Eighth International Symposium on

Space Terahertz Technology

March 25 - 27, 1997

Science Center
Harvard University
Cambridge, Massachusetts, USA

JPL

PROCEEDINGS

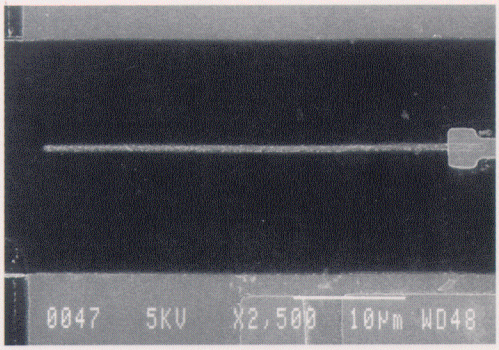

Distibuted SIS Mixer

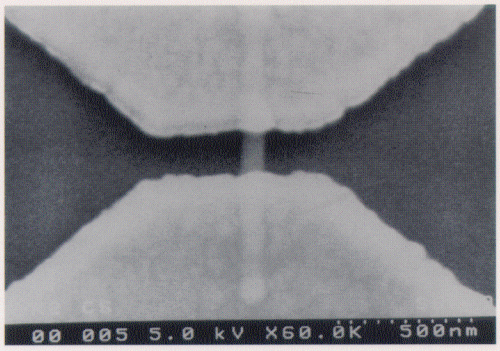

Hot Electron Bolometer Mixer

Sponsored by : JPL Center for Space Microelectronics Technology and Harvard University

Organized by : Harvard-Smithsonian Center for Astrophysics

PROCEEDINGS

of the

EIGHTH INTERNATIONAL SYMPOSIUM ON

SPACE TERAHERTZ TECHNOLOGY

Tuesday - Thursday March 25 - 27, 1997

Science Center
Harvard University
Cambridge, Massachusetts

Sponsored by: JPL Center for Space Microelectronics Technology and Harvard University

Organized by: Harvard-Smithsonian Center for Astrophysics

Organizing Committee

Raymond Blundell, Harvard-Smithsonian Center for Astrophysics
Edward Tong, Harvard-Smithsonian Center for Astrophysics

PREFACE

The Eighth International Symposium of Space Terahertz Technology was held at the Harvard University Science Center in Cambridge, Massachusetts, on March 25-27, 1997. The Symposium was attended by more than 140 scientists and engineers from all over the world. The theme of the Symposium centered on the detection, generation, and manipulation of radiation in the terahertz spectral region for both space- and ground-based applications including astronomy and remote sensing of the Earth's atmosphere. The program included twelve sessions covering a wide variety of topics including: Schottky, SIS, and hot electron bolometer mixers; local oscillator sources, either fundamental, varactor frequency multiplied or generated from heterodyne downconversion; and various new developments in optics, antennas, and waveguide devices. In addition, there were invited presentations that outlined the recent progress and future opportunities in ground-based, airborne, and spaceborne observatories for submillimeter astronomy.

The Symposium was sponsored by the NASA Office of the Center for Space Microelectronics Technology, Jet Propulsion Laboratory and was organized by the Harvard-Smithsonian Center for Astrophysics. We would like to thank all of the participants of the Eighth International Symposium of Space Terahertz Technology, in particular the session chairs whose work helped to make the event a success. We would also like to thank Harvard University for the use of the meeting facilities.

The Ninth International Symposium on Space Terahertz Technology will be held in Pasadena, CA, and will be hosted by the Center for Space Microelectronics Technology, Jet Propulsion Laboratory, on March 17-19, 1998.

Edward Tong
Raymond Blundell

For more information on the next Symposium please contact:

Dr. William R. McGrath
Jet Propulsion Laboratory
MS 168-314
4800 Oak Grove Drive
Pasadena, CA 91101

Telephone: 818-354-8542
FAX: 818-393-4683
Email: rob@rob-mac.jpl.nasa.gov

The SEM photographs on the front cover, showing a 150 nm wide distributed SIS device and a 80 x 80 nm niobium HEB device, are supplied by Bruce Bumble (JPL Center for Space Microelectronics Technology).

EIGHTH INTERNATIONAL SYMPOSIUM ON SPACE TERAHERTZ TECHNOLOGY

Tuesday - Thursday, March 25-27, 1997

Science Center
Harvard University
Cambridge, Massachusetts

Sponsored by: JPL Center for Space Microelectronics Technology and Harvard University

Organized by: Harvard-Smithsonian Center for Astrophysics

DAY 1: TUESDAY, MARCH 25

Opening Session		**Chair:**	**Raymond Blundell**
Opening Remarks	Carl Kukkonen	JPL	8
Submillimeter Astronomy - The Next Steps	K. Menten	MPIfR	

Session 1: HEB 1		**Chair:**	**Anthony Kerr**
Phonon-Cooled NbN HEB Mixers for Submillimeter Wavelengths	J. Kawamura, R. Blundell, C-Y.E. Tong, G. Gol'tsman, E. Gershenzon, B. Voronov S. Cherendichenko	SAO MSPU	23
Phonon-Cooled Ultra Thin NbN Hot Electron Bolometer Mixers at 620 GHz	H. Ekström, E. Kollberg, P. Yagubov, G. Gol'tsman, E. Gershenzon, S. Yngvesson	CTH MSPU U.Mass.	29
Superconducting Transition and Heterodyne Performance at 730 GHz of a Diffusion-Cooled Nb Hot-Electron Bolometer Mixer	J.R. Gao, M.E. Glastra, R.H. Heeres, W. Hulshoff, D.W. Floet, H. van de Stadt, T.M. Klapwijk, Th. de Graauw	U.Groningen SRON	36
Noise and RF Bandwidth Measurements of a 1.2 THz HEB Heterodyne Receiver	A. Skalare, W.R. McGrath, B. Bumble, H.G. LeDuc	JPL	47
A Low-Noise Superconductive Nb Hot-Electron Mixer at 2.5 THz	B.S. Karasik, M.C. Gaidis, W.R. McGrath, B. Bumble, H.G. LeDuc	JPL	55
Conversion Loss of a Resistive State Superconducting Mixer	O. Vendik, E. Kollberg	Etech.U. CTH	67

DAY 2: WEDNESDAY, MARCH 26

Session 4: Semiconductors		**Chair: Neal Erickson**	
Accurate Circuit and Device Equations for Designing 50-600 GHz GaAs Schottky Diode Varactor Frequency Doublers	R.E. Lipsey, S.H. Jones, T.W. Crowe	U.Va.	166
Fabrication and Optimisation of Planar Schottky Diodes	A. Simon, C.I. Lin, H.L. Hartnagel, P. Zimmermann, R. Zimmermann	Inst.Hochfreq. Rad.Physics	179
Advances in Submillimeter Wave Semiconductor-Based Device Designs and Processes at JPL	R.P. Smith, S.C. Martin, M. Kim, J. Bruston, D. Humphrey, N. Erickson, P.H. Seigel	JPL FCRAO	184
Fixed-Tuned Submillimeter Waveguide Multipliers Using MMIC Technology	J. Bruston, R.P. Smith, S.C. Martin, A. Pease, M. Kim, P.H. Seigel	JPL	198
Planar GaAs Schottky Barrier Diodes	S.M. Marazita, W.L. Bishop, T.M. Cunningham, P.J. Koh, T.W. Crowe, R.M. Weikle, II	U.Va.	208
Substrateless Schottky Diodes for THz Applications	C.I. Lin, A. Simon, M. Rodriguez-Gironés, H.L. Hartnagel, P. Zimmermann, R. Zimmermann	Inst.Hochfreq. Rad.Physics	224

Session 5: HEB II		**Chair: Rob McGrath**	
Fabrication of High-Tc Hot-Electron Bolometric Mixers for Submillimeter Heterodyne Applications	M.J. Burns, A.W. Kleinsasser, B. Karasik, M. Gaidis, W.R. McGrath	JPL	230
Large Bandwidth of NbN Phonon-Cooled Hot-Electron Bolometer Mixers on Sapphire Substrates	S. Cherednichenko, P. Yagoubov, K. Il'in, G. Gol'tsman, E. Gershenzon	MSPU	245
NbN Hot Electron Bolometric Mixer for 2.5 THz: The Phonon Cooled Version	E. Gerecht, C.F. Musante, Z. Wang, K.S. Yngvesson, J. Waldman, G.N. Golts'man, P.A. Yagoubov, S.I. Svechnikov, B.M. Voronov, S.I. Cherednichenko, E.M. Gershenzon	U.Mass. MSPU	258
Noise-Bandwidth of Diffusion Cooled Hot-Electron Bolometers	P.J. Burke, R.J. Schoelkopf, D.E. Prober, A. Skalare, W.R. McGrath, B. Karasik, M. Gaidis, B. Bumble, H.G. LeDuc	Yale JPL	272

DAY 3: THURSDAY, MARCH 27

Session 8: SOURCES II		**Chair: Jacob Kooi**	
The Complete Analysis of a 91.33 to 274 GHz Schottky Barrier Varactor Frequency Tripler	R.E. Lipsey, C. Mann, S.H. Jones, J. Thornton	U.Va. Rutherford Lab	385
Power and Spatial Mode Measurements of a Sideband Generator Submillimeter-Wave Source	E.R. Mueller, J. Waldman, W.E. Nixon	DeMaria U.Mass. USA NGIC	404
Terahertz Emission from *p*-Type Germanium Lasers Doped with Novel Acceptors	O.D. Dubon, D.R. Chamberlin, W.L. Hansen, E.E. Haller, L.A. Reichertz, G. Sirmain, E. Bründermann, A.M. Linhart, H.P. Röser	UCB DLR ISST	423
Tunable THz-laser for applications in FIR Astronomy	E. Bründermann, A.M. Linhart, L.A. Reichertz, G. Sirmain, H.P. Röser, O.D. Dubon, D.R. Chamberlin, W. L. Hansen, E.E. Haller	DLR ISST UCB	430
Investigations of High-Resistivity, Undoped GaP Crystal for Quasi-Phasematched Difference Frequency Generation to Produce Terahertz Frequency Local Oscillators	G. Herman, S. Sandford	SAIC NASA	436

Session 9: Optics		**Chair: Scott Paine**	
Investigation of Surface Profiles of a Reflector from Near-field Beam Measurements	M.T. Chen, C.-Y.E. Tong	ASIAA SAO	437
Modal Analysis of Partially-Coherent Submillimetre-Wave Quasioptical Systems	S. Withington, J.A. Murphy	U.Cambridge St. Patrick's	446
Gaussian Beam Mode Analysis of Imaging Arrays	J.A. Murphy, S. Withington	St. Patrick's U.Cambridge	466
LO Beam Array Generation at 480 GHz by Use of Phase Gratings	T. Klein, G.A. Ediss, R. Güsten, H. Hauschildt, C. Kasemann	MPIfR	482
Hologram CATR for Millimeter and Submillimeter-Wavelengths: A Progress Report	T. Hirvonen, P. Piironen, J. Ala-Laurinaho, A. Lehto, A.V. Räisänen	HUT	490

Welcome and Introduction

Presentation to

Eighth International Symposium on Space Terahertz Technology

Carl Kukkonen
Director, Center for Space Microelectronics Technology

JPL

March 24-27, 1997

Submillimeter Heterodyne Sensor

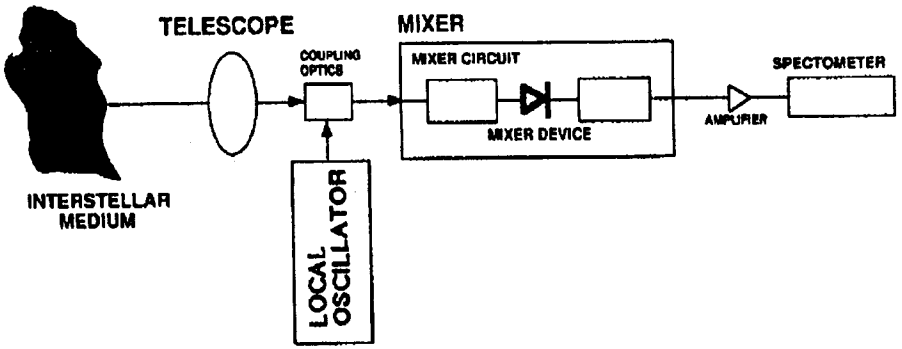

Why Submillimeter Technology

Addresses fundamental questions of astrophysics

- Birth and death of stars
- Galactic evolution

Required data

- Composition (H_2O, O_2,O, C) mass, density, temperature and velocity of material in interstellar medium

Challenge

Demonstrate 1.2 THz Key Component Technology

- Mixer
- Local Oscillator

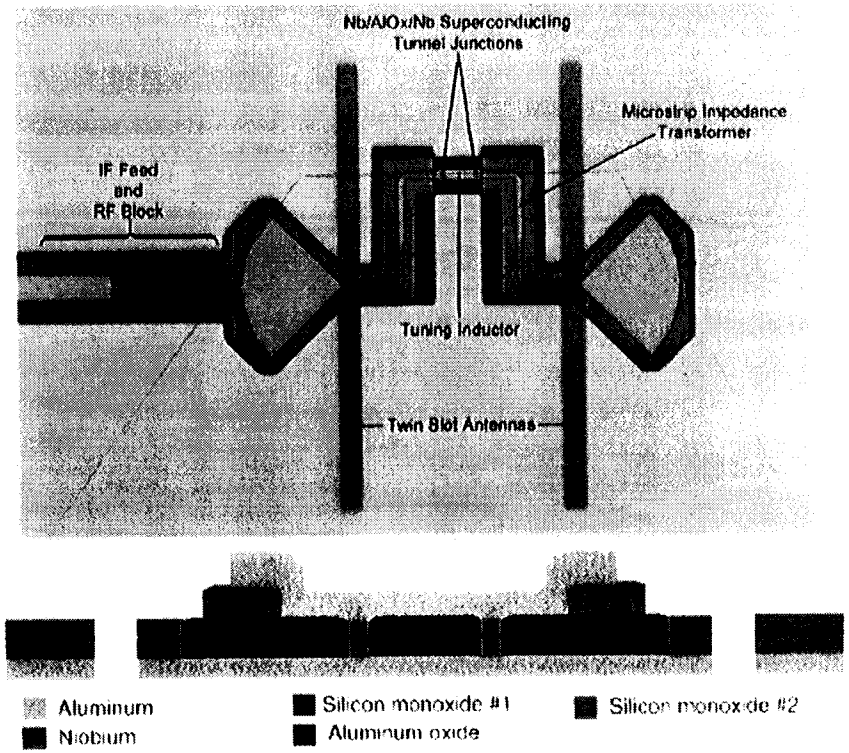

Terahertz Astrophysics Observing Platforms

- **Submillimeter Wave Astronomy Satellite (SWAS)**
  - Small Explorer Mission
  - Heterodyne receivers near 480 and 560 GHz
  - Observe interstellar water, oxygen, and carbon
  - Launch date 1998

- **Far Infrared Submillimeter Telescope (FIRST) - ESA Mission**

  <u>Baseline Capabilities</u>
  - Passively cooled 3 m telescope 250-600 GHz SIS mixer
  - High resolution spectroscopy 85-300 μm, photoconductor and bolometer arrays
  - Broad band photometry 85-900 μm bolometer arrays

  <u>Potential NASA Contributions</u>
  - Orbit: Increase observing time and sensitivity
  - 4 m telescope
  - Enhanced detectors: SIS to 1.2 THz; HEB Channel (1.9-2.7 THz)
  - Vibrationless sorption cooler system

Terahertz Astrophysics Observing Platforms

- The Stratospheric Observatory for Infrared Astronomy (SOFIA)
  - 2.5 m aperture airborne telescope for wavelengths between 1 mm and 10 microns
  - Funded by NASA
  - Successor to the Kuiper Airborne Observatory
  - First flights in 2000-2001
- Antarctic Submillimeter Telescope and Remote Observatory (AST/RO)
  - South Pole Observatory operational this year funded by NSF
  - 1.7 m aperture for 0.5 mm wavelengths
  - Built, running and taking data
- Heinrich Hertz / SubMillimeter Telescope Observatory (HHT/ SMTO)
  - Located on Emerald Peak of Mt. Graham, approximately 75 miles north-east of Tucson, Arizona
  - 10 m aperture for wavelengths between 1.3 mm and 350 microns
  - Joint University of Arizona / Max-Planck Institut fur Radioastronomie project
  - Operational and taking data

Terahertz Astrophysics Observing Platforms

- NRAO - Millimeter Array in Chile
  - 40 Telescopes
  - 8 m diameter
  - Construction start 1998
  - Operational 2005
  - Frequency: 200 -850 GHz
- South Pole 10 m Telescope
  - Operational 2003
  - AST/RO - NSF Funded Program
  - Frequency SIS & Bolometers up to 1.5 THz

Terahertz Astrophysics Observing Platforms

- **Microwave Instrument for the Rosetta Orbiter (MIRO)**
  - **Approved for the Rosetta Orbiter - Launch 2003**
  - **Two channel continuum and spectroscopic heterodyne receiver system**
    - **Submillimeter Wave Receiver - Frequency: 540 GHz**
    - **Millimeter Wave Receiver**
- **Submillimeter Array (SMA)**
  - **Harvard Smithsonian Center for Astrophysics**
  - **6 telescopes upgraded to 9**
  - **6 m diameter**
  - **On Mauna Kea, Hawaii**
  - **Operational 2000**
  - **Operational under (200 - 800 GHz)**

Terahertz Astrophysics Observing Platforms

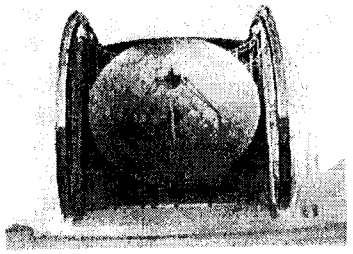

- Caltech Submillimeter Observatory
  - A cutting-edge facility for astronomical research and instrumentation development
  - Located on "submillimeter ridge" near the summit of Mauna Kea, Hawaii
  - 10 m Telescope
  - Frequencies: 200 - 800 GHz

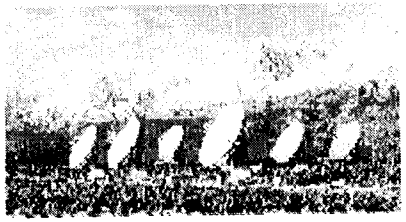

- Owens Valley Radio Observatory
  - Largest university-operated radio observatory in the world
  - Located five hours north of Pasadena, near the Sierra Nevada range
  - Six 10m telescopes
    - Frequency ranges 80-116 GHz and 210-270 GHz
  - 40m Telescope
  - 5m Telescope
  - Two 27m Telescopes

Status of NASA Submillimeter Sensors Astrophysics Program

- Superconducting Mixers
  - Nb SIS Mixers meet needs of FIRST for frequencies up to 1 THz
  - Challenge is to improve performance to 1200 GHz
    - Approach
      - Nb or NbTiN SIS mixers
      - Hot Electron Bolometers
  - Above 1 THz Hot Electron Bolometer
    - Diffusion Cooled (Nb)
    - Phonon Cooled (NbN)
- Solid State Local Oscillator Sources
  - Multiplier chains meet power requirements of FIRST for frequencies up to about 1.2 THz
  - Challenge is to provide
    - Wide bandwidth with fixed tuning
    - Reliability
  - Higher Power and Stable Photomixer L.O. (1-3 THz)

Eighth International Symposium on Space Terahertz Technology, Harvard University, March 1997

NASA Terahertz Space Missions for Earth Observations

- **Earth Observing Satellite Microwave Limb Sounder**
  - **Study of chemistry of stratospheric ozone on a global scale**
  - **118 GHz**
    - **Temperature and Pressure**
  - **190 GHz**
    - **Continuity with UARS MLS for O_3, ClO, and H_2O**
  - **240 GHz**
    - **O_3, CO - Temperature and Pressure**
  - **640 GHz**
    - **Ozone chemistry (O_3, HCl, ClO, NO_2 and others)**
  - **2.5 THz**
    - **Ozone chemistry (OH), Temperature and Pressure**

- **Approved mission, instrument engineering model build in 1997**
- **Launch date 2002**

Mission to Planet Earth
Technology Insertion

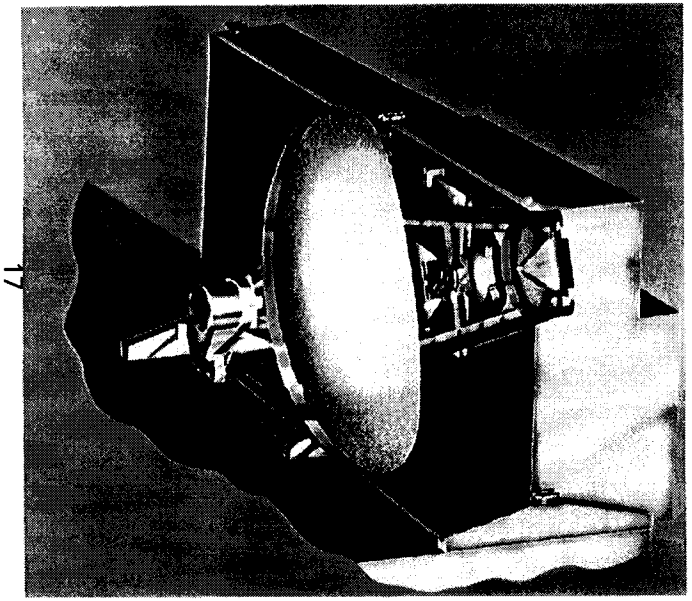

Microwave Limb Sounder

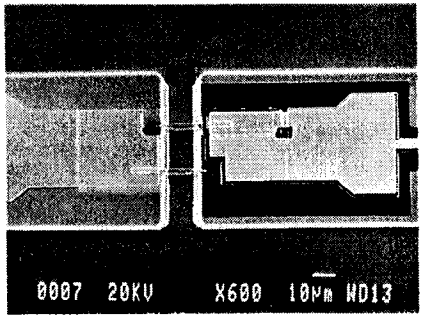

JPL 640 GHz QUID (Quartz upside-down integrated Device) Diode Pair

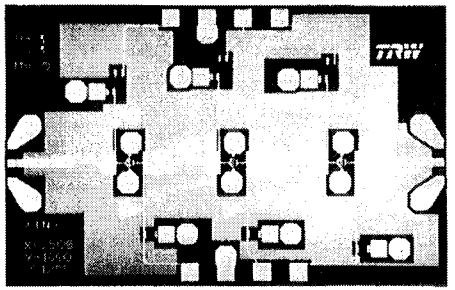

TRW 160 GHz InP MMIC LNA Chip (3 stage)

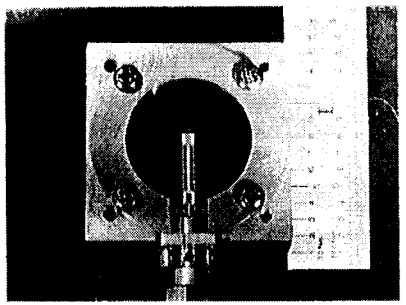

JPL MMIC Mixer Prototype for 2.5 THz

MMIC Development for IMAS

IMAS: Integrated Multispectral Atmospheric Sounder to Measure Temperature and Pressure of the Atmosphere with MMIC Radiometer at 54, 118 and 183 GHz

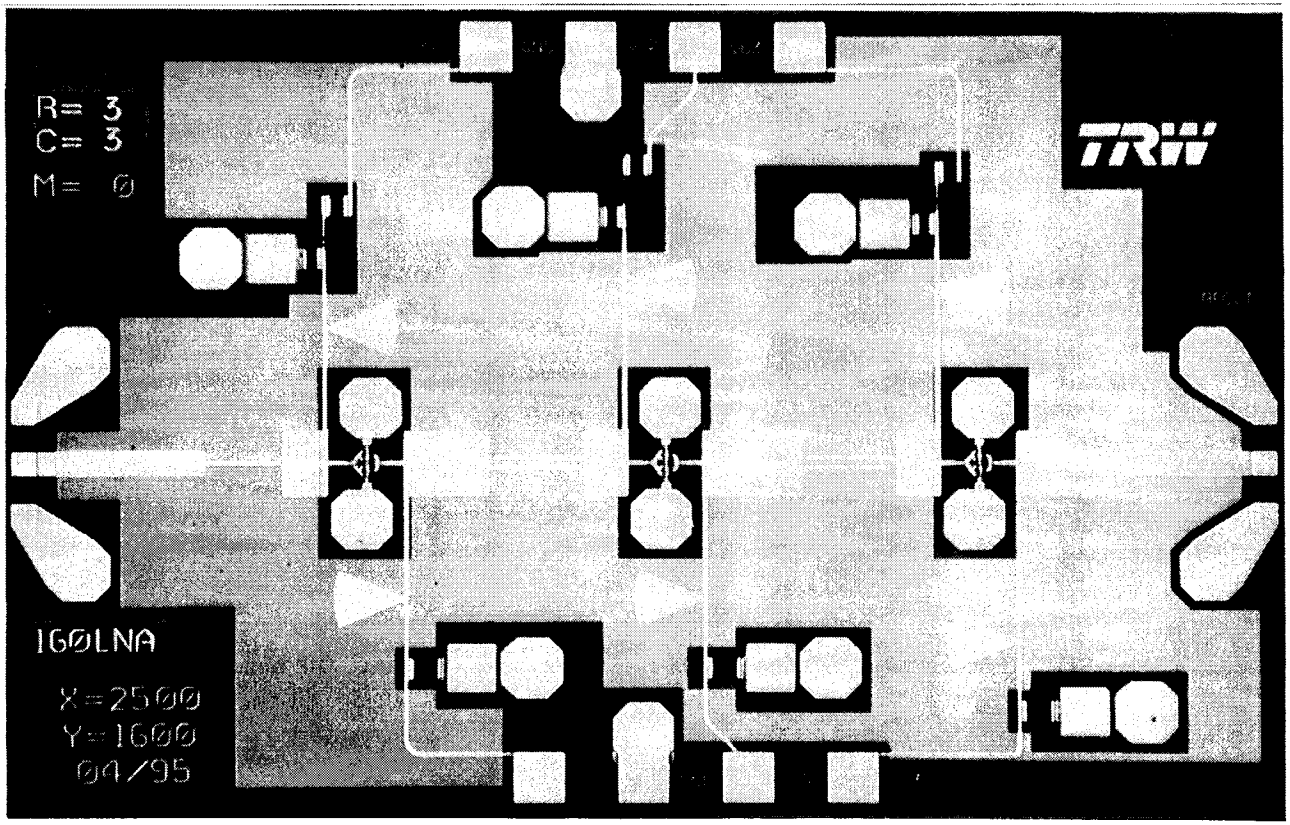

TRW 160 GHz InP MMIC LNA Chip (3 stage)

Measured gain: 8 dB at 155 GHz (including waveguide-to-chip input and output transition and input horn)!

Measured noise figure: 6.4dB (965K) at 155 GHz !

- World's highest frequency LNA with measurable gain
- World's first noise measurement on a MMIC amplifier above 140 GHz
- World's lowest noise room temperature amplifier above 120 GHz

H. Wang (TRW), P.H. Siegel, T. Gaier, R.J. Dengler (JPL)

Eighth International Symposium on Space Terahertz Technology, Harvard University, March 1997

Mission to Planet Earth
Technology Insertion

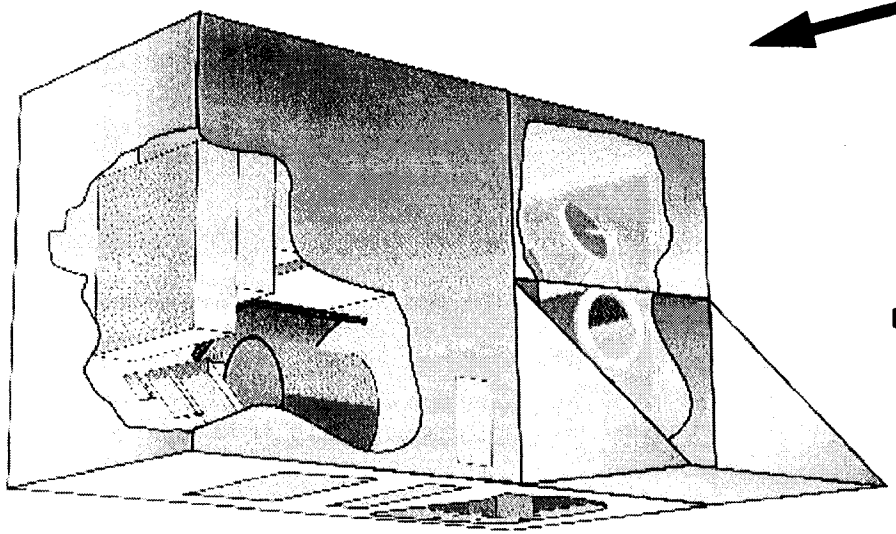

Integrated Multi-Spectral
Atmospheric Sounder

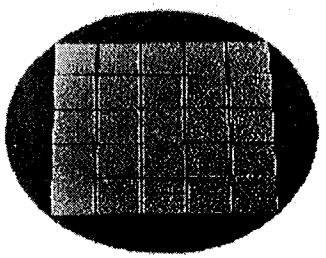

Twenty Five 256 x 256 QWIP Focal PlaneArrays (FPAs) on 3 inch GaAs Wafer

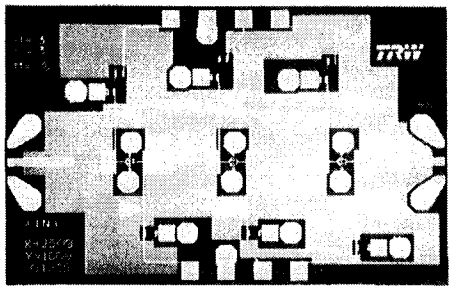

TRW 160 GHz InP MMIC LNA Chip (3 stage)

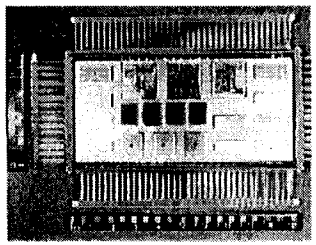

Advanced Flight Computer: 33-chip Module

Kukkonen Challenge 1993

- First SIS mixer with
  - Frequency > 1 THz
  - T_{sys} < 1000 K DSB

Awarded 1995

- First Solid State Local Oscillator Source
  - Frequency > 1 THz
  - Output power > 100 microwatts

  (100 GHz Bandwidth) Unclaimed

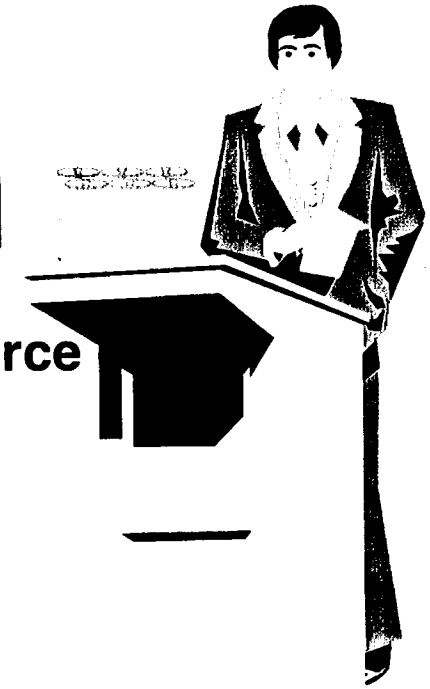

Kukkonen Terahertz Prize

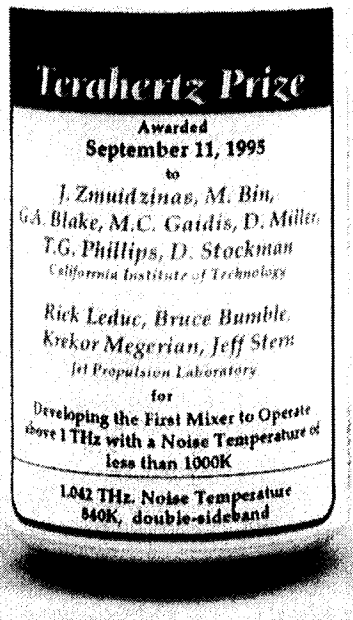

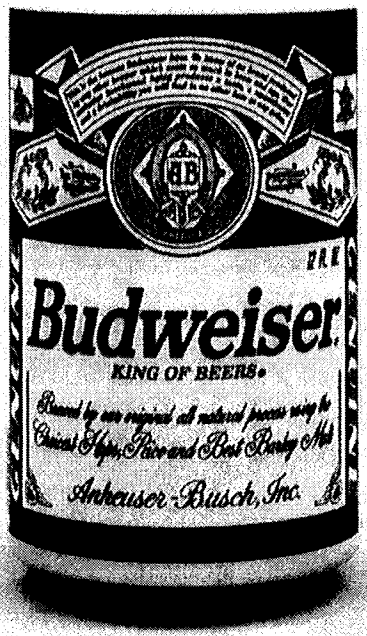

1997 Kukkonen Challenge

Local Oscillator

Frequency: 1-3 THz (500 GHz Tunability)

Power: 10-50 μwatts

Phonon-cooled NbN HEB Mixers for Submillimeter Wavelengths

J. Kawamura, R. Blundell, C.-Y. E. Tong
Harvard-Smithsonian Center for Astrophysics
60 Garden St.
Cambridge, Massachusetts 02138

G. Gol'tsman, E. Gershenzon, B. Voronov, S. Cherendichenko
Moscow State Pedagogical University
Moscow, 119435, Russia

Abstract

The noise performance of receivers incorporating NbN phonon-cooled superconducting hot-electron bolometric mixers is measured from 200 GHz to 900 GHz. The mixer elements are thin-film (thickness ~ 4 nm) NbN with ~5 to 40 μm^2 area fabricated on crystalline quartz substrates. The receiver noise temperature from 200 GHz to 900 GHz demonstrates no unexpected degradation with increasing frequency, being roughly $T_{RX} \approx 1$–2 K GHz^{-1}. The best receiver noise temperatures are 410 K (DSB) at 430 GHz, 483 K at 636 GHz, and 1150 K at 800 GHz.

Introduction

Superconducting hot-electron bolometric mixers are emerging as the alternative technology to SIS mixers for heterodyne detection above 1 THz. This technology promises good sensitivity (T_{RX} < 1 K GHz^{-1}), low local-oscillator power requirement (< 1 μW), and a large useable IF bandwidth (several GHz). This type of mixer should have good performance up to infrared wavelengths. It also utilizes the same components as those used in an SIS-based receiver system (except a magnetic field is not needed), making the technological transition convenient and straightforward.

The goal of our present series of experiments is to study the performance of the phonon-cooled NbN hot-electron mixer [1, 2] at frequencies where we have a good understanding of the measurement techniques, and where we can also make direct comparisons to the performance of SIS mixers. In our experiments near 200 GHz [3], we demonstrated the operation of the superconducting HEB mixer in a practical receiver, measuring its linearity, stability and saturation level, and also detecting molecular line emission from a laboratory gascell. The sensitivity of the receiver was T_{RX} = 750 K (DSB) at 244 GHz, with 1.5 GHz IF and 500 MHz bandwidth. While this sensitivity is not competitive with that of SIS receivers operating in the same frequency band, similar noise performance should in principle be possible at frequencies beyond 1 THz, unlike for current SIS mixers made from niobium.

Following this successful proof-of-principle experiment, which proved that the superconducting HEB mixer is a properly behaving heterodyne detector, we built and tested a receiver operating at 400 GHz [4]. The block and mixer are nearly scaled versions of those operating at 200 GHz. Measurements at these frequencies yielded good receiver

noise performance, typically better than 2 K GHz^{-1}, and at some frequencies better than 1 K GHz^{-1}. The best receiver noise temperature in this frequency band is 410 K at an LO frequency of 430 GHz. We attribute the improvement in the noise performance to better quality NbN film [5]. In this paper we report measurements made at higher frequencies, in the 600 GHz and 900 GHz bands.

Mixer and Receiver

The mixer element is an electron-phonon cooled [lattice-cooled] HEB mixer. The mixer element is formed from reactive magnetron sputtering of NbN on *z*-cut crystalline quartz [5]. The substrate material is chosen because the waveguide block is designed for its dielectric constant, and is chosen over fused quartz because of its superior thermal conductance. The film is etched to form a bridge with 5 μm^2 to 40 μm^2 area across two overlaid TiAu electrodes which couple the mixer to the waveguide. Because the length and width are not critical dimensions in the operation of the mixer, a mixer with a range of impedance can easily be fabricated. Additionally, by adjusting these dimensions the local-oscillator power requirement can be varied as its value depends on the volume of the mixer.

For our mixers the typical film thickness is 40 Å, and the bridge is 5–20 μm wide and 2 μm long. The room temperature resistance is ~ 1500 Ω / . The film has $T_c \sim 8$ K, $\Delta T_c \sim 1$ K, and j_c ($T = 4.2$ K) ~ 1×10^6 A cm^{-2}. The mixer has an IF bandwidth of about 2 GHz, which is sufficient for our present measurements. Further increase in IF bandwidth is possible by reducing the film thickness or by improving the quality of the film [5]. Changing the substrate to one on which better film can be grown is possible, but would obviously entail a different design for the mixer. The (absorbed) local-oscillator power is ~ 1 μW.

freq. band [GHz]	waveguide dimension [a × b mm]	substrate size [t × w × l mm]
200	1.1 × 0.28	0.13 × 0.51× 7.5
400	0.51 × 0.12	0.058 × 0.28 × 6.3
600	0.37 × 0.091	0.041 × 0.16 × 2.0
900	0.25 × 0.066	0.030 × 0.13 × 2.0

Table 1. Waveguide and substrate dimensions

The receivers operating at 600 GHz and 900 GHz are scaled versions of those operating at 200 GHz [3] and 400 GHz [4]. Further details of the mixer design can be found in [6]. The dimensions of the waveguide mixer are summarized in Table 1. The mixer is suspended across a waveguide, and the mixer block has a mechanically driven backshort. The mixer is operated at $T_{physical} \geq 4.2$ K. The waveguide is coupled to the input beam with a corrugated feed, which illuminates an off-axis paraboloid. The beam passes through several layers of porous Teflon IR filters at 4.2 K and 80 K, and through a 0.5 mm Teflon window, which seals the cryostat. A Martin-Puplett diplexer employing free-standing wire-grids is used to ensure adequate LO coupling.

The local-oscillator power is supplied by a multiplied solid state source, except those measurements made above 820 GHz. For those measurements a backward-wave oscillator is used.

Measurements

The receiver sensitivity is measured using the *Y*-factor method of alternately placing a hot load at 295 K and a cold load at 77 K at the input of the receiver. Previous measurements [3] have shown that the mixers used in our study do not suffer from direct detection saturation effects due to the broad band response to the input radiation. Furthermore, all the receiver noise temperatures reported are *not* corrected to account for losses. The sensitivity refers to the double-sideband receiver noise temperature. Except for the measurements near 200 GHz, the IF output power is detected after a 200 MHz wide filter centered at 1.4 GHz.

The current-voltage (*I-V*) curves of 600 GHz and 900 GHz mixers are shown in Figure 1, with the insets showing the IF power output as a function of DC voltage bias in response to hot and cold loads placed at the input of the receiver. These *I-V* characteristics are similar to those of mixers giving the best noise performance at the lower frequency bands, although it is not possible definitively to predict which mixer will give good RF noise performance by mere inspection of its *I-V* curve. In our experiments, we pre-select mixers with high T_c, high j_c, low resistance, and a large ratio of the critical current to current measured in the resistive region, which is usually fairly constant over a broad bias range. About 6 mixers were tested at both 600 GHz and 900 GHz, and the noise performance of all the mixers was typically better than 3 K GHz^{-1}.

LO frequency [GHz]	DSB L_c [dB]	T_{mix} [K]	T_{RX} (DSB) [K]
244	~ −18	~ 500	750
430	−10.5	370	410
636	−13	400	483
800	−16	990	1150

Table 2. Best noise performance in each frequency band, with estimates of the conversion loss and mixer noise temperature.

Table 2 summarizes the performance of the mixers that gave the best noise performance in each frequency band. In the same Table, estimates of the DSB conversion loss and mixer noise temperature are also stated. The sensitivity of the receivers is plotted as a function of LO frequency in Figure 2. The frequency of each point is verified by measuring it with the Martin-Puplett interferometer.

Conclusion

We have used the electron-phonon cooled version of the superconducting hot-electron bolometric mixer in a waveguide receiver, and performed noise temperature measurements from 200 GHz to 900 GHz. The best receiver noise temperatures are better than 1 K GHz^{-1}. Further improvements in the noise temperature should be possible when the mixer

design is optimized, specifically when the RF and IF mixer impedance are better matched to their respective circuits.

References

[1] E. M. Gershenzon, G. N. Gol'tsman, I. G. Gogidze, Y. P. Gousev, A. I. Elantev, B. S. Karasik, and A. D. Semenov, Sov. Phys. Superconductivity **3**, 1583 (1990).

[2] Y. P. Gousev, G. N. Gol'tsman, A. D. Semenov, E. M. Gershenzon, R. S. Nebois, M. A. Heusinger, and K. F. Renk, J. Appl. Phys. **75**, 3695 (1994)

[3] J. Kawamura, R. Blundell, C.-Y. E. Tong, G. Gol'tsman, E. Gershenzon, and B. Voronov, J. Appl. Phys. **80**, 4232 (1996)

[4] J. Kawamura, R. Blundell, C.-Y. E. Tong, G. Gol'tsman, E. Gershenzon, B. Voronov, and S. Cherednichenko, Appl. Phys. Lett. **70**, 1619 (1997)

[5] P. Yagoubov, G. Gol'tsman, B. Voronov, L. Seidman, V. Siomash, S. Cherednichenko, and E. Gershenzon, Proc. 7th Int. Symp. Space Terahertz Tech., Charlottesville, Virginia, 1996, pp. 290–302; S. Cherednichenko, P. Yagoubov, K. Il'in, G. Gol'tsman, and E. Gershenzon, This conference proceedings, 1997.

[6] R. Blundell, C.-Y. E. Tong, D. C. Papa, R. L. Leombruno, X. Zhang, S. Paine, J. A. Stern, H. G. LeDuc, and B. Bumble, IEEE Trans. Microwave Theory Tech. **43**, 933 (1995)

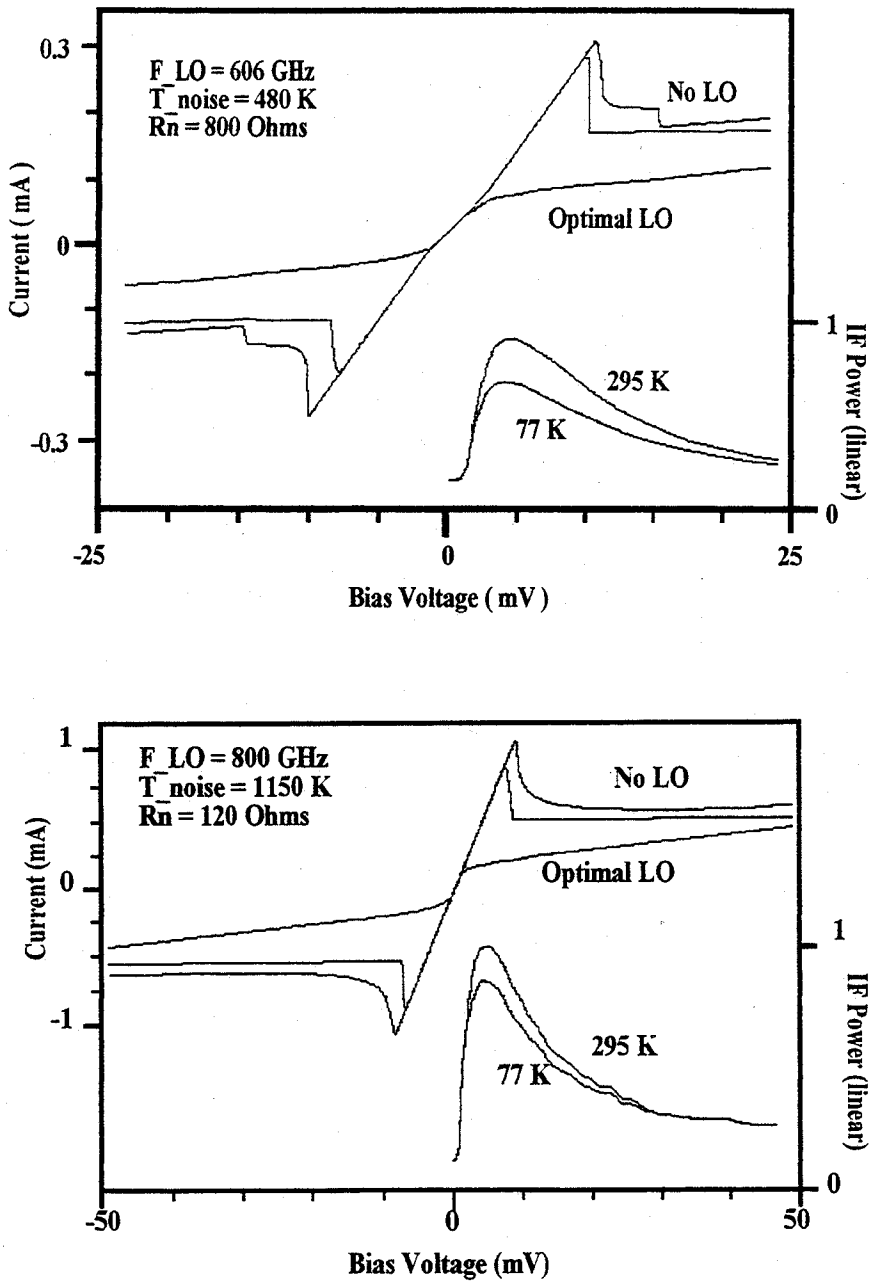

Figure 1. I-V curves of mixers operating at 600 GHz (top) and 800 GHz (bottom). The lower right hand corner in each figure shows the IF power as a function of DC voltage bias in response to hot and cold loads placed at the receiver input.

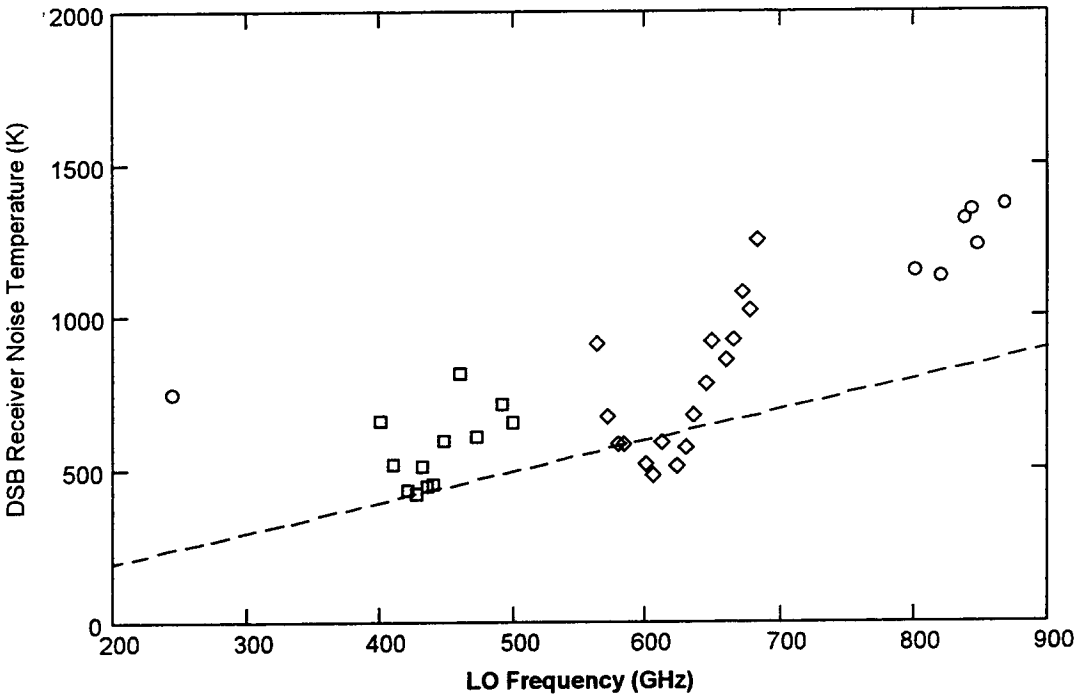

Figure 2. Performance of the best mixer in each frequency band. The dashed line indicates 1 K GHz^{-1}.

Phonon cooled ultra thin NbN hot electron bolometer mixers at 620 GHz

H. Ekström, E. Kollberg

Chalmers University of Technology, Gothenburg Sweden

P. Yagoubov, G. Gol'tsman, E. Gershenzon

Moscow State Pedagogical University, Moscow, Russia

S. Yngvesson

University of Massachusetts, Amherst, MA, USA

ABSTRACT

We have measured the noise performance and gain bandwidth of 35 Å thin NbN hot-electron mixers integrated with spiral antennas on silicon substrate lenses at 620 GHz. A double-sideband receiver noise temperature less than 1300 K has been obtained with a 3 dB bandwidth of ≈5 GHz. The gain bandwidth is 3.2 GHz. A lower noise temperature of 1100 K has been achieved with an improved set-up. The mixer output noise dominated by thermal fluctuations is about 50-60 K, and the SSB receiver and intrinsic conversion gain is about -18 and -12 dB, respectively. Without mismatch losses and excluding the loss from the beamsplitter, we expect to achieve a receiver noise temperature of less than 700 K.

INTRODUCTION

The superconducting hot-electron bolometer (HEB) mixer has proved to be a strong competitor to mixers based on traditional superconducting tunnelling devices or Schottky diodes for frequencies above 1 THz. The mixing mechanism in a HEB depends on the non-linearity of electron heating and the temperature dependent resistance near T_c [1]. The HEB is consequently not limited by parasitic reactances or by the superconducting energy gap as SIS devices, and is therefore expected to have a good performance up to tens of THz. Schottky mixers which also work in the terahertz region are noisier and require orders of magnitude more LO power.

A disadvantage of bolometric mixers is a very narrow IF bandwidth mainly determined by the electron energy relaxation time. The semiconductor InSb and first Nb HEB had a bandwidth of about 1 MHz and 100 MHz, respectively [2, 3]. In both types the electron energy relaxed through interaction with phonons. A larger bandwidth has been obtained in devices of NbN which have shorter electron-phonon relaxation time. Another limitation to the relaxation time is the phonon escape time from film to substrate, determined both by the thermal resistance in the film substrate

interface and the film thickness. Thus for ultra thin 35 Å NbN devices an IF bandwidth larger than 3 GHz has been measured at 4.2 K [4], enough for most practical applications.

Another approach for increasing the IF bandwidth is to make the device very short. If the device length $L < \sqrt{12 D \tau_{e-ph}}$ (D is the diffusion constant and $\tau_{e\text{-}ph}$ is the inelastic electron phonon interaction time), the out-diffusion of hot electrons into the normal leads dominates over electron-phonon interaction as the main cooling mechanism [5-10].

An important property of the HEB is that the output noise should be dominated by thermal fluctuation noise which has the same frequency dependence as the IF signal [1, 11-13]. Thus the receiver noise bandwidth will be larger than the gain bandwidth. Here we present measurements of DSB receiver noise bandwidth and gain bandwidth for an ultra thin phonon cooled NbN HEB mixer operating in a 620 GHz quasi optical receiver.

MEASUREMENT SET-UP

The measurements were performed with HEB devices made from ≈35 Å thick NbN films with $T_c \approx 10$ K sputtered on silicon substrates by reactive magnetron sputtering in an argon-nitrogen gas mixture [4]. The film is patterned to form a 1 μm long and 13 μm wide bolometer strip across the centre gap of a Ti-Au spiral antenna, which has a frequency range from 300 to 1250 GHz with an impedance of 75 Ω. The substrate on which the device and antenna are integrated, is glued to an anti-reflection coated extended hyper hemispherical silicon lens with a diameter of 12.5 mm.

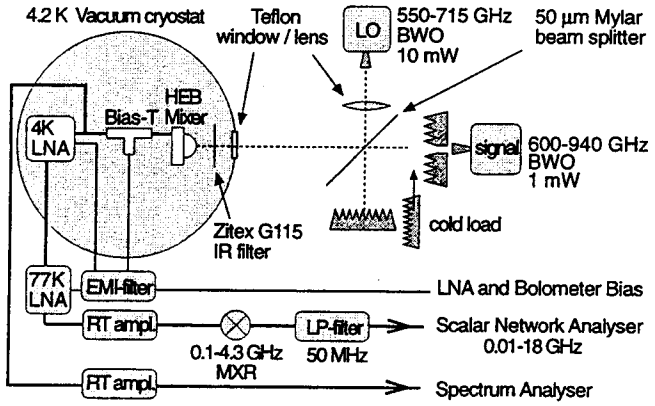

Fig. 1 Measurement set-up

Table 1. RF losses

element	loss [dB]
50μm beam-splitter	0.8
1 mm Teflon window	0.4
Zitex G115 IR filter	0.1
silicon lens	1.8
RF mismatch loss antenna-bolometer	< 2.4
total RF loss	< 5.5

The mixer is mounted in a LHe-cooled vacuum cryostat equipped with a 1 mm thick Teflon window and a 380 μm Zitex G115 IR radiation filter. We use two backward wave oscillators (BWO) as signal and local oscillator (LO) sources with a common frequency range 600- 715 GHz, Fig. 1 for IF bandwidth measurements. The radiation from the LO is focused by a Teflon lens and combined with the signal by a 50 μm thick Mylar beam-splitter. The optical losses are estimated to be about 3 dB, Table 1.

For DC bias and IF signal output the device is attached to a coplanar 50 Ω line soldered to a SMA connector, and connected to a bias-T. Data for the amplifiers used for noise measurements at different IF frequencies are shown in Table 2. Following the last amplifier is a second mixer and a 50 MHz low pass filter at the input of a scalar network analyser. For gain bandwidth measurements the IF signal from the HEB is directly fed to a spectrum analyser, amplified by a 0.01-20 GHz room temperature amplifier.

Table 2

IF freq. [GHz]		0.7	1.5	3.9
LHe LNA	(GHz)	0.68-0.92 [1)]	1.3-1.8 [4)]	3.6-4.2 [5)]
		4 K/17 dB	5 K/33 dB	12 K/33 dB
LN_2 LNA	(GHz)	0.1-2.5 [2)]	–	–
		20 K/40 dB	–	–
RT ampl.		120 K/30 dB [3)]	120 K/30 dB [3)]	150 K/30 dB [5)]
RT ampl.		–	150 K/32 dB [6)]	500 K/20 dB [7)]

[1] NRAO
[2] Miteq
[3] Miteq
[4] Russian
[5] Russian
[6] Russian AGASTA
[7] Avantek

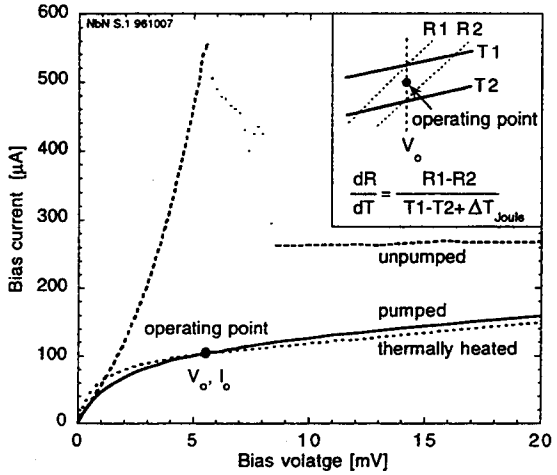

Fig. 2. IV characteristics. Inset shows part of the IV at the operating point, with two curves at different temperatures (T1,T2) and the corresponding resistances (R1,R2) at bias voltage V_o, for calculation of dR/dT.

The optimum bias with respect to minimum receiver noise temperature is found by adjusting the LO-power and the bias voltage at the operating temperature 4.5 K, Fig. 2. The absorbed LO and DC power, are about 2.5 μW and 0.5 μW respectively, and are derived from the IV characteristics assuming that the response to DC and RF power is the same and due to electron heating only.

$$P_{LO} = \frac{V_1 I_1 - V_o I_o}{1 - x} \qquad (1)$$

Points 0 and 1 are where the isotherm intersects two IV curves with LO powers P_{LO} and xP_{LO}.

At the optimum bias a change of current or voltage by ±10% does not have any significant influence on the noise performance, Fig. 3.

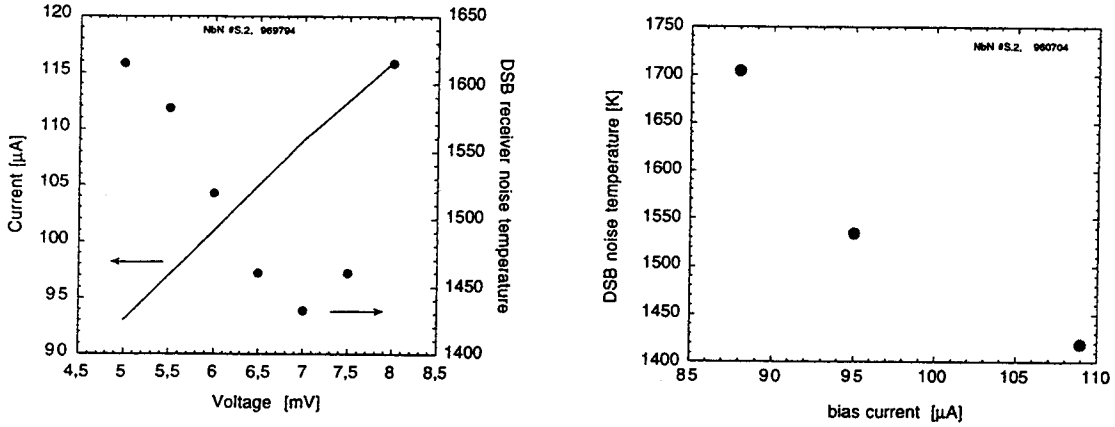

Fig. 3. DSB receiver noise temperature vs a) bias voltage and b) bias current (LO power). No minima is found for an optimum amount of LO power. Further reduction of LO power results in unstable and hysteretic conditions

RESULTS

The gain bandwidth of the HEB is measured with fixed frequency and power of the signal BWO, while the frequency of the LO BWO is tuned to obtain an IF signal in the frequency range 0-7 GHz. An attenuator is used to keep the LO power at a constant optimum level, as indicated by the bias current. As seen in Fig. 4 the gain bandwidth is slightly larger than 3 GHz.

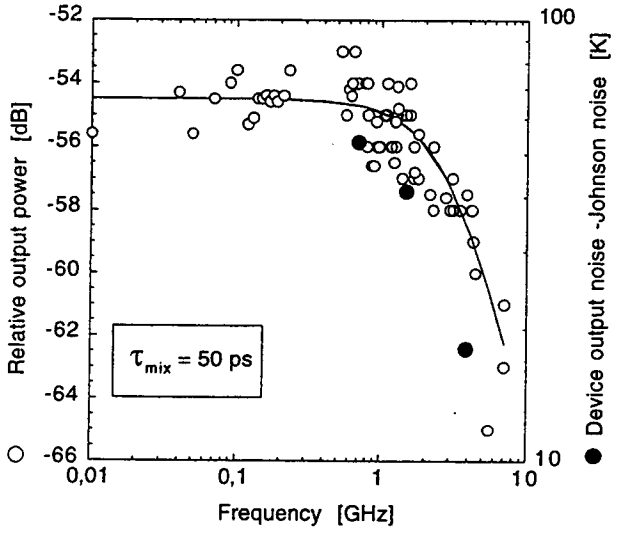

Fig. 4. Relative IF output power and device output noise temperature excluding Johnson noise vs frequency

To measure the device output noise temperature, T_{out}, two noise levels were obtained on a scalar network analyser; one with the device in the operating point, P_r, and a second with the device in the

superconducting state, P_s, giving rise only to Johnson noise, T_J, due to the series-resistance in the contacts. An additional noise source is the load of the circulator at the input to the amplifier. The load temperature, T_s=4.5 K, is reflected by the device and is added to the IF amplifier noise temperature, T_{IF}. The ratio of P_r to P_s is then obtained from the equation given below.

$$\frac{P_r}{P_s} = \frac{T_{out}/L_r + T_s(1-1/L_r) + T_{IF}}{T_J/L_s + T_s(1-1/L_s) + T_{IF}} \tag{2}$$

Here L_r and L_s are the mismatch losses in the operating point and superconducting state, respectively. In the latter state T_J=T_s. T_{IF} is noise the contribution from the IF-chain, and is obtained with the device in normal state acting as a white noise source and producing only Johnson noise at two temperatures just above T_c. All quantities except T_{out} in Eq. (2) are now known, and we can thus obtain T_{out} at different IF frequencies by measuring P_r/P_s.

The similar frequency dependence of the output noise and IF signal, Fig. 3, as well as the relatively large low frequency value of the output noise, 50-60 K, compared to the Johnson noise, T_J ($\approx$ electron temperature $\theta \approx T_c$), proves that the dominating noise process in the device is due to fluctuations in the equivalent electron temperature. An expression for the fluctuation noise is [11]

$$T_{FL} = \frac{I_o^2}{R_L}\left(\frac{dR}{dT}\right)^2 \frac{\theta^2}{c_e V}\tau \tag{3}$$

I_o is the bias current, R_L is the load resistance, $c_e = \gamma\theta$ is the electron specific heat (γ=Sommerfield constant 0.21 mJ $cm^{-3}K^{-2}$). The electron temperature θ in the mixing operating point (V_o,I_o in Fig. 2) is determined by thermally heating the whole device without LO power. In this way the same point (V_o,I_o) is reached at a temperature of the environment of 8.7 K. By adding the excess temperature due to Joule heating $T_{DC} = P_{DC}/G = I_oV_o\tau/c_eV$ = 0.3 K we obtain θ=9 K. V is the bolometer volume, and the electron energy relaxation time τ=52 ps is obtained from the mixing time constant, τ_{mix} in Fig. 3, according to [3, 14]

$$\tau = \frac{\tau_{mix}}{1 - \tau_{mix}\dfrac{dR}{dT}\dfrac{I_o^2}{c_eV}\dfrac{R_o - R_L}{R_o + R_L}} \tag{4}$$

R_o is the DC resistance in the bias point. dR/dT=63 Ω/K is found from the IV-char. according to inset in Fig. 2. This derivation is done at the operating point which is reached by thermal heating without LO power. The change in resistance at constant voltage V_o for a change of physical temperature of 0.05 K is measured, and adding a difference in Joule heating of 0.012 K. The value for the fluctuation noise obtained by Eq. (3) is 31 K. Another contribution to the output noise is from Johnson noise $\approx$ 9 K. For a pumped device, there is as well a contribution from the 300 K hot load. The SSB conversion loss is $\approx$18 dB (see below). Thus, the hot load contribution is about 10 K. This gives a total output noise temperature of 50 K, in excellent agreement with the measured value of 50 K at 1.5 GHz IF frequency and 60 K at 700 MHz IF.

However, it should be pointed out that there is an error in the calculated value of about ±20 K. The factor α by which the mixer noise bandwidth will be larger than the gain bandwidth, due to the dominating fluctuation noise is given by [1, 12].

$$\alpha = \sqrt{\frac{T_{out}(0)}{T_J}} = \sqrt{\frac{T_{FL}(0)+T_{load}+T_J}{T_J}} \qquad (5)$$

where $T_{out}(0)$ is the output noise in the low frequency limit. Since we have different noise contributions from the IF chain in the different bands, Table 2, the noise contribution from the IF is excluded in Eq. (5) so as to enable us to compare it with the measured receiver noise bandwidth. We also want to judge the performance of the HEB independently of our particular IF chain. With $T_J \approx 9$ K and $T_{out}(0) \approx$ 50-60 K we should have a mixer noise bandwidth about 2.3-2.5 times larger than the gain bandwidth, i.e. ≈ 7.5-8 GHz. The DSB receiver noise temperature, T_{DSB}, was determined from the Y-factor with a hot/cold load (300/80K) at a signal frequency of 620 GHz and at IF frequencies of 700 MHz, 1.5 and 3.9 GHz. The response was obtained within a 40 MHz band at each IF frequency. The best DSB receiver noise temperature is 1280 K with a 50 μm beam splitter and ≈1100 K with a 12 μm beamsplitter. Fig. 5 shows the measured noise temperatures at the different IF frequencies including an error of ≈±50 K. The frequency dependence gives a 3 dB receiver noise bandwidth of roughly 5 GHz. Subtracting the noise contribution from the IF chain (which includes an error of ≈ ±25%), shows that the HEB device has a 3 dB mixer noise bandwidth of about 8 GHz, 2.5 times larger than the gain bandwidth, in agreement with the value derived from Eq. (5).

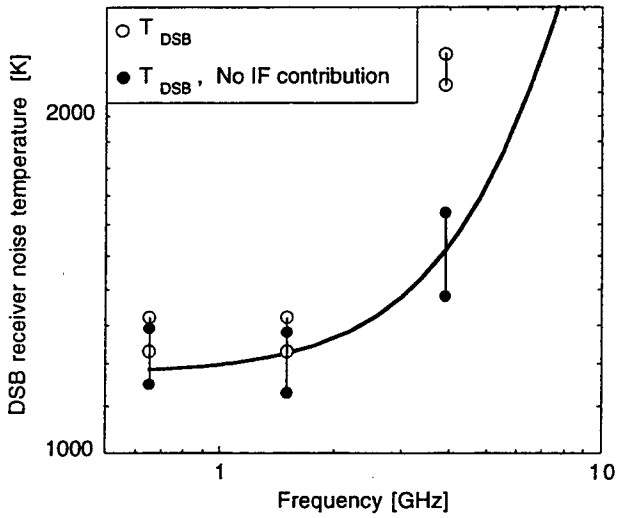

Fig. 5. DSB receiver noise temperature vs IF frequency with and without contributions from the IF chain.

The RF (350 Ω) and IF (120 Ω) impedance mismatch loss is about 2 and 1 dB, respectively. With no mismatch losses, which can be obtained with shorter devices, and excluding beamsplitter

loss, it is possible to achieve a DSB receiver noise temperature of about 700 K with devices of this type of NbN film.

An estimation of the single-sideband receiver conversion gain from the output and receiver noise measurements is obtained by

$$G_{SSB} = \frac{T_{out} \cdot L_{IF} + T_{IF}}{2 \cdot T_{DSB}} \qquad (6)$$

and gives ≈-18 dB gain. Excluding the RF and IF mismatch and the loss in optics (≈3 dB) we have an intrinsic conversion gain of ≈ -12 dB.

In summary, we have measured the mixer gain and receiver noise bandwidth of ultra thin NbN HEB at 620 GHz to 3.2 and ≈5 GHz, respectively. Excluding the noise contribution from the IF chain, the mixer noise bandwidth is ≈8 GHz. For an optimised receiver with the same device, a receiver noise temperature of 700 K DSB is possible to obtain.

This work has been supported by ESA /contact AOP/WK/330038), Swedish National Space Board (Contract Drn. 22/95), INTAS Grant No.94-3965, and Russian program on Condensed matter Grant # 93169. We are thankful to NRAO for the loan of the 4K LNA, V. Belitsky for useful discussions and B. Voronov for fabrication of NbN devices.

REFERENCES

[1] E. M. Gershenzon, G. N. Gol'tsman, I. G. Gogidze, A. I. Elant'ev, B. S. Karasik and A. D. Semenov, Sov. Phys. Superconductivity, **3**, 1582-1597, (1990)

[2] T. G. Phillips and K. B. Jefferts, Rev. Sci. Instrum., **44**, 1009-1014, (1973)

[3] H. Ekström, B. Karasik, E. Kollberg and S. K. Yngvesson, IEEE Trans. Microwave Theory Tech., **43**, 938-947, (1995)

[4] P. Yagoubov, G. Gol'tsman, B. Voronov, L. Seidman, V. Siomash, S. Cherednichenko and E. Gershenzon, *Proceedings of the 7th Int. Symp. on Space Terahertz Technology*, Charlottesville, VA, 1996, pp. 290-302,

[5] D. E. Prober, Appl. Phys. Lett., **62**, 2119-2121, (1993)

[6] A. Skalare, W. R. McGrath, B. Bumble, H. G. LeDuc, P. J. Burke, A. A. Verheijen, R. J. Schoelkopf and D. E. Prober, Appl. Phys. Lett., **68**, 1558-1560, (1996)

[7] B. S. Karasik, M. Gaidis, W. R. McGrath, B. Bumble and H. G. LeDuc, *Proceedings of the Applied Superconductivity*, Pittsburg, 1996, pp. (to be published)

[8] A. Skalare, W. R. McGrath, B. Bumble and H. G. LeDuc, *Proceedings of the Applied Superconductivity*, Pittsburgh, 1996, pp. (to be published),

[9] K. Fiegle, D. Diehl and K. Jacobs, *Proceedings of the Applied Superconductivity*, Pittsburgh, 1996, pp. (to be published),

[10] P. J. Burke, R. J. Schoelkopf, D. E. Prober, A. Skalare, W. R. McGrath, B. Bumble and G. H, LeDuc, Appl. Phys. Lett., **68**, 3344-3346, (1996)

[11] H. Ekström and B. Karasik, Appl. Phys. Lett., **66**, 3212-3214, (1995)

[12] B. S. Karasik and A. I. Elantiev, Appl. Phys. Lett., **68**, 853-855, (1996)

[13] R. J. Schoelkopf, P. J. Burke, D. E. Prober, B. Karasik, A. Skalare, W. R. McGrath, M. C. Gaidis, B. Bumble and H. G. LeDuc, *Proceedings of the Applied Superconductivity*, Pittsburgh, 1996, pp. (to be published),

[14] J.-X. Yang, Ph.D. Thesis in Deparment of Electrical and Computer Engineering, University of Massachusetts, Amherst, (1992)

Superconducting Transition and Heterodyne Performance at 730 GHz of a Diffusion-cooled Nb Hot-electron Bolometer Mixer

J.R. Gao[a,b], M.E. Glastra[a], R.H. Heeres[a], W. Hulshoff [b], D. Wilms Floet[a], H. van de Stadt[b], T.M. Klapwijk[a] and Th. de Graauw[b]

[a] Department of Applied Physics and Materials Science Center, University of Groningen, Nijenborgh 4, 9747 AG Groningen, The Netherlands

[b] Space Research Organization of the Netherlands, PO Box 800, 9700 AV Groningen The Netherlands

Abstract

We report two typical experimental results of waveguide diffusion-cooled Nb hot-electron bolometer (HEB) mixers. The device is a thin (10 nm) Nb bridge with a length of 0.3 μm and a width of 0.9 μm and is defined using photolithography. In the first experiment, the resistance of a HEB is studied as a function of temperature. We observe two critical temperatures, which correspond to the T_c of the Nb bridge and the T_c of the Nb under the Au pads, respectively. These two T_c define a superconducting transition width ΔT of a HEB. The reduced T_c of the Nb under the Au pads is explained by the superconducting proximity effect. In the second experiment, we measure relative conversion efficiency vs intermediate frequency (IF) by using two coherent sources, a carcinotron and a Gunn oscillator, and determine an IF roll-off ($IF_{roll\text{-}off}$) between 0.6 and 1.2 GHz, in agreement with a value estimated in terms of the diffusion-cooled model.

1. Introduction

Recent work on diffusion-cooled Nb hot-electron bolometer (HEB) mixers reported by the Jet Propulsion Laboratory and other groups[1-5] has demonstrated that they are promising heterodyne detectors in the THz frequency range. It has been shown that HEB mixers have low noise and a reasonable wide intermediate frequency roll-off ($IF_{roll\text{-}off}$), but no clear upper limit of operating frequency and no requirement of high local oscillator (LO) power. HEB mixers are expected to compete with NbN SIS mixers around 1.5 THz, but to be superior at much higher frequencies. It is known that coupling a signal at radio frequency (RF) and a signal from a LO to a superconducting HEB can generate a response at IF frequency, provided that the superconductor is biased near the middle point of the transition due to the heating of LO and DC power. So a superconducting HEB can be operated as a mixer. For a practical HEB mixer, it is required that an $IF_{roll\text{-}off}$, defined as the IF frequency at which the relative conversion efficiency decreases by 3 dB, should be $\geq$ 1.5 GHz. A diffusion-cooled Nb HEB suggested by Prober[1] can satisfy this requirement because the hot electron are cooled via out-diffusion, but not via electron-phonon process. This new cooling process can result in a shorter thermal response time and thus a higher $IF_{roll\text{-}off}$. A typical diffusion-cooled HEB consists of a thin ($\sim$ 10 nm) and narrow ($\sim$ 100 nm) superconducting Nb bridge, which is attached to two Au pads serving as heat sinks. The separation of the two pads defines the bridge. A short bridge ($\sim$ 200 nm) is needed to ensure a fast out-diffusion

cooling.

Several heterodyne measurements have been reported using diffusion cooled Nb HEBs. Those are in the waveguide mixers at 530 GHz[2] and in quasi-optical mixers at 1.3 THz[3] using double dipole antenna by Skalare *et al*, in quasi-optical mixers at 2.5 THz using twin-slot antenna by Karasik *et al*[4], and waveguide mixers at 800 GHz by Fiegle *et al*[5]. Also, the dependence of $IF_{roll\text{-}off}$ on bridge length is studied by Burke *et al*[6] and the output noise spectrum by Schoelkopf *et al*[7].

It is known theoretically that the superconducting transition width ΔT of a HEB and details of resistance vs temperature within the ΔT play a critical role in determination of mixer properties, such as conversion efficiency, mixer noise temperature and requirement of LO power. However, the origin of the transition is not clear. In this paper we will address this basic problem and also report measurements of the $IF_{roll\text{-}off}$. Furthermore, we will present our preliminary receiver noise measurements around 730 GHz.

2. Devices and Fabrication

Part of the HEB device is schematically illustrated in Fig. 1a. It consists of a Nb strip with a thickness of 10 nm and a width of 0.9 μm, attached to two Au contact pads (60 nm thick), acting as heat-sinks and RF probes. The separation of the Au contact pads in this case is 0.3 μm, defining the bridge length. The devices are fully fabricated using the standard photolithography and realized in the following way. Starting with a fused quartz wafer, a 10 nm thick Nb is sputtered over the whole area. The Au pads are patterned using photolithography, followed by an Au sputtering deposition and a lift-off process. To remove the native oxides of Nb, a short RF Ar sputter etching of 1 min is applied before the Au deposition. To improve adhesion we add a thin (6 nm) Al layer between Nb and Au. Then the choke structure, which is a Nb and Au bilayer, is defined by sputtering and a lift-off process. The Au layer is for electrical contacts and to prevent Nb etching during the last step. In this last step, bridges are formed by etching the Nb and applying photoresist as a mask. Fig. 1b gives a SEM micrograph of a completed HEB. Before heterodyne measurements, devices are diced and polished so that the substrate has a width of 90 μm and a thickness of 50 μm.

There are two points we need to explain here. Firstly, to establish film growing parameters for Nb thin films we choose a simple fabrication process, namely the photolithography. The present process can lead to bridge dimensions as small as 300 nm. Secondly, since $IF_{roll\text{-}off}$ is determined by both the bridge length and interfaces between Au and Nb, it is essential to form an oxide-free interface. For the devices studied, we apply a RF Ar sputter etching of 1 min, which is shorter than the standard process for Nb SIS (2.5 min). Thus, we expect a possible reduction of $IF_{roll\text{-}off}$, although we do not have clear evidence of oxide barriers from the DC measurements.

3. DC Measurements and Superconducting Transition

The resistance (R) of a HEB is measured as a function of temperature (T) by applying a standard lock-in technique using a low current. The sample is mounted in a dipstick with a vacuum can and the temperature is varied by changing heating currents. Fig. 2 shows R vs T curves for two different devices. Below 5.5 K the resistance is zero and above 6.5 K it reaches the normal state resistance R_N. Between these two temperatures the resistance increases with temperature. We will explain that in our case the two values, 5.5 K and 6.5

K, correspond to the critical temperature T_c(Nb/Au) of Nb under the Au contacts and the critical temperature T_c(Nb) of the Nb bridge, respectively. The difference between the T_c(Nb) and the T_c(Nb/Au) defines the transition width ΔT of a HEB. The low T_c(Nb/Au) is due to the superconducting proximity effect. This conclusion is supported by additional measurements and a numerical calculation.

The different R_N values between the two devices in fig. 2 are due to the difference in bridge size, which is negligible if devices are close to each other on the wafer.

The first experimental result to support our conclusion is the measurement of R vs T for Nb films with different thicknesses or different levels of impurities. The latter is manipulated by using different sputtering rates. We find that the Nb films have a transition width ΔT smaller than 0.1 K regardless of thickness and sputtering rate. In general, a lower sputtering rate can cause a reduction of T_c. The reason for this is that more contaminations existing in the background of a sputtering system are introduced to the film. Very likely, the presence of oxygen and water in the sputtering system is the cause of the reduction[9]. Reducing the thickness gives the same effect.

The second experimental result[10] to support our conclusion is the separate measurement performed in a device structure allowing determination of the T_c(Nb) and the T_c(Nb/Au) simultaneously. We observe a reduced T_c(Nb/Au).

We calculate the reduction of T_c using a model by Werthamer[8] based on the proximity effect. Fig. 3 shows the calculated normalized critical temperature T_c/T_{c0} of Nb under Au or Al layer as a function of metal thickness D_n. Details of the numerical calculation are given elsewhere[10]. For comparison, our experimental data, together with the data from others[11], are included. As expected, the T_c of Nb will decrease with increasing the metal thickness. It is also clear that this reduction depends on which metal is used. The difference between Au and Al is mainly caused by the fact that Al is a superconductor and Au not. We notice from our calculations that the parameters, the electronic specific heat γ for Nb and T_{c0} for Al, have a clear influence on T_c. However, we find that varying the electron mean free path for Al or Au gives only little effects.

The quantitative difference between the calculated and experimental results is obvious. One possible reason is that, as mentioned before, the native oxide layer may not be fully removed. This would cause a less transparent interface and weaken the proximity effect. There is also another complication. For our devices, there is a very thin Al layer between Nb and Au. The influence for this layer is not clear. But it is reasonable to assume that the result should be close to one calculated for an Au layer.

So far we only explain the double T_c characteristic. Another interesting feature, that is the temperature dependence of the resistance within the transition width ΔT, is probably also a result of the proximity effect. However, in this case, we have to deal with the proximity effect along the bridge, by considering the Nb bridge as *a superconductor* and the contacts which are Nb/Au bilayer as *a normal metal*. Unfortunately, such a system is beyond Werthamer's theory. A different model is required to extend our calculations.

4. Heterodyne Measurements

4.1 *Heterodyne Measurement Setup*

The heterodyne measurements are performed in a modified waveguide receiver test setup originally designed for Nb SIS mixers. The waveguide mixer block has been previously used for Nb SIS mixers around 700 GHz[12,13]. Major modifications are made with respect to the bias-T connector and the IF chain. For the former a bias-T connector suitable for 0.1 to 4

GHz is chosen and for the latter Miteq wide-band low temperature FET amplifiers are used. For the Y-factor measurements, an amplifier[14] operating between 0.1 to 2 GHz with a noise temperature of 15 K at liquid nitrogen temperature, together with two room-temperature amplifiers operating between 0.1- 1 GHz, is used. A low pass filter of 0.5 GHz is applied to limit the bandwidth for the receiver noise measurements to 0.1-0.5 GHz. For the $IF_{roll\text{-}off}$ measurements, the second amplifier (0.1 to 8 GHz) with a gain flatness of ± 1.5 dB (max.) is used in combination with a room temperature amplifier with the same bandwidth.

Three different local oscillators are employed, a carcinotron, a backward wave oscillator (BWO), and a Gunn oscillator.

4.2 *FTS Response*

As the first step to characterize HEB mixers, we evaluate the direct response of a HEB using a Fourier transform spectrometer (FTS). The normal state resistance of the device is 13 Ω. The measurements are done by raising the temperature of a HEB within the transition region. Although they can also be performed at the bath temperature, signals are less stable. Fig. 4 shows FTS direct response spectra, different curves corresponding to different positions of the backshort tuner. The continuous curve corresponds to the case that the backshort is close to the HEB. Peak response, as expected, takes place at around 700 GHz. It is evident that the HEB mixer has a much wider instantaneous bandwidth than SIS mixers. The response starts around 500 GHz, which is the waveguide cut-off frequency, and ends around 960 GHz, where the RF loss through the substrate channel may become significant. It is worthwhile to note that, in contrast to SIS mixers, the instantaneous bandwidth is not set by the HEB mixer, but set by the waveguide, or by an antenna in the case of quasi-optical HEB mixers[3,4]. In the FTS spectra a dip at 750 GHz is due to water vapour absorption.

4.3 *Determination of* $IF_{roll\text{-}off}$

We study relative conversion efficiency vs IF by mixing the two monochromatic signals from a carcinotron and a Gunn oscillator. The former is used as a LO to pump the mixer, while the latter acts as a RF signal. Their frequencies are chosen around 700 GHz and their frequency difference specifies an intermediate frequency. Mixed signals are monitored with a spectrum analyser. The measurements are carried out at $T_{bath}=4.6$ K, which is read from a temperature sensor placed in the mixer block.

The amplitude of the mixed signal as a function of IF is measured by varying the LO frequency, but keeping the pumping power constant. The power is monitored through ΔI (at a constant bias voltage) which is the current difference with and without the LO power. The pumping power is chosen in such a way that the output of the mixed signal is maximal. Fig.5 illustrates the normalized amplitude of the mixed signal as a function of IF for two different bias voltages, 0.25 and 0.35 mV. No corrections are applied for small fluctuations in the gain of the IF chain. We fit the theoretical expression for the frequency dependence of the conversion efficiency, $[1+(f_{IF}/IF_{roll\text{-}off})^2]^{-1}$, to the experimental data. We find that our data obey the function reasonably well and obtained an $IF_{roll\text{-}off}$ of 0.6 GHz at 0.25 mV and 0.9 GHz at 0.35 mV. For the same device we also determined the $IF_{roll\text{-}off}$ at a lower temperature (3 K) and higher bias voltages. Depending on the bias voltage, the $IF_{roll\text{-}off}$ ranges from 0.6 to 1.2 GHz. No clear differences are found between 3 and 4.6 K.

In another measurement we used a combination of a carcinotron and a BWO. Due to the BWO the mixed signal is broad (80 MHz). By taking the averaged signal amplitude the results still show similar behaviour as previous ones.

It is known that the $IF_{roll\text{-}off}$ for a HEB follows $IF_{roll\text{-}off}=(2\pi\ \tau_{th})^{-1}$, where is the thermal response time $\tau_{th}=C/G$. Here C is the thermal capacitance of a HEB and G the thermal

conductance. To calculate the $IF_{roll\text{-}off}$, we need to know the C and G. We calculate the C value using $C=\gamma TV$, where γ is the coefficient of electronic specific heat (700 J/K^2m^3); T critical temperature of the bridge (6.5 K); and V volume (2.7×10^{-21} m^3). W estimate the G value of a HEB, fabricated in the same wafer but with R_N=23 Ω, by measuring the resistance as a function of temperature for different currents[10,13]. In this case G equals 32 nW/K. Since the resistance of the device used for the $IF_{roll\text{-}off}$ measurement is 13 Ω, we find the G value being 57 nW/K by scaling the resistances. In this way, we derive a τ_{th} of 0.21 ns and thus an $IF_{roll\text{-}off}$ of 0.8 GHz. This value is roughly in agreement with those of the $IF_{roll\text{-}off}$ measurements. Since the experimental $IF_{roll\text{-}off}$ values are much higher than that one would expect from electron-phonon cooling HEBs[6], we conclude that the cooling process in our devices is indeed dominated by diffusion.

We notice that, if we calculate the G by using the Wiedemann-Franz law, the $IF_{roll\text{-}off}$ should be 2.5 GHz for the present device. There are several possible reasons to explain the difference. Firstly, the interfaces may, as mentioned before, not be highly transparent. We expect that, if we take a long RF sputter etching time before the deposition of the Au pads, this effect can be diminished. Secondly, since the operating temperature is below the T_c(Nb/Au) (the Nb under the Au pads), this Nb is likely still superconducting, although the Nb bridge can be in the resistive state due to LO pumping. Because of the presence of superconductor/metal interfaces, hot electrons may have difficulties to diffuse out. Finally, variations in bridge length (see fig. 1b) due to mis-alignment of photolithography can certainly have an additional effect.

4.4 *Receiver Noise Measurements*

Fig. 6 shows a Y-factor measurement of the HEB mixer together with the pumped I-V curve at a LO frequency of 730 GHz and T_{bath}=4.6 K. Here ac output power is a measure of the response between hot and cold loads and is proportional to the Y-factor. The LO power that pumps the HEB, is supplied by a carcinotron. The maximum Y-factor is 0.18, giving a receiver noise temperature of 5500 K. Since this is a very preliminary measurement, we will not discuss this result further before we have optimized the IF chain. One interesting feature that needs to be discussed is the operating bias point. We can see clear hot/cold response only at bias voltages below the drop-back point, which differs from the results reported by others[2-5]. In other words, if we use the current-bias mode for measurements, it is difficult to measure response in the IF output. For this reason, all the measurements are performed in the voltage-bias mode.

4.5 *Local Oscillator Power*

We estimate LO power using a technique commonly applied for HEBs[15]. The coupled LO power is approximately given by the difference in DC heating power taken from two points (from a constant resistance line) in the pumped and unpumped curves, respectively. We find that the coupled LO power is 130 nW at 4.6 K and 160 nW at 3 K for the $IF_{roll\text{-}off}$ measurements, and is about 90 nW for the receiver noise temperature measurement.

5. Conclusions

We fabricate waveguide diffusion-cooled Nb HEB mixers using photolithography. Two basic aspects have been studied. Firstly, the resistance of a HEB is studied as a function of temperature. We observe two critical temperatures, which correspond to the T_c of the Nb

bridge and the T_c of the Nb under the Au pads, respectively. For a HEB these two T_c define a superconducting transition width. In our case theΔT equals about 1 K. The origin of the transition is interpreted by the superconducting proximity effect. Secondly, we measure relative conversion efficiency vs intermediate frequency by mixing two coherent signals and obtain an $IF_{roll\text{-}off}$ ranging from 0.6 to 1.2 GHz, which is in agreement with the value estimated in terms of the diffusion-cooled model. Furthermore, the first noise measurements show a receiver noise temperature (DSB) of 5500 K at 730 GHz. For all the measurements the local oscillator power needed is $\leq$160 nW.

ACKNOWLEDGEMENT: The authors would like to thank S. Bakker for performing photolithography, J.B.M. Jegers for his assistance in sputtering and RIE etching, and H. Schaeffer and H. Golstein for their assistance in measurements. We also would like thank P.R. Wesselius and P.A. J. de Korte for their support and encouragement. This work is financially supported by the Stichting voor Technische Wetenschappen (STW).

References

1. D.E. Prober, *Appl. Phys. Lett.* **62**, 17 (1993).
2. A. Skalare, W.R. McGrath, B. Bumble, H.G. LeDuc, P.J. Burke, A.A. Verheijen and D.E. Prober, *Appl. Phys. Lett.* **68**, 1558(1996).
3. A. Skalare, W.R. McGrath, B. Bumble, and H.G. LeDuc, *IEEE Trans. Appl. Super.* 1997 (in press).
4. B.S. Karasik, M.C. Gaidis, W.R. McGrath, B. Bumble, and H.G. LeDuc, *IEEE Trans. Appl. Super.* 1997 (in press).
5. K. Fiegle, D. Diehl, and K. Jacobs, *IEEE Trans. Appl. Super.* 1997 (in press).
6. P.J. Burke, R.J. Schoelkopf, D.E. Prober, A. Skalare, W.R. McGrath, B. Bumble, and H.G. LeDuc, *Appl. Phys. Lett.*, **68**, 3344(1996)..
7. R.J. Schoelkopf, P.J. Burke, D.E. Prober, A. Skalare, B. Karasik, W.R. McGrath, M.C. Gaidis, B. Bumble, and H.G. LeDuc, *IEEE Trans. Appl. Super.* 1997 (in press).
8. N.R. Werthamer, *Phys. Rev.* **132**, 2440 (1963); J.J. Hauser, H.C. Theuerer and N.R. Werthamer, *Phys. Rev.* **136**, A637 (1964).
9. C.C. Koch, J.O. Scarbrough, and D.M. Kroeger, *Phys. Rev.* B**9**, 888(1974).
10. R.H. Heeres, *M. Sc. thesis*, University of Groningen, The Netherlands, 1996.
11. A. Skalare, W.R. McGrath, B. Bumble, H.G. LeDuc, P.J. Burke, A.A. Verheijen and D.E. Prober, Proc. *5th Int. Symp. on Space Terahertz Technology*, p. 157, May 10-12, 1994, Univ. of Michigan, Ann Arbor, Michigan; and P. J. Burke, private communication.
12. G. de Lange, C.E. Honingh, J.J. Kuipers, H.H. A. Schaeffer, R.A. Panhuyzen, T.M. Klapwijk, H. van de Stadt and Th. de Graauw, *Appl. Phys. Lett.* **64**, 3039 (1994).
13. H. van de Stadt, A. Baryshev, P. Dieleman, J.R. Gao, H. Golstein, Th. de Graauw, W. Hulshoff, T.M. Klapwijk. S. Kovtonyuk, and H. Schaeffer, *Proc. 30th ESLAB Symp. On Submillimetre and Far-Infrared Space Instrumentation*, 231, 1996, Noordwijk, The Netherlands.
14. On the amplifier, we applied a bias voltage of 5 V, as suggested by Miteq. However, we later noticed that a bias of 3-4 V may improve S/N ratio and also reduce the power. The gain is reduced slightly.
15. H. Ekström, B. Karasik, E. Kollberg, and K.S. Yngvesson, *Proc. 5th Int. Symp. on Space Terahertz Technology*, p.169, May, 1994, Univ. of Michigan, Ann Arbor, Michigan

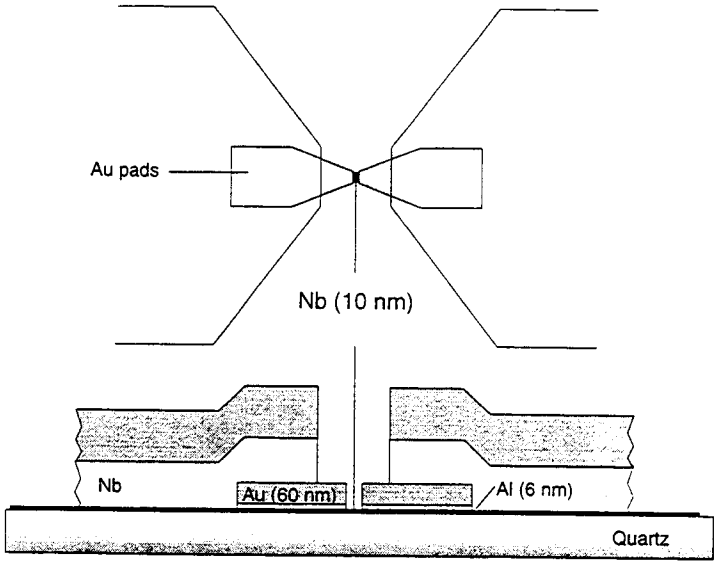

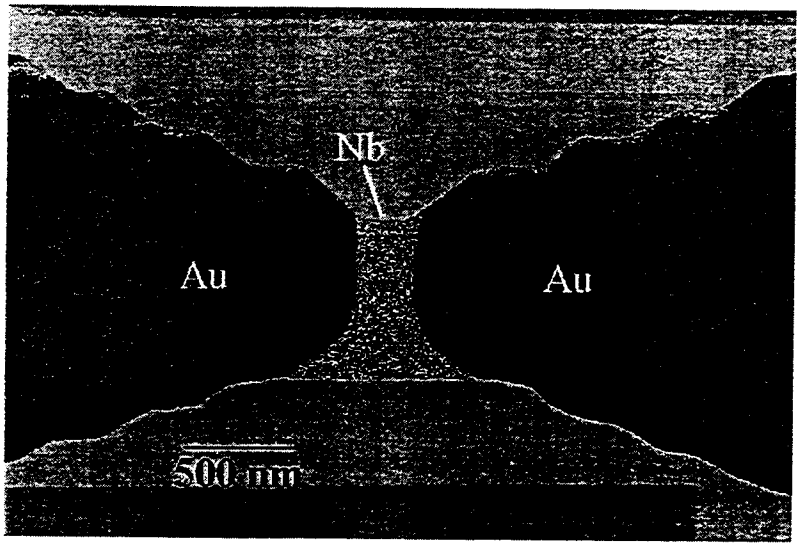

FIG. 1(a) schematic top and cross-sectional views of a hot-electron bolometer mixer; (b) SEM micrograph of the centre part of a completed HEB.

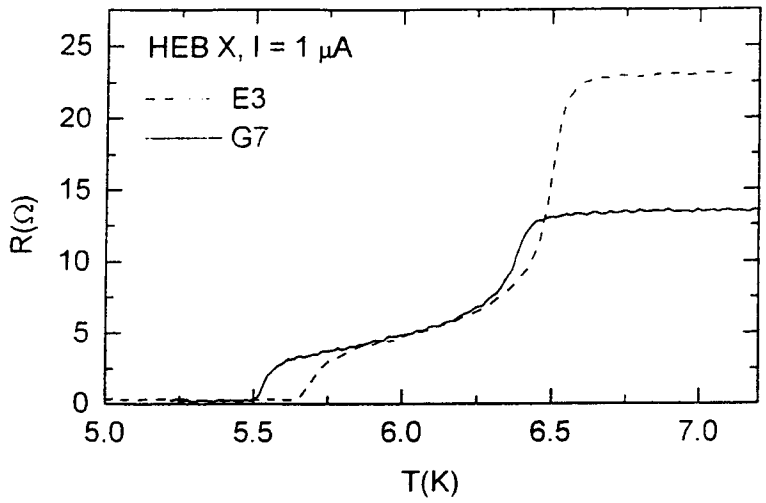

FIG. 2. Resistance as a function of temperature for two different HEBs. The temperature values, 5.5 K and 6.5 K, correspond to the T_c of the Nb under the Au pads and the T_c of the Nb bridge, respectively.

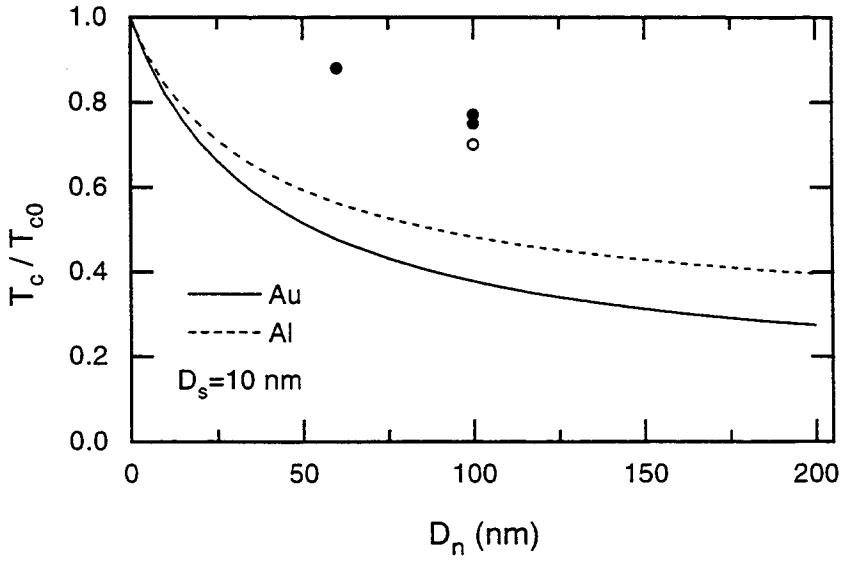

FIG. 3. Calculated normalized critical temperature T_c / T_{c0} of 10 nm thick Nb under a normal metal layer, which is either Au or Al layer, as a function of the thickness D_n. The curves are theoretical values and the data points are experimental values. The data point indicated by " ∘ " is taken from ref. 11. T_{c0} is the original critical temperature of 10 nm thick Nb, that is 6.5 K in our case.

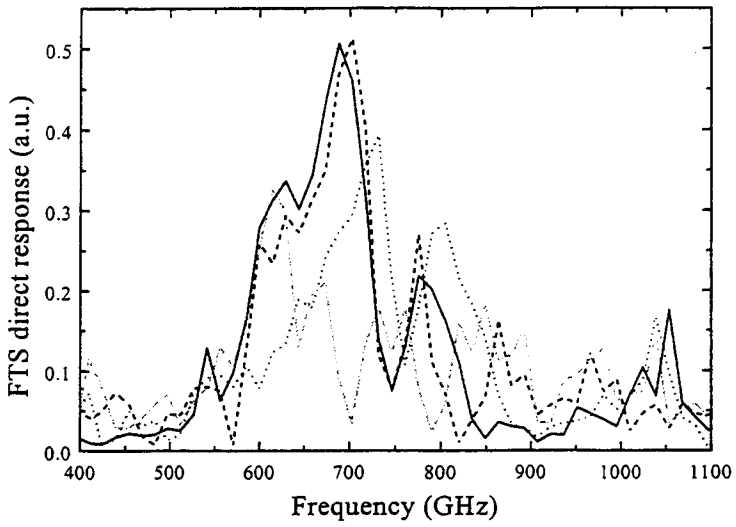

FIG. 4. FTS Spectra of a HEB mixer in a 750 GHz waveguide mixer block. Different curves correspond to measurements with different positions of the backshort tuner. The continuous curve corresponds to the case that the backshort is close to the HEB.

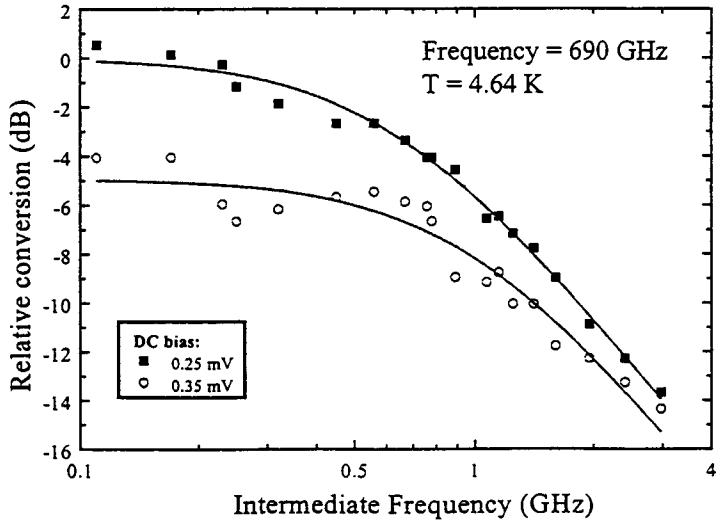

FIG. 5 Relative conversion efficiency of a HEB mixer is measured as a function of intermediate frequency at two bias voltages. The data points are the measurements and the curves are the fits (see the text).

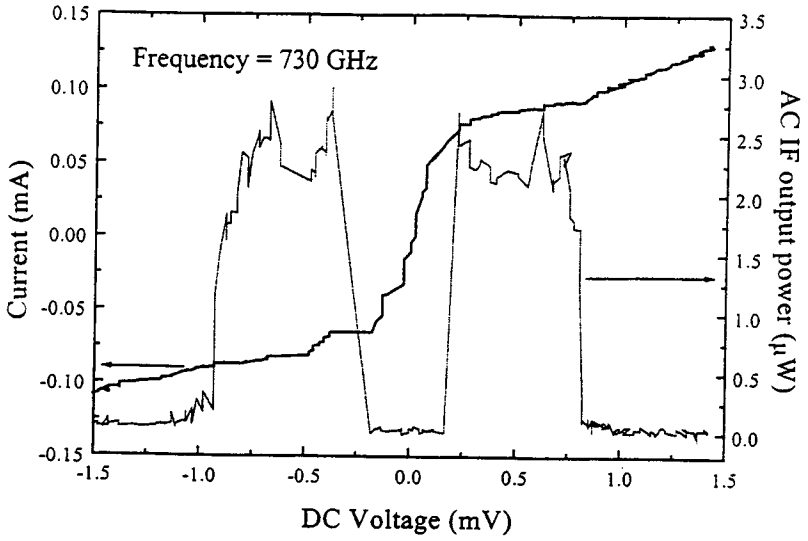

FIG. 6 AC IF output power of a HEB mixer, that responds to hot/cold load, as a function of DC bias voltage and the pumped *I-V* curve. Measurements are done at a LO frequency of 730 GHz and at a bath temperature of 4.6 K.

NOISE AND RF BANDWIDTH MEASUREMENTS OF A 1.2 THz HEB HETERODYNE RECEIVER

A.Skalare, W.R. McGrath, B. Bumble, H.G. LeDuc

Center for Space Microelectronics Technology
Jet Propulsion Technology, California Institute of Technology
Pasadena, CA 91106

Abstract

Receiver noise and RF coupling bandwidth have been measured for a quasioptically coupled diffusion-cooled hot-electron bolometer mixer at a local oscillator frequency of 1267 GHz and an intermediate frequency of 1.4 GHz. A lowest receiver equivalent noise temperature of 1880 K double-sideband was measured, with an upper limit for the mixer noise temperature of 950 K double-sideband. The amount of absorbed local oscillator power in the bolometer device was approximately 6 nW. The effective instantaneous RF bandwidth measured with a Fourier transform spectrometer was 730 GHz.

Introduction

In the last few years, superconducting transition-edge hot-electron bolometers (HEB's) have emerged as prime candidates for use in low-noise heterodyne receivers at frequencies exceeding 1 THz [1,2,3,4,5,6]. The reason is that their performance does not degrade above the superconducting gap frequency, as is the case for SIS mixers, since bolometers operate through heating of the electron gas in the device. The most urgent need for these receivers is within the field of astrophysics, where the strong requirements on detector sensitivity justify the use of cryogenic temperatures below 10 K. Conventional bolometers have traditionally not been considered for such applications, as their intermediate frequency bandwidth has been limited to less than the 500 MHz to 1 GHz that would be required. Recent measurements have shown that superconducting HEB's can satisfy both the sensitivity and IF bandwidth requirements of molecular spectroscopy in astrophysics [2,3,4,5,6,7].

Two varieties of superconducting HEB's have been reported. The phonon-cooled variety studied by other research groups [3,4,8] uses interaction between the hot electrons and the lattice as a cooling mechanism, and will not be treated here. The diffusion-cooled superconducting HEB, which is the topic of this paper, instead relies on electron out-diffusion as the main cooling mechanism for the heated electrons. This requires that the device is very short, less than 1 μm [1,2,7], since the thermal response time and therefore also the intermediate frequency bandwidth depend on the time required for the heated electrons to escape via the ends of the bolometer. This type of HEB requires normal metal contacts, which suppress the superconducting energy gap at the device ends, thereby ensuring that Andreev reflection will not slow down the escape of the electrons.

In this paper we present measurements of receiver noise and RF bandwidth of a quasioptically coupled diffusion-cooled superconducting HEB at 1267 GHz. Additional details of the device operation are discussed elsewhere [6].

Bolometer Device & Experimental Setup

The device is a 150 nm wide and 300 nm long strip, that is e-beam patterned and etched from a 10 nm thick Nb film using a recently developed self-aligned fabrication technique [9]. This process provides a robust thermal and electrical contact between the Nb microbridge and the gold contact pads, which is important for the mixer operation. Fig. 1 shows an SEM of a completed bolometer. It is integrated with a gold double-dipole antenna [10,11,12] on a crystal quartz substrate to form the planar mixer circuit, see fig.2. A $\lambda/4$ thick quartz plate with a gold reflector is placed on top of the device substrate which is then glued to a hyperhemispheric lens of crystal quartz. An additional plastic lens is used to create an essentially parallel beam in front of the mixer assembly. This mixer assembly, together with a HEMT intermediate frequency amplifier is cooled to an operating temperature of about 2 K in a vacuum cryostat. Y-factor measurements were performed in an evacuated box that was attached to the vacuum cryostat, as shown in fig.3, thereby eliminating the need for atmospheric corrections to the measured Y-factors, and thus allowing for accurate measurements of receiver noise. The box contains a 10 μm thick polyethylene beamsplitter to couple in the local oscillator power, and a rotating mirror to switch between the hot (295 K) and cold (85 K) loads. The 1267 GHz local oscillator is a submillimeter gas laser using a difluoromethane (CH_2F_2) line, that is pumped by a CO_2-laser operating at the 9R6 line. Two Zitex filters at 77 K and at 2 K are used to reduce the amount of infrared radiation coming in through the cryostat window. The intermediate frequency chain consists of a cooled isolator, a cooled 1.4 GHz HEMT amplifier, two FET amplifiers operating at room temperature, and a crystal direct-detector. A bandpass filter outside the cryostat sets the IF bandwidth for noise measurements to 300 MHz. The entire chain has an equivalent noise temperature of 6.3 K and a total gain of 85 dB.

Measurements

The frequency dependence of the RF power coupling to the bolometer was measured using a Fourier transform spectrometer (FTS) with the bolometer operated as a direct detector. The measured coupling center frequency was approximately 1 THz, with an effective coupling bandwidth of 730 GHz as shown in fig.4. This is in good agreement with the antenna design frequency, which was 1100 GHz, and with the one octave 3 dB bandwidth that has been measured for this type of antenna at lower frequencies [12]. This indicates that the coupling bandwidth is defined by the antenna rather than the bolometer. The dip near the center of the coupling band (see fig.4) corresponds to a third-order Fabry-Perot resonance between the quartz lens and the plastic lens in the mixer block, which we believe is enhanced by the mismatch between the f/6 beam of the spectrometer and the high focal number beam of the mixer.

A measurement of the direct detection response of the bolometer when switching between a hot (295 K) and a cold (77 K) blackbody load in the receiver signal beam indicates that the coupled broadband RF power is of the order 0.4 nW. In combination with the 730 GHz bandwidth this indicates that the total beam-path loss between the loads and the bolometer is approximately 7 dB.

Figure 5 shows the measured data for heterodyne receiver measurements. The best Y-factor response occurs in the resistive branch of the device IV curve at bias levels just above the instability point where the device switches into the superconducting state. The largest Y-factor value, measured at a constant DC bias voltage of 0.345 mV was 1.084, giving a receiver noise temperature of 2430 K double-sideband (DSB). This value does, however, contain a systematic error due to a slight shift in the electron temperature of the device from the broadband thermal radiation coupled from the calibration hot and cold loads. The temperature shift causes a change in the DC resistance and in the amount of thermal fluctuation noise generated by the device. This temperature shift can be avoided by maintaining constant resistance during the measurement instead of constant voltage, since the device resistance is a unique function of the electron temperature. This gives a slightly higher DC bias current, and therefore a higher mixer conversion [13] for the "cold" data point than for the "hot" one, leading to a conservative (slightly underestimated) value of the real Y-factor. The Y-factor measured in this way at a constant resistance of 54 Ω is 1.107, corresponding to an equivalent noise temperature of 1880 K DSB. It should be pointed out that the shift in temperature is not the same as a saturation of the mixing process; in fact the effect occurs also when no local oscillator is present. Due to the thermal response time of the device, only broadband power coupled within a few GHz of bandwidth around the LO frequency can actually take part in the mixing process. This power is only a few pW, which is not enough to cause saturation.

An upper limit estimate for the mixer noise temperature can be calculated by subtracting the IF amplifier chain noise, and by taking into account that the antenna is operating at 1267 GHz where the coupling is 1.6 dB lower than optimum (see fig.4). Other coupling losses such as reflections at lens surfaces, losses in the infrared filters and ohmic losses in the antenna are less accurately known to us, and are therefore not taken into account. This upper limit for the mixer noise is 950 K DSB.

The absorbed LO power in the device can be estimated from the direct detection response of the bolometer to be approximately 6 nW. This very low number is a result of the fairly high sheet resistance of the niobium film; the two-squares long device has a resistance of 140 Ω. The sheet resistance is linked via the Wiedemann-Franz law to the thermal conductivity of the electron gas, and therefore affects the bolometric response. Lower resistance devices generally require higher amounts of LO power, see [2,5,7]. In addition, for lower resistance devices (20-30Ω) than the one described here the broadband thermal radiation from the hot and cold loads has a negligible effect in Y-factor measurements [2,5], since the higher thermal conductance effectively reduces the temperature shift of the electrons.

Planned measurements

We are currently preparing to do two types of measurement with the devices described in this paper:

The first is a gas cell measurement using a rather strong absorption line of deuterized ammonia (NH_2D) at 1268 GHz, with either a backward wave oscillator (BWO) or the 1267 GHz CH_2F_2 laser line as a local oscillator. This measurement is warranted since it is the is the best way of conclusively verifying that the detector is operating in a 100 % heterodyne mode.

The second experiment is a measurement of resistance and IF output noise from the bolometer as a function of ambient temperature and the amount of LO pump power. Preliminary measurements have shown that an unpumped device can generate a significant

amount of thermal fluctuation noise when biased thermally right at the superconducting transition temperature. The amount of noise generated appears to be higher than what an LO-pumped device produces when operated as a mixer. This may indicate that only a portion of the microbridge is operating precisely at the transition, and that the mixer can therefore be further optimized. This is reasonable, since the diffusion-cooled microbridge must operate with a temperature gradient along its length. A local oscillator that is stable over an extended period of time is required for this experiment because of the time constants involved in varying the temperature of the fixture that holds the mixer. We will therefore use either a BWO or a lower-frequency (630 GHz) solid-state source rather than a gas laser.

Summary

We have made the first measurements at terahertz frequencies with a diffusion-cooled hot-electron bolometer. A receiver noise temperature of 1880 K (DSB) was measured at 1267 GHz, with a mixer noise temperature below 950 K (DSB). The amount of local oscillator power absorbed in the device was approximately 6 nW, which is the lowest amount reported for any heterodyne receiver operating above 1 THz. The RF coupling bandwidth was 730 GHz, as measured with a Fourier transform spectrometer.

Acknowledgments

We acknowledge D. Prober, P. Burke and R. Schoelkopf of Yale University and B. Karasik of the Jet Propulsion Laboratory for many useful discussions. We are also grateful to T. Crawford, M. Gaidis and M. Shumate for supporting our laser LO system, and to H. Pickett for the use of the Fourier Transform Spectrometer. In addition, we appreciate the loan of a quartz lens and mount from J. Zmuidzinas. The research in this paper was performed by the Center for Space Microelectronics Technology, Jet Propulsion Laboratory, California Institute of Technology, and was sponsored by the National Aeronautics and Space Administration, Office of Space Science.

References

[1] D. E. Prober, "Superconducting Terahertz Mixer using a Transition-Edge Microbolometer", Appl. Phys. Lett. **62** (17), pp. 2119-2121, (1993).

[2] A. Skalare, W.R. McGrath, B. Bumble, H.G. LeDuc, P.J. Burke, A.A. Verheijen, R.J. Schoelkopf, D.E. Prober, "Large bandwidth and low noise in a diffusion-cooled hot-electron bolometer mixer", Appl. Phys. Lett. 68 (11), pp.1558-1560, (1996)

[3] P. Yagubov, G. Gol'tsman, B. Voronov, S. Svechnikov, S. Cherednichenko, E. Gershenzon, V. Belitsky, H. Ekstrom, E. Kollberg, "Quasioptical phonon-cooled NbN hot-electron bolometer mixer at Thz frequencies", Proc. 7th Int'l. Symp. on Space Terahertz Technology, University of Virginia, Charlottesville, VA, March 1996, pp. 303-317.

[4] J. Kawamura, R. Blundell, C.-Y. E. Tong, G. Gol'tsman, E. Gershenzon, B. Voronov, J. Appl. Phys. **80**, p. 4232 (1996).

[5] B. S. Karasik, M.C. Gaidis, W.R. McGrath, B. Bumble, H.G. LeDuc, "A Low-Noise 2.5 THz Superconductive Nb Hot-Electron Mixer", To appear in IEEE Trans. Applied Superconductivity.

[6] A. Skalare, W.R. McGrath, B. Bumble, H.G. LeDuc, "Receiver measurements at 1267 GHz using a diffusion-cooled transition-edge bolometer", To appear in IEEE Trans. Applied Superconductivity.

[7] P.J. Burke, R.J. Shoelkopf, D.E. Prober, A. Skalare, W.R. McGrath, B. Bumble, H.G. LeDuc, "Length scaling of bandwidth and noise in hot-electron superconducting mixers", Appl. Phys. Lett. **68** (23), pp. 3344-3346 (1996)

[8] G.N. Gol'tsman, A.I. Elant'iev, B.S. Karasik, E.M. Gershenzon, "Antenna-coupled superconducting electron-heating bolometer", Proc. Fourth Int. Symp. on Space Terahertz Technology, p. 623, University of California, Los Angeles, March 30-April 1, 1993.

[9] B. Bumble, H.G. LeDuc, "Fabrication of a diffusion cooled superconducting hot electron bolometer for THz mixing applications", To appear in IEEE Trans. Applied Superconductivity.

[10] D. B. Rutledge, D. P. Neikirk, D. P. Kasilingam, "Integrated Circuit Antennas", *Infrared and mm Waves*, K. J. Button (Ed.), Vol.10, Ch.1, Academic Press, New York, 1983

[11] P.T. Parrish, T.C.L.G. Sollner, R.H. Mathews, H.R. Fetterman, C.D. Parker, P.E. Tannenwald, A.G. Cardiasmenos, "Printed Dipole-Schottky Diode Millimeter Wave Antenna Array," *SPIE Millimeter Wave Technology*, pp.49-52, Vol.337, 1982

[12] A. Skalare, Th. de Graauw, H. van de Stadt, "A planar dipole array antenna with an elliptical lens", Microwave and Optical Tech. Lett., Vol.4, No.1, Jan 5, 1991.

[13] F. Arams, C. Allen, B. Peyton, E. Sard, "Millimeter Mixing and Detection in Bulk InSb", Proc. IEEE **54**, 308 (1966)

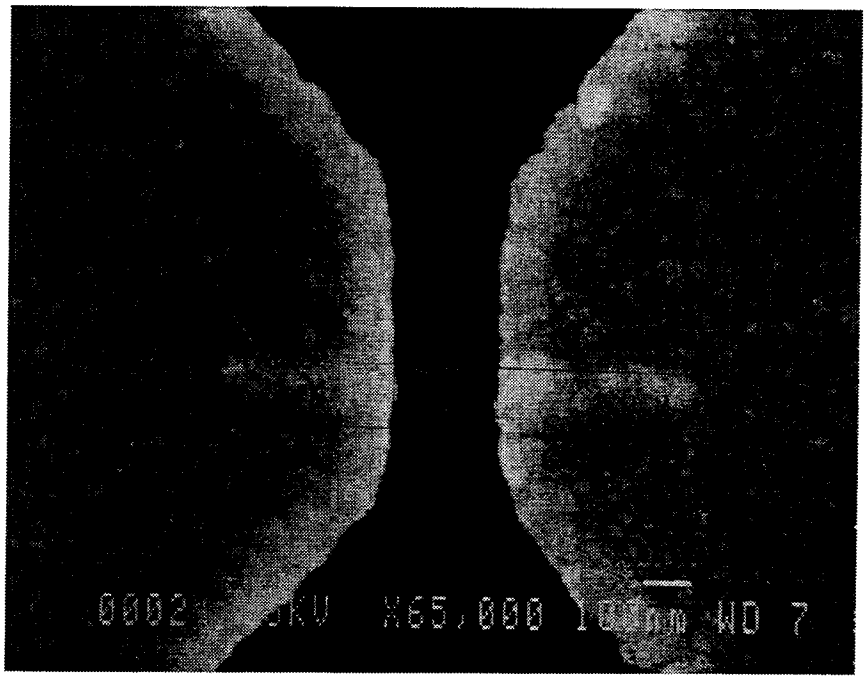

Fig.1: SEM photo of a submicron Nb HEB.

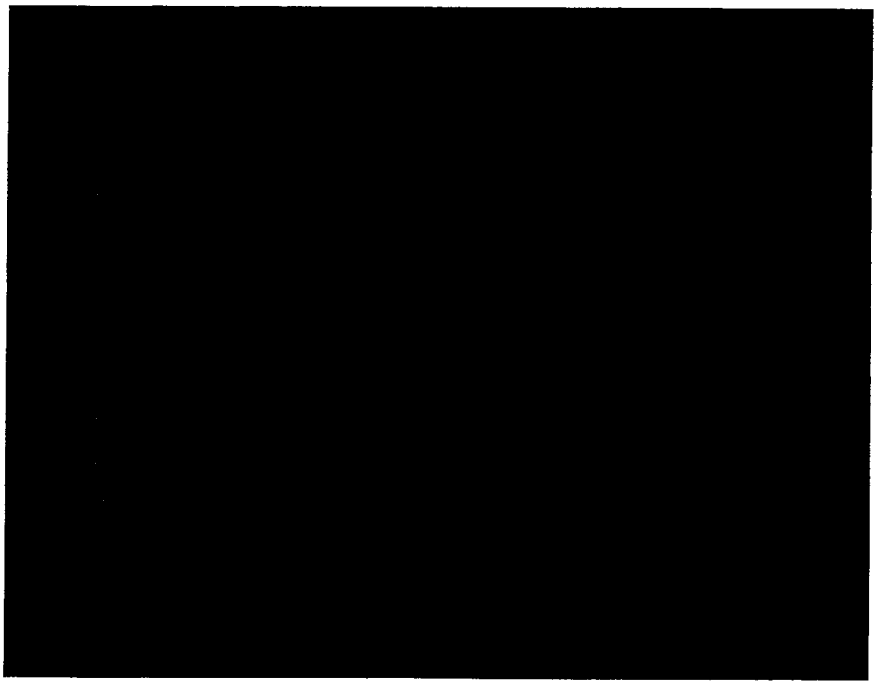

Fig.2: Double-dipole antenna and coplanar transmission line embedding circuit and RF bandstop filter. These elements are fabricated in gold. The Nb microbolometer is located in the center of the antenna circuit.

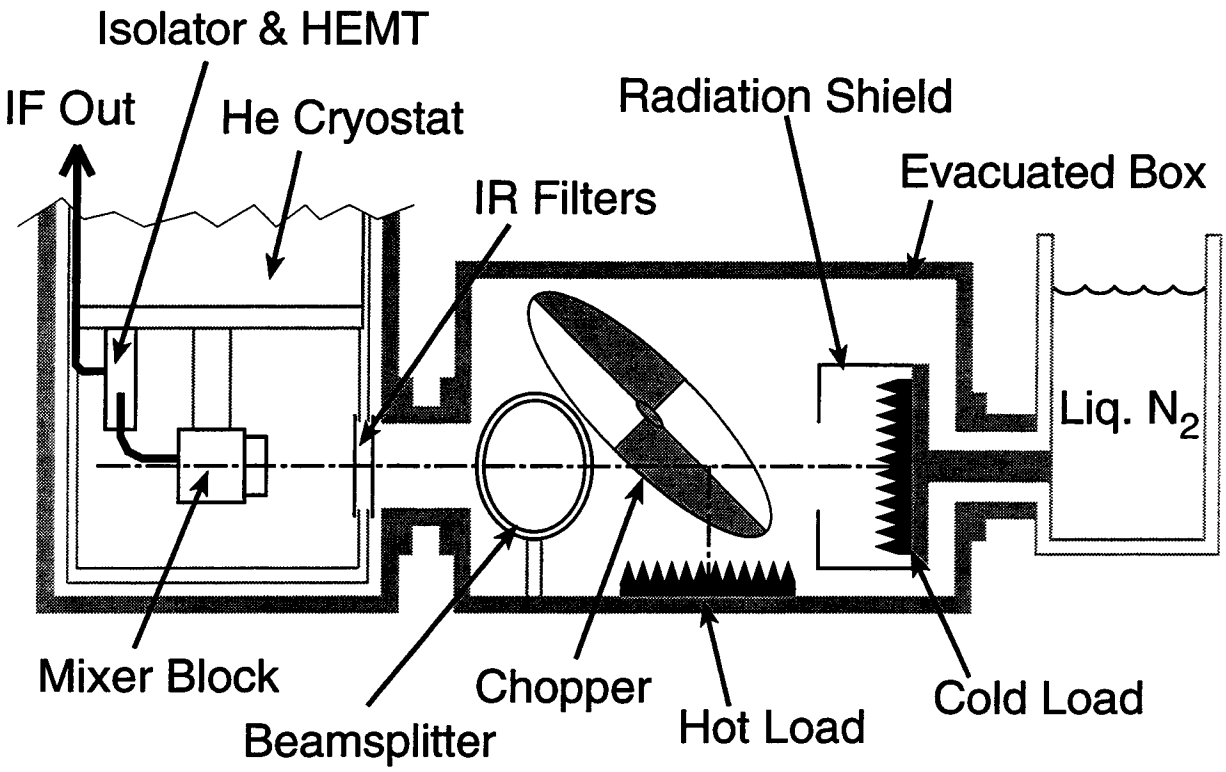

Fig.3: Schematic of the vacuum cryostat and the evacuated Y-factor measurement box.

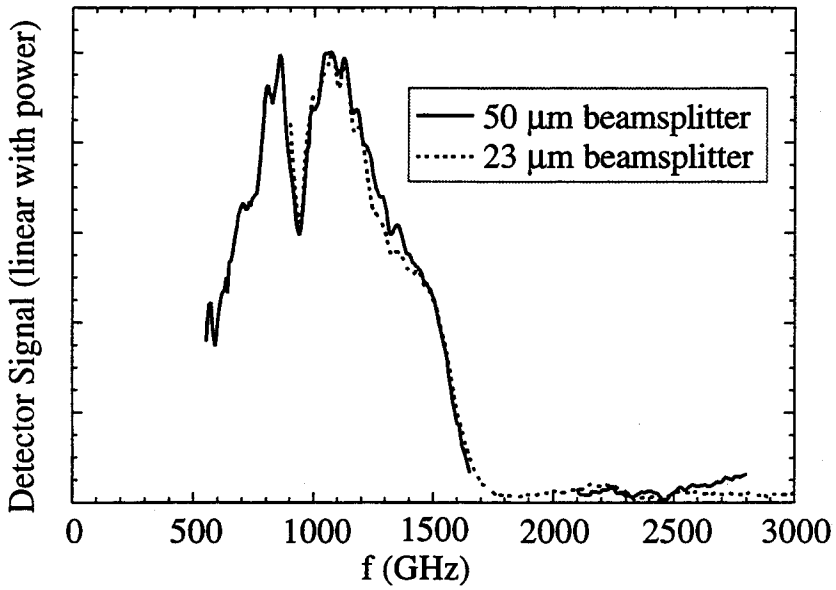

Fig.4: Relative coupled rf power versus frequency as measured with a Fourier transform spectrometer. To first order, the frequency dependence of the FTS itself has been calibrated away. Two different beamsplitters were used in the spectrometer which shows that there were no systematic errors due to this particular element.

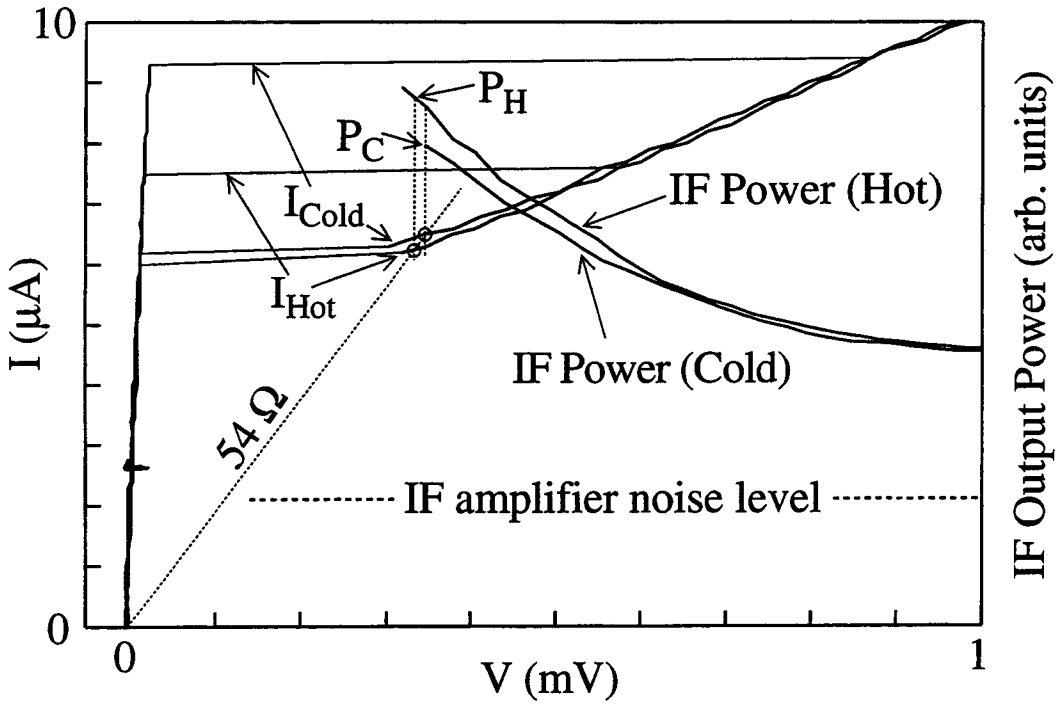

Fig.5: A pumped IV-curve at 1.2 THz and the output intermediate frequency power when coupling to a hot and a cold blackbody radiator. The periodic "wiggles" in the IV-curves are due to numerical truncation in the digitized data and are not present in the actual device. The integration time used in acquiring the IF power data was fairly low, which causes some point-to-point variation in the power readings shown. At high enough bias currents both IF power curves increase linearly with the dc current (not shown here), which is a result of the diffusion cooling mechanism in conjunction with the Wiedemann-Franz law for the thermal conductivity.

A Low-Noise Superconductive Nb Hot-Electron Mixer at 2.5 THz

B.S. Karasik*, M.C. Gaidis, W.R. McGrath, B. Bumble, and H.G. LeDuc
Center for Space Microelectronics Technology, Jet Propulsion Laboratory,
California Institute of Technology, Pasadena, CA 91109, USA

We report on the development of a quasioptical Nb hot-electron bolometer mixer for a 2.5 THz heterodyne receiver. The devices are fabricated from a 12 nm thick Nb film, and have a 0.30 μm×0.15 μm in-plane size, thus exploiting diffusion as the electron cooling mechanism. The rf coupling was provided by a twin-slot planar antenna on an elliptical Si lens. A specially designed 2.5 THz system, using a CO_2-pumped FIR laser as local oscillator (LO), with rf hot/cold loads enclosed in vacuum to avoid atmospheric absorption, was used in the experiment. The experimentally measured double sideband (DSB) noise temperature of the receiver was as low as 2750 ± 250 K, with an estimated mixer noise temperature of ≈ 900 K. These results demonstrate the low-noise operation of the diffusion-cooled bolometer mixer above 2 THz.

I. INTRODUCTION

A number of on-going astrophysical and atmospheric programs are aimed at spectroscopic exploration of the terahertz (THz) frequency range. There is an urgent need here for low-noise mixers for heterodyne receivers. Currently available SIS mixers and Schottky-diode mixers exhibit significant degradation in noise performance above 1 THz [1] (see Fig. 1). A unique superconducting hot-electron bolometer (HEB) mixer has been proposed [2-3] as an alternative to address these high-frequency needs. The HEB mixer is expected to operate up to at least several 10's of THz, due to the relatively frequency independent absorption of rf radiation in a superconductor above the gap frequency. Theory [4] predicts the HEB mixer noise temperature due to intrinsic noise mechanisms to be as low as ~ 100 K, which is of the order of the quantum limit at THz frequencies. Also the required local oscillator (LO) power can be made very low (less than 100 nW for Nb devices) if the device size and sheet resistance are appropriately chosen. Two different approaches have been pursued to develop a practical HEB mixer. The first device approach employs an ultrathin (< 40 Å) NbN film where, due to the fast phonon escape, the mixer 3-dB IF signal bandwidth, f_{3db}, is determined by the intrinsic electron-phonon interaction time τ_{ep} to be $f_{3db} = 1/(2\pi\tau_{ep}) \approx$3-4 GHz [5]. The other major approach utilizes thicker (≈ 100 Å) low-resistive high quality Nb films, in which out-diffusion of electrons to normal metal contacts serves as the dominant electron cooling mechanism. For Nb device lengths L less than 0.4 μm, useful IF bandwidths have been demonstrated in the range of 2-6 GHz [6-7].

In this work we developed and tested a quasioptical diffusion-cooled HEB mixer at 2.5 THz. Record sensitivity was obtained at this frequency demonstrating the superiority of HEB mixers at THz frequencies.

II. MIXER DESIGN AND EXPERIMENTAL SET-UP

The bolometer device used in this experiment consists of a 0.30 μm long by 0.15 μm wide

* Electronic mail: karasik@merlin.jpl.nasa.gov

microbridge made of a 12 nm thick Nb film sputtered-deposited on a high-resistivity ($\rho \approx$ 4-5 kΩ cm) silicon substrate. The length of the bridge was defined by the gap between the 150 nm thick gold contact pads using a unique self-aligned fabrication process [8]. The surrounding mixer embedding circuit and planar antenna are fabricated from 300 nm thick gold. This process gives automatic registration of the Nb under the gold to provide dependable electrical and thermal contact. Figure 2 shows an SEM of a completed device. To protect the device against oxidation the entire area surrounding the microbridge was passivated with a 40 nm thick layer of SiO. More details of the device fabrication are given elsewhere [8]. The critical temperature of the film was 6.8 K, the transition width was 0.2-0.3 K, and the sheet resistance was 11-13 Ω/sq. After patterning of the device, the critical temperature decreased typically to 6.5 K without significant change of other film parameters. The critical current density at 4.2 K was measured to be 1.5×10^7 A/cm^2.

The mixer rf embedding circuit was made using a twin-slot antenna and coplanar waveguide transmission (CPW) line [9] located at the second focus of an elliptical Si lens of 12.7 mm diameter [10]. Figure 3 shows this planar circuit. Our antenna design uses a slot length of 36.5 μm, a slot width of 2.0 μm, and a center-to-center slot spacing of 19.0 μm. A $Z_o = 39\ \Omega$ CPW feed connects to the HEB, with center strip width of 2.0 μm and gaps of 0.5 μm each. The rf impedance presented to the HEB device at the feed point was designed to be 70 Ω, and was strongly determined by the 0.5 μm gap in the CPW line. The IF and dc line integrates an rf choke with 4 high- and 4 low-impedance CPW sections each of 12 μm length. The (85 Ω) high-impedance sections have center strip widths of 1.0 μm and gaps of 4 μm each. The (34 Ω) low-impedance sections have center strip widths of 7.0 μm and gaps of 1 μm each. A 250 μm thick Si chip carrying the twin-slot antenna and rf choke-filter was glued to the lens and wire-bonded to a coplanar waveguide IF circuit on Duroid™ substrate which, in turn, was soldered to an SMA connector.

Our mixer test system (see Fig. 4) consisted of a CO_2-pumped methanol FIR laser as an LO source, and a vacuum box containing two blackbody loads with similar emissivities for Y-factor measurements of the receiver noise temperature. The box is connected to the LHe vacuum cryostat, allowing operation without a pressure window in the signal path. The box and cryostat are evacuated to remove the effect of atmospheric absorption which is significant at 2.5 THz. Thus accurate measurements of receiver noise are possible without any corrections applied. We use a 200 μm thick Zitex™ G108 [11] infrared filter to block background 300 K radiation. The LO beam was diplexed into the signal path using a 12.7 μm thick Mylar beam splitter. One of the blackbody loads was attached to the cold finger of a liquid N_2 dewar and reached a temperature of typically 90 K. The signal from the hot and cold loads was switched by a mechanical chopper with a reflecting blade at a rate typically around 100 Hz. The first-stage of the IF system consisted of a cooled broadband HEMT amplifier with a bandwidth 1.5-3.0 GHz and a noise temperature of $\approx$ 9 K. This was followed by room-temperature amplifiers, a narrow bandpass filter (a set of different filters with bandwidths ranging from 25 to 300 MHz was used), and a commercial crystal detector. The average IF response, V_{dc}, (*i.e.*, the dc voltage across the IF crystal detector) and the change in IF response synchronous with the chopper, ΔV, were simultaneously measured using a voltmeter and a lock-in amplifier. The Y-factor is then given by $(V_{dc}+\Delta V/2)/(V_{dc}-\Delta V/2)$, and the DSB mixer noise temperature, T_M, is $T_M = (T_H - T_C Y)/(Y-1)$, where T_H and T_C are the effective Planck temperatures of the hot and cold loads.

III. EXPERIMENTAL PROCEDURE

A. RF Antenna and Coupling Test.

The antenna frequency response was measured using a Fourier Transform Spectrometer (FTS). For this measurement, the device operating temperature was set to a value near T_c, and the bias voltage was adjusted to obtain a large direct-detection response in the bolometer. The detector response was corrected

for the calculated frequency dependence of the beamsplitter in the spectrometer. The remaining frequency dependence is dominated by the antenna response. From the result shown in Fig. 5(A), the center frequency is about 1900 GHz and the 3-dB bandwidth is approximately 1.1 THz. These results conform with the expected performance for twin-slots [9] and demonstrate that this type of antenna functions well above 2 THz. Previously, twin-slot antennas have been successfully demonstrated only slightly above 1 THz [12].

One can see that the center frequency was offset by almost 25% from the desired 2.5 THz center frequency. We have investigated the antenna rf performance, attempting to understand this discrepancy with the 2.5 THz design. A detailed model simulation revealed a significant dependence of center frequency on the HEB device resistance. Figure 5(B) shows the result of simulations for 3 different device resistances. The antenna was designed to provide a match to a 70 Ω HEB with a 2.5 THz center frequency. The 23 Ω HEB device, actually tested as a mixer, would be expected to best match the antenna at about 2.25 THz which is only 18% higher than the experimental result. To examine these issues further, we have tested a 35 Ω device with the same antenna design as used for the previous 23 Ω device. In this case, we find the theory is about 7% higher than the measured center frequency. We have not yet been able to test more devices of this type on the FTS to evaluate the statistical significance of this deviation, but find it to be quite close to the errors one could expect from the theoretical model simulations. Tests with more devices of varying resistances will also reveal the significance of the device resistance on match to theory. The rf choke filter was assumed ideal in the simulations, but may also play a role in the observed discrepancy. The first rf filter section presented to the antenna is a low-impedance section which flares at 45° to match the dimensions of the CPW inside the twin-slot antenna. One other 49 Ω device tested with a modified rf filter in which the first section does not have the 45° flare, showed less than 1% deviation from theory, but the lack of more tests prevents us from yet concluding that the rf choke is responsible for the 7-18% shift seen above. It is also likely that the Zitex G108 or G115 IR filters used in the experiment causes a small downshift, as it exhibits a rolloff beginning only slightly above 2.5 THz. The Zitex is responsible for the deviation between the calculated and measured response above 3 THz. Finally it is useful to note that the theory predicts approximately 1.5 dB of loss at the LO frequency of 2.522 THz for the 23 Ω, whereas the FTS measurements suggest up to 3 dB improvement may be possible for an optimized device/antenna combination.

The coupling efficiency of the bolometer to the radiation (which includes all the losses and reflections in the warm and cold optics, as well as embedding circuit losses) was measured using the direct detection response of the HEB to the hot and cold loads (*i.e.*, without any LO applied). Plotting the two current-voltage (IV) characteristics ("hot" and "cold") one can calculate the absorbed radiation power, P_{abs}, assuming the rf power heats the device in the same fashion as the dc bias Joule heating. Here, $P_{abs} = P_{dc}(\text{hot}) - P_{dc}(\text{cold})$, applied for a constant resistance line (Pdc is the Joule power). The device coupling efficiency can be found as $\eta = P_{abs}/\Delta P_{inc}$, where ΔP_{inc} is the difference between the powers of black body radiation from the hot and cold loads, integrated over the measured rf bandwidth of the mixer. This yields a total optical coupling efficiency of $\eta \approx -7.2$ dB.

B. Y-factor and LO power.

Mixer experiments were performed with two very similar devices, and both demonstrated comparable performance. Only the data for one are discussed here. Figure 6 shows both unpumped and optimally LO-pumped IV characteristics at 4.3 K. Normally, only small or no negative resistance was observed in the optimal IV curve. The LO power (P_{lo}) absorbed in the bolometer was evaluated from the pumped and unpumped IV characteristics as $P_{lo} = P_{dc(\text{unpumped})} - P_{dc(\text{pumped})}$, applied for a constant resistance line. Within the uncertainty of this simple technique, $P_{lo} \approx 80$ nW was obtained. In addition, special precautions have been taken (including very careful alignment, absorbers to catch stray reflections, and aperturing of the laser beam) to reduce reflections and LO standing wave effects to a negligibly small

level. This was required to obtain a stable ac component ΔV for Y-factor measurements. Also the offset of the output noise caused by the direct detection of the THz radiation within the antenna bandwidth was verified as too small to contribute significantly to the observed mixing signals. In particular, we have checked that the highest possible IF noise offsets caused by the direct detection at different temperatures (LO power turned off) were still much smaller than the mixing response.

The bias dependencies of both V_{dc} and ΔV are given in the same figure. One can see than the IF output power starts to rise when approaching the dropback point at the IV curve, indicating the onset of strong mixing performance (at this point the dynamic resistance becomes very large and the self-heating effects increase). This behavior was also observed at 1.5 K, where both the position of the operating point and the mixer noise temperature were almost the same as at 4.3 K. The only difference was a somewhat larger amount of LO power required to pump the mixer at 1.5 K. Also, for bias voltages in the negative differential resistance region, the generation of oscillations in the device were observed. This bias region was avoided for mixer measurements.

C. IF Impedance and Mixer Bandwidth.

In order to estimate the IF bandwidth inherent in the mixer device we performed IF impedance measurements within a 0.05-4 GHz frequency range. It has been demonstrated experimentally for phonon-cooled Nb [13,14] and NbN [15] devices that the HEB impedance changes from a high differential resistance value at low frequencies to a lower ohmic resistance R at high frequencies. The crossover occurs at the frequencies related to the intrinsic electron temperature relaxation time, τ_T. Thus, a measurement of the HEB impedance versus frequency allows τ_T to be determined. The mixer bandwidth, f_{3dB}, is then given by:

$$f_{3dB}^{-1} = \frac{\tau_T}{1 + C\dfrac{R - R_L}{R + R_L}}, \tag{1}$$

where R_L is the IF load (50 Ω), and C is the self-heating parameter.

For these measurements, a 0.3 μm long device with small contact pads was mounted in a gap in the center conductor of a microstrip transmission line fabricated on 0.5 mm thick Duroid with dielectric constant 10.2. The line was placed in a dewar and connected through semirigid cables with a HP8510 network analyzer to measure the S_{21} parameter. The testing rf power level was greatly attenuated to avoid any influence of the test signal on the device resistive state. Calibrations were done with the HEB device in the superconductive state ($Z \approx 0$) and normal state ($Z = R_n$). This allowed the HEB IF impedance to be de-imbedded from the microstrip test fixture. According to theory [4] the HEB impedance is given by

$$Z(\omega) = R\frac{1+C}{1-C}\frac{1 + j\omega\dfrac{\tau_T}{1+C}}{1 + j\omega\dfrac{\tau_T}{1-C}}. \tag{2}$$

Large values of the parameter C are required in order to observe a pronounced frequency dependence of the impedance. Equivalently, the device has to be biased to the operating point with a large differential resistance. In the experiment this was accomplished by heating the device to some temperature above 4.2 K. Figure 7 shows the IV curve and the position of the operating point for these measurements. Figure 8 shows the Z(f) dependence (both real and imaginary parts) along with the fitted curves from Eq. 2 The associated mixer bandwidth is found to be f_{3dB} = 1.4 GHz. This quantity is in good agreement with recently reported bandwidth measurements on diffusion-cooled Nb devices of the same length [6,7].

IV. NOISE TEMPERATURE AND LOSSES

The experimental values of the DSB receiver noise temperature are plotted vs IF in Fig. 9. The different points correspond to the different bandpass filters used. A best receiver noise of 2500-3000 K was measured at IF's below 1.4 GHz, *i.e.* the noise bandwidth is consistent with the mixer bandwidth implied by the impedance measurements. If we remove the IF system noise and correct for the measured 1.5-dB loss in the off-resonant antenna, an upper limit of about 900 K is obtained for the mixer noise temperature. This performance is comparable to that for similar diffusion-cooled HEB mixers at 533 GHz [6] and at 1.2 THz [16], and demonstrates the relative frequency-independence of the mixer performance. It should be noted that this receiver performance is 3-to-5 times better than competing Schottky-diode receivers at 2.5 THz, and the required LO power is at least four orders of magnitude lower.

TABLE I
BALANCE OF THE RECEIVER LOSSES

Element	Loss (dB)
Si lens (reflection)	1.5
Si lens (absorption)	<0.3
Beamsplitter	0.5
Zitex filter	≤0.5
Mixer center frequency offset	3.0
Twin-slot antenna backlobe loss	0.5
CPW conduction losses	1.0
TOTAL:	7.3

We believe that this measured performance, while very good, is certainly not the best possible for an optimized device. Table I shows a loss budget at the mixer rf path. One can estimate that the DSB noise temperature at the device itself (after eliminating the 7.3 dB rf loss) may be as low as ≈ 500 K. Such corrections always involve substantial uncertainty, but at least are indicative of the noise performance of this type of HEB mixer. In addition, a better optimized design of the antenna circuit and use of an appropriate anti-reflection coating for the Si lens can reduce the receiver noise temperature to below 1000 K.

V. CONCLUSION

Excellent performance of a diffusion-cooled Nb hot-electron bolometer mixer has been demonstrated at 2.5 THz. A DSB receiver noise temperature of ≤ 3000 K has been measured at $f_{IF} \leq 1.4$ GHz, along with only 80 nW coupled LO power. The mixer performance is expected to improve by at least 1.5-2 dB with better antenna design and impedance match. This demonstrates that diffusion-cooled HEB mixers can work up above 2 THz with no significant degradation in performance. This is a major improvement for heterodyne sensor technology and is expected to be extremely useful for numerous astrophysical and atmospheric applications.

ACKNOWLEDGMENT

The authors are thankful to A. Skalare for numerous discussions and valuable contributions during set up of the experiment, G. Rebeiz for calculation of the twin-slot antenna and J. Zmuidzinas for the use of his computer program to model the twin-slot antenna impedance. M. Shumate is acknowledged for setting up the FIR laser. We also acknowledge T. Crawford and H. Pickett for the use of FTS and assistance with the measurements.

The research described in this paper was performed by the Center for Space Microelectronics Technology, Jet Propulsion Laboratory, California Institute of Technology, and was sponsored by the National Aeronautics and Space Administration, Office of Space Science.

REFERENCES

[1] These data are borrowed from different sources: Schottky diode data are taken from the Proc. 7th Int. Symp. on Space Terahertz Technology (STT-7), University of Virginia, Charlottesville, VA, March 1996; most recent SIS data are from STT-7 and Ref. 11; NbN HEB data are from STT-6, STT-7, Ref. 5, J. Kawamura et al., J. Appl. Phys., vol. 80, pp. 4232-4234, October 1996; Appl. Phys. Lett., vol. 70, March 1997, and A.D. Semenov et al. Appl. Phys. Lett., vol.69, pp. 260-262, July 1996; Nb HEB data are from Ref. 6,16 and this work.

[2] E.M. Gershenzon, G.N. Gol'tsman, I.G. Gogidze, Y.P. Gusev, A.I. Elant'ev, B.S. Karasik, and A.D. Semenov, "Millimeter and submillimeter range mixer based on electronic heating of superconducting films in the resistive state," *Sverhprovodimost' (KIAE),* vol. 3(10), pp. 2143-2160, October 1990 [*Sov. Phys. Superconductivity*, vol. 3(10), pp. 1582-1597, 1990];

[3] D.E. Prober, "Superconducting terahertz mixer using a transition-edge microbolometer," *Appl. Phys. Lett.* vol. 62(17), pp. 2119-2121, 26 April 1993.

[4] B.S. Karasik and A.I. Elantiev, "Noise temperature limit of a superconducting hot-electron bolometer mixer," *Appl. Phys. Lett.*, vol. 68, pp. 853-855, February 1996; "Analysis of the noise performance of a hot-electron superconducting bolometer mixer," *Proc. of the 6th Int. Symp. on Space Terahertz Technology*, 21-23 March 1995, Caltech, Pasadena, pp. 229-246.

[5] P. Yagubov, G. Gol'tsman, B. Voronov, S. Svechnikov, S. Cherednichenko, E. Gershenzon, V. Belitsky, H. Ekström, E. Kollberg, A. Semenov, Yu. Gousev, and K. Renk, "Quasioptical phonon-cooled NbN hot-electron bolometer mixer at THz frequencies," Proc. 7th Int. Symp. on Space Terahertz Technology, University of Virginia, Charlottesville, VA, March 1996, pp. 303-317.

[6] A. Skalare, W.R. McGrath, B. Bumble, H.G. LeDuc, P.J. Burke, A.A. Verheijen, R.J. Schoelkopf, and D.E. Prober, "Large bandwidth and low noise in a diffusion-cooled hot-electron bolometer mixer," *Appl. Phys. Lett.*, vol. 68, pp. 1558-1560, March 1996.

[7] P.J. Burke, R.J. Schoelkopf, D.E. Prober, A. Skalare, W.R. McGrath, B. Bumble, and H.G. LeDuc, "Length scaling of bandwidth and noise in hot-electron superconducting mixer," *Appl. Phys. Lett.*, vol. 68, pp. 3344-3346, June 1996.

[8] B. Bumble and H.G. LeDuc, "Fabrication of a diffusion cooled superconducting hot electron bolometer for THz mixing applications", *IEEE Transactions on Applied Superconductivity*, vol. 7, pp.3560-3563, June 1997.

[9] D.F. Fillipovic, S.S. Gearhart, G.M. Rebeiz, "Double-slot antennas on extended hemispherical and elliptical silicon dielectric lenses," *IEEE Trans. on Microwave Theory and Technique,* vol. 41, pp. 1738-1749, October 1993.

[10] The Si lenses have been fabricated at Janos Technology Inc., Townshed, VT 05353-7702.

[11] Zitex G108, Norton Performance Plastics, Wayne, NJ 07470-4699.

[12] M. Bin, M.C. Gaidis, J. Zmuidzinas, T.G. Phillips, and H.G. LeDuc, "Low-noise 1 THz niobium superconducting tunnel junction mixer with a normal metal tuning circuit," *Appl. Phys. Lett.*, vol. 68, pp. 1714-1716, March 1996.

[13] A.I. Elantev and B.S. Karasik, "Effect of high frequency current on Nb superconductive film in the resistive state," *Fiz.Nizk.Temp.*, vol. 15, pp. 675-683 (1989) [Sov. J.Low Temp. Phys. vol. 15, pp. 379-383 (1989)].

[14] H. Ekström, B.S. Karasik, E. Kollberg, K.S Yngvesson, "Superconducting bolometric mixers," *IEEE Trans. Microwave and Guided Wave Letters,* vol. 4, pp. 253-255 (1994).

[15] H. Ekström, B.S. Karasik, E. Kollberg, G.N. Gol'tsman, and E.M. Gershenzon, "350 GHz hot electron bolometer mixer," *Proc. of the 6th Int. Symp. on Space Terahertz Technology*, 21-23 March 1995, Caltech, Pasadena, pp. 269-283.

[16] A. Skalare, W.R. McGrath, B. Bumble, H.G. LeDuc, "Receiver measurements at 1267 GHz using a diffusion-cooled superconducting transition-edge bolometer", *IEEE Transactions on Applied Superconductivity*, vol.7, pp. 3568-3571, June 1997; and this conference issue.

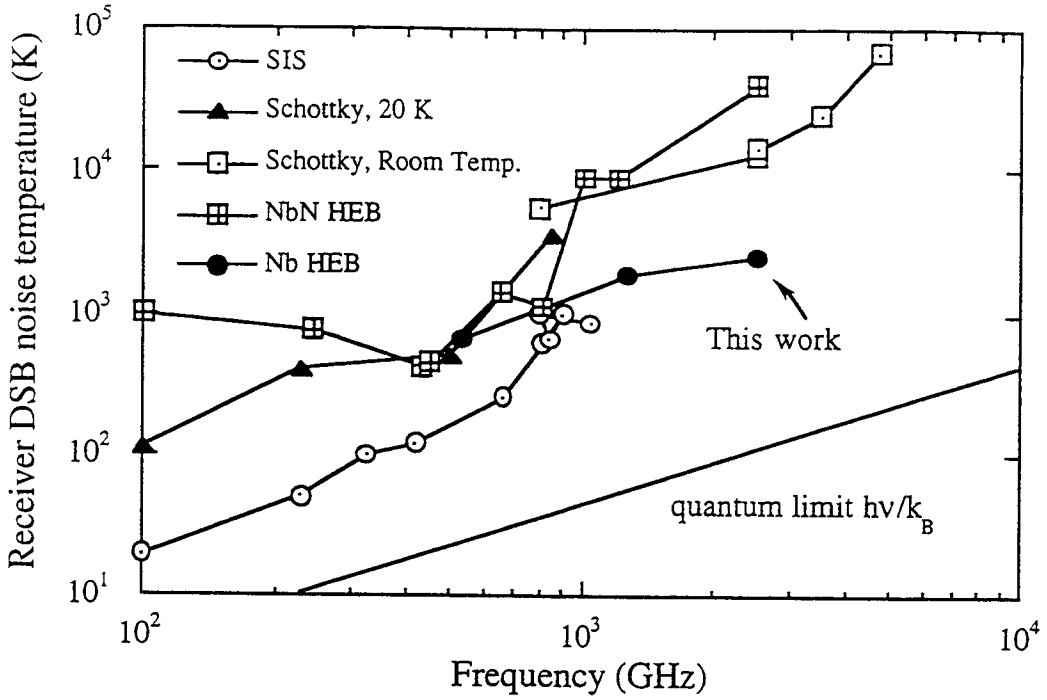

Fig. 1. State-of-the-art in heterodyne receiver noise performance at submillimeter wavelengths.

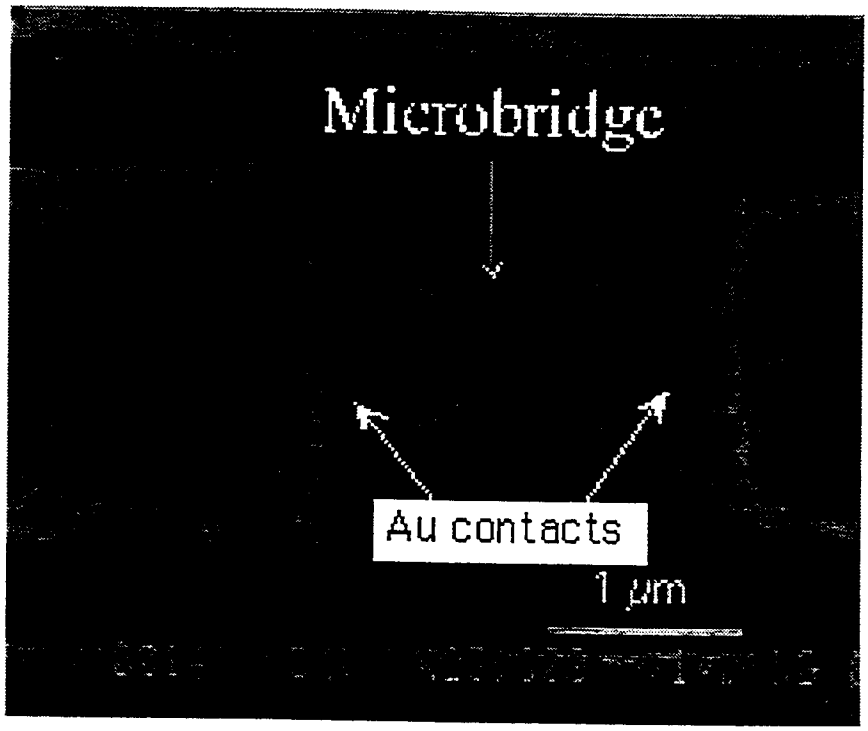

Fig. 2. SEM photo of the 0.30 μm by 0.15 μm Nb HEB device between the gold contacts.

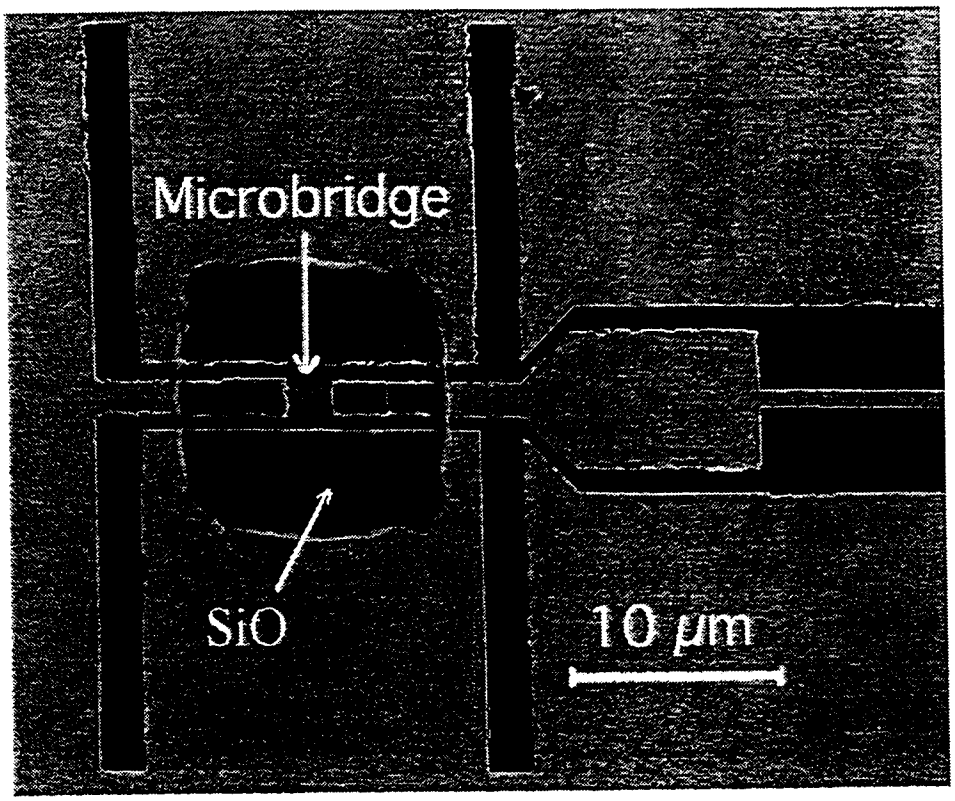

Fig. 3. Photo of the planar mixer circuit consisting of the twin-slot antenna and coplanar waveguide transmission line. The circuit elements to the right are the IF and dc lines with an integrated rf choke filter.

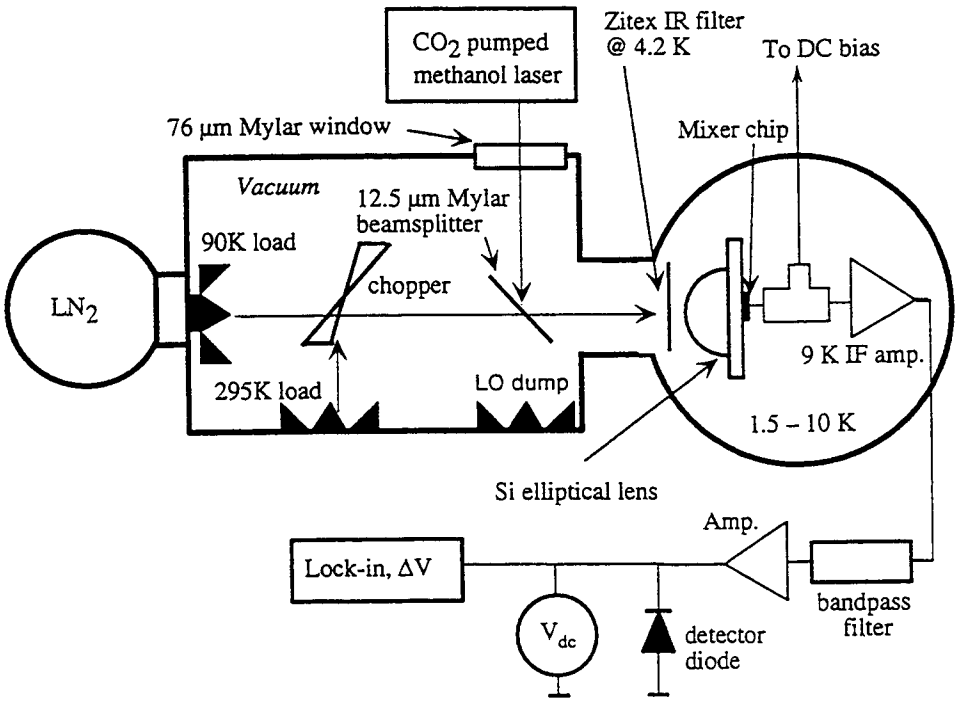

Fig. 4. Block diagram of the 2.5 THz mixer/receiver test system.

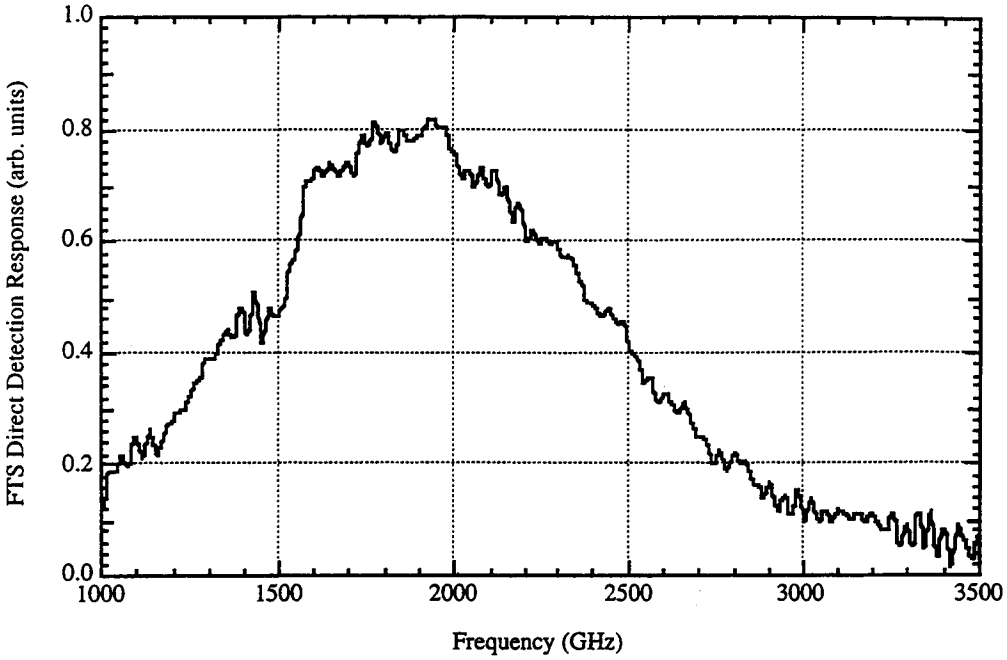

Fig. 5(A). FTS spectrum measured for the 23 Ω HEB, corrected for the calculated 23 μm FTS beamsplitter efficiency. The HEB was operated as a direct detector. The frequency response is determined mainly by the planar antenna and shows that the twin-slot circuit works well at terahertz frequencies.

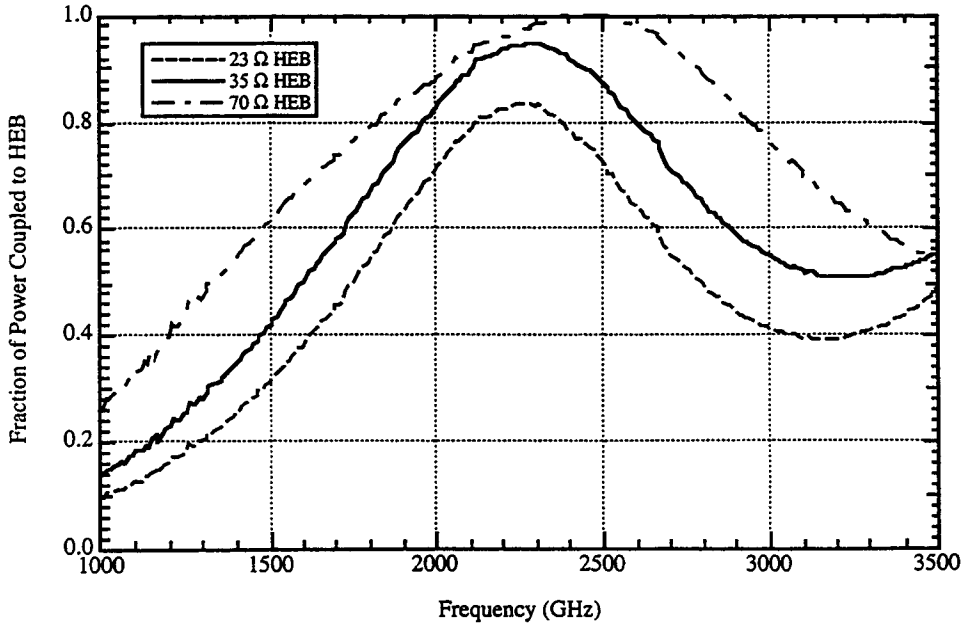

Fig. 5(B). Coupling efficiency of twin-slot antenna and coplanar waveguide to the HEB, calculated for 23 Ω, 35 Ω, and the ideal 70 Ω device resistance.

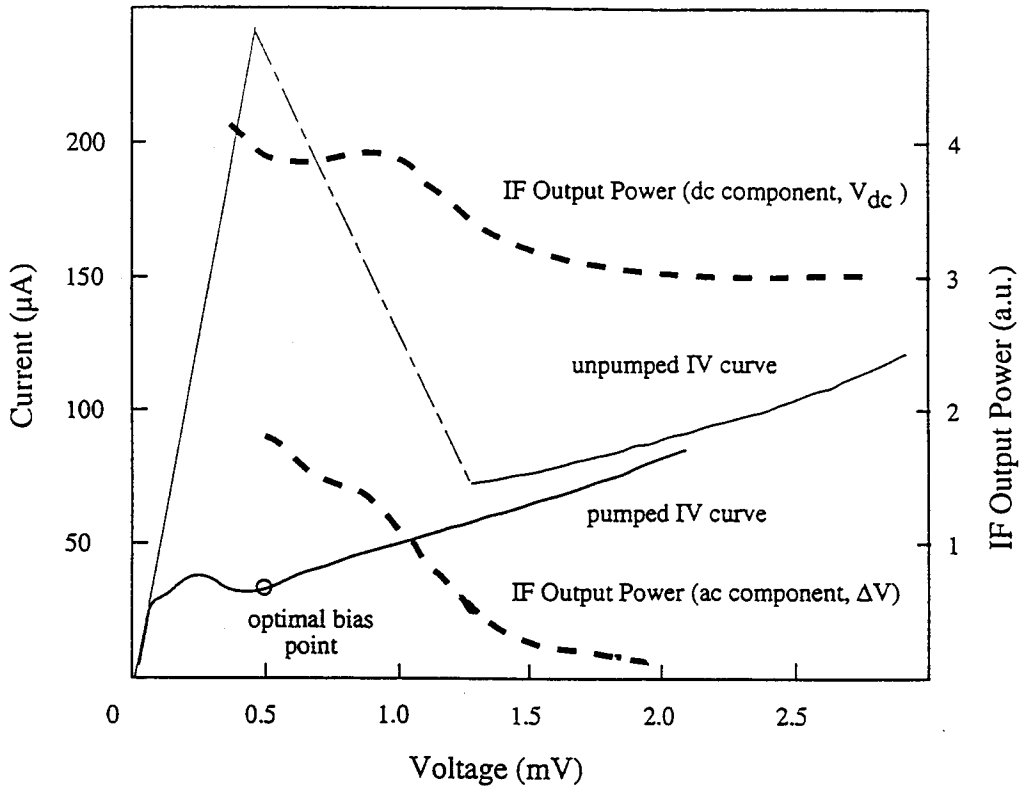

Fig. 6. Current-voltage characteristics and the dc (V_{dc}) and ac (ΔV) components of the IF output power. V_{dc} and ΔV are arbitrary scaled in reference to each other.

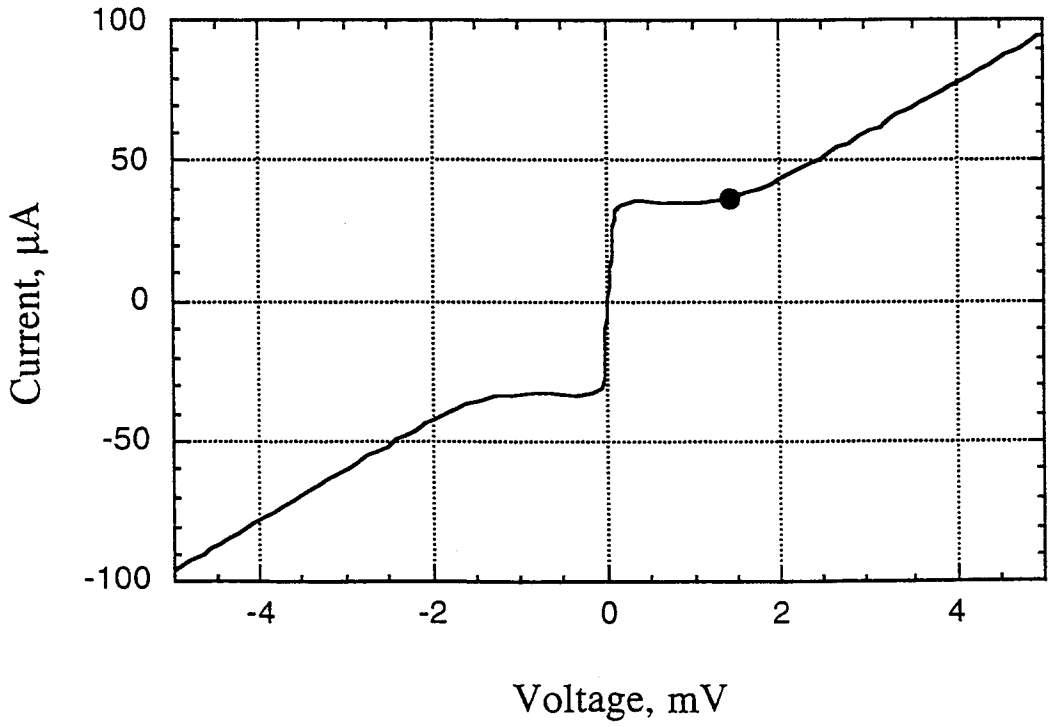

Fig. 7. The IV characteristic and the position of the operating point (filled circle) for the impedance measurements.

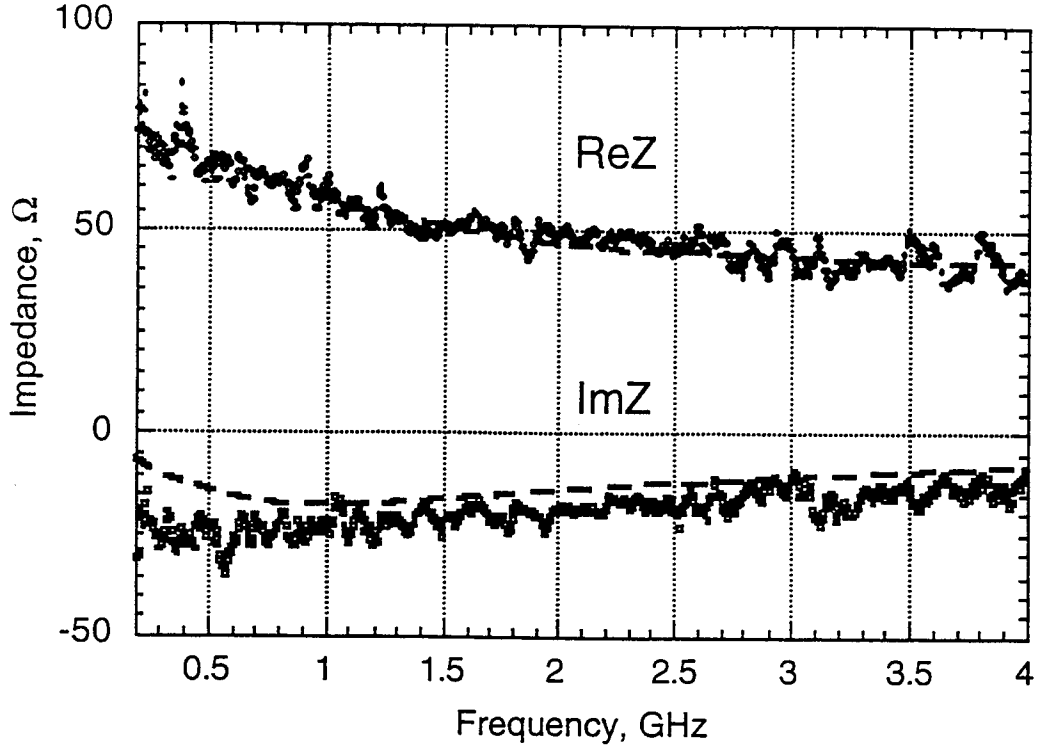

Fig. 8. HEB IF impedance for a 0.3 μm long microbridge. The dashed lines are the fit by Eq. 2 with C = 0.3

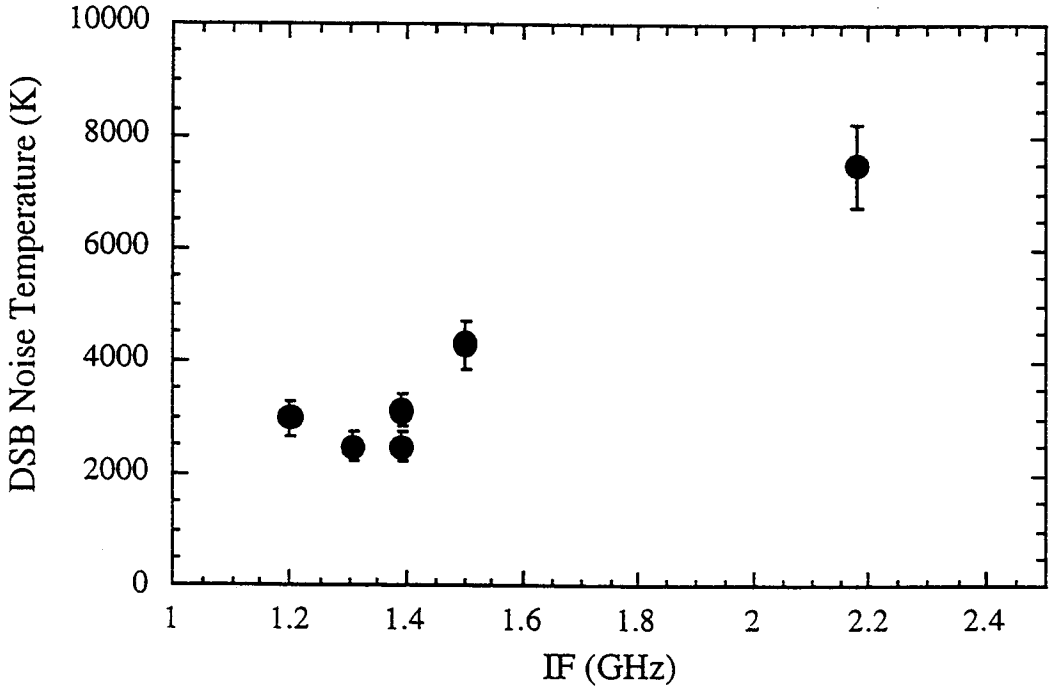

Fig. 9. The receiver noise temperature vs intermediate frequency.

CONVERSION LOSS OF A RESISTIVE STATE SUPERCONDUCTING MIXER

by

Orest Vendik, Electrotechnical University, St. Petersburg, Russia

Erik Kollberg, Chalmers University of Technology, Göteborg, Sweden

Abstract

We have investigated theoretically superconducting hot-electron type mixers operating in a frequency regime, where the signal and LO is below the bandgap frequency of the superconducting device. Then the signal and LO may see a device impedance that is modulated by the IF current, which leads to creation of an image current. Three cases are investigated: open and short-circuited image, and equal impedance at the signal and image frequency. We find that for open circuited image it is theoretically possible to obtain a conversion gain G = 0 dB, while for short-circuited image $G_{opt} \approx -7.7$ dB and for equal impedance at the signal and image frequency $G_{opt} \approx -4.7$ dB. These results can be compared to the optimum conversion gain of -6 dB for the classical bolometer mixer.

1. Introduction

Hot-electron bolometer (HEB) mixers utilising superconducting films in the resistive state [1-3], have a potential to offer low conversion loss and noise temperature from frequencies of a few GHz to several THz. Below about 700 GHz, the frequency approximately corresponding to the superconductor bandgap of niobium (Nb), Nb trilayer S-I-S mixers show unchallenged performance [4- 6]. Particular for frequencies above about one THz HEB mixers are predicted to have superior performance compared to any other type of mixer such as SIS and Schottky mixers.

However, also at lower microwave frequencies the superconducting resistive state mixer may be very useful. E. g. in a microwave system, that needs cooling e. g. in order to use superconducting narrow band low loss filters, it may be practical to have the mixer integrated in the same circuit. Besides low noise, a large dynamic range is often required. Both requirements can be fulfilled by choosing the device volume large enough, of requiring large enough LO power. Experiments at 20 GHz using HEB-devices made from thin and narrow strips of niobium, show excellent mixer performance, with a conversion loss < 6 dB and noise temperature of only a few hundred K [3].

The common theory of HEB mixers is essentially the same as the one presented in the early paper by Arams [7], originally developed for InSb type submillimeter wave bolometric mixers. The basic assumptions used in this theory may are not necessarily true for a superconducting HEB mixer, particularly not for "low frequency" operation. The theoretical work reported below has the Arams' results as a special case.

2. Approach to the mixer analysis

A superconducting HEB device (Fig. 1) normally consists of one superconducting strip with micrometer dimensions or smaller, which is deposited on a substrate of e. g. silicon, single crystalline quartz or sapphire. The strip is cooled to the superconducting state and then under the influence of DC and microwave power undergoes the transition to the resistive state, where the superconductor will gradually become normal.

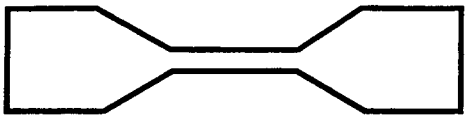

Fig.1 Layout of a typical bolometric superconducting thin film device.

The resistance of the device in the resistive state may be explained by several possible physical phenomena, such as formation of normal domains, phase slip centers, and moving magnetic vortices[1]. The DC and microwave currents transfer the electron subsystem of the device into a nonequilibrium state. It is common to describe these nonequilibrium electrons as hot electrons. In general, however, it is not possible to define a precise thermodynamic temperature of the electron subsystem, although we may consider an "effective electron temperature".

In designing a theory for mixing, we will discuss two cases, Case **A** when the signal frequency (f_S) and the local oscillator (LO) frequency is (f_{LO}) *larger* than the frequency corresponding to the quasiparticle bandgap ($2\Delta/h$) and Case **B** when the signal and the LO frequency is *lower* than $2\Delta/h$. These two cases are illustrated in Fig. 2. For both cases the response time of the device is related to the time constant τ, which determines decay rate of the excess energy absorbed by the heated electrons. The available maximum IF is determined by this relaxation time of the electrons, i. e. $f_{IF} < 1/(2\pi\tau)$ [3].

Case A:

In Arams' theory, which is applicable to Case **A** and commonly used to explain HEB-mixer conversion loss [7], it is assumed that when the LO and signal currents are added in the bolometer, the device is fast enough to respond to the difference frequency (IF) ($|f_{LO}-f_S|=f_{IF}$) power variation, but not to frequencies of the order the signal and the LO frequency. It is also assumed that the signal and LO device impedance is constant, i. e. not modulated by the IF signal. Since the device resistance at f_{LO} or f_S,is constant, there will of course be no generation of any high frequency harmonics $n\times f_{LO}$ or $n\times f_S$. The modulation of the dissipated power at the IF will cause a modulation of the electron temperature, causing a related resistance modulation (R(t)) noticeable at DC and at the IF. The DC bias current applied to the device will consequently cause a "DC" voltage modulation $I_{DC}\times R(t)$ at the IF and an IF signal can be extracted in a separate IF load resistance (see Fig. 3 below).

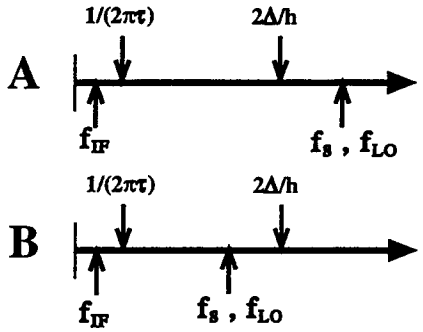

Fig. 2 The signal, local oscillator, and intermediate frequencies compared to the characteristic frequencies of the superconducting device. $1/(2\pi\tau)$ is the relaxation frequency of the electron subsystem of the device, $2\Delta/h$ is the bandgap frequency of the superconductor. For Case **A** the signal and LO resistance of the strip is equal to R_N, while in Case **B** the signal and LO resistance of the strip is modulated by f_{IF}.

[1]Note that the validity of the circuit-based model which we will present in the next section does not depend on the details of the microscopic model.

Case B:

However, for f_{LO}, $f_s < 2\Delta/h$ some parts of the strip will be superconducting also for the high frequency components(Fig. 2, Case **B**). In this case the superconducting bridge should be described as a resistor with a mean value of the resistance determined by the DC and LO power but complemented with a *modulation term at the IF*. The modulated resistor is interacting with all current components present, i.e. with the IF, LO, input and image signals. This is the case in several recent experimental mixers (Nb [3], NbN [2]). Particularly mixers based on HTS [8-11] with very high band gap frequencies case **B** of Fig. 2 should be dominating. Indeed for f_{LO}, $f_S<2\Delta/h$ the *Arams theory is not valid.*

It is known that development of the thermal domains in the superconducting film bridge can result in a negative dynamic resistance region of the *I-V* curve [3]. If negative resistance is available, it can be used for increasing the conversion gain, and even make it larger than one. This phenomenon will not be discussed here.

3. Modelling the resistance of the superconducting bridge

Assuming ohmic heating, proportional to the current squared ($I(t)^2$), to be a dominating physical reason for the resistance variations, we suggest the following simplistic equation for describing the current dependent resistance, i. e.

$$R(I(t)) = -R_0 + A_0\langle I(t)^2\rangle \tag{1}$$

The operator $\langle\ \rangle$ indicates an averaging of the total current squared over a time interval determined by the time constant τ of the bolometric device. The signal and LO frequency terms in the spectrum of $R(I(t))$ are suppressed, while the IF term is saved. The model we adopt for the current dependent resistance is further illustrated in Fig. 3. The solid line shows the DC and IF resistance vs. the sum of the high frequency and low frequency currents.

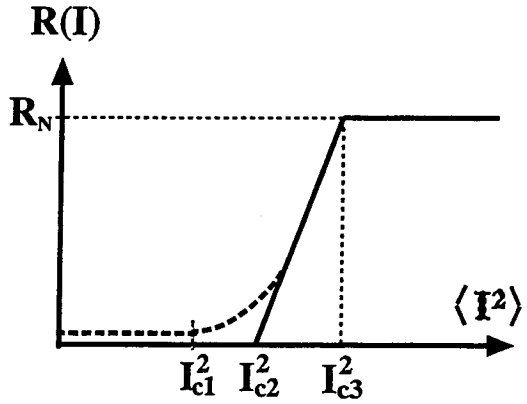

Fig. 3. The model assumes that the resistance of a the superconducting thin film bridge on the averaged depends on the square of the current. The solid line is the DC resistance. The dashed line shows the resistance experienced by the microwave current.

Thus, for DC *and* IF current one has:

$$R(I) = \begin{cases} 0 & for \quad \langle I^2\rangle \le I_{c,2}^2 \\ R_N \dfrac{\langle I^2\rangle - I_{c,2}^2}{I_{c,3}^2 - I_{c,2}^2} & for\ I_{c,2}^2 \le \langle I^2\rangle \le I_{c,3}^2 \\ R_N & for \quad I_{c,3}^2 \le \langle I^2\rangle \end{cases} \tag{2}$$

where R_N is the resistance of the bridge in the normal state.

We shall consider the case when the sum of DC and LO current squared is in the region $I_{c,2}^2 \le \langle I^2 \rangle \le I_{c,3}^2$. For this particular case $R(I)$ can be written as:

$$R(I) = -R_N \frac{I_{c,2}^2}{I_{c,3}^2 - I_{c,2}^2} + R_N \frac{1}{I_{c,3}^2 - I_{c,2}^2} \cdot \langle I^2 \rangle \tag{3}$$

Comparing (3) with the equation (1) gives:

$$R_0 = R_N \frac{1}{k^2 - 1}, \quad A_0 = \frac{R_N}{I_{c,2}^2} \cdot \frac{1}{k^2 - 1} = \frac{R_0}{I_{c,2}^2} \tag{4}$$

where

$$k = \frac{I_{c,3}}{I_{c,2}} \tag{5}$$

The coefficient k ($k > 1$) characterizes the slope of the resistive state characteristic.

The dashed line in Fig. 3 indicates the high frequency resistance of the superconducting bridge. The region between $I_{c,1}$ and $I_{c,2}$ has been investigated for NbN films at liquid helium temperature and was termed the potentialless (no DC resistance) resistive state [12]. To obtain mixing in the potentialless resistive state we must have a situation as shown in Fig. 2B, i. e. $1/(2\pi\tau) < f_s$, $f_{LO} < \Delta/h$.

4. Modelling the mixer.

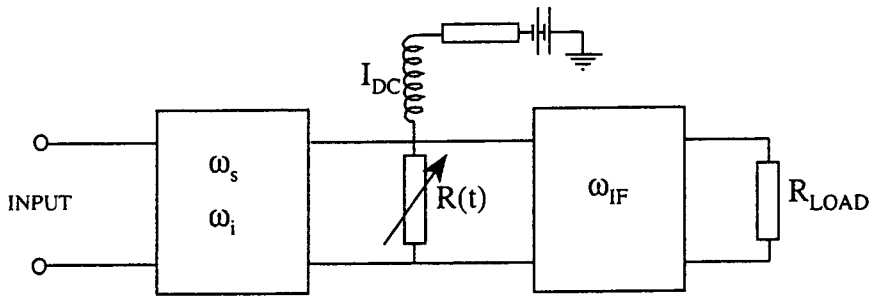

Fig. 4 Block diagram of the mixer.

Fig. 4 presents a block diagram of the mixer. Notice that the embedding impedances of the mixer may be different for the signal and the image frequency respectively.

The total current in the device is

$$I(t) = \underset{A}{I_{dc}} + \underset{B}{I_{LO}\cos\omega_{LO}t} + \underset{C}{I_s\cos\omega_s t} + \underset{D}{I_i\cos\omega_i t} + \underset{E}{I_{IF}\cos\omega_{IF}t} \tag{6}$$

where I_{dc}, I_{LO}, I_s, and I_{IF} are the DC, LO, signal, image and the intermediate frequency currents respectively. The capital letters A - E in equation (6) denotes the different terms and will be used below. The following relations between frequencies are assumed

$$\begin{aligned} \omega_{LO} + \omega_{IF} &= \omega_i \\ \omega_{LO} - \omega_{IF} &= \omega_s \end{aligned} \tag{7}$$

and we will use

$$\begin{aligned} I_{dc} \cong I_{LO} &>> I_s \cong I_i \cong I_{IF} \\ \omega_{LO} \cong \omega_s &\cong \omega_i >> \omega_{IF} \end{aligned} \tag{8}$$

For simplicity, let us suppose that the impedance with respect to all frequencies of the mixer current are real and consequently no phase shifts between current and voltage components take place. Substituting (6) into (1) and neglecting the high frequency terms (ω_{LO}, ω_i, ω_s) and the quadratic terms of the small signal current amplitudes (I_s^2, I_i^2, I_{IF}^2 etc.), one obtains:

$$R(t) = -R_0 + \underset{a}{A_0(I_{dc}^2 + 0.5I_{LO}^2)} + \underset{b}{A_0 I_{LO} I_S \cos\omega_{IF}t} + \underset{c}{A_0 I_{LO} I_i \cos\omega_{IF}t} + \underset{d}{2A_0 I_{dc} I_{IF} \cos\omega_{IF}t} \tag{9}$$

The small letters a - d defining the different terms in eq. (9) will be used for the discussion below. The voltage drop over the resistive bridge can now be calculated as $U(t)=R(t)\cdot I(t)$. The resulting frequency components are listed in Table 1.

TABLE 1

	U(t) = R(t) I(t) =	ω_s	ω_i	ω_{IF}
$a\times A$	$= R_B \cdot I_{dc} +$			
$a\times B$	$+ R_B \cdot I_{LO}\cos\omega_{LO}t +$			
$a\times C$	$+ R_B \cdot I_s \cos\omega_s t +$	+		
$a\times D$	$+ R_B \cdot I_i \cos\omega_i t +$		+	
$a\times E$	$+ R_B \cdot I_{IF}\cos\omega_{IF}t +$			+
$b\times A$	$+ A_0 \cdot I_{LO} I_s I_{dc} \cos\omega_{IF}t$			+
$b\times B$	$+ A_0 \cdot I_{LO} I_s I_{LO} 0.5(\cos\omega_s t + \cos\omega_i t) +$	+	+	
$b\times C$	0			
$b\times D$	0			
$b\times E$	0			
$c\times A$	$+ A_0 \cdot I_{LO} I_i I_{dc} \cos\omega_{IF}t$			+
$c\times B$	$+ A_0 \cdot I_{LO} I_i I_{LO} 0.5(\cos\omega_s t + \cos\omega_i t) +$	+	+	
$c\times C$	0			
$c\times D$	0			
$c\times E$	0			
$d\times A$	$+ 2A_0 I_{dc} I_{IF} I_{dc} \cos\omega_{IF}t +$			+
$d\times B$	$+ A_0 I_{dc} I_{IF} I_{LO}(\cos\omega_s t + \cos\omega_i t)$	+	+	
$d\times C$	0			
$d\times D$	0			
$d\times E$	0			

In the table the terms from the expressions (6) and (9), A, B, C, D, E and a, b, c, d are used. R_B is a constant resistance which is seen by the DC, IF, signal and LO currents and is equal to

$$R_B = -R_0 + A_0(I_{dc}^2 + 0.5I_{LO}^2) \tag{10}$$

Equating the terms of the frequency components ($\omega_s, \omega_i, \omega_{LO}$) to the corresponding voltage drops which appear over the resistance bridge, one obtains the following system of equations:

$$\begin{aligned} &\text{for } \omega_s && Z_{11}I_s + Z_{12}I_i + Z_{13}I_{IF} = U_s \\ &\text{for } \omega_i && Z_{21}I_s + Z_{22}I_i + Z_{23}I_{IF} = U_i \\ &\text{for } \omega_{IF} && Z_{31}I_s + Z_{32}I_i + Z_{33}I_{IF} = U_{IF} \end{aligned} \tag{11}$$

where

$$\begin{aligned} Z_{11} &= R_B + 0.5A_0I_{LO}^2 & Z_{12} &= 0.5A_0I_{LO}^2 & Z_{13} &= A_0I_{dc}I_{LO} \\ Z_{21} &= 0.5A_0I_{LO}^2 & Z_{22} &= R_B + 0.5A_0I_{LO}^2 & Z_{23} &= A_0I_{dc}I_{LO} \\ Z_{31} &= A_0I_{dc}I_{LO} & Z_{32} &= A_0I_{dc}I_{LO} & Z_{33} &= R_B + 2A_0I_{dc}^2 \end{aligned} \tag{12}$$

These equations reflect the fact that both the LO and signal see a resistance that is *modulated* by the IF current, causing new current and voltage components at $f_{LO} \pm f_{IF} = f_s$ or f_i, where $f_i = 2f_{LO} - f_s$ is the image frequency.

For additional information about the meaning of the resistance R_B see Appendix 2

5. Mixer performance for different image frequency load impedances

Let us suppose that the embedding impedance at the output (intermediate) frequency is R_L and at the image frequency is R_i. Then

$$U_{IF} = -R_L \cdot I_{IF}, \quad U_i = -R_i \cdot I_i \tag{13}$$

For convenience we introduce a factor b which we use to define R_i accordingly

$$R_i = b \times \frac{U_s}{I_s} \tag{14}$$

Three cases will be analysed:

b=∞	for opencircuited image
b=1	for equal impedance at the image and the short circuit
b=0	for shortcircuited image

Equation (11) can now rewritten in the form

$$\begin{aligned} Z_{11}I_s + Z_{12}I_i + Z_{13}I_{IF} &= U_s \\ Z_{21}I_s + \left(Z_{22} + b \times \frac{U_s}{I_s}\right)I_i + Z_{23}I_{IF} &= 0 \\ Z_{31}I_s + Z_{32}I_i + (Z_{33} + R_L)I_{IF} &= 0 \end{aligned} \tag{15}$$

where the elements Z_{ij} are defined above. It is possible to derive an expression for the input impedance U_S/I_S (see Appendix 1), allowing expressions for the signal, image and IF currents. Then it is possible to determine the input power P_s and the IF output power P_{IF} as

$$P_s = 0.5U_sI_s, \qquad P_{IF} = 0.5I_{IF}^2R_L. \tag{16}$$

The conversion gain is finally defined as

$$G = \frac{P_{IF}}{P_s} \tag{17}$$

5.1. Infinite impedance at the image frequency.($Z_i = \infty$)

For the special case when the image is terminated by an infinite impedance (b=∞, I_i=0), it is possible to find an analytical solution. Equation (11) is simplified to

$$\begin{aligned} Z_{11}I_s + Z_{13}I_{IF} &= U_s \\ Z_{31}I_s + (Z_{33} + R_L)I_{IF} &= 0 \end{aligned} \tag{18}$$

For the signal and IF current we get

$$I_s = U_s\left(Z_{11} - \frac{Z_{31}Z_{13}}{Z_{33}+R_L}\right)^{-1} \qquad I_{IF} = -I_s\frac{Z_{31}}{Z_{33}+R_L} \tag{19}$$

which together with (16) and (17) yields

$$G = \frac{Z_{31}^2 R_L}{(Z_{33}+R_L)\left(Z_{11}(Z_{33}+R_L) - Z_{13}Z_{31}\right)} \tag{20}$$

A maximum G is obtained for

$$R_L^{opt} = Z_{33}\cdot\sqrt{1-M} \tag{21}$$

where

$$M = \frac{Z_{31}^2}{Z_{22}Z_{33}}. \tag{22}$$

After some transformations one obtains the optimized conversion gain:

$$G^{opt} = \frac{1-\sqrt{1-M}}{1+\sqrt{1-M}} \tag{23}$$

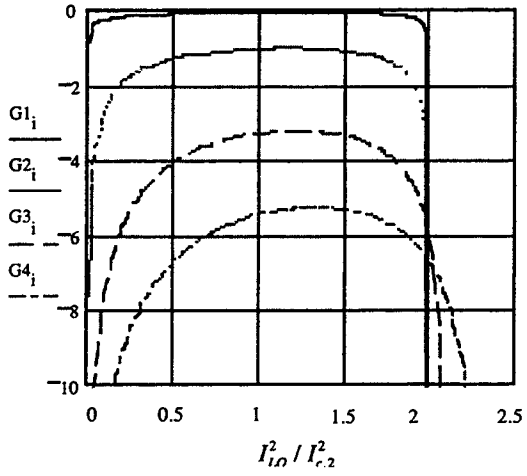

Fig. 5. Conversion gain (dB) for R_i=∞ vs. $I_{LO}^2 / I_{c,2}^2$ for α=1.00005, 1.005, 1.05 and 1.15 respectively.

For convenience we introduce the parameter α

$$\alpha = \left(I_{DC}^2 + 0.5I_{LO}^2\right) / I_{c,2}^2 \tag{24}$$

Notice that α is proportional to the total power absorbed and that it indicates the bias point in the R(I) vs. $\langle I^2 \rangle$ diagram, Fig. 4. In Fig. 5 is depicted G^{opt} vs. $I_{LO}^2 / I_{c,2}^2$ for different values of α. Notice that $I_{LO}^2 / I_{c,2}^2$ is proportional to the LO power.

The maximum conversion gain is obtained for $\alpha \rightarrow 1$, yielding the optimum value for $0.5 \cdot I_{LO}^2 / I_{c,2}^2$ of $2-\sqrt{2} = 0.5858$. This means that optimum performance is expected when the absorbed LO power is approximately equal to the DC power $\left(0.5\, I_{LO}^2 \equiv I_{dc}^2\right)$.

The impedance levels are as well of interest. In Table 2 below the impedances are normalized with respect to $R_0=R_N/(k^2-1)$ (see equation (3)), viz.

$$R_{L,opt} = \frac{U_{IF}}{I_{IF}} = r_L R_0 \qquad R_{s,opt} = \frac{U_s}{I_s} = r_s R_0 \qquad R_B = \frac{U_{DC}}{I_{DC}} = r_B R_0 \tag{26}$$

Table 2

r_B	$I_{LO}^2 / I_{c,2}^2$	G^{Opt} dB	r_S	r_L
0.00005	1.17	-0.105	0.00706	0.01002
0.005	1.19	-1.045	0.0711	0.1002
0.05	1.23	-3.216	0.233	0.330
0.15	1.34	-5.267	0.608	0.441

Notice that $r_B=\alpha-1$. Maximum conversion gain is obtained when the parameter $r_B \rightarrow 0$ and $\alpha \rightarrow 1$ while the signal and output impedances approaches zero ohms . This means that the mixer is operating with a very low power dissipation and practically without heating. The nature of the nonlinearity in this regime could be due to kinetic effects (depairing of Cooper pairs when the current slightly exceeds the critical value). This is an interesting difference as compared to the bolometric regime where heating is assumed.

5.2. Equal impedance at signal and image frequency ($R_i = R_s$)

For this case b =1. We have calculated the conversion gain vs. $I_{LO}^2 / I_{c,2}^2$ and for

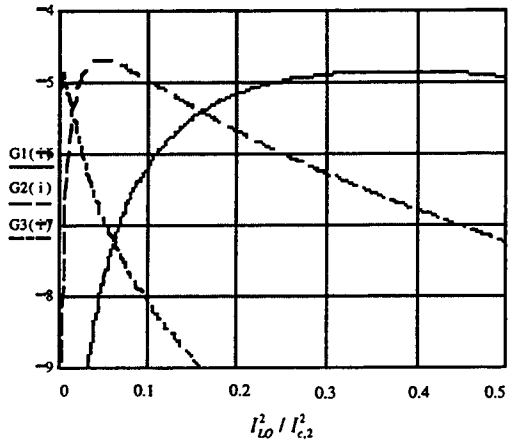

Fig. 6 Conversion gain (dB) vs. $I_{LO}^2 / I_{c,2}^2$ for α=1.00005 (r_B=0.00005), r_L=0.1, 0.01, 0.001 for G1(i), G2(i) and G3(i) respectively in the case of the equal signal and image frequency impedance. Maximum conversion gain is obtained approximately for r_L=0.01 (G2-curve) and $I_{LO}^2 / I_{c,2}^2$=0.05.

different load resistances r_L (see Fig 6). Note that the maximum conversion gain $\approx$ -4.7 dB is not strongly dependent on r_L. However, decreasing the IF load resistance r_L increases the conversion gain and requires lower LO power.

5.3. Zero impedance at image frequency ($R_i = 0$)

For shortcircuited image, the maximum gain is lower than for the opencircuited image, or for equal signal and image impedances. A maximum conversion gain of -7.7 dB is obtained when $\alpha \rightarrow 1$. The dependence on r_L is not so strong, and for r_B=0.00005 (α=1.00005) a value of 0.01 is close to optimum yielding a result for the conversion that is only moderately dependent on the LO power (Fig. 7).

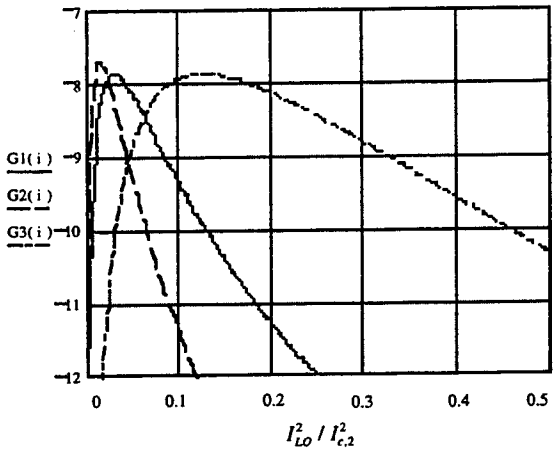

Fig. 7. Conversion gain (dB) vs. $I_{LO}^2 / I_{c,2}^2$ for α=1.00005 (r_B=0.00005), r_L= 0.1, 0.01, 0.001. The case of zero image frequency impedance. For G1(i), the $I_{LO}^2 / I_{c,2}^2$ scale is expanded by a factor of 20. Maximum conversion gain is obtained approximately for $I_{LO}^2 / I_{c,2}^2$=0.01 (G2-curve).

5.4. Discussion

In table 3 is shown the conversion gain for different values of r_l and optimized $I_{LO}^2 / I_{c,2}^2$.

Table 3: Optimum mixer performance for r_B=0.00005

	r_L=0.1				r_L=0.01				r_L=0.001			
	G_{max} dB	optim. $\frac{I_{LO}^2}{I_{c,2}^2}$	$\left(\frac{P_{LO}}{P_{DC}}\right)_{opt}$	$\frac{r_s}{r_B}$	G_{max} dB	optim. $\frac{I_{LO}^2}{I_{c,2}^2}$	$\left(\frac{P_{LO}}{P_{DC}}\right)_{opt}$	$\frac{r_s}{r_B}$	G_{max} dB	optim. $\frac{I_{LO}^2}{I_{c,2}^2}$	$\left(\frac{P_{LO}}{P_{DC}}\right)_{opt}$	$\frac{r_s}{r_B}$
R_i=∞	-0.276	0.26	0.149	142	-0.105	1.17	1.41	141	-0.276	1.86	13.2	141
R_i=Z_S	-4.85	0.005	0.0025	2.40	-4.69	0.05	0.026	2.48	-4.86	0.375	0.231	2.40
R_i=0	-7.87	0.0015	0.00075	1.42	-7.70	0.014	0.0070	1.41	-7.87	0.125	0.067	1.41

The reason why the maximum possible conversion loss is as high as 0 dB for opencircuited image, and as low as 7.7 dB for shortcircuited image is related to power loss μ $0.5R(t)\cdot I(t)^2$ in the bolometric resistance. The current $I(t)$ is larger for the short-circuited case than for the open-circuited case when I_i=0. Small r_B as compared to r_L and r_S indicate low losses in the device itself.

The formula for the conversion gain of the classical mixer as originally derived by Arams [7] is obtained assuming I_i=0 and R_S=R_i=R_B (see Appendix C). The classical

theory for the bolometric mixer yields an the optimum load impedance R_L is equal to $(dV/dI)_{DC}$ in the operating point, i. e. (much) larger than the R_B, and the optimum LO is small compared to the DC power (see reference [3], Fig. 4). According to Table 3, this is also a result of the present analysis. The analysis also shows that the optimum source impedance R_s is larger than the DC resistance R_B,

6. Taking Into Account the Intrinsic Microwave Loss of the Device

The largest conversion gain is obtained, if the effective current formed by the sum of DC and LO current squared is just larger than $I_{c,2}^2$. The intrinsic microwave resistance of the bridge is presented by the dashed line in Fig. 3. We now assume that this additional resistance of the bridge is the microwave resistance of the bridge when it is in the superconducting equilibrium state. Hence, we suggest the following approximation for this intrinsic microwave resistance R_{MW} and the normal resistance of the bridge R_N,

$$R_{MW} = R_{MW,SUR} \cdot \frac{l}{w} \qquad R_N = R_{N,SUR} \cdot \frac{l}{w} \tag{27}$$

where $R_{MW,SUR}$ is the microwave surface resistance of the film in the superconducting state, and $R_{N,SURF}$ is the surface resistance of the film in normal state. l and w are the length and the width of the bridge respectively. The loss related to R_{MW} is due to a voltage redistribution over a series connected resistance. Thus a corrected conversion gain can by written as follows:

$$G^{cor} = G^{opt} \cdot \frac{R_{s,opt}}{R_{s,opt} + R_{MW}} = G^{opt} \cdot \frac{1}{1 + \frac{\delta}{r_s}} \tag{28}$$

where

$$\delta = \frac{R_{MW}}{R_N} \cdot (k^2 - 1) \tag{29}$$

δ is a phenomenological parameter responsible for the contribution of the intrinsic microwave resistance of the bridge. For f =10 GHz we may estimate the microwave surface resistance of a superconducting film to be $R_{sur} = 10^{-3}$ Ohm/□ and the normal state film resistance to R_N =1 Ohm/□ . For l/w = 5 and k = 1.4 we then have $\delta = 10^{-3}$. In Table 4, we have calculated the corrected mixer gain for R_L/R_0=0.01, R_B/R_0=0.0005. and $\delta = 10^{-3}$.

Table 4: Correction of the conversion gain for r_L=0.01, r_B=0.0005. and $\delta = 10^{-3}$

	r_S	G^{cor}/G^{opt}	$(G_{max})^{cor}$ dB
$R_i = \infty$	0.07	0.98	-0.2
$R_i = R_S$	0.0012	0.55	-7.3
$R_i = 0$	0.0007	0.42	-11.5

Notice that in practice a conversion gain below -3 dB should be possible to achieve. However, the impedance levels may be quite low. For R_0=5 Ohm we have R_S=0.35 Ohm and R_L=0.05 Ohm.

7. Conclusion

A microwave mixer based on a superconducting bridge partly in a resistive state has been investigated assuming that the signal and the LO frequency is below the quasiparticle bandgap frequency. In our model, the resistance of the superconducting film is dependent on the current squared and is inertial with respect to the signal and LO frequencies. The mixer circuit is assumed matched at the signal input and intermediate frequency output.

We found that the conversion gain can be as low as -4.7 dB for equal embedding resistance at the signal and image frequency. The conversion gain improves and approaches 0 dB if R_i->∞. However, if the image is shortcircuited, the conversion gain goes down and is only about -7.7 dB as best. These differences are due to the losses in the device itself. Maximum gain is obtained operating the mixer as close to the critical current $I_{c,2}$ as possible, which also means that the input and output impedances are very low. Adding the microwave losses to the model suggests that the bias current should be increased. The ordinary Arams' case is a special case of the theory presented above.

The case **B**, corresponding to when the signal and the LO frequency is below the quasi particle bandgap frequency, is in practice valid only for comparatively "low" frequencies. What this means in practice is not known in detail. At "ordinary" microwave frequencies this case must be seriously considered, and for mixers using high temperature superconductors the upper limiting frequency may well be at several hundred GHz.

At "ordinary" microwave frequencies it should be possible to design a circuit preventing any image frequency current. A couple of interesting engineering problems can be identified: **i.** how to develop a device (thin film bridge) with an as large as possible nonlinearity and with low intrinsic microwave loss,es and **ii.** how to design impedance transforming circuits with very low intrinsic loss. The first problem is probably the more difficult, while the second problem for reasonably low frequencies can be solved using a superconducting matching circuit.

8. Acknowledgements

The authors would like to acknowledge Prof. Sigfrid Yngvesson for his useful remarks. We as well would like to thank for financial support from the Swedish Royal Academy of Sciences and the Swedish National Board for Industrial Research.

References

[1] E.M.Gershenzon et al, "Millimeter and Submillimeter Range Mixer Based on Electronic Heating of Superconducting Films in the Resistive State", *Sov.Phys.Superconductivity*, 3, pp.1582-1597, 1990.

[2] B.S. Karasik, G.N. Gol'tsman, B.M. Voronv, S.T. Svechnikov, E.M.Gershenzon, H. Ekström, S. Jacobsson, E. Kollberg, and K.S. Yngvesson,"Hot Electron Quasioptical NbN Superconducting Mixer", *IEEE Trans. Appl. Supercond.*, vol. 5, pp. 2232-2235, 1995

[3] H. Ekström, B. Karasik, E. Kollberg, and K.S. Yngvesson, "Conversion Gain and Noise of Niobium Hot - Electron Mixer", IEEE Trans. on MTT, vol. MTT-43, N0. 4, pp. 938 - 947, 1995

[4] R. Blundell, C.E. Tong, "Submillimeter Receivers for Radio Astronomy," *Proc. IEEE*, vol. 80, pp.1702-1720, 1992.

[5] J.Mees, et al, "An Airborne SIS-Receiver for Atmospheric Measurements at 630 and 720 GHz", *Proceedings of the Fifth International Symposium on Space Terahertz Technology*, 1994

[6] Zimmermann R&R&P, "All solid state radiometers for environmental studies to 700 GHz," *Proceedings of the Third International Symposium on Space Terahertz Technology*, pp. 706-723, 1992.

[7] F.Arams, et al., "Millimeter Mixing and Detection in Bulk InSb", *Proc. IEEE*, vol. 54, pp.308-318, 1966.

[8] H. Chaloupka, M. Jeck, S.G. Kolesov, O.G. Vendik, " Frequency Conversion in High-Tc Superconductor Microwave Circuits", *Proc. of 22nd European Microwave Conference*, v.1, pp. 189-194, 1992.

[9] T.B. Samoilova, "Nonlinear Microwave Effects in Thin Superconducting Films", *Supercond. Sci. Technol.*, vol. 8, pp. 259-277, 1995.

[10] J.Wang, D.P. Butler, Z. Celik-Butler, " Modeling of High Tc Superconductor Parametric Amplifiers and Mixers", *Physica C*, vol. 231, pp. 271-276, 1994.

[11] M. Jeck et al. Investigation of Electrical Nonlinearity of HTS Thin fFlms as Applied to Realization of a Microwave IC Mixer", *Journal of Superconductivity*, vol. 8, No. 6, pp. 705-714, 1995

[12] A.B. Kozyrev et al. "Destruction of the Superconductive State in Thin Film by Microwave Pulses", *Solid State Commun.*, vol. 77, No. 6, pp. 441-445, 1991.

Appendix 1: Calculation of the signal, image and if currents.

$$I_s = \frac{U_s}{\Delta}\left[\left(Z_{22} + b\frac{U_s}{I_s}\right)(Z_{33} + R_L) - Z_{23}Z_{32}\right] \tag{A1.1}$$

$$I_i = \frac{U_s}{\Delta}\left[Z_{21}(Z_{33} + R_L) - Z_{23}Z_{31}\right] \tag{A1.2}$$

$$I_{IF} = \frac{U_s}{\Delta}\left[Z_{21}Z_{32} - \left(Z_{22} + b\frac{U_s}{I_s}\right)Z_{31}\right] \tag{A1.3}$$

$$\begin{aligned}\Delta = Z_{11}&\left[\left(Z_{22} + b\frac{U_s}{I_s}\right)(Z_{33} + R_L) - Z_{23}Z_{32}\right] - Z_{12}\left[Z_{21}(Z_{33} + R_L) - Z_{23}Z_{31}\right] + \\ &+ Z_{13}\left[Z_{21}Z_{32} - \left(Z_{22} + b\frac{U_s}{I_s}\right)Z_{31}\right] = a_1 + b\frac{U_s}{I_s}a_2\end{aligned} \tag{A1.4}$$

From (A1.1) and (A1.4) we get a second degree equation:

$$a_1 + b\frac{U_s}{I_s}a_2 - \frac{U_s}{I_s}(Z_{22}Z_{33} + Z_{22}R_L - Z_{23}Z_{32}) - b\left(\frac{U_s}{I_s}\right)^2(Z_{33} + R_L) = 0 \tag{A1.5}$$

From (A1.5) we obtain the input impedance U_S/I_S. Hence, by inserting U_S/I_S into (A1.1)-A(1.4) the currents I_S, I_i, and I_{IF} can now be calculated.

Appendix 2. Deriving the I - V curve from the model of the current dependent resistor.

Using (10) the expression for DC I - V characteristics of the nonlinear resistor can be written as:

$$U_{dc} = R_B \cdot I_{dc} = -R_0 I_{dc} + A_0 \cdot I_{dc}^3 + 0.5A_0 \cdot I_{LO}^2 I_{dc} \qquad \text{(A2.1)}$$

We get

$$\left(\frac{dU}{dI}\right)_{dc} = -R_0 + 3A_0 \cdot I_{dc}^2 + 0.5A_0 \cdot I_{LO}^2 . \qquad \text{(A2.2)}$$

Substituting (4) into (A2.1) one obtains

$$U = \frac{R_N I_{c,2}}{k^2 - 1}\left(0.5\frac{I_{LO}^2}{I_{c,2}^2} + \frac{I_{dc}^2}{I_{c,2}^2} - 1\right) \cdot \frac{I_{dc}}{I_{c,2}} . \qquad \text{(A2.3)}$$

The same in normalized form:

$$z = (x^2 + 0{,}5y^2 - 1) \cdot x \qquad \text{(A2.4)}$$

where

$$x = \frac{I_{dc}}{I_{c,2}}, \qquad y = \frac{I_{LO}}{I_{c,2}}, \qquad z = \frac{U}{R_N I_{c,2} / (k^2 - 1)} . \qquad \text{(A2.5)}$$

Fig. A2.1 shows the normalized I - V curves for different values of the LO power. Qualitatively the curve obtained are in agreement with the known form of pumped I - V curves (see e. g. [9]).

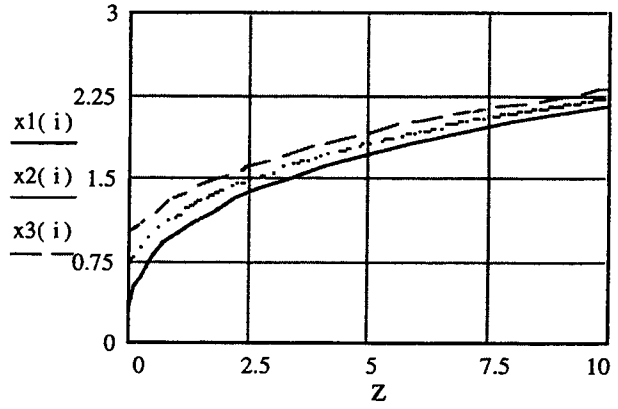

Fig. A2.1 IV curves (x1, x2 and x3) calculated using equation A2.4 for $0.5y^2$=1, 0.5 and 0 respectively..

Appendix 3. Comparison with Arams' theory for bolometric mixers.

In order to find the equivalence of the Arams' theory, we must arrange the model so that the signal and LO power absorbed have the same effect on the nonlinear resistance as the IF power. This leads to the conclusion that we should use R_B as the device impedance for LO, signal and DC currents. If we do so, we can transform (10) - (12) into the following simplified system.

$$\begin{aligned} R_B \cdot I_s &= U_s \\ A_0 \cdot I_{dc} I_{LO} I_s + (R_B + 2A_0 \cdot I_{dc}^2) I_{IF} &= U_{IF} \end{aligned} \tag{A3.1}$$

Introducing the load resistance ($U_{IF} = -R_L \cdot I_{IF}$) we obtain :

$$I_{IF} = I_s \cdot \frac{A_0 \cdot I_{dc} I_{LO}}{R_B + 2A_0 \cdot I_{dc}^2 + R_L} \tag{A3.2}$$

which together with (A2.2) leads to

$$G = (A_0 \cdot I_{dc} I_{LO})^2 \cdot \frac{R_L}{R_B} \left(\left(\frac{dU}{dI} \right)_{DC} + R_L \right)^{-2} \tag{A3.3}$$

The gain of the ordinary bolometric mixer can be expressed as (see Eq. (5) of reference [3]):

$$G = \frac{1}{2} \frac{P_{LO}}{P_{DC}} \frac{R_L}{R_B} \left(1 - \frac{R_B}{(dU/dI)_{DC}} \right)^2 \left(1 + \frac{R_L}{(dU/dI)_{DC}} \right)^2 \tag{A3.4}$$

Assuming that

$$P_{DC} = R_B \cdot I_{DC}^2 \qquad P_{LO} = \frac{1}{2} R_B \cdot I_{LO}^2 \tag{A3.5}$$

and using (A2.2) and (10) to develop the terms within the parenthesises of (A3.4), equation (A3.4) can be transformed into the same form as Eq. (A3.3).

ANALYSIS OF THE BANDWIDTH PERFORMANCE OF SIS MIXERS WITH DISTRIBUTED JUNCTION ARRAYS

Sheng-Cai Shi, Takashi Noguchi, and Junji Inatani

Nobeyama Radio Observatory
National Astronomical Observatory of Japan
Nobeyama, Minamisaku, Nagano, 384-13 Japan
E-mail: shencai@nro.nao.ac.jp; noguchi@; intani@

ABSTRACT: In this paper, the bandwidth performance of the distributed junction array, i.e., a number of junctions connected in parallel with a tuning inductance separating every two junctions, is theoretically investigated. The small-signal equivalent circuit model of the distributed junction array is constructed in a general form of multi-sideband frequency ports in order to employ the quantum theory of mixing. Detailed simulation results are presented.

I. INTRODUCTION

Broadband SIS-junction devices are of benefit in developing tuneless or fixed-tuned mixers that are highly desirable at submillimeter wavelengths and for complex systems such as multibeam receivers and interferometer arrays. Typically, submillimeter SIS mixers use junctions of a relatively large $\omega R_n C_j$ product (say 4), as far as the junction's critical current density (J_c), which is limited to around 10 kA/cm^2 for Nb junctions, is concerned. The bandwidth of such SIS mixers is governed mainly by the $\omega R_n C_j$ product, i.e., approximately the Q-factor of the resonance circuit tuning out the junction capacitance. Recently, Tong et al. [1] proposed a junction device made of a nonlinear thin-film transmission line, which has demonstrated encouraging performance (less J_c-independence, large bandwidth, and low noise). Such a type of junction, however, has a very small line-width (~0.1 μm), requiring the electron-beam lithograph for the junction fabrication.

Here we propose another type of junction device, i.e., the distributed junction array made up of a number of junctions connected in parallel with a tuning inductance separating every two junctions. In practice, the distributed junction array is the extension of conventional twin-junction devices [2-3].

II. THEORETICAL MODEL OF DISTRIBUTED JUNCTION ARRAYS

The distributed junction array, as illustrated in Fig. 1, appears like a lossy transmission line as a single junction can be approximately regarded as the parallel combination of a resistance and capacitance. It has only a single port, feeding both the RF and LO signals. All the junctions in such an array are dc-biased at the same voltage. While an LO signal is applied,

however, the SIS junctions must be impressed by different LO voltages (in both amplitude and phase, appearing frequency dependent) due to the phase shift by the tuning inductance, thereby having different small-signal characteristics. Nevertheless, it would be straightforward to simulate the mixing behavior of distributed junction arrays using the quantum theory of mixing, while their equivalent conversion admittance and noise correlation matrices are constructed. A method similar to that in [2-3] is adopted here.

II.a LO-voltage distribution

To understand the distribution of the LO voltage in a distributed junction array, strictly speaking, it is necessary to carry out a large-signal analysis. Here we employ a simple method, i.e., assuming a sinusoidal LO voltage applied to each junction, as it has been very effective in simulating SIS mixers, especially for those using SIS junctions of a considerably large capacitance (a typical case for submillimeter SIS mixers).

Fig. 2 demonstrates an equivalent circuit for the k-th SIS junction of an N-junction array, including its preceding tuning inductance that is described by a chain matrix $[C]^p$ at the LO frequency ω_p. The LO voltage and current at port $(k\text{-}1)$ (V_p^{k-1}, I_p^{k-1}), i.e., the LO voltage applied to and the LO current flowed out of the $(k\text{-}1)$-th junction, can be written

$$V_p^{k-1} = C_{11,p}V_p^k + C_{12,p}\left[I_p^k + I_{j,p}^k + j\omega_p C_j V_p^k\right] \tag{1}$$

$$I_p^{k-1} = C_{21,p}V_p^k + C_{22,p}\left[I_p^k + I_{j,p}^k + j\omega_p C_j V_p^k\right] \tag{2}$$

where V_p^k and I_p^k denotes the LO voltage and current at port k, respectively, $I_{j,p}^k$ is the LO current induced in the k-th junction (only its intrinsic branch, given by Eq. (4.41) in [4]), C_j is the single-junction's geometric capacitance, and $C_{11,p}$, $C_{12,p}$, $C_{21,p}$, and $C_{22,p}$ are the elements of the chain matrix $[C]^p$. Notice that I_p^k is equal to zero while k=N (i.e., at the last junction). Apparently the LO voltage developed to each junction can be calculated using Eqs. (1-2), once the LO voltage across the last junction, V_p^N, is determined (actually optimized for the SIS mixer performance).

II.b Equivalent conversion admittance matrix

Fig. 3a shows the equivalent circuit of the k-th junction at the m'-th sideband, including its shot-noise current source and an equivalent one representing the shot noise due to all the following junctions. It is assumed that only the small-signal voltage at the m'-th sideband (i.e., $\omega_{m'} = m'\omega_p + \omega_0$, here ω_0 is the IF frequency), $V_{m'}$, is developed to this junction, according to the definition of the conversion admittance matrix

$$Y_{mm'} = \left.\frac{I_m}{V_{m'}}\right|_{V_j=0,\, j\neq m'}, \quad m, m' = \cdots, -2, -1, 0, 1, 2, \cdots \tag{3}$$

where I_m is the small-signal current induced at the m-th sideband (i.e., $\omega_m = m\omega_p + \omega_0$). Let us first omit those noise current sources. The small-signal voltage at port (k-1) at the m'-th sideband is therefore given by

$$V_{m'}^{k-1} = C_{11,m'}V_{m'}^{k} + C_{12,m'}\left[I_{m'}^{k} + I_{j,m'}^{k} + j\omega_{m'}C_jV_{m'}^{k}\right] \tag{4}$$

and the small-signal current at port (k-1) induced at the m-th sideband by

$$I_{m}^{k-1} = C_{21,m}V_{m'}^{k}\delta_{mm'} + C_{22,m}\left[I_{m}^{k} + I_{j,m}^{k} + j\omega_{m}C_jV_{m'}^{k}\delta_{mm'}\right] \tag{5}$$

Replacing the junction (intrinsic branch) currents $I_{j,m'}^{k}$ and $I_{j,m}^{k}$ with $Y_{m'm'}^{k}V_{m'}^{k}$ and $Y_{mm'}^{k}V_{m'}^{k}$ respectively, and small-signal currents $I_{m'}^{k}$ and I_{m}^{k} with $Y_{m'm',e}^{k}V_{m'}^{k}$ and $Y_{mm',e}^{k}V_{m'}^{k}$, into (4) and (5) and using (3), give the elements of the equivalent conversion admittance matrix at port (k-1), $[Y_e^{k-1}]$

$$Y_{mm',e}^{k-1} = \frac{C_{21,m}\delta_{mm'} + C_{22,m}\left[Y_{mm',e}^{k} + Y_{mm'}^{k} + j\omega_{m}C_j\delta_{mm'}\right]}{C_{11,m'} + C_{12,m'}\left[Y_{m'm',e}^{k} + Y_{m'm'}^{k} + j\omega_{m'}C_j\right]} \tag{6}$$

where $[Y^k]$ and $[Y_e^k]$ are designated as the k-th junction's conversion admittance matrix (defined by QTM [4] for the corresponding LO voltage, including the LO-voltage phase effect [2-3]) and the equivalent conversion admittance matrix at port k, respectively. Notice that $Y_{mm',e}^{N} = 0$ and $Y_{mm',e}^{0}$ represents the elements of the array's equivalent conversion admittance matrix.

II.c Equivalent noise correlation matrix

In terms of the theory of noisy fourpoles [5], the two shot-noise current sources in Fig. 3a can be described by a noise-voltage source $E_{m'}^{k-1}$ and a noise-current source $I_{m'}^{k-1}$ in parallel with the input admittance seen before the chain matrix (refer to Fig. 3b). The magnitudes of the two equivalent noise sources are expressed as

$$E_{m'}^{k-1} = C_{12,m'}\left(I_{s,m'}^{k} + I_{se,m'}^{k}\right) \tag{7}$$

$$I_{m'}^{k-1} = C_{22,m'}\left(I_{s,m'}^{k} + I_{se,m'}^{k}\right) \tag{8}$$

The total short-circuit noise current at port (k-1) at the m'-th sideband is therefore written

$$\begin{aligned} I_{se,m'}^{k-1} &= E_{m}^{k-1}Y_{in,m'}^{k-1} - I_{m'}^{k-1} \\ &= \left(C_{12,m'}Y_{m'm',e}^{k-1} - C_{22,m'}\right)\left(I_{s,m'}^{k} + I_{se,m'}^{k}\right) \end{aligned} \tag{9}$$

The correlation matrix of this equivalent noise-current source has elements of this form

$$H_{mm',e}^{k-1} = C_{e,m}C_{e,m'}^{*}\left[H_{mm'}^{k} + H_{mm',e}^{k}\right] \tag{10}$$

where $H^k_{mm'}$ and $H^k_{mm',e}$ are the elements of the k-th junction's shot-noise correlation matrix (defined by QTM [4] for the corresponding LO voltages, including the LO-voltage phase effect [2-3]) and of the equivalent shot-noise correlation matrix at port k, respectively, and $C_{e,m}$ is a transfer factor defined as

$$C_{e,m} = C_{12,m} Y^k_{mm,e} - C_{22,m} \tag{11}$$

It should be pointed out that $H^N_{mm',e} = 0$, and that $H^0_{mm',e}$ and the thermal-noise component at port *0* combine the total noise correlation matrix for the distributed junction array.

III. Simulation Results and Analyses

Using the quantum theory of mixing, together with the equivalent circuit model established above, we have simulated the mixing behavior of the distributed junction array in the frequency range of 100~1000 GHz for three examples of two (a particular case, i.e., twin-junction device), eight, and sixteen junctions, respectively. All the junctions were assumed to have the same critical current density as 3 kA/cm^2 (relatively low for Nb junctions) that corresponds to a $\omega R_n C_j$ product of about eleven at 500 GHz. Therefore, a sharp junction I-V curve of a quality factor of around 35 mV was employed in the simulation. The tuning inductance (L) was studied for three different values, having $\omega L/R_n$ @ 500 GHz equal to .117, .192, and .258 (around its resonance value at 500 GHz) for the twin-junction array but equal to .042, .067, and .092 for the eight- and 16-junction arrays. Assumed a pure resistance and to be identical at all the frequencies, the RF and IF terminations for the three examples had normalized (to the junction array's equivalent normal-state resistance, i.e., R_n/N, here N is the junction number) values of one and ten, respectively. Note that quite a large IF termination was used in conjunction with small values of the junction array's equivalent normal-state resistance (typically of order of several ohms) and the intention of neglecting an IF impedance transformer.

Figs. 4-6 demonstrate the simulated mixer noise temperature and conversion gain for the three examples, respectively. Note that at each frequency the dc-bias and the LO (at the last junction) voltages were optimized for the receiver noise temperature by assuming an IF noise temperature of 10 K. Obviously, with the increase of the junction number, the overall bandwidth performance of the distributed junction array is improved immensely and becoming less insensitive to the tuning inductance. In comparison to the mixer conversion gain, however, the mixer noise temperature degrades rapidly at certain frequencies that may differ according to the junction number, the $\omega R_n C_j$ product, and the tuning inductance. It has been found that these frequencies actually correspond to the minima of the optimized LO voltage seen before the junction array, just as exhibited in Fig. 6b. Increasing the tuning inductance is helpful to the reduction of this fluctuation, but for arrays of a large number of junctions too large an inductance would deteriorate the mixer performance considerably at high frequencies.

Regarding the local bandwidth (i.e., one between two singular frequencies), which is supposed to be of frequency independence according to a constant J_c, it simply decreases with the increase either of frequency or of the junction number. For arrays of the same junction number the smaller the tuning inductance is, the larger local bandwidths become.

Another 16-junction array of the critical current density equal to 6 kA/cm^2, which doubles the one examined before, has also been investigated. The simulation results are displayed in Fig. 7. Apparently the frequency response of the mixer noise temperature is improved in comparison to that in Fig. 6a, while that of the mixer conversion gain is very similar.

It has been concluded that the distributed junction array's bandwidth can be enlarged by increasing either the junction number or the critical current density. The latter, however, is clearly of no benefit in fabricating SIS junctions. And for both cases, the array's input impedance would be reduced so as to make it difficult to match the RF termination. Keeping these in mind, we suggest that the junction number N and critical current density J_c are chosen according to a fixed NJ_c product (say 35 kA/cm^2). Regarding the optimum tuning inductance, it is not so critical for arrays of a large number of junctions and may be determined in terms of the relation, $\omega L/R_n$=0.07 (at 500 GHz).

IV. SUMMARY

The mixing behavior of the distributed junction array has been theoretically investigated. Its bandwidth performance can be improved considerably using a large number of junctions (e.g., >10), and appears insensitive to the tuning inductance in comparison to the case of a single junction. One example, assuming sixteen Nb junctions of the critical current density as low as 3 kA/cm^2, has demonstrated a mixer conversion gain (SSB) of −3.5~−7.5 dB and a mixer noise temperature (SSB) varying from 15 to 150 K over the frequency range of 100~1000 GHz. Hence distributed junction arrays, even composed of very low-J_c junctions, should be of good use for submillimeter-wave SIS mixers.

ACKNOWLEDGMENT

Authors thank Jonas Zmuidzinas for valuable discussions.

REFERENCE

[1] C.E. Tong, R. Blundell, B. Bumble, J.A. Stern, and H.G. LeDuc, "Quantum limited heterodyne detection in superconducting non-linear transmission lines at sub-millimeter wavelengths," *Appl. Phys. Lett.*, vol. 67, pp. 1304-1306, Aug. 1995.

[2] J. Zmuidzinas, H.G. LeDuc, J.A. Stern, and S.R. Cypher, "Two-junction tuning circuits for submillimeter SIS mixers," *IEEE Trans. Microwave Theory Tech.*, vol. 42, no. 4, pp. 698-706, 1994.

[3] T. Noguchi, S.C. Shi, and J. Inatani, "Parallel connected twin junctions for millimeter and submillimeter wave SIS mixers: analysis and experimental verification," *IEICE Trans. Electronics*, vol. E78-c, no. 5, pp. 481-489, May 1995.

[4] J. R. Tucker and M.J. Feldman, "Quantum detection at millimeter wavelengths," *Rec. Mod. Phys.*, vol. 57, no. 4, pp. 1055-1113, Oct. 1985.

[5] H. Rothe and W. Dahlke, "Theory of noisy fourpoles," *Proc. IRE*, vol. 44, pp. 811-818, June 1956.

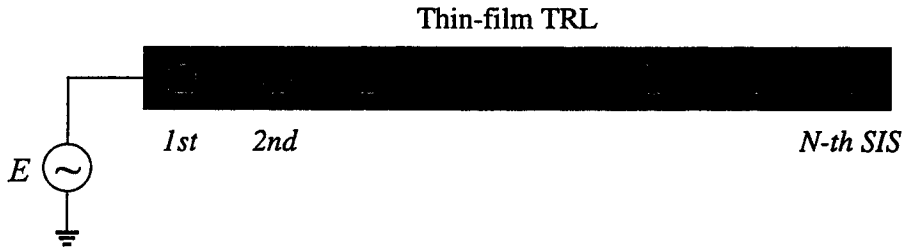

Fig. 1 Schematic of the distributed junction array composed of N junctions. Every two junctions are seperated by a tuning inductance.

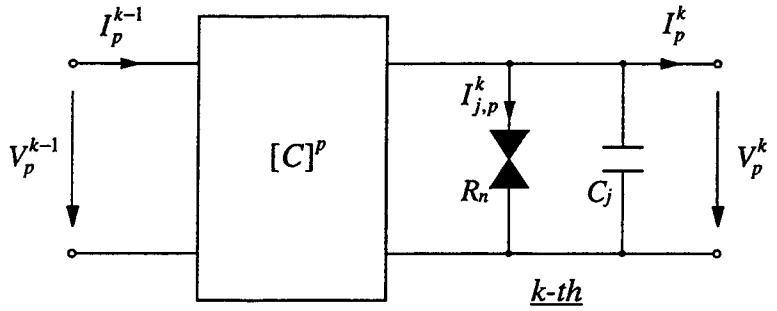

Fig. 2 LO equivalent circuit for the k-th junction and its preceding tuning inductance (described by a chain matrix [C]).

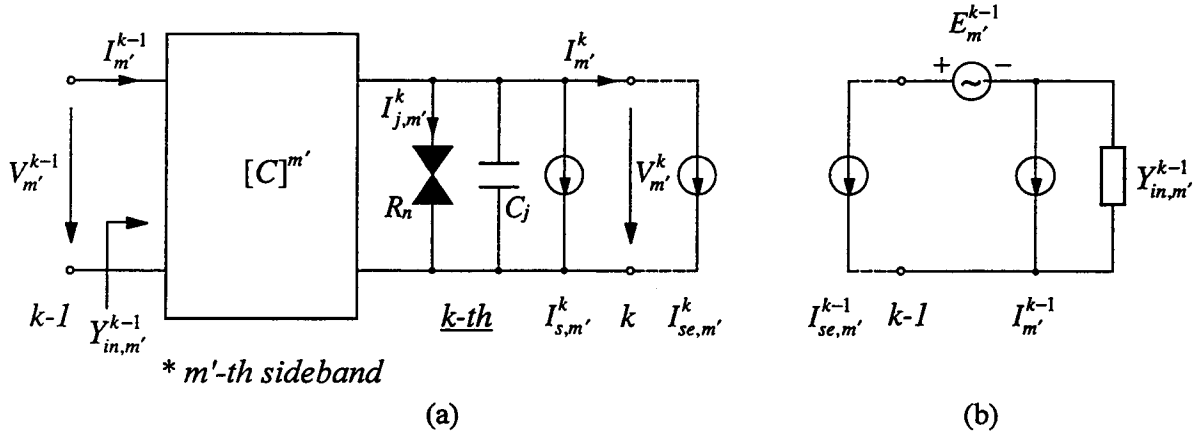

Fig. 3 (a) Small-signal equivalent circuit for the k-th junction and its preceding tuning inductance at the m'-th sideband. (b) Noise equivalent circuit at port (k-1), representing all the shot noise sources due to the k-th and following junctions.

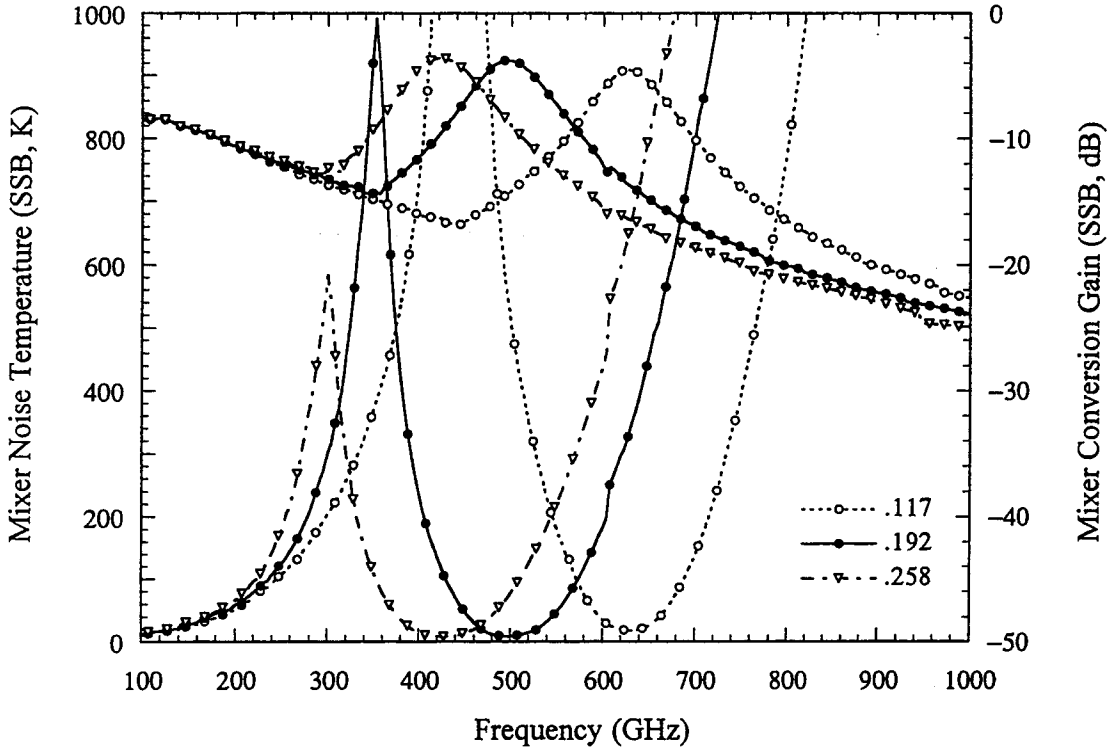

Fig. 4 Simulated mixer noise temperature and conversion gain for a twin-junction (J_c=3kA/cm2) array, as a function of frequency. Results are shown for three inductances (wL/R_n at 500 GHz).

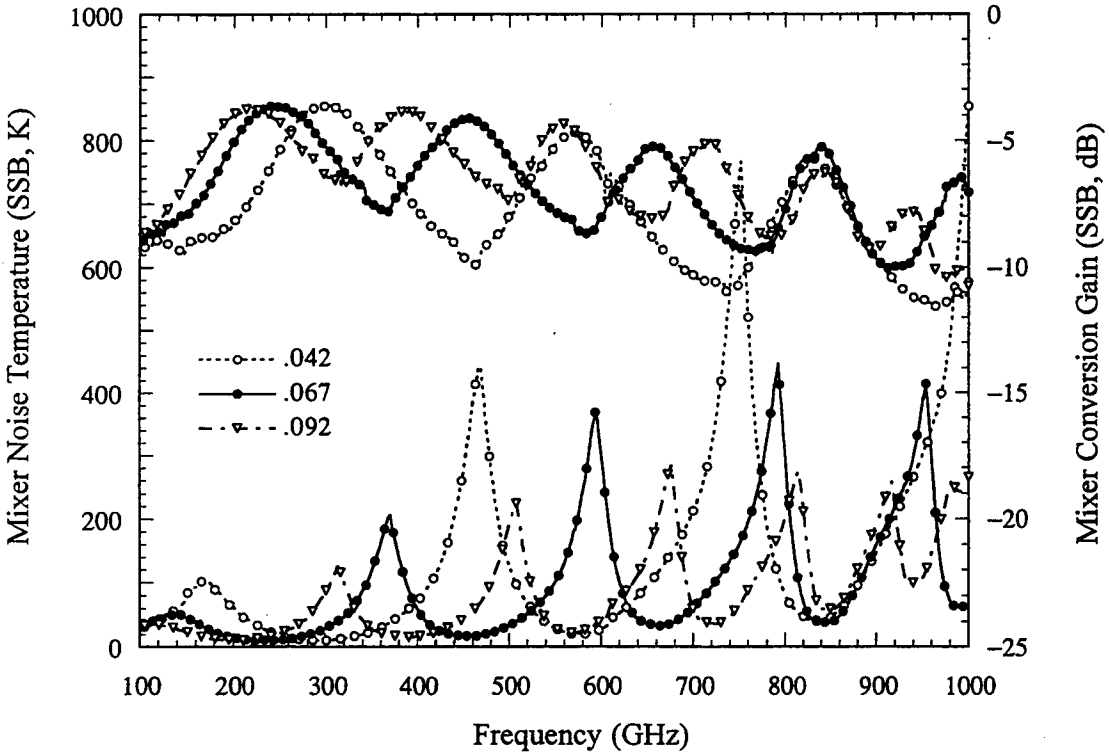

Fig. 5 Simulated mixer noise temperature and conversion gain for a 8-junction (J_c=3kA/cm2) array, as a function of frequency. Results are shown for three inductances (wL/R_n at 500 GHz).

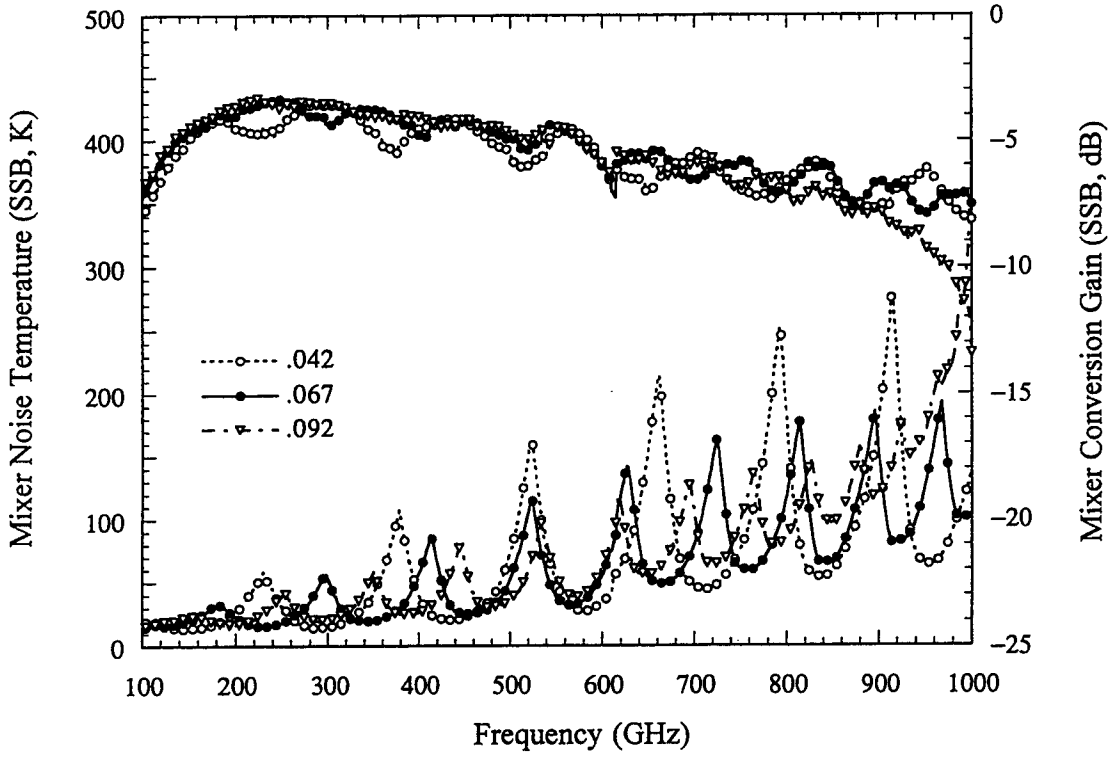

Fig. 6a Simulated mixer noise temperature and conversion gain for a 16-junction (J_c=3kA/cm2) array, as a function of frequency. Results are shown for three inductances (wL/R_n at 500 GHz).

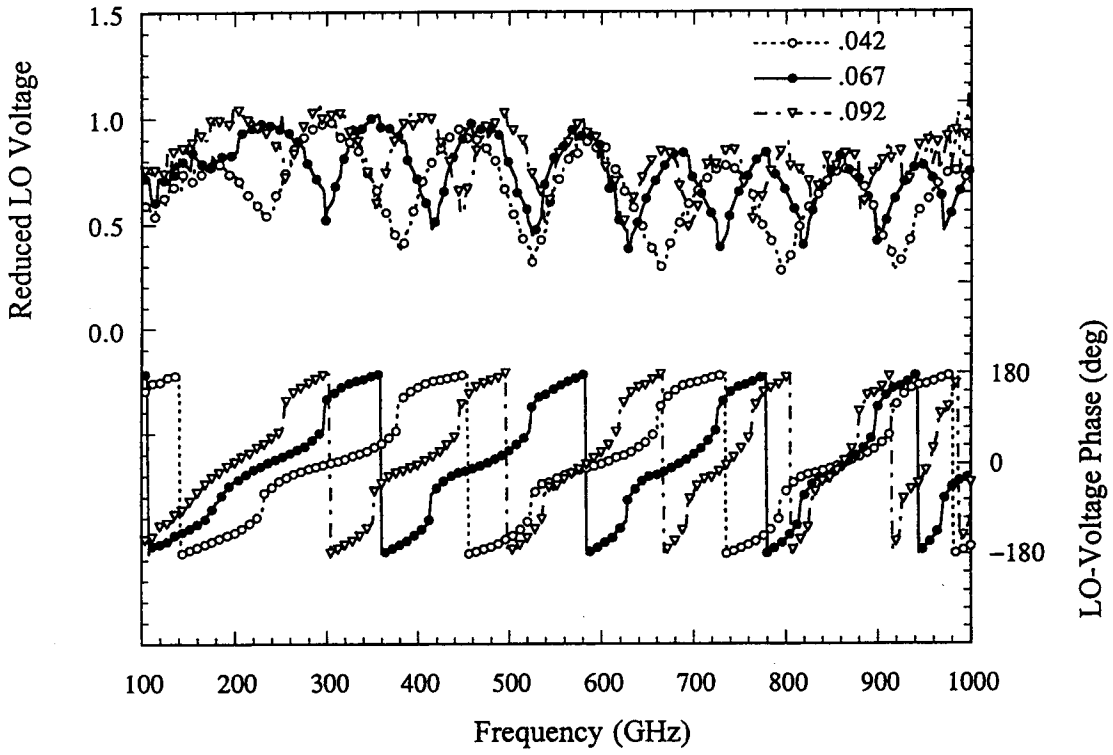

Fig. 6b Optimized LO voltage (magnitude and phase) for a 16-junction (J_c=3kA/cm2) array, as a function of frequency. Results are shown for three inductances (wL/R_n at 500 GHz).

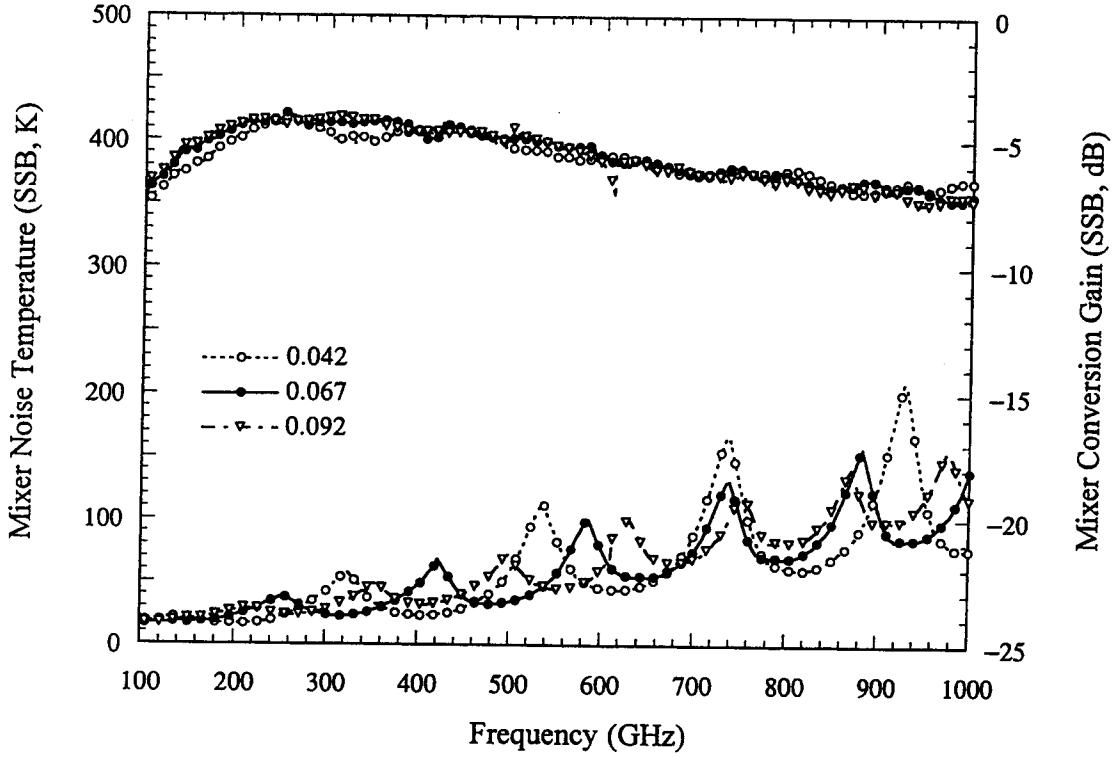

Fig. 7a Simulated mixer noise temperature and conversion gain for a 16-junction (J_c=6kA/cm2) array, as a function of frequency. Results are shown for three inductances (wL/R_n at 500 GHz).

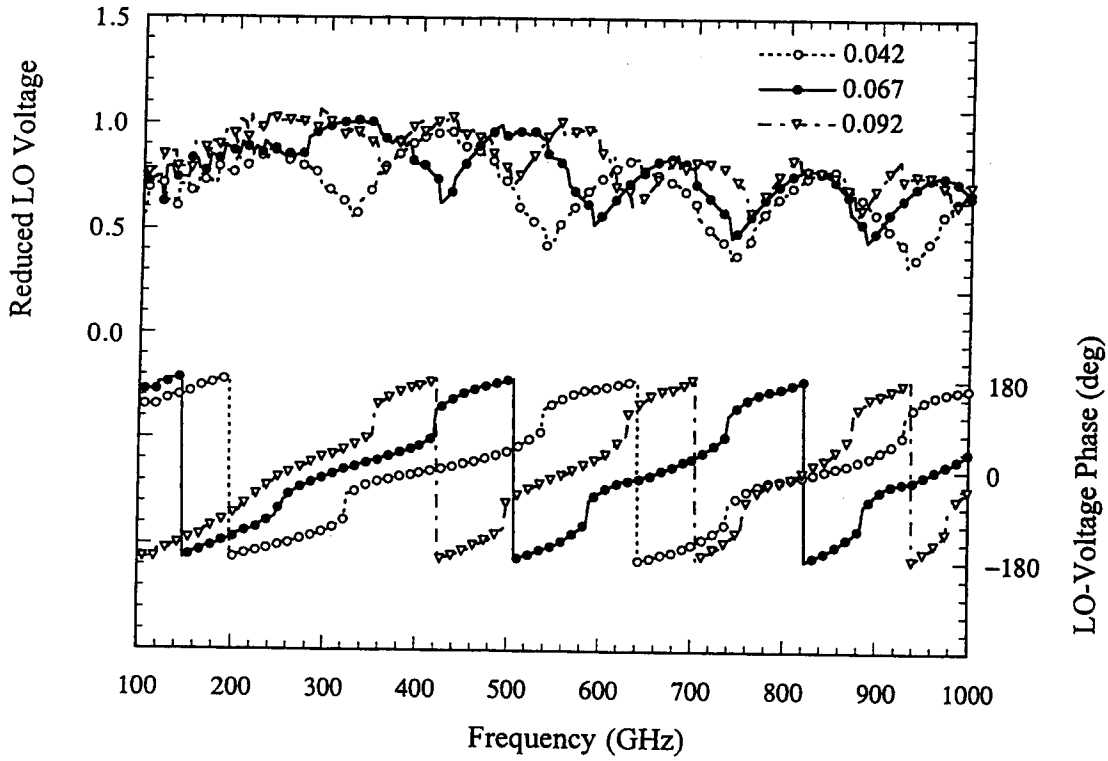

Fig. 7b Optimized LO voltage (magnitude and phase) for a 16-junction (J_c=6kA/cm2) array, as a function of frequency. Results are shown for three inductances (wL/R_n at 500 GHz).

NUMERICAL MODELING OF THE QUASIPARTICLE NON-LINEAR TRANSMISSION LINE

C.-Y. Edward Tong, Linda Chen* and Raymond Blundell

Harvard-Smithsonian Center for Astrophysics,
60 Garden St., Cambridge, MA 02138.

*Dept. of Mathematics, University of Chicago,
Chicago, IL 60615.

An analysis is presented for the behavior of the quasiparticle non-linear transmission line driven by a high frequency local oscillator. The theory developed includes a large-signal non-linear analysis, a small-signal analysis and a noise analysis. This model is used to simulate the conversion loss and noise temperature of distributed quasiparticle mixers based on the non-linear transmission line. The numerical code has been verified by comparing the theoretical conversion loss and mixer noise temperature with that of an experimental mixer that operates in the 400 GHz band. Reasonable agreement between the calculated and measured data has been obtained.

The numerical simulation shows that good conversion efficency and low mixer noise temperature are realizable at relatively low source resistance where the optimum line lengths are spaced half guided wavelength apart. From the results of the claculation, one can also derive the optimum critical current density of the long SIS junctions used for this type of non-linear transmission line based SIS mixer.

The theory also predicts that if the non-linear transmission line is terminated by an RF load, the signal waveform along the line may be amplified parametrically if the idler frequency is inductively terminated. The inductive load for the idler should roughly tune out the capacitance of the entire line at the same frequency. In one specific simulation, for example, a peak gain of 5.2 could be obtained with a line length of 5.4 guided wavelengths at 460 GHz. The required pumping power is about 300 nW and the input return loss is about -16 dB. The corresponding single-side-band mixer noise temperature is only about 58 K. This new possibility of low-noise stable parametric amplification may present new opportunities to low-noise receiver systems at sub-millimeter frequencies.

The full text of this manuscript appears in the I.E.E.E. Transactions on Microwave Theory and Techniques, vol. 45, pp. 1086 - 1092, July 1997.

Determining input loss in SIS receivers

C. E. Honingh, S. Haas, D. Hottgenroth, K. Jacobs, and J. Stutzki.

I. Physikalisches Institut, Universität zu Köln
Zülpicher Straße 77
50937 Köln
Germany

Abstract

We present measurements on two high frequency S(uperconductor) I(nsulator) S(uperconductor) heterodyne receivers at 660 GHz and 810 GHz. Their noise temperatures are 163 K and 860 K, respectively. The contribution of the high frequency (RF) input loss to this number is measured with the commonly used method of intersecting lines. The result is compared to a more rigorous analysis using the full quantum theory of mixing. We will show that in this frequency range the method of intersecting lines in general leads to an overestimation of the RF input loss. Even at 660 GHz, with a well matched SIS junction, the input noise contribution is overestimated by about 25 percent. This is due to the summation of the contributions due to the vacuum fluctuations, which is the highest contribution, the mismatch at the intermediate frequency (IF), and the fact that the mixer output noise is not completely independent of local oscillator (LO) power. At 810 GHz, due to a much stronger loss-induced mismatch of the SIS junction, the mixer output noise varies considerably with LO-power. The large loss of approximately 8 dB directly in front of the mixer enhances this contribution to the measured RF input loss. The contribution of the IF-mismatch is likewise enhanced. Together with the contribution of the vacuum fluctuations, this can lead to an overestimation of the RF input noise by more than 100 percent, depending on the actual mismatch of the mixers. We therefore conclude that, for the severe mismatch that occurs in Nb based SIS mixers above 700 GHz, the method of intersecting lines gives incorrect results and the full analysis should be applied.

1 Introduction

The noise temperature of niobium SIS mixers is now, by better junctions and by better design, reduced to only a few times the quantum limit, especially at frequencies below 700 GHz. Frequently receiver noise temperatures at these frequencies are dominated by the other noise sources than the mixer [1], [2]. The reduction in signal to noise ratio by losses in the focusing optics or in the unavoidable cryostat windows often constitutes at least 25% of the total receiver noise.

Accurate analysis of the distribution of the total receiver noise over its various contributions is important. Not only to locate the areas where a receiver might be improved, but also to compare several designs, often from different laboratories.

In recent years a particularly attractive and quick method, the so called intersecting line method (ISLM), developed in Ref. [3] and [4], has come in general use to determine the noise contribution of the RF-input loss, in front of the mixer. The main advantage of the method is that no additional parameters of the mixer have to be determined. From the receiver noise temperature and the conversion loss at a number of local oscillator settings, the input noise is determined by a simple linear fit. This measurement can be done at any telescope receiver without extra facilities.

The accuracy of the method was discussed in Ref [4] and it was concluded that the method should be as accurate as the measurement of the receiver noise temperature and that the several correction terms should all be smaller than the quantum temperature hf/k, except for mixers that are severely mismatched to the local oscillator (LO). The influence of the noise originating from the vacuum fluctuations, the quantum noise, is only briefly discussed for mixers that are perfectly matched to the LO. It is concluded that for that case the unavoidable quantum noise in fully included in T_{rf}.

We noticed, from our own experience and from other measurement data [1], [4] - [6] , that the estimate of the noise contribution of the input loss by this method is always somewhat high and that the losses responsible for the measured input noise temperature of the system can only be partly explained from an inspection of the optics. Especially our measurements just below and just above the gap frequency of niobium at 660 GHz and 810 GHz, with comparable optics, raised questions about the accuracy of the ISLM. The optics of the 810 GHz test set up always contributed at least three times as much noise to the receiver as the 660 GHz test set-up, according to the input noise temperature measured by the ISLM.

In this paper we will determine the contribution of the RF losses to the noise temperature of the receivers at both frequencies in two ways. The results of the ISLM and of a more elaborate approach, where the noise contribution of all the components of the receiver is determined separately with help of the quantum theory of mixing [7] will be compared. We will argue that the ISLM will only give a correct result in the case of a mixer with an almost ideal embedding impedance and a low RF loss in the warm as well as in the cold optics or electronic circuitry in front of the mixer.

2 Method

We will in short describe the two methods that we use to determine the high frequency input loss of SIS mixers. They both are based on the measurement of the output power of the total receiver in a certain bandwidth as a function of the input power of the receiver. As input source we use a blackbody of 295 K (hot) and 77 K (cold) physical temperature.

All temperatures used in the equations, unless explicitly stated as physical temperatures, are noise temperatures that represent equivalent noise input powers given by kBT, with k the Boltzmann constant, B the detection bandwidth and T the noise temperature.

In both methods we use the output power of the receiver P_{out} written as:

$$P_{out} = \left\{ \left(P_{in} + kT_{rf}\right) G_{rf} G_{mix} G_{4.2K} G_{if} + P_{mix}^{out} G_{if} + kT_{if} G_{if} \right\} B \qquad (1)$$

with P_{in} the input power of the receiver, kT_{rf} the noise power added by the RF input losses and G_{rf} the transmission of the RF input section. $G_{4.2K}$ is the transmission at 4.2K physical temperature, inside the dewar, G_{if} is the total IF gain, T_{if} is the noise temperature of the IF amplifier(s), and B is the detection bandwidth. P_{mix}^{out} is the output noise of the mixer per unit bandwidth, and G_{mix} is the total mixer gain

For the ISLM its convenient to write the total receiver noise temperature T_{rec}. , using the notation of Eq. (1) , as

$$kT_{rec} = kT_{rf} + \frac{P_{mix}^{out} + kT_{if}}{G_{rf}G_{4.2K}} \frac{1}{G_{mix}} \tag{2}$$

T_{rec}. is measured several times for different sub-optimum local oscillators powers. The ISLM uses the fact that for LO powers below the optimum level P_{mix}^{out} is approximately constant, as had been shown in Ref. [8]. With this assumption T_{rf} is found from the intercept of T_{rec} at different LO powers against the corresponding value of $1/G_{mix}$ A more complete description of the intersecting line method (ISLM) can be found in Ref.'s [3] and [4].

In the second method for determining T_{rf} we use again Eq. (1) for the output power of the mixer, but now the terms other than that with T_{rf} are determined separately. For that purpose we apply the quantum theory of mixing (QTM) in the three port approximation [7]. To do so the receiver output power has to be measured as a function of bias voltage at the optimum LO power level, and without LO-power. In addition the junction IV-curve has to be measured at the same local oscillator settings.

The bandwidth is set by an accurate bandfilter in the IF chain. The IF gain and noise temperature are determined by the well established shotnoise method [9], that uses the output noise of the junction without LO power as calibrated input noise source for the IF amplifiers.

G_{mix} and P_{mix}^{out} are calculated from the QTM. G_{mix} is given by the sum of the conversion from the upper side band, Gm_{01} , and from the lower side band , Gm_{0-1}, to the IF

$$G_{mix} = Gm_{01} + Gm_{0-1} = 4G_{load}\left(G_{usb}|Z_{01}|^2 + G_{lsb}|Z_{0-1}|^2\right) \tag{3}$$

G_{load} is the real part of the terminating admittance at the IF port of the mixer, G_{usb} that at the upper side band port and G_{lsb} that at the lower side band port. Z_{ij} is the ij-element of the conversion matrix Z obtained by inverting the matrix YT ,

$$YT_{ij} = Y_{ij} + \begin{pmatrix} Y_{usb} & 0 & 0 \\ 0 & Y_{load} & 0 \\ 0 & & Y_{lsb} \end{pmatrix} \qquad i,j = -1,0,1 \tag{4}$$

with Y_{ij} the small signal admittance matrix that connects the small signal voltages and currents in the junction. The elements of Y_{ij} are given by equations (4.49-4.51) in Ref [7]. The diagonal matrix contains the full embedding admittance of the mixer, given by the terminating admittance at the upper side band, Y_{usb} , at the lower side band, Y_{lsb} , and at the IF port, Y_{load}. The embedding impedances for different frequencies are determined from the measured DC IV-curves with and without local oscillator power.

To determine the output noise of the mixer per unit bandwidth we use the expression derived in Ref. [11], which has the advantage that the contribution of the quantum noise to the output noise of the mixer is explicitly stated.

$$P_{mix}^{out} = G_{load} \sum_{i,j=-1,0,1} Z_{oi}\overline{Z_{oj}}H_{ij} + \tfrac{1}{2}h \sum_{i=-1,0,1} Gm_{oi}\left|i f_{lo} + f_{if}\right| \tag{5}$$

of which the first term is the contribution of the shotnoise and the second term is identified as the mixer noise output due to the unavoidable half quantum of noise input per side band due to the vacuum fluctuations [12]. As is clearly explained in this reference the sum of both terms gives the correct output noise of the mixer for every embedding impedance.

The shotnoise term in Eq. (5) is derived in Ref. [7], where the elements of the current correlation matrix H are given by Eq. (4.69). The input power per unit bandwidth from the blackbody load of temperature T at frequency f is calculated by the Planck formula [11],

$$P(T,f) = \frac{hf}{\exp\left(\frac{hf}{kT}\right) - 1} \tag{6}$$

T_{rf} and G_{rf} are related via

$$T_{rf} = \frac{(1 - G_{rf})}{G_{rf}} T_{295K} + \frac{(1 - G_N)}{G_N G_{rf}} T_{77K} \tag{7}$$

with G_N the known transmission of the infrared filter of the dewar at 77 K. An equivalent noise temperature for $G_{4.2K}$ is neglected because the noise power $kBT_{4.2K}$ is very small.

G_{rf} (and so T_{rf}) and $G_{4.2K}$ are determined by fitting the calculated receiver output power according to Eq. (1) to the measured output power, for the hot and the cold input. By adapting $G_{4.2K}$ the overall gain is changed but the noise input stays equal, and so this parameter is mainly adapted to fit the output power at a hot input. Next, by G_{rf} which hardly changes the calculated output for a hot input, the output for a cold load input is fitted.

This gives a second way to determine T_{rf} that is much more elaborate and complicated. In the next section the result of the two methods will be compared.

3 Results

All measurements are done in a liquid helium dewar at a temperature of 4.2 K. The vacuum window of the dewar and the 77 K-infrared filter are sealed with Teflon or Mylar foils. The thickness of the foils is optimized to achieve a transmission of about 98 % in the current frequency band.

For 660 GHz the local oscillator and the signal are combined with a beamsplitter. The calculated reflection of the beamsplitter is 5%. At 800 GHz we use a Martin-Puplett diplexer with a transmission loss of about 7 %.

The mixers are fixed tuned waveguide mixers and are described in detail in Ref. [2] and [13] In the present measurement set up the lowest receiver noise temperature at 660 GHz is 163 K ,

and at 810 GHz 860 K. The center frequency of the cooled HEMT amplifier is 1.4 GHz and its noise temperature is 4 K. The IF output power is measured in a 100 MHz bandwidth around the

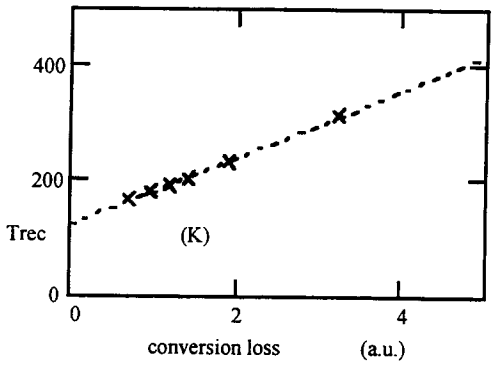

Fig. 1 Receiver noise temperature against conversion loss for different LO powers at 660 GHz.

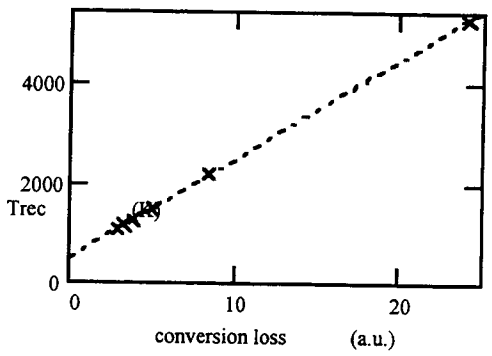

Fig. 2 Receiver noise temperature against conversion loss at different LO power levels at 810 GHz.

center frequency.

The result of the hot/cold load measurements at different local oscillator powers below the optimum are given in Fig. 1 for 660 GHz and in Fig. 2 for 810 GHz. The intersection point with the vertical axis is 125K at 660 GHz and 470 K at 810 GHz. These temperatures represent again equivalent noise powers.

The measured output power as a function of bias voltage for a hot and a cold input at optimum LO-power are given in Fig. 3 and 4 for 660 GHz and 810 GHz resp. by the solid lines. The calculated output powers are given by the (+) signs for the hot load input and the (o) signs for the cold load input. The wiggles on the calculated curves stem from noise in the measured IV-curves of the junctions.

To obtain the agreement as shown in the Fig. 3 and 4 (G_{rf}, $G_{4.2K}$) is chosen (0.78, 0.75) for 660 GHz and (0.59, 0.36) at 810 GHz. Using Eq. 7 these values for G_{rf} give T_{rf} equal to 82K for 660 GHz and 183K for 810 GHz.

The embedding impedance normalized to the junction normal state impedance is 0.5 + 0.1i for 660 GHz and 0.15 - 0.04i at 810 GHz. The embedding impedances are not obtained from a real fit to the pumped IV-curve in the sense of Ref. [10]. They are determined from calculations of the embedding circuitry and then slightly adapted to obtain best agreement between the measured and calculated pumped IV-curve.

4 Discussion

At both frequencies the two values of T_{rf}, determined by the two methods, do not correspond. In addition the difference in T_{rf} of 125K at 660 GHz and 470K at 800 GHz, as obtained by the ISLM, is much larger than expected from an inspection of the optics.

To investigate the difference between the two methods we focus on the assumption that P_{mix}^{out} is constant. Smaller effects due to mismatch at the IF port of the mixer are not discussed. It can be seen immediately from Eq. (2), that any component of P_{mix}^{out} depending linearly on G_{mix} results in

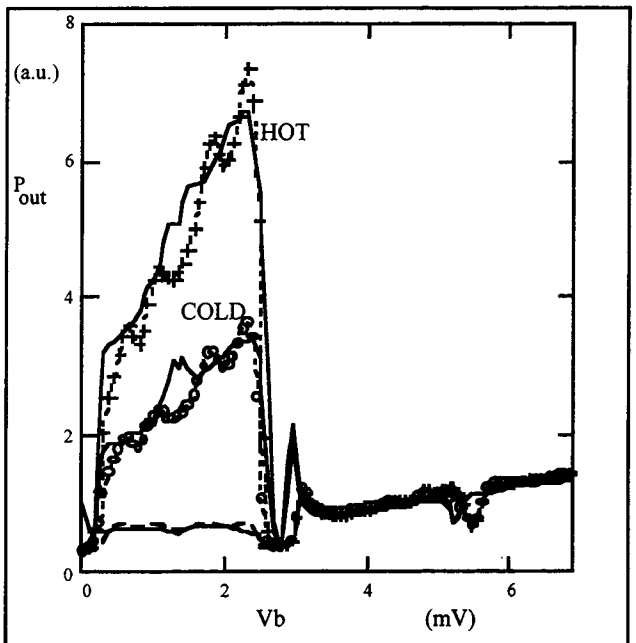

Fig. 3 Measured (solid line) and calculated receiver IF output power as a function of bias voltage at a hot and cold load input at 660 GHz, and without LO-power.

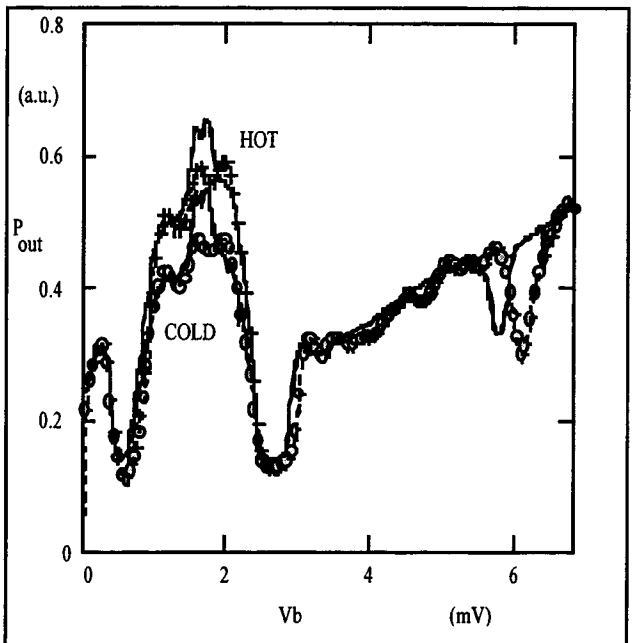

Fig. 4 Measured (solid line) and calculated receiver IF output power as a function of bias voltage at a hot and cold load input at LO-frequency 810 GHz

a constant contribution to Trf which would have no effect on the quality of the linear fit to the results.

If we insert Eq. (3) and (5) in Eq. (2), given that the term with Gm_{OO} in Eq. (5) is approximately constant, it is clear that the quantum noise term of Eq. (5) will always add to T_{rf}. Unfortunately, for a mixer with a lossy input coupling, the contribution of the quantum noise to T_{rf} is larger by the unknown factor $1/(G_{rf}G_{4.2K})$.

Furthermore, if we investigate the dependence of the shotnoise term on G_{mix}, we get the result as is given in Fig. 5 and 6. The mixer output power is calculated for the embedding impedances given above at several LO-power levels. In each figure two curves are given. The lower curve shows the dependence of only the shotnoise term on G_{mix}. The upper curve is a linear fit to the total output noise, calculated for eight different values of the LO power. We verified that for an embedding impedance equal to one (normalized to the junction normal state resistance) the calculated shotnoise output is indeed almost constant with G_{mix}.

Already at 660 GHz, where the receiver noise temperature is quite low, the imperfect embedding impedance causes a positive slope of 11 K. At 810 GHz, due to the imperfect compensation of the junction capacitance by the lossy integrated tuning structures [13], the embedding impedance is worse than at 660 GHz. Consequently the slope of the lower line is higher, 38 K, which is well above 0.5 hf/k.The total output noise, given in both Fig.'s by the upper line has a slope which is approximately 0.5 hf/k higher than the slope of the lower curve. For 660 GHz the total slope is 27K, and at 810 GHz it is 58K.

We can use the values for G_{rf} and $G_{4.2K}$ to calculate a correction to the T_{rf} that has been measured by the ISLM. The small value of $G_{4.2K}$ (0.36) at 810 GHz resulting from the second method to determine T_{rf} is not unreasonable if compared to the calculated transmission of the integrated tuning structure [13].We subtract the value of the slope of the upper curves in Fig. 5

and 6 devided by $G_{rf}G_{4.2K}$. This corrected value of T_{rf} is in good agreement with the value determined directly from the second method. Phrased differently: A simulation of the ISLM-using the QTM and the values for G_{rf} and $G_{4.2K}$ as determined by the second method, yields a value for T_{rf} that is in good agreement with the value measured by the ISLM for both mixers.

We conclude that the assumption that the mixer output noise is independent of the mixer gain for low local oscillator power does not hold for both our mixers and that thus the ISLM gives too high values for T_{rf}.

Even if the embedding impedance would be perfect and the input loss both at ambient temperature *and* at 4.2 K would be negligible, a half quantum of unavoidable noise would be included in T_{rf}. As is shown in Ref.[14] this is due to the fact that we calculate the receiver noise temperature from the hot/cold load measurement using the Planck formula (Eq. 6) for the input noise from the loads. This is consistent since the quantum noise is included in the output noise of the mixer (Eq.5).

As is shown in Ref. 14, the receiver noise temperature determined from the hot/cold load measurement is lower by exactly 0.5 hf/k if the quantum noise is included in the input signal. The input noise power per unit bandwidth (P) from the calibration loads is than calculated using the Callen & Welton formula $P= 0.5\ hf\coth(0.5\ hf/kT)$ instead of the Planck formula. This emphasizes that to appreciate published values of T_{rf} measured by the ISLM for almost perfect mixers, one needs specific information about the calculation of the receiver noise temperature [1] [4].

For this analysis we prefer to use the Planck formula to calculate the input signal of the mixer because the contribution of the quantum noise to the output of the mixer can then be written explicitly in Eq. 5. If the quantum noise is included in the input signal one has to be very careful in introducing the input losses and the added quantum noise of these losses to end up with the correct output noise power of the mixer.

From a practical point of view one could attempt to correct a value of T_{rf} measured by the ISLM. Subtraction of $0.5hf/k(1/G_{rf})$ or $0.5hf/k(1/G_{rf} - 1)$, depending on how T_{rec} is calculated, gives a better estimate for the quality of the input coupling. G_{rf} can determined from the measured T_{rf} assuming that all of the loss occurs at 295K. This works reasonably well as long as $G_{4.2K}$ is close to one. For niobium SIS mixers above the gap frequency of niobium, which generally have a low value for $G_{4.2K}$ due to the unavoidable loss in the integrated tuning structure, values of T_{rf} measured by the ISLM and adapted in this way will still be much too high. In that case an estimate for $G_{4.2K}$ is necessary and the full analysis should be applied.

Acknowledgments

We thank Stephan Wulff for polishing and dicing the junction substrates. We thank A. Kerr and M. Feldman for helpful discussions about the consistency of their (Ref.14) and our way to include the quantum noise into the analysis. This work was supported by the Bundesministerium für Forschung und Technologie, Verbundforschung Astronomie, grant 05-KU134(6), and the

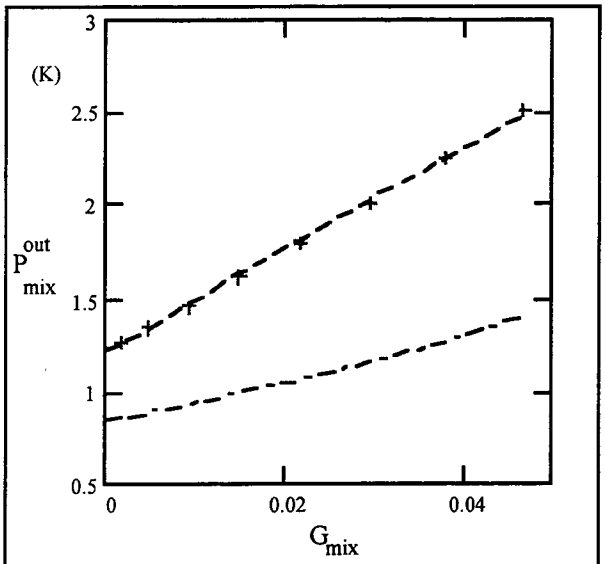

Fig. 5 Calculated mixer output noise at 660 GHz against mixer gain, for different LO power levels. The dash-dotted curve, the dependence of the shotnoise on Gmix, has a slope of 11.4K. The slope of the curve including the quantum noise is 27K, given by the upper line fitted to the calculated points.

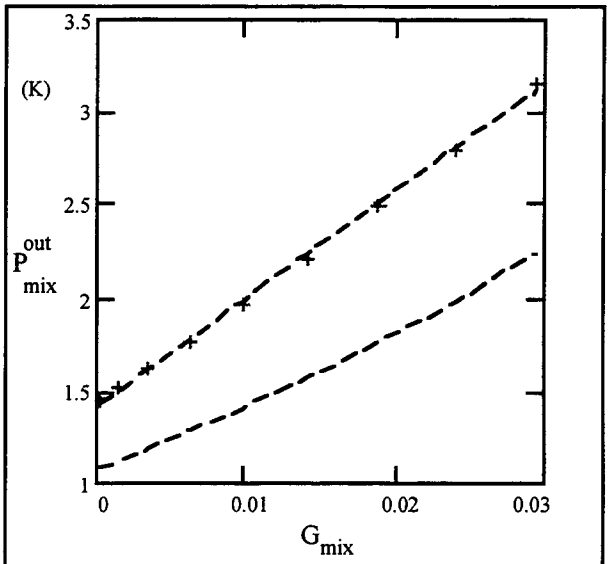

Fig. 6 Calculated mixer output noise at 810 GHz against mixer gain, for different LO power levels. The slope of the upper curve, given by the straight line fitted to the calculated points, is 58K.The lower curve gives only the contribution of the shotnoise to the mixer output noise and has a slope of 38K.

Deutsche Forschungsgemeinschaft, grant SFB301.

References

[1]C.-Y. E. Tong, R. Blundell, S. Paine, D. C. Papa, J. Kawamura, X. Zhang, J. A. Stern, and H. G. LeDuc, "Design and characterization of a 250-350-GHz Fixed-Tuned Superconductor-Insulator-Superconductor Receiver", *IEEE Trans. Microwave Theory Tech.* **44**, (1996), pp. 1548-1556.

[2] S. Haas, C. E. Honingh, D. Hottgenroth, K. Jacobs, and J. Stutzki, "Low Noise Tunerless Waveguide SIS Receivers for 440-500 GHz and 630-690 GHz", *Int .J. Infrared Millimeter Waves* **17**, (1996), pp. 493-506

[3]R. Blundell, R. E. Miller, and K. H. Gundlach, "Understanding noise in SIS receivers", *Int. J. Infrared Millimeter Waves* **13**, (1992), pp. 3-14

[4]Qing Ke and M. J. Feldman, "A technique for noise measurements of SIS receivers", *IEEE Trans. Microwave Theory Tech.* **42** , (1994), pp. 752-755.

[5]J.Kooi, Caltech., U.S.A. , personal communication

[6]P. Dieleman, S.R.O.N Groningen, the Netherlands, personal communication

[7]J. R. Tucker, M. J. Feldman, "Quantum detection at millimeter wavelengths", *Rev. Mod. Phys.* **57**, (1985), pp. 1055-1113

[8]Qing Ke and M. J. Feldman, "Constant output noise temperature of the superconducting quasiparticle mixer", *IEEE Trans. Appl. Supercond.* **3**, (1993), pp. 2245-2249.

[9]D. P. Woody. "Measurement of the noise contribution to SIS heterodyne receivers", *IEEE Trans. Appl. Supercond.* **5**, (1995) , pp. 3312-3315

[10] A. Skalare, " Determining embedding circuit parameters from DC measurements on quasiparticle mixers", *Int. J. Infrared Millimeter Waves* **10**, (1989), pp. 1339-1353

[11] M. J. Wengler, and D. P. Woody, "Quantum noise in heterodyne detection", *IEEE J. Quantum Electron.* **5**, (1987), pp. 613-622.

[12] M. J. Feldman, "Quantum noise in the quantum theory of mixing", *IEEE Trans. Magn.* **23**, (1987), pp. 1054-1057.

[13] D. Hottgenroth, C. E. Honingh, S. Haas, K. Jacobs, and J. Stutzki, "Design and analysis of a waveguide SIS mixer above the gap frequency of niobium", to be published in *Int. J. Infrared Millimeter Waves* March (1997)

[14] A. R. Kerr , M. J. Feldman, and S.-K. Pan, "Receiver noise temperature, the quantum noise limit, and the role of the zero point fluctuations", this conference.

Receiver Noise Temperature, the Quantum Noise Limit, and the Role of the Zero-Point Fluctuations*

A. R. Kerr[1], M. J. Feldman[2] and S.-K. Pan[1]

[1]National Radio Astronomy Observatory**
Charlottesville, VA 22903

[2]Department of Electrical Engineering
University of Rochester
Rochester, NY 14627

Abstract

There are in use at present three different ways of deducing the receiver noise temperature T_R from the measured Y-factor, each resulting in a different value of T_R. The methods differ in the way the physical temperatures of the hot and cold loads, T_h and T_c (usually room temperature and liquid nitrogen), are converted into radiated power "temperatures" to deduce T_R from Y. Only one of these methods is consistent with Tucker's quantum mixer theory and the constraints of Heisenberg's uncertainty principle. The paper also examines the minimum *system* noise temperatures achievable with single- and double-sideband receivers.

Introduction

After talking to people at the 1996 Symposium on Space Terahertz Technology, it was clear that there was some confusion, or at least difference of opinion, on how to deduce the noise temperature of a receiver from the measured Y-factor. There was also disagreement on the fundamental quantum noise limit of single- and double-sideband mixer receivers. With the (DSB) noise temperatures of the best SIS receivers now approaching 2hf/k (~30 K at 300 GHz), these questions need to be resolved. This paper compares the three interpretations of the Y-factor measurement currently in use, and discusses the fundamental quantum limit on the sensitivity of coherent receivers.

The Y-factor Method

In a Y-factor measurement, two noise sources are connected individually to the receiver input, and the ratio, Y, of the receiver output powers is measured. From the Y-factor the intrinsic noise of the receiver can be deduced, either as an equivalent input noise power or as an equivalent input noise temperature. While noise temperatures are most commonly used, the discussion will be clearer if we consider noise powers initially.

---

*Originally printed as Electronics Division Internal Report No. 304, National Radio Astronomy Observatory, Charlottesville VA 22903, September 1996.

**The National Radio Astronomy Observatory is a facility of the National Science Foundation operated under cooperative agreement by Associated Universities, Inc.

Let P^n be the equivalent input noise power of the receiver in a bandwidth B, the measurement bandwidth. B is defined by a bandpass filter at the receiver output (for a coherent receiver (*e.g.*, amplifier or mixer) an input filter is unnecessary). With a power P_{in} incident on the receiver in bandwidth B, the measured output power of the receiver $P_{out} = G\left[P^n + P_{in}\right]$, where G is the gain of the receiver. With hot and cold loads in front of the receiver the measured Y-factor is:

$$Y = \frac{P^n + P_{hot}}{P^n + P_{cold}} \quad . \tag{1}$$

The equivalent input noise power is found by inverting this equation:

$$P^n = \frac{P_{hot} - Y P_{cold}}{Y - 1} \quad . \tag{2}$$

Frequently the hot and cold loads are simply black-body radiators (well matched waveguide or free-space loads) heated or cooled to accurately known physical temperatures T_{hot} and T_{cold}.

Power Radiated by a Black Body

The Planck radiation law is often used to calculate the thermal noise power in a bandwidth B about frequency f (B << f), radiated into a single mode (*e.g.*, a waveguide mode), by a black body at physical temperature T:

$$P^{Planck} = kTB\left[\frac{\frac{hf}{kT}}{\exp\left[\frac{hf}{kT}\right]-1}\right] , \tag{3}$$

where, h and k are the Planck and Boltzmann constants. In the present context, a more complete description is given by the dissipation-fluctuation theorem, or generalized Nyquist theorem, of Callen & Welton [1]:

$$P^{C\&W} = kTB\left[\frac{\frac{hf}{kT}}{\exp\left[\frac{hf}{kT}\right]-1}\right] + \frac{hfB}{2} \tag{4}$$

$$= \frac{hfB}{2}\coth\left(\frac{hf}{2kT}\right) .$$

This is simply the Planck formula with an additional half photon per Hz, hfB/2,

and it is this additional half photon, the zero-point fluctuation noise, that is the source of some confusion. Some authors believe that the zero-point fluctuations should be excluded from consideration of noise powers because they do not represent *exchangeable* power. However, the view of Devyatov *et al.* [2] is that, although the zero-point fluctuations deliver no real power, the receiver nevertheless "...develops these quantum fluctuations to quite measurable fluctuations..." at its output. The zero-point fluctuations, they argue, should be associated with the incoming radiation and not with the receiver itself: at the receiver input "...one can imagine two zero-point fluctuation waves propagating in opposite directions..." with no net power flow.

It is interesting to note [3] that in the limit of small hf/kT, it is the Callen and Welton formula (4) which gives the Rayleigh-Jeans result P = kTB, while the Planck formula (3) gives P = kTB - hfB/2, half a photon below the Rayleigh-Jeans result.

Noise Temperatures

The noise power P^n in a bandwidth B is conveniently represented by a *noise temperature* $T^n = P^n/kB$. The noise temperature is simply a shorthand notation for the noise power per unit bandwidth. The noise temperature of a black body radiator at physical temperature T is obtained from the noise power (3, 4) as:

$$T^{Planck} = T\left[\frac{\frac{hf}{kT}}{\exp\left[\frac{hf}{kT}\right]-1}\right], \qquad (5)$$

$$T^{C\&W} = T\left[\frac{\frac{hf}{kT}}{\exp\left[\frac{hf}{kT}\right]-1}\right] + \frac{hf}{2k} = \frac{hf}{2k}\coth\left(\frac{hf}{2kT}\right). \qquad (6)$$

These expressions differ by the zero-point fluctuation noise temperature, hf/2k, whose magnitude is 0.024 K per GHz. In the Rayleigh-Jeans limit of small hf/kT, the noise temperature based on the Callen & Welton formula approaches the physical temperature of the black body ($T^{C\&W} \rightarrow T$), while the noise temperature based on the Planck formula is half a photon below the physical temperature ($T^{Planck} \rightarrow T - hf/2k$). Fig. 1 shows T^n evaluated according to (5) and (6), as functions of the physical temperature T of the black body, for a frequency of 230 GHz. Also shown are the differences between T^{Planck}, $T^{C\&W}$, and T^{RJ}.

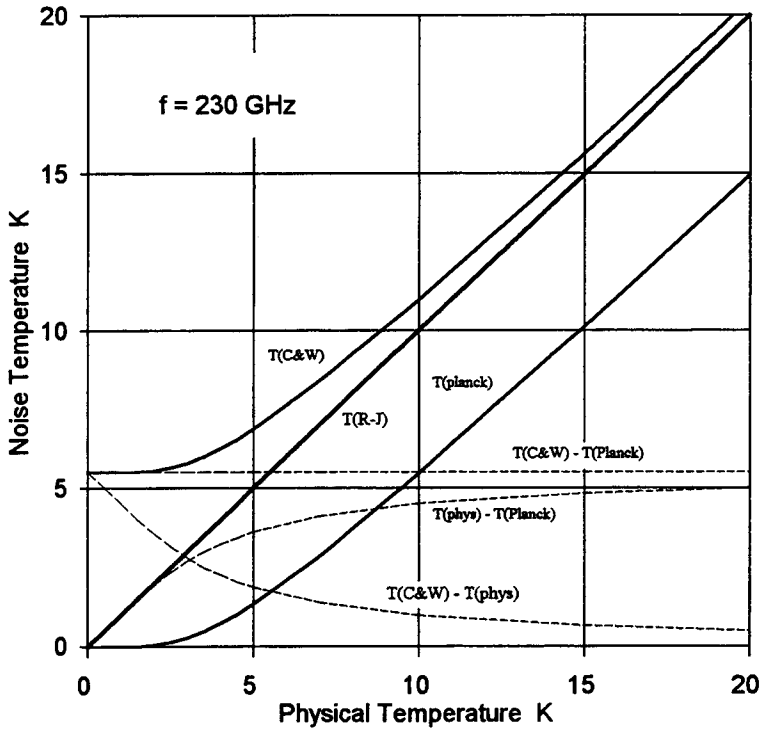

Fig.1. Noise temperature vs physical temperature for black body radiators at 230 GHz, according to the Rayleigh-Jeans, Planck, and Callen & Welton laws. Also shown (broken lines) are the differences between the three radiation curves. The Rayleigh-Jeans curve converges to the Callen & Welton curve at high temperature, while the Planck curve is always hf/2k below the Callen & Welton curve.

Receiver noise temperature from the Y-factor

Equation (2) for the equivalent input noise power of a receiver can be written in terms of noise temperatures using $T^n = P^n/kB$. Thus the *equivalent input noise temperature*[1] of the receiver,

$$T_R^n = \frac{T_{hot}^n - Y T_{cold}^n}{Y - 1} \quad . \tag{7}$$

Three different interpretations of this equation are in use at present. They differ in the values of T_{hot}^n and T_{cold}^n assumed for the hot and cold loads at physical temperatures T_{hot} and T_{cold}. Most often, the Rayleigh-Jeans formula is

[1] This definition of receiver noise temperature is now generally accepted in the millimeter and submillimeter receiver community. There are two older definitions of receiver noise temperature which are based on hypothetical measurements rather than on the simple Y-factor measurement: (i) The physical temperature of the input termination of a hypothetical noise-free device, which would result in the same output noise power as the actual device connected to a noise-free input termination. (ii) The physical temperature of the input termination required to double the output noise of the same receiver with its input termination at absolute zero temperature. Using either of these older definitions causes further complications, beyond the scope of this paper. This question was dealt with at length in [5].

used, in which T_{hot}^{n} and T_{cold}^{n} are equal to the physical temperatures. Some workers use the Planck formula (5), while others use the Callen & Welton formula (6). The three approaches result in three different values of T_R^n, which we denote T_R^{RJ}, T_R^{Planck}, and $T_R^{C\&W}$:

$$T_R^{RJ} = \frac{T_{hot} - Y T_{cold}}{Y - 1} \quad , \tag{8}$$

$$T_R^{Planck} = \frac{T_{hot}^{Planck} - Y T_{cold}^{Planck}}{Y - 1} \quad , \tag{9}$$

and

$$T_R^{C\&W} = \frac{T_{hot}^{C\&W} - Y T_{cold}^{C\&W}}{Y - 1} \quad . \tag{10}$$

It will become clear in the following sections that only eq.(10) gives a receiver noise temperature consistent with quantum mixer theory [4] and the constraints of the uncertainty principle.

For a given value of Y, the difference between the Planck and Callen & Welton formulas (9, 10) is just half a photon:

$$T_R^{Planck} = T_R^{C\&W} + \frac{hf}{2k} \quad . \tag{11}$$

This constant half photon difference is independent of the hot and cold load temperatures. The difference between the Rayleigh-Jeans and Callen & Welton formulas (8, 10) depends on the physical temperatures of the hot and cold loads, and on frequency. Fig. 2 shows the receiver noise temperature, calculated according to eqs. (8-10), as a function of Y-factor for a 230 GHz receiver, measured with hot and cold loads at physical temperatures 300 K and 77 K. The small difference between the Rayleigh-Jeans and Callen & Welton results is shown by the dashed curve and referred to the right-hand scale. The negative receiver noise temperatures correspond to physically impossible values of the Y-factor. The physical limits on T_R^n will be discussed below.

The difference between receiver noise temperatures obtained using the Rayleigh-Jeans and Callen & Welton laws is not always as small as in the example in Fig. 2. Only if $hf/kT \ll 1$ for the hot and cold loads will $T_R^{RJ} \approx T_R^{C\&W}$. For example, if a 230 GHz receiver were measured using 4 K and room temperature loads, $hf/kT_{cold} = 2.8$, and T_R^{RJ} is ~2.3 K larger than $T_R^{C\&W}$. Another example is an 800 GHz receiver measured using 77 K and room temperature loads; then $hf/kT_{cold} = 0.5$, and T_R^{RJ} would be ~2.0 K larger than $T_R^{C\&W}$.

So far there has been no mention of single- or double-sideband operation. That is because the above discussion applies to both SSB and DSB receivers; a Y-factor measurement on a SSB or DSB receiver gives, via equation (7), the SSB or DSB receiver noise temperature.

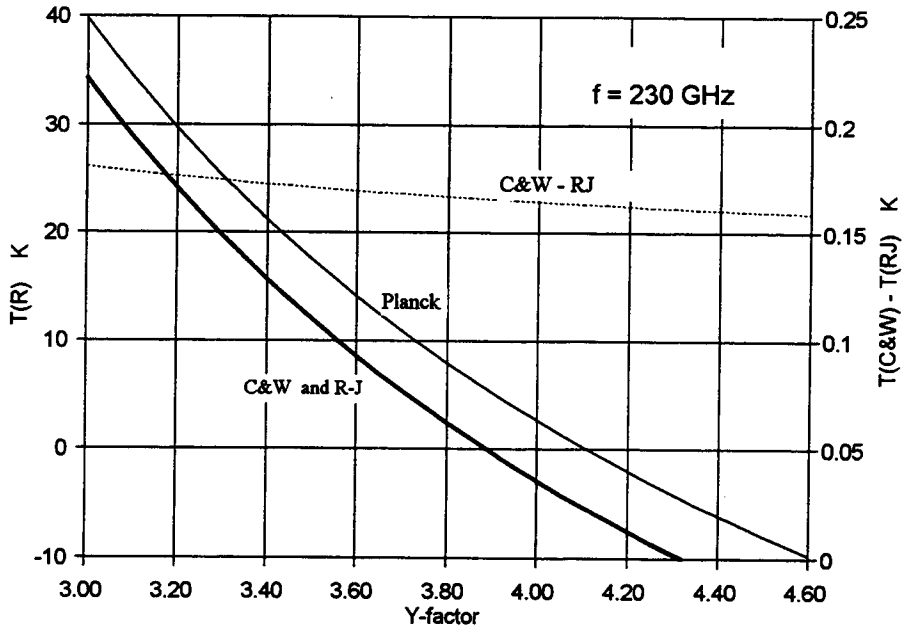

Fig. 2. Receiver noise temperature as a function of Y-factor for a 230 GHz receiver measured with T_{hot} = 300 K and T_{cold} = 77 K. The Rayleigh-Jeans curve is obtained when the hot and cold load noise temperatures are equal to their physical temperatures. The Planck and Callen & Welton curves are obtained using equations (5) and(6) for the hot and cold load noise temperatures. The small difference between the Planck and Callen & Welton curves is indicated by the dashed line (right-hand scale).

Single- and Double- Sideband Mixer Receivers

Mixer receivers can operate in several modes, depending on the configuration of the receiver and the nature of the measurement. In single-sideband operation, the receiver is configured so that, at the image sideband, the mixer is connected to a termination within the receiver. There is no external connection to the image frequency, and the complete receiver is functionally equivalent to an amplifier followed by a frequency converter. In double-sideband operation, on the other hand, the mixer is connected to the same input port at both upper and lower sidebands. A DSB receiver can be used in two modes: (i) to measure narrow-band signals contained entirely within one sideband — this is SSB operation of a DSB receiver. For detection of such narrow-band signals, power collected in the image band of a DSB receiver degrades the measurement sensitivity. And (ii), to measure broadband (or continuum) sources whose spectrum covers both sidebands — this is DSB operation of a DSB receiver. For continuum radiometry, the additional signal power collected in the image band of a DSB receiver improves the measurement sensitivity.

A Y-factor measurement on a DSB receiver, interpreted according to eq. (7), gives the so-called *DSB receiver noise temperature*. This is the most commonly quoted noise temperature for mixer receivers because it is easy to measure. It is also common to derive a *SSB noise temperature* (for a DSB receiver) by measuring the sideband gains, and referring all the receiver noise to a single

sideband, the signal sideband. Then, for the DSB receiver,

$$T^n_{R,SSB} = T^n_{R,DSB}\left[1 + \frac{G_i}{G_s}\right] , \qquad (12)$$

where G_s and G_i are the receiver gains at the signal and image frequencies[2], measured from the hot/cold load input port. If the upper and lower sideband gains are equal, $T^n_{R,SSB} = 2T^n_{R,DSB}$. If $G_i << G_s$, the Y-factor measurement directly gives $T^n_{R,SSB}$. When a DSB mixer receiver is used to receive a narrow-band signal contained entirely within one sideband, noise from the image band contributes to the output of the receiver. The overall SSB system noise temperature

$$T^n_{sys,SSB} = \frac{P_{out}}{kBG_s} = T^n_s + T^n_i\left(\frac{G_i}{G_s}\right) + T^n_{R,SSB}$$

$$= T^n_s + T^n_i\left(\frac{G_i}{G_s}\right) + T^n_{R,DSB}\left(1 + \frac{G_i}{G_s}\right) , \qquad (13)$$

where T_s^n and T_i^n are the noise temperatures of the signal and image terminations.

Fundamental Limits on T_R

The fundamental limits imposed by the Heisenberg uncertainty principle on the noise of amplifiers, parametric amplifiers, and mixer receivers have been studied by a number of authors over the last thirty five years, and their work is reviewed, with particular attention to mixer receivers, in [5] and [6]. The following general statement can be made: The minimum output noise power of a measurement system using a mixer receiver, SSB or DSB, is hf (*i.e.* one photon) per unit bandwidth, referred to one sideband at the receiver input. Hence, the minimum *system* noise temperature is hf/k referred to one sideband at the receiver input — exactly the same result as for a system incorporating an amplifier. The origin of this *quantum* noise has been much discussed [7, 3, 5, 6], and will be explained with the aid of Figs. 3 and 4, which depict four minimum-noise measurement systems using mixer receivers.

Fig. 3 shows two SSB receivers, 3(a) with a short-circuited image, and 3(b) with an image-frequency termination equal to the signal source resistance. For both 3(a) and 3(b), Tucker's quantum mixer theory predicts [4, 5, 8] a minimum receiver noise temperature of hf/2k. In 3(a) the zero-point fluctuations associated with the input termination (at 0 K) contribute half a photon (hf/2k) to the overall system noise temperature, and the mixer contributes the remaining

[2] For simplicity, we assume there is no significant conversion of higher harmonic sideband signals present at the input port. If the receiver gain is not negligible at frequencies $nf_{LO} \pm f_{IF}$, $n > 1$, then additional terms of the form G_n/G_s must be added in the parentheses on the right side of eq. (12).

half photon , which can be shown to originate in the electron shot noise in the mixer. In (b), the zero-point fluctuations associated with the signal source and (internal) image termination each contribute half a photon, which accounts for all the system noise; the mixer itself contributes no noise, which is exactly the result obtained from mixer theory. Here, the down-converted components of the mixer shot noise exactly cancel the IF component, with which they are correlated, a result well known in classical mixer theory.

Fig. 4 shows a DSB mixer receiver used in two different measurement modes: 4(a) to measure a signal present only in one sideband (the SSB mode for a DSB receiver), and 4(b) to measure a broadband signal present in both sidebands (the DSB or continuum mode). In 4(a), zero-point fluctuations associated with the input termination (at 0 K) contribute half a photon (hf/2k) in each sideband, and the mixer need contribute no noise, consistent with mixer theory. The same is true in 4(b), in which the presence of the signal in both sidebands doubles the signal power at the output of the system, and the signal-to-noise ratio at the output is twice that of the SSB receivers in Fig. 3. It is this apparent doubling of the receiver gain that leads to the concept of the DSB gain, $G_{DSB} = 2G$ (provided the signal and image gains are equal, *i.e.*, $G_s = G_i = G$).

It is clear from Figs. 3 and 4 that the minimum *receiver* noise temperatures for SSB and DSB receivers are, respectively, hf/2k and zero. The minimum *system* noise temperature, on the other hand, depends on the nature of the particular measurement; for SSB measurements using either SSB or DSB receivers, the minimum system noise temperature is hf/k, while for broadband continuum measurements using a DSB receiver, the minimum (DSB) system noise temperature is hf/2k.

From the discussion above, it is clear that in all computations of receiver or system noise temperatures, the zero-point fluctuations associated with resistive terminations at the signal and image frequencies must be included. Equations (4) and (6) must therefore be used in calculating noise powers or temperatures, and the receiver noise temperature must be obtained from the Y-factor according to eq.(10), in which the Callen & Welton law is used for the noise temperature of hot and cold loads.

It is appropriate here to address the question of how to compare SSB and DSB receivers: should a DSB receiver be judged against a SSB receiver by comparing their SSB and/or DSB receiver noise temperatures (for the DSB receiver with equal sideband gains, $T^n_{R,SSB} = 2T^n_{R,DSB}$)? The answer depends on the application. The mode of the measurement (*i.e.*, narrow-band or broadband) must be specified, and in the case of broadband measurements, also the source noise temperature at the signal and image frequencies. This enables the appropriate system noise temperatures to be calculated and compared. When the context is broadband (continuum) radiometry, simply comparing the (SSB) receiver noise temperature of an SSB receiver with the DSB receiver noise temperature of a DSB receiver is appropriate, but when narrow-band (SSB) signals are to be measured no such simple comparison is meaningful.

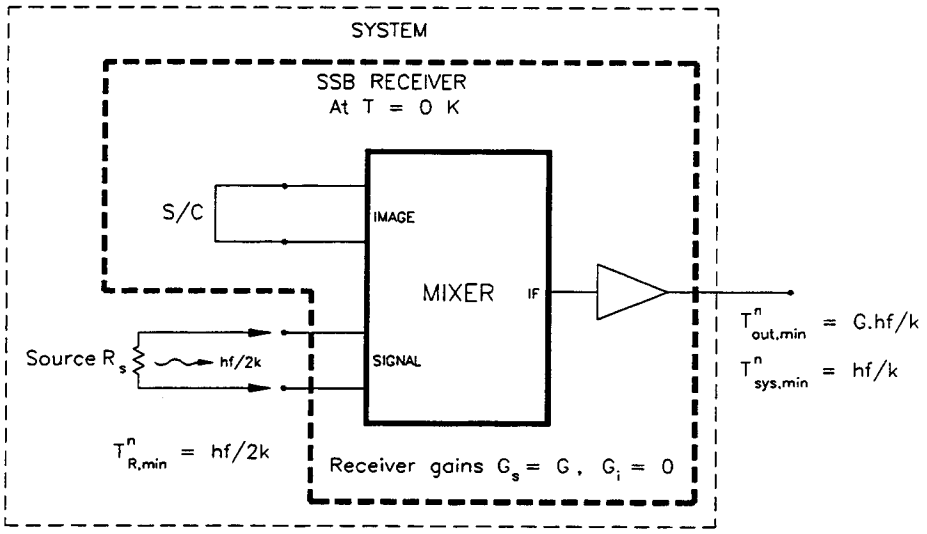

MINIMUM NOISE TEMPERATURES FOR AN SSB RECEIVER WITH S/C IMAGE TERMINATION

Fig. 3(a)

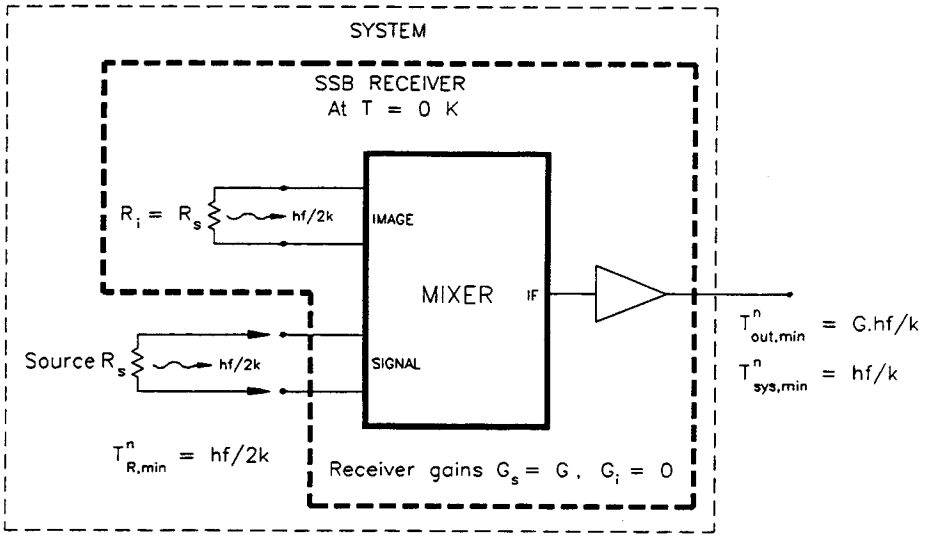

MINIMUM NOISE TEMPERATURES FOR AN SSB RECEIVER WITH RESISTIVE IMAGE TERMINATION

Fig. 3(b)

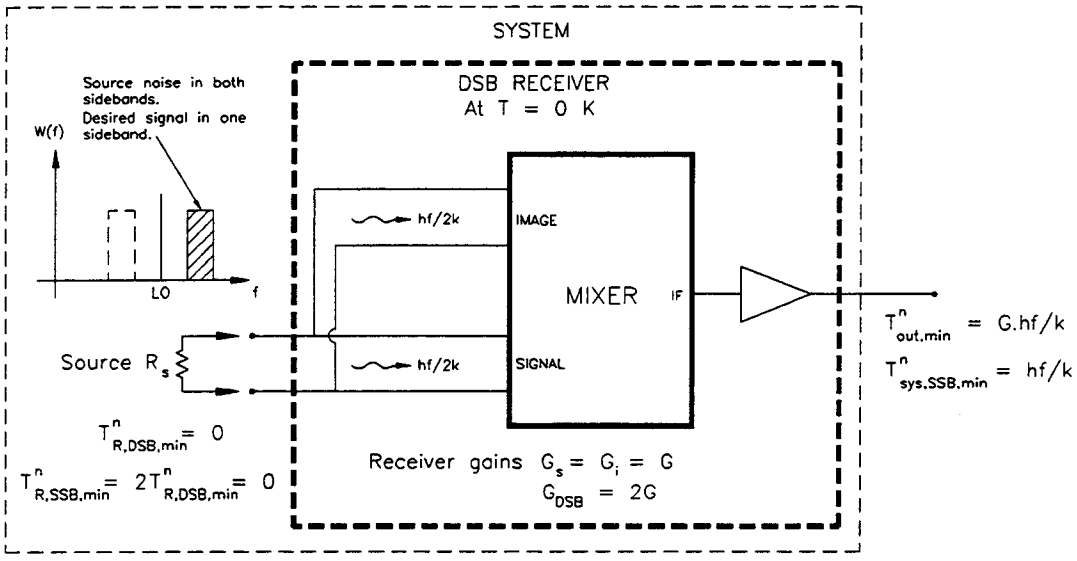

MINIMUM NOISE TEMPERATURES FOR A DSB RECEIVER
Narrow–Band (SSB) Measurements

Fig. 4(a)

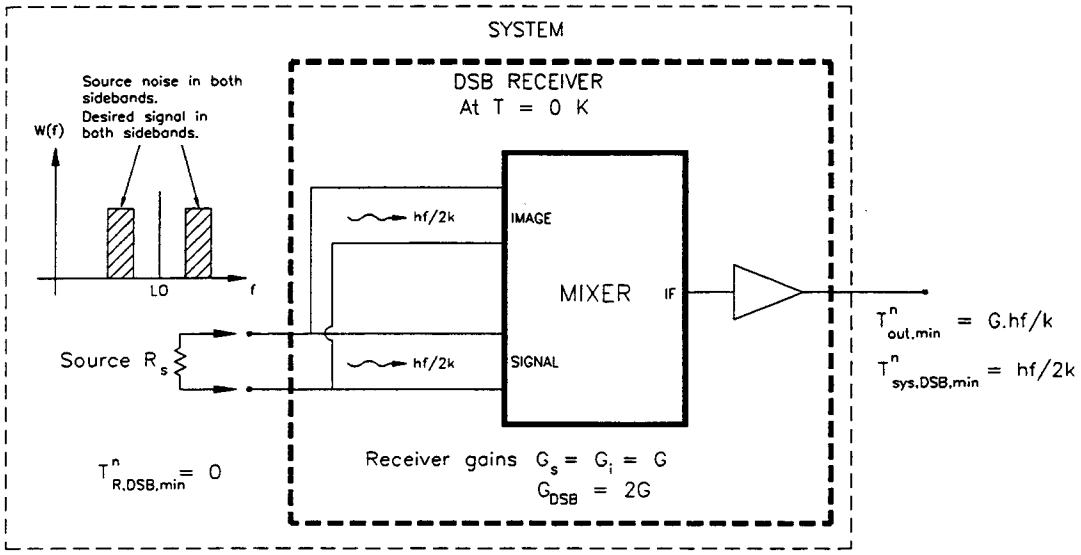

MINIMUM NOISE TEMPERATURES FOR A DSB RECEIVER
Continuum (DSB) Measurements

Fig. 4(b)

Conclusion

Tucker's quantum mixer theory predicts a minimum receiver noise temperature of hf/2k for a SSB receiver, and zero for a DSB receiver, results which are consistent with the limitations imposed by the Heisenberg uncertainty principle. With signal (and image) sources at absolute zero temperature, the minimum receiver output noise, referred to the input (and, in the case of a DSB receiver, referred to one sideband) is hf/k, twice the zero-point fluctuation noise. To be consistent with this, the Callen & Welton law (eq.(6)) and not the Planck law (eq.(5)) must be used in deriving the required source noise temperatures. This ensures that the zero-point fluctuation noise associated with the source is included at the input, and in both sidebands in the case of a DSB mixer.

For many practical cases, the Rayleigh-Jeans law is a close approximation to the Callen & Welton law, and eq. (7) with $T^n = T$ can often be used with insignificant error. When using liquid nitrogen and room temperature blackbodies in measuring the Y-factor, little error is incurred at frequencies up to ~ 1 THz. Use of the Planck law (eq.(5)) for the hot- and cold-load noise temperatures in deriving receiver noise temperatures from measured Y-factors, is inappropriate, and results in receiver noise temperatures higher by half a photon (hf/2k) than they should be (7.2 K at 300 GHz).

In comparing SSB and DSB receivers, the particular application must be considered. When the context is broadband (continuum) radiometry, the (SSB) receiver noise temperature of an SSB receiver can be meaningfully compared with the DSB receiver noise temperature of a DSB receiver, but when narrow-band (SSB) signals are to be measured no such simple comparison is meaningful and the overall *system* noise temperatures for the intended application must be considered.

References

[1] H.B. Callen and T.A. Welton, "Irreversibility and generalized noise," Phys. Rev., vol. 83, no. 1, pp. 34-40, July 1951.

[2] I. A. Devyatov, L.S. Kuzmin, K. K. Likharev, V. V. Migulin, and A. B. Zorin, "Quantum-statistical theory of microwave detection using superconducting tunnel junctions," J. Appl. Phys., vol. 60, no. 5, pp. 1808-1828, 10 Sept. 1986.

[3] M. J. Wengler and D. P. Woody, "Quantum noise in heterodyne detection," IEEE J. of Quantum Electron. vol. QE-23, No. 5, pp. 613-622, May 1987.

[4] J.R. Tucker, "Quantum limited detection in tunnel junction mixers," IEEE J. of Quantum Electron. vol. QE-15, no. 11, pp. 1234-1258, Nov. 1979.

[5] J.R. Tucker and M.J. Feldman, "Quantum detection at millimeter wavelengths," Rev. Mod. Phys., vol. 57, no. 4, pp. 1055-1113, Oct. 1985.

[6] M.J. Feldman, " Quantum noise in the quantum theory of mixing," IEEE Trans. Magnetics, vol. MAG-23, no. 2, pp. 1054-1057, March 1987.

[7] C. M. Caves, "Quantum limits on noise in linear amplifiers," Phys. Rev. D, Third series, vol. 26, no. 8, pp. 1817-1839, 15 October 1982.

[8] A. B. Zorin, "Quantum noise in SIS mixers," IEEE Trans. Magnetics, vol. MAG-21, no. 2, pp. 939-942, March 1985.

Second-Harmonic Broad-Band 60-200 GHz InP Transferred Electron Device and Oscillators

S.H. Jones, M.F. Zybura*, J.E. Carlstrom+, T. O'Brien
Applied Electrophysics Laboratory, University of Virginia, Charlottesville, VA
*Litton Solid State, Santa Clara, CA
+Department of Astrophysics, University of Chicago, Chicago, Ill

Abstract

Theoretical and experimental analysis of a single-style second-harmonic InP Transferred Electron Oscillator is presented for the 60-200 GHz frequency band. It is experimentally shown that this single device is extremely broad band and produces moderate amounts of second-harmonic output power (8-85 mW) between 170-63 GHz. Four different cavity designs are considered. A continuously tunable cavity is shown to produce 30-40 mW of power over the 120-147.5 GHz range without any detectable frequency jumps or power dips. A combination of High Frequency Structure Simulator, Microwave Design Software, and Drift-Diffusion-Harmonic-Balance analysis is used to fully self-consistently analyze the TEO operation. Simulations are capable of predicting operating frequencies to within several GHz and output powers to within about 20% accuracy.

Introduction

Many high frequency heterodyne receivers for radio astronomy and atmospheric science research require low noise, reliable, and moderate power sources in the 60-200 GHz regime. Presently, many heterodyne receivers in this frequency band are using InP Transferred Electron Devices (TED) as the local oscillator (LO) source. Also, to generate LO power at the higher frequencies above about 110 GHz, Schottky Barrier Varactor frequency multipliers driven by InP Transferred Electron Oscillators (TEO) are commonly used. Most the InP TEDs in use today are NN+ type devices developed and manufactured by Litton Solid State, and are current limiting or Stable Depletion Layer (SDL) devices [1,2]. These devices are similar to conventional N+NN+ Gunn Diodes, but differ in the mode of operation since an NN+ structure with a very low barrier non-ohmic cathode is incorporated [2]. Although researchers have demonstrated excellent results in the 60-200 GHz regime using N+NN+ Gunn diodes [3,4], the SDL NN+ devices are often preferred for their low operating currents(150-250 mA), lower operating temperature, higher efficiency (2-10%), and commercial availability.

In general, second-harmonic TEOs are realized by reactively terminating the large fundamental oscillation, and coupling to the second-harmonic output power resulting from the strong nonlinear conductance and reactance of the device [5]. The advantage of this design is the low noise associated with the high Q of the fundamental oscillation, combined with the easy tuning and minimal load pulling of the second-harmonic output power. However, as described here, the high Q resonator at the fundamental frequency limits the bandwidth of any one oscillator cavity. In this paper we offer experimental results demonstrating that a single InP, SDL mode, second-

harmonic TEO can operate over the very broad band of about 63-170 GHz; the theoretical results indicate that device operation from 60-200 GHz with this single device is very reasonable given proper cavity design. All the results reported here are for moderate power (10-100mW), and second-harmonic TEO operation. The emphasis of this report is to verify both experimentally and theoretically that the intrinsic bandwidth of high frequency, SDL mode, InP TEDs is on the order of 100 GHz; the typically narrow operational-bandwidth that is observed for most TEOs is associated with the high unloaded circuit Q and other cavity properties. Hence, a number of different broad-band and narrow-band cavities had to be used in this investigation in order to achieve good oscillator operation over the entire range of 63-170 GHz. Certainly, to optimize performance over some narrow-band within this 60-200 GHz range both the diode and cavity design should be fully optimized. However, the device described here does perform well over the entire frequency range, and as expected performs particularly well near the center of the band.

Oscillator Properties and Numerical Simulation

Device Properties

The broad-band device investigated here is a 62.5 um diameter NN+ InP current-limiting TED [1]. The N-type active layer is nominally doped to $1x10^{16}$ cm^{-3} and is about 1.8 um long. An integral heat sink fabrication process is used to reduce thermal resistance, and the N+ substrate region is only 10 um thick to minimize parasitic resistive loss. A very shallow barrier cathode contact serves to restrict current flow and force the SDL mode of operation. Details of the fabrication process, operation, and design for this device are given in references 1,2. The devices are packaged in standard pill-packages incorporating a quartz dielectric-ring to enclose the device. The inner diameter of the quartz ring is nominally 250 um, the outer diameter is about 300 um, and the ring is about 25 um thick. Au preformed-crosses are typically used to bond the InP device anode to the package lid via the quartz dielectric-ring stand-off. For the highest frequency 170 GHz devices, a six-lead preformed-star was used. This bonding configuration is needed to reduce the series inductance to the diode and increase the operating frequency. A schematic of the device is given in Figure 1. The quartz ring package is not shown in the figure; it is bonded to the heatsink and surrounds the diode.

Cavity Properties

Several second-harmonic cavities and bias-choke structures were used to experimentally explore the maximum bandwidth capability of the described device,. The inherent narrow bandwidth of the high Q cavity at the fundamental makes it very difficult to achieve high performance over a broadband (although the device is inherently broad band). Hence, four separate cavities all similar to those described by Carlstrom [5] were used to achieve reasonable power and performance across the entire 64-170 GHz band (using the single-style device described above). A number of different devices

having the same specifications and very similar operating characteristics were used throughout this investigation. Figure 2 shows the basic cavity configuration.

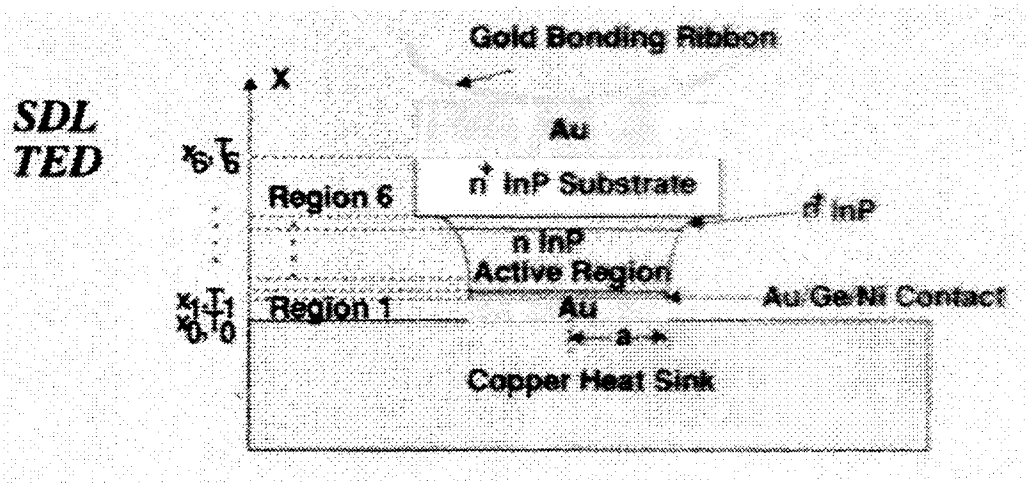

Figure 1 Cross Sectional Schematic of the SDL TED

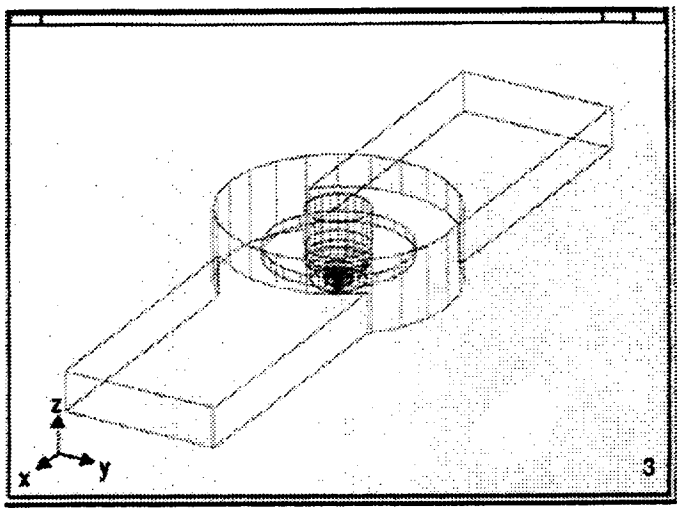

Figure 2 (a) Second-harmonic TEO cavity oblique view

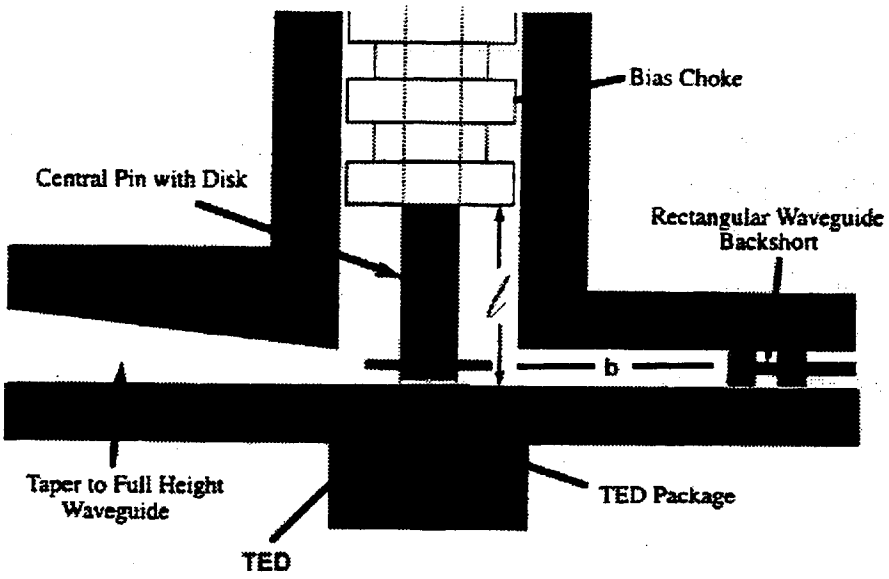

Figure 2 (b) Second Harmonic TEO cavity cross sectional view

Broad-band continuously-tunable Carlstrom-style cavities were used for the 94 - 147 GHz (noted wr8-Carl in table 1) as well as the 70-100 GHz band (noted wr10-Carl in table 1). For these cavities the frequency is continuously tunable by mechanically adjusting the height (l) of the inner coaxial resonator. This alters the resonant frequency of the fundament tone; as l is decreased the frequency is increased. The dimensions of the horizontal waveguide section correspond to wr8 and wr10 waveguide respectively. Also, wr6 and wr10 fixed-frequency cavities were used to investigate select frequencies between 170 and 110 GHz respectively (noted wr10-wr6 and wr6 in table 1). For the fixed-tune cavities the height (l) is not adjustable. The power-backshort and output waveguide section in all cases are cutoff at the fundamental operating frequency to insure high Q at the fundamental and minimal load pulling while adjusting the output power. All cavities have adjustable waveguide backshorts to adjust b, and control the second-harmonic impedance presented to the diode. This controls the second-harmonic power at the output. Adjustment of b only slightly changes the frequency since the fundamental is cutoff in the backshort section and the frequency is predominantly controlled by height (h) of the inner coaxial resonator. The wr10-wr6 cavity in Table 1 has wr10 dimensions for the inner cavity and backshort, but a wr10 to wr6 transition at the output to cutoff the fundamental oscillation at the output.

Numerical Simulation

Theoretical investigations of the devices, the cavities, and the devices operating in the cavities were completed using numerical simulation and computer aided design techniques. The properties of the device were explored using unique numerical simulation codes that self-consistently incorporate physical device simulation and harmonic-balance nonlinear circuit simulation [6]. Electron transport and current flow

within the device is achieved by self-consistently solving Poisson's Equations, the 0^{th} and 1^{st} moments of the Boltzmann Transport Equation (current equations) , and the Heat Equation. Since the devices are perfectly cylindrical and relatively large, a one-dimensional finite difference Crank-Nicholson technique is used to solve the set of time and space dependent nonlinear differential equations under large signal excitation. Both electric field dependent and temperature dependent electron mobility and diffusivity are incorporated into the current equations to account for complex transport phenomena under high frequency and large signal operation. The dependence of electron mobility and diffusivity on electric field and temperature was extracted from Monte Carlo analysis of electron transport in the InP material. A unique Accelerated Fixed Point harmonic balance technique [7] is combined with the electron transport analysis to complete the actual oscillator simulation. This combined analysis is referred to as the Drift-Diffusion-Harmonic-Balance analysis (DDHB), and requires detailed knowledge of the circuit embedding impedance as seen by the device. Embedding impedance at the fundamental frequency and at the first six harmonics are inputs to the DDHB code. The other inputs to the DDHB code include device area, cathode barrier height, device doping profile, active layer length, heat sink and substrate parameters, and DC bias. Oscillator characteristics such as power, current and voltage verses time, and device temperature profile are self-consistently and autonomously calculated. Numerical convergence for the DDHB occurs when the Kurokawa conditions for two-terminal oscillators are satisfied (linear circuit embedding impedance is equal-and-opposite to the nonlinear device impedance at all six harmonic frequencies) [8]. Since the DDHB simulations include device, circuit, and thermal analysis, very accurate results for oscillator power and behavior are achievable.

High Frequency Structures Simulator (HFSS) is used to numerically simulate the electromagnetic fields in the cavities at a specific frequency. HFSS is a three dimensional electromagnetic solver that uses finite element techniques to solve Maxwell's equations. Also, using HFSS the exact embedding impedance presented to the device can be calculated for a range of frequencies, backshort positions, pin and disk geometry, and package geometry. For the fixed-tuned wr6 cavity and the wr8-Carl cavity (see Figure 2 and table 1) the entire oscillator structure including the device package has been simulated with HFSS. This allows one to view the internal fields and cavity behavior, and makes it possible to accurately calculate the embedding impedance that is needed for the DDHB simulations. The embedding impedance is calculated by de-embedding and normalizing the S-parameters calculated by HFSS, and then using MDS to calculate the impedance at the position of the diode from the S-parameters. The HFSS probe is a 60 um diameter coaxial probe placed at the precise location of the diode. Correlation between theory and experiment is accurate to within 20% when using the combined analysis techniques of HFSS, MDS, and DDHB [6]. To fully explore the coupled effects of cavity and device properties on the oscillator operation, simulations were completed to calculate the output power as a function of backshort position and cavity geometry. This required several hundred DDHB simulations to be completed and scores of HFSS simulations. To reduce computation time, distributed computing techniques are used for the DDHB code.

Results and Discussion

Theoretical Analysis of Inherent InP Device Properties

Using the DDHB simulator, the small signal negative resistance of the 1.8 um long TED was explored. Simulations were run for fundamental frequencies (f1) ranging from 25-100 GHz (second-harmonic frequencies, f2, between 40-200 GHz). For this analysis the device was driven with a small AC signal (20 mV) at f1 and a DC bias of 8-10 volts. The current and voltage verses time, diode impedance, and power were self-consistently calculated at each operating point, and the first six harmonic tones. The small signal negative resistance of the diode (ReZ_{diode}) at the fundamental frequency ranged from about -10 ohms to -0.7 ohms for 25 GHz to 100 GHz respectively. This corresponds well with the small signal analysis presented in reference 2, and indicates that oscillator operation is predicted over a very broad band. Upon turning on the diode there is a current pulse applied to the high Q resonator, and a subsequent harmonic impulse response. If the resonator center frequency is within the frequency band of negative resistance, the harmonic response near the center frequency will be amplified. As the voltage amplitude of the signal increases, the diode negative resistance decreases (see Figure 3 and 4) until the $ReZ_{diode} = -ReZ_{circuit}$.

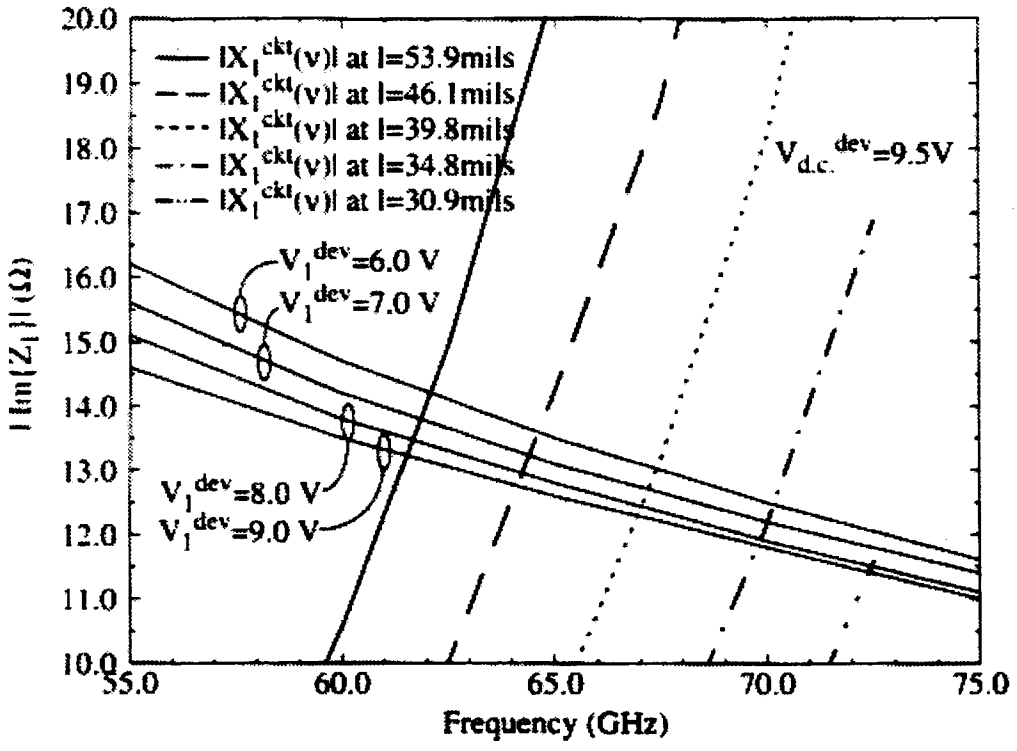

Figure 3 Operating Points as predicted by the DDHB and HFSS simulations

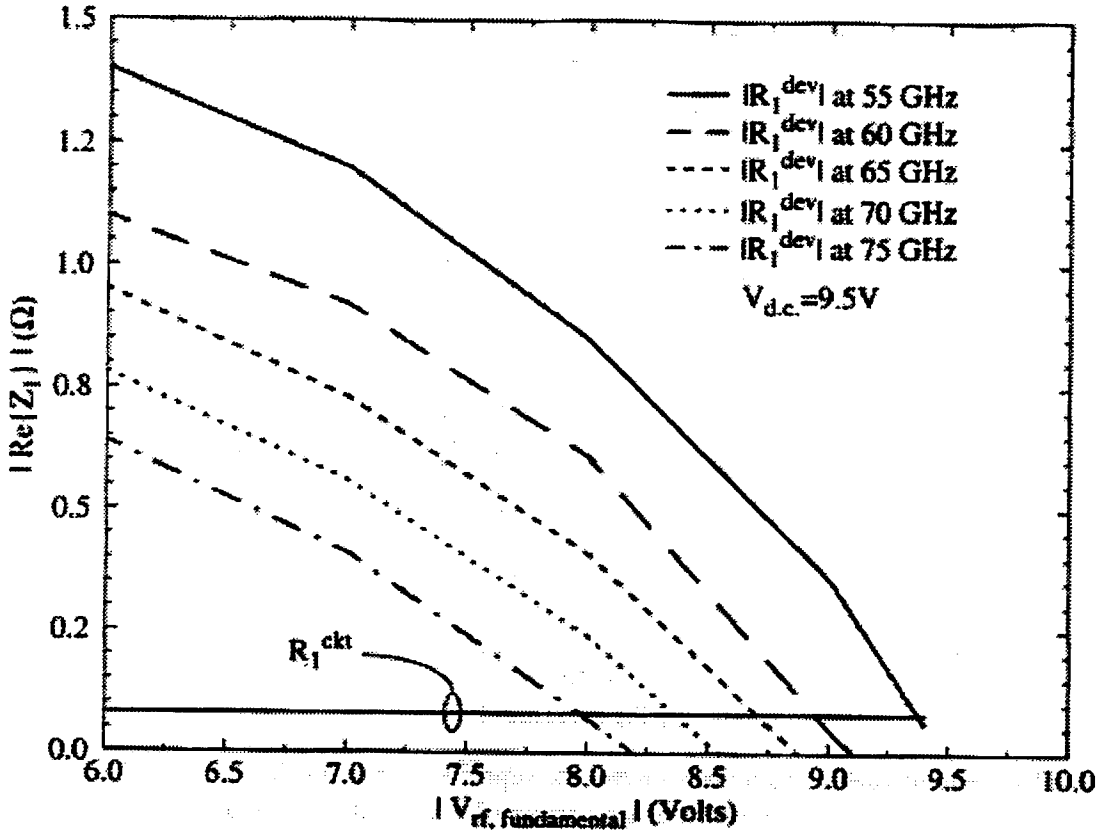

Figure 4 Operating Points as predicted by DDHB and HFSS simulations

The frequency changes until $ImZ_{diode} = -ImZ_{circuit}$, $f1 = 1/(ImZ_{diode}\, ImZ_{circuit})^{1/2}$, and a stable oscillation is established (Kurokawa condition, [8]). Since the fundamental frequency is reactively terminated, the magnitude of the voltage oscillation increases until $ReZ_{diode} = -R_{parasitic}$, where $R_{parasitic}$ is the parasitic resistance of the device contacts, and the cavity loss. Hence, voltage oscillations will occur if the magnitude of the $ReZ_{circuit} + R_{parasitic}$ is less than the magnitude of ReZ_{diode}. However, as indicated by the Kurokawa condition, stable oscillations are only possible if the condition $ImZ_{diode} = -ImZ_{circuit}$ can be achieved, and the magnitude of the derivative of the diode resistance with respect to the RF voltage, $dReZ_{diode}/dV_{rf}$, at the fundamental is less than one. If this condition is not possible, then the requirement that $ReZ_{diode} = -R_{parasitic}$ is also not possible as the RF voltage increases. Large Signal DDHB simulations were completed over the frequency range of 25-100 GHz (similar to Figure 4) to directly calculate the simplified stability criteria $dReZ_{diode}/dV_{rf} < 1$. At all frequencies over the band and DC biases between 8-10 volts the stability criteria was achieved. These small signal and large signal DDHB simulations therefore predict that stable oscillation is expected over the frequency range of about f1 = 25-100 GHz for DC bias between 8-10 volts. Second-

harmonic operation and moderate power is therefore predicted over the frequency range of f2 = 50-200 GHz.

The steady state oscillator behavior was analyzed by simulating the above described device at each frequency in the band, at a DC bias of 10 volts, and a second-harmonic embedding impedance of $Z_{circuit}$ = 7+j7 ohms. Figure 5 shows the theoretical maximum second-harmonic output power verses frequency for this device under these conditions.

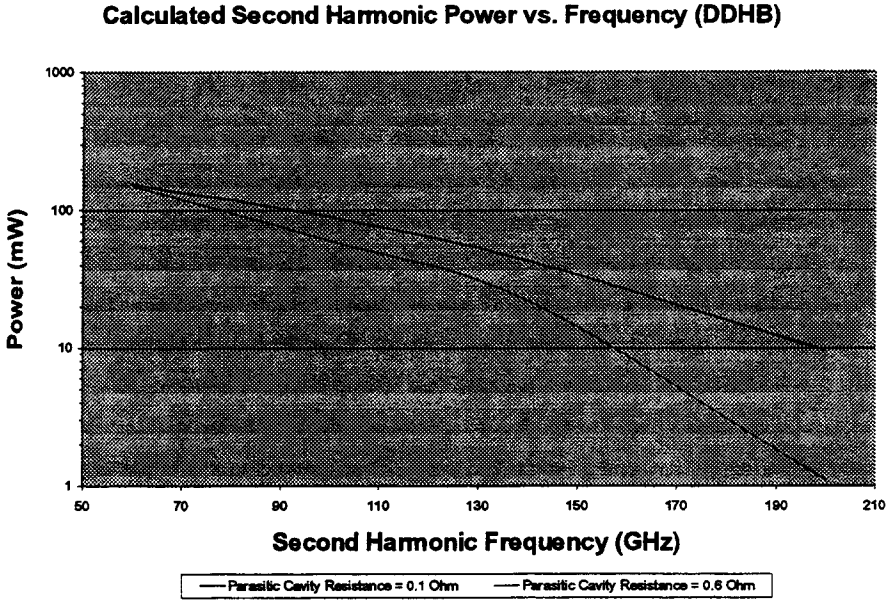

Figure 5 Simulated Maximum Second Harmonic Power vs. Frequency

As seen the DDHB simulations predict that this single device can produce 150-10 mW of second-harmonic output power over the entire range of 60-200 GHz if the appropriate embedding impedance is presented to the diode. The effects of $R_{parasitic}$ at the fundamental frequency are also included. At the fundamental frequency ReZ_{diode} = - $R_{parasitic}$ and the ImZ_{diode} ranged from 22-8 ohms for f1 = 30-100 GHz respectively. Since the waveguide is cutoff at the fundamental, the real part of the fundamental circuit impedance is nearly zero ohms. The ReZ_{diode} is essentially equal to the parasitic resistance of the device plus any cavity losses. When the cavity loss increases from 0.1 ohm to 0.6 ohm at f1, there is a significant reduction in the second-harmonic output power. As the real part of the impedance increases at the fundamental, power is internally dissipated in the cavity, and the magnitude of the voltage oscillation is greatly reduced. For negative resistance diode oscillators, the magnitude of the fundamental voltage oscillation is reduced as the square of the real part of the fundamental impedance. This is exactly the case for these diodes as shown in Figure 4. Hence, as the real part of the fundamental embedding impedance increases, the magnitude of fundamental voltage is reduced, and subsequently, the magnitude of the second-harmonic voltage (V_{rf2}) is

reduced. Since the power delivered at the second-harmonic frequency (P2) is given by P2 = $V_{rf2}^2/2ReZ_{2diode}$, the output power is reduced for all possible load impedance. Since the small signal negative resistance is smaller at higher frequencies, the increase of $R_{parasitic}$ to 0.6 ohms reduces the second-harmonic output power more severely at higher frequencies. Therefore, these DDHB simulations indicate that 150-10 mW of second-harmonic output power is achievable from a single-style TED provided the fundamental frequency is reactively terminated and the second-harmonic circuit impedance is near 7 + j7 ohms. Although not shown here, 100% variation in the second-harmonic circuit impedance (from 7 +j7 ohms) only produced approximately a 50% variation in the second harmonic output power.

Theoretical Analysis of Inherent Cavity and Oscillator Properties

Although the above analysis indicates that the InP TEDs are inherently very broad band devices, the oscillators are typically narrow band since the cavities are very high Q at the fundamental frequency (low Q at the second-harmonic). Hence, HFSS analysis of the intrinsic cavity properties such as impedance and unloaded Q have been completed. Since the variation in the ImZ_{diode1} with bias voltage is relatively small, only 100-300 MHz of bias frequency-tuning is typically possible with these devices. Varactor tuning the $ImZ_{circuit1}$ and subsequently frequency tuning is possible for very narrow bands, but reduces the oscillator performance by introduce parasitic loss into the high Q fundamental resonator. Therefore, mechanically adjusting the coaxial resonator height (l) is the only practical technique for broad band frequency tuning. As described below, the wr8-Carl cavity demonstrated the largest continuous tuning bandwidth of the four cavities investigated. Therefore, extensive HFSS simulations were completed for this cavity. The cavity was analyzed for different coaxial resonator heights (l in Figure 2), and corresponding fundamental frequency ranges from 49-72 GHz, second-harmonic frequencies ranging from 99-145 GHz, and appropriate third harmonic frequencies. HFSS was used to visual the electromagnetic fields for different cavity configurations and at different frequencies. Also, using a combination of HFSS and Microwave Design Software (MDS) the circuit impedance seen by the diode was directly calculated. Figure 2b illustrates how the entire cavity and device package was carefully drawn and incorporated into the HFSS analysis.

Figures 6 and 7 show snapshots of the time varying electric field in the wr8-Carl cavity 140 and 108 GHz respectively. The plot for f2 = 140 GHz corresponds to the precise dimensions of the wr8-Carl cavity that was used to experimentally measure about 40 mW of output power at 140 GHz. Although not shown, at 70 GHz the fields are confined to the coaxial resonator within the center of the cavity. Although not illustrated here, the time variation of the electric field at 70 GHz is a TEM oscillation driven by the diode and disc region.. As expected, the 140 GHz oscillation is coupled to the output and power is delivered to the load. The disk serves as transformer to reduce the load impedance as seen by the diode. The cavity was simulated at the fundamental, second-harmonic, and third-harmonic frequency for coaxial resonator heights corresponding to observed second-harmonic output power at 99, 100, 108, 116, 119, 120, 125, 130, 140,

and 145 GHz. Operation at all these frequencies with the exception of f2 = 108 GHz is very similar to that shown in Figure 6..

At f2 = 108 GHz a strong resonance occurs between the disc and the upper coaxial section that shorts-out the diode at the second harmonic. Figure 7 shows the relatively weak second-harmonic fields being shorted between the disc and the coaxial wall. This essentially demonstrates the phenomena of a power dip in the broad band operation of the TEO. The second-harmonic oscillator is well behaved over most the 99-145 GHz band as l is decreased until the severe resonance condition at the second-harmonic occurs near 108 GHz.

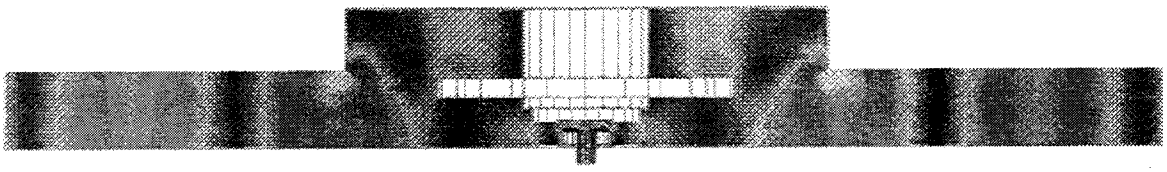

Figure 6 HFSS simulation of the wr8-Carl cavity at 140 GHz

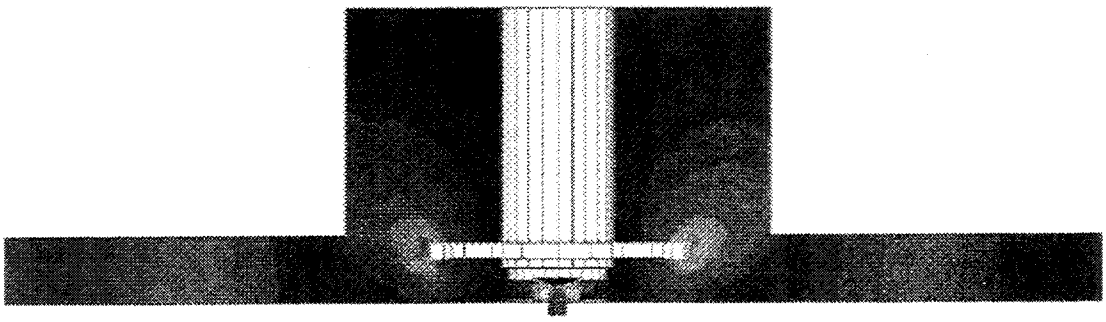

Figure 7 HFSS simulation of wr8-Carl cavity at 108 GHz

To further illustrate the effects of cavity geometry on the device embedding impedance, HFSS and MDS were used to directly calculate the embedding impedance at many frequencies between 99-145 GHz (second-harmonic), and 49.5-72.5 GHz (fundamental). Also, the impedance at each frequency verses the position of the power backshort was calculated. Figures 8, 9 show the calculated circuit impedance seen by the diode at 70, 140, and 108 GHz as a function of the power backshort position (varying b in Figure 2).

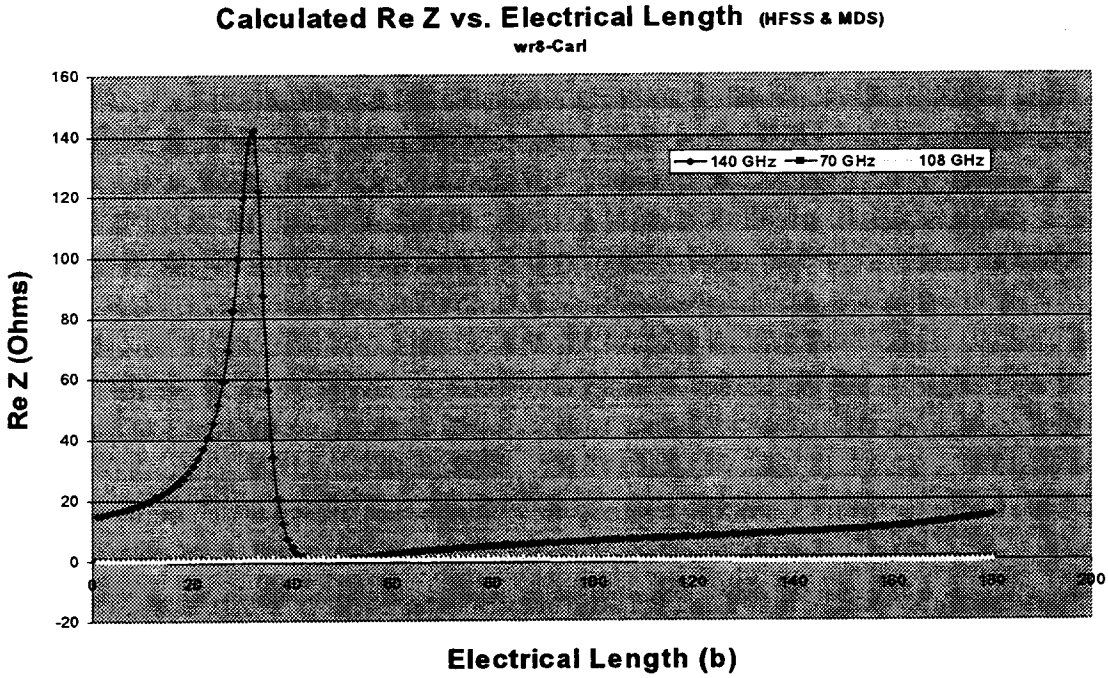

Figure 8 Re Z as a function of backshort position

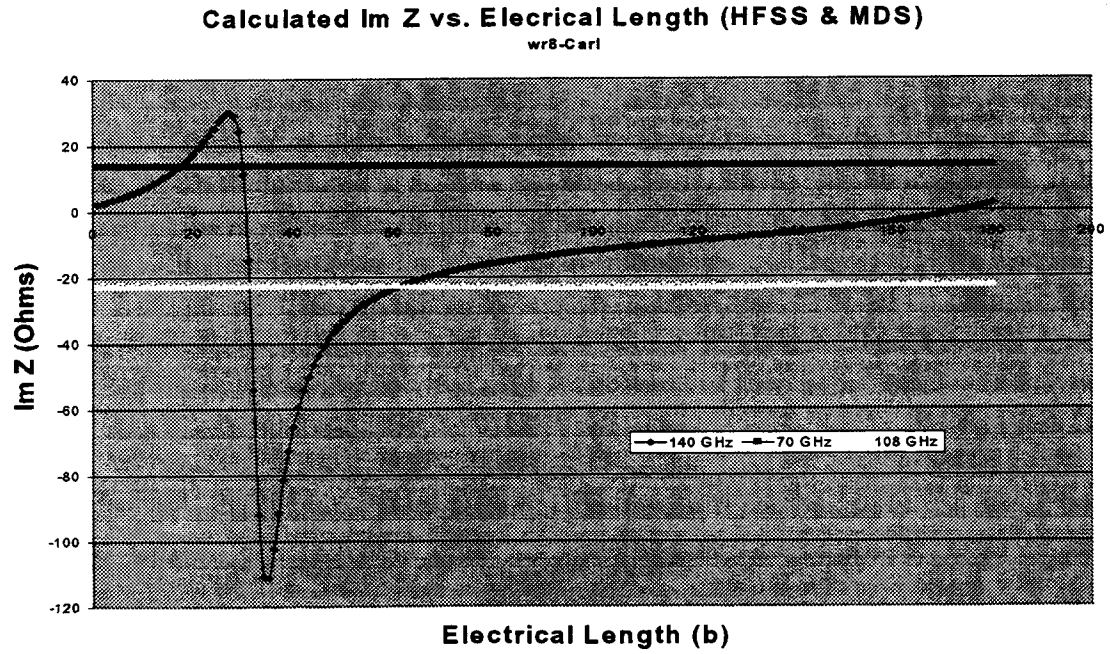

Figure 9 Im Z as a function of backshort position

At the 70 GHz fundamental frequency, the circuit impedance is purely inductive and independent of the power backshort position. However, at the 140 GHz second-harmonic frequency the impedance moves along a circle on the smith chart as the power backshort is adjusted; the impedance is plotted on a linear scale in Figures 8 and 9. Hence, with a properly designed cavity the near optimal second harmonic impedance of approximately 7+j7 ohms can be easily achieved with this cavity design. However, the TEO bandwidth is bounded at low frequency by the second-harmonic resonance condition at 108 GHz. As shown in Figure 8, the second harmonic impedance is shorted at 108 GHz and not tunable by the power backshort. Although not shown, the fundamental impedance at 54 GHz is well behaved. The resonance at 108 GHz can be moved slightly by changing the package dielectric or the width of the disc. However, changing the package dielectric only slightly effects the resonance. Increasing or decreasing the disc diameter greatly compromises the impedance transformation across the remainder of the band limiting performance at other frequencies. Therefore, the 108 GHz power dip is strongly related to *l*, and difficult to remove without compromising performance at other higher frequencies. The TEO bandwidth is limited at higher frequencies by the cutoff frequency of the wr8 backshort and output waveguide. Above about f1 = 73.5 GHz the fundamental power is coupled to the output and the loaded Q at f1 is greatly reduced. As described above, the magnitude of the RF voltage at f1 is greatly reduced when the fundamental is coupled to an external load or, if the resistance of the load is large enough the oscillations are terminated. Hence, the upper frequency of second harmonic operation for this wr8 cavity is about 147 GHz; at higher frequencies the output power is dominated by the fundamental frequency.

The theoretical operating point of the oscillator can be predicted by using HFSS and MDS together with the DDHB simulator. By plotting the embedding impedance for different values of *l* verses frequency in combination with the intrinsic diode impedance verses V_{rf1} and frequency, the operating point is defined by the points of intersection. The points of intersection are where the Kurokawa conditions hold. Figure 3, 4 demonstrate this analysis for the wr8-Carl cavity for f1 = 55-75 GHz. The operating frequency for a given *l* is determined by the mutual intersection of the circuit and device lines shown in figures 3a,b. For example, when *l* = 53.9 mils (solid line) the points of mutual intersection are approximately 61.5 GHz and Vrf = 8.75 volts. Therefore, the self-consistent analysis of HFSS, MDS, and DDHB simulation predict a second-harmonic output at 123 GHz for *l* = 53.9 mils. The experimentally measured oscillator operating point for this *l* value in the wr8-Carl cavity at 10 volts DC bias is 120 GHz. Therefore, this complex analysis is accurate to within about 3 GHz. The other operating points predicted in Figures 3, 4 are also within 2-4 GHz accurate. As described below, the power delivered to the load at each operating point is also accurately predicted. This analysis shows that the mechanical tuning of the wr8-Carl cavity can offer continuous and smooth frequency tuning over a relatively large bandwidth; the wr8-Carl TEO is expected to have at least 27.5 GHz of bandwidth from 120-147.5. However, to achieve more than 30 GHz of TEO bandwidth in this frequency regime is probably very difficult using any mechanical or electrical tuning technique. Certainly, the fixed-tune cavities

(non-adjustable *l*) are limited to bias tuning which is approximately 100-300 MHz/volt for these diodes.

Experimental Results and Comparisons to Theory

To confirm the inherently broad band nature of this diode (under the constraints of limited bandwidth cavities) a set of identical diodes from several fabrication batches were tested in the four cavities described above. As shown in table 1 this design is capable of broad band second-harmonic operation, and at least 55 mW at 67 GHz , 85 mW at 122 GHz, 55 mW at 140 GHz, 29 mW at 151 GHz, and 8 mW at 170 GHz.

Cavity Style	2nd Harmonic Power (mW)	Output Frequency (GHz)
wr6	8	170
wr6	6	167
wr6	29	151
wr6	49	146
wr6	55	140
wr10-wr6	42	137
wr10-wr6	65	127
wr10-wr6	85	122
wr8-Carl	30-40	120-147.5
wr8-Carl	20-25	99-105
wr10-Carl	30	93
wr10-Carl	55	67
wr10-Carl	30	63

The results in Table 1 were attained by exploring many different pin and disc diameters and back short positions in each of the four cavities. Second-harmonic operation was confirmed by directly observing the third-harmonic power at exactly 3/2 the frequency of the measured tone. If the output power was a result of fundamental operation the next higher frequency tone would be at exactly twice the frequency. These experimental results confirm the theoretic analysis described above and show that this device has at least 84.5 GHz of bandwidth. The degradation in performance near 170 GHz is thought to be primarily due to improper impedance matching. The wr6 cavity used here was designed and optimized for operation near 140 GHz, and is probably not possible of achieving the proper impedance at 170 GHz with any set of pin and disc diameters. Similarly, the low frequency measured at 63 GHz is probably not the lowest possible frequency, but was the lowest achievable with the wr10-Carl cavity and limited pin and disc diameters.

Figure 10 demonstrates that the wr8-Carl cavity has continuous operation from 99-147.5 GHz, but a major power dip between 108 and 115 GHz. Over 30 mW of power is continuously produced from 120-147.5 GHz. This behavior is fully predictable using

HFSS, MDS and DDHB simulation. Figure 11 shows the experimental and theoretical second-harmonic power for the wr8-Carl cavity at 140 GHz and 108 GHz as a function of backshort position. The output power has been simulated using the DDHB code with the embedding impedance calculated from HFSS. As expected, the output power varies with backshort position as the impedance moves around a circle on the smith chart.

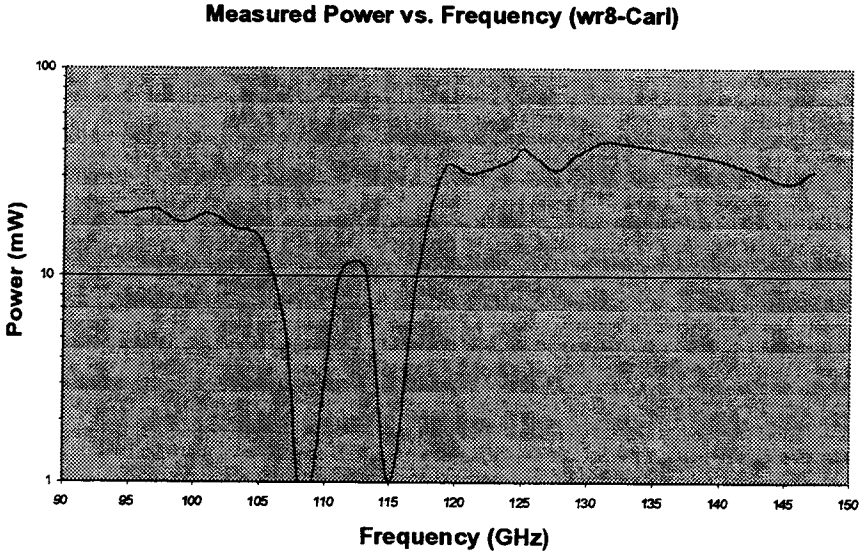

Figure 10 Power vs. Frequency Measured with the wr9-Carl cavity

Comparison of Figures 8 through 11 indicate the optimal impedance as well as the backshort position that essentially shorts the second-harmonic power. Reasonable amounts of second-harmonic power are generated even for backshort positions that present a capacitive load to the diode. Although the diode must be capacitive at the fundamental, at the second-harmonic the diode can appear inductive. This is a direct outcome of the nonlinearity of the device impedance which produces undriven harmonic currents and voltages with phase relationships controlled by the linear embedding impedance of the circuit. For 108 GHz the output power is very low and independent of back short position since a strong resonance occurs within the coaxial section; the device is essentially shorted at the second-harmonic.

Conclusion

We have shown experimentally that a single-style InP second-harmonic TED can produce moderate amounts of output power over the frequency range of 63-170 GHz. An accurate theoretical analysis using HFSS, MDS, and DDHB has been used to show that this device is capable of operation from 60- 200 GHz with proper cavity design. A mechanically tuned cavity is described that continuously tunes from 99-147.5 GHz with no detectable frequency jumps, and produces 30-40 mW of power over the 120-147.5

GHz band. Future experimental and theoretical investigations are focused on new diode and cavity designs capable of moderate output power (10-30 mW) in the 200-150 GHz regime.

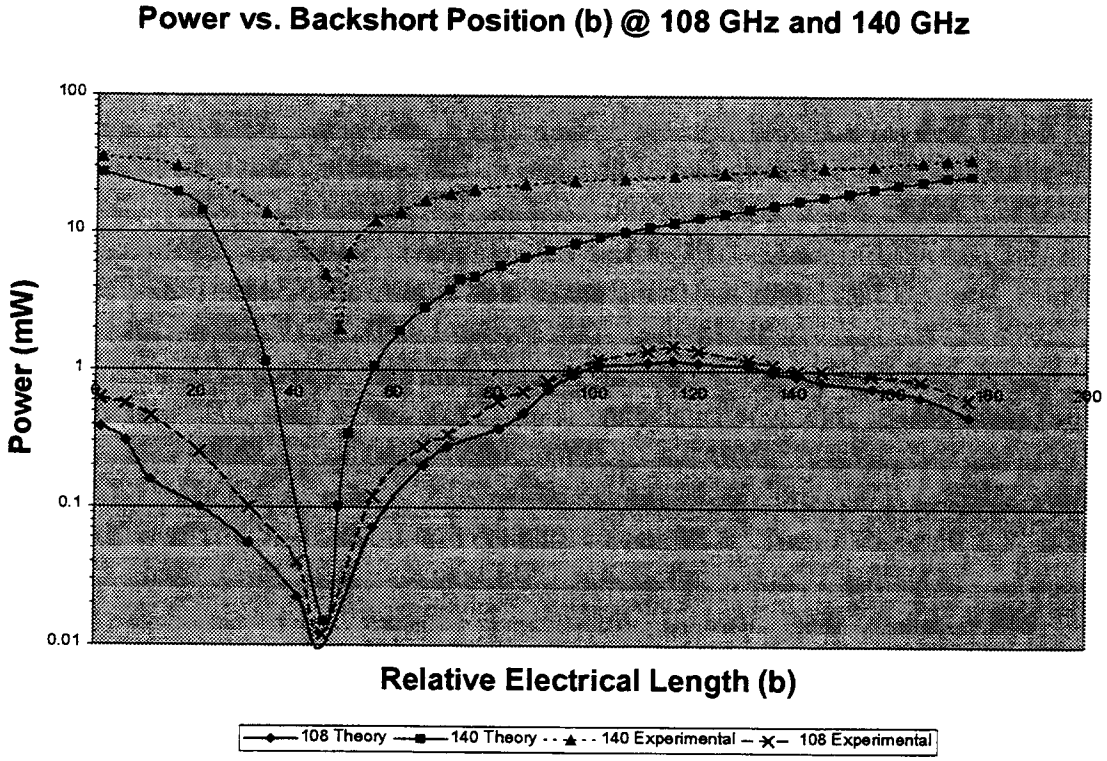

Figure 11 Theoretical and Experimental power vs. backshort position for the wr8-Carl cavity

References

1. J.D. Crowley, C. Hang, R.E. Dalrymple, D.R. Tringali, F.B. Frank, L. Wandinger, B. Wallace, Electron. Lett., 30, 499 (1994).
2. M.F. Zybura, S.H. Jones, B.W. Lim, J.D. Crowley, J.E. Carlstrom, Solid State Electronics, vol. 39, No. 4, pp 547-533 (1996).
3. H. Eisle, G.I. Haddad, Proceedings of the 1995 Symposium on Space Terahertz Technology, Pasadena, CA (1995).
4. A. Rydberg, Int. J. Infrared Millimeter Waves, 11, 383, (1990).
5. J.E. Carlstrom, R.L. Plambeck, D.D. Thornton, IEEE MTT, MTT-33, No. 7, (1989).
6. M.F. Zybura, J.R. Jones, S.H. Jones, G. Tait, IEEE MTT, vol 43, No. 4, (1995).
7. G. Tait, IEEE Microwave and Guided Wave Lett., vol 4, No. 12, (1994).
8. K. Kurokawa, Bell Systems Technical Journal, (1969).

Why Don't Back-to-Back Abrupt Junction Frequency Triplers Work?

R. F. Bradley and A. R. Kerr
National Radio Astronomy Observatory*
Charlottesville, VA 22903

N. R. Erickson
Five College Radio Astronomy Observatory
University of Massachusetts
Amherst, MA 01003

Abstract

The recent interest in direct frequency tripling, *i.e.*, tripling without idler circuits, is due primarily to advances in the fabrication of planar, two-terminal nonlinear circuit elements having a symmetrical capacitance-voltage characteristic. Over the past few years, several research groups have put considerable effort into the development of triplers based on uniformly doped (abrupt-junction) back-to-back varactors only to measure little if any power conversion despite an apparently reasonable C_{max}/C_{min} ratio, the common figure of merit. Although a symmetrical capacitance-voltage function is desirable for efficient direct tripling, the dynamics of direct tripling using symmetrical varactors is more complex than first expected.

We describe the nonlinear circuit behavior of back-to-back varactors using the elastance-charge function, and discuss the phenomenon of self-biasing. We conclude by showing that *it is physically impossible for a back-to-back uniformly doped varactor circuit to convert power from the pump frequency to any harmonic.*

---

*The National Radio Astronomy Observatory is a facility of the National Science Foundation operated under cooperative agreement by Associated Universities, Inc.

Introduction

The back-to-back varactor diode analyzed in this paper is shown schematically in Fig. *1(a)*. Physically, the device may consist of either a series connection of two identical varactors with no external connection to the center node, or it can be a monolithic semiconductor structure. In either case, it has often been assumed that this device should work as a frequency tripler, with efficiency dependent on the capacitance ratio C_{max}/C_{min}.

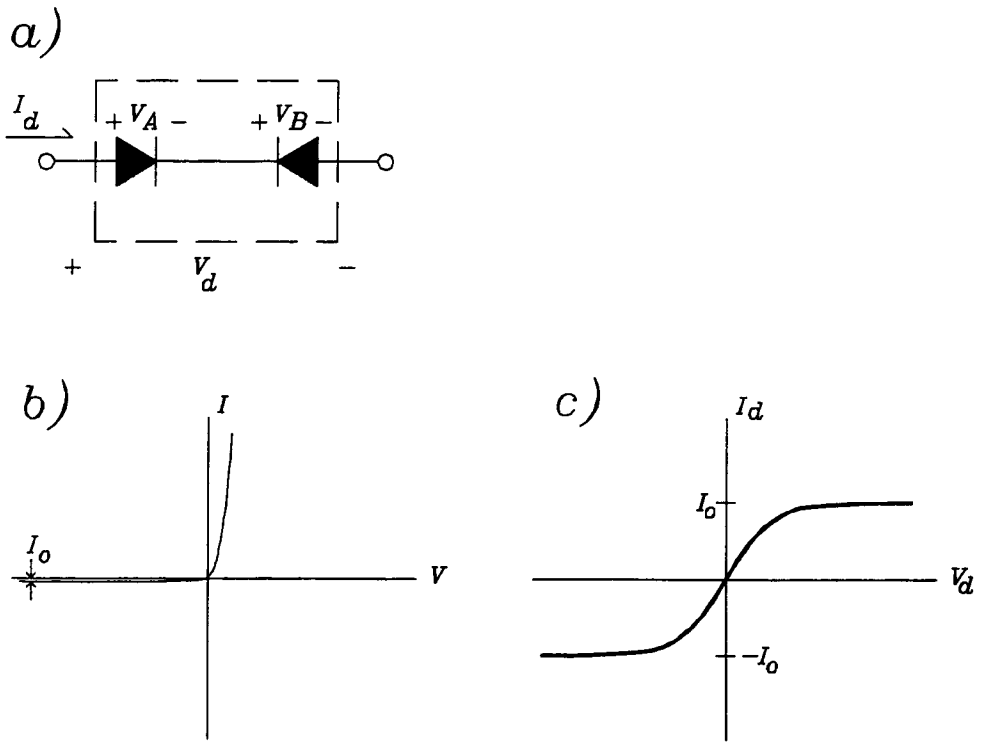

Figure 1 *a*) Schematic representation of the back-to-back diode varactor, *b*) I-V characteristic of a single diode, and *c*) I-V characteristic of the back-to-back varactor.

Figure *1(b)* shows the I-V curve of a single diode. The dc current in the pair of diodes is limited by the leakage current of the "off" diode. For two identical diodes in series,

$$i = i_o(e^{\alpha V_A} - 1) = -i_o(e^{-\alpha V_B} - 1) \quad , \tag{1}$$

and the voltage across the pair is

$$V_d = V_A + V_B = \frac{1}{\alpha}\ln\left[\frac{i}{i_o} + 1\right] - \frac{1}{\alpha}\ln\left[1 - \frac{i}{i_o}\right] \quad . \tag{2}$$

Combining terms and solving for i_d gives the dc I-V characteristic of the back-to-back varactor:

$$i_d = i_o \tanh\left(\frac{\alpha V_d}{2}\right) \quad . \tag{3}$$

An I-V curve according to eqn. 3 is sketched in Fig. *1(c)*.

The equivalent circuit of the back-to-back varactor, ignoring the series resistance, is shown in Fig. 2. The incremental impedance is

$$Z_d = \frac{1}{(g_A + j\omega C_A)} + \frac{1}{(g_B + j\omega C_B)} \quad . \tag{4}$$

For the individual diodes, $g = \alpha(i - i_o)$. Then, at zero bias,

$$Z_d = \left.\frac{2}{g_A + j\omega C_A}\right|_{V=0} = \frac{2}{\alpha i_o + j\omega C_{jo}} \quad . \tag{5}$$

Using typical values for $i_o = 10^{-11}$ A, $\alpha = 39$ V^{-1}, and $C_{jo} = 10$ fF gives a corner frequency above which the back-to-back varactor looks primarily capacitive at zero bias:

$$f_x = \frac{1}{2\pi}\frac{\alpha i_o}{C_{jo}} \approx 400\ kHz \quad . \tag{6}$$

At large bias voltages, the current in the back-to-back pair is essentially the leakage current of one diode. Near the breakdown voltage V_{BR},

$$\begin{aligned} Z_d &= \frac{1}{\left[g_A\big|_{i=-i_o} + j\omega C_A\big|_{V_{BR}}\right]} + \frac{1}{\left[g_B + j\omega C_B\right]\big|_{i=i_o}} \\ &= \frac{1}{\left[0 + j\omega C_A\big|_{V_{BR}}\right]} + \frac{1}{\left[2\alpha i_o + j\omega C_B\big|_{i=i_o}\right]} \quad . \end{aligned} \tag{7}$$

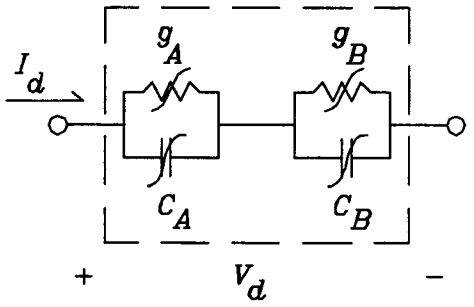

Figure 2 Equivalent circuit of the back-to-back varactor.

Since C_B at $i = i_o$ is approximately C_{jo}, it follows that at frequencies substantially above $2f_x$, the back-to-back diode is predominately capacitive at all bias voltages, with

$$C \simeq \frac{C_A C_B}{C_A + C_B} \quad , \tag{8}$$

which is a function of bias. The C_{max}/C_{min} ratio can be measured as a function of the bias voltage using an RF bridge with a low-level test signal. A typical plot of C_{max}/C_{min} is given in Fig. 3.

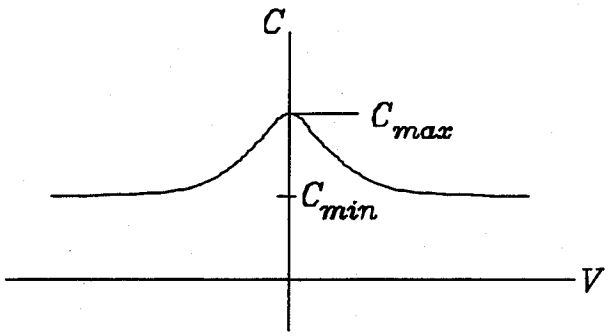

Figure 3 Sketch of typical C-V curve for the back-to-back varactor as measured using an RF bridge.

Among the many devices that exhibit a symmetrical C-V curve, the most popular candidates for millimeter-wave direct triplers have included 1) a pair of identical uniformly doped varactors, 2) a pair of identical hyperabrupt-junction varactors, 3) a quantum barrier varactor, 4) a pair of identical BIN or delta-doped varactors, and 5) a bbBNN varactor. The C_{max}/C_{min} ratio has been used in an attempt to rank the frequency tripling performance of each device. It was widely believed that the higher this ratio the better the tripling performance. However, this ratio, measured under small-signal conditions, is not an adequate indication of the large-signal behavior of the back-to-back diode in a tripler circuit. What is overlooked is the phenomenon of *self-biasing* caused by rectification at the diodes.

Self-Biasing

Self-biasing is well known in single-diode mixers when the dc bias source is replaced with a resistor R_b. The LO causes rectified current in the bias circuit, thus

generating a (reverse) bias voltage across R_b. If R_b becomes infinite, the self-bias voltage increases (in the reverse direction) until the diode conducts no net charge over the pump cycle (if there is nowhere for the rectified current to flow, there can be no net current in the diode). This is illustrated in Fig. 4. The presence of a capacitor (usually the first element of a low-pass filter) in series with the RF circuit provides the necessary charge storage. Note that this circuit is simply that of a half-wave rectifier, which is the best example of self-biasing.

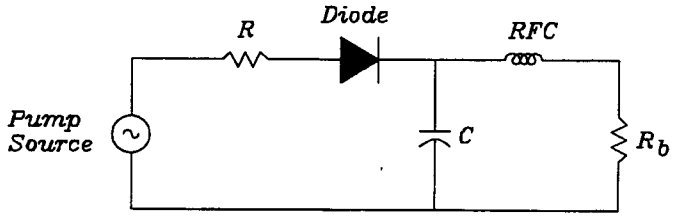

Figure 4 Self biasing in a single-diode mixer.

In the case of a pair of back-to-back diodes driven by a large-amplitude high frequency pump voltage, each diode presents a very high resistance path to the rectified current of the other. Both diodes self-bias, so there is no net current in either. The capacitance of each diode provides charge storage for the other. This is illustrated in Fig. 5.

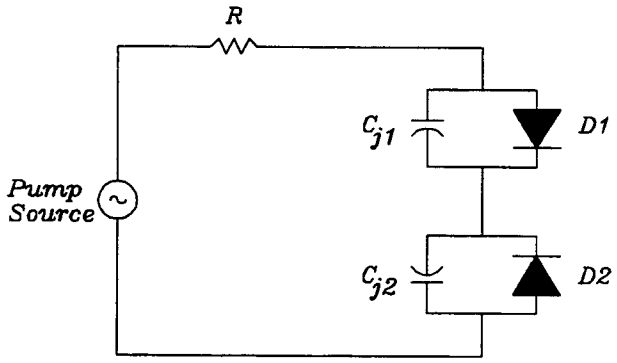

Figure 5 Simplified schematic diagram of a back-to-back varactor driven by a pump source.

Note the similarity between this circuit and a full-wave rectifier.

The effect of self-biasing is to clamp the peak of the diode voltage waveform at a small positive (forward) value, V_{CL} (which is zero for an ideal rectifier). For the back-to-back pair, the self-bias voltage adjusts itself so that during the part of the pump cycle in which the diode is reverse biased, the small amount of charge which leaks through the conductance of the diode in the reverse direction is equal to the charge which flows in the forward direction during the forward-biased part of the pump cycle.

Back-to-Back Uniformly Doped Varactor Tripler

We now examine the large-signal behavior of a pumped back-to-back varactor consisting of a pair of identical uniformly-doped diodes as shown in Fig. 6.

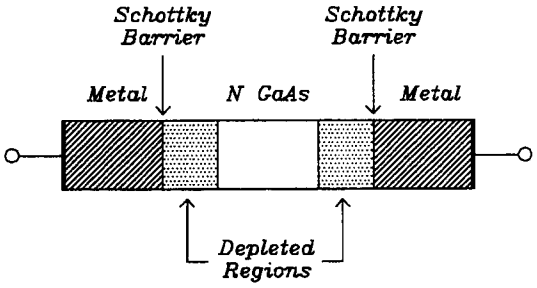

Figure 6 Diagram illustrating the physical structure of the back-to-back varactor.

Each of the twin diodes has a C-V curve which can be analyzed using Poisson's equation. Within the depletion region of each diode, $Q = N_d wA$, where N_d is the doping concentration, w is the depletion region width, and A is the cross-sectional area. Since we are considering a series combination of capacitances, it is easier to examine the *elastance*, S, the inverse of the capacitance, which for each diode is[**],

[**] Note that the elastance and capacitance used here are the incremental quantities $S = dV/dQ$ and $C = dQ/dV$, as appropriate for analysis of frequency multipliers.

$$S = \frac{1}{C} = \frac{w}{\epsilon A} = \frac{Q}{\epsilon N_d A^2} \tag{9}$$

At high frequencies, in the steady state, the large amplitude pump current in the back-to-back pair is almost entirely in the junction capacitance. This is a result of self-biasing which prevents either diode from going significantly into conduction and limits the forward voltage across each diode to the small value V_{CL}. Thus one can think of a fixed amount of charge oscillating between the two diodes with a corresponding modulation of their depletion layer widths, and, hence, of their elastances. The total elastance of the series pair $S_T = S_1 + S_2$. It is the time variation of this total elastance caused by the pump which determines the effectiveness of the back-to-back varactor as a frequency multiplier.

For a uniformly doped abrupt-junction diode, the elastance is proportional to the charge in the depletion layer. Hence, at the terminals of the back-to-back varactor there is no net elastance variation produced by the pump once steady-state operation is reached. The situation is analogous to two parallel plate capacitors in series, with the two internal plates connected by a rigid conducting rod; the total capacitance of the structure remains constant for any position of the rod.

The operation of the pumped back-to-back varactor in the steady-state condition can be represented graphically as shown in Fig. 7. Let $Q_1(t)$ and $Q_2(t)$ be the total depletion layer charges of the two diodes, and let $Q_P(t)$ be the charge waveform produced in the varactor by the pump. Since the leakage currents are negligible, $Q_P(t) = Q_1(t) - Q_2(t)$. If Q_{SB} is the depletion layer charge of the diode biased at the self-bias voltage, the charges on the individual diodes are $Q_1(t) = Q_{SB} + Q_P(t)$ and $Q_2(t) = Q_{SB} - Q_P(t)$. For purposes of illustration, it is assumed that the pump charge waveform is sinusoidal: $Q_P(t) = Q_{PO} \sin(\omega_P t)$.

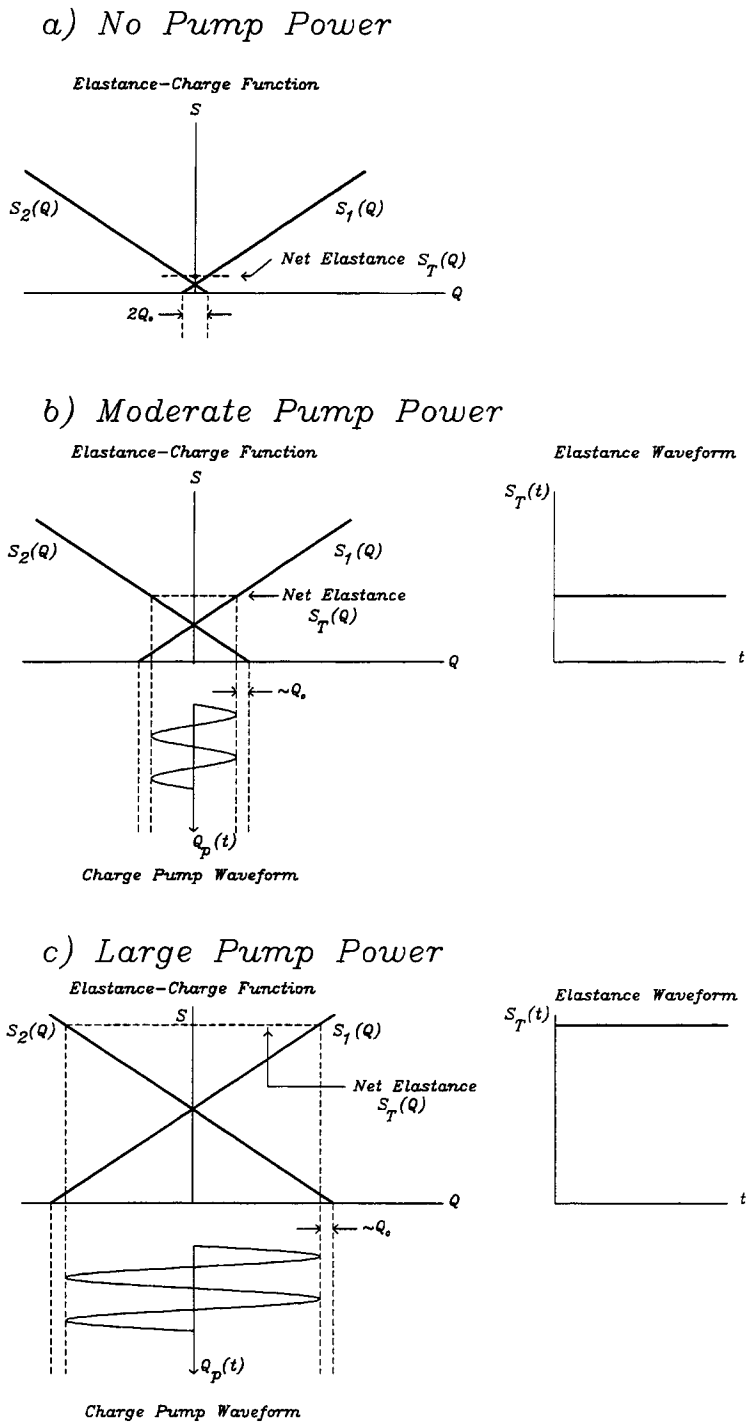

Figure 7 The steady-state elastance-charge functions and elastance waveforms for the back-to-back varactor under three pump amplitude conditions.

In Fig. *7(a)* no pump power is applied to the varactor. The depletion layer charges of both diodes have their zero-bias values Q_O. In Fig. *7(b)* pump power is applied to the back-to-back varactor, and each diode self-biases to a charge Q_{SB}. The charge on each diode now varies between $Q_{SB} + Q_{PO}$ and $Q_{SB} - Q_{PO}$. The self-bias voltage adjusts itself so that the voltage waveforms at the two diodes do not extend significantly into the region of forward conduction. Fig. *7(c)* is the same as *(b)* but with a larger pump amplitude. It is clear that in all cases the total elastance of the varactor remains constant at the value corresponding to the self-bias point.

Discussion

We have shown that a frequency multiplier cannot be made using back-to-back diodes if their doping profile is uniform. Although the pump causes a large-amplitude current to flow in the two diodes, self-biasing occurs, and the pump current flows almost entirely in the junction capacitance. If the doping is uniform, the pump produces no modulation of the overall elastance of the pair of diodes.

If the doping is non-uniform, application of the analysis described here shows that the pump modulates the overall elastance of the pair of diodes, and frequency multiplication is possible. The choice of an optimum doping profile for tripling (or other-order multiplication) is outside the scope of the present paper.

The omission of the series resistance of the diodes in the analysis does not affect the above conclusions. The pump current flows through the series connection of the series resistance and junction elastance, so self-biasing still occurs, and the overall elastance of a back-to-back pair of uniformly doped diodes remains fixed.

Wideband Fixed-Tuned Millimeter and Submillimeter-Wave Frequency Multipliers

N. R. Erickson
Millitech Corp.
PO Box 109
S. Deerfield, MA 01373

Abstract

Varactor frequency multipliers have been built with fixed mechanical tuning, which cover a fractional bandwidth >25%. These multipliers include balanced doublers and single diode triplers, with the tripler output frequency tuning up to 730 GHz. The efficiency of such a fixed tuned tripler in the 250-320 GHz band, using new design and fabrication techniques, is comparable to that of previous mechanically tuned devices. A doubler design for 200-240 GHz is not so well characterized but also appears comparable to previous tunable models.

Introduction

Millimeter and submillimeter wave frequency multipliers are required for a wide variety of applications ranging from laboratory spectroscopy to remotely operated receiver LO's on radio telescopes. While the ability of the operator to interact with the multiplier varies with the application, in every case the use of the multiplier would be simpler if there were no need to mechanically tune the device. In addition, for applications requiring considerable tuning on a frequent basis the backshorts within the multipliers can wear out relatively quickly, diminishing the power or even shorting out the waveguide with metal chips. For all of these reasons, it is highly desirable to completely eliminate mechanical tuners.

From a historical perspective, mechanical tuners are a sign of immaturity of a technology. In many microwave devices (such as waveguide mixers), tuners were initially required and have been eliminated over time. In other cases (such as mm amplifiers) tuners were never even considered as an option, and the devices have always been required to operate fixed tuned, regardless of the limitations this imposed. In the case of multipliers, tuners have many times been required to meet user expectations of power and bandwidth, but recent advances in circuit design are rapidly eliminating this need.

Bandwidth limitations of varactor multipliers

Varactor diodes are simply nonlinear capacitors having no inherent resistance except for an entirely undesirable series resistance. They develop their useful resistive component through a coupling of the input circuit to the output via the frequency conversion process. An ideal varactor (with $R_s = 0$), measured with a small test signal, thus will reflect all of its input power. Even under the case of a large input signal, varactors remain highly reactive loads, with a typical input Q around 5. This reactance produces inherent limitations to the bandwidth possible without significant mismatch.

Practical considerations to the realization of circuits also play an important role in the achievable bandwidth. Most circuits are built using coaxial or stripline circuits and in both cases, it is difficult to fabricate matching elements with very high or low impedance. In addition, for simplicity of construction, it is desirable to avoid shunt elements such as stub lines, and to use series elements only.

For predictable operation the output spectrum should be essentially a single harmonic. Single diode multipliers offer no way to discriminate between harmonics except through filter structures and are limited by overlapping harmonics in band. For doublers this still permits a very wide band approaching 1.5:1 or 35% fractional bandwidth, but for triplers the fourth harmonic overlap into the band sets a limit of only 28% bandwidth. Practical mm-wave tripler circuits closely approach this limit. Multiple diode circuits exploiting symmetry, called balanced multipliers, have inherent rejection of alternate harmonics. In principle, circuits having a higher degree of balance are possible, in which only harmonics of multiples of 3 or more are produced, but none seem to be practical at mm-wave frequencies.

Balanced doublers are practical up to 400 GHz because their circuits are so easy to realize using a variety of full wave rectifier designs. Balanced doublers require no filters to separate frequencies and some are easy to bias. Balanced triplers, by contrast, require much more complex circuitry which includes filters and difficult bias circuitry. Thus far no successful mm-wave varactor balanced tripler has been reported (with performance even comparable to single diode designs). Using whisker contacted diodes, balanced doublers have a bandwidth limit of 25% due to the limitations of circuit elements available. At this bandwidth, the efficiency is about half that of the fully optimized (narrow band) value. Planar diode doublers appear to be able to do much better because of the integrated approach to the fabrication of the diodes. Bandwidths of 30-35% seem possible based on circuit simulations.

All wideband fixed tuned circuits require very accurate circuit fabrication. Thus far this has been the primary restriction on their use above 300 GHz, and has lead to variable performance even in this frequency range.

Balanced doubler design

The basic design of the balanced doubler has been previously described [1], but in this work the design is extended to cover a wide band. This circuit is nearly ideally suited for wide band use because: it requires no filters which can compromise the matching circuits; the input and output circuits are nearly completely decoupled in the design; and the simplicity of the circuit leads to very high inherent efficiency. The whiskered design for a balanced doubler may use two diodes or two contacts to a single diode chip. In either case the diodes are in series across a waveguide in the input circuit. The output circuit consists of a TEM line (coax or stripline) to which the diodes are coupled in parallel. This line acts as a mode filter and is coupled back into a second waveguide for a lower loss connection to the output. The design of a practical balanced doubler is shown in Fig. 2.

The design process for this circuit is mostly cut and try. There is no easy way to model this circuit except with scale models or finite element simulators. Scale modeling is very difficult because two diode ports are needed having the correct phase of excitation. Finite element simulators (such as HP-HFSS) make this job much easier because it is possible to exploit the circuit symmetry and to model only a single diode port. The symmetry plane is an electric wall at

the input and a magnetic wall at the output. This symmetry plane automatically imposes the correct excitation conditions upon the two diode ports.

A troublesome feature of this circuit is a tendency for the second harmonic to excite the TM11 mode in the input waveguide. This mode looks very much like the output coaxial mode but does not require an inner conductor, and so is readily excited. This sets a general constraint on the design of the input waveguide which is to ensure that this mode is below cut-off for a sufficient distance to prevent any loss of power out the input.

The varactor diode is best modeled as a linear element in the circuit design. While it is certainly possible to optimize a circuit of this type using a nonlinear simulator, it is a very inefficient process, and is unlikely to produce a truly optimized result. This is because of the long computing time required and the numerical noise introduced in nonlinear simulators. In addition, a nonlinear simulator is not easily used to visualize the matching problems involved, and so the user can not usefully interact in the optimization process, changing the form of the circuit as required. The linear model for a diode is derived using a nonlinear simulator in a very basic embedding circuit. The process is to derive the optimum embedding impedances at the input and the output for the desired input power level. In this process the varactor bias voltage must be constrained to the low end of the optimum range. If the bias voltage is allowed to freely float, the result may be a rather high Q load. Constraining the voltage may cause a 10-20% decrease in optimized efficiency, but is generally a good trade-off for a reduced Q and increased bandwidth. In fact, even this process is not really needed. A general rule of thumb that serves very well is to model the varactor as a simple series RC circuit at the input and output. At both frequencies assume the capacitance is 0.40 $C_j(0)$. This is true only for a varactor pumped with a ~15 V p-p waveform, but the value will increase only up to 0.5 $C_j(0)$ for much lower drive levels. The choice of resistance is not so simple but is also much less important. This is because the exact resistance value chosen has almost no affect upon the circuit optimization, as long as the value is not too large. The reason is that it is impossible to match to the very low resistance values typical of varactor loads over any significant bandwidth [2], and so achievable circuits nearly always have resistive components higher than that of the varactor. The more carefully the circuit is optimized, the more true this will be. It is generally safe to pick a resistance which is about 0.2 times the varactor reactance at the input, and to then use this as the varactor load at both frequencies. If a very wide band is simulated, it may be helpful to add a 1/f frequency dependence to the resistance.

The circuit design process begins by picking a basic geometry for the diode, whisker, output coax and waveguide. This geometry is modeled in HFSS, and solved for the port S parameters in the input frequency band with a waveguide port, a backwall port and a diode port and with an electric symmetry wall. Next solve the same geometry for the output band without the waveguide port, and substituting a coaxial port for the backwall and a magnetic wall for the symmetry plane. This core circuit is shown in Fig. 1. Now terminate the input waveguide port in its own characteristic impedance and do the same for the coaxial port. Use the linear diode model as a load on the varactor port and compute the wideband match at each frequency band, with diode C_j, input backwall location, and center frequency (f_c) as optimization variables. The variation in center frequency is equivalent to an overall scale factor change in the circuit, and saves the additional simulation of scaled structures. Then vary individual dimensions in the circuit structure to see their effect upon the wideband match. Most of these dimensions are too constrained (or are equivalent to linear circuit variables) to produce much difference in results.

The most useful variables are the waveguide width and the coaxial pin diameter. The decoupling of the input and output circuits means that the pin diameter has little effect on the input, while the waveguide width has almost no effect on the output. It is desirable to tune the input circuit so that the waveguide backwall is fairly close to the diode in order to move the unconstrained part of the output matching circuit as close as possible to the source. The pin may have a step in impedance within the waveguide, with the impedance generally lower for a short distance close to the diode. This low impedance section adds capacitance to the output and helps to tune out the whisker inductance. The whisker length is chosen as a compromise between the input and output requirements, with the backwall location and the coaxial pin compensating for the very different reactance at the two frequencies. The optimum geometry chosen should be based upon the inherent wideband match which may be achieved without the aid of additional circuitry, although this serves only as a rough selection criteria.

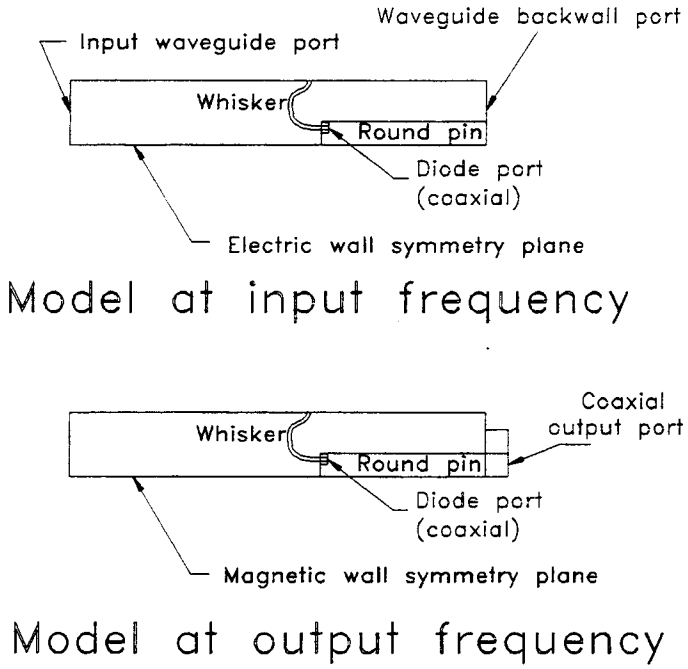

Figure 1. Cross section of the "core" circuit of a balanced doubler. Only half of the waveguide and pin and one diode need to be modeled through the use of symmetry planes.

Having arrived at an optimum "core" circuit model, it is time to design the input and output wideband matching circuits. This process is still iterative, but is much more predictable than the design of the "core" circuit. This still requires as many variables as possible including C_j and f_c, and the final circuit may require a rescaling to match the desired output frequency. In the process of adjusting C_j, keep in mind that the value of C_j strongly affects the optimum operating power level and so is not a completely free variable. However, variations in the whisker length can partially compensate for changing varactor capacitance, so capacitance is a useful variable.

Finally, having arrived at a plausible design, it is necessary to determine if the dimensions chosen can actually be machined using conventional tools. This can be a very extreme constraint on the design if it is to be machined at a reasonable cost, but is not a serious limitation if electroformed construction is allowed. Before actually cutting metal, one might wonder if any

further test is needed to prove the design. Experience with the HFSS simulator has shown that results are sufficiently accurate that circuits will work nearly exactly as designed, and any variations observed are most likely due to errors in fabrication. It may be useful to test the assumptions used in the linear diode model by modeling the full circuit in a nonlinear simulator as a check of the actual performance to be expected. However, none of the circuits to be described have been subjected to any detailed nonlinear simulation. This step is not really essential, and the linear diode model suffices for most purposes.

200-240 GHz Balanced Doubler

The first device to be described is a doubler designed for use as a driver for a tripler for 600-720 GHz. This doubler was intended to produce 10 mW output power, since the tripler was being designed at the same time and the required drive was unknown. The diode chosen was UVa type 6P4 with $C_j(0)$=20 fF, and R_s=10 ohms. The optimum input power for this device in this frequency range is 50 mW, and the expected efficiency was about 20%, including the wideband circuit mismatch losses.

The circuit was designed using the procedure described above, and the predicted performance showed a good input/output match over the full 200-240 GHz band, with a VSWR <2.5:1. The output broadband match was achieved with a series half wave low impedance line, which has a similar (although lesser) wideband matching effect to a stub line. This half wave line is actually optimized as two quarter λ lines of somewhat different impedance, but it is important to realize that these two line sections do not constitute an impedance transformer. These lines use a round inner conductor, but have a square outer conductor to make the machining easier.

The entire circuit was machined in split block fashion. The layout of the doubler is shown in Fig. 2. Both of the waveguides are split near the E plane centerline, with most of the coaxial outer conductor machined in one half of the block. The whisker pins enter at right angles to the diode. The pins are secured into close fitting slots by slightly peining the edges of the slots. In this improbable geometry, contact of the whisker to the diode is made by setting the whisker slightly off center on the pin and just twisting the pin. This contact may be made without the use of any fixture other than a pair of pliers and a microscope. After the first diode is contacted, the contact to the second anode is determined by the shift in the IV curve and the reduction in R_s.

The diode and the output matching filter pin are supported on a metallized alumina wafer (for insulation) with the pin captured in a channel in a block soldered to the alumina. The use of a slot permits the precise alignment of the pin axially. All of the features in the entire block are machined in the same set-up using a high precision CNC mill. This ensures that there are no alignment errors as can occur if multiple set-ups are used. There are no difficult features to machine except for the output waveguide which has .10 mm width and a depth of .55 mm. This slot is broached with a single tooth cutter in repeated passes under numerical control. The transformer matching to full height WR4 waveguide is machined with conventional mill cutters.

The diodes are contacted with the blocks opened in order to observe the contacting process (which is essential given the unconventional geometry). If all the parts are positioned

properly and the blocks are sufficiently flat, closing up the blocks will not disturb the contacts to typical large area varactors. This is not necessarily true for diodes <2 μm diameter where the contacts cannot stand small motions.

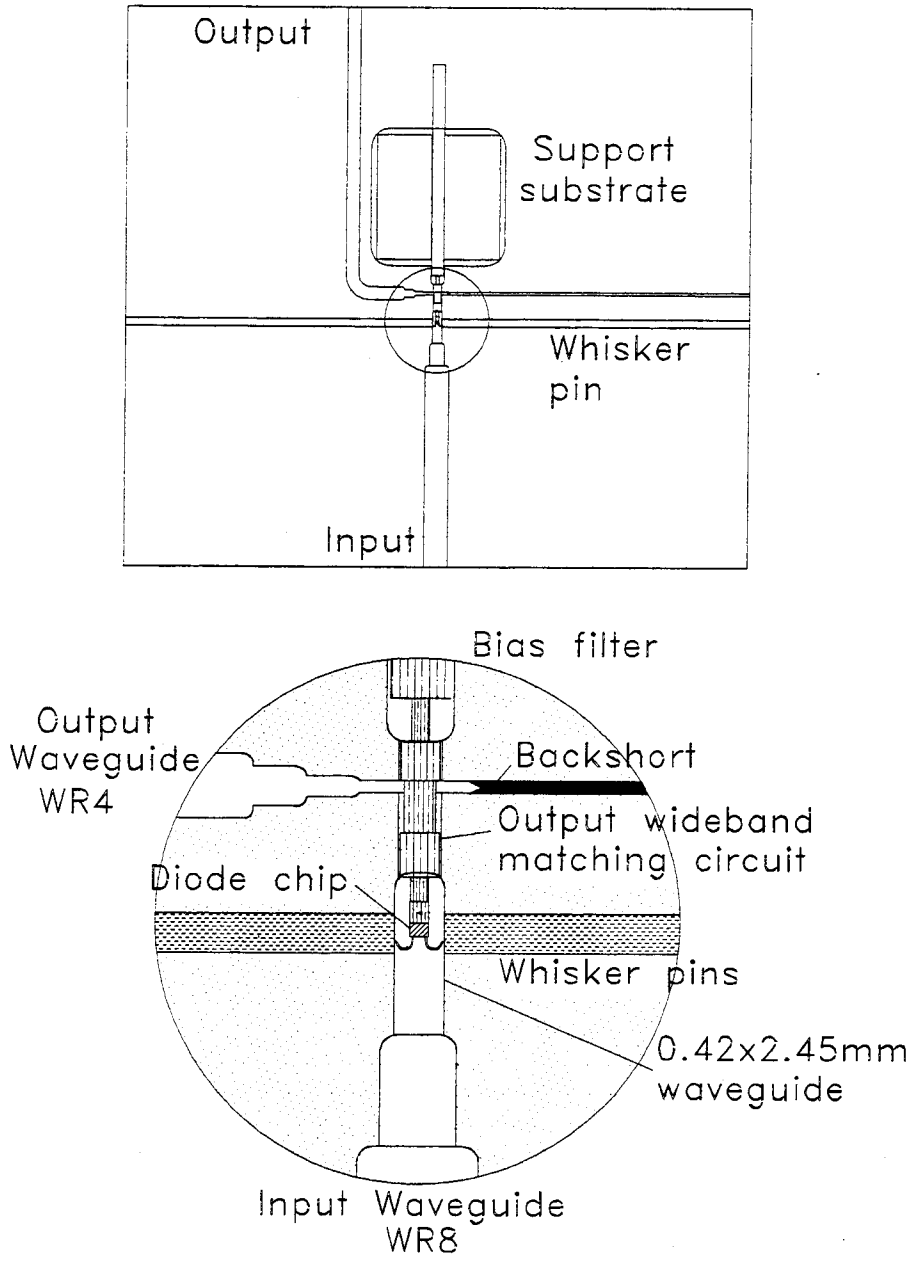

Figure 2. Balanced doubler for 200-240 GHz, with detail of critical area.

There is only one backshort to adjust for final tuning. The best full-band setting is with the short set at the closest position to the coaxial pin which optimizes the output for the highest frequency in the band. There is no other tuning required except to set the bias voltage.

The operational bandwidth exceeds the design band; a range of 194-250 GHz has been tested, but the efficiency is poorly calibrated because no isolator was used on the input. The primary difficulty with measurements is a need for fairly high input power. For an input power below 30 mW, almost no output is obtained while the best results are with >50 mW input. The available Gunn oscillators produced a marginal amount of power and could not produce this much power though the loss of an isolator. It is not correct to assume that the input power is just that which the Gunn will deliver into a matched load since the oscillators are not matched, and may deliver considerably more into the correct mismatch. However, at ~70 mW input near the peak Gunn output, the efficiency is ~20% (midband).

This high power operation arises because the optimum bias for the varactor is 6-7 V, even at low power. For efficient operation the varactor voltage waveform should swing between a small positive (forward) voltage and a large reverse voltage. At 6 V bias this will not happen until around 50 mW input. It is not clear if this situation could have been predicted through a complete nonlinear simulation or if it arises because of an error in assembly (such as excessive whisker length). In any case a lower capacitance varactor ($C_j(0)$=16 fF) would work well at lower power, since it would match at a lower bias, and it should have comparable peak efficiency.

600-720 GHz Fixed-Tuned Tripler

A similar design procedure was used to develop a wide band tripler, which was intended to produce an output in the 600-720 GHz range. This tripler uses a single diode and is similar to others previously described [1,3]. The input matching circuit is based on a coaxial resonator with $\lambda/2$ length at the output frequency. The wideband matching to the input is accomplished with a special coaxial filter design, while the output match with the diode mounted in the output waveguide is inherently wideband. A varactor was chosen with the lowest available capacitance. This device is UVa type 2T8 with $C_j(0)$=4fF and R_s=15 ohms.

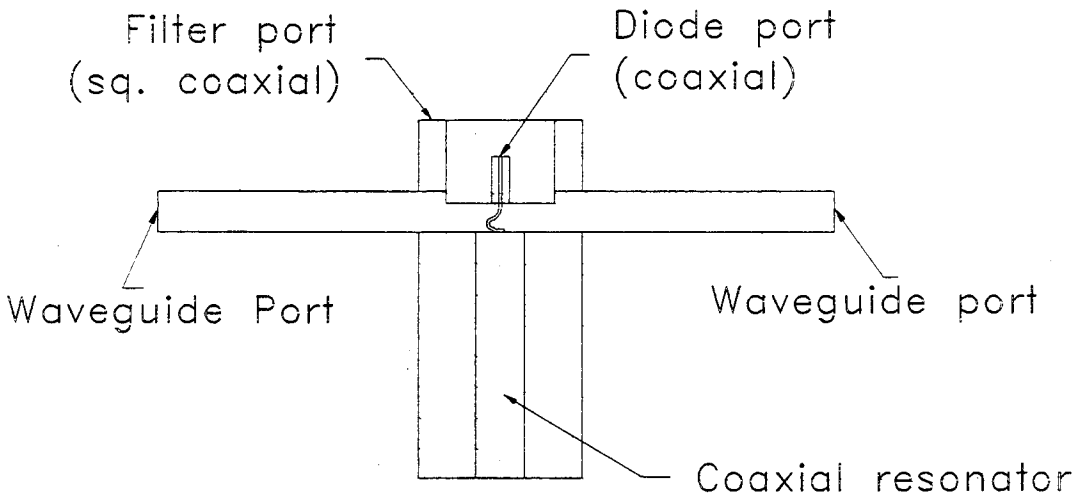

Figure 3. Cross section of "core" circuit of tripler.

The core of the circuit (subjected to HFSS simulation) is the output waveguide where the diode is mounted. This part of the circuit as it would be drawn in HFSS is shown in Fig. 3. In this design a linear diode model was used as in the doubler, with similar resistance and capacitance values. The primary additional circuit requirement for a tripler is a need for an inductive termination at the second harmonic. The output matching was found to be the biggest constraint on circuit design, introduced in part by the relatively high capacitance of the diode. A waveguide height of <38 μm was found to be essential for fixed backshort tuning. In addition an outer diameter to the coaxial resonator of more than 0.15 mm caused too much dispersion in output matching because of the large opening in the waveguide wall.

The coaxial resonator is a good solution to the need for input inductance, but to minimize its effect at the higher harmonics its impedance should be chosen as low as possible, and for this device the impedance is 70Ω. With λ/2 length there is very little effect in the output band, but the stub is very capacitive in the second harmonic band. This leads to a problem since the optimum idler termination is inductive. Inductance may be added selectively to the second harmonic by enhancing the inductance of the whisker. The whisker coupling to the waveguide behaves as a radial mode resonator for frequencies below cutoff. Increasing the width of the output waveguide near the diode increases the inductance up to the point of resonance at λ/2 width. In order to suppress the radiation of the second harmonic and to bound this resonator, it is necessary to reduce the waveguide width a short distance away. Including the location of the backshort, a roughly square resonator is formed. While this solution adds inductance, it really only works well near the top of the band, and for lower frequencies there is not enough circuit inductance for best efficiency.

After developing this core circuit, the design of an input matching coaxial line is fairly easy. A five section matching filter was designed using impedances of 14 and 70Ω, with 18Ω along the diode. This filter must have a good (short circuit) stopband at the second and third harmonics but is permitted to have any behavior between the specified bands. The filter is built using a square outer conductor with circular inner sections except for the first section comprising just the diode chip which is square.

The final circuit design was realized in a rather complex block using three pieces which meet at a T joint. The layout of the critical part of the circuit is shown in Fig.4. The remainder of the block is configured much as in the doubler of Fig. 2. The output waveguide is milled as a shallow channel (split along the H plane) in one piece in order to achieve the very low height required. The input waveguide and the coaxial filter were machined in a pair of blocks split along the waveguide E plane for best accuracy. The coaxial filter was supported as in the doubler above. The two input parts must have a very smooth joint where they cross the output waveguide. The coaxial resonator is made using a pin with a shoulder to ensure a good ground. Poor grounding of this pin (even a 1-2μm gap) can greatly increase the circuit loss. These considerations make the block a very difficult part to machine, but it probably can be simplified as lower capacitance diodes become available or better methods of cutting waveguide are developed.

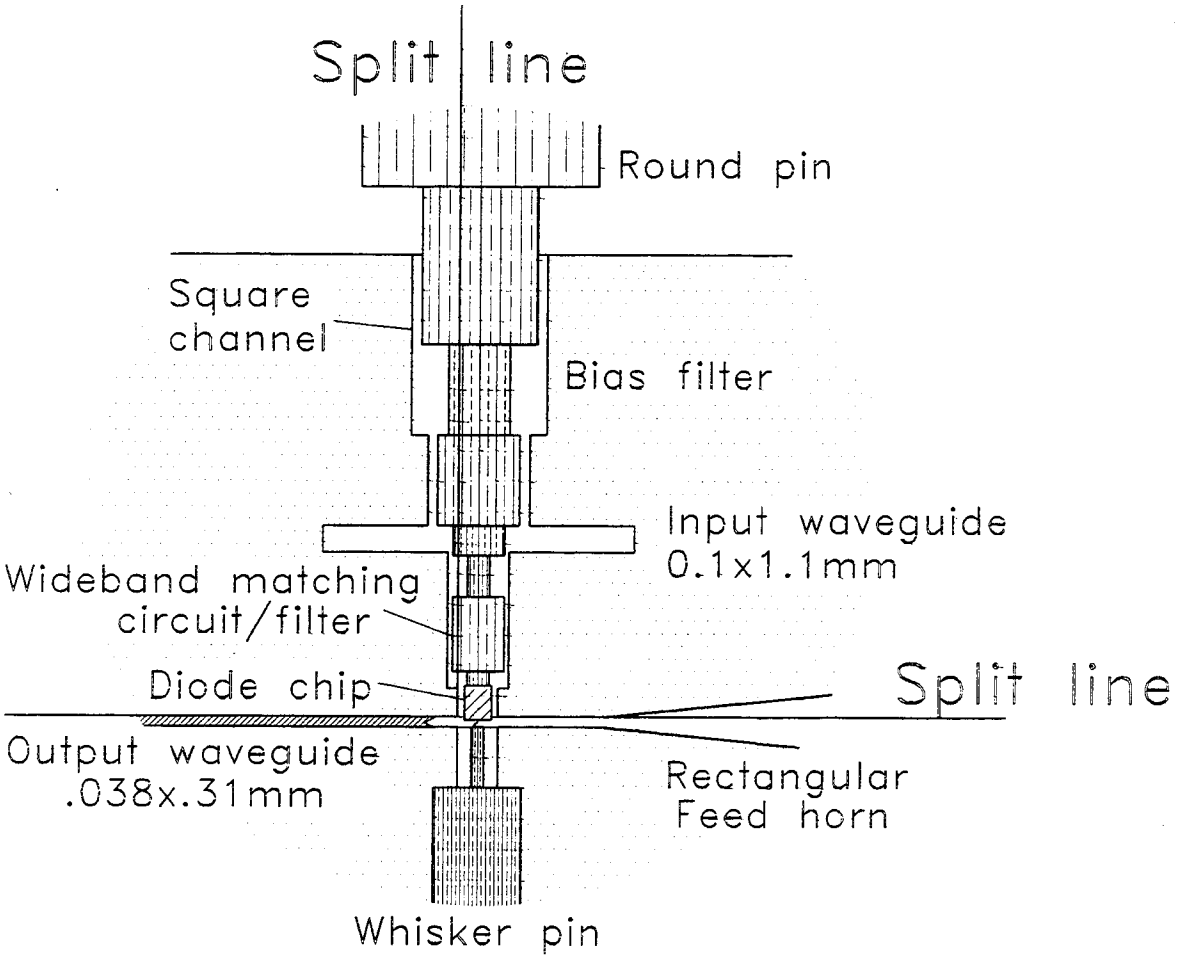

Figure 4. Cross section detail through fixed tuned tripler for 600-720 GHz.

The assembly and contacting process were relatively easy considering the frequency involved. There were no alignment problems between the coaxial pin and the outside, and the contacting was readily done by sliding the choke pin in its groove. Full band operation was obtained without any circuit modification at an efficiency of 0.5-1.0%. Operation is in a varactor mode with a bias of 1.5-3 V at an input power of 3-10 mW. The input and output power are shown in Fig. 5. The individual powers were measured at different times and may not be at exactly the same frequency. The overall shape to the curves is largely due to the available Gunn oscillator power. Power at both frequencies was measured with a calorimeter [3] and should be accurate to within 10%. There is one apparent hole in the output spectrum near 696 GHz, but the input power is also low here. It is not clear if the doubler or tripler is responsible for this hole, or if perhaps some other tuning of the backshorts would eliminate this problem. It is relatively easy to find a set of backshort positions that work but it is difficult to be certain that they are really the best over the full band. In addition, the interactions between the doubler and tripler make it difficult to tune at all frequencies, and require an adjustable phase shifter to obtain full frequency coverage.

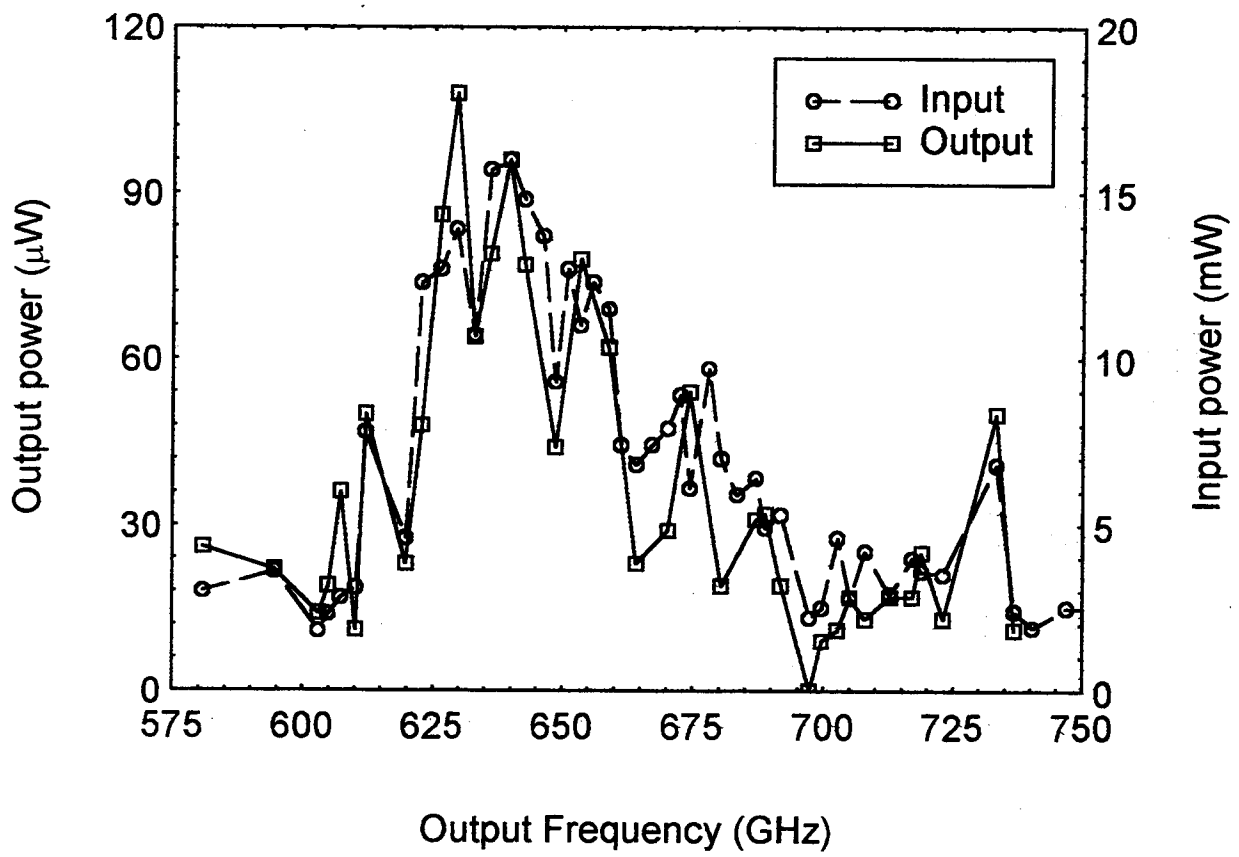

Figure 5. Input and output power for 600-720 GHz tripler. Input power is from 200-240 GHz doubler.

250-320 GHz Fixed Tuned Tripler

A similar design was used in a tripler for 250-320 GHz, but due to the lower frequency the fabrication was much simpler. All of the features in this device were machined in a block split in the E plane with no really difficult features. The output waveguide was broached with a single tooth cutter while the remainder of the output waveguide was milled as full height WR3. The transition between these waveguides included the high pass filter required to suppress second harmonic radiation and was milled as a "channel transformer" with varying depth milled features in a cross section resembling a + sign [4]. The channel transformer is very useful device for this application because the waveguide cutoff frequency in the channel region is always higher than that of the uniform rectangular cross section at the ends. This cutoff frequency can be varied using just the depth of one cut relative to the other. However the cutoff frequency and the impedance are tied together so it is a bit tricky to design an impedance transformer with a given impedance ratio and cutoff frequency.

The assembly was very easy relative to previous wafer style triplers at a similar frequency and the initial performance matched expectations. The input backshort was easily set using a measurement of the small signal input return loss. This small signal tuning works well because the

series resistance of the diode is typically only a factor of three smaller than the optimum input resistance under large signal drive. As long as the bias voltage is set to produce the correct effective capacitance (typically 4-5 V), the general shape of the frequency response of S11 is essentially independent of power level except that its magnitude will decrease at higher power. The output backshort is tuned for the best power output at the maximum frequency in the band, as this has typically been found to optimize the full band. The overall performance is excellent, and is comparable to older mechanically tuned models optimized at each frequency over a similar band.

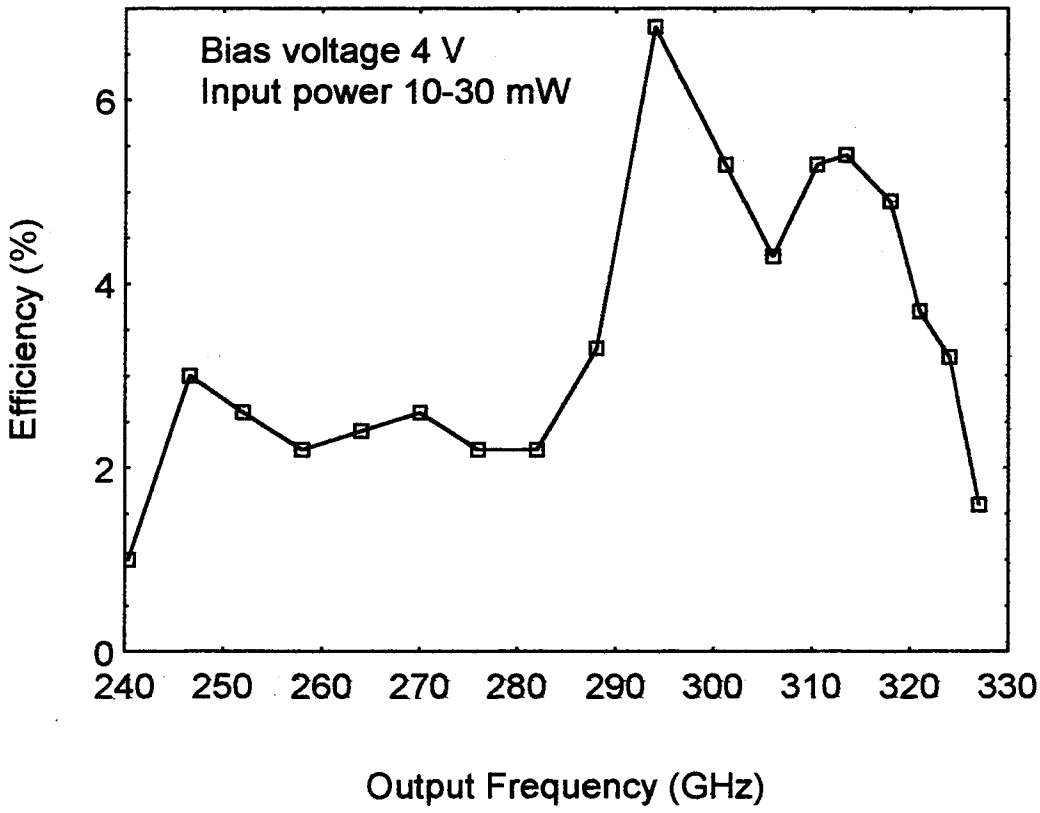

Figure 6. Efficiency of fixed tuned tripler for 250-320 GHz.

Cascading multipliers and interstage interactions

Cascading of multipliers is difficult because all wideband varactor multipliers are inherently poorly matched. An input/output VSWR = 2.5-3:1 is typical for the devices described above and this will degrade further at low power levels or if the bias is set incorrectly. Cascading of circuit elements with a VSWR >2:1 produces significant power ripple, and generally is undesirable even for linear elements. Varactor devices present additional problems because of their nonlinearity, and are even prone to instabilities such as parametric oscillations [5]. Typical cascaded multipliers measured over a wide band will show some frequencies where useful output may not be obtained or where power is very sensitive to frequency. Adding a tunable phase shifter between stages generally permits operation at any frequency, since it eliminates the worst case interaction, but it adds loss and requires mechanical tuning.

Ideally one would add an isolator between all stages, but mm-wave wideband isolators have fairly high loss, and are not available at all above 220 GHz. While a loss of 2 dB may be marginally acceptable at 100 GHz, a loss of 4.5 dB is not at 200 GHz, and so isolators are not really a good option at present.

In principle the input and output may be matched through the use of a balanced construction using wideband 90° hybrids on the input and output with parallel multiplier circuits. This only works well if the multipliers are identical in efficiency and phase, and this may never be true at high frequencies. In addition, the bandwidth of the hybrids is limited and the required operating power doubles.

This unsatisfactory situation is now improving. In recent work the author has made wideband isolators with much lower loss than previous models, although they use the same basic design as present Faraday rotation isolators [6]. The differences are a much shorter ferrite length (with a correspondingly higher magnetic field), and much reduced lengths of waveguide on either end. The loss of a WR10 model is <1.0 dB across the band, while a WR6 model has typically <1.5 dB midband loss with 2 dB worst case, and this loss can probably be reduced further. It even seems possible to build a WR3 model, although the loss may be significantly higher.

Conclusions

These devices represent a sample of designs that are now possible for wideband applications. These same designs can in principle be scaled to any frequency but peculiarities of each frequency range usually require some redesign. The balanced doubler with whisker contacts is feasible up through at least 400 GHz, while a planar diode version has been designed with very wide bandwidth at 150 GHz.

The tripler to 720 GHz is pushing the limits of the techniques used but is practical at any lower frequency. Lower capacitance varactors may extend the frequency upward, while with reduced bandwidth its fabrication becomes somewhat easier.

These types of devices should be able to completely replace tunable multipliers in the near future. With the increasing capabilities of planar diodes and new designs using them, many of these same circuits should soon become feasible with planar diodes up through 400 GHz.

References

[1] Erickson, N.R., "High efficiency submillimeter frequency multipliers," 1990 IEEE MTT-S Int'l. Microwave Symposium, p. 1301.

[2] Matthaei, G.L., Young L., and Jones E.M.T., "*Microwave Filters, Impedance-Matching Networks and Coupling Structures*," (section 4.09), Artech House Books, Dedham, MA, 1980.

[3] Erickson, N.R., and Tuovinen, J., "A waveguide tripler for 720-880 GHz," Proceedings of the Sixth Int'l. Symposium on Space THz. Tech., pp. 191-198, Mar. 1995.

[4] Siegel, P.H., Peterson, D.W. and Kerr, A.R., "Design and analysis of the channel waveguide transformer," IEEE Trans. Microwave Theory Tech., June 1983, pp. 473-484.

[5] Penfield, P. and Rafuse, P.R., *Varactor Applications*, MIT Press, Cambridge, MA, 1962.

[6] Millitech Corporation, S. Deerfield, MA series FBI isolators.

Monolithic Schottky-Collector Resonant Tunnel Diode Oscillator Arrays to 650 GHz

M. Reddy[1], S.C. Martin[2], A.C. Molnar[1], R.E. Muller[2], R.P. Smith[2], P.H. Siegel[2], M. J. Mondry[1], M. J. W. Rodwell[1] and S.J. Allen, Jr.[3]

[1]Department of Electrical and Computer Engineering
University of California, Santa Barbara, CA 93106

[2]California Institute of Technology
Jet Propulsion Laboratory, Pasadena, CA 91109

[3]Center for Free-electron Laser Studies
University of California, Santa Barbara, CA 93106

Abstract:
We report the design, fabrication, and performance of monolithic, slot-antenna coupled Schottky-collector resonant tunnel diode (SRTD) oscillator arrays. A 64-element oscillator array oscillated at 650 GHz while a 16-element array produced 28 μW at 290 GHz.

Introduction:
Resonant tunnel diode (RTD) waveguide oscillators have been reported at frequencies as high as 712 GHz [1], well beyond the highest frequency transistor oscillators built to date [2]. Power levels achieved by discrete waveguide RTD oscillators are limited by constraints imposed on maximum device area for suppressing parasitic bias circuit oscillations [3]. Higher power levels can be obtained with monolithic RTD oscillators in which these constraints are eliminated by on-wafer bias stabilizers [4]. Power levels can then be further increased using quasi-optical array RTD oscillators [5]. Here, we report monolithic Schottky-collector RTD (SRTD) oscillator arrays with on-wafer Schottky-diode bias stabilizers. Different circuits operated at frequencies ranging from 100 GHz to 650 GHz. A 64-element array oscillated at 650 GHz. To our knowledge this is the highest oscillation frequency achieved by a monolithic oscillator. Additionally, a 16-element array produced 28 μW at 290 GHz.

Design:
The single element RTD oscillator circuit (Fig.1) consists of a 0.1 μm InGaAs SRTD located in the center of a slot antenna terminated by air-bridged capacitors, resonant at the desired frequency of oscillation, f_{osc}. The SRTDs have a peak current density of $5x10^5$ A/cm^2 at a peak voltage of 0.95 V, a current peak to valley ratio of 1.7, a measured peak negative conductance of -19 mS/μm^2, a parasitic capacitance of 3.0 fF/μm^2, a parasitic resistance of 2.2 Ω-μm^2 and a quantum well lifetime of 0.12 ps. These parameters are

normalized to the SRTD effective area which is twice the SRTD junction area to account for the spreading of electric field beneath the 0.1 μm Schottky-collector. From the DC and microwave parameters, the 0.1 μm InGaAs SRTD has an estimated maximum frequency of oscillation f_{max}, of 2.2 THz [6], although such high f_{max} values are difficult to verify experimentally.

A low-impedance Schottky-diode and series resistor is located within $\lambda_{osc}/4$ from the SRTD for suppressing both DC bistability and parasitic oscillations in the bias circuit at frequencies below the antenna's resonance [4]. The positive conductance of the low-impedance diode- resistor combination is larger than the absolute value of the SRTD's maximally negative conductance. The low-impedance diode's high turn-on voltage means that the diode-resistor combination can provide the low differential impedance while using only a small fraction of the current, and thus power consumption, that a resistor would use without the diode. The low-impedance Schottky diode is fabricated on AlInGaAs to give an appropriate amount of current and conductance in the negative-resistance voltage range of the RTD.

At the antenna's resonant frequency, the low-impedance Schottky-diode is decoupled from the SRTD and the SRTD is shunted only by the antenna's radiation impedance in series with the MIM capacitors. To ensure oscillation, the SRTD junction area is chosen such that the SRTD's negative conductance exceeds the antenna radiation conductance at f_{osc}. Interactions between neighboring slot antennas were ignored. In addition, the slot antennas were shortened in order to tune out the capacitances of the SRTDs.

More specifically, the approach used to design an oscillator of a given frequency is as follows: (1) Starting with a slot antenna with a resonant frequency somewhat higher than the design frequency, an appropriate SRTD with a sufficiently large negative conductance is chosen. (2) In order to move the oscillation frequency to the design value, the slot antenna size is altered to satisfy the relation:

$$Im[Y_{ant}] + Im[Y_{srtd}] = 0$$

at the design frequency, where $Im[Y_{ant}]$ and $Im[Y_{srtd}]$ are the imaginary parts of the admittances of the antenna and SRTD, respectively. SRTDs are chosen from the library of devices shown in table 1. Devices with stripe lengths > 4 μm had been observed to fail due to overheating, so devices with stripe lengths of 6 and 8 μm consisted of two 3 μm or 4 μm stripe length SRTDs connected in parallel.

Larger SRTD junction areas provide design margin but also detune the slot antenna from its resonant frequency due to an increased parasitic SRTD capacitance. The maximum SRTD junction area per single element oscillator was 0.8 μm^2 to prevent device burnout at the high operating current density. SRTD oscillator arrays were designed with varying slot antenna lengths and varying SRTD junction areas with the objective of building oscillators in the 100 GHz to 1000 GHz frequency range. The arrays were obtained by

repeating the single element slot antenna coupled oscillator (Fig. 1) into rows and columns. The separation between the adjacent elements for various frequency array designs was chosen to be less than the corresponding half wavelength in the substrate to ensure a single main lobe in the radiation pattern of the antenna arrays.

Array fabrication requires monolithic integration of 0.1 μm InGaAs SRTDs, Schottky-diode bias stabilizers, MIM capacitors, N++ resistors, slot antennas and airbridges. The molecular beam epitaxial layer structure (Fig. 2) consists of graded bandgap AlInGaAs Schottky-diode [7] layers grown beneath the InGaAs SRTD layers. The SRTD layers consist of 5 monolayer AlAs barriers in the double barrier heterostructure which yield current densities in the vicinity of $5x10^5$ A/cm^2. Fabrication (Fig. 3) starts with exposing the Schottky-diode surface layers by etching away the SRTD layers in regions where the bias stabilizer is required. A non-selective etch (3:1:50, H_3PO_4 : H_2O_2 : H_2O) is used to etch away most of the layers and stop within the 1000 Å AlInAs layer. A selective etch (1:1:4:1, CH_3CHOOH : HBr : HCl : H_2O) then removes the remaining AlInAs layer and stops on the InGaAs cap layer of the Schottky-diode. Subsequently, ohmic contacts to the N++ layers of both the SRTD and the Schottky-diode are formed by first recess etching and then depositing and annealing Au-Ge-Ni metal. The 0.1 μm Schottky-collector for the SRTD is then defined using an airbridge electron beam collector process [8] (Fig. 4). Mesa isolation is achieved using a wet etch (3:1:50, H_3PO_4 : H_2O_2 : H_2O) and is followed by interconnect metal deposition (Ti/Pt/Au). A 1000 Å thick, PECVD SiN film is then patterned to access both the bottom plate of the MIM capacitors and the surface layers of the Schottky-diode. Posts and evaporated airbridges provide the second level of interconnections, the top plate of the MIM capacitors and the stabilizer diode's Schottky-contact metal. A layout of an array is shown in Figure 5.

Results:

The arrays were tested with a quasi-optical conFiguration (Fig. 6). The 23 mm diameter Si hyperhemispherical lens on which the oscillator array is placed forms the array's external resonant cavity, determining both the oscillation frequency and the oscillator Q. For arrays oscillating below 250 GHz, the oscillator array output was detected directly using a broad band bowtie-antenna-coupled Schottky diode harmonic mixer. The harmonic mixer downconverts the signal frequency to the 2-12 GHz passband of a spectrum analyzer. A 2-element array oscillated at 109 GHz (Fig. 7(a)). A second 2-element array having shorter slot length oscillated at 196 GHz (Fig. 8). A 16-element array oscillated at 94 GHz [9](Fig. 7(b)). This array radiated 5% of its output power into a secondary cavity mode at 108 GHz.

For arrays oscillating above 250 GHz, the signals were detected by a liquid helium cooled Ge bolometer or a less sensitive but calibrated Thomas acousto-optic bolometer. A Fabry-Perot interferometer measures the signal wavelength and hence the frequency. A 64-element array produced oscillations at 650 GHz (Fig. 9). Other arrays oscillated at 290 GHz, 300 GHz, 310 GHz, 470 GHz and 560 GHz (Table 2).

The output power of a 16-element array oscillating at 290 GHz was measured to be 28 +/- 2 μW by the acousto-optic power detector. This corresponds to a 440 W/cm^2 power per unit SRTD junction area. This measured power does not correct for reflection and diffraction losses in the beam path, which may be substantial. Power measurements of the higher frequency oscillator arrays using the acousto-optic detector proved difficult as the power levels were close to the instrument's threshold and a Ge bolometer was then used instead. Direct electrical connection to the individual SRTDs is not possible at submm-wave frequencies. Therefore, we cannot conclusively establish that every array element is oscillating. However, we note that except for the 100 GHz designs (where both the 2-element and the 16-element arrays have similar total SRTD junction areas) the detected signal levels of the 16-element oscillator arrays are approximately an order of magnitude larger than the 2-element oscillator arrays.

For designs above 500 GHz, the slot length becomes comparable to the capacitor, stabilizer diode and the SRTD dimensions. The physical layout then fails to conform well to a slot antenna. We believe that the highest oscillation frequency (650 GHz) obtained is limited by these layout considerations. More recent work [10] indicates that much more compact SRTD layouts could be fabricated, and the use of structure simulators could be used to correct for any such effects in future designs.

Acknowledgements:

The UCSB work is supported by ONR under contract N00014-93-0378, NSF (QUEST) and AFOSR. The JPL work was performed at the JPL Center for Space Microelectronics Technology, and was sponsored by the NASA Office of Space Science. The authors wish to acknowledge discussions with H.S. Tsai and R.A. York from the University of California, Santa Barbara.

Design	A (μm^2)	Length (μm)	G_n(mS)	C_{rtd}(fF)	L_{qw}(pH)	$Rs(\Omega)$
SR2	0.4	2.0	7.6	1.2	15.8	5.5
SR3	0.6	3.0	11.4	1.8	10.5	3.66
SR4	0.8	4.0	15.2	2.4	7.9	2.76
SR5	1.2	6.0	22.8	3.6	5.26	1.94
SR6	1.6	8.0	30.4	4.8	3.96	1.38

Table 1: Small-signal model parameters for the various 0.1 μm SRTDs in the device library. In this table, A represents the effective area as inferred from capacitance extraction, which is twice the SRTD junction area.

# of array elements	Total SRTD area (μm^2)	Slot length (μm)	Osc. freq (GHz)
16	3.2	544	94
2	1.6	430	109
2	1.6	217	196
16	6.4	157	290
16	12.8	121	300
2	1.6	121	310
16	6.4	84	470
16	6.4	53	560
64	19.2	51	650

Table 2: Summary of results obtained with various SRTD oscillator arrays designed with parameter variation of total SRTD junction area, slot antenna length and number of unit cell elements in the array.

References:

[1] E.R. Brown, J.R. Soderstorm, C.D. Parker, L.J. Mahoney, K.M. Molvar and T.C. Mcgill, "Oscillations up to 712 GHz in InAs/AlSb resonant-tunneling diodes," Appl. Phys. Lett., vol. 58, no. 20, pp 2291-2293, May, 1991.

[2] S.E. Rosenbaum, B.K. Kormanyos, L.M. Jelloin, M. Matloubian, A.S. Brown, L.E. Larson, L.D. Nguyen, M.A. Thompson, L.P.B. Katehi and G.M. Rebeiz, " 155 and 213-GHz AlInAs/GaInAs/InP HEMT MMIC Oscillators", IEEE Transactions on Microwave Theory and Techniques, vol. 43, no. 4, pp. 927-932, April, 1995.

[3] C. Kidner, I. Mehdi, J.R. East and G.I. Haddad, "Bias circuit instabilities and their effect on dc current-voltage characteristics of double-barrier resonant tunneling diodes," Solid-State Electron., vol. 34, no. 2, pp 149-156, Feb., 1991.

[4] M. Reddy, R.Y. Yu, H. Kroemer, M.J.W. Rodwell, S.C. Martin, R.E. Muller and R.P. Smith, "Bias stabilization for resonant tunnel diode oscillators," IEEE Microwave and Guided Wave Lett., vol. 5, no. 7, pp. 219-221, July, 1995.

[5] M.P. De Lisio, J.F. Davis, S.J. Li, D.B. Rutledge and J.J. Rosenberg, "A 16-element tunnel diode grid oscillator," IEEE AP-S International Symposium, Newport Beach, CA, June, 1995.

[6] M. Reddy, M.J. Mondry, M.J.W. Rodwell, S.C. Martin, R.E. Muller, R.P. Smith, D.H. Chow and J.N. Schulman "Fabrication and dc, microwave characteristics of submicron Schottky-collector AlAs/$In_{0.53}Ga_{0.47}As$/InP resonant tunneling diodes," J. Appl. Phys., vol. 77, no. 9, pp. 4819-4821, May, 1995.

[7] D.H. Lee, S.S. Li, N.J. Sauer, and T.Y. Chang, "High quality $In_{0.53}Ga_{0.47}As$ Schottky diode formed by graded superlattice of $In_{0.53}Ga_{0.47}As/In_{0.52}Al_{0.48}As$," Appl. Phys. Lett. , vol. 54, no. 19, pp. 1863-1865, May, 1989.

[8] R.E. Muller, S.C. Martin, R.P. Smith, S.T. Allen, M. Reddy, U. Bhattacharya and M.J.W. Rodwell, "Electron-beam lithography for the fabrication of air-bridged, submicron Schottky-collectors," J. Vac. Sci. Technology B, vol. 12, no. 6, pp. 3668-3672, Nov/Dec, 1994.

[9] M. Reddy, M.J. Mondry, A.C. Molnar, U. Bhattacharya, M.J.W. Rodwell, S.C. Martin, R.E. Muller and R.P. Smith, "Monolithic RTD array oscillators at 100 GHz and 200 GHz with on-wafer bias stabilization," Late news, 54th Annual Device Research Conference, Santa Barbara, CA, June, 1996.

[10] R.P. Smith, S.C. Martin, M. Kim, J. Bruston, D. Humphrey, N. Erickson, and P.H. Siegel, "Advances in Submillimeter Wave Semiconductor-Based Designs and Processes at JPL," to be published in the Proceedings of the 8th Space Terahertz Symposium, Cambridge, MA, March, 1997.

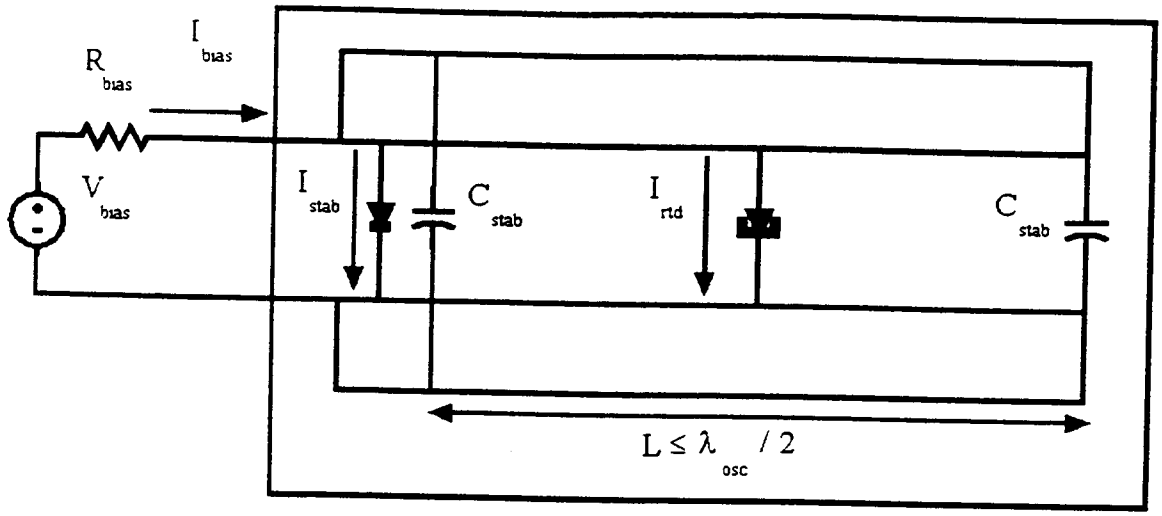

Figure 1: Circuit schematic of a monolithic slot-antenna coupled SRTD oscillator.

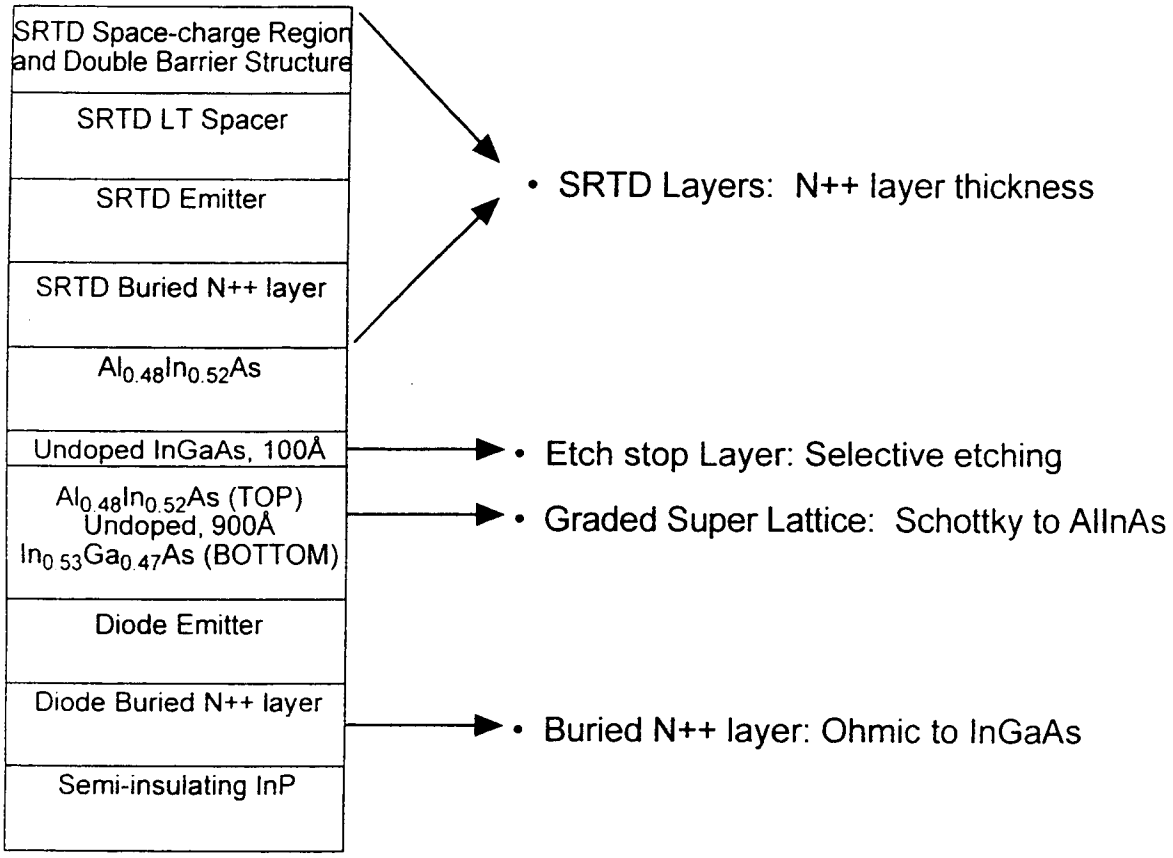

Figure 2: Layer structure grown by molecular beam epitaxy (MBE) for SRTDs, bias stabilization diodes, and resistors on semi-insulating InP substrates.

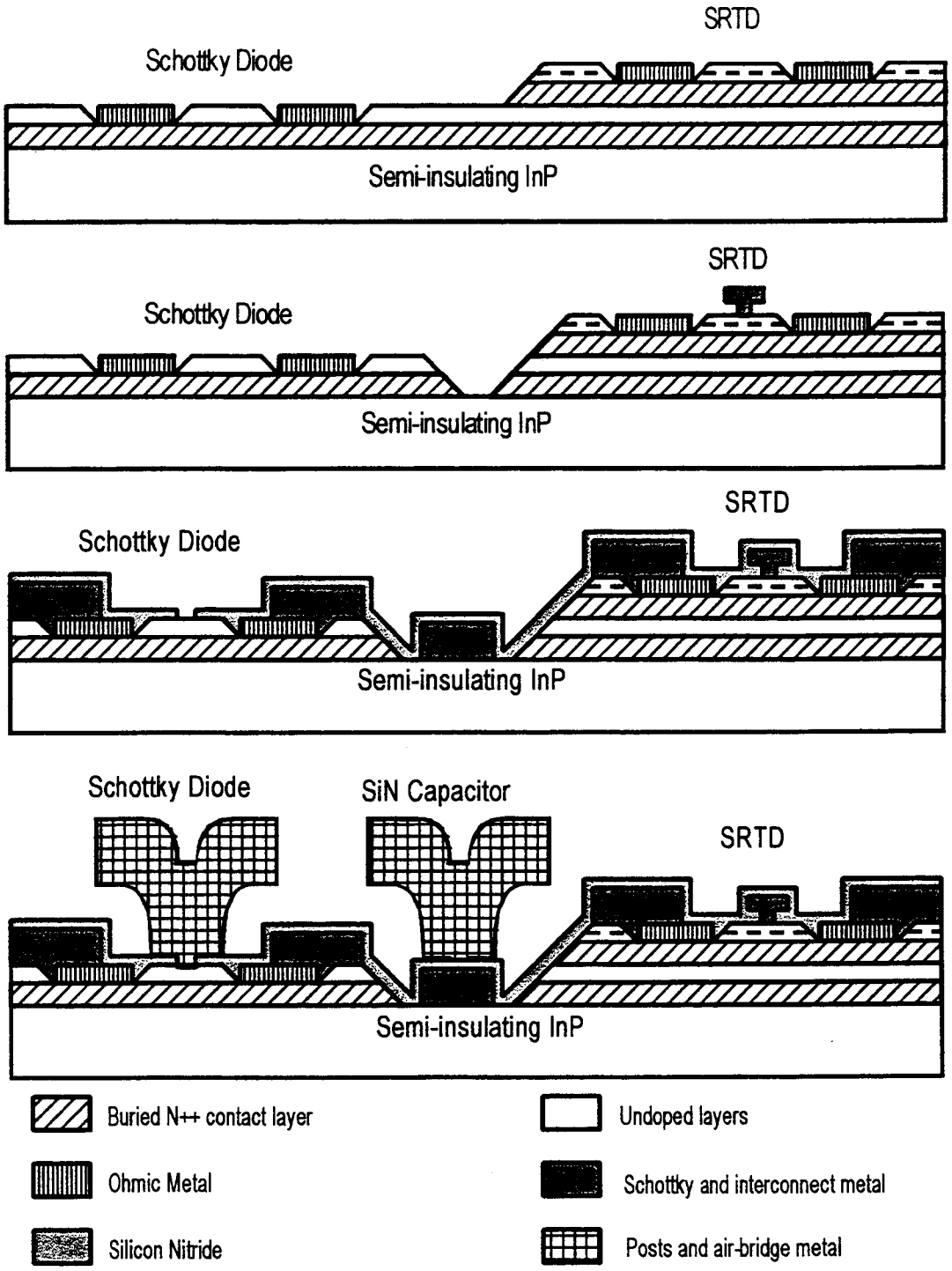

Figure 3: The process steps are: a) etching down to the stabilizer region, then depositing and annealing the ohmic contacts, b) defining the Schottky collectors and etching the mesas, and c) depositing interconnect metal, and then depositing and patterning silicon nitride for passivation and capacitor dielectrics, and d) fabricating the air-bridges and capacitor top plates.

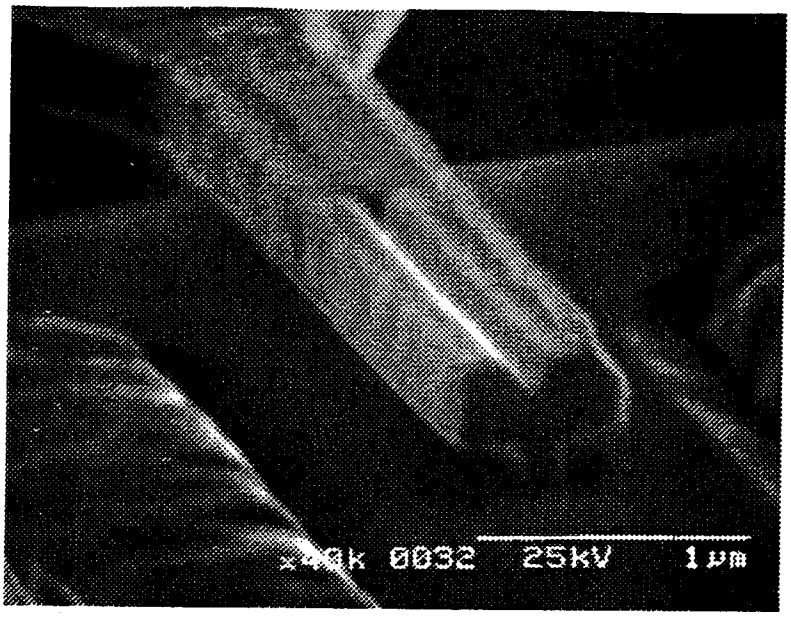

Figure 4: SEM photograph of a 0.1 μm InGaAs SRTD

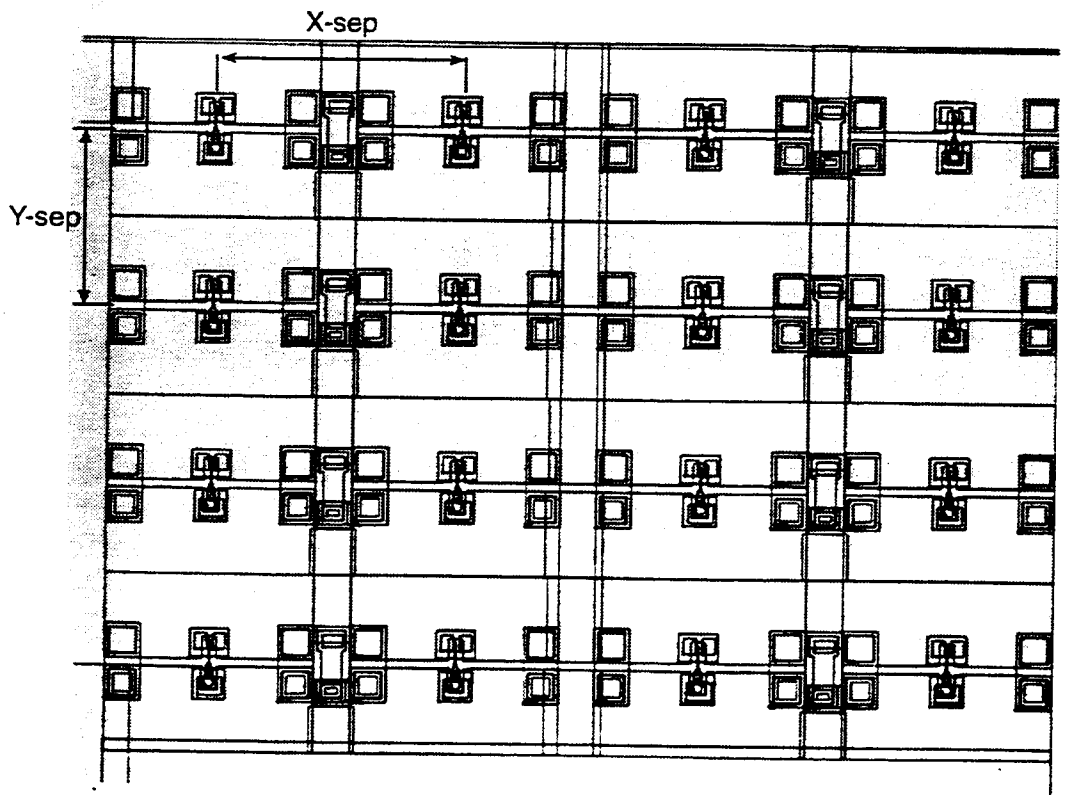

Figure 5: Mask layout of a 16-element array oscillator. The layout for array designs is obtained by simply repeating the single-element layout in the X and Y directions.

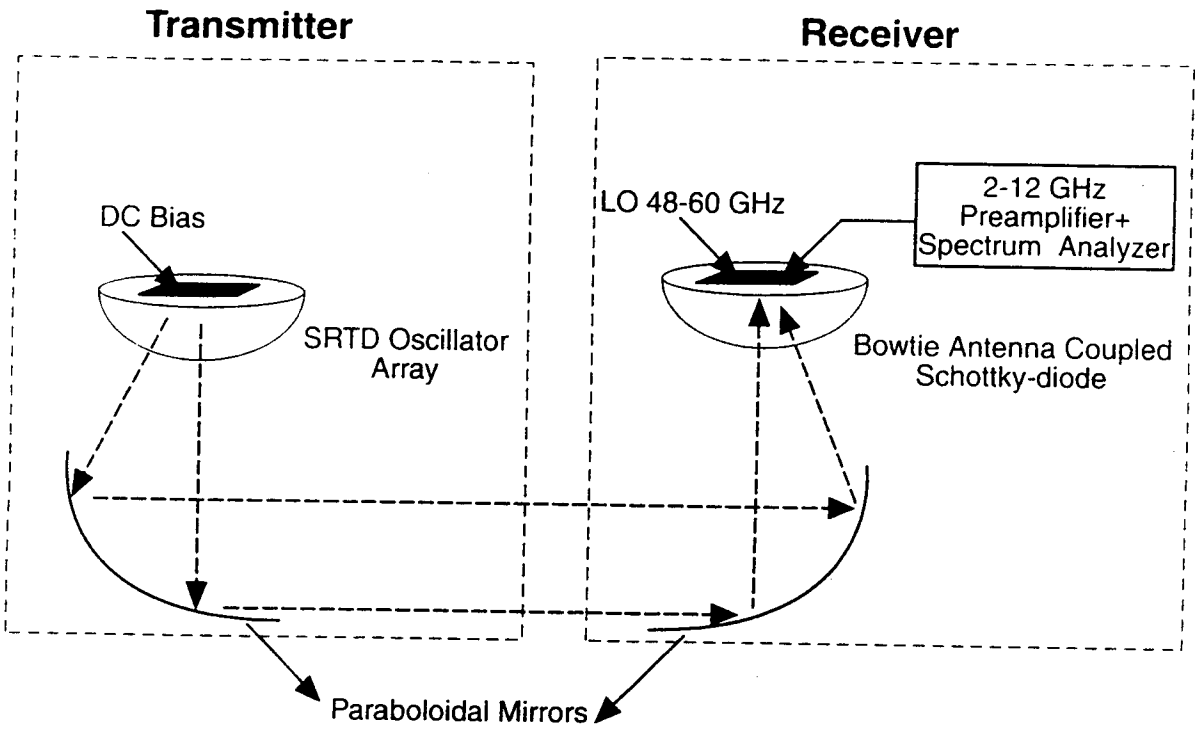

Figure 6: Quasi-optical oscillator array on a silicon lens which forms the oscillator's resonant cavity.

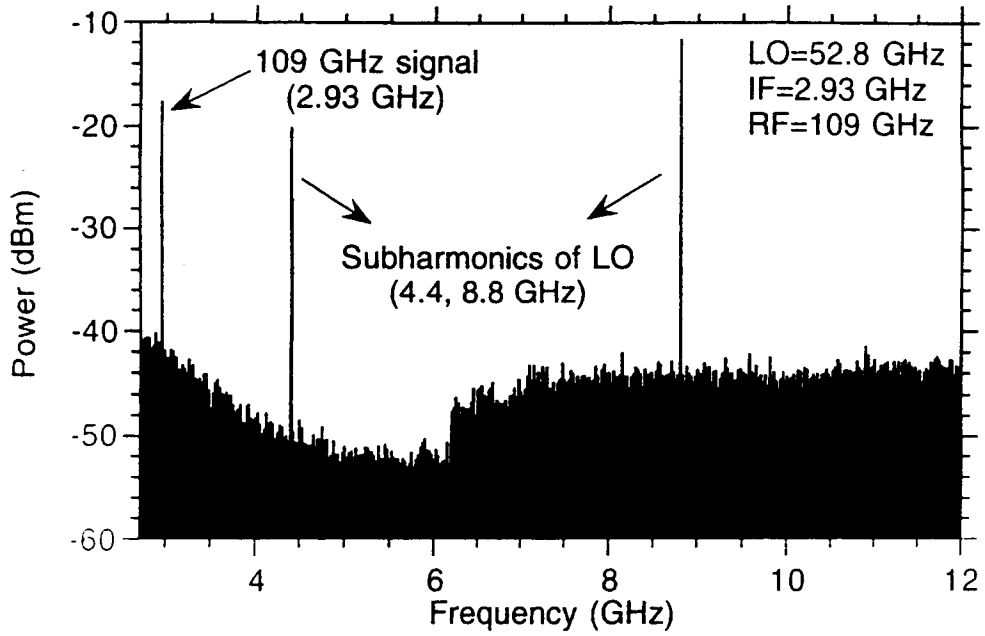

a.

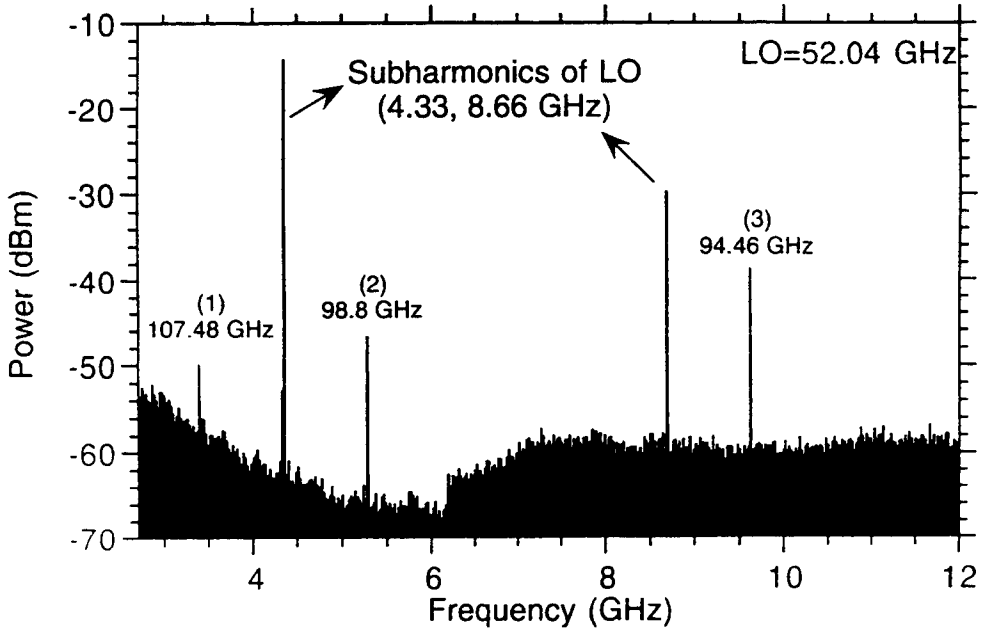

b.

Figure 7: Measurements of oscillator arrays: Spectra of (a) 2-element and (b) 16-element arrays at near 100 GHz showing multiple oscillation frequencies for the 16-element array. In both cases the linewidth is limited by the measurement system.

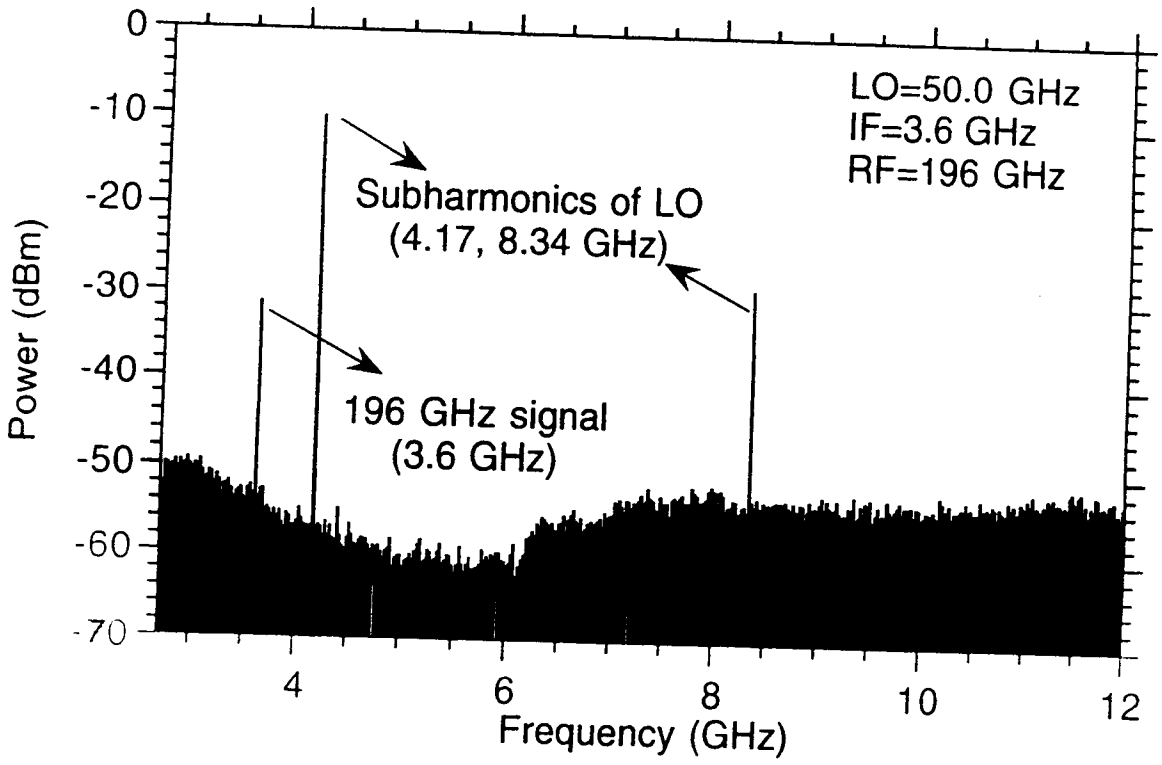

Figure 8: Spectrum of a 2-element array at 196 GHz tested with a Schottky-diode harmonic mixer.

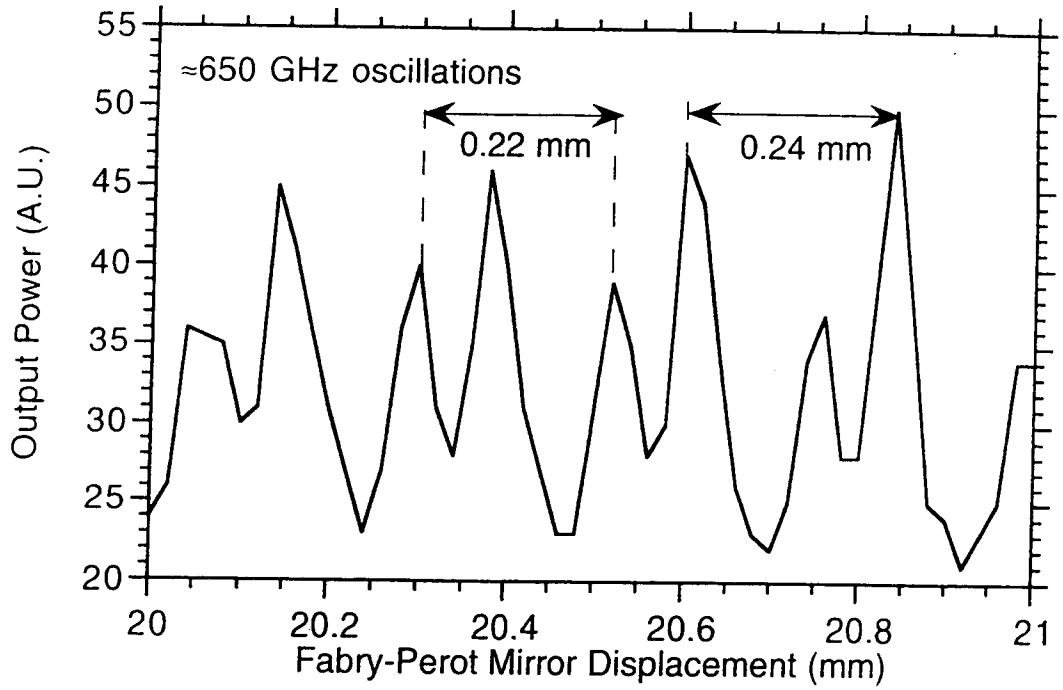

a.

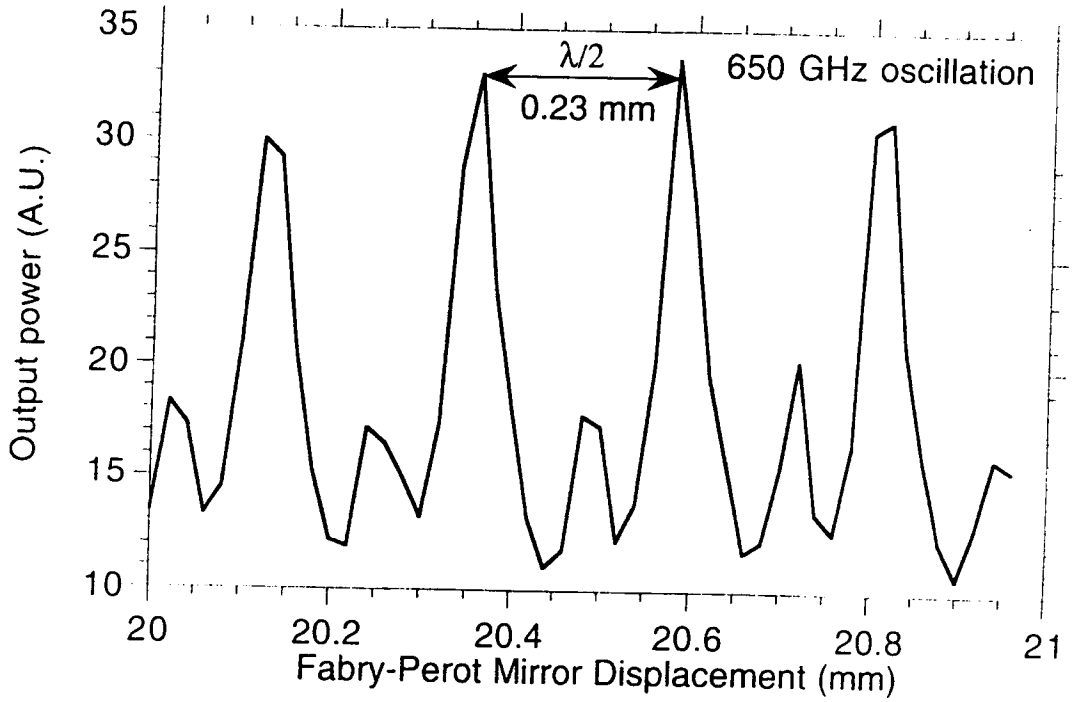

b.

Figure 9: Detected power of a 64-element array as a function of Fabry-Perot interferometer cavity length showing transmission peaks separated by 0.23 mm (a 650 GHz signal). In (b) the substrate was separated from the silicon lens by a 0.8 mm air gap.

FIBER-COUPLED PHOTOMIXERS OPERATING AT CRYOGENIC TEMPERATURES

S. Verghese,[1] K. A. McIntosh, E. R. Brown[2]
Lincoln Laboratory, Massachusetts Institute of Technology
244 Wood Street, Lexington, MA 02173

ABSTRACT

Optical heterodyne conversion, or photomixing, occurs in epitaxial low-temperature-grown GaAs between two voltage-biased metal electrodes on which two laser beams are focused with their frequencies offset by a desired difference frequency. Compared with optoelectronic THz emitters such as time-domain photoconductive switches, the photomixer is useful when a constant wave source is needed with high spectral brightness and narrow linewidth.

The spectral region $30 - 1000\,\mu$m lies beyond the capabilities of both solid-state optical sources on the short wavelength side and of electronic sources on the long wavelength side. Heterodyne measurements in this region can reveal the spectroscopic signatures of molecules that are important for atmospheric sensing and for astrophysical measurements. Recent advances in superconducting THz receivers [1, 2] have created a compelling need for a tunable single-frequency local oscillator with output power $> 1\,\mu$W from roughly 1 to 2.5 THz.

The photomixer generates a THz difference frequency by photoconductive mixing of two tunable single-frequency lasers in low-temperature-grown (LTG) GaAs [3]–[5]. Both Ti:sapphire and diode-laser pairs have been used with no measurable difference observed in the photomixer performance. In one of our designs, the combined laser beams are focused on an 8×8-μm area with interdigitated 0.2-μm-wide electrodes that are separated by a 1.8-μm gap and voltage biased at approximately 30 V. The electrodes are at the drive point of either a spiral or a dipole [4] antenna that radiates through the GaAs substrate that is mounted on a Si hyperhemisphere lens. Compared to other fast photoconductors, high-quality LTG GaAs is well suited to this application because of its short carrier lifetime (< 0.25 ps), high electrical breakdown field ($> 5 \times 10^5$ V/cm), and its relatively high mobility ($> 100\,\mathrm{cm}^2/\mathrm{Vs}$).

Our recent efforts have focused on increasing the maximum THz power available from the photomixer. The available THz power is approximately proportional to P_i^2, where P_i is the total optical power incident on the photomixer. Our room-temperature photomixers can

[1] simonv@ll.mit.edu
[2] On leave of absence to DARPA/ETO, 3701 N. Fairfax Dr., Arlington VA 22203-1714

withstand a total optical power of $P_i \approx 60\,\mathrm{mW}$ ($9 \times 10^4\,\mathrm{W/cm^2}$) when biased at 30 V. Above that power, a combination of optical and ohmic heating causes catastrophic failure of the device. Cryogenic operation at 77 K was expected to increase the maximum withstandable optical power because the base temperature is reduced by 223 K and because the thermal conductivity of the GaAs substrate increases by a factor of 6 at 77 K relative to 300 K [6]. In principle, this would allow operation with increased pump power and would result in much higher emission of THz power. In this paper, we report on the increase in emitted THz power that was realized experimentally upon cooling to 77 K.

The cooled photomixer was operated in a liquid-nitrogen cryostat with fiber-optic coupling used to route the optical beams. Figure 1 shows the fiber-optic coupling scheme. Combined light from two continuous-wave Ti:sapphire lasers operating between $813 - 819$ nm was coupled into a 4-m length of polarization-maintaining optical fiber [7]. The fiber entered the cryostat through a 1-cm-long length of stainless steel tubing that was filled with low vapor-pressure epoxy. The cleaved end of the fiber was positioned over the photomixer active area and was cemented to a position roughly $50\,\mu$m away from the photomixer chip. At this distance, the mode field of the light in the fiber expands to approximately fill the $8 \times 8\,\mu$m active area. The result is a robust package that allows independent alignment of the THz and optical beams and is immune to thermal motion in the cryostat. For comparison, measurements were also performed using free-space coupling to the photomixer through an optical window.

Figure 2 shows a comparison of the THz output power for photomixers operating at 300 and 77 K. The THz power was measured with a calibrated 4.2-K bolometer. Curve (a) is a bandwidth curve for a fiber-coupled photomixer operating at 300 K with $P_i = 20\,\mathrm{mW}$ and a bias voltage of $V = 30\,\mathrm{V}$. Curve (b) was measured for a free-space-coupled photomixer operating at 300 K, with $P_i = 30\,\mathrm{mW}$, and $V = 20\,\mathrm{V}$. The bandwidth of the fiber-coupled device is in agreement with the free-space-coupled device. The output power is proportional to P_i^2 and to V^2. Therefore, curves (a) and (b) were expected to agree in amplitude, as well. Curve (c) was measured from the free-space-coupled photomixer used in (b) after it was cooled to 77 K. The shapes of the curves (b) and (c) are similar and the 3-dB bandwidth of $\sim 0.9\,\mathrm{THz}$ was preserved as the device was cooled to 77 K. This suggests that the ultrafast trapping of carriers by the midgap defect states is not very temperature dependent. Curves (d) and (e) are measured from a fiber-coupled device at 77 K with optical pump powers of 40 and 60 mW respectively. The amplitude of the measured output power scales roughly as the square of the optical pump power. The point on curve 2(f) is from a free-space coupled photomixer operating at 77 K with $P_i = 90\,\mathrm{mW}$. This point is our highest measured output power ($0.2\,\mu$W) at 2.5 THz to date. The line shows the expected scaling of the THz output to lower frequencies. The

0.2-μW point was limited by the available power from the cw Ti:sapphire lasers. Damage-threshold measurements made with a single, more powerful Ti:sapphire laser suggest that the photomixer can withstand approximately $P_i = 96$ mW before failure. A detailed understanding of the failure mechanism is being explored [8].

In summary, cooled photomixers can withstand increased power from the pump lasers and consequently have been shown to emit unprecedented levels of power. A fiber coupling scheme allowed for more robust alignment and packaging compared to free-space coupling. There was no observed reduction in bandwidth when the photomixer was cooled to 77 K. This work was supported in part by the National Aeronautics and Space Administration, Office of Space Access and Technology, through the Center for Space Microelectronics Technology, Jet Propulsion Laboratory, California Institute of Technology and by the Air Force under Contract F19628-95-C-0002.

References

[1] D. E. Prober, *Appl. Phys. Lett.*, **62**, 2119 (1993); A. Skalare, W. R. McGrath, B. Bumble, H. G. LeDuc, P. J. Burke, A. A. Verheijen, and D. E. Prober, *IEEE Trans. Appl. Supercond.* **5**, 2236 (1995).

[2] G. N. Gol'tsman, B. S. Karasik, O. V. Okunev, A. L. Dzardanov, E. M. Gershenzon, H. Ekstroem, S. Jacobsson, and E. Kollberg, *IEEE Trans. Appl. Supercond.* **5**, 3065 (1995).

[3] K. A. McIntosh, E. R. Brown, K. B. Nichols, O. B. McMahon, W. F. Dinatale, and T. M. Lyszczarz, *Appl. Phys. Lett.* **67**, 3844 (1995).

[4] K. A. McIntosh, E. R. Brown, K. B. Nichols, O. B. McMahon, W. F. Dinatale, and T. M. Lyszczarz, *Appl. Phys. Lett.* **69**, 3632 (1996).

[5] S. Verghese, K. A. McIntosh, and E. R. Brown, to appear in *IEEE Trans. Microwave Theory Tech.*, August 1997.

[6] J. S. Blakemore, *J. Appl. Phys.* **53**, R123 (1982).

[7] Single-mode, polarization-maintaining optical fiber, 850-nm center wavelength. Model FS-4625-PM, 3M Specialty Optical Fibers, West Haven, CT.

[8] S. Verghese, K. A. McIntosh, and E. R. Brown, submitted to *Appl. Phys. Lett.* on 30 April, 1997.

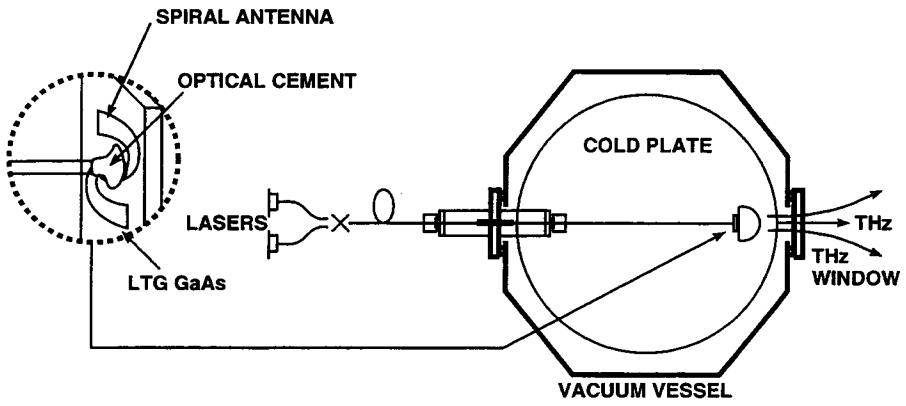

Figure 1: Schematic diagram of the cryogenic LTG-GaAs photomixer coupled to two lasers via optical fiber. Both diode lasers and Ti:sapphire lasers have been used.

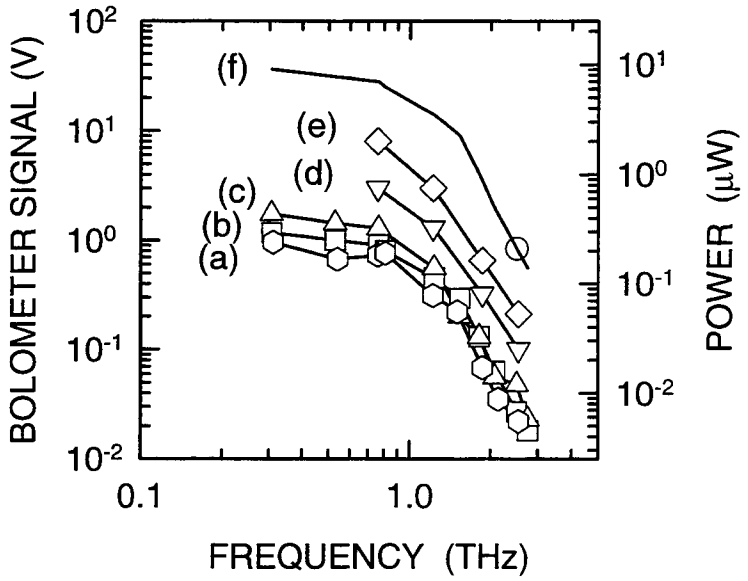

Figure 2: Measured bandwidth curves for photomixers operating at room temperature and at liquid nitrogen temperature. (a) 300-K operation of a fiber-optic coupled photomixer with 30-V bias and $P_i \approx 20\,\mathrm{mW}$. (b) 300-K operation of a free-space coupled photomixer with 20-V bias and $P_i = 30\,\mathrm{mW}$. (c) 77-K free-space coupled photomixer under same conditions as curve (b). (d) 77-K fiber-coupled photomixer with 30-V bias and $P_i \approx 40\,\mathrm{mW}$. (e) 77-K fiber-coupled photomixer with 30-V bias and $P_i \approx 60\,\mathrm{mW}$. (f) 77-K free-space coupled photomixer with 30-V bias and $P_i \approx 90\,\mathrm{mW}$.

Accurate Circuit and Device Equations for Designing 50-600 GHz GaAs Schottky Diode Varactor Frequency Doublers

R. E. Lipsey, S. H. Jones, and T. W. Crowe
Department of Electrical Engineering, University of Virginia, Charlottesville, VA 22903

Abstract

The use of GaAs Schottky barrier varactors (SBVs) for high frequency multiplication has long been establish. In order to theoretically analyze the performance of these devices, several different approaches have been realized among which are equivalent circuit modeling, drift-diffusion modeling, and Monte Carlo modeling. Equivalent circuit modeling, such as the analytical models derived by Penfield and Rafuse , offer a fast and efficient method for analyzing these non-linear devices. However, the solutions of these analytical models rely heavily on undetermined coefficients. In an attempt to solve the problems associated with the Penfield and Rafuse technique, Burckhardt empirically solved for the undetermined coefficients, creating closed form expressions. These analytical models have demonstrated reasonable accuracy for SBVs in the frequency range of 1-50 GHz. However, at high frequencies, the usefulness of these analytical models is limited due to their inability to model high frequency electron transport phenomenon . To accurately model high frequency transport phenomena in GaAs SBVs, a Monte Carlo Harmonic-Balance (MCHB) simulator has been developed and offers considerably better precision over results obtained from Harmonic-Balance simulation incorporating equivalent circuit modeling for the diodes. Although the MCHB and DDHB methods offer superior accuracy, they are time and CPU intensive and can take from several hours to several weeks to reach a complete multiplier design. To decrease simulation complexity and maintain precision, we have derived a set of analytical design equations with semi-empirical coefficients derived from the MCHB simulator. Since these expressions for device and circuit impedance, efficiency, output power, and d.c. bias are independent of each other and rely solely on nominal device specifications, they allow for co-design from both a device and circuit point of view in a relatively simple, efficient, and accurate manner. Results from the set of design equations are compared to both MCHB simulations and experimental results for the UVA 5T1 100 to 200 GHz frequency doubler.

I. Introduction

The use of GaAs Schottky barrier varactors (SBVs) for high frequency multiplication has long been established. In order to theoretically analyze the performance of these devices, several different approaches have been realized among which are equivalent circuit modeling, drift-diffusion modeling, and Monte Carlo modeling. Equivalent circuit modeling, such as the analytical models derived by Penfield and Rafuse [1] , offer a fast and efficient method for analyzing these non-linear devices. However, the solutions of these analytical models rely heavily on undetermined coefficients. In an attempt to solve the problems associated with the Penfield and Rafuse technique, Burckhardt [2] empirically solved for the undetermined coefficients, creating closed form expressions. These analytical models have demonstrated reasonable

accuracy for SBVs in the frequency range of 1-50 GHz. However, at high frequencies, the usefulness of these analytical models is limited due to their inability to model high frequency electron transport phenomenon [3-4]. To accurately model high frequency transport phenomena in GaAs SBVs, a Monte Carlo Harmonic-Balance (MCHB) [5] simulator incorporating the Monte Carlo simulator of [6-7] has been developed and offers considerably better precision over results obtained from Harmonic-Balance simulation incorporating equivalent circuit modeling for the diodes [8-9]. Although the MCHB method offers superior accuracy, it is time and CPU intensive and can take from several hours to several weeks to reach a complete multiplier design. To decrease simulation complexity and maintain precision, we have derived a set of analytical design equations with semi-empirical coefficients derived from the MCHB simulator. Since these expressions for device and circuit impedance, efficiency, output power, and d.c. bias are independent of each other and rely solely on nominal device specifications, they allow for co-design from both a device and circuit point of view in a relatively simple, efficient, and accurate manner. Results from the set of design equations are compared to both MCHB simulations and experimental results for a frequency doubler to 200 GHz using a UVA 5T1 varactor diode.

II. Device and Circuit Equations

The following analysis determines a set of equations for the optimal performance of SBV frequency doublers. This set of equations describes the relationship between voltage, current, and power derived from the equivalent circuit model shown in figure 1. Parasitic impedances due to the substrate have been lumped into the linear equivalent circuit embedding impedances and are appropriately accounted for in the calculations of power and efficiency. The following analysis is similar to that of [1-2], but includes the effects of both the nonlinear resistance and capacitance elements.

Given that

$$C(t)\frac{dv(t)}{dt} = i(t) \qquad (1)$$

and

$$R(t) = \frac{\rho}{a}(l - w(t)) \qquad (2)$$

where ρ is the resistivity of the undepleted active region, a is area of the anode, l is the length of the diode active region, and w(t) is the time dependent depletion width, equations (1) and (2) can be rewritten as

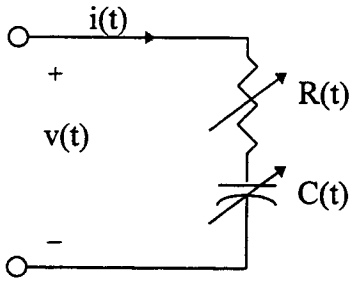

Figure 1 Equivalent varactor circuit model

$$v(t) = \int \frac{1}{C(t)} i(t)dt = \int S(t)i(t)dt \tag{3}$$

and $$R(t) = \frac{\rho}{a}(l - \frac{\varepsilon a}{C(t)}) = \frac{\rho}{a}[l - \varepsilon a S(t)]. \tag{4}$$

Therefore, the time dependent voltage across the diode terminals can be written as

$$v(t) = \frac{\rho l}{a} i(t) - \varepsilon\rho S(t)i(t) + \int S(t)i(t)dt \tag{5}$$

Following the approach of Penfield and Rafuse [1], if an input pump frequency of ω_0 is fed into a harmonic multiplier such as a GaAs SBV, only integer multiples of the form $k\omega_0$ are present. Thus the Fourier representation of the voltage, current, and elastance take the form

$$v(t) = \sum_{k=-\infty}^{\infty} V_k e^{jk\omega_0 t} \tag{6}$$

$$i(t) = \sum_{k=-\infty}^{\infty} I_k e^{jk\omega_0 t} \tag{7}$$

$$S(t) = \sum_{k=-\infty}^{\infty} S_k e^{jk\omega_0 t}. \tag{8}$$

The waveforms v(t), i(t), and S(t) are all real which permits the simplification that

$$\begin{aligned} V_{-k} &= V_k^* \\ I_{-k} &= I_k^* \\ S_{-k} &= S_k^* \end{aligned} \tag{9}$$

where * indicates the complex conjugate. Since the Fourier coefficients are simply phase modified time-averaged values of the time-varying waveforms,

$$V_k = \frac{1}{T_0} \int_{-\frac{T_0}{2}}^{\frac{T_0}{2}} v(t) e^{-\frac{j2\pi kt}{T_0}} dt = \left\langle v(t)e^{-jk\omega_0 t} \right\rangle \tag{10}$$

and similarly

$$I_k = \left\langle i(t)e^{-jk\omega_0 t} \right\rangle \tag{11}$$

$$S_k = \left\langle S(t)e^{-jk\omega_0 t} \right\rangle. \tag{12}$$

Substituting equations (10), (11), and (12) into equation (5) yields

$$V_k = \frac{\rho l}{a} I_k - \varepsilon\rho \left\langle S(t)i(t)e^{-jk\omega_0 t} \right\rangle + \frac{1}{jk\omega_0} \left\langle S(t)i(t)e^{-jk\omega_0 t} \right\rangle \tag{13}$$

Finally, combining like terms and substituting equations (7) and (8) into equation (13) yields

$$V_k = \frac{\rho l}{a} I_k + \left(\frac{1}{jk\omega_0} (1 - j\varepsilon\rho k\omega_0) \right) \sum_l I_l S_{k-l} \tag{14}$$

where both k and l range from $-\infty$ to $+\infty$. Equation (14) describes the equivalent varactor circuit model in the frequency domain.

Since our analytical model only describes the operation of abrupt junction Schottky barrier diodes, the time-dependent elastance may be expressed as

$$S(t) = \frac{1}{qN_d\varepsilon}Q(t) = \frac{1}{C(t)} \tag{15}$$

where N_d is the doping concentration of the active layer of the device. Because the current and charge are related, we can relate equation (15) to the current via

$$i(t) = \frac{dQ(t)}{dt} = qN_d\varepsilon\frac{dS(t)}{dt}. \tag{16}$$

In the frequency domain, the current can be expressed as

$$\begin{aligned}\sum_k I_k e^{jk\omega_0 t} &= qN_d\varepsilon\frac{d}{dt}\sum_k S_k e^{jk\omega_0 t} \\ &= qN_d\varepsilon(jk\omega_0)\sum_k S_k e^{jk\omega_0 t}.\end{aligned} \tag{17}$$

Since both the summations and phases are identical, we can compare term by term which results in

$$I_k = jk\omega_0(qN_d\varepsilon)S_k. \tag{18}$$

We define the Complex Modulation Ratio, M_k, as the normalized elastance coefficient,

$$M_k = \frac{S_k}{S_{avg}} \tag{19}$$

where $S_{avg} = (S_{max} + S_{min})/2$, S_{max} is defined as the reciprocal of the capacitance at reverse breakdown, and S_{min} is defined as the reciprocal of the capacitance at zero bias. Substituting equations (18) and (19) into equation (14) gives the expression for the harmonic voltage at k

$$V_k = \frac{\rho l}{a}I_k + (qN_d\varepsilon)S_{avg}^2(1 - \varepsilon\rho jk\omega_0)\sum_r M_r M_{k-r} \tag{20}$$

The combination of equations (18) and (20) allow us to calculate the device impedance and efficiency. The input impedance at the n^{th} harmonic (where *n* represents a specific value of *k*) is given by

$$Z_n = \frac{V_n}{I_n} = \frac{\rho l}{a} + S_{avg}(1 - j\varepsilon\rho n\omega_0)\frac{\sum_r M_r M_{n-r}}{jn\omega_0 M_n} \tag{21}$$

If we extract only the real part of equation (21), we arrive at the expression for the resistance of the diode at the n^{th} harmonic

$$R_n = \mathrm{Re}\{Z_n\} = \frac{\rho l}{a} + S_{avg}\left[\frac{A_n}{n\omega_0} - \varepsilon\rho B_n\right] \tag{22}$$

where A_n and B_n are real coefficients related to the real parts of the complex modulation ratio summations. The diode reactance at the n^{th} harmonic is given by the imaginary part of equation (21)

$$X_n = \mathrm{Im}\{Z_n\} = S_{avg}\left[\frac{C_n}{n\omega_0} - \varepsilon\rho D_n\right] \tag{23}$$

where C_n and D_n are real coefficients related to the imaginary parts of the complex modulation ratio summations. The device efficiency is given by the ratio of the output power at the harmonic of interest to the available input power to the device. Given the complex modulation ratios at each harmonic, each frequency can be considered individually and the expression for the input power at the fundamental frequency ($n = 1$), using equations (18-19) and (22), becomes

$$P_{1,in} = 2(R_1 + R_p)|I_1|^2 = 2(qN_d\varepsilon)^2 S_{avg}^2 \omega_0^2 m_1^2 (R_1 + R_p) \tag{24}$$

where $m_n = |M_n|$. R_p is the device parasitic resistance in the substrate and the contact regions of the device as well as the circuit. R_p is always positive and was lumped with the linear embedding circuit impedance at the beginning of this analysis. The second harmonic output power for a doubler is given by a similar expression as equation (24) with the substitution of R_2 for R_1 which results in

$$P_{2,out} = 2(R_2 + R_p)|I_2|^2 = 2(qN_d\varepsilon)^2 S_{avg}^2 4\omega_0^2 m_2^2 (R_2 + R_p). \tag{25}$$

Since power is generated at the second harmonic, both R_2 and P_2 are negative for typical doubler designs. As Penfield and Rafuse point out [1], the modulation ratio m_2 is always less than m_1 since the varactor is not an ideal nonlinear capacitor. Also, at frequencies approaching the diode cutoff frequency $m_2 \approx 0$ since the second harmonic current is approximately zero. We approximate m_2 with the following

$$m_2^2 \approx \frac{1}{4}\alpha m_1^2 (1 - \beta f_0 / f_c) \quad \text{for } \beta f_0 \le f_c \text{ where}$$

$$f_c = \frac{1}{2.2 R_{max} C_{max}} \tag{26}$$

where α and β represent the relationship between the modulation ratios m_1 and m_2 and f_c represents the cutoff frequency. R_{max} is the maximum resistance across the diode active region which we define to be $(\rho\ell / a)$ and C_{max} is defined as the capacitance across the active region at zero bias. The product of R_{max} and C_{max} represents the charging time of the device and the factor of *2.2* accounts for the rise and fall time (the time it takes the device to charge to 90 % and discharge to 10 % of its final value). The inclusion of the cutoff frequency in the modulation ratio aids in the modeling of the effects of diode length and doping on efficiency. The second harmonic power generation efficiency is given by the ratio of the second harmonic output power (25) to the available input power (24) with the substitution of equation (26) for the modulation ratios which becomes

$$\eta = -\frac{P_{2,out}}{P_{in}} = -\alpha \frac{R_2 + R_p}{R_1 + R_p}\left(1 - \beta \frac{f_0}{f_c}\right). \tag{27}$$

As seen, the parasitic resistance contributes to a decrease in efficiency since it serves to increase the magnitude of the of denominator and decrease the magnitude of the numerator in equation (27).

In order to determine the required d.c. bias for optimal performance, we relate the magnitude of the first harmonic voltage to the d.c. bias. Since increased efficiency is observed with increased non-linearity in the capacitance, it is desirable to pump the diode

as close to forward turn-on and breakdown as possible. However, at small incident pump powers, the magnitude of the voltage may not be large enough to reach forward conduction or breakdown. Therefore, since the greatest nonlinear effects in the capacitance are realized when the diode is close to forward turn-on, the d.c. bias should be set approximately equal to the magnitude of the voltage at the first harmonic. The elastance of the diode can be related to the charge by

$$\frac{S - S_{\min}}{S_{\max} - S_{\min}} = \frac{q - Q_{\min}}{Q_{br} - Q_{\min}} \tag{28}$$

where S and q are the unknown elastance and charge at a particular time, respectively, Q_{br} is the charge at reverse breakdown voltage (V_{br}), Q_{min} is the charge at the minimum applied voltage. The voltage is related to the charge and elastance by

$$V_{Br} = \int_{Q_{\min}}^{Q_{br}} S\,dq \quad \text{or}$$

$$Q_{br} - Q_{\min} = \frac{2}{S_{\max} + S_{\min}} V_{br} \tag{29}$$

Since equation (18) can also be written as

$$I_k = j\omega_0 k M_k (Q_{br} - Q_{\min}) \tag{30}$$

we can express the current in terms of the breakdown voltage by substitution of equation (29) into equation (30) which gives the following

$$I_k = j\omega_0 k M_k \frac{2}{S_{\max} + S_{\min}} V_{br} \tag{31}$$

By substituting equation (31) into equation (14) and substituting $|V_{dc}| = |V_1|$ with n=1, gives the following expression for the d.c. bias

$$V_{dc} = \frac{1}{(S_{\max} + S_{\min})} \left(\frac{\rho \ell}{a} V_{br} \omega_0 \chi + S_{avg} V_{br} (1 - \varepsilon \rho \omega_0) \kappa \right) \tag{32}$$

where χ and κ are associated with the complex modulation ratios. Since the MCHB simulator used does not account for breakdown effects, calculated d.c. bias points may bias the device too close to breakdown. Therefore, the general very important guideline applies

$$\left| V_{dc,calculated} \right| \le \left| \frac{1}{2} V_{br} \right| \tag{33}$$

III. Design Equations and Coefficients for Doublers

In order to utilize the derived set of varactor equations, all the unknown coefficients representing the modulation ratios, which generally are unknown, must be determined. We have solved a global and unified set of coefficients for the analytical equations (22)-(23), (27), and (32) using very accurate numerical simulation results (the MCHB simulator described in [5]). Our analysis considers the case of a GaAs Schottky barrier abrupt junction frequency doubler. We have combined multiple real ratios for each equation into one real coefficient as needed. This results in the following set of design equations for optimal doubler performance

$$R_1 = \frac{\rho l}{a} + S_{avg}\left(\frac{A}{\omega_0} - \varepsilon\rho B\right) \tag{33}$$

$$R_2 = \frac{\rho}{a} + S_{avg}\left(\frac{C}{2\omega_0} - \varepsilon\rho D\right) \tag{34}$$

$$X_1 = S_{avg}\left(\frac{E}{\omega_0} - \varepsilon\rho F\right) \tag{35}$$

$$X_2 = S_{avg}\left(\frac{G}{2\omega_0} - \varepsilon\rho H\right) \tag{36}$$

$$\eta = -\alpha\frac{R_2 + R_p}{R_1 + R_p}(1 - \beta\frac{f_0}{f_c}) \quad \text{for } f_0 \le f_c \tag{37}$$

$P_{2,out} = \eta P_{1,in}$, where P_2 is power generated

$$|V_{dc}| = \frac{\rho l\omega_0}{a(S_{max} + S_{min})}V_{br}\chi + \frac{S_{avg}}{S_{max} + S_{min}}V_{br}(1 - \varepsilon\rho\omega_0)\kappa \tag{38}$$

$$|V_1| = |V_{dc}|$$

where A, B, C, D, E, F, G, H, α, β, χ, and κ are the unknown combined modulation ratios. These equations form a complete set of diode and circuit specifications for optimal performance of GaAs SBV frequency doublers. Given a specified diode, the embedding circuit for optimal performance is uniquely determined and the maximum efficiency and output power can be calculated. Also, given a specified circuit, the relationship between the doping and geometry of a diode can be optimally determined for that circuit. For steady state operation and optimal efficiency, the following expressions hold true

$$Z_{1,diode} = Z^*_{1,circuit} \quad \text{and} \tag{39}$$

$$Z_{n,diode} = -Z_{n,circuit} \ (n \neq 1). \tag{40}$$

Equations (33) - (36) are used to calculate $Z_{n,diode}$.

In order to determine the coefficients, MCHB simulations were run on three different diodes with nominal parameters summarized in table 1 to determine the left hand side of equations (33) - (38). The choice for using three diodes was based on two conditions. First, as can be seen in equations (33) - (38), each equation has two dependent coefficients which would require a minimum of two diode simulations. Second, we wanted to find the coefficients based on an overdetermined set of equations which allows for a minimum mean squared error solution instead of a uniquely determined solution based on two specific diodes. Diodes with doping and length specifications spanning the typical parameters used for high frequency doublers were chosen. For each diode, four different input powers were simulated at both 100 and 275 GHz. The best fit for these overdetermined expressions in equations (33) - (38) was found. For equations (33) - (38), the conventional parameter for resistivity has been used. We can solve for the resistivity through its definition

$$\rho = \frac{1}{q\mu_n N_d} \tag{41}$$

where q is the charge of an electron, N_d is the doping concentration, and we assume μ_n to be the doping dependent constant low-field mobility value of an electron in GaAs. The elastances are calculated as defined earlier. Since ℓ, the length of the diode active region, and a, the area defined by the Schottky contact, are known, we can explicitly solve for the undetermined coefficients. The results from the MCHB simulations are summarized in table 2. The resultant coefficients are summarized in table 3.

Table 1 Nominal Diode Parameters Used to Solve for Unknown Coefficients [10]

Diode	Diode Doping Density (cm^{-3})	Diode Thickness (μm)	Anode Diameter (μm)	Mobility (cm^2/Vs)	Breakdown Voltage (V)
1	2.0×10^{16}	1.5	7.0	6580	31.5
2	3.5×10^{16}	1.0	6.3	6400	20
3	4.0×10^{16}	0.8	4.7	6340	18

Table 2 Results from Monte Carlo/Harmonic-Balance Simulator for Diodes 1, 2, and 3 (i.e. Right Hand Side of Equations (33) - (38))

Input Frequency (GHz)	$P_{1,in}$ (mW)	Diode	R_1 device	R_2 device	X_1 device	X_2 device	$P_{2,out}$ (mW)	$\|V_1\|$ (V)
100	7.5	1	30.3	-27.5	-243.2	-122.6	-2.07	5.29
		2	22.9	-25.0	-213.0	-108.5	-2.92	5.33
		3	35.9	-37.6	-282.3	-147.1	-3.44	5.59
	18.8	1	55.9	-57.3	-273.0	-139.4	-3.58	7.19
		2	39.0	-39.0	-228.3	-116.4	-4.86	7.14
		3	64.1	-58.9	-315.9	-157.6	-5.72	7.95
	29.6	1	81.7	-83.2	-305.9	-153.3	-5.12	8.38
		2	53.4	-51.6	-231.7	-118.9	-5.98	7.84
		3	79.4	-72.7	-320.6	-162.1	-6.92	8.89
	47.0	1	102.1	-99.4	-375.7	-193.4	-5.91	11.77
		2	73.4	-75.7	-272.4	-135.9	-7.57	9.89
		3	96.4	-102.2	-358.7	-181.8	-8.25	11.44
275	7.5	1	17.0	-17.5	-53.6	-30.1	-0.08	1.59
		2	8.6	-11.4	-38.6	-23.0	-0.26	1.47
		3	12.0	-14.7	-69.9	-38.0	-0.49	2.29
	18.8	1	48.1	-48.3	-100.5	-52.9	-0.28	3.04
		2	24.2	-26.4	-57.2	-30.7	-0.74	2.34
		3	35.1	-35.5	-111.5	-63.1	-0.89	3.67
	29.6	1	52.4	-55.9	-143.0	-72.5	-0.38	5.01
		2	35.2	-33.2	-82.2	-47.0	-0.82	3.53
		3	34.9	-33.2	-123.9	-64.2	-1.51	5.48
	47.0	1	37.8	-41.9	-171.6	-88.1	-0.44	8.52
		2	33.8	-30.2	-112.3	-64.1	-1.21	5.98
		3	29.2	-35.6	-158.2	-79.2	-1.89	8.75

Table 3 Resultant Coefficients

f_{input} = 100 GHz

$P_{1,in}$ mW	A	B	C	D	E	F	G	H	α	β	χ	κ
7.5	0.113	1.681	-0.25	2.727	-0.94	6.623	-1.00	2.519	0.485	5.18	-5.25	0.825
18.8	0.173	-0.08	-0.24	7.02	-1.00	9.025	-0.98	5.149	0.394	7.27	-7.47	1.15
29.6	0.166	-3.93	-0.19	11.35	-0.85	18.01	-0.89	8.452	0.289	5.67	-7.73	1.25
47.0	0.226	-5.13	-0.52	8.966	-0.82	28.65	-0.78	15.73	0.187	4.16	-8.34	1.526

f_{input} = 275 GHz

$P_{1,in}$ mW	A	B	C	D	E	F	G	H	α	β	χ	κ
7.5	0.027	0.505	-0.07	4.681	-0.55	1.509	-0.62	0.845	0.068	4.26	-0.75	0.308
18.8	0.036	-3.72	-0.02	9.216	-0.58	7.6	-0.74	3.306	0.064	3.78	-0.94	0.458
29.6	0.118	-3.59	0.088	10.96	-0.41	15.56	-0.59	6.977	0.069	4.15	-1.18	0.657
47.0	0.259	-0.09	-0.33	6.727	-0.79	15.50	-0.94	7.374	0.049	4.02	-1.74	1.05

Given the coefficients in table 3 and equations (33) - (38), optimal device and circuit parameters can be quickly calculated for a broad range of input powers and frequencies. Higher harmonic embedding impedances have been shorted.

IV. Design Example

An example of how the design equations and coefficients can be used follows. For this exercise, we wish to compare the results with known experimental results for the UVA 5T1 diode [10]. The nominal device parameters are summarized in table 4. Note that the parameters for this diode are unlike diodes 1, 2, and 3 used for the coefficient extraction.

Table 4 Nominal Diode Parameters for the 5T1 [10]

Diode	Diode Doping Density (cm^{-3})	Diode Thickness (μm)	Anode Diameter (μm)	Mobility (cm^2/Vs)	Breakdown Voltage (V)
5T1	1.0×10^{17}	0.6	4.7	5620	10

Step 1: Choosing a diode length, diode doping, and bias point

First, the diode length is chosen, which for the UVA 5T1 is specified as 0.6 μm. Next, the diode doping density is chosen. Since we are using the UVA 5T1 as an example, the diode doping density, N_d, is 1.0×10^{17} cm^{-3}. Once the doping is chosen, the avalanche breakdown voltage, V_{abr}, should be calculated. The expression for avalanche breakdown voltage is given as

$$V_{abr} = \frac{1}{2qN_d}\varepsilon\xi_{max}^2 = 10 \text{ V} \qquad (42)$$

where ξ_{max} is the maximum electric field obtainable in the diode. An empirical equation we have derived from the measured diode breakdown voltages of actual diodes for ξ_{max} is

$$\xi_{max} = 1.3x10^{-12}(Vcm^2)\cdot N_d(cm^{-3}) + 4x10^5(\frac{V}{cm}). \quad (43)$$

For the UVA 5T1, ξ_{max} is 530 kV/cm which yields a breakdown voltage of 10 V. Because the diode can suffer both avalanche breakdown with and without punch through, the avalanche breakdown voltage (which corresponds to avalanche breakdown without punch through) and the punch through voltage (which determines when punch through occurs and indicates the onset of breakdown) must both be calculated. The smaller of the two voltages should be chosen as the design breakdown voltage, V_{Dbr} , and used in the design equations (33)-(38). The punch through voltage, V_{pt} , is given by

$$V_{pt} = \frac{1}{2\varepsilon} qN_d l^2 = 25 \text{ V}. \quad (44)$$

Therefore, for this example, the design breakdown voltage, V_{Dbr} , is given by the avalanche breakdown voltage and is 10 V. Once the design breakdown voltage is found, the d.c. bias of the device should be determined from equation (38) and for an input power of 16 mW and an input frequency of 100 GHz, we determine that the magnitude of the d.c. bias should be set at 4.5 V. If the calculated d.c. bias is greater than $V_{Dbr}/2$ which violates equation (32), the input power could be reduced until equation (32) is satisfied; if the device was punch through limited ($V_{pt} < V_{br}$), the length of the device can be increased; or if the device was not punch through limited, the doping can be decreased. If any changes are made to the power, length, or doping, the above process must be repeated until the calculated d.c. bias does not violate equation (32).

Step 2: Determining the optimal embedding impedances, device area, and Q of the diode

Once the length and doping have been determined an anode diameter must be specified which for our example is 4.7 μm. The next step in the solution process is to solve for the resistivity of the device which can be found using equation (41) and is calculated to be 0.01 Ω-cm. Next, the minimum and maximum elastances must be calculated. These are calculated from the minimum and maximum depletion widths. The depletion width, W, is given by

$$W = \sqrt{\frac{2\varepsilon(1+|V|)}{qN_d}} \quad (45)$$

where |V| is the absolute value of the applied voltage (approximately zero for the minimum depletion width corresponding to the minimum elastance and V_{Dbr} for the maximum depletion width corresponding to the maximum elastance). For the UVA 5T1, we calculate that the maximum depletion width, W_{max}, is 0.40 μm and the minimum depletion width, W_{min}, is 0.12 μm. Next, the maximum and minimum capacitances are calculated

$$C = \frac{a\varepsilon}{W} + \frac{3a\varepsilon}{d_{anode}} \quad (46)$$

where d_{anode} is the device anode diameter, a is the anode area, and W is the depletion width (C_{min} corresponds to W_{max} and C_{max} corresponds to W_{min}). For the UVA 5T1 whisker contacted diode, the anode area is defined by the anode diameter and is given by

$a = \pi\,(d_{anode} / 2)^2$. For the UVA 5T1, we calculate C_{min}= 6.3 fF and C_{max}= 17.8 fF. This result yields the following for the minimum and maximum elastances

$$S_{max} = \frac{1}{C_{min}} = 1.6x10^{14}\ F^{-1}$$
$$S_{min} = \frac{1}{C_{max}} = 5.6x10^{13}\ F^{-1}. \qquad (47)$$

Then, given the coefficients in table 3, the optimal device impedances can be solved for using equations (33) - (36). A comparison of the calculated results and experimental data are presented in table 5. Since the circuit embedding impedances for the experimental data are unknown, results for the impedances of the device and circuit are compared to the accurate MCHB simulator. With the impedances calculated, the Q ($Q_n = X_n / R_n$) for the diode can be calculated. For the UVA 5T1, the calculated value for Q at the first harmonic is approximately 6 ($Q \approx 6$).

Step 3: Determining the output power and second harmonic doubling efficiency

Once the maximum and minimum elastances and the device impedances have been calculated, the second harmonic doubling efficiency can be calculated with equation (37) and the coefficient from Table 3. The cutoff frequency is determined using equation (26) and we find that

$$f_c = \frac{1}{2.2 R_{max} C_{max}} = 6.62\ THz. \qquad (48)$$

Thus, the calculated doubling efficiency for the UVA 5T1 diode is found to be approximately 31 % which results in 5.0 mW of output power at the second harmonic. R_p has been set equal to zero for this example. Hence, for optimal performance at an input frequency of 100 GHz and an input power of 16 mW ($\eta \approx 31$ %), the embedding circuit impedances should be set to $Z_1 = 30.5 + j\ 180.5$ and $Z_2 = 25.3 + j\ 91.1$ and the d.c. bias should be set to -4.5 V. Estimated performance at other frequencies and powers or using different diode parameters can be quickly calculated using table 3.

Table 5 Comparison of Design Equations, Simulated, and Experimental Results for the UVA 5T1 Frequency Doubler at an Input Frequency of 100 GHz

Input Power (mW) f_{in} = 100 GHz	**R_1 calc.**	**R_1 sim.**	**R_1 exp.**	**X_1 calc.**	**X_1 sim.**	**X_1 exp.**	**R_2 calc.**	**R_2 sim.**	**R_2 exp.**
16	30.5	23.1	NA	-180.5	-174.2	NA	-25.3	-24.5	NA

Input Power (mW) f_{in} = 100 GHz	**X_2 calc.**	**X_2 sim.**	**X_2 exp.**	**$P_{2,out}$ mW calc.**	**$P_{2,out}$ mW sim.**	**$P_{2,out}$ mW exp.**	**$\|V_{d.c.}\|$ calc.**	**$\|V_{d.c.}\|$ sim.**	**$\|V_{d.c.}\|$ exp.**
16	-91.1	-87.9	NA	5.0	9.0	4.1	4.5	5.0	5.0

Although the calculated impedances cannot be compared to experimental data, they accurately reflect the values predicted by the MCHB simulator and the calculated output power and d.c. bias accurately reflect the experimental data. Many different simulations of various combinations of doping, active layer length, and anode diameter

were performed. The results using the set of design equations yielded consistently accurate results with both MCHB simulation and experimental data where available.

V. Conclusions

A set of design equations for high frequency GaAs SBV frequency doublers has been derived. These equations maintain the simplicity of equivalent circuit modeling while offering superior accuracy. The improvements in accuracy arise from the semi-empirical coefficients contained within the equation set that are derived from a high performance Monte Carlo Harmonic-Balance simulator. These coefficients are found for a variety of powers and two frequencies and can be used to solve for either the nominal diode parameters or the device operating point. Thus, the set of design equations allow for co-design from both a device and circuit standpoint in a simple, efficient, and accurate manner.

Acknowledgments

This research has been sponsored by NSF grant #ECS-9412931. The authors greatly appreciate many important discussions with Tom Crowe, Rob Jones, Greg Tait, and Chris Mann. The authors would also like to recognize the work of Richard Bradley who's dissertation [11] provided an enlightening summary of the Penfield and Rafuse approach in [1].

References

[1] P. Penfield and R. P. Rafuse, *Varactor Applications*, The M.I.T. Press,Cambridge, Massachusetts, 1962.

[2] C. B. Burckhardt, "Analysis of Varactor Frequency Multipliers for Arbitrary Capacitance Variation and Drive Level," *The Bell System Technical Journal*, Apr. 1965, pp. 675-692.

[3] L. F. Horvath, J. R. Jones, S. H. Jones, and G. B. Tait, "Numerical Device/Harmonic-Balance Circuit Analysis of Schottky Barrier Varactors," *Proceedings of the 1995 International Device Research Symposium*, Vol. 1, pp. 259-262, Dec.. 1995.

[4] J. R. Jones, S. H. Jones, G. B. Tait, "Self-Consistent Physics Based Numerical Device/Harmonic-Balance Circuit Analysis of Heterostructure Barrier and Schottky Barrier Varactors including Thermal Effects," *Proceedings of the Sixth International Symposium of Space Terahertz Technology*, March 1995, p. 423.

[5] R. E. Lipsey, S. H. Jones, J. R. Jones, T. W. Crowe, L. F. Horvath, U. V. Bhapkar, and R. J. Mattauch, "Monte Carlo Harmonic-Balance and Drift-Diffusion Harmonic-Balance Analyses of 100-600 GHz Schottky Barrier Varactor Frequency Multipliers," Submitted to *IEEE Elec. Dev.*, November 1996.

[6] U. V. Bhapkar, "Monte Carlo Simulation of GaAs Schottky Diodes for Terahertz Frequencies," Doctoral Dissertation, University of Virginia, August 1995.

[7] U. V. Bhapkar and R. J. Mattauch, "Monte Carlo Simulation of Terahertz Frequency Schottky Diodes," *Proceedings of the 1995 International Semiconductor Device Research Symposium*, Vol. 1, pp. 263-265, Dec. 1995.

[8] P. H. Siegel, A. R. Kerr, and W. Hwang, "Topics in the Optimization of Millimeter-Wave Mixers," *NASA Tech. Papers*, No. 2287, Mar. 1984.

[9] E. L. Kollberg, T. J. Tolmunen, M. A. Frerking, and J. R. East, "Current Saturation in Submillimeter Wave Varactors", *IEEE Trans. on Microwave Theory Tech.*, Vol. 40, No. 5, May 1992, pp. 831-838.

[10] T. W. Crowe, W. C. B. Peatman, Ru. Zimmermann, and Ra. Zimmermann, "Consideration of Velocity Saturation in the Design of GaAs Varactor Diodes," *IEEE Microwave Guided Waves*, Vol. 3, No. 6, June 1993, pp. 161-163.

[11] R. F. Bradley, "The Application of Planar Monolithic Technology to Schottky Varactor Millimeter-Wave Frequency Multipliers," Doctoral Dissertation, University of Virginia, 1992.

FABRICATION AND OPTIMISATION OF PLANAR SCHOTTKY DIODES

A. Simon#, C. I. Lin#, H. L. Hartnagel#
P. Zimmermann*, R. Zimmermann*,

Institut für Hochfrequenztechnik, Merckstr. 25, 64283 Darmstadt
Fax: + 6151/164367, e-mail: hfmwe015@hrzpub.th-darmstadt.de
* Radiometer Physics GmbH, Bergerwiesenst. 15, 53340 Meckenheim
Tel. +2225/15953, Fax: +2225/14441

Abstract

Aiming at a more reliable and cheaper fabrication the replacement of whisker contacted Schottky diodes for applications in the THz frequency range is an important topic of investigation. The recent status of planar Schottky diodes using the quasi-vertical approach is shown. Mixer diodes with anode diameters of 0.8 - 2 μm and cut-off frequencies up to 9 THz have been fabricated that offer characteristics comparable to whiskered diodes with the same diode parameters.

Introduction

GaAs Schottky barrier diodes are used as frequency multiplier in all-solid-state local oscillators and as mixer element in heterodyne receivers in the THz frequency range. Especially whisker-contacted Schottky diodes have been the preferred nonlinear element at frequencies above 300 GHz. The main limitation of whiskered diodes is that there is no integration possible. Therefore, the development of competitive planar Schottky barrier diodes has been put forward in the last decade. The first planar device that has shown that the replacement of whisker-contacted devices is possible, is the surface channel diode [1]. Another approach that has been proposed three years ago is the quasi-vertical Schottky diode [2]. This paper describes the technology developments that made available mixer diodes using the quasi-vertical approach. First results of planar varactor diodes are shown.

Diode Design

The main idea of the quasi-vertical approach is to transfer the optimum geometry of the substrateless whiskered Schottky diode to a planar device. The main features are shown in fig. 1

The benefits of the substrateless Schottky diodes are:

- Minimum series resistance
- Little affected by the skin effect
- Excellent power handling capabilities

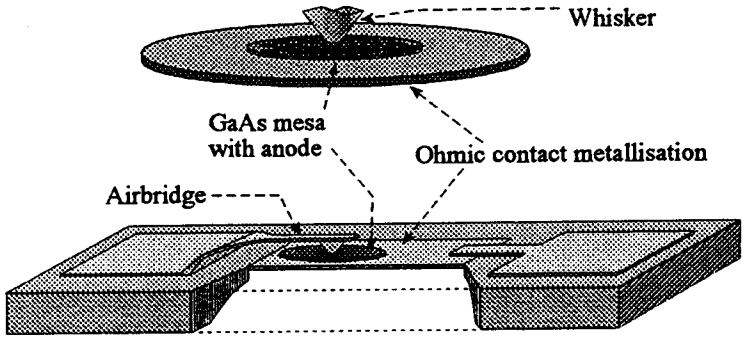

Fig. 1 **Structure of the substrateless whiskered Schottky diode and quasi-vertical planar Schottky diode**

These benefits are mainly caused by the reduction of the GaAs dimensions. Typical dimensions of whiskered diode chips have been drastically reduced. A reduction of the lateral dimension from 100-250 µm to 20-30 µm gives a reduction of the series resistance caused by the skin effect. The low thermal conductivity of GaAs leads to heating effects at high power levels. Therefore the reduction of the chip thickness from 70-80 µm to 2-3 µm leads to a significant improvement in the power handling capabilities. Additionally the contribution of the substrate to the series resistance is minimized. Fig. 2 gives a comparison of the series resistance of a substrateless diode and a planar surface channel diode for identical diode parameters [3,4].

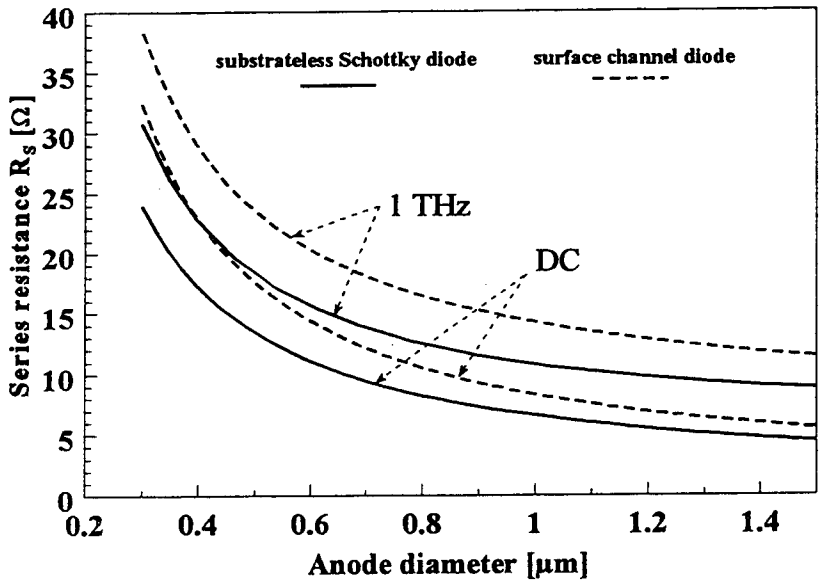

Fig. 2. Series resistance for different diode geometries

The difference in series resistance is about 20-30 %. The basic active region of the quasi vertical planar Schottky diodes is identical to the substrateless Schottky diode. Therefore, the above

remain the same as for whiskered diode chips where many experiences are available.

In the design of planar devices reducing stray capacitances that limit the performance is important. Mainly two contributions to the parasitic capacitance have to be considered. The main contribution regards to the contact pads that typically cause a parasitic capacitance of 10 fF on GaAs substrate for planar devices. With respect to an integration using a proper design, this contribution vanishes. Therefore, the main contribution that has to be reduced is the parasitic capacitance of the airbridge. Using a finite-difference technique, we have investigated the influence of the airbridge parameters on the parasitic capacitance. We could achieve the most effective reduction in fabricating a high airbridge that is at least two microns higher than the diode mesa. Even with an airbridge width of 4 microns the contributions do not exceed 2 fF.

Fabrication Technology

The main disadvantage of the quasi vertical planar Schottky diode was the lack of a suitable, mature fabrication technology. Especially technologies for a proper structurisation of small contacts from the backside of the wafer were not available. In addition existing airbridge technologies had to be modified with respect to small airbridge dimensions and airbridge height of at least four microns. Using a new two-stage spray etching technique, we have overcome the structurisation problem (fig. 3). Fig. 4 shows that we have established an airbridge technology according to the requirements.

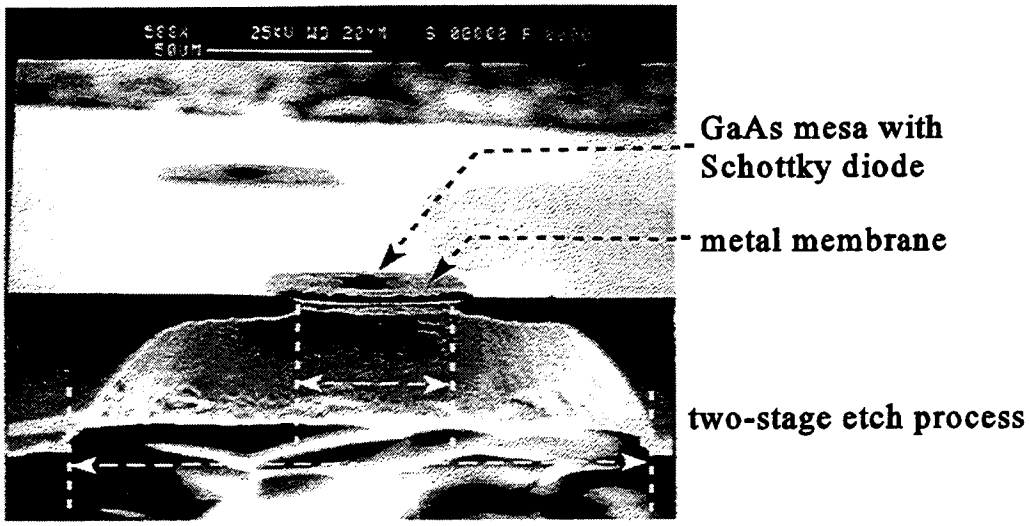

Fig. 3 Two-stage etching technique for contact structurisation

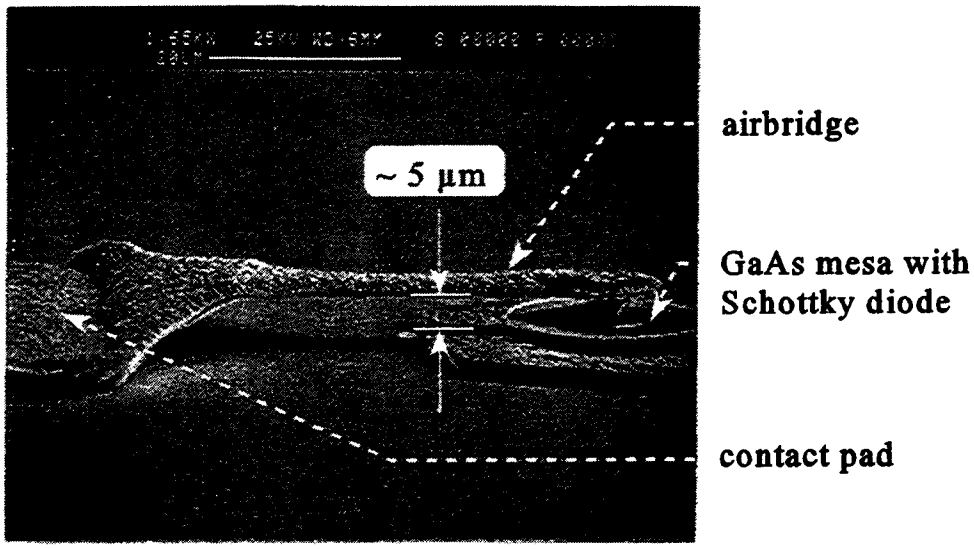

Fig. 4 SEM-picture of quasi vertical diode

Results

The characteristic parameters of different planar mixer diodes are given in the table below. There is no remarkable difference between these diodes and substrateless whisker diodes with the same diode parameters.

	DAP0308	DAP0312	DAP0320
n_{epi} [cm^{-3}]	$3 \cdot 10^{17}$	$3 \cdot 10^{17}$	$3 \cdot 10^{17}$
d_{epi} [nm]	70	100	100
d_a [µm]	8	12	2
R_S [Ω]	15-20	9.2	5
C_{jo} [fF]	1.1	2.2	5.8
η	1.13	1.1	1.08
V_{br} [V]	5-5.8	5-5.8	4.9-5.1
f_c [THz]	9	7.9	5.5

The parasitic capacitance of single devices is 9-10 fF. This is mainly due to the contribution of

The parasitic capacitance of single devices is 9-10 fF. This is mainly due to the contribution of the contact pads (>8fF). First varactors with a low series resistance, zero-bias junction capacitances in the range between 10fF and 20 fF and a capacitance variation of $C_{jo}/C_{min} > 2.4$ have been fabricated. Using substrateless whiskered diodes capacitance modulations of >3 are possible. This indicates that there is a further improvement possible.

Conclusion

The technology for quasi-vertical planar Schottky diodes has been established. Several improvements in the technology made available planar quasi-vertical mixer diodes with anode diameters of 0.8µm, 1.2 µm and 2 µm and corresponding cut-off frequencies up to 9 THz. The characteristics are comparable to whiskered diodes with the same diode parameters.

Acknowledgement

The authors would like to express their acknowledgements to Dr. H. Grothe and Dr J. Freyer, both from the Technical University of Munich, Germany, for supplying the high-quality epitaxial material.
The research described in this paper was partly sponsored by the european space agency, esa/estec, Noordwijk

References

[1] W. L. Bishop, K. Mckinney, R. L. Mattauch, T. W. Crowe und G. Green, "A novel whiskerless Schottky diode for millimeter and submillimeter wave applications ," *IEEE MTT-S Int. Microwave Symp. Dig.*, Juni 1987, pp 607-610

[2] A. Simon, A. Grüb, V. Krozer, K. Beilenhoff and H.L. Hartnagel, "Planar THz Schottky Diode Based on a Quasi-Vertical Diode Structure", *4th Int. Symp. on Space Terahertz Technology*, pp 392-403, 1993

[3] K. Bhaumik, B. Gelmont, R. J. Mattauch und M. Shur, " Series impedance of GaAs planar Schottky diodes operated to 500 GHz ," *IEEE Trans. Microwave Theory & Techniques*, Band 40, Nr. 5, (1992), pp 880-885

[4] J. R. Jones, " CAD of Millimeter Wave Frequency Multipliers: An Experimental and Theoretical Investigation of the Heterostructure Barrier Varactor ", Dissertation, University of Virginia, Januar 1996

ADVANCES IN SUBMILLIMETER WAVE SEMICONDUCTOR-BASED DEVICE DESIGNS AND PROCESSES AT JPL

R. Peter Smith, Suzanne C. Martin, Moonil Kim, Jean Bruston, Dexter Humphrey, Neal Erickson*, and Peter H. Siegel

California Instiute of Technology
Jet Propulsion Laboratory
4800 Oak Grove Drive,
Pasadena, CA 91109

*Five College Radio Astronomy Observatory
619 Lederle Graduate Research Center
University of Massachusetts, Amherst
Amherst Massachusetts, 01003

Abstract

Planar submillimeter wave circuits are slowly replacing whisker-contacted devices at frequencies above 100 GHz, but in many cases the size constraints dictated by the short wavelengths found at high frequencies have not been adequately addressed. In the last year we have been responding to the challenges of implementing submillimeter wave circuits in GaAs by using processing technologies somewhat new to this field as well as developing unique processing capabilities. This approach has allowed for greater flexibility in circuit design and the ability to fabricate circuits for frequencies up to 2.5 THz. Changes in our device processing include: (1) using either direct-write electron-beam or 5x projection lithography for all pattern definition, (2) doing mesa etching by RIE (reactive ion etching), and (3) incorporating an advanced planarization/air-bridge fabrication technique for submicron structures. Together, these process changes have enabled us to control process dimensions to sub-micron, or even deep sub-micron, levels. The circuits fabricated using these techniques include a number of waveguide and quasi-optical multipliers to be used at frequencies from 160 GHz to 640 GHz, and a quasi-optical mixer for 2.5 THz. While all of these circuits are made to be completely "planar" in the sense that there are no connections that lead away from the plane of the circuit, the relatively large amount of topography presents additional challenges when compared with the fabrication of HEMT-based MMICs used at lower frequencies.

Introduction:

Schottky-barrier diode circuits for submillimeter wave applications have improved significantly in the past several years, but in many ways the devices and circuits have not taken advantage of recently developed techniques used for microwave MMICs (Monolithic Microwave Integrated Circuits). In particular, practices developed for the design and fabrication of monolithic circuits should make it possible to economically produce better-performing devices with integrated matching and bias structures that can greatly simplify circuit assemblies, improving both the performance and ruggedness of the circuits.

Taking this approach, we fabricated a number of submillimeter wave circuits within the last year. These circuits include:

- A 320 to 640 GHz quasi-optic frequency doubler,
- A 160 to 320 GHz and a 320 to 640 GHz MMIC doubler, along with a 160 to 640 MMIC quadrupler,
- New designs of the 80 to 160 and 160 to 320 GHz planar varactor arrays previously fabricated and reported by the University of Virginia [1], and
- A 2.5 THz integrated mixer.

Performance of these circuits will only be mentioned briefly, as the purpose of this paper is to discuss particular processing techniques. These techniques have the potential to improve submillimeter wave circuit performance and to extend the use of planar circuits to even higher frequencies.

Device Improvement:

The approach used to improve device and circuit performance concentrated on developing fabrication techniques for circuits with up to 4 microns of topography that enable: (1) definition of small structures into the submicron regime, (2) tight dimensional control of circuit elements, and (3) tight layer-to-layer alignment tolerances. The resulting processes make possible a wider latitude of circuit designs, permitting the inclusion of more circuit elements and multiple devices, a reduction in device parasitics, and the possibility of higher frequency circuits designs.

In contrast with the wet etches and contact lithography typically used for submillimeter wave circuit fabrication, industry has moved to using dry etches and projection and electron-beam lithography for MMIC fabrication. Adoption, by industry, of these newer techniques was made partly for the economics of high throughput and high yield, but also for enabling the fabrication of structures with smaller dimensions and

tighter tolerances between layers - in other words, to make the "extrinsic" device as similar as possible to the "intrinsic" device.

A Schottky diode's frequency response is typically limited by the series resistance, R_s, and the junction capacitance. R_s can be reduced in a number of ways. Assuming the usual device structure shown in Figure 1, much of the series resistance is determined by the area of the anode and the thickness and doping level of the topmost epitaxial layer, all of which are dictated by the application. However, the parasitic components of R_s can be reduced [2] by increasing the length-to-width ratio of the anode, reducing the ohmic contact-to-anode spacing, and by increasing the thickness of the buried n+ layer (Table 1). The last of these techniques encounters diminishing returns due to the effect of skin-depth that occurs in high frequency circuits.

The overall device structure is necessarily larger than the intrinsic device, which gives rise to extrinsic capacitances, losses, and phase lags. By reducing various device dimensions, these extrinsic parameters can be reduced. Through the use of the newer lithography tools and by replacing wet etches with dry etches, we have greatly reduced mesa sizes in order to reduce these extrinsic parameters. These improvements will be pointed out in the specific circuit descriptions below.

Finally, for circuits operating at terahertz frequencies, device sizes and features need to be very small and dimensions well controlled. As part of the fabrication of anodes for fixed-tuned monolithic circuits, we developed a newer version of our T-anode e-beam lithography process [3] that introduces a temporary planarization layer after mesa etching. The new process enables us to take full advantage of the tighter mesa geometries that result from the use of stepper lithography and reactive-ion etching (RIE) of mesas while permitting us to make a 0.05 μm^2 device with a length-to-width ratio of 5 in order to reduce R_s as much as possible.

Circuit Fabrication:

Each of the circuits described in this article had a unique process flow. However, we will describe only the 320-to-640 GHz quasi-optic doubler in detail and then discuss differences in the fabrication processes used for the other circuits.

320-to-640 GHz quasi-optic doubler:
The process flow for the 320-to-640 GHz circuit is shown in Figure 2. SEM views of the circuit and the diode quad-bridge are shown in Figure 3. All layers in this process were defined by our I-line 5x projection aligner. The smallest dimensions were approximately 1 micron, and tolerances between layers before they would interfere were less than a micron in many cases. Since this circuit was our first to be processed on the projection

aligner, we were doing process development simultaneously with device fabrication. Details on the circuit design approach are listed in [4].

Fabrication starts with the definition of the ohmic contacts, which are recessed a few thousand angstroms to the buried n+ layer. For this step, a wet etch (consisting of a 1:1:38 solution of hydrogen peroxide:phosphoric acid:water) is preferable, as dry etches tend to damage the etched surface, leading to poorer contact characteristics. The etch is shallow enough that the silicon nitride etch mask is only undercut by a small fraction of a micron during this etch. A conventional Ni/Ge/Au/Ni/Ag/Au ohmic metalization is deposited by electron beam evaporation. The ohmic contacts are annealed in a rapid thermal annealer after the mesas have been defined and the silicon nitride mask has been removed.

Next, the mesas were patterned, then etched in an RIE system using a chlorine/boron-trichloride/argon mixture. Because the design of the circuit demanded that the diode quad-bridge be as compact as possible, the nominal mesa-to-mesa spacing is approximately 3 microns, but variations were included on the mask that ranged from 1 micron to 5 microns. All of the mesa separations showed reasonable dc characteristics, although lower breakdown voltages were observed in some cases for the one micron spacings. It isn't known whether the one micron inter-mesa distance is too small to suppress breakdown current with some substrates and processes or whether the photoresist did not fully clear out of the 1 micron gap and thus the subsequent etch did not fully isolate the mesa structures for those devices that exhibited low breakdown voltages.

The anodes and the bulk of the circuitry were metalized in the same processing step. The lithography for this step proved to be the most challenging part of the circuit fabrication. The basic approach used for the step is much like that used for many Schottky metalizations - a photoresist layer optimized for good metal lift-off is defined on top of a rounded, cross-linked, bridge-base photoresist layer. Problems included: (1) the 1 μm x 4 μm anodes are defined partly by the bridge base layer and partly by the metalization mask itself. Thus, the area of the anode is not only dependent on a single lithographic step, but also on an overlay accuracy. (2) The height differential between the tops of the mesas and the semi-insulating substrate is greater than the depth of field of the projection aligner. This problem required us to choose between double exposing the wafers using two separate masks or running two completely separate process steps. (3) The spiral matching circuits included two micron lines and spaces in patterns that would be considered to be very difficult to lift off even with much larger geometries. (4) The ground plane around the outside of the quad-bridge is located only one micron away from the mesas, where the photoresist is much thicker, necessitating a relatively high exposure time. Despite these issues, we obtained a reasonable yield.

The circuit was then passivated using a 1200 angstrom thick silicon nitride dielectric layer, deposited in a Plasmatherm PECVD reactor. Contact vias were opened in the nitride using a CF_4/O_2 etch. . After additional patterning, a final air-bridge metal was deposited to supply the top plate of the bias line capacitors and tie them to the neighboring ground planes. This metalization also forms the air-bridge structure seen in Figure 3(b), which is intended to suppress slot-line modes that may otherwise propagate along the coplanar waveguide. Finally, the wafers were lapped to a thickness of approximately 125 μm before being scribed into individual die.

The rf measurement results will be reported at a later date, but preliminary results show up to 1.4 mW output power from a quad bridge made of 1 μm x 4 μm diodes. The minimum loss was about 16 dB with 0.53 mW associated output power.

MMIC multipliers:
Details on the microstrip MMIC multipliers appear in [5]. The process was essentially similar but significantly simpler than the process for fabricating the quasi-optic doublers due to the lack of small structures off- mesa on the semi-insulating GaAs layer. In addition, overlay dimensions other than ohmic-to-Schottky were significantly larger.

However, wafer thinning is much more critical to microstrip performance, and the high frequencies of these circuits necessitate the thinnest wafers possible in order to suppress the propagation of undesired radiation through the substrate. Once the MMICs were through front-side processing, a sequence of lapping and polishing steps was used to thin the wafers. The difficulty of maintaining a reasonable yield for these relatively large circuits while thinning samples to tens of microns, required that we trade off some performance with final chip thickness. For this design, we chose a target thickness of 50 μm. We were able to deliver at least some circuits with thicknesses within a few microns of this target. Figure 4 shows an SEM of a typical device.

DC characteristics of these diodes were excellent. For example, a 1.2 x 7 micron diode that was predicted to have a minimum possible series resistance of 5 Ω (without considering the limited ohmic contact area) and a breakdown voltage of 7 V, was measured to have an R_s of 5.9 Ω and a breakdown voltage of 5.9 V.

Array multipliers:
The highest multiplier power outputs measured to date at about 160 GHz and 320 GHz were obtained using varactor diode arrays mounted in waveguides [1]. Unfortunately, current requirements demand significantly higher power outputs. It is believed that higher power could be obtained by simply increasing the number and anode area of the diodes in proportion such that the approximate active impedance of the devices stays the same - in this case, we increased the number of devices in each leg from two to three and increased the anode area by 1.5. For the new design the mesa areas of the devices are

much smaller in order to reduce parasitic, distributed capacitances. The devices are shifted towards the ground contacts, and the spacings between them are adjusted in order to reduce phasing problems. The nominal doping of the circuits is the same as previously reported [1] - approximately $1.2x10^{17}/cm^3$ for the topmost layer for 160 GHz circuits, and approximately approximately $2.5x10^{17}/cm^3$ for the topmost layer for 320 GHz circuits. The buried n+ layer is significantly thinner than previously reported - 1 micron for the rf results reported below, and 2 microns for the latest devices.

SEM photographs of the overall circuits and a device are shown in Figure 5. The fabrication process was exactly as described for the MMIC multipliers except that the last metalization layer included a nickel barrier layer to permit soldering, and that a selective $Cl/BCl_3/SF_6$ etch was used for the mesa etch for the most recent lot. DC parameters from the latest run, taken before thinning, are shown in Table 2. The best rf data from the first run of devices indicated a record power output of 76 mW at 160 GHz with an efficiency of 22% for devices with anode sizes of 3 μm x 7 μm x 2 fingers despite much higher-than-anticipated capacitances and the thin n+ layer.

2.5 THz mixers:

Mixer devices monolithically integrated with slot antennas, IF filters, and IF coplanar waveguide lines were fabricated on GaAs [6] with a topmost layer doped to $1x10^{18}/cm^3$ and a 1 micron buried n+ layer. The extremely small sizes and overlay tolerances along with the short turnaround time led us to use our JEOL electron beam lithography system for several of the layers instead of the optical projection aligner.

Other than using the different lithography tools, most of the process was much as described above with the exception of the anode process. We had previously reported a new e-beam anode process that could be used with wet-etched mesas defined after the anode layer [3]. For the current layouts, the mesa sizes and separations were so small that they had to be defined by dry etching prior to anode formation.

In order to fabricate air-bridged T-anodes [3] on top of the already-defined mesas, it was necessary to temporarily fill in the gap between the mesas. This was done by spinning PMMA to a thickness of 4 microns, and then iteratively flood exposing the sample with deep-UV and developing the PMMA until the tops of the mesas were just clear of the PMMA. The usual tri-layer PMMA/copolymer/PMMA resist structure can then be processed on top of the planar PMMA layer as previously reported.

In addition, it is possible to make connections off-mesa by grading the e-beam exposure of the thick, planarizing PMMA layer. We were unable to optimize this process in the short time that we had available, but working devices were obtained by exposing and developing the T-anodes and off-mesa interconnect metal in one lithography step.

Finished devices (Fig. 6) had anode areas of 0.1 x 0.5 μm^2 and 0.1 x 1 μm^2. The lowest measured R_s value was about 30 Ω. Modeling leads us to believe that much of this resistance may be due to the very small ohmic pads necessitated by the compact coplanar environment of the devices.

Conclusions:

We have reported on a number of monolithic integrated circuits fabricated within the last year for submillimeter wave applications. It is clear that overall device sizes and geometries must be more compact and more accurate than for lower frequency circuits. By using better forms of lithography and other processes that allow us to reduce device sizes and overlay tolerances, and by optimizing the device geometries in order to take advantage of these device improvements, we have shown that monolithic circuits can be made with reproducible and predictable devices with state-of-the-art performance.

Acknowledgements:

The research described in this paper was performed by the Center for Space Microelectronic Technology, Jet Propulsion Laboratory, California Institute of Technology, and was sponsored by the National Aeronautics and Space Administration, Office of Space Science and Office of Earth Science.

[1] P.J. Koh, W.C.B. Peatman, T.W. Crowe, and N.R. Erickson, "Novel planar varactor diodes," Proceedings of the Seventh International Symposium on Space Terahertz Technology, Charlottesville, Va., 1996, p. 143-156. Also N.B. Erickson, B.J. Rizzi, and T.W. Crowe, "A high power doubler for 174 GHz using a planar diode array," 4th International Symposium on Space Terahertz Technology. Also personal communication from I. Mehdi and S.C. Martin, 1996.

[2] S.I. Long and S.E. Butner, Gallium Arsenide Digital Integrated Circuit Design, p. 126, McGraw Hill, New York, 1990.

[3] R. E. Muller, S. C. Martin, R. P. Smith, S. A. Allen, M. Reddy, U. Bhattacharya, and M. J. W. Rodwell, " Electron beam lithography for the fabrication of air-bridged, sub-micron Schottky collectors," J. Vac. Sci. Technol. B vol. 12, no. 6, p. 3668, 1994. Also M. Reddy, M. J. Mondry, M. J. W. Rodwell, S. C. Martin, R. E. Muller, and R. P. Smith, D. H. Chow, J. N. Schulman, "Fabrication and dc, microwave characteristics of submicron Schottky-collector AlAs/$In_{0.53}Ga_{0.47}As$/InP Resonant Tunneling Diodes," Appl. Phys. Lett., vol. 77, no. 9, p. 4819, 1995.

[4] M. Kim, J. Bruston, R.P. Smith, S.C. Martin, P.H. Siegel, "A slot-antenna bridge-frequency multiplier design suitable for submillimeter wavelengths," Proceedings of the IEEE Antennas and Propogation Symposium, 1996, pp. 1258-1261.

[5] Jean Bruston, R. Peter Smith, Suzanne C. Martin, Andrew Pease, Moonil Kim and Peter H. Siegel, "Fixed-tuned submillimeter waveguide multipliers using MMIC technology," Proceedings of the 8th International Symposium on Space Terahertz Technology, Cambridge, Massachussetts, March 1997.

[6] P.H. Siegel, "An open-structure mixer using an all-GaAs integrated diode/antenna wafer for millimeter and submillimeter wavelengths," JPL New Technology Report NP0-19371/8972, January, 1994.

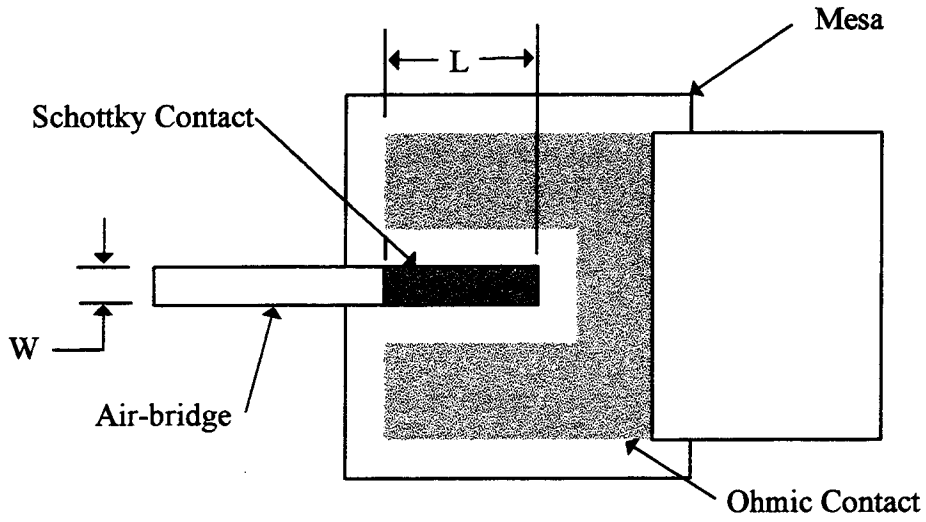

Figure 1. Basic geometry for the mesa area of a Schottky diode.

Buried layer thickness	R_s
0.5 μm	4.3 Ω
1.0 μm	3.2 Ω
2.0 μm	2.6 Ω
4.0 μm	2.3 Ω

1.a.

Length	Width	R_s
2.0 μm	4.0 μm	3.1 Ω
4.0 μm	2.0 μm	2.6 Ω
8.0 μm	1.0 μm	2.3 Ω
16.0 μm	0.5 μm	2.0 Ω

1.b.

Tables 1.a. and b. Calculated [2] series resistance of a Schottky diode as a function of (a) buried layer thickness and (b) length and width with eight μm^2 anode areas. For both tables, the top layer doping is 2.6×10^{17} /cm^3 with a thickness of 210 nm, the buried layer is doped to a level of 5×10^{18} /cm^3, there is a 1.5 μm anode-to-ohmic contact spacing, and the contact resistivity is 10^{-7} cm^2. For table 1.a., L=4 μm and W=2 μm. For table 1.b., the buried layer thickness is 2 μm.

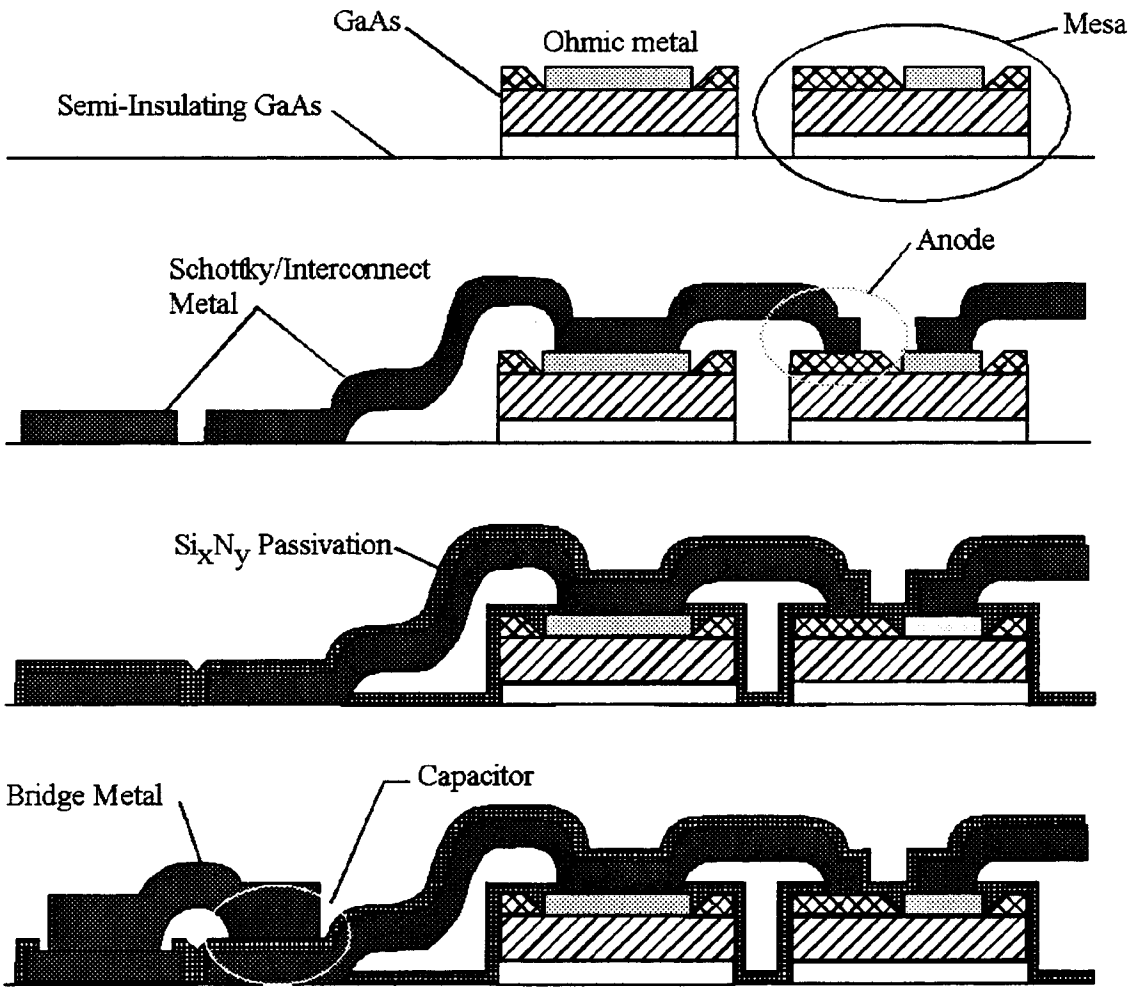

Figure 2: Process flow for quasi-optic, 640 GHz doublers.

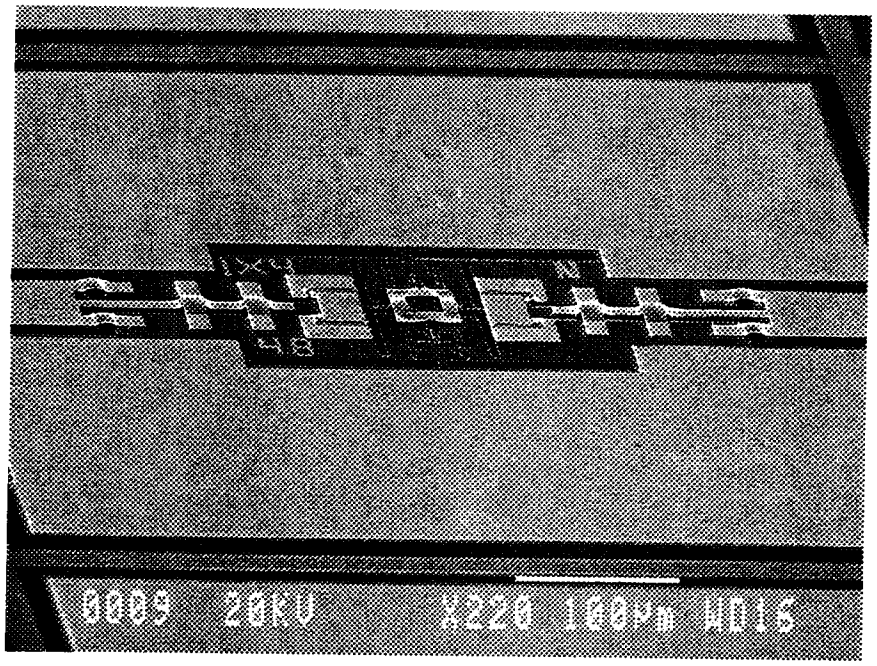

(a)

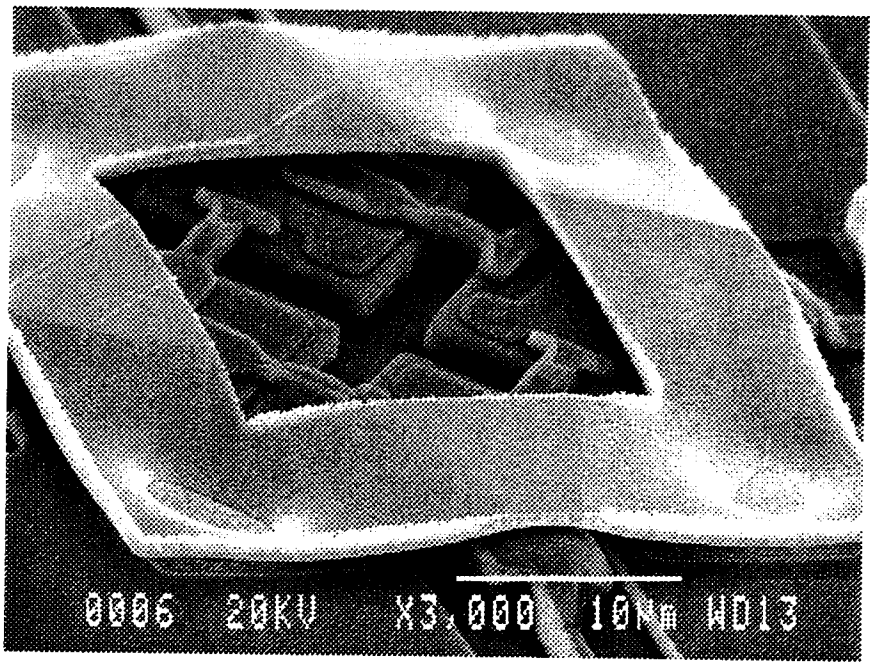

(b)

Figure 3: SEM photographs of the quasi-optic doublers. In (a), the diode bridge can be seen between the faint horizontal input slot antennas and the vertical output slot antennas. The bias lines extend to the right and left sides of the picture. Fig. 3.b. shows a close up of the four diodes. The large air-bridge structure across the top of the bridge is meant to suppress slot modes by tying together the ground planes.

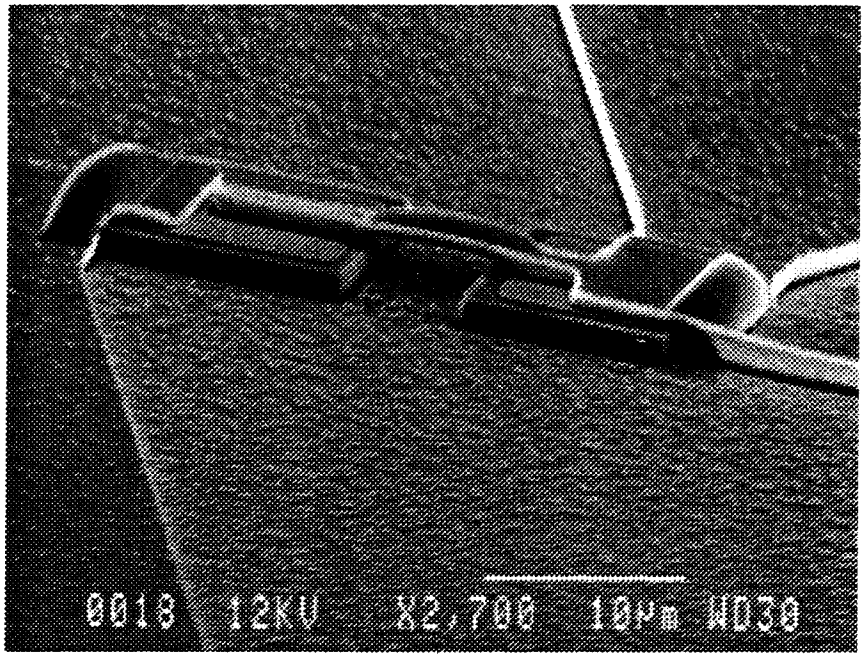

Figure 4. SEM photograph of a diode from one of the microstrip multipliers. The anode is on the left-hand mesa. Radia stubs extend to the upper right and lower left corners of the photograph.

Wafer 0.031XT: $N_d \sim 1.2 \times 10^{17}/cm^3$

Size (µm x µm)	Is (fA)	Ideality factor	Rs (Ω)
3 x 7 x 2	37 fA	1.13	2.96
3 x 7 x 2	44	1.14	2.82
1.5 x 14 x 2	54	1.15	2.56
1.5 x 14 x 2	70	1.15	2.53
1.7 x 4 x 2	27	1.18	4.32
3 x 8.4 x 2	51	1.13	3.1
3 x 8.4 x 2	53	1.13	3.0

0.019 SU $N_d \sim 2 \times 10^{17}/cm^3$

Size (µm x µm x n)	Is (fA)	Ideality factor	Rs (Ω)
1.7 x 4 x 2	42	1.16	3.67
1.5 x 3 x 2	32	1.17	4.42
1.5 x 14 x 2	75	1.14	2.57

Table 2. DC parameters of devices from recent wafers with varactor diodes as shown in figure 5. The sizes [illegible] device. The series resista[illegible]ce of approximately 0.7 Ω.

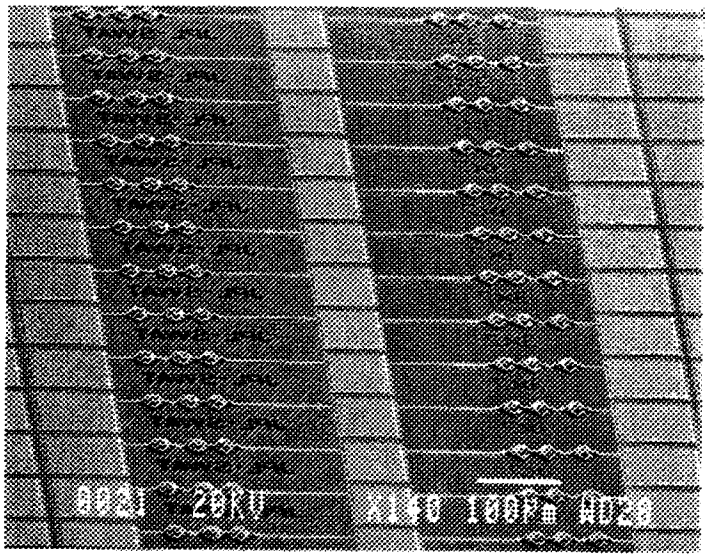

(a)

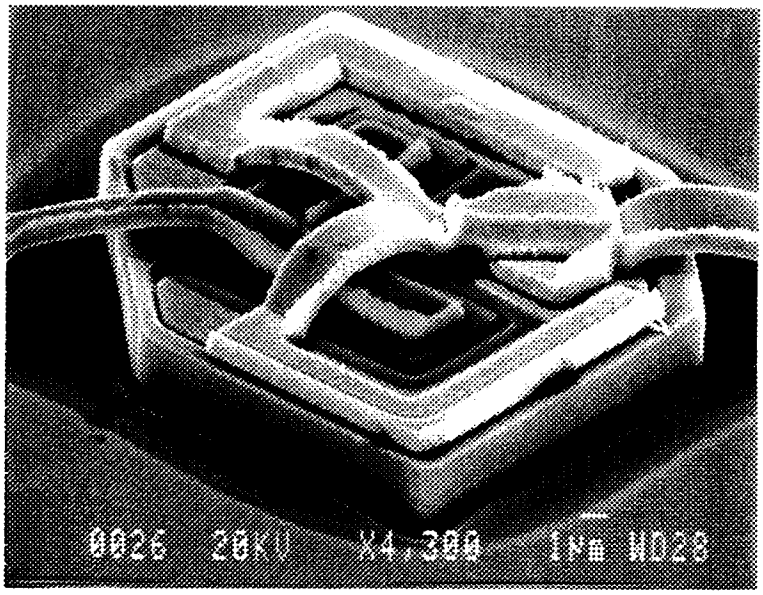

(b)

Figure 5: SEM photographs of (a) 6-element arrays and (b) a single diode. In (b), the bridge to the anodes comes from the left side of the photograph. The active device area is formed by two 3 x 7 μm^2 rectangular anodes.

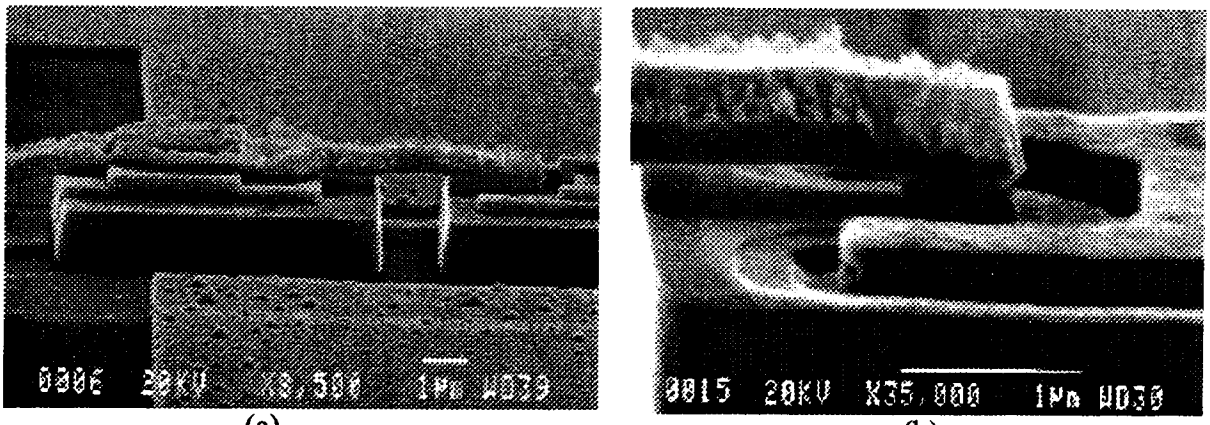

(a) (b)

Figure 6: Close-up views of 0.1 x 0.5 μm^2 diodes in coplanar waveguide/slot antenna structures for 2.5 THz detection. The active mesa area is approximately 4.5 x 5 μm^2.

FIXED-TUNED SUBMILLIMETER WAVEGUIDE MULTIPLIERS USING MMIC TECHNOLOGY

Jean Bruston, R. Peter Smith, Suzanne C. Martin, Andrew Pease, Moonil Kim
and Peter H. Siegel

California Instiute of Technology
Jet Propulsion Laboratory
4800 Oak Grove Drive,
Pasadena, Ca 91109-8099

ABSTRACT

We have developed tools and fabrication processes which led to the design and fabrication of a MMIC waveguide doubler to 320 GHz and a MMIC waveguide quadrupler to 640 GHz. This includes extensive diode modeling and analysis and optimization [1], design and fabrication of input and output ridge-waveguide-to-microstrip transitions, to provide the fixed tuned input and output ports, and the design and fabrication of the MMIC multiplier chips containing the active devices and all matching elements and bias circuitry [2].

To date, measurements have yielded 10 μW at 640 GHz and 420 μW (2.7% efficiency) at 320 GHz, with 15 mW of pump power at 160 GHz. We believe these are the first working waveguide MMIC multipliers above 200 GHz. The waveguide block concept used for these multipliers is very efficient for mounting/dismounting devices, allowing rapid and repeatable measurements of different chips.

However, these measurement results are much poorer than expected from our original analysis, and we have taken a more detailed look to explain the discrepancy. After including the diode physical structure and radiation loss in the circuit models, we have been able to obtain excellent agreement between our measured performance and that predicted from our finite element analysis. With this improved circuit model in hand we have designed a new MMIC doubler which is expected to perform significantly better than the original chip. Due to the limitations of microstrip (substrate thickness) above 300 GHz, we have begun a CPW design with the more accurate device model as well.

INTRODUCTION

There are now a significant number of space applications in the Earth remote sensing, planetary and astrophysics areas which require solid state local oscillator sources in the 300 to 1000 GHz range. Although some new approaches look very promising in the long term (photomixers, fundamental or harmonic oscillators...), solid state harmonic multipliers based on varactor diodes still offer the best performance in the near term. For many years, the most common implementation has been the discrete Schottky barrier honeycomb diode mounted in a waveguide block and contacted via a fine whisker wire [3]. More recently, the whisker contacted

diode has been replaced by the planar discrete diode, used in a similar mount configuration [4]. Both of these approaches have led to very good results, and whisker contacted diodes are still the only way to reach the higher submillimeter wave frequencies. A recent planar diode result (an array of six varactor diodes on a single planar chip) has yielded amazing output power in the 100 to 300 GHz frequency range (76 mW at 160 GHz, and 8 mW at 320 GHz [5]). However, all of these discrete diode approaches have limited circuit flexibility, are complicated to analyze and difficult to assemble. Also, the output power available above 400 GHz is low in the case of the whisker diode, and non existent in the case of the discrete planar device.

Because we need high efficiency, high output power, reliable wide-band multipliers up to 1 THz, we have proposed a new approach, which pushes further the integration of the multiplier device and surrounding circuitry, moving toward a true GaAs MMIC implementation. The MMIC's we are now fabricating at 300 and 600 GHz are composed of GaAs chips containing the active device(s), all matching and bias circuitry and transitions to a new waveguide block configuration, in which the chip is coupled to inline input and output waveguides by means of micromachined E-plane ridges [6,2].

We believe that a benefit of this approach is that it provides a very flexible, potentially wide band structure, in which one can easily accommodate many different chip designs and devices. Like MMIC's at lower frequencies, we have found that a very thorough analysis of the entire structure is required to accurately predict the performance.

DESIGN AND FABRICATION

The basic concept used for all the multiplier designs presented here is shown in Figure 1. Thin metallic ridge transitions, similar to those employed by [6], are used to convert the input and output signals from fundamental waveguide to a microstrip mode. All other RF functions - frequency multiplication, matching and filtering - are then performed on chip. No tuning capability, other than adjustment of the bias voltage, is present. The chip is held in place under the ridge transitions with a spring loaded mechanical micrometer drive assembly and no soldering is required. Wire bonds are used to couple bias into the chip through channels perpendicular to the input and output waveguide (not shown in the Figure).

Because of their proven performance in this frequency range, we have implemented the multiplier circuits with planar Schottky barrier diodes. Our designs are based on the derived equivalent circuit of the strip or T-gate rectangular diode [1]. The rectangular anode devices have lower than average series resistance compared to traditional planar varactors, making them ideal candidates for higher frequency circuits. We implemented a Schottky barrier diode model, including saturation effect [7], appropriate for the rectangular anode geometry, in an harmonic balance program. The electrical parameters of the diode are described as a function of the epilayer doping, Nd and the anode length and width, L and W. Using the diode model, we optimized the physical parameters of the diode, i.e. doping profile and anode geometry, for specific input power and frequency, and determined the optimum embedding impedances for each harmonic [1].

The diodes are matched to the waveguide input/output ports at the fundamental and harmonic frequencies through traditional microstrip elements - stubs and high/low impedance filters. Bias is coupled in through bypass capacitors formed on-chip. The matching circuit must provide both filtering and impedance matching from the real impedance of the ridge transitions to the complex impedance of the diode, at the input, output, idler and higher harmonic frequencies. Figure 2 shows a picture of the 320 GHz doubler chip. Since the diode is in series in the circuit, it must be shorted at the input frequency on the output side (right of the diode). A quarter wavelength open radial stub provides this short. Similarly, another stub shorts the diode at the output frequency on the input side (left of the diode). A high-low impedance matching circuit converts the 30 Ohm real impedance of the ridge to the optimized complex diode impedances at 160 GHz. Similarly on the output side, another high-low impedance circuit matches the diode impedance at 320 GHz to the final 50 Ohm microstrip line which couples to the output waveguide ridge. As we are working at high frequencies (320 and 640 GHz), the substrate must be mechanically as thin as possible. The circuits have been designed for a 50 μm thick GaAs substrate, the thinnest substrate we felt could be reasonably handled. The nominal diode size for which we designed our circuit is 10x1.3 μm^2. Variations of 1.2x7 and 1.3x12were also included on the mask set.

Details of the MMIC fabrication process can be found in [5]. The recessed and alloyed ohmic contacts were formed (bottom to top) of Ni/Ge/Au/Ni/Ag/Au. Mesas were reactive-ion etched using chlorine and boron trichloride. The air-bridge Schottky contacts were made of evaporated Ti/Pt/Au. 1500 angstroms of silicon nitride passivation/dielectric was deposited over the top in a plasma-enhanced chemical vapor deposition system. A subsequent nitride etch and air-bridge metal step formed the necessary isolation for bias, input, and output connections. Before scribing, the wafer was mechanically lapped to 50 μm. DC characterization of the chips shows very good yield. The I(V) and C(V) characteristics are as expected, and Rs is as good if not better than that predicted with our device model.

The ridge transition works like a Chebychev step transformer that matches the impedance difference between the waveguide mode (~500 Ohm) and the microstrip mode (50 Ohm). The ridges are fabricated from BeCu using a double sided photoetch technique. The 160 GHz ridge is formed from .003" BeCu and the 320 and 640 GHz ridges from .0015" sheet. The sheets, containing many ridges, are etched in ferric chloride and then gold plated. We obtained an overall accuracy of 2-7 μm for the final dimensions. After separation from the "spider mount" (Figure 3) the individual ridges can be readily handled and are soldered permanently into position in the split-block waveguide mount.

The multiplier mount which contains the ridge transitions and multiplier chip is formed in three parts, two of which are used to permanently fix the ridges in place at the center of the waveguide. A separate top piece protects the chip and, when removed, allows access for positioning and wire bonding the bias line during assembly. The waveguides and transitions are formed in the split block (Figure 4), but once the ridges have been positioned and soldered in place the two halves are permanently mated. Insertion of the GaAs chip is made possible by a spring loaded moving post controlled by a micrometer with a simple cam mechanism. During contacting, the chip is placed in position in a recess under the two ridges and moved upwards

into final position where it is pressed lightly against the ridges on both sides (Figure 5). Once contact is made, the micrometer is locked and no further adjustments are required.

Measurements of the transmission properties of the ridge and the block were performed in a test mount at 180 GHz. A block similar to that described above has been fabricated, with identical input and output waveguides to allow a back to back ridge measurement with a straight 50 Ohm transmission line in-between. The measured transmission through the two transitions and the wafer with the 50 ohm line are shown in Figure 6. When the measured waveguide loss of 0.5 dB and calculated substrate loss of 1 dB are subtracted, the ridge transitions show an insertion loss of better than 0.75 dB each over 40% bandwidth.

MEASUREMENTS

Assembly of the block starts with permanent fixing of the two ridges. The ridges are first positioned and then epoxied in cavities provided on one half of the split waveguide block, such that they fall in the center of the E-field plane of the waveguide (Figure 4). They are then soldered to the block to provide a DC path to the chip. As will be seen later, positioning the ridges is critical. Several contacts and actual RF measurements are necessary to verify that the ridges are in their optimum position. Rotation and height are easily controlled by positioning the ridges against a chip placed in the waveguide. The longitudinal position of the ridge along the waveguide axis is more difficult to set, and requires precise measurement of the dimensions. Once the ridges have been fixed in place, the two block halves can be permanently mated, and no further adjustments are needed. For making measurements on actual MMIC chips, the chip is placed on top of the moving post, which is then driven up until the ridges come in contact with the microstrip lines (Figure 5). Mounting and dismounting a chip takes only a few minutes.

Since there is no tuning besides DC bias, RF measurements are very simple to perform. A BWO tube providing around 15 mW output power in the 145 to 175 GHz band is used as a source. This is followed by a variable attenuator and then the multiplier block. At 320 GHz, a 140-220 GHz Anritsu power meter (used out of band) is used to detect the signal. At 640 GHz, the output is radiated through a feed horn machined into the split block, and a planar diode Schottky detector [8] is used to initially detect the signal and determine optimum bias and frequency response. In both cases, a Thomas Keating acousto-optic bolometer was used to calibrate the detected power. For return loss measurements, a directional coupler can be inserted between the attenuator and the input waveguide of the multiplier block.

Using the set up described, we measured a maximum output power of 420 μW at 320 GHz, corresponding to an efficiency of 2.7%. At 640 GHz, we are near the sensitivity limit of the Keating power meter and measure approximately 10 μW.

Measurements over a range of chips with the same anode area gave similar output power (300-420 mW) at 320 GHz. We also observed that the DC current detected in the diode conforms to what is expected from analysis with a reverse bias of 2 V, the detected current was 100 μA, showing that there is good input power coupling. The effect of diode biasing follows

the expected trend for high quality varactors, with optimum power conversion at a reverse bias which is about half the breakdown voltage.

When the ridge transitions are not optimally aligned, we still measure repeatable performance among chips of a particular diode size, but output power and input coupling efficiency are both degraded (maximum output power around 100 μW, very low detected current), and the frequency for maximum output power is shifted.

The best performance was obtained with the smallest diode size (1.2x7 μm^2). The nominal anode gave poorer input coupling, and almost no output power (maximum around 100 μW).

The strong effect of the ridge position on the chip performance is consistent with the behavior of the Chebyschev transformer when the last section is varied in electrical length. If the ridges are mounted slightly off in longitudinal position, the transformation provided by the last ridge step and microstrip line is directly affected. Future ridges will mitigate this effect by using tapered transitions.

PERFORMANCE ANALYSIS

Since the diodes appeared to be behaving properly, we suspected that the poor multiplier performance was due to neglected properties of the circuit itself. For expediency during the initial design of the MMIC, some effects were knowingly neglected, such as the diode mesa and air bridge geometry, microstrip radiation effects, and tolerances of the ridge transitions. In order to check the accuracy of our measurements and to understand the reason for our poorer than expected performance, we conducted a more careful analysis of the complete 320 GHz doubler using a combination of finite element and harmonic balance analysis, in which we included the diode mesa/air bridge and radiation effects. The approach consisted in describing each individual circuit element in Ansoft's Maxwell Eminence, deriving the S parameters, integrating together all the pieces, and finally applying harmonic balance techniques to derive the full circuit performance (including ridges).

An example of the individual structure analysis is shown Figure 7, where the air bridge and mesa's have been accurately modeled (a photo is shown as Figure 8). In our original design the effect of the diode mesas and air bridge were modeled as simple transmission lines. The finite element structure includes two microstrip ports and a diode port defined using a "coaxial probe", where the Schottky contact lies. The S parameters of that structure are then imported to a circuit simulator, and the diode embedding impedances are compared with those of the diode only, and those of the diode with the transmission line equivalent circuit. It can be seen in Figure 9, that the effect of the mesa/air bridge combination is quite large, especially at 320 GHz, where the embedding impedance becomes inductive when in fact it was designed to be capacitive. Although the effect is due to the overall structure, and therefore difficult to describe by means of a simple equivalent circuit, it is understandable that its effect is significant, considering that the

overall structure length is of the same order as the quarter wavelength radial stub shown in Figure 8.

Similarly, we have computed the S parameters of the output microstrip circuit associated with the output ridge (Figure 10). In our original analysis, only conductive and dielectric losses were taken into account. The finite element analysis adds radiative loss. Figure 11 shows the comparison of the two cases and the significance of the radiative loss. A closer examination shows that most of the radiation occurs at 320 GHz in the two radial stubs.

Finally, we have integrated all these elements together with our diode model in an harmonic balance circuit simulator (MDS), and compared the computed performance of the MMIC with measurements at 320 GHz. Figure 12 shows the result, a pretty good match. The same analysis also shows good agreement between measurements and computed performance for the other diode sizes we have fabricated. A separate analysis in which we have shifted the ridges longitudinally also confirms the trends observed during measurements, i.e. shifted maximum output power frequency and a degraded power level. These results make us confident that our multiplier is in fact working as designed - although not up to expectations! However, with the more accurate analytic description in hand, we can now redesign the circuit to realize its full performance potential.

CONCLUSION

We have demonstrated full MMIC multipliers with output power at frequencies as high as 640 GHz. The first iteration of our 320 GHz doubler design has demonstrated that this approach has the potential to realize reasonable performance, and an efficiency of 2.7% has already been obtained. The current performance, especially at 640 GHz, is much poorer than what we were expecting, but a more accurate analysis of the physical structure gives good agreement with measurements and has allowed us to understand where the deficiencies of our design lie. Analysis indicates that these problems can be easily fixed, and a second iteration is already in progress and should provide greatly improved performance at 320 GHz (Figures 13 and 14).

The design, measurements and analysis described in this paper also helped us to identify some inherent problems with the present circuit realization, especially above 320 GHz. We have found that the microstrip ridge and its step transformer design introduce too tight a tolerance for simple mounting in the block. Also, at higher frequencies, the problem of radiation in the thick GaAs substrate is disastrous. A solution to both of these problems consists in the use of coplanar transmission line (CPW), and tapered ridges for the transitions. Such a design is now under way.

ACKNOWLEDGMENTS

This work was sponsored by the JPL Center for Space Microelectronics Technology, NASA Office of Space Access and Technology. The authors would like to thank Pete Bruneau for fabricating the waveguide blocks.

REFERENCES

[1] Jean Bruston, R. Peter Smith, Imran Mehdi and Peter H. Siegel, "Analysis and Optimization of Planar Rectangular T-anode Schottky Barrier Diodes for Submillimeter-wave Multipliers", *26th European Microwave Conference, September 1996.*

[2] J. Bruston, M. Kim, S.C. Martin, I. Mehdi, R.P. Smith and P.H. Siegel, "Design and Analysis of Broad-Band Fixed-Tuned Submillimeter-Waveguide Multipliers using MMIC Style Circuit Topology," *Seventh International Symposium on Space Terahertz Technology, March 12-14, 1996.*

[3] R. Zimmermann, T. Rose and T. Crowe, "An All Solid State 1 THz Radiometer for Space Applications," *Sixth International Symposium on Space Terahertz Technology, March 21-23, 1995.*

[4] N.R. Erickson, J. Tuovinen, B.J. Rizzi, T.W. Crowe, "A Balanced Doubler Using a Planar Diode Array for 270 GHz," *Fifth International Symposium on Space Terahertz Technology, March 21-23, 1995.*

[5] R.P. Smith, S.C. Martin, M. Kim, J. Bruston, D. Humphrey , P.H. Siegel, "Advances in Submillimeter Semiconductor-based Device Designs and Processes," *Eighth International Symposium on Space Terahertz Technology, March 25-27, 1997.*

[6] D. Winkler, A.H. Worsham, N.G. Ugras, D.E. Prober, N.R. Erickson and P.F. Goldsmith: " A 75-110 GHz SIS mixer with integrated tuning and coupled gain," *Nonlinear Superconductive Electronics and Josephson Devices, Plenum Press, NY.1991, pp.73-79.*

[7] E.L. Kollberg, T.J. Tolmunen, M.A. Frerking and J.R. East: "Current saturation in submillimeter wave varactors," *IEEE Transaction on Microwave Theory and Techniques, vol.40, no.5, May 1992, pp.831-838.*

[8] P.H. Siegel and I. Mehdi, "The Spare-Diode Detector: A New Planar-Diode Detector Circuit with State-of-the-Art Performance for Millimeter and Submillimeter Wavelengths," *JPL New Technology Report, December 1996, 8 pages.*

FIGURES

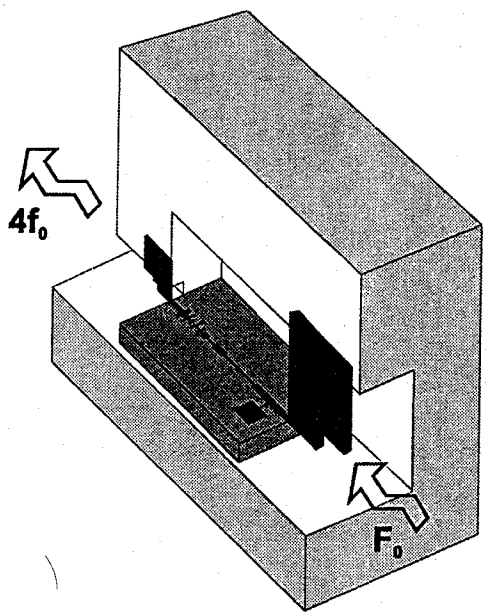

Figure 1 - Conceptual drawing of a MMIC multiplier in its ridge/waveguide block.

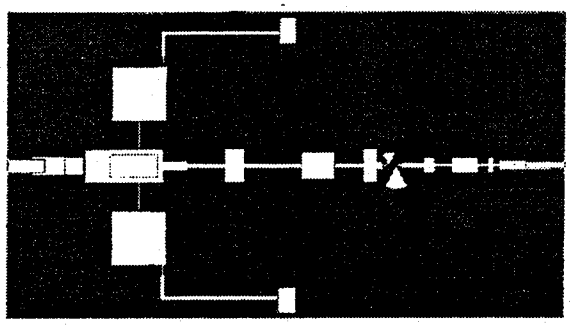

Figure 2 - Picture of the 320 GHz MMIC doubler chip.

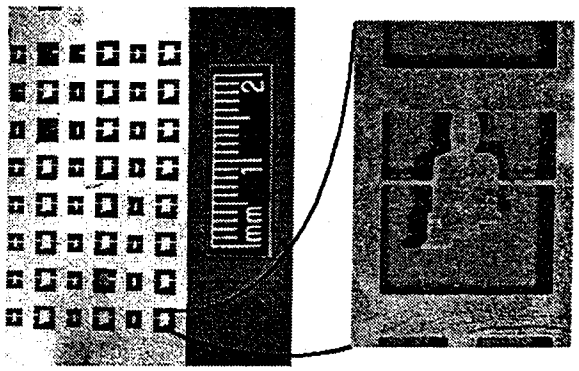

Figure 3 - Picture of the photoetched BeCu ridge sheet and close up of one ridge.

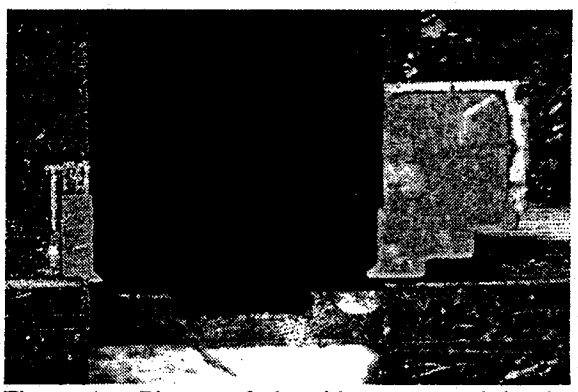

Figure 4 - Picture of the ridges mounted in the waveguide block (here a 160 GHz ridge and a 640 GHz ridge in the quadrupler block).

Figure 6 - A MMIC multiplier chip mounted in its ridge waveguide block. One can barely distinguish the ridge tips on the left and right of the chip, contacting the microstrip lines.

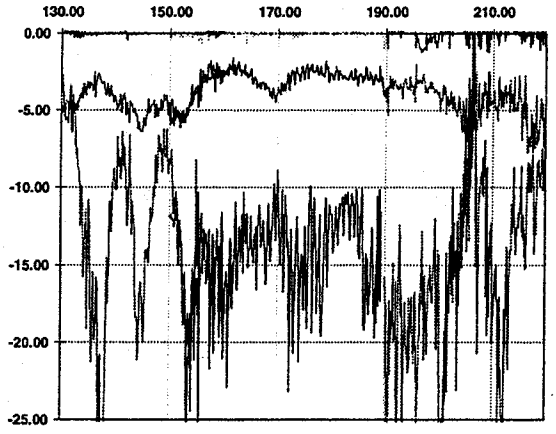

Figure 5 - S21 and S11 of a back-to-back ridge transition (two ridges and a 50 Ohm through line), ridge designed for 180 GHz.

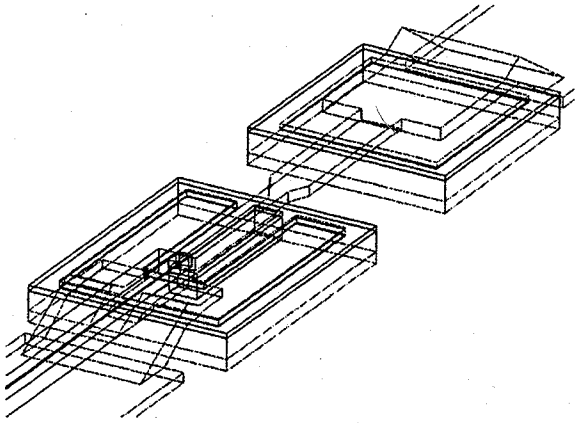

Figure 7 - Geometry of the diode mesas and air bridge as described in the finite element analysis.

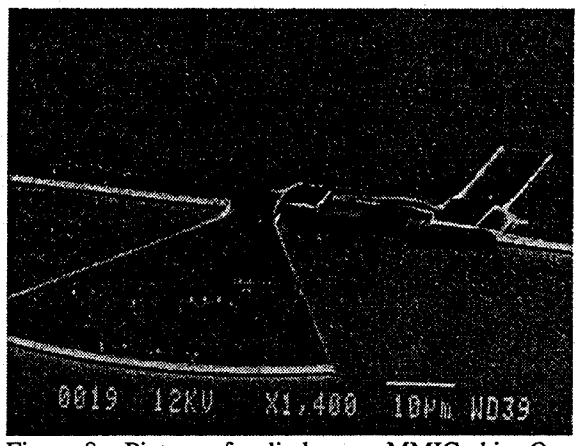

Figure 8 - Picture of a diode on a MMIC chip. One can see the mesas, air bridges, a 320 GHz quarter wavelength radial stub, and a 640 GHz quarter wavelength stub.

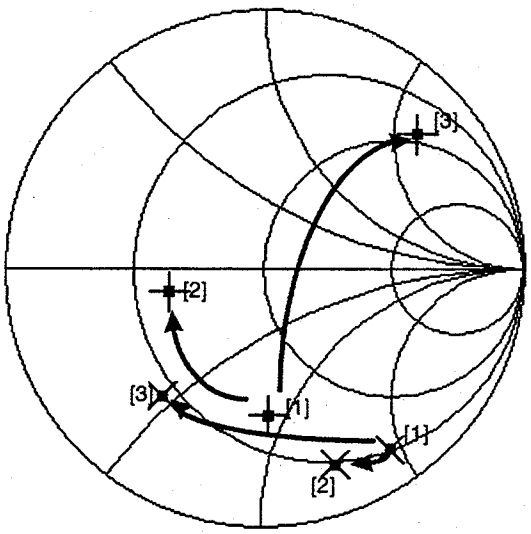

Figure 9 - Embedding impedances at 160 GHz (X) and 320 GHz (+), for the diode alone [1], for the diode with transmission line equivalent circuit of the mesas/air bridge [2], and with the finite element analysis of the mesas/air bridges [3].

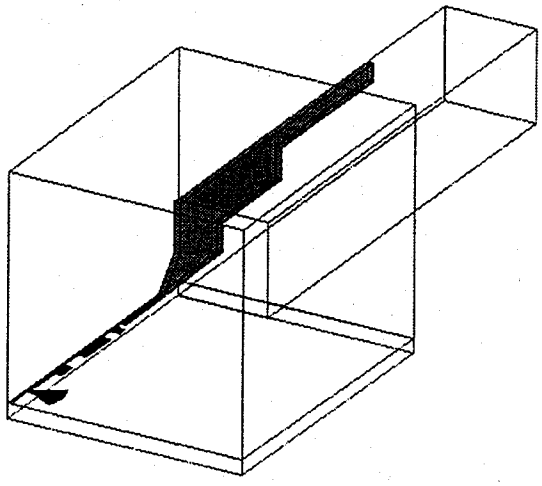

Figure 10 - Geometry of the output microstrip circuit and output ridge of the 320 GHz MMIC doubler, as described in the finite element analysis.

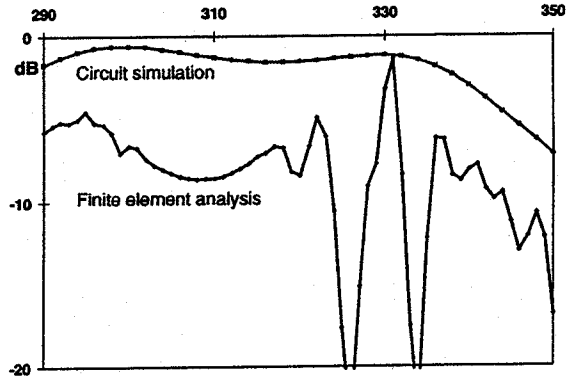

Figure 11 - Comparison of the performance of the output circuit of the 320 GHz MMIC doubler, analysed with a circuit simulator and with finite element.

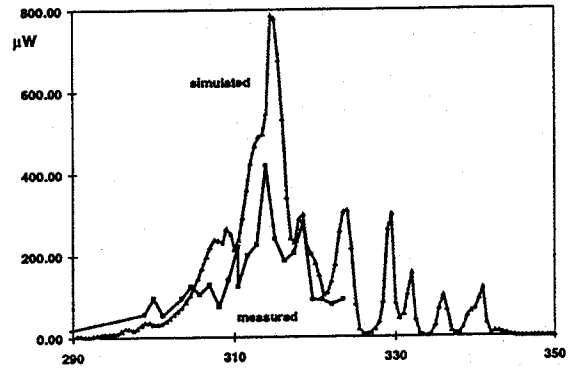

Figure 12 - Comparison of the measured and computed performance of the 320 GHz MMIC doubler using finite element analysis for each component.

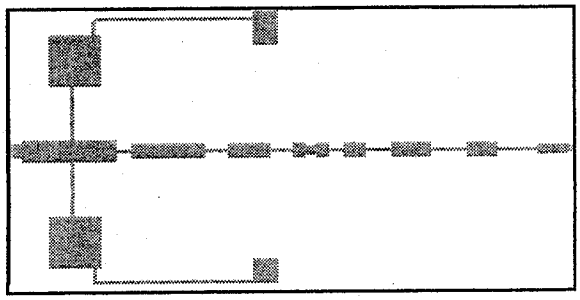

Figure 13 - Second iteration design of a 320 GHz MMIC doubler using full finite element analysis.

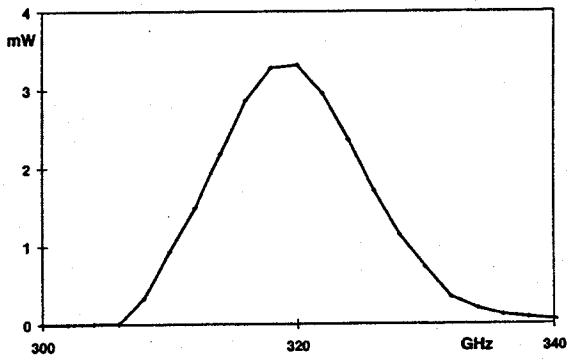

Figure 14 - Performance computed with finite element analysis and harmonic balance of the second iteration design of the 320 GHz MMIC doubler. Input power is 15 mW at 160 GHz.

PLANAR GaAs SCHOTTKY BARRIER DIODES

Steven M. Marazita, William L. Bishop, Thomas M. Cunningham,
Philip J. Koh, Thomas W. Crowe, and Robert M. Weikle, II

Applied Electrophysics Laboratories
Department of Electrical Engineering
University of Virginia
Charlottesville, VA 22901

Abstract

GaAs Schottky barrier diodes continue to be heavily used in millimeter and submillimeter wavelength heterodyne receiver applications where cryogenic cooling is not an acceptable option. This is because the diode technology is well known, reliable, and yields acceptable sensitivities at room temperature. Planar GaAs mixer diodes can now replace the older whisker contacted diodes to at least 600 GHz, and THz devices are easily within grasp.

This presentation will update the status of planar mixer diode technology at the University of Virginia. Recent developments include methods to reduce anode dimensions and parasitic shunt capacitance, fabrication of GaAs diodes on quartz substrates with integrated circuit elements, and fabrication of a diode pair with an integrated log-periodic antenna and separate diode biasing for subharmonic mixing. The paper will conclude with a summary of the status of mixer performance based on planar diodes and a discussion of the potential for THz mixers.

I. Introduction

Over the past several decades, there has been a surge of research in the detection of radiation in the submillimeter-wave portion of the electromagnetic spectrum (300 GHz to 3 THz). This research has been spurred in part by the desire of astrophysicists to map submillimeter-wave electromagnetic signatures in interstellar space. These signatures provide researchers with a better understanding of interstellar chemistry, star formation, and galactic structure. Research has also been driven by the need to observe radiation emitted from a number of molecules in the Earth's atmosphere. Detection of these emissions is critical to the study of the ozone layer and greenhouse warming. The detection of emissions from molecules involved in ozone depletion cycles such as O_3, ClO, and OH is particularly important.

The Microwave Limb Sounder (MLS) on the Earth Observing System (EOS), for example, will employ heterodyne radiometers operating from 240 GHz to 2.5 THz. These radiometers require mixers with sufficient spectral sensitivity, bandwidth, and low noise temperature. The mixers must also be highly robust to survive the launch and the lifetime of the satellite. The highest frequency receivers to date use quarter-micron diameter mixer diodes and have achieved record sensitivity at 2.5 THz [1][2]. However, these mixers are based on whisker-contacted diodes which are difficult to space qualify due to the fragility of the whisker contact. It is therefore essential that the new mixer diodes be fabricated using planar technology, thus eliminating the fragile whisker.

Several groups have developed planar Schottky diode technology with an integrated

finger replacing the whisker [3][12][13]. These chips have been used in waveguide receivers and yielded excellent performance up to about 600 GHz [4]. These results are promising, but work must be done to optimize planar chips for operation in the THz range.

At UVA we have investigated several key issues which could pertain to successful THz device operation. These include fabrication of GaAs planar diodes on quartz substrates with integrated circuit elements, methods of reducing parasitic shunt capacitances and anode dimensions in the planar diode structure, and fabrication of an anti-parallel anode pair with an integrated log-periodic antenna incorporating separate diode biasing for subharmonic mixing. This paper presents the latest fabrication achievements in these areas and some preliminary RF results.

II. Quartz Substrate and Circuit Element Integration

As operating frequencies in a mixer are pushed to higher limits, minimizing the parasitic capacitances in the planar diode structure and the precise alignment of the diode to the RF circuit become increasingly important. One method of reducing the parasitic pad to pad capacitance is to remove the high dielectric GaAs substrate and replace it with a low dielectric material such as quartz, leaving only a small, thin GaAs active area around the device anodes. UVA successfully has integrated this technology into their planar diode process with the diode bonded face up on quartz [5]. NASA's Jet Propulsion Laboratory also has developed a quartz substrate integration technology, QUID, which has

demonstrated promising results at 200 and 600 GHz [6-8]. This technology incorporates integrated RF circuitry fabricated along with the mixer diode, eliminating the alignment error associated with soldering a discrete device into an RF circuit. UVA and JPL are cooperatively developing this technology at 240 and 640 GHz for implementation on the MLS of EOS. The most recent results at 240 GHz use RF circuitry designed at JPL integrated with UVA planar diodes and QUID substrate replacement.

The fabrication process is similar to the standard planar diode process [3] with a few notable changes. Since the device is subharmonically pumped, it incorporates two anti-parallel diodes and hence two anodes and ohmic contact pads per device. The anode contact mask layer typically forms the finger and contact pads only. In this process, the RF/LO/IF mixer circuitry is integrated with the two anti-parallel fingers and anode contact pads of the device. Figure 1 shows an SEM of the device after the anode contact layer with integrated filters has been completed. Figure 2 shows the device after the surface channel etch has been performed. At this point, the frontside processing is complete.

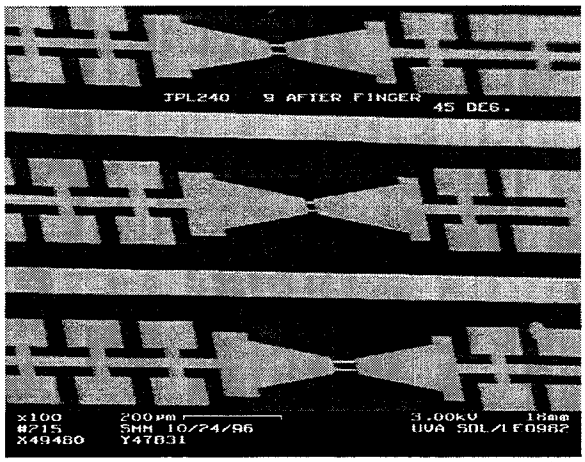

Figure 1: Devices after anode contact layer

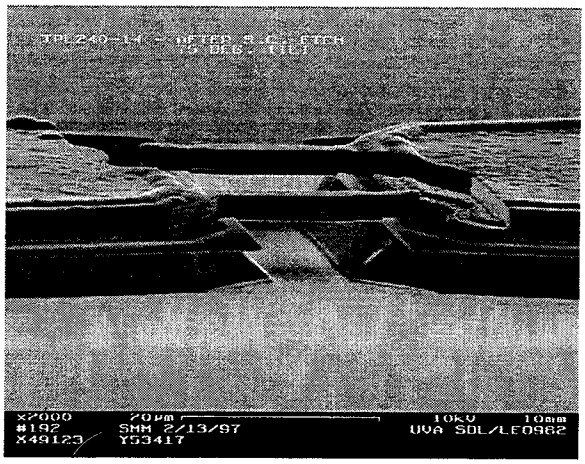

Figure 2: Device after surface channel etch

The backside processing of the devices begins with inverting the wafer and bonding it face down with epoxy to a 6 mil quartz substrate. The critical steps in this process are to ensure that the cured epoxy contains no air bubbles and that the epoxy is thin and of uniform thickness across the wafer. During the development of the wafer bonding and epoxy curing process, there were many problems with air bubble formation during the required 80°C curing cycle. By using a two day room temperature cure under vacuum, followed by post-curing at 80 and 120 °C, this problem has been solved. We use a homemade rubber membrane press under vacuum to minimize the cured epoxy thickness and consistently achieve thicknesses of 1-2 μm over the entire wafer. The GaAs substrate is removed using a selective wet etch composed of 96% H_2O_2:4% NH_4OH which etches GaAs approximately 60 times faster than AlGaAs. The GaAs material incorporates an AlGaAs etch stop layer between the n+ buffer layer and the substrate to provide a stopping point for the substrate removal etch from the backside. Figure 3 shows a wafer after the substrate has been removed. The dark area is epoxy and the lighter area is AlGaAs.

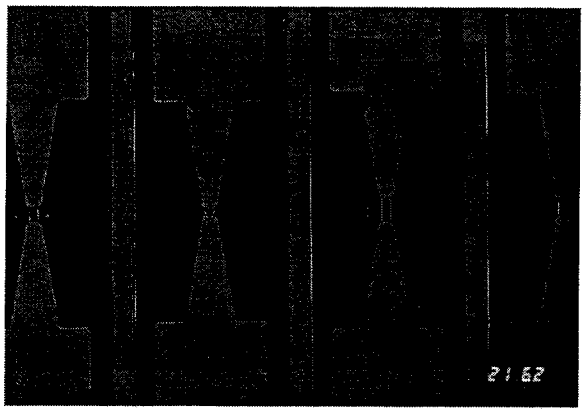

Figure 3: Backside of wafer after substrate removal

A photoresist pattern is applied to mask the active areas and ohmic contacts from the backside. Cl-RIE is used to remove the remaining AlGaAs and n+ GaAs buffer from outside the photoresist pattern. CF_4 RIE is utilized to etch the SiO_2 layer underneath the GaAs, and an Argon sputter etch removes the chrome adhesion layer on top of the filter circuitry to reveal the frontside gold filters from the backside of the wafer. Figure 4 shows the photoresist pattern on top of AlGaAs and epoxy, and Figure 5 shows the wafer after all dry etching is complete. In this figure the light areas are now gold. At first we were using a combination of wet etchants to perform the backside etching. The batch

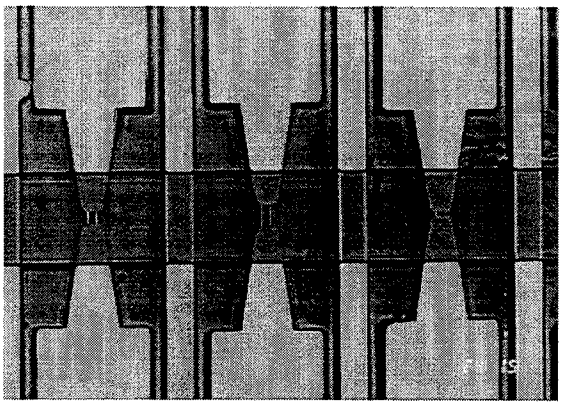

Figure 4: Photoresist pattern for backside etching

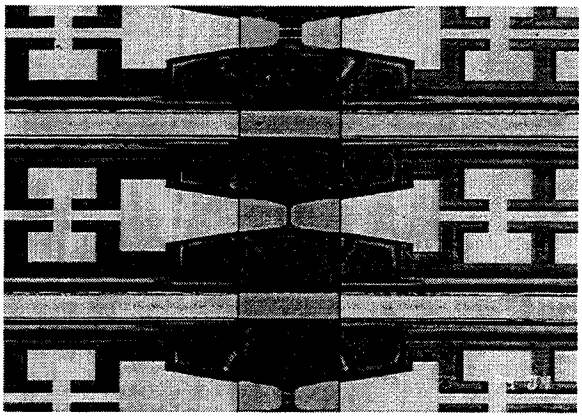

Figure 5: Devices after backside processing

yield was very low due to etchants leaking underneath the photoresist and epoxy, attacking the device's active areas. By switching to an entirely dry etch process, we improved the yield from approximately 7% to over 70%.

The last step in the process is to dice the wafer into individual mixers. The final chip dimensions are 8600 x 230 μm (340 x 9 mils). Figure 6 shows an SEM of a finished chip. The devices are fabricated on $2x10^{17}$ n-type GaAs epi and have anode diameters of approximately 1.3 μm. The I-V parameters are as follows: R_s=12-14 ohms,

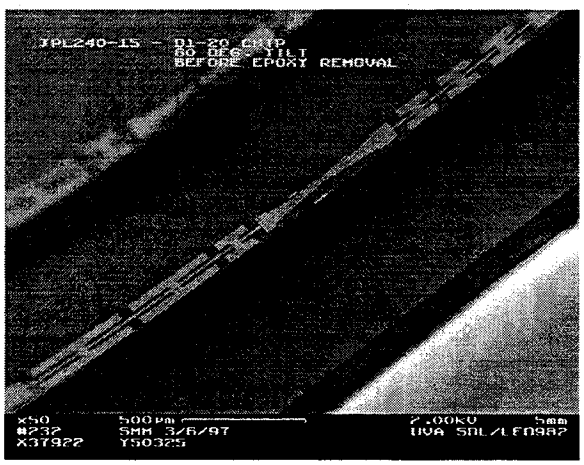

Figure 6: Complete 240 GHz mixer

$V_{knee}(1\mu A)$=670 mV, ΔV=73-74 mV, C_{j0}=2 fF per anode, and C_{total}=16 fF with parasitics. This batch of mixers performed very well at 230 GHz: DSB T_{mix}=716 K, P_{LO}=4.95 mW, L_{conv}=5.18 dB, Z_{IF}=139.8 ohms, IF=1.5 GHz using JPL block 240A2. These numbers look very promising. Additionally, we have developed a technique at UVA to remove the epoxy from the surface channel to reveal an air channel once again. Figures 7 and 8 show before and after the epoxy was removed from a device. This procedure reduces its parasitic capacitance by over 20%. The RF performance seems to

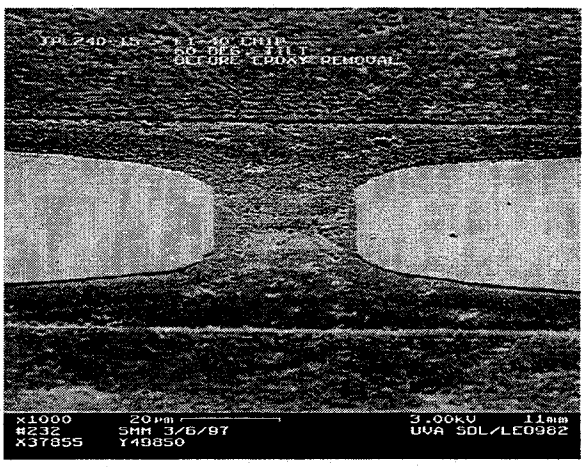

Figure 7: Before epoxy removal

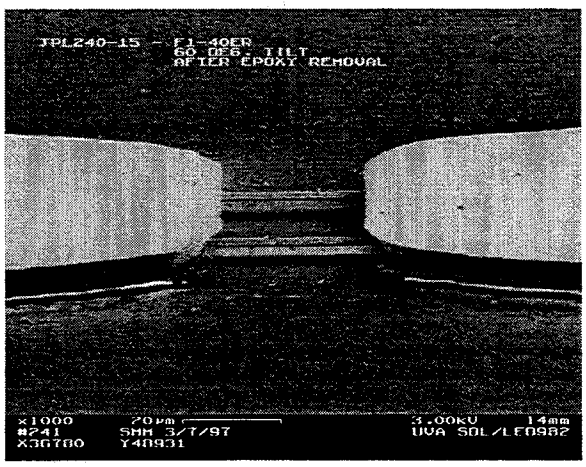

Figure 8: After epoxy removal

improve considerably after this step. JPL measured the RF performance for a different device which had the epoxy removed and was from the same wafer as quoted previously: at 235 GHz, DSB T_{mix}=537 K, P_{LO}=3.98 mW, L_{conv}=4.93 dB, Z_{IF}=176.1 ohms, IF=2.0 GHz. We believe that this is one of the best reported results at 235 GHz for a subharmonically-pumped integrated mixer. It shows a marked improvement over the device with epoxy in the surface channel. This is only one result, however, and more testing needs to be done to confirm this trend.

III. Finger Overlay Capacitance Reduction

Finger overlay capacitance arises due to the anode contact finger sitting on top of SiO_2 and GaAs around the device anode and to the wall of surface channel. We currently are applying an air bridge technology to planar varactor diodes with great success, reducing this capacitance to a negligible amount [9]. Figure 9 shows a recent planar varactor diode with the air bridge interconnect. This technique replaces a 0.5 μm layer

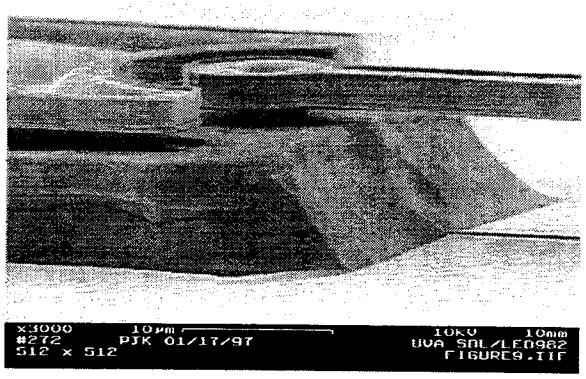

Figure 9: Planar varactor diode with air bridge interconnect to anode

of oxide of dielectric constant 6 with a 1 μm layer of dielectric constant 1 (air), yielding approximately a factor of 12 reduction in overlay capacitance. It also makes the position of the surface channel wall relative to the anode less critical. We feel that this technology can also be applied to mixer diodes if the small area anodes necessary for high frequency operation provide a robust contact. At THz frequencies any parasitic capacitance reduction techniques should improve device performance.

IV. Anode Dimension Reduction

Development is continuing at UVA on the Electroplate Window Shrink (EWS) process which uses conventional deep-ultraviolet lithography and an electroplated metal mask to define 0.25 μm and smaller Schottky contacts to GaAs for 2.5 THz whisker-contacted mixer diode development [10]. Figure 10 shows the most recent batch of 2.5 THz mixer diodes fabricated at UVA. The process has seen great improvements in anode uniformity, DC I-V characteristics, and minimization of C_{TOTAL}. Table 1 compares the

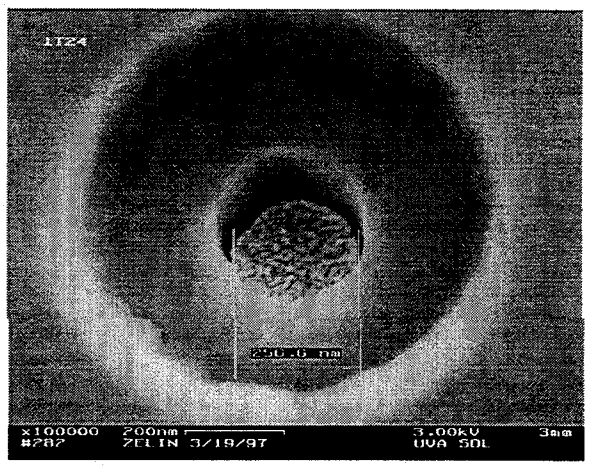

Figure 10: 0.25 μm Schottky contact to GaAs

I-V and capacitance data for the new batch 1T24 mixer diodes with the first generation batch 1T23:

Device	V_{KNEE}@ 1 μA (mV)	ΔV @ 1-10 μA (mV)	V_{BR} @ -1 μA (V)	R_S @ 1 mA (Ω)	C_{TOTAL} (fF)
1T23	680-700	89-92	2.1-2.4	25-36	0.5-0.65
1T24	720-730	85-86	3.4	26-38	0.32-0.5

Table 1: I-V and capacitance data comparing 1T23 and 1T24

The most notable changes in the above parameters are the reduction in ΔV, increase in V_{br}, and reduction in total capacitance. These factors should contribute to better RF performance for these devices. We are currently awaiting RF test data.

This technology is applicable to the next generation THz planar mixer diodes as anode dimensions will need to be scaled into the sub-0.5 μm regime to further reduce parasitic anode capacitance.

V. Separately Biasable Subharmonic Mixer Diodes with Integrated Antennas

Subharmonically pumped diodes seem very attractive for high frequency mixer applications since the LO frequency only needs to be one-half of the RF frequency. Since LO power is not abundant at THz frequencies, this is an attractive configuration for THz mixers. However, pumping the anti-parallel diodes into their turn-on regimes requires

significantly more power than single-ended mixers if individual anode DC biasing is not provided. This work focuses on fabricating separately biasable anti-parallel planar diodes integrated with a log periodic receiving antenna. The antenna is designed to operate from 250 GHz to approximately 1.2 THz. Using chlorine RIE, a split was cut down the center of one side of the antenna so that each diode could be DC biased individually. Figure 11 is an SEM from a batch of mixers fabricated at UVA. The split is the dark band down the

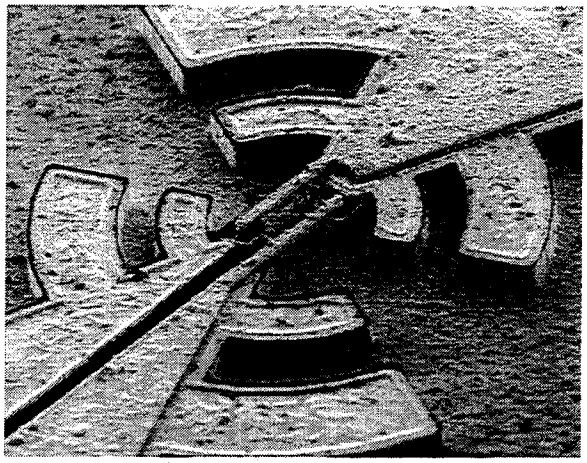

Figure 12: Subharmonically pumped separately biasable planar mixer diode with integrated log periodic antenna

center of the log periodic structure on the left side of the figure. It penetrates into the semi-insulating GaAs substrate. The DC I-V characteristics are similar to other planar diodes from UVA with 0.75 μm anodes on $4x10^{17}$ cm^{-3} epitaxial layer doping. We are awaiting RF test results on the performance of these devices both as a receiving antenna and a mixer.

VI. Summary and Conclusions

Several groups are actively developing millimeter and submillimeter wavelength mixers based on planar Schottky barrier diodes. Gencorp-Aerojet has a 200 GHz subharmonically pumped receiver operating from 150 to 300 GHz with a 6 to 18 GHz IF bandwidth. The best performance is DSB T_{rec}=496 K at 200 GHz with P_{LO}<4 mW [11]. NASA's Jet Propulsion Laboratory is investigating integrated subharmonic mixers at a variety of frequencies [6][7][8] and cooperatively with UVA [this work]. UVA is also actively researching fundamentally pumped planar mixers at 585 GHz and 690 GHz with DSB T_{rec}=2380 K and 3200 K, respectively [4].

GaAs Schottky diodes are presently the most promising technology for space based spectroscopy applications such as atmospheric limb sounding. These compact, all-solid-state systems require no complex cooling technology and are highly reliable. Furthermore, the rapid advance of planar Schottky diodes will reduce system costs and increase reliability. Planar Schottky mixers are now competitive to at least 700 GHz. Some of the key issues for planar devices as we push towards higher frequencies are:

1. Higher levels of integration - The alignment of the diode to the surrounding circuitry is too critical for discrete devices at THz frequencies.
2. Lower parasitics and shorter finger lengths ($< 20\ \mu$m) for better bandwidth
3. Reduced chip dimensions to fit in higher frequency waveguide structures

As these issues and others are overcome in the near future, this technology should advance to the THz frequency range.

VII. Acknowledgements

The authors acknowledge the collaboration of JPL on the integrated planar mixer research. This work was supported by NASA-NGT-51396, NASA-NAGW-4007, JPL-960017, and NSF-AST-9320183.

VIII. References

[1] H.-W. Hübers, W.C.B. Peatman, T.W. Crowe, G. Lundershausen and H.P. Röser, "Noise Temperature and Conversion Losses of Submicron GaAs Schottky-Barrier Diodes," Presented at the Fourth Intl. Symp. Space THz Tech., Los Angeles, CA, March 1993.

[2] P.A.D. Wood, D.W. Porterfield, William L. Bishop and T.W. Crowe, "GaAs Schottky Diodes for Atmospheric Measurements at 2.5 THz," Proc. Fifth Intl. Symp. Space THz Tech., Ann Arbor, pp.355-368, May 1994.

[3] W.L. Bishop, R.J. Mattauch, T.W. Crowe and L. Poli, "A Planar Schottky Diode for Submillimeter Wavelengths," 15th Int. Conf. on Infrared and Millimeter Waves, Orlando, FL, Dec. 1990.

[4] J.L. Hesler, W.R. Hall, T.W. Crowe, R.M. Weikle, II, B.S. Deaver, Jr., R.F. Bradley, and S.-K. Pan, "Fixed-Tuned Submillimeter Wavelength Waveguide Mixers Using Planar Schottky Barrier Diodes," To be published in the IEEE Trans. Microwave Theory Tech., May 1997.

[5] W.L. Bishop, T.W. Crowe, R.J. Mattauch, and P.H. Ostdiek, "Planar Schottky Barrier Mixer Diodes for Space Applications at Submillimeter Wavelengths," Microwave and Optical Tech. Lett., Special Issue on Space THz Tech., Vol. 3, No. 1, pp. 44-49, Jan. 1991.

[6] I. Medhi, M. Mazed, R. Dengler, A. Pease, M. Natzic, and P.H. Siegel, "Planar GaAs Schottky diodes integrated with quartz substrate circuitry for waveguide subharmonic mixers at 215 GHz", IEEE-International Microwave Symposium 1994 Digest, pp. 779-782.

[7] I. Medhi, S. Martin, R. Dengler, R.P. Smith, and P.H. Siegel, "Fabrication and performance of planar Schottky diodes with T-gate-like anodes in 200 GHz subharmonically pumped waveguide mixers," IEEE Microwave and Guided Wave Letters, vol. 6, no. 1, January 1996.

[8] I. Medhi, T. Lee, D. Humphrey, S. Martin, R.J. Dengler, J.E. Oswald, A. Pease, R.P. Smith, and P.H. Siegel, "600 GHz Planar-Schottky-Diode Subharmonic Waveguide Mixers," IEEE-MTT International Microwave Symposium, San Francisco, CA, June 17-21, 1996.

[9] Philip J. Koh, William C.B. Peatman, Thomas W. Crowe, and Neal R. Erickson, "Novel Planar Varactor Diodes", Seventh International Symposium on Space Terahertz Technology, Charlottesville, VA, March 1996.

[10] William L. Bishop, Steven M. Marazita, Perry A.D. Wood, and Thomas W. Crowe, "A Novel Structure and Fabrication Process for Sub-Quarter-Micron THz diodes", Seventh International Symposium on Space Terahertz Technology,

Charlottesville, VA, March 1996.

[11] I. Galin, "A Mixer up to 300 GHz with Whiskerless Schottky Diodes for Spaceborne Radiometers," 7th Intl. Symp. Space THz Tech., Charlottesville, VA, pp. 474-476, March 1996.

[12] J.W. Archer, R.A. Batchelor, and C.J. Smith, "Low-Parasitic, Planar Schottky Diodes for Millimeter-Wave Integrated Circuits," IEEE Trans. Microwave Theory Tech., Vol. MTT-38, No. 1, pp. 15-22, Jan. 1990.

[13] A. Simon, A. Grueb, V. Krozer, K. Beilenhoff, H.L. Hartnagel, "Planar THz Schottky Diode Based on a Quasi-Vertical Structure," 4th Intl. Symp. Space THz Tech., UCLA, pp. 392-403, March 1993.

Substrateless Schottky Diodes for THz Applications

C.I. Lin[#], A. Simon[#], M. Rodriguez-Gironés[#], H.L. Hartnagel[#]
P. Zimmermann[*], R. Zimmermann[*]

[#] Institut für Hochfrequenztechnik, Technische Hochschule Darmstadt, 64283 Darmstadt, Germany
Tel : 49-6151-162562, Fax : 49-6151-164367, e-mail : hfmwe013@hrzpub.th-darmstadt.de
[*] Radiometer Physics GmbH, Bergerwiesenstr. 15, 53340 Meckenheim, Germany
Tel : 49-2225-15953, Fax : 49-2225-14441

Abstract

Although planar Schottky diodes have been significantly improved, whisker contacted Schottky diodes still dominate as nonlinear devices in mixer and frequency multiplier applications in the sub-millimeter regime. Because of the skin effect the performance of whisker contacted Schottky diodes above 1 THz is limited. A novel device structure of a whisker contacted schottky diode, the substrateless Schottky diode, was proposed in 1995 [1] and the final fabrication process was defined in 1996 [2]. This structure improves some shortcomings of whisker contacted Schottky diodes. This paper presents the state-of-the-art development of this structure and discusses recent multiplier results. Tripler efficiencies of 12% (6mW) at 279 GHz and 6.7% (1mW) at 474 GHz show that the substrateless Schottky diode extends the capabilities of whisker contacted Schottky diodes in the THz regime.

Introduction

Many recent research activities are focused on planar Schottky diodes, but whisker contacted diodes still provide better RF performances. For the submillimeter regime the performance of a conventional whisker contacted Schottky diode is limited by the skin effect. In order to overcome this problem the first structure of a substrateless Schottky diode has been proposed by Seidel in 1989 [3]. In 1995 Simon proposed a novel structure that demonstrated excellent performance in a mixer at 545 GHz [1]. After the optimization of the fabrication process the yield and reproducibility of substrateless Schottky diodes has been improved significantly [2]. Fig.1 shows the structure of the substrateless Schottky diode.

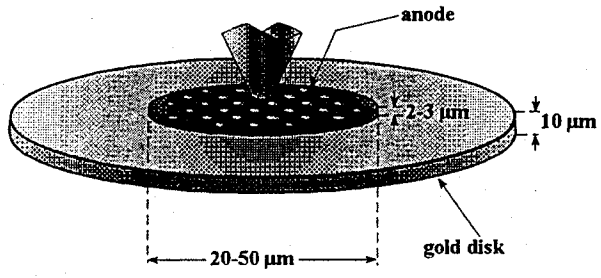

Fig.1 Drawing of a substrateless diode

Compared with the conventional diode chip the thickness of the n^+-GaAs substrate is strongly reduced from 100 µm to 2µm. Using a 5-10 µm thick Gold disc promotes the mechanical stability of the device and simplifies the handling. Due to the reduced geometry substrateless Schottky diodes offer several advantages compared with conventional whisker contacted Schottky diodes [2]:

- Due to minimized dimensions the structure is less affected by the skin effect [4].
- The n^+-substrate thickness is reduced to a few microns reducing its contribution to the resistance.
- Small distance between the active n-layer and the backside metal provides a good heat sink. Therefore, substrateless Schottky diodes can operate more reliably at high current densities without thermal degradation and the contribution to the system noise is reduced.
- Reduced semiconductor surface area decreases the leakage current.
- Reduced device volume allows a better coupling of the input signal into the diode within the waveguide.

Due to these advantages substrateless Schottky diodes give a prospect to attain improved performance of mixers and frequency multipliers in the submillimeter regime.

Fabrication process

Fig. 2 shows the material used to produce substrateless Schottky diodes, which is the same as the quasi-vertical planar Schottky diodes [5]. In fact both structures have very similar process steps from backside processing to Schottky contact formation. Thus, another advantage of substrateless Schottky diodes is the possibility to use its fabrication process in controlling the fabrication of quasi-vertical planar Schottky diodes.

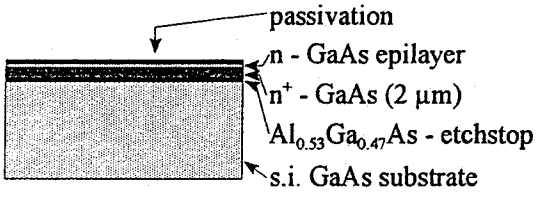

Fig.2 Layers of a MBE-wafer for substrateless Schottky diodes

The process steps for the substrateless Schottky diode fabrication are outlined below:

- Passivation (SiO_2 / polyimide) on the active n-layer

- Backside process steps

  1.Sample thinning to 70 µm from the backside

  2.Samples thinning to 30 µm from the backside in the middle of the chip

  3.Backside ohmic contact/metal disks structure definition (⌀=100 µm) through selective spray etching to etchstop layer (H_2O_2/NH_4OH).

  4.Etchstop layer removal using spray etching ($H_2O_2/NH_4OH/H_2O$)

  5.Ohmic contact (Ni/GeAu/Ni) evaporation and annealing at 480°C for one minute

  6.Ohmic contact Gold plating to achieve a 10 µm thick Gold substrate

- Frontside process steps

  1.Schottky contact definition using Reactive Ion Etching, pulse plating with Platinum and Gold [6].

  2.Mesa definition using selective spray etching (H_2O_2/NH_4OH)

  3.On chip measurements

- Device separation

  1. GaAs-substrate removal from the backside using selective spray etching (H_2O_2/NH_4OH)

Device characteristics

Since last year several batches of substrateless GaAs Schottky diodes have been successfully fabricated and measured. Table 1 records the used materials and electrical characteristics of different varistors and varactors for mixer and frequency multiplier applications:

Device	N_d [cm^{-3}]	$d_{n\text{-}epi}$ [nm]	d_{anode} [µm]	R_s [Ω]	n	C_{jo} [fF]	V_{br} [V]	C_{j0}/C_{min}	f_c [GHz]
1030SDK	8E16	560	5	5	1.04	20	9.5	2	1.6
P1030SDK	8E16	560	5	5.7	1.03	20	18	3.2	3.1
1030SGF	8E16	560	3.5	11.5	1.05	9	8.5	2.2	1.9
733SIB	3E17	100	0.8	14	1.14	1.5	5.1	--	7.6
733SJA	3E17	100	0.5	17	1.17	0.7	5.8	--	13.4
867SIB	5E17	70	0.5	15	1.22	1.2	3.3	--	8.84

Table 1 : Characteristics of fabricated substrateless Schottky diodes

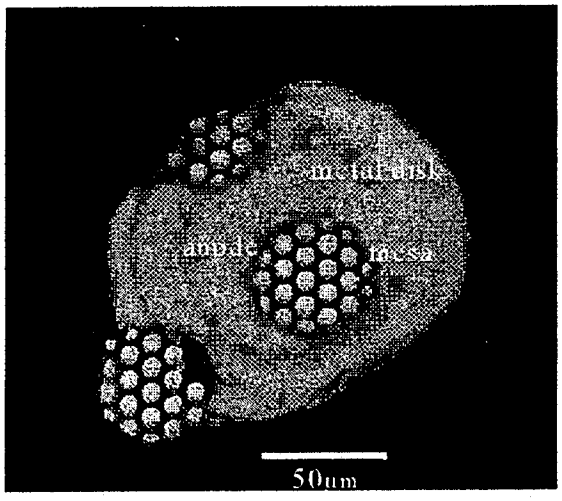

Fig.3a : Picture of device P1030SDK

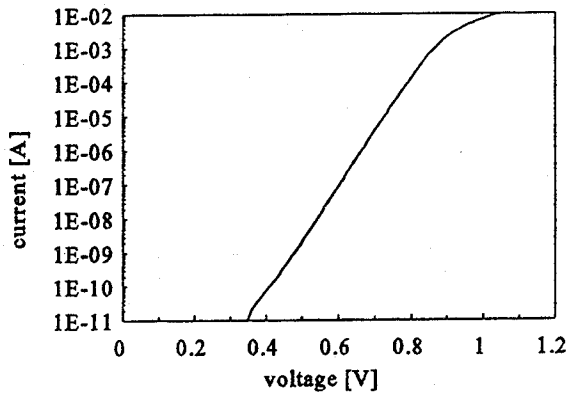

Fig.3b: I/V-characteristics of device P1030SDK

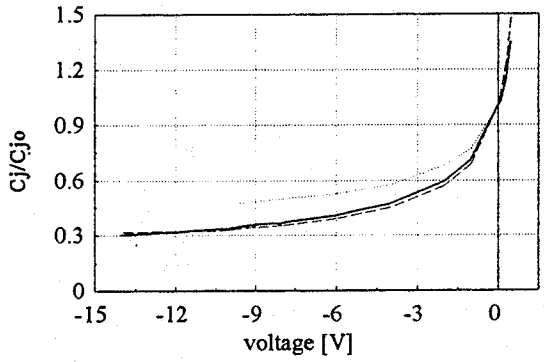

Fig.3c:C/V-curves of device 1030SDK, P1030SDK and simple simulated result
(solid line:simulation, dash line:P1030SDK, dot line:1030SDK)

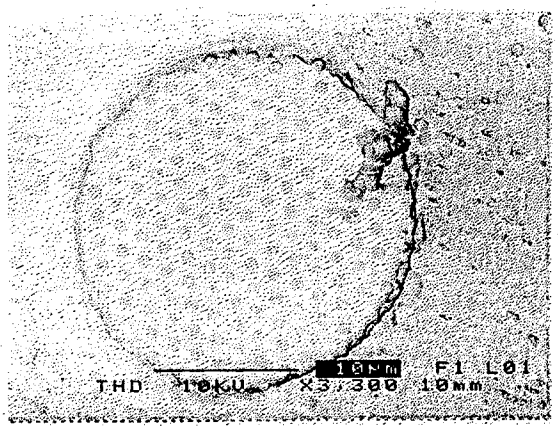

Fig.4a: SEM-picture of a mesa of device 733SIB

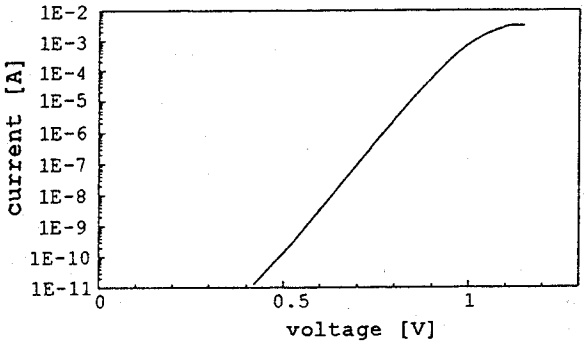

Fig. 4b : I/V-characteristics of this diode

Fig. 3a and fig. 4a show different devices. Fig. 3b and fig. 4b show the forward I/V-characteristics of diode P1030SDK (varactor) and 733SIB (varistor). It is important to note that these forward I/V-characteristics are nearly ideal values even at a current less than 1nA and follow a straight line within a very large voltage regime. That means, the complicated backside fabrication process does not have any influence on the quality of the Schottky contacts at the frontside.

Fig. 3c shows the C/V-curves of devices 1030SDK, P1030SDK and simulated results. PECVD-SiO_2 and polyimide are used for the passivation of 1030SDK and P1030SDK, respectively. Because of the in oxide-related fixed charges, device 1030SDK has a lower breakdown voltage and a smaller capacitance modulation [7]. Polyimide passivation offers a much higher breakdown voltage and an excellent capacitance modulation (P1030SDK). Therefore, polyimide can be used as a good passivation layer without the problem of fixed charges. Due to difficulties in the fabricaton the polyimide process still needs to be optimized for an anode diameter of less than 2 μm.

Radiometer Physics GmbH has tested devices 1030SDK, P1030SDK and 1030SGF, in different triplers for the frequencies 93GHz/279GHz, 125GHz/375GHz and 158GHz/474GHz. Table 2 shows the achieved output powers and efficiencies, which are comparable or better than the best results of conventional whisker contacted diodes.

Tripler	input power	output power	efficiency
93GHz/279GHz	50 mW	6 mW	12%
125GHz/375GHz	50 mW	3 mW	6%
158GHz/474GHz	15 mW	1 mW	6.7%

Table 2 : RF results of devices in tripler.

Some 733SIB devices have been delivered to University Erlangen, Germany and assembled in a corner-cube mixer. First RF measurements of the video sensitivity at 600 GHz show similar results (150mV /mW) compared with the results of two referent conventional Schottky diodes (120mV/mW and 200mV/mW). Further measurements for 2.5THz are in progress.

Conclusion

A reliable fabrication process for substrateless Schottky diodes has been presented. The proposed device structure offers reduced overall dimensions and improved power handling capabilities. The achieved output power and efficiencies of frequency triplers (6 mW, 3 mW and 1 mW at 279 GHz, 375 GHz and 474 GHz) demonstrate the capabilities of the substrateless Schottky diode in the submillimeter

regime. Furthermore, the presence of oxide-related fixed charges has been avoided by polyimide passivation. Polyimide passivation offers a higher breakdown voltage and an increased capacitance modulation. The processing of the polyimide passivation for diodes with anode diameters smaller than 2 μm still needs to be optimized.

Acknowledgment

The authors would like to express their acknowledgments to Dr. H. Grothe and Dr. J. Freyer, both from the Technical University of Munich, Germany, for supplying the high-quality epitaxial materials.

References

[1] A. Simon, A. Grüb, M. Rodriguez-Gironés and H. L. Hartnagel, "A Novel Micron-Thick Whisker Contacted Schottky Diode Chip", Sixth Int. Symp. on Space Terahertz Technology, pp 5-12, 1995

[2] C. I. Lin, A. Simon and H. L. Hartnagel, "Fabrication of Substrateless Schottky Diodes for THz Applications", Fourth Int. Workshop on Terahertz Electronics, Erlangen, 1996

[3] L. K. Seidel and T. W. Crowe, "Fabrication and Analysis of GaAs Schottky Barrier Diodes Fabricated on Thin Membranes for Terahertz Applications", Int. Journal IR and Millimeter Waves, Vol.10, No.7, pp 779-787, 1989

[4] U. V. Bhapkar, T. W. Crowe, "Analysis of the High Frequency Series Impedance of GaAs Schottky Diodes by a Finite Difference Technique", IEEE Trans. Microwave Theory Tech., Vol. 40, No. 5, pp. 886-894, 1992

[5] A. Simon, C. I. Lin and H. L. Hartnagel "Fabrication and Optimization of Planar Schottky Diodes", this proceedings

[6] A. Grüb, C. I. Lin and H. L. Hartnagel, "Electrolytic Deposition Techniques for the Fabrication of Submicron Anodes", Sixth Int. Symp. on Space Terahertz Technology, pp 54-65, 1996

[7] S. M. Sze, "Physics of Semiconductor Devices", 2nd Ed., John Wiley Inc., pp. 390-395

FABRICATION OF HIGH-T_C HOT-ELECTRON BOLOMETRIC MIXERS FOR SUBMILLIMETER HETERODYNE APPLICATIONS

M.J. Burns, A.W. Kleinsasser, B. Karasik, M. Gaidis, and W.R. McGrath

Center for Space Microelectronics Technology, Jet Propulsion Laboratory, California Institute of Technology, Pasadena, CA 91109, USA

Abstract

Superconducting hot-electron bolometers are the most promising candidate for heterodyne mixers at frequencies above 1 THz. These devices operate by heating of electrons in the superconductor, and thus have no energy gap related frequency limitation, such as exists in SIS mixers, for example. Nb hot-electron bolometric mixers have recently demonstrated superior performance to competing Schottky mixers at frequencies above 1 THz, but of course must be operated at liquid helium temperatures. $YBa_2Cu_3O_{7-\delta}$ hot-electron bolometric mixers introduce the possibility of sensitive, low power heterodyne detectors operating at temperatures approaching 90 K for high-background applications, such as earth observing missions. We describe the fabrication of high-T_c devices based on ultrathin (<20 nm) $YBa_2Cu_3O_{7-\delta}$ films for use as 2.5 THz mixers.

Introduction

Heterodyne receivers based on superconductor-insulator-superconductor junctions for use in submillimeter astronomical and atmospheric studies at frequencies up to 1 THz have been produced [1,2]. At higher frequencies, Schottky diode mixers or direct detection techniques are generally used. Superconducting hot-electron bolometers (HEB), consisting of a thin film microbridge, have been proposed for use in heterodyne applications in the terahertz (THz) range [3,4]. Superconducting hot-electron bolometric mixers require orders of magnitude less local oscillator power than semiconductor mixers, allowing for solid state local oscillators rather than the large lasers

required of Schottky diode mixers. Nb HEB mixers operating at 2-4 K have shown excellent performance at 530GHz [5], and recently demonstrated low noise at 1.2THz [6] and 2.5THz [7]. While some initial experiments on device physics and heterodyne performance [8,9] have been carrier out on high-temperature superconductor (HTS) bolometric mixers, no optimized devices have been reported to date.

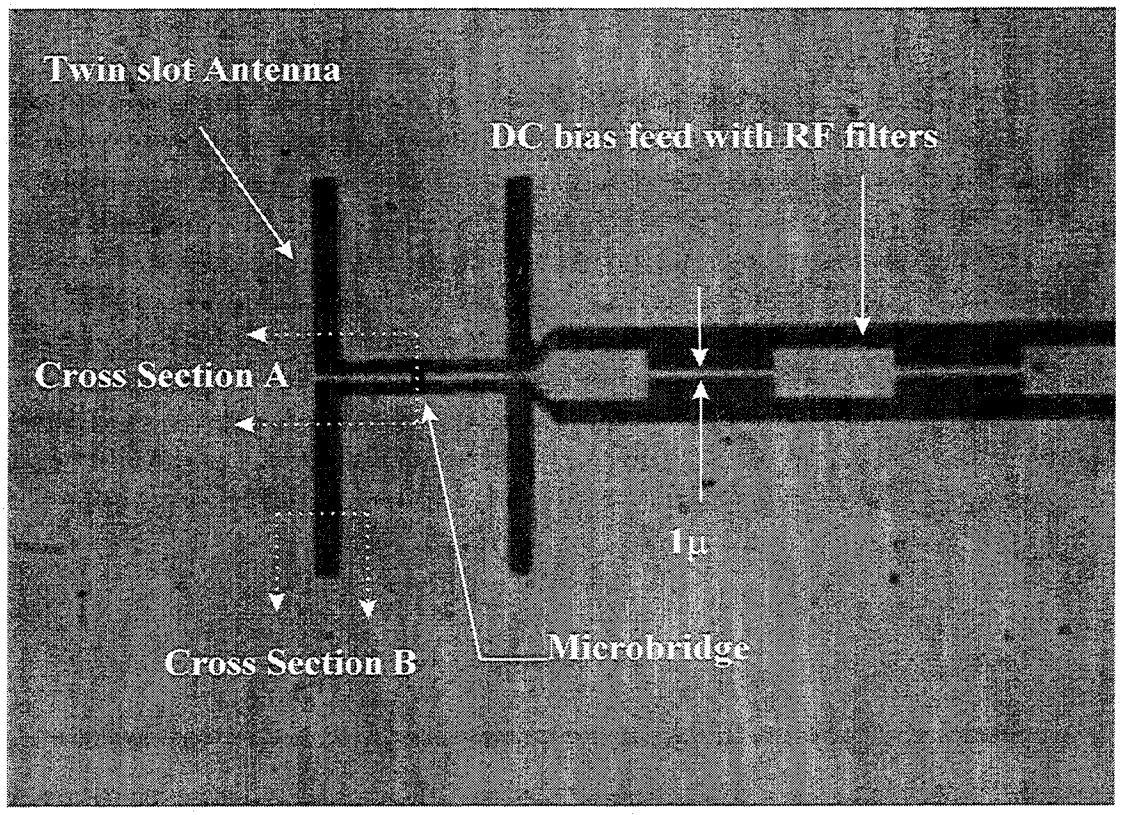

Figure 1 -- Finished 2.5THz hot electron bolometric mixer showing twin slot antenna, DC bias feed with filters, and the active element microbridge. Dark areas are where all material has been removed, thus exposing the dark substrate. Light areas are Au. Dashed lines show two cuts for the cross sections of Figure 3. Cross section A is across the twin slot and microbridge, cross section B is illustrative of the dark areas where the substrate is exposed.

The lower local oscillator power requirements of superconducting hot-electron bolometric mixers makes them particularly attractive for remote sensing

systems with constraints on the availability of power or mass, such as on balloon or space-based platforms. Hot-electron bolometric mixers made from HTS operating in the range of 60-85 K are particularly attractive for space based applications since they can be cooled with existing space qualified closed-cycle refrigerators.

In this paper we describe the fabrication of nominally of microbridge bolometers based on ultrathin (<20 nm) $YBa_2Cu_3O_{7-\delta}$ films for HEB mixer applications at 2.5 THz [10]. A photograph of a finished 2.5 THz twin-slot mixer with a $YBa_2Cu_3O_{7-\delta}$ device is shown in Fig. 1, and a microbridge connected to dc contact pads is shown in Fig. 2.

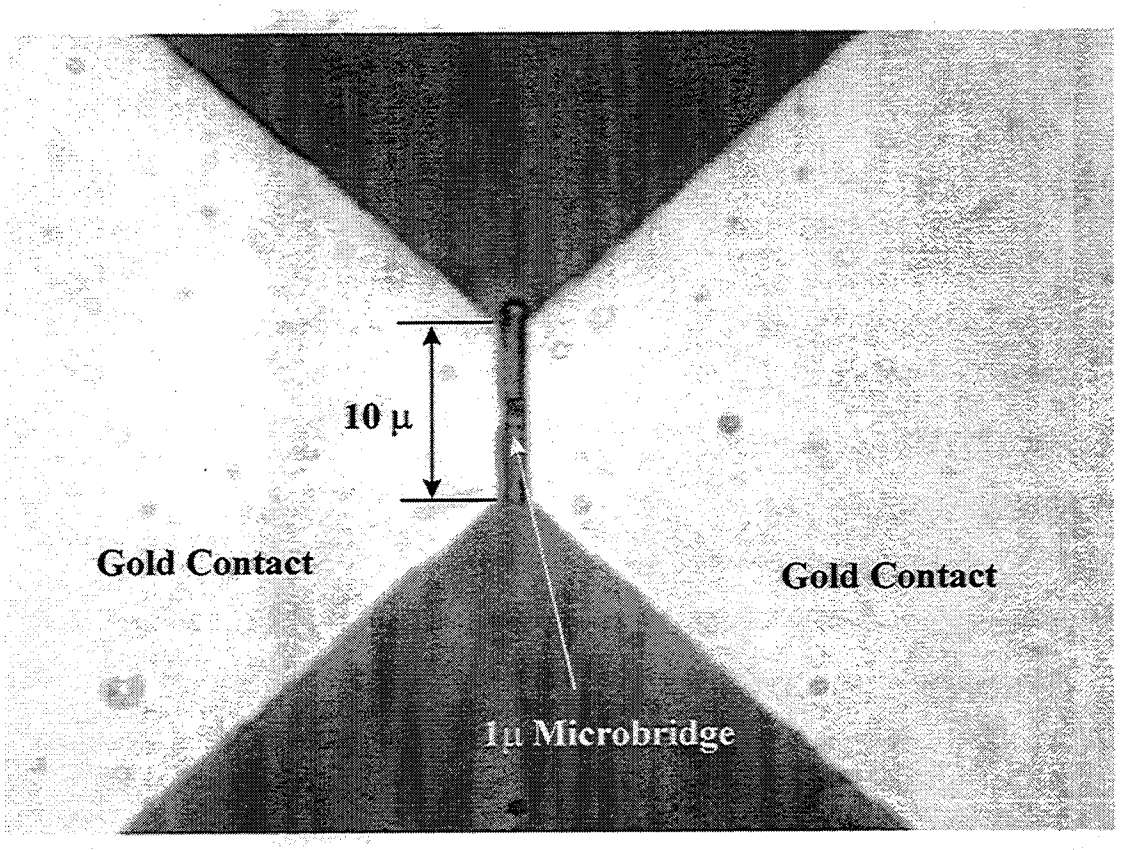

Figure 2 -- Finished microbridge located in the center of dc contact pads.

Requirements

The design and operating principles of our 2.5 THz HTS hot-electron bolometric mixer are described in detail elsewhere [10]. Hot-electron bolometric mixer operation depends on heating the electrons by the incoming rf radiation, resulting in a nonequilibrium energy distribution. Cooling occurs via electron-phonon interactions whereby the hot electrons give their energy to phonons which escape into the substrate. Alternatively, cooling can occur by diffusion of the hot electrons out of the device and into the normal-metal electrical contacts [4]. Due to the short electron mean-free-paths in HTS materials, the electron-phonon cooling mechanism dominates in HTS hot-electron bolometric mixers.

In space applications, system-level power restrictions constrain mixers to operate at low local oscillator power levels, with major implications for device size. As a result of these considerations, the major device design requirements [10] for HTS hot-electron bolometers are described below. The first four requirements pertain to the substrate. While a large number of substrates can individually meet these conditions, it is important for optimal mixer performance to meet all simultaneously.

The substrate must have a high thermal conductivity and be compatible with epitaxial $YBa_2Cu_2O_{7-\delta}$ (YBCO) growth. This requirement can be met by a number of substrates compatible with high-quality YBCO films. MgO, $LaAlO_3$, Al_2O_3 and $YAlO_3$ have thermal conductivities at 90 K of 3.4, 0.35, 6.4 and 0.2-0.4 W K^{-1} cm^{-1}, respectively. For comparison, yttrium stabilized zirconia (YSZ) has a thermal conductivity at 90 K of only 0.015 W K^{-1} cm^{-1} [10].

The thermal boundary resistance (R_b) between the HTS film and the substrate should be as small as possible. This second requirement can be met by several of the aforementioned substrates. The values of R_b, inferred from measurements of

the phonon escape time, between YBCO and MgO, $LaAlO_3$ and Al_2O_3 at 90 K are 5, 10, and 11 x 10^{-4} K cm^2 W^{-1} respectively [11-15].

Substrates need to have a small loss-tangent at both 2.5 THz and at the IF frequency. This fourth requirement can also be met by a number of the aforementioned substrates. MgO, $LaAlO_3$, Al_2O_3 and $YAlO_3$ have loss tangents of 7, 5, 8, and 10, x 10^{-6}, respectively at 90 K and ~10 GHz. For comparison, yttrium stabilized zirconia (YSZ) has a loss tangent of 400 x 10^{-4} at 90 K at ~10 GHz [10].

Substrates need to have a convenient dielectric constant at both 2.5THz and at the IF frequency. This fifth requirement can also be met by a number of HTS compatible substrate materials. The dielectric constants of MgO, Y_2O_3, Si-on-Al_2O_3 and $YAlO_3$, measured in a Fourier transform infrared spectrometer at JPL, are 10.0, 12.9, 9.9 and 21.2, respectively, at 77 K and 2.5 THz.

The film must be ultra-thin (10-20 nm) to minimize the phonon escape time and allow for optimum mixer performance at GHz IF's [10]. In addition, the HTS mixer film volume must be small enough to allow device operation at microwatt local oscillator power levels. This third requirement dictates that the mixer be constructed from films patterned to submicron dimensions [10].

In this work, ~20 nm YBCO thick films on $YAlO_3$ substrates were used to fabricate hot-electron bolometric mixers.

Growth and Patterning

Growth of the superconductor and gold (Au) contact layers are performed completely *in situ* without exposure of interfaces to the ambient environment. The devices are grown on 250 μm thick, 1x1cm^2 (001) $YAlO_3$ substrates polished on both sides. The nominal growth process is: The substrates are mounted on Haynes alloy plates using Ag paint. These are transferred into the HTS deposition system via a load-lock. The substrates are buffered using a 20 nm

$PrBa_2Cu_3O_{7-\delta}$ (PBCO) layer deposited by pulsed laser deposition at 790°C, 400 mTorr of O_2, at a fluence of 1.6 J/cm^2 at λ=248nm. Substrate are heated radiatively, and monitored by a thermocouple that is cross checked by an optical pyrometer prior to film growth. The PBCO layer is followed by a 20 nm YBCO layer deposited at 810°C, 200 mTorr of O_2, and 1.6 J/cm^2. The deposited bilayer is cooled *in situ* at 40°C/minute in a 500-650 Torr O_2 atmosphere from the growth temperature down to room temperature. Next 100 nm of Au is deposited *in situ* by DC magnetron sputtering in a 1 mTorr Ar atmosphere. The resulting trilayer structure is illustrated in Fig. 3a-i. Typical transition temperature (T_c) for these trilayers, as determined by AC susceptibility, is 83-86 K with a transition width of less than 2 K.

After the trilayer growth process, the substrate is mechanically removed from the Haines alloy plate. Photoresist (AZ5214) is spun onto the blank trilayers to a thickness of 1.5 μm and soft-baked at 95 °C for 2 minutes. The sintered Ag paste residue remaining from substrate mounting on the Haines plate is dry honed from the substrate with a razor, followed by swabbing with 100% HNO_3 and rinsing in water. The photoresist is then removed with acetone and the devices are rinsed in 100% ethanol and blow-dried with dry N_2.

The initial patterning of the PBCO/YBCO/Au trilayer into the antenna, RF filter, IF/DC contacts and bolometer microbridge is performed using optical contact lithography. Photoresist is spun onto the unpatterned trilayers to a thickness of 0.5 mm and soft-baked at 95°C for 2 minutes. The resist is exposed through a chrome contact mask and developed. The resist is soft-baked again at 95°C for 1 minute and ashed for 30 seconds in a 40 mTorr oxygen plasma in a Semi Group 1000TP reactive ion etch (RIE) tool at 120 watts, with a DC substrate self-bias of -320 volts [16]. The minimum feature size with good definition for this process is 1 μm.

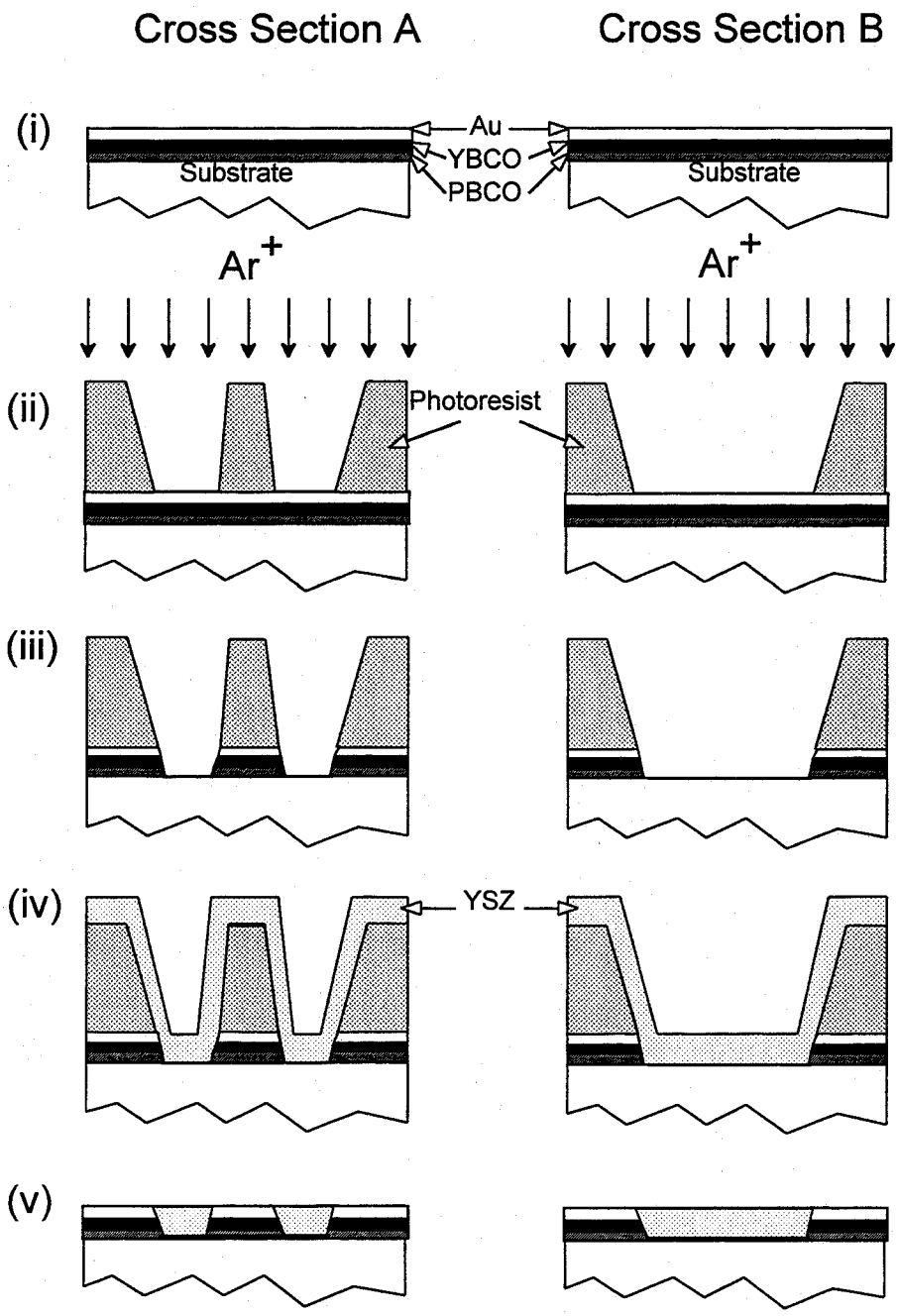

Figure 3a – First five process steps for cross sections A & B of the device in Fig. 1. The steps are described in the text.

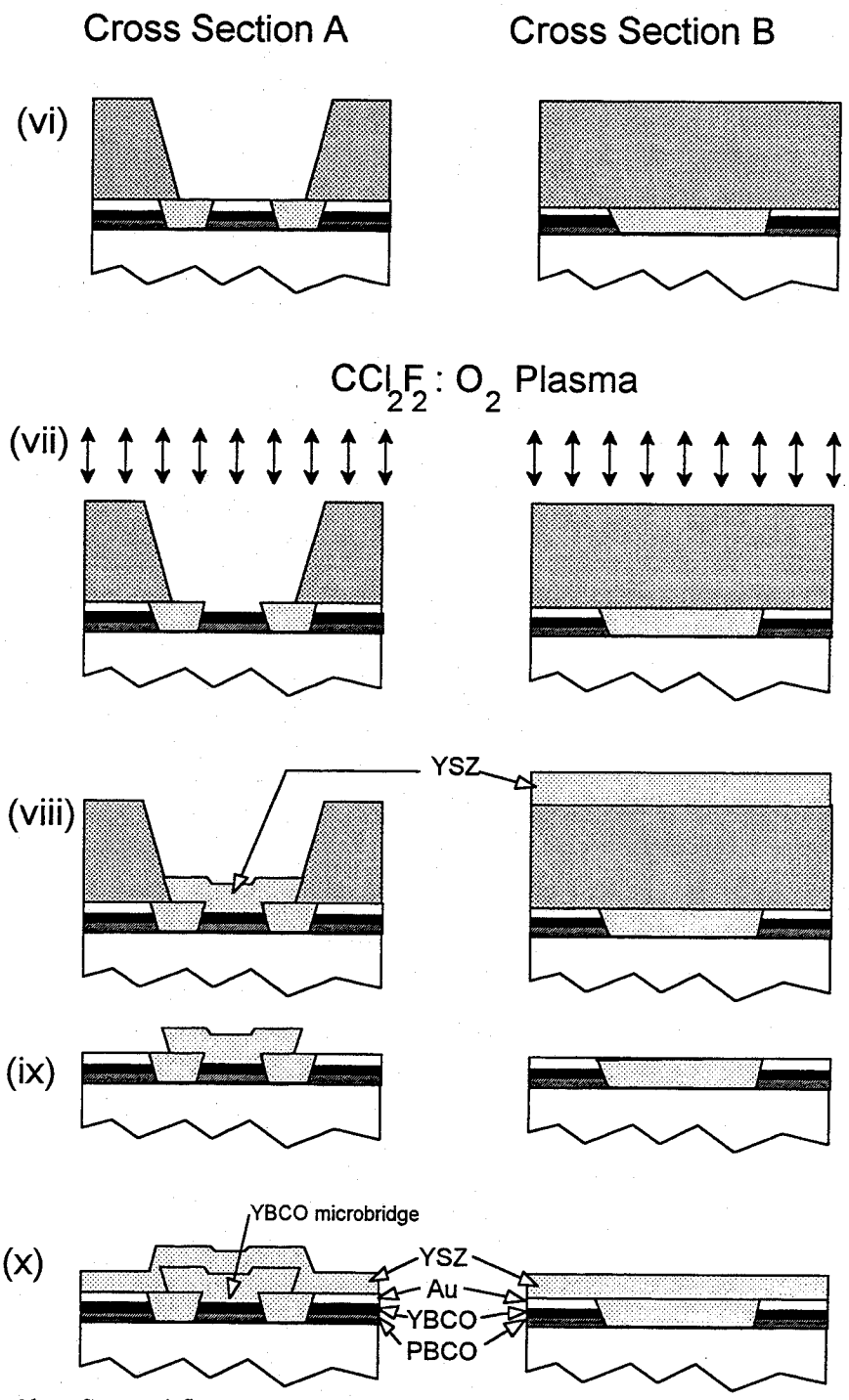

Figure 3b – Second five process steps for cross sections A & B of the device in Fig. 1. The steps are described in the text.

Next, the devices are placed into the load-lock of the deposition system in which an ion mill is located. The etching process uses normally incident 500 eV Ar^+ ions at 1 mA/cm^2 for 5 minutes (Fig. 3a-ii). The pressure is 2.0×10^{-4} Torr. The substrates are not cooled, however the temperature remains below 100 °C during the etching process and no polymerization of the photoresist is observed. The resulting layer structure is illustrated in Fig. 3a-iii.

After milling, the devices are transferred from the load-lock directly into the deposition system where 60 nm of YSZ is deposited at room temperature by pulsed laser deposition, resulting in the layer structure shown in Fig. 3a-iv.

The photoresist is then removed by ultrasonically cleaning the devices in acetone for 1-2 minutes. The devices are rinsed in 100% ethanol and blow dried with dry N_2. The first resist layer is thus used for two purposes, the process of patterning the antenna and feed structure, and for a self-aligned step of capping device side walls with a YSZ layer, resulting in the layer structure shown in Fig. 3a-v.

At this point in the process, another layer of photoresist is spun on the device to a thickness of 0.5μm, soft-baked, exposed, and developed using the procedure described above. The mask for this step opens a small window in the resist, exposing the 1 μm-wide bolometer bridge, which is still covered with 100 nm of Au as shown in Fig. 3b-vi. The device is then placed in the RIE system for the following procedure illustrated in Fig. 3b-vii: (1) Oxygen ashing for 5 minutes in a 200 mTorr oxygen plasma at 60 watts with approximately -80 self bias. (2) Etching for 50 minutes in a 200 mTorr 1:10 O_2:CCl_2F_2 plasma at 60 watts with approximately -20 volts self bias. The approximate Au removal rate is 2.5 nm/minute. We have found that over etching does not damage *c*-axis-oriented YBCO. (3) Oxygen ashed for 2 minutes in a 200 mTorr oxygen plasma at 30 watts with approximately -40 volts self bias. It should be noted that without the

YSZ side-wall coating covering the *a-b* plane edges of the YBCO layer, lines as wide as 50 μm are no longer superconducting after the Au RIE process, presumably due to chlorine being driven into the film along the *a-b* planes. With the YSZ side-wall coating, we have successfully used this 3-step Au removal process on 20 nm thick YBCO lines as narrow as 400 nm and maintained T_c above 80 K. Such a line test structure, and its superconducting transition are shown in Figure 4. However it should be noted that the yield on devices declines precipitously as the microbridge size drops below 3 μm^2.

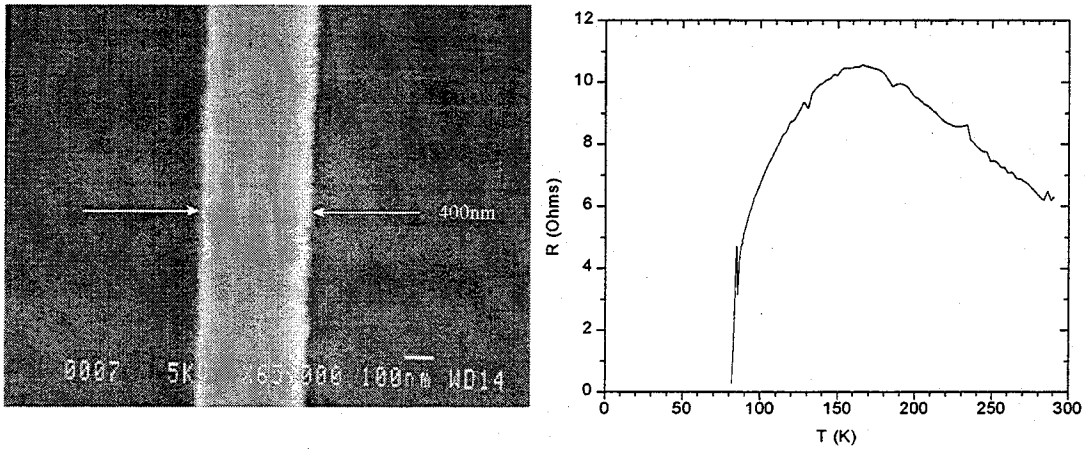

Figure 4 -- Narrow line (400nm wide) of 20nm thick YBCO after the Au removal process described in the text. Superconducting transition approximately 80K.

Next the devices are placed in the pulsed laser deposition system load-lock, pumped down and immediately transferred into the deposition chamber, where 100 nm of YSZ is deposited by pulsed laser deposition, filling in the area where the Au was just removed (Fig. 3b-viii). The total time from removal from the RIE to pumping down in the load lock is always less than 10 minutes, and typically less than 5 minutes. The photoresist is then removed by ultrasonically cleaning the devices in acetone for 1-2 minutes. The devices are rinsed in 100% ethanol

and blow dried with dry N_2. The resulting layer structure for the device after this process step is illustrated in Fig. 3b-ix.

The devices are next placed back into the deposition system where 100 nm of YSZ is deposited by pulsed laser deposition onto the entire substrate at room temperature. The resulting layer structure for the device after this final deposition step is illustrated in Fig. 3b-x.

Photoresist is next spun onto the 1x1cm^2 substrates (now containing 19 chips) to a thickness of 1.5 μm and soft-baked at 95 °C for 2 minutes. The substrates are mounted on a dicing saw and cut into individual chips. The photoresist is then removed with acetone and the devices are rinsed in 100% ethanol and blow dried with dry N_2. Photographs of a finished device in a twin-slot mixer is shown in Fig. 1, as is a simple microbridge with dc contacts in Fig. 2.

Electrical Tests

For DC device tests, individual die are mounted in 28-pin Keocera ceramic chip packages which plug into the bottom of a cryogenic dipping probe. Four wires are ultrasonically bonded to the YSZ-covered Au contacts. With proper settings, the wire bonds make contact through the nominally 100 nm thick YSZ over-layer. The wire bond connections are chosen in order to allow 4-terminal device measurements on the twin slot devices, eliminating resistance contributions from the probe and instrumentation wiring. The wire bond connections in the devices with dc contacts allow only 2-terminal measurements..

Resistance versus temperature measurements are taken using a computer controlled system. For some measurements, a Keithley 220 DC current source connected to two leads applies ±1 mA and the voltage response of the device under test is measured for both current polarities using an HP 3457A multimeter. The difference is used to eliminate contributions from thermally induced

voltages in the probe and instrumentation wiring. For other measurements a lock-in amplifier is used with a low frequency current source.

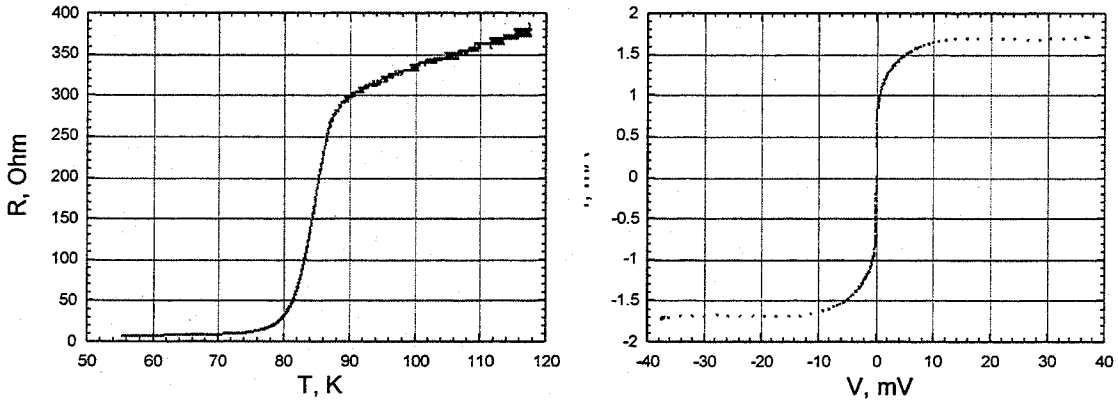

Figure 5 -- An R vs. T and a 77K I-V curve for a 1x1x0.02 μm^3 microbridge with dc contacts of the type shown in Fig. 2. The R vs. T curve includes the 10Ω lead resistance.

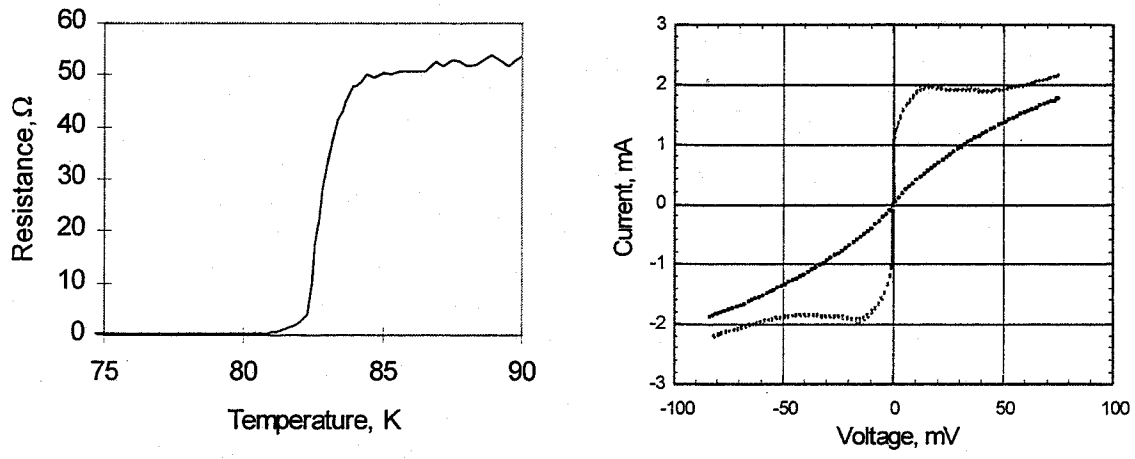

Figure 6 -- A R vs. T and an I-V curve with and without applied local oscillator power for a 1x1x0.02 μm^3 microbridge in a 2.5Thz twin slot antenna as shown in Fig. 1.

After processing, the microbridge T_c determined from the *R* vs. *T* data is generally 2-3K lower than the T_c of the initial trilayer film measured by AC susceptibility. The transition widths are also slightly broader. Fig. 5 shows *R* vs. *T* and a 77K I-V curve for a 1x1x0.02 μm^3 microbridge with dc contacts as shown in Fig 2. There is a baseline resistance of about 10 ohms from the probe wiring.

The samples are RF tested by mounting in an aluminum block and placed in an optical cryostat.[17] The 2.5 THz local oscillator consists of a methanol far-infrared laser, pumped by a λ=9.6μm CO_2 laser. *I-V* curves at 77 K, with and without applied local oscillator power (estimated power absorbed in the device is about 100 μW), are also shown in Fig 6. With the application of local oscillator power, the critical current of the microbridge at 77 K can be almost entirely suppressed from is initial value of approximately $5x10^6$ A/cm^2.

Conclusion

We have designed and fabricated superconducting hot-electron bolometers based on a recently developed model [10]. The devices utilize ultra-thin YBCO ($\leq$20 nm) films patterned into 1μm by 1μm microbridges and passivated with YSZ. These bridges maintain T_c on the order of 80 K and J_c's >$1x10^6 A/cm^2$ at 77 K. We have demonstrated that the devices were successfully coupled to a 2.5 THz local oscillator source when operated at 77 K.

Acknowledgments

The authors thank L.P. Lee, B. Bumble, H.G. LeDuc and D.B. Tanner for useful discussions, and H.M. Pickett and T.J. Crawford for the 2.5THz Fourier transform infrared spectrometer substrate measurements. The research described in this paper was performed by the Center for Space Microelectronics Technology, Jet Propulsion Laboratory, California Institute of Technology, and

was sponsored by the National Aeronautics and Space Administration, Office of Mission to Planet Earth, and the Office of Space Science.

References

[1] M. Bin. M.C. Gaidis, J. Zmuidzinas, T.G. Phillips, H.G. LeDuc, "Low-noise 1 THz niobium superconducting tunnel junction mixer with a normal-metal tuning circuit", *Appl. Phys. Lett.* ***68***, 1714 (1996)

[2] M. Bin. M.C. Gaidis, J. Zmuidzinas, T.G. Phillips, H.G. LeDuc, "THz SIS mixers with normal-metal Al tuning circuit", *Supercond. Sci. Tech.* ***9***, A136 (1996)

[3] E.M. Gershenzon, G.N. Gol'tsman, I.G. Gogidze, Y.P. Gusev, A.I. Elant'ev, B.S. Karasik and A.D. Semenov, "Millimeter and submillimeter range mixer based on electronic heating of superconducting films in the resistive state", *Sov. J. Supercond.* ***3,*** 1582 (1990)

[4] D.E. Prober, "Superconducting terahertz mixer using a transition-edge microbolometer," *Appl. Phys. Lett.* ***62***, 2119 (1993)

[5] A. Skalare, W.R. McGrath, B. Bumble, H. G. LeDuc, P.T. Burke, A.A. Verheijen, R.J. Schoelkpf, and D.E. Prober, "Large bandwidth and low-noise in a diffusion-cooled hot-electron bolometer mixer", *Appl. Phys. Lett.* ***68***, 1558 (1996)

[6] A. Skalare, W.R. McGrath, B. Bumble, and H. G. LeDuc, "Receiver measurements at 1267 GHz using a diffusion-cooled superconducting transition-edge bolometer", to appear in the Proceedings of the 1996 Applied Superconductivity Conference (*IEEE Trans. Appl. Superconductivity*)

[7] B. S. Karasik, M. C. Gaidis, W.R. McGrath, B. Bumble, and H. G. LeDuc, "A low-noise 2.5 THz superconductive Nb hot-electron mixer", to appear in the Proceedings of the 1996 Applied Superconductivity Conference (*IEEE Trans. Appl. Superconductivity*)

[8] V.A. Trifonov, B.S. Karasik, M.A. Zorin, G.N. Gol'tsman, E.M. Gershenzon, M. Lindgren, M. Danerud, D.M. Winkler, " 9.6mm wavelength mixing in a patterned $YBa_2Cu_3O_{7-\delta}$ thin film", *Appl. Phys. Lett.* ***68***, 1418 (1996)

[9] Yu. P. Gousev, A.D. Semenov, E.V. Pechen, A.V. Varlashkin, R.S. Nebosis, and K.F. Renk, "Coupling of terahertz radiation to a high-T_c superconducting hot electron bolometer mixer", *Appl. Phys. Lett.* ***69***, 1 (1996)

[10] B. S. Karasik, W.R. McGrath, and M. Gaidis, "Analysis of a high-T_c hot-electron superconducting mixer for terahertz applications", *J. Appl. Phys. 81, 1581 (1997).*

[11] G.L. Carr, M. Quijada, D.B. Tanner, C.J. Hishumugi, G.P. Williams, S. Estemand, B. Dutta, F. DeRosa, A. Inam, T. Venkatesan, and X. X. Xi, "Fast bolometric response by high-Tc detectors measured with subnanosecond synchrotron radiation", *Appl. Phys. Lett.* ***57***, 2725 (1990)

[12] N. Bluzer, "Temporal relaxation of nonequilibrium in Y-Ba-Cu-O measured from transient photoimpedance response" *Phys. Rev. B* ***44***, 10222 (1991)

[13] C.D. Marshall, I.M. Fishman, R.C. Dorfman, C.B. Eom, and M.D. Fayer, "Thermal diffusion, interfacial thermal barrier, and ultrasonic propagation in $YBa_2Cu_3O_{7-\delta}$ thin films: surface-selective transient-grating experiments", *Phys. Rev. B* ***45***, 10009 (1992)

[14] A.V. Sergeev, A.D. Semenov, P. Kouminov, V. Trifonov, I.G. Goghidze, B.S. Karasik, G.N. Gol'tsman, and E.M. Gershenzon, "Transparancy of a $YBa_2Cu_3O_{7-\delta}$-film/substrate interface for thermal phonons measured by means of voltage response to radiation", *Phys. Rev. B* ***49***, 9091 (1994)

[15] M. Danerud, D. Winkler, M. Lindgren, M. Zorin, V. Trifonov, B.S. Karasik, G.N. Gol'tsman, and E.M. Gershenzon, "Nonequilibrium and bolometric photoresponse in patterned YBa2Cu3O7-d thin films", *J. Appl. Phys.* ***76***, 1902 (1994)

[16] Reference herein to any specific commercial product, process, or service by trade name, trademark, manufacturer, or otherwise, does not constitute or imply its endorsement by the United States Government or the Jet Propulsion Laboratory, California Institute of Technology.

[17] B.S. Karasik, M.C. Gaidis, W.R. McGrath, M.J. Burns, and A.W. Kleinsasser, To be published.

Large bandwidth of NbN phonon-cooled hot-electron bolometer mixers on sapphire substrates.

S.Cherednichenko, P.Yagoubov, K.Il'in, G.Gol'tsman, and E.Gershenzon

Department of Physics, Moscow State Pedagogical University, Moscow 119435, Russia

ABSTRACT

The bandwidth of NbN phonon-cooled hot electron bolometer mixers has been systematically investigated with respect to the film thickness and film quality variation. The films, 2.5 to 10 nm thick, were fabricated on sapphire substrates using DC reactive magnetron sputtering. All devices consisted of several parallel strips, each 1 μ wide and 2 μ long, placed between Ti-Au contact pads. To measure the gain bandwidth we used two identical BWOs operating in the 120-140 GHz frequency range, one functioning as a local oscillator and the other as a signal source. The majority of the measurements were made at an ambient temperature of 4.5 K with optimal LO and DC bias. The maximum 3 dB bandwidth (about 4 GHz) was achieved for the devices made of films which were 2.5-3.5 nm thick, had a high critical temperature, and high critical current density. A theoretical analysis of bandwidth for these mixers based on the two-temperature model gives a good description of the experimental results if one assumes that the electron temperature is equal to the critical temperature.

INTRODUCTION

In recent years, significant advances have been made in the development of heterodyne receivers of a submillimeter waverange with a noise temperature approaching the quantum limit [1]. These receivers utilize Nb superconducting-insulator-superconducting (SIS) tunnel junction mixers. However, at frequencies higher than the energy gap for Nb (700 GHz) and especially higher than 1 THz the noise temperature grows drastically. Only Shottky diode mixers are used here, but they are much noisier and require a high local oscillator (LO) power.

Unlike direct detectors, conventional bolometers impose practically no restrictions as far as high frequencies are concerned, but these devices are slow and cannot be used as mixers. Although semiconducting hot-electron bolometers HEB (n-InSb) which appeared in the 60 s have a higher performance, they are still very far from being satisfactory for any major applications. The reason is that the intermediate frequency bandwidth (IF) is in this case limited to about 1 MHz. A substantial expansion of the bandwidth of the HEB mixers became possible when two-dimensional electron gas in GaAs/AlGaAs heterostructures were studied [2]. HEB mixers became much more promising after superconducting HEBs were developed [3]. In the devices of the latter type, when the electrons are phonon-cooled, the performance is in principle restricted by

the electron-phonon interaction time at a critical superconducting transition temperature $\tau_{eph}(T_c)$, which yields for an Nb mixer a bandwidth of about 500 MHz.

A further expansion of the bandwidth for this type of HEBs was made possible with the application of NbN, a superconducting material with a lesser time $\tau_{eph}(T_c)$=15 ps [4], which corresponds to about ~10 GHz mixer bandwidth. However, it is much more difficult to achieve a wide bandwidth for a HEB mixer than for a detector. To do so, ultrathin films with a high critical temperature T_c and critical current density j_c(4.2 K) must be available. The plane sizes have no impact whatever on the mixer bandwidth and can be randomly chosen to obtain the required values of the optimum LO power, dynamic range and impedance. As the NbN ultrathin film technology was developing, the HEB mixer bandwidth reached 1 GHz [5], then 2 GHz [6], and, finally, preliminary results were reported in [7] which included a bandwidth of 4 GHz accompanied by a low noise temperature at frequencies of 500-700 GHz and an optimal P_{LO} on the device ~1 μW.

Another way of achieving a wide bandwidth of hot-electron bolometer mixers, the out-diffusion of hot electrons into normal metal leads, was proposed in [8] and implemented in [9]. This method does not require any changes in the superconducting material, a thinner film, or a high critical temperature (a Nb film 10 nm thick with T_c=5 K proves to be quite satisfactory). However, very small in-plane sizes are a must: the length of the bridge should be as small as 0.08 μ for a 6 GHz bandwidth [10], which can be achieved using normal metal (100 nm thick Au) contacts and direct write e-beam lithography in a self-aligned process. Thus, for a diffusion-cooled HEB, the IF bandwidth appears to be connected with the LO power and the dynamic range of the mixer. For a 6 GHz bandwidth, P_{LO}=10 nW [10]. On the one hand, such a low value of LO power is an important issue at high submillimeter wave frequencies where LO power is difficult to generate. On the other hand, however, so small a dynamic range can be a problem since it can lead to an increase of a nonheterodyne response from thermal loading of the hot/cold loads [11].

In this paper we present the results of a systematic study of the bandwidth of phonon cooled NbN HEB mixer based on ultrathin films with high T_c and j_c (4.2 K) at a 140 GHz frequency.

EXPERIMENTAL

Ultrathin NbN films have been deposited on sapphire substrates by reactive dc magnetron sputtering in the Ar+N_2 gas mixture [12]. The maximum values of the critical film parameters (T_c and j_c) are reached at the discharge current value of 300 mA, the partial N_2 pressure of $1.7 \cdot 10^{-4}$ mbar and the substrate temperature 850°C. The Ar pressure proved to have no substantial effect on the film deposition rate or film composition. For this reason, the pressure level was chosen in such a way as to maintain a stable discharge, namely $4.5 \cdot 10^{-3}$ mbar. The deposition rate was 0.5 nm/s. It was

defined as a ratio of the film thickness, measured with a Talystep profilometer/profilograph, and its deposition time.

Fig. 1 gives the values of the critical temperature for the NbN film batch used in this work. The film thickness varies between 2.5 and 10 nm (Table 1). The thinnest films (2.5 nm thick) had T_c about 8.5 K and the transition width of about ~1.2 K. In the specified thickness range the sheet resistance of the films varied between 1000 and 70 Ohm/□, whereas the average resistivity was 150 μOhm•cm. The changes of these parameters during further contact metallization, ion milling and sputtering processes were insignificant.

Geometrically, NbN films in HEB mixers are several parallel strips 1 μ wide which are spaced 1 μ. For patterning, photolithography followed by ion milling was used. The strips were placed between Ti-Au contact pads 2-3 μ apart from each other. The number of NbN strips varied between 1 and 16 depending on the film thickness, to ensure that the normal state bolometer resistance stayed within the 200-300 Ohm range.

The experimental device was mounted on a waveguide flange, as shown on Fig. 2. The setup used for bandwidth measurements is presented in Fig. 3. Two backward wave oscillators (BWO) operating at 120-145 GHz were used as local oscillator and signal sources. The LO and signal radiation were coupled by a beam splitter and a beamguide into the cryostat. Two attenuators included in the quasioptical path line allowed to adjust the signal and LO power, and to maintain an optimum LO power during the retuning. The IF signal received from the mixer was amplified by a room temperature wideband amplifier (0.1-4 GHz) and was sent to the input of the spectrum analyzer.

The results of the investigations of the bandwidth of NbN HEB mixers are presented in Fig. 4-8. The data obtained under quasi-equilibrium conditions at $T \approx T_c$. allow the simplest interpretation and are at the same time quite informative of the physical processes responsible for the bandwidth. To obtain these data, low LO and dc powers were chosen: they were much lower than those optimal for mixing. In fact, a HEB mixer is functioning under these conditions as a direct detector for LO and signal beating oscillations. The results of these experiments demonstrate (Fig. 4) that the cut-off frequency is, respectively, 1.2 GHz, 2.8 GHz and 3.3 GHz for NbN mixer film thickness 10 nm, 5 nm and 4 nm. For thinner films, the cut-off frequency is approaching, or even exceeding, the upper limit of the measured frequency range (4 GHz).

The bandwidth of NbN HEB mixers in the optimal operating point at low temperature is often narrower than at $T \approx T_c$. The data for five mixers at T=4.5 K are given in Fig. 5. It can be seen that the bandwidth is growing as the films get thinner. However, practically no growth is observable for the thinnest films. It must be noted that the obtained bandwidth values for mixers made of thin films (d=2.5-3.5 nm) are only valid for high quality films. For films of a comparatively poor quality that had lower values of the critical temperature (T_c) and the critical current density (j_c) at T=4.2 K, the bandwidth is narrower than for quality films of the same thickness

(Fig. 6). At the same time, the data on the wide mixer bandwidth obtained at the 140 GHz frequency are fully confirmed by the measurements done at higher frequencies (660 GHz). In the latter experiments (Fig. 7) a quasi-optical mixer was used, which was made of a spiral antenna-coupled NbN HEB on a sapphire substrate. The results of bandwidth measurements of NbN HEB mixers on sapphire substrates are summarized in Fig. 8.

DISCUSSION

As was already mentioned, the results of bandwidth measurements taken at $T \approx T_c$ and P_{LO} and P_{dc} values much lower than those optimally required for the mixer are the simplest to interpret. Under these (quasi-equilibrium) conditions, the exact value of the electron temperature $\Theta=T=T_c$ is known, so one can be certain that the value of the self-heating parameter $C = I^2 \frac{\partial R/\partial\Theta}{c_e V}\tau_\Theta << 1$ (I is the bias current, c_e is the electron specific heat, V is the volume of the mixer, $\tau_\Theta = \tau_{eph} + \frac{c_e}{c_{ph}}\tau_{es}$ is the electron temperature relaxation time, where c_{ph} is the phonon specific heat and τ_{es} is the phonon escape time). The latter fact allows to disregard a possible effect of the frequency dependence of mixer impedance in the intermediate frequency range close to $f \approx 1/2\pi\tau_\Theta$ as well as the feedback effect in the bias circuit [13]. For this reason, it is quite easy to calculate the frequency dependence of the amplitude of the variable constituent of the electron temperature $\Delta\Theta_{IF}(f)$ and hence the proportional IF voltage on the device within the two-temperature model [14]

$$U_{IF}(f) \sim \Delta\Theta_{IF}(f) = \frac{\Delta\Theta(0)(1+j\omega\tau_0)}{(1+j\omega\tau_1)(1+j\omega\tau_2)}, \qquad (1)$$

where $\tau_0^{-1} = \tau_{es}^{-1} + \tau_{eph}^{-1} c_e/c_{ph}$,

$$\tau_{1,2}^{-1} = \frac{\tau_{es}^{-1} + \tau_{eph}^{-1}(c_e/c_{ph}+1)}{2}\left[1 \pm \sqrt{1 - 4\frac{\left(\tau_{es}^{-1} + \tau_{eph}^{-1}(c_e/c_{ph}+1)\right)^2}{\tau_{es}\tau_{eph}}}\right],$$

$\tau_{es}=13$ ps•d(nm) (see below), $\tau_{eph}=5\cdot10^2\cdot T^{-1.6}$ ps [4], $c_e=1.6\cdot10^{-4}\cdot T$ J/cm²•K [15], $c_{ph}=9.8\cdot10^{-6}\cdot T^3$ J/cm²•K [15].

For the thinnest NbN films used (d=2.5 nm), the escape time of the nonequilibrium phonons from the film into the substrate τ_{es} is much shorter than the time of their reabsorption by the electrons $\tau_{phe} = \tau_{eph}\frac{c_{ph}}{c_e}$. In this case the mixer bandwidth could be described by a single time constant τ_{eph} in a relatively simple hot electron model. However, for the thickest films used (d=10 nm) , the τ_{es} and τ_{phe} times are close to each other and such a simplification would be too rough. As well be seen from the analysis

given below, the NbN films 3-3.5 nm thick which are now used to make practically operating HEB mixers also require that not only the electron but also the phonon heating should be considered, which means that the calculations must be carried out according to formulas (1).

Thorough experiments of bandwidth measurements and the comparison with the calculated data showed a very good correlation when the known τ_{eph}, c_e and c_{ph} values were used [15], but the τ_{es} value was somewhat different from that quoted in [15] for NbN films on sapphire. So, the curves 1-3 in Fig. 4 are produced according to (1) using τ_{es}=13 ps•d(nm), while [15] quotes τ_{es}=8 ps•d(nm). We believe that the difference is explained by more precise measuring of NbN film thickness in the present work.

We shall start the discussion of the results of the study of the NbN HEB in the optimum operating point at T=4.5 K with the mixers № 11 and 4 made of NbN films having 3.0-3.5 nm thick. The films of this quality and thickness seem to be a matter of the keenest practical interest. They have been used in HEB mixers studied in [7, 16]. It should be noted that the comparison of the bandwidth measurement results in the optimum operating point at frequencies of 140 and 660 GHz (Fig. 7) shows their full coincidence. Even though this result could be expected theoretically, it is nonetheless important because it demonstrates the practical applicability of the results obtained in the present work to terahertz range mixers. To compare the relative conversion gain vs intermediate frequency dependency with that theoretically calculated (Fig. 5) one needs to know the electron temperature value at the optimal point of the mixers. It can be defined by superimposing the IV curve under the optimal LO power on a set of IV curves derived for various ambient temperatures without a LO power. As can be seen in Fig. 9, a good correspondence may be obtained for the IV curve at T=10 K. Taking into account that Joule power $P_{dc}=I_0 \cdot V_0$, we can calculate an additional heating in the operating point ΔT_{dc}=0.5 K. The ultimate calculation of the electron temperature value in the operating point is Θ=10.5 K.

This Θ value can be now used to calculate the relative conversion gain vs intermediate frequency. The result gives a good description of the experimental data for this mixer. For other mixers, the above procedure of comparing IV curves was not applied, so the remaining curves are obtained by adjusting the calculations according to formulas (1) to the experimental data.

It is worthy of note that the high quality of the films and, specifically, the high critical temperature T_c and the high critical current density j_c(4.2 K), along with the small thickness, is a necessary condition to ensure that the phonon-cooled HEB mixers have a wide bandwidth. This is illustrated by Fig. 6 where data are presented for three mixers with the same NbN film thickness (d=3.0-3.5 nm). The № 4 mixer has high T_c and j_c values while the other two have lower values. It can be seen that the bandwidth of the latter two mixers is almost twice as narrow as that of the former mixer, this corresponds to the electron temperature Θ=5.5-5.7 K. This value is much lower than the

T_c for these mixers. This fact may be accounted for by a uniformity of the NbN films used to manufacture the mixers.

Such NbN films (with lower T_c and j_c) usually have a granular structure with weak intergranular links, and the superconducting transition shows a "tail" at low temperatures. The critical current density of such films is lower than that of the homogeneous films. When the current flow is higher than the critical current, these films develop a resistance, which is due to the transition to the normal state of those granular areas which are close to weak links because the superconductivity is substantially suppressed in such areas. When the current is growing, this resistance may be high enough, even though the value of the current itself is essentially lower that for HEB mixers made from high quality films. A substantial part of the LO power cannot be applied to HEB mixers produced from granular films, either. The reason is that with the growth of the electron temperature j_c drops even more and the resistance growth is observed with a still lower current value. The bandwidth of such a mixer is comparatively narrow and corresponds to the electron temperature Θ, which is much lower then T_c (see Fig. 6). As the films become more homogenous, the "tail" in the temperature dependence curve of the resistance is reducing and, most importantly, the critical current density is growing. For the best NbN films used in this work to produce HEB mixers, j_c(4.2 K) reaches the value of $4 \cdot 10^6$ A/cm^2 at d=3.5 nm , while the resistance drops almost to zero and keeps very close to T_c. Such uniform films lack granular structure with weak links, so the value of the critical current is defined by vortex tear-off from pinning centers. The resistance generated in such conditions at a low T brings an overheating and the film is divided into thermal domains in which Θ is much greater than T and is close to T_c. This corresponds to an unstable IV-curves area (Fig. 9), so the current drops while remaining practically the same when the voltage continues to grow (see Fig. 9). The absorption of a sufficiently high LO power heats the electron subsystem substantially, the IV curves become smooth and the film resistance is accounted for by a uniform viscous vortex flow. In this IV-curve the critical current is much lower, hence the optimal bias current of the mixer is also lower. It is however true, within a certain limit, that the higher the critical current for the unpumped device, the larger the value of the optimal P_{LO}, the closer to T_c is the electron temperature under the optimum conditions of the mixer and the wider the operating IF bandwidth.

This can be illustrated by Fig. 8, which summarizes the measurement data and gives a dependency curve of 3 dB bandwidth calculation, which was produced using frequency dependencies (1). When calculating this curve, we assumed that the electron temperature Θ was equal to T_c, and experimentally determined the dependency of the latter value on film thickness (Fig. 1). It is only natural that the data on the bandwidth given in Fig. 4 very well agree with the curve. However, the mixer bandwidth measured in the optimal operating point at T=4.5 K does not always correspond to the curve. For example, the mixers № 1, 4 and 11 we obtain bandwidth values which are close to those

calculated. These mixers were produced from ultrathin high quality films. Mixers № 2 and 3 show a slightly narrower bandwidth. It could be observed (see Table 1) that the T_c and j_c for these mixers can be only a trifle lower than for mixers № 4 and 11. As shown in the above discussion, however, the difference is great for mixers № 12 and 13.

Mixers № 5-10, which were made of films 4-10 nm thick, deserve a special consideration. The experimental data show (Fig. 5, 8) that as the thickness is growing the systematic deviation of the measured mixer bandwidth in the optimal operating point at T=4.5 K from that predicted is getting all the greater (see the curve in Fig. 8). For the calculated frequency dependencies in Fig. 5 this fact is interpreted as a lowering of the electron temperature in the optimal point with the film thickness growth.

However, this additional bandwidth narrowing may be accounted for by other reasons. A possible reason is a dependence of the HEB mixer impedance on the frequency, which has so far not been taken into account at all. The most significant changes of the impedance module and phase, however, are occurred just in the frequency range close to the upper frequency boundary of the 3 dB bandwidth. These changes can have an impact on the results of the frequency measurement. In the present work, we did not measure the impedance and so are unable to offer any experimentally based conclusions as to how great such an impact could be.

Another possible reason of the disagreement between the experimental and the calculated result is self-heating of the mixer due to a feedback in the dc circuit. This phenomena is reflected in particular in the formula for the HEB mixer bandwidth

$$\Delta B_m = \Delta B\left(1 + C\frac{R - R_L}{R + R_L}\right)$$

where ΔB - is the 3 dB bandwidth calculated from frequency dependencies (1). A characteristic feature of the effect is that depending on the R_L/R ratio the mixer bandwidth can be narrower or wider than ΔB. This should become essential when the self-heating parameter C is getting closer to 1. In the experiments, however, when the operating point was shifted along the optimal IV-curve, no change in mixer bandwidth was observed. This may be due to the fact that the values of C do not approach 1 at any point and that $\Delta B_m = \Delta B$.

ACKNOWLEDGMENTS

This work has been supported by Russian Program on Condensed Matter (Superconductivity Division) under Grant № 93169. The authors wish to thank B.M. Voronov for his assistance in the fabrication of the devices.

REFERENCES

[1] J.Carlstrom and J.Zmuidzinas "Millimeter and Submillimeter Techniques", in "Review of Radio Science 1993-1995", ed. W.R.Stone, Oxford, The Oxford University Press, 1996.

[2] J.X.Yang, F.Agahi, D.Dai, C.Musante, W.Grammer, K.M.Lau, and K.S.Yngvesson, IEEE Trans. Microwave Theory Tech. **MTT-41**, 581, (1993).

[3] E.M.Gershenzon, G.N.Gol'tsman, I.G.Gogidze, Yu.P.Gousev, A.I.Elant'ev, B.S.Karasik, and A.D.Semenov, Sov. J.Superconductivity **3**, 1582 (1990).

[4] Yu.P.Gousev, G.N.Gol'tsman, A.D.Semenov, E.M.Gershenzon, R.S.Nebosis, M.A.Heusinger, and K.F.Renk, "Broadband Ultrafast Superconducting NbN Detector for Electromagnetic Radiation", J.Appl.Phys., **75**, 7, 3695 (1994).

[5] G.N.Gol'tsman, B.S.Karasik, O.V.Okunev, A.L.Dzardanov, E.M.Gershenzon, H.Ekstrom, S.Jacobsson, E.Kollberg. "NbN Hot Electron Superconducting Mixers for 100 GHz Operation." IEEE Transactions on Applied Superconductivity, **5**, 2, 3065 (1995).

[6] O.Okunev. A.Dzardanov, G.Gol'tsman, and E.Gershenzon. "Performances of Hot-electron Superconducting Mixer for Frequencies Less Than the Gap Energy: NbN Mixer for 100 GHz Operation." Proc. of the 6th Int. Symp. on Space Terahertz Tech., Caltech, Pasadena, 247, (1995),

[7] P.Yagoubov, G.Gol'tsman, B.Voronov, S.Svechnikov, S.Cherednichenko, E.Gershenzon, V.Belitsky, H.Ekstrom, E.Kollberg, A.Semenov, Yu.Gousev, K.Renk, "Quasioptical phonon-cooled NbN hot-electron bolometer mixer at THz frequencies", Proc. of the 7th Int. Symp. on Space Terahertz Tech., Charlottesville, VA, 303, (1996),

[8] D.E.Prober, "Superconducting terahertz mixer using a transition-edge microbolometer", Appl. Phys. Lett. **62**, 17, 2119, (1993).

[9] A.Scalare, W.R.McGrath, B.Bumble, H.G.LeDuc, P.J.Burke, A.A.Verheijen, R.J.Schoelkopf, and D.E.Prober, "Large bandwidth and low noise in a diffusion-cooled hot-electron bolometer mixer", Appl. Phys. Lett. **68**, 11, 1558, (1996).

[10] P.J.Burke, R.J.Schoelkopf, D.E.Prober, A.Scalare, W.R.McGrath, B.Bumble, and H.G.LeDuc, "Length scaling of bandwidth and noise in hot-electron superconducting mixers", Appl. Phys. Lett. **68**, 23, 3344, (1996).

[11] A.Scalare, W.R.McGrath, B.Bumble, H.G.LeDuc, "Receiver Measurements at 1267 GHz using a Diffusion-Cooled Superconducting Transition-Edge Bolometer", presented at ASC, Pittsburgh, 1996. To appear in IEEE Transactions on Applied Superconductivity 1997.

[12] P.Yagoubov, G.Gol'tsman, B.Voronov, L.Seidman, V.Siomash, S.Cherednichenko, and E.Gershenzon, "The bandwidth of HEB mixers employing ultrathin NbN films on sapphire substrate", Proc. of the 7th Int. Symp. on Space Terahertz Tech., Charlottesville, VA, 290, (1996),

[13] B.S.Karasik and A.I.Elant'ev, "Analysis of the Noise Performance of a Hot-Electron Superconducting Bolometer Mixer", Appl. Phys. Lett. **68**, 853, (1996).

[14] N.Perrin and C.Vanneste, "Response of superconducting films to a periodic optical irradiation", Phys. Rev. B**28**, 5150, (1983).

[15] A.D.Semenov, R.S.Nebosis, Yu.P.Gousev, M.A.Heusinger, and K.F.Renk", Phys. Rev. B**52**, 581, (1995).

[16] H.Ekstrom, E.Kollberg, P.Yagoubov, G.Gol'tsman, E.Gershenzon, S.Yngvesson, "Gain and noise bandwidth of NbN hot-electron bolometric mixers", submitted to Appl. Phys. Lett., (1997).

Table 1. Critical temperature T_c, critical current density at T=4.2 K j_c(4.2 K), film thickness d and 3 dB bandwidth for NbN HEB mixers ΔB.

	T_c, K	j_c(4.2 K), A/cm^2	d, nm	ΔB, GHz
1	8.5	$9.3 \cdot 10^5$	2.5	4
2	9.2	$1.0 \cdot 10^6$	3.0	3
3	9.8	$1.8 \cdot 10^6$	3.5	3
4	10.2	$1.1 \cdot 10^6$	3.5	3.5
5	10.3	$2.1 \cdot 10^6$	4	2.7
6	10.4	$1.6 \cdot 10^6$	4	2.5
7	11.8	$4.1 \cdot 10^6$	5	1.9
8	11.8	$3.9 \cdot 10^6$	5	1.8
9	14.2	$6.5 \cdot 10^6$	10	0.9
10	14.2	$1.3 \cdot 10^6$	10	0.9
11	11	$3.9 \cdot 10^6$	3.5	3.5
12	8.5	$7.0 \cdot 10^5$	3.5	1.8
13	8.5	$5.0 \cdot 10^5$	3.5	1.9

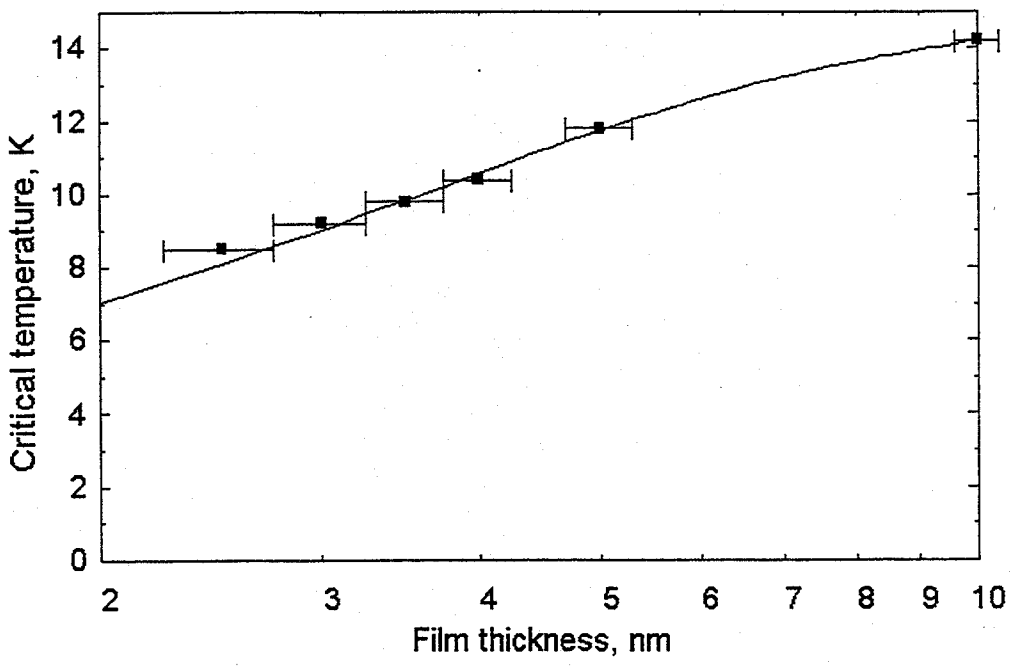

Fig. 1 Critical temperature vs film thickness (devices # 1, 2, 3, 6, 7, 9). The solid line is the typical T_c(d) dependence for our films.

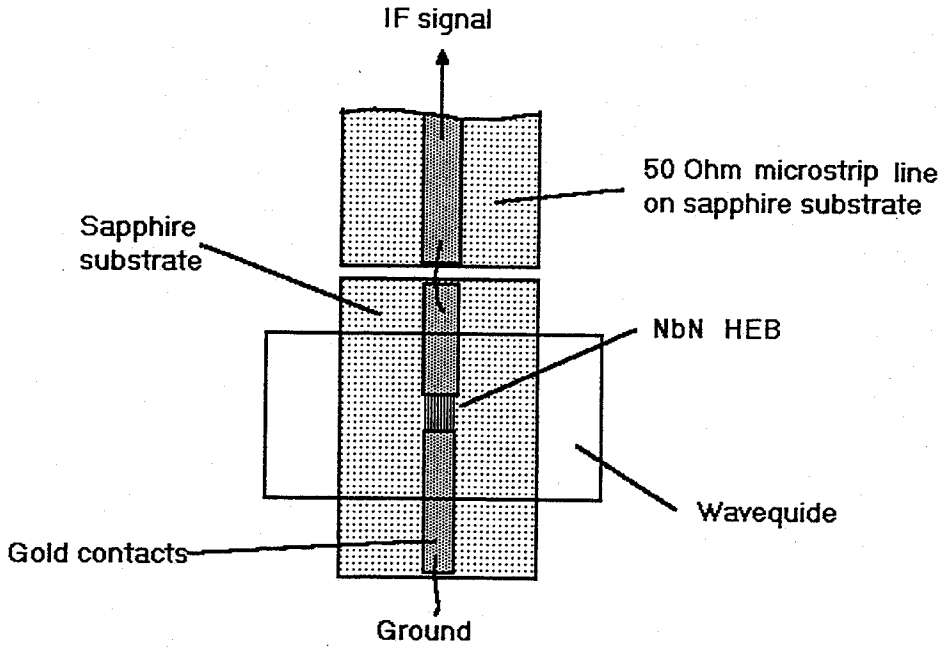

Fig. 2 View of the mixer chip on the waveguide flange.

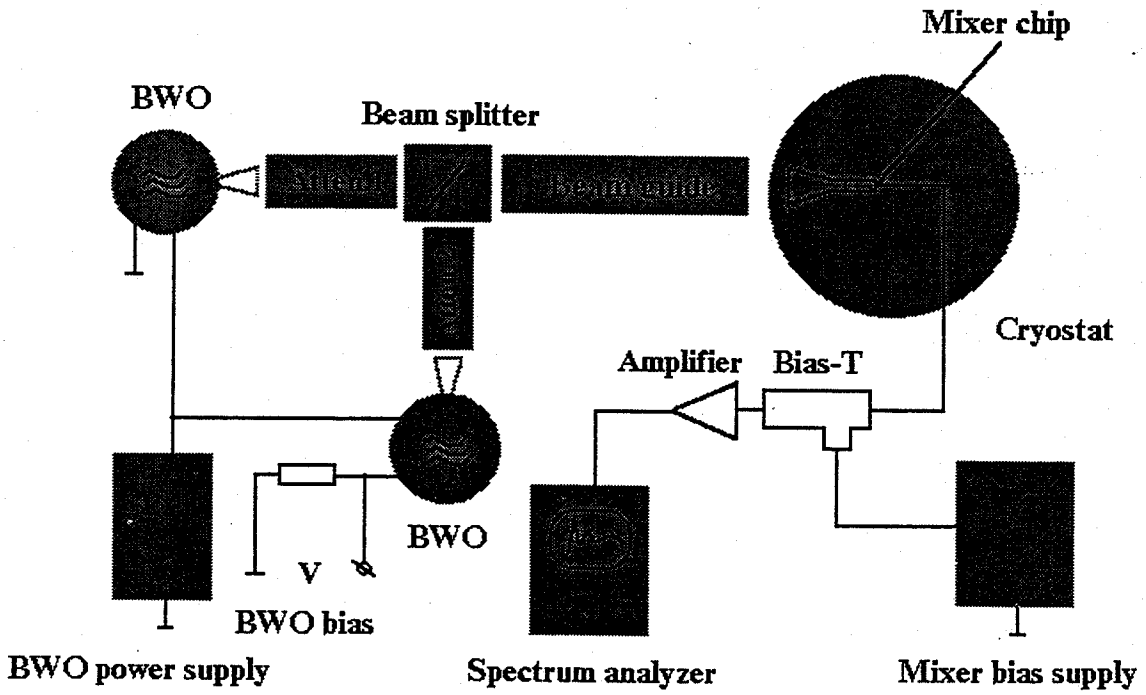

Fig. 3 Set-up for bandwidth measurements.

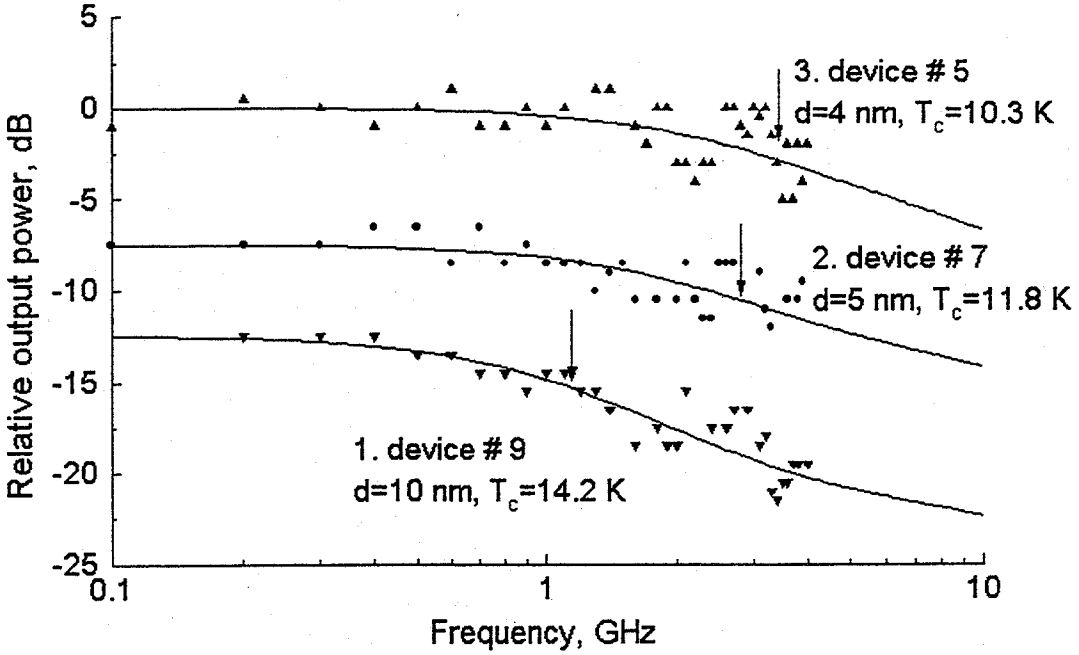

Fig. 4 Relative output power for devices # 5, 7, 9 measured at $T=T_c$ (points) and calculated for $\Theta=T_c$ (solid line). The arrows show 3 dB cut-off frequencies.

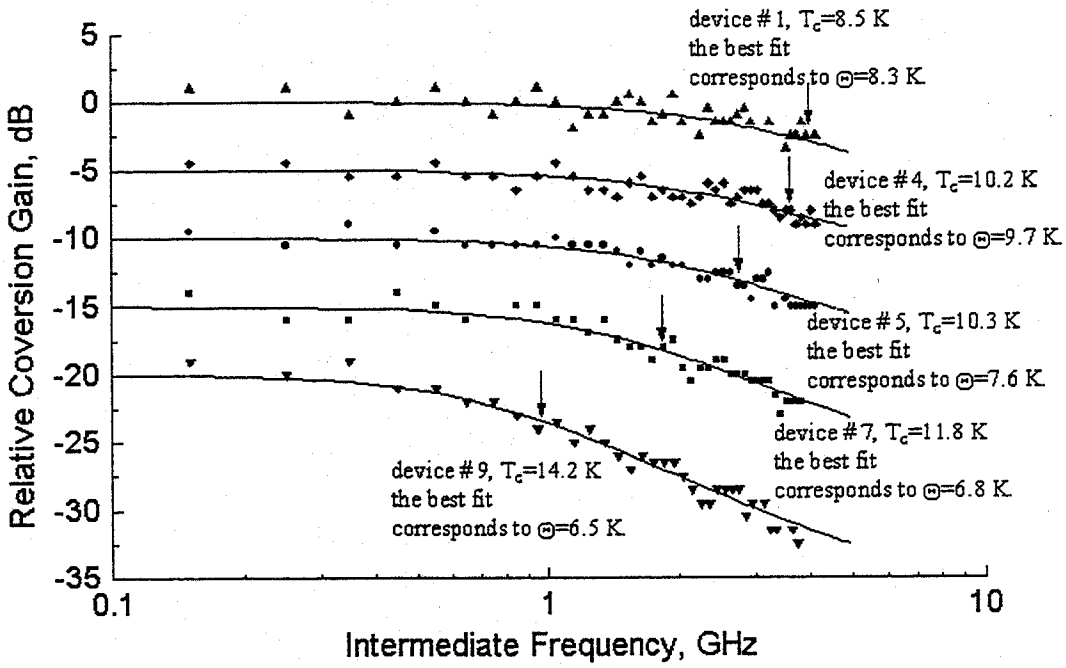

Fig. 5 Relative conversion gain for devices # 1, 4, 5, 7, 9 measured at T=4.5 K under optimal LO and dc bias; the arrows show 3 dB cut-off frequencies.

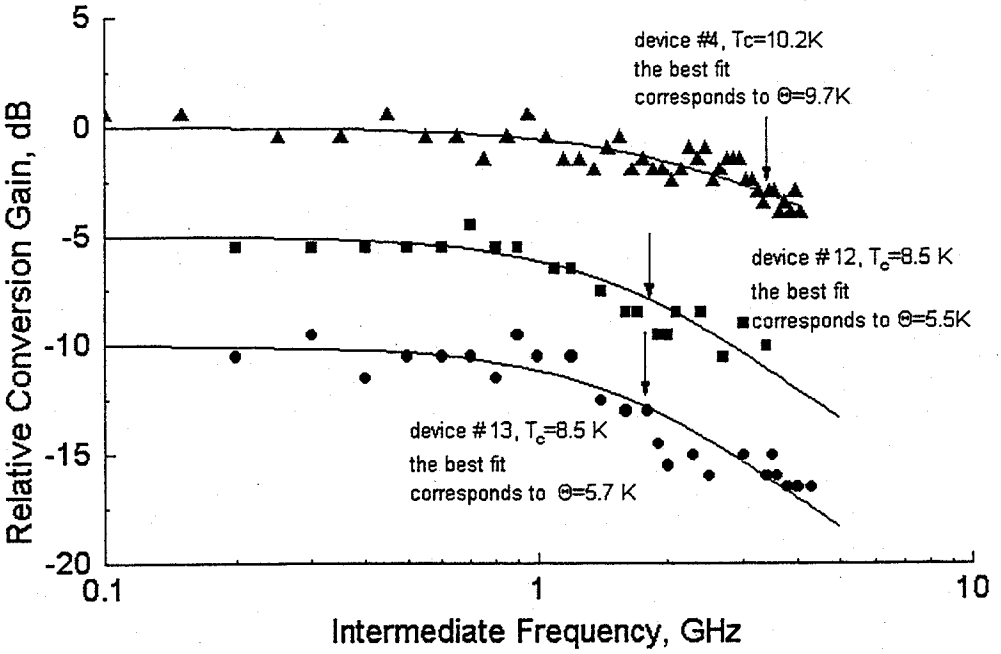

Fig. 6 Relative conversion gain for devices # 4, 12, 13 measured at T=4.5 K under optimal LO and dc bias; the arrows show 3 dB cut-off frequencies.

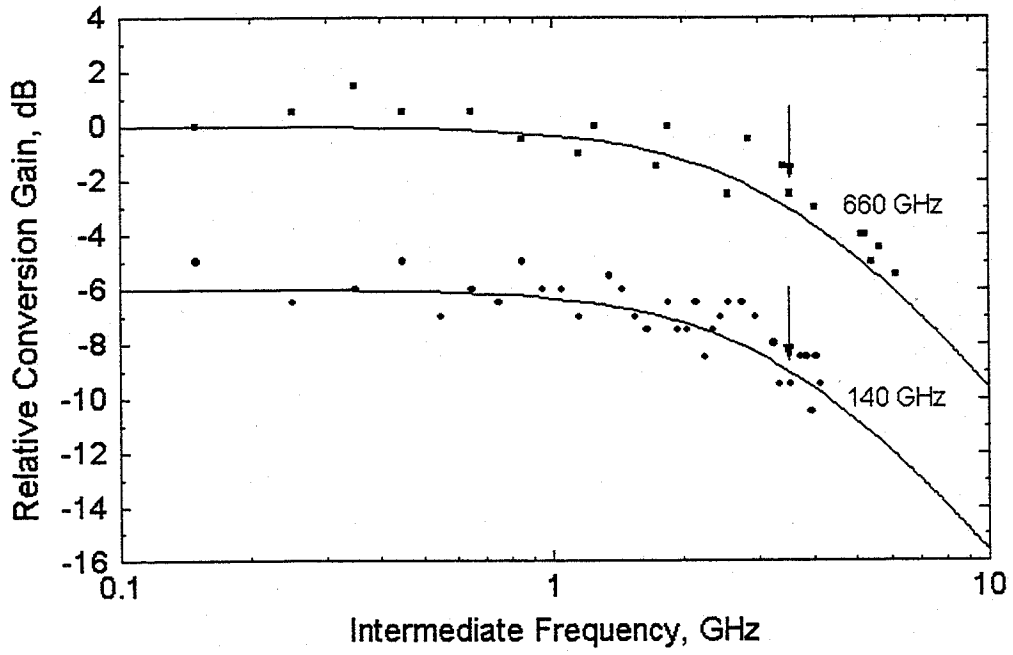

Fig. 7 Relative conversion gain for device # 11 measured at 140 and 660 GHz under optimal LO and dc bias.

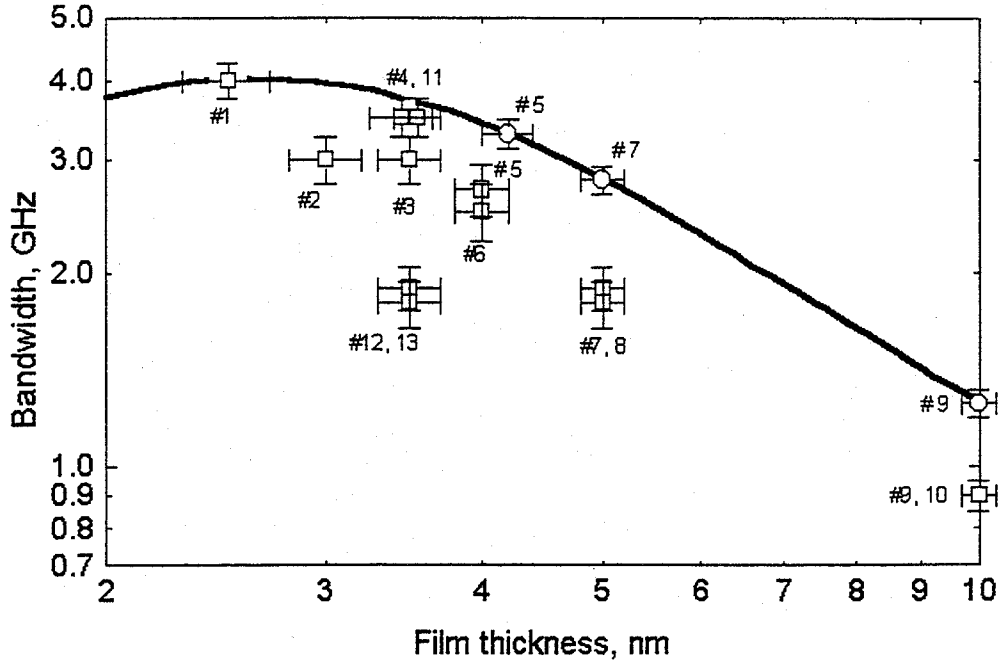

Fig. 8 3 dB bandwidth vs film thickness calculated taking into account $T_c(d)$ dependence typical for our films and experimental results for all devices at T=4.5 K, optimal P_{LO} and P_{dc} □; for three devices at $T=T_c$, small P_{LO} and P_{dc} ○.

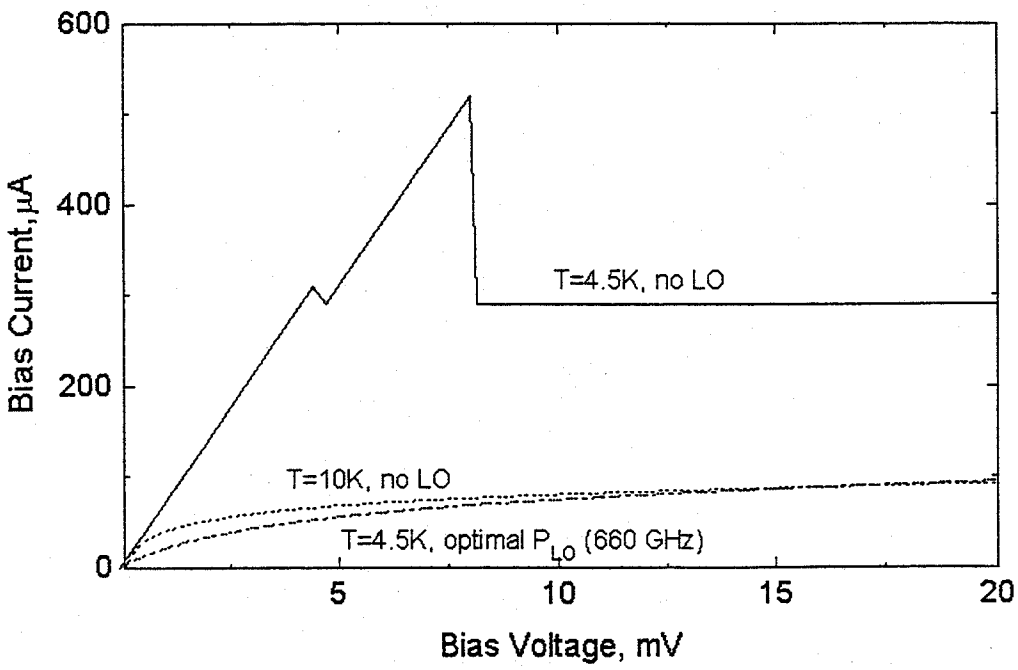

Fig. 9 IV-curves for device # 11.

NbN HOT ELECTRON BOLOMETRIC MIXER FOR 2.5 THz: THE PHONON COOLED VERSION

E. GERECHT, C. F. MUSANTE, Z. WANG, AND K. S. YNGVESSON

Department of Electrical and Computer Engineering, University of Massachusetts, Amherst, MA 01003

J. WALDMAN

Submillimeter Technology Laboratory, University of Massachusetts at Lowell Research Foundation, Lowell, MA 01854

G. N. GOLTS'MAN, P. A. YAGOUBOV, S. I. SVECHNIKOV,

B. M. VORONOV, S. I. CHEREDNICHENKO, AND E. M. GERSHENZON

Department of Physics, Moscow State Pedagogical University, Moscow, Russia

ABSTRACT

We describe an investigation of a NbN HEB mixer for 2.5 THz. NbN HEBs are phonon-cooled devices which are expected, according to theory, to achieve up to 10 GHz IF conversion gain bandwidth. We have developed an antenna coupled device using a log-periodic antenna and a silicon lens. We have demonstrated that sufficient LO power can be coupled to the device in order to bring it to the optimum mixer operating point. The LO power required is less than 1 microwatts as measured directly at the device. We also describe the impedance characteristics of NbN devices and compare them with theory. The experimental results agree with theory except for the imaginary part of the impedance at very low frequencies as was demonstrated by other groups.

I. INTRODUCTION

NbN Hot Electron Bolometric (HEB) mixers represent a promising approach for achieving receiver noise temperatures of a few times the quantum noise limit at frequencies above 1 THz. These HEB mixers have so far demonstrated a DSB noise temperature as low as 500 K at 630 GHz [1] and 1140 at 870

GHz [2]. Figure 1. shows receiver noise temperatures for existing receivers and also predicted performance of HEBs which are currently under development. The conversion loss and intrinsic noise temperature of HEB mixers are expected to be essentially independent of frequency, up to at least several THz, and thus noise temperatures of about 1000 K or less can be expected for these frequencies. NbN HEB mixers have been shown to have sufficient bandwidths for the anticipated applications such as future receiver frontends for THz astronomical observation from space. Note that HEB theory predicts that the receiver noise bandwidth should be wider than the conversion gain bandwidth. A receiver noise bandwidth of 5 GHz and a conversion gain bandwidth of 3 GHz were measured by [3]. The LO power required is less than one microwatt which can be further decreased by reducing the active area of the device. The power level required by NbN HEB mixers make them suitable for use with future solid state tunable THz sources [4]. However, the LO power is not at the level to cause the device to saturate by thermal radiation which is a problem with some diffusion cooled HEB mixers. The main problems remaining to be solved before THz NbN HEB mixers are

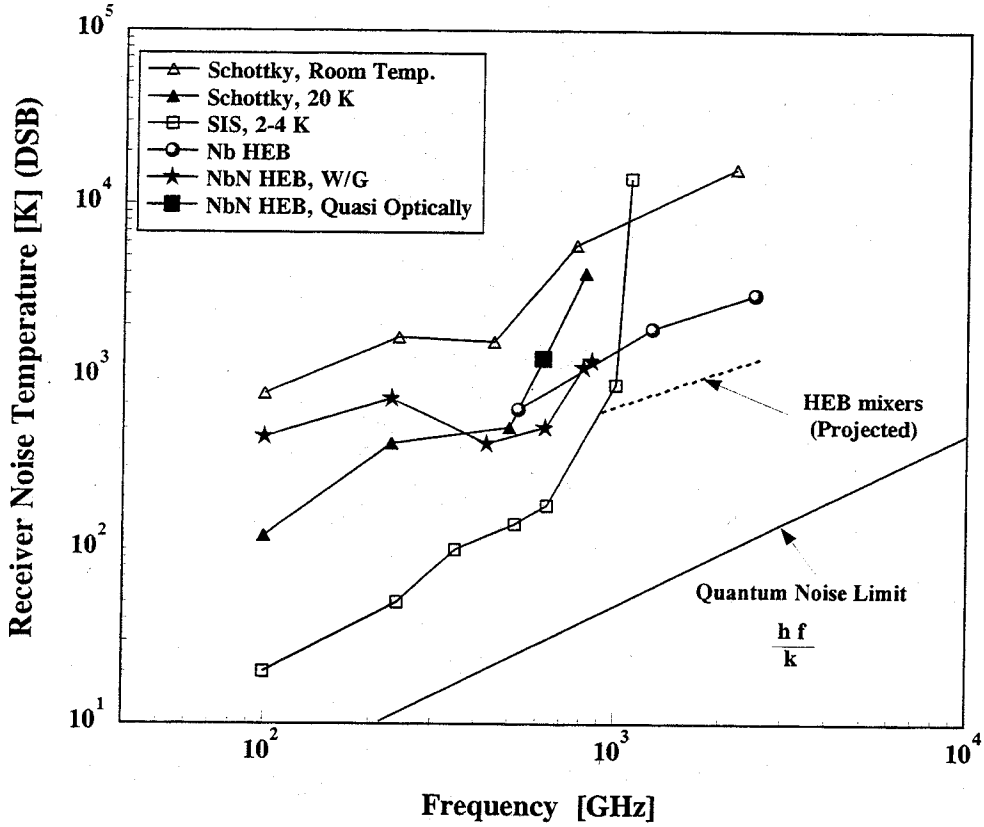

Figure 1: Receiver noise temperature for receivers in the THz frequency range.

ready for use in practical applications are (i) efficient optical coupling to the device, (ii) further investigation of the properties of very thin NbN films which are required to maximize the bandwidth performance, and (iii) development of measurement techniques for very low-noise, wide-band receivers in the THz range.

We have earlier performed experiments with fairly large (700 μm x 350 μm) NbN HEB devices which demonstrated for the first time that efficient HEB mixing was possible in NbN at 2.5 THz [5]. These results were reported at the previous Space THz Technology Symposium [6]. Based on this experience, we have designed a new NbN device, which is coupled to the THz radiation by a log-periodic antenna through an extended hemispherical lens. This paper describes the development of this new configuration and our first results from measurements with this mixer.

The IF bandwidth of NbN HEB devices cannot be easily measured at THz frequencies. This measurement requires one fixed source for the RF input and a tunable source for the LO, or vice versa. The tunable source may be a photonic mixer source, or a sideband generator, which produces a tunable sideband from a fixed laser frequency [7]. Such measurements have so far not been performed due to the complexity of setting up the experiment. Instead, one typically infers the bandwidths of THz mixers from measurements at lower frequencies of either impedance, mixer IF response, or IF output noise. We present new measurements of the IF impedance of a NbN HEB device.

II. DEVICE DESIGN AND FABRICATION

NbN Films

The NbN films were fabricated on silicon substrates at Moscow State Pedagogical University (MSPU) by magnetron reactive sputtering in an argon/nitrogen gas mixture. For this work we have primarily used films of thickness 3.5-4 nm in order to maximize the conversion gain bandwidth. The production of such thin films is presently still an evolving technology. The substrate has to be heated during the process and the partial pressures of nitrogen and argon need to be controlled separately. The details of the process are described in [8]. Some difficulties in reproducing high quality films still exist. The surface quality of the silicon substrates appears to be a very important factor. Furthermore, the characteristics of some of the devices, such as critical current, critical temperature and, occasionally, contact resistance, deteriorated after

one or several cool-downs to liquid helium temperature. Another problem which occurs in some device batches is that there is a process which makes the conversion gain drop by several dB from the lowest frequencies (MHz) to a few hundred MHz. The conversion gain is then less in the portion of the IF band (GHz) where the noise temperature is measured. This phenomenon has been observed for similar devices used by [3] and also in our work. These problems will undoubtedly be solved. Very thin NbN films on sapphire substrates have been more reproducible as shown in another paper at this conference [9]. The optimum thickness, based on the sapphire work, appears to be close to 3.5-4 nm. The films used for the devices we have tested so far have T_c = 7.5 - 9 K and the transition width is about 0.5-1 K. The surface resistance value for a typical film is about 450 Ω/square.

Optical Design

Optical design considerations are crucial for efficiently coupling LO and signal power into the device. It is clear that quasi-optical coupling to the device is the only alternative for frequencies as high as 2.5 THz. We chose to use an extended hemispherical silicon lens coupled to a log-periodic spiral antenna (see Figure 2) as successfully demonstrated and analyzed at 250 GHz and 500 GHz by [10]. A similar design

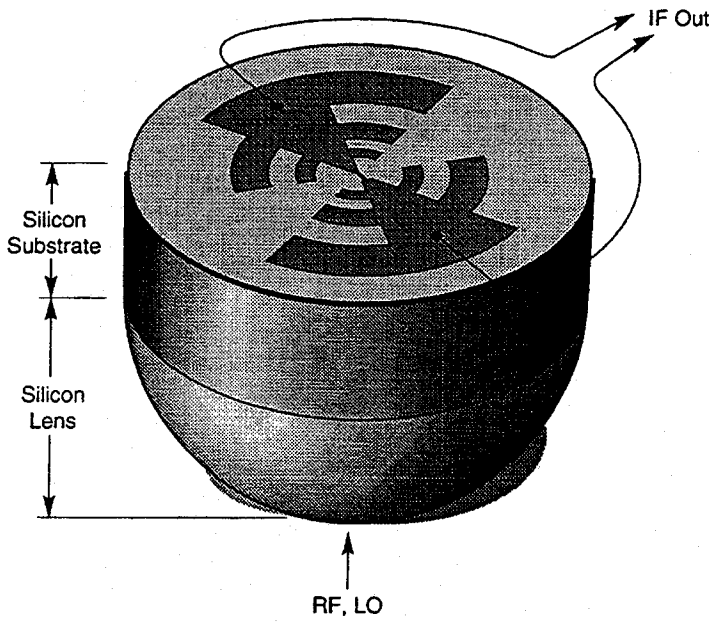

Figure 2: Log-Periodic antenna fabricated on an extended hemispherical silicon lens.

was also integrated with a Schottky-barrier diode and used at 760 GHz by [11]. The log-periodic spiral antenna is convenient at this stage since it can be used over a very wide frequency range; later versions will employ twin-slot or twin-dipole antennas tuned to specific frequencies. We scaled the dimensions of the lens and the antenna used in the 250 GHz experiments by a factor of ten, resulting in a lens diameter of 1.3 mm. We chose an extension length, beyond the hemispherical lens, of 0.33 times the lens radius. The characteristics of the lens radiation pattern can then be predicted from the results of [10]: A beamwidth of about 5-6 degrees and directivity of 30 dB as well as a gaussian coupling efficiency of 50-60 %. We can also predict the amount of beam-scan which would result from misalignment of the center of the antenna with respect to the center of the lens: a 20 micrometer misalignment results in a 5 degree beam scan. This makes it imperative to use an accurate alignment procedure which will be described below. We are not employing a matching layer at this stage. The manufacturing of such a small silicon lens turned out to be a significant challenge which was, however, overcome[1]. An alternative would have been to utilize a larger hyperhemispherical lens but this would have necessitated the incorporation of a second lens in the dewar in order to bring the beam to a focus.

The choice of a smaller lens has advantages in terms of being adaptable for extending the receiver system to a focal plane array as illustrated in Figure 3. The figure shows a "fly's eye" configuration with individual lenses for each pixel. Larger lenses are more limited in terms of the number of elements which can be accommodated in the focal plane without severe aberrations. Also significant is the fact that the element spacing in this focal plane array is sufficiently large to match the typical size (about 1 mm x 1 mm) of MMIC amplifier chips. We anticipate employing commercial MMIC IF amplifiers which would be inserted into etched wells in the silicon substrate/motherboard. The routing of all transmission lines would be done on a separate dielectric (BCB) which we are presently exploring for other applications.

Device Fabrication

Devices have been fabricated at MSPU as well as at UMASS/Amherst. The processes are somewhat different at the two locations but in what follows we will emphasize the UMASS process. The fabrication technique developed here begins with the deposition of 3.5-4 nm NbN on a silicon wafer as described

[1] The lenses were made by Janos Technology, Townshend, VT

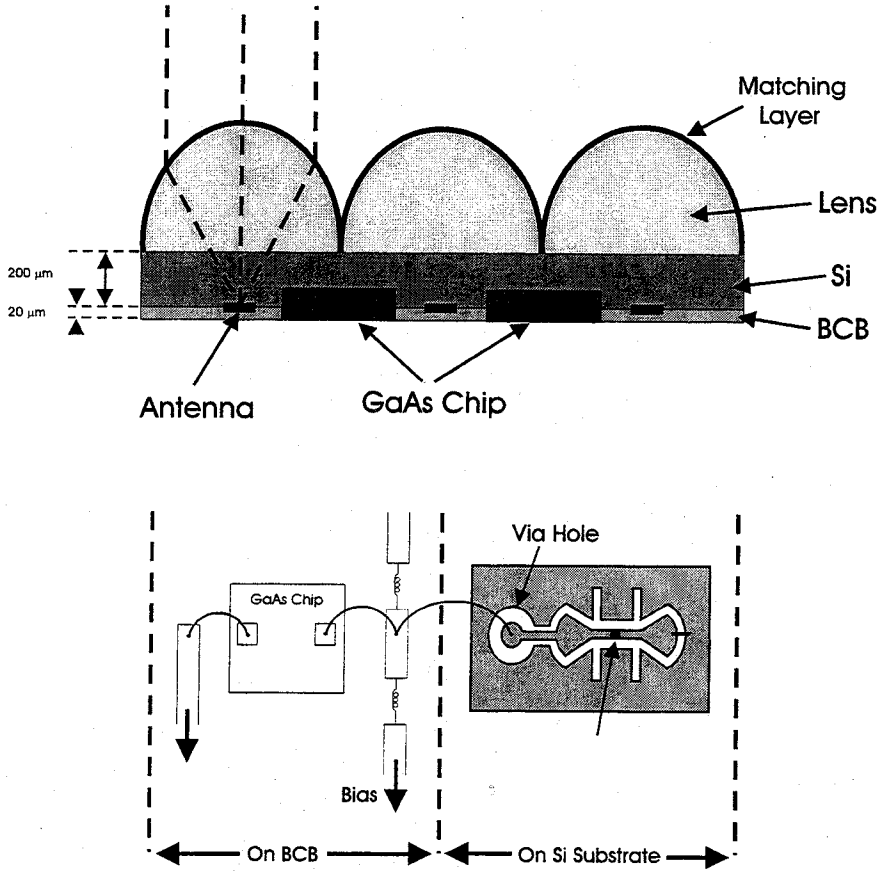

Figure 3: Lens array with NbN mixers for focal plane imaging system: fly's eye configuration.

above. Presently we are employing analysis techniques such as EDAX and XPS to further enhance our understanding of the film structure and the effects that various processing steps have on the films. The gold log-periodic antenna is fabricated using liftoff. After the pattern has been defined in the photoresist, a 40 nm thick layer of Nb is applied by sputtering. This layer is used to guarantee the lowest possible contact resistance. Next, 20 nm of Ti and 100 nm of Au are deposited by E-beam evaporation followed by the liftoff step. The NbN strips are then defined and etched using Reactive Ion Etching (RIE). Next, the substrate is thinned to a thickness equal to the lens extension length. The position of a square alignment window for the lens is then defined in a photoresist layer on the opposite side of the substrate from the antenna and device using an infrared mask aligner. The alignment window is etched by RIE to a depth of 100 nm and the lens is attached to the silicon substrate using purified bees wax. The substrate is mounted on a holding frame made of OFHC copper and the antenna contacted through indium wires. The final dimensions of the device strips

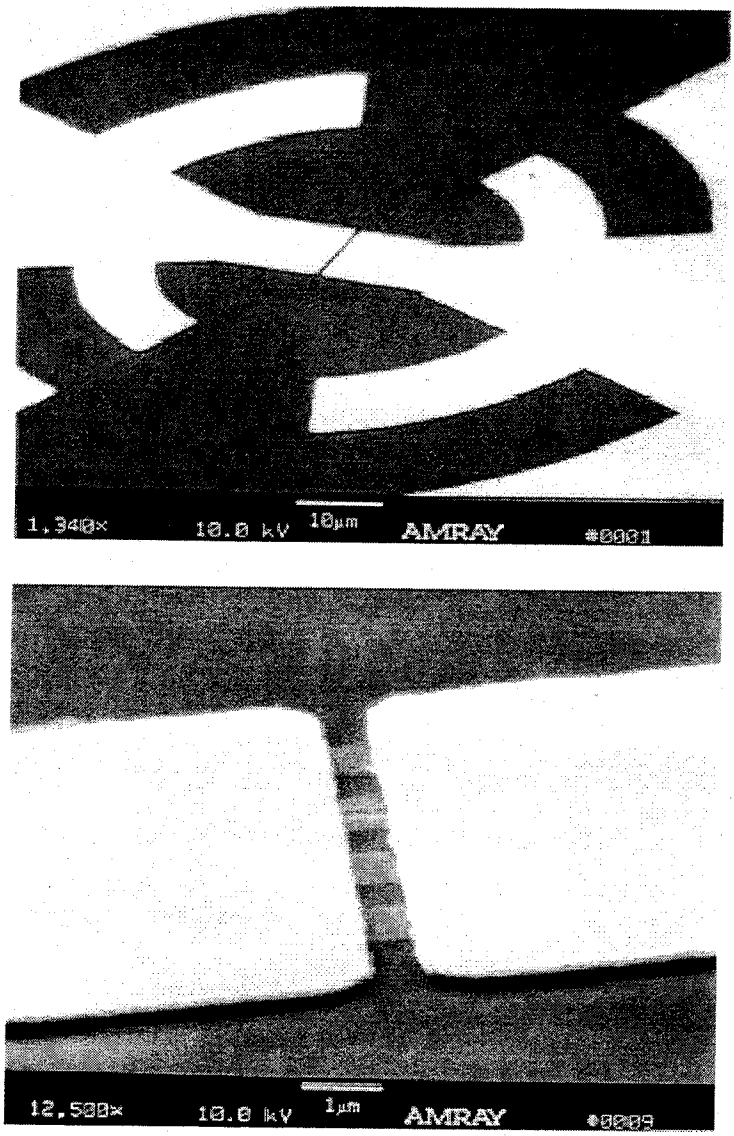

Figure 4: SEM photographs of the NbN device.

are about 0.6 µm long by 1.0 µm wide. The number of strips is from one to three. The mask also has a different pattern for which the smallest teeth, which determine the highest frequency of the antenna, are twice as large, i.e. the highest frequency is 1.25 THz. This antenna can have up to five strips. Figure 4 shows an SEM picture of a device with four strips recently fabricated at UMASS/Amherst. Finally, the holding frame and the device are mounted onto a copper post which is attached to the cold plate of an IRLABS liquid helium dewar. A heater and temperature sensor are also attached to the copper post close to the device.

The contact resistance of good devices is less than 1 Ω. The normal resistance of the device should be matched to the antenna impedance (100 Ω). The devices fabricated so far have a normal resistance as low as 200 Ω. A better match could be obtained if a thicker film were used but with a tradeoff for somewhat narrower bandwidth.

III. EXPERIMENTAL SETUP

Optical Setup

The optical coupling loss as well as the receiver noise temperature are measured using a laser setup shown in Figure 5. An FIR methanol laser is pumped by a CO_2 laser and reflected by a 1 mil mylar beam splitter. The laser beam is then focused by an off-axis paraboloidal mirror through a 0.75 mm polyethylene window onto the device. Shorter IR wavelengths are further attenuated by a sheet of cooled Zitex. The beam splitter allows radiation from a hot-cold load to be directed into the beam path. This blackbody radiation is obtained by chopping between a room temperature absorber and a liquid nitrogen bath. The device is biased through a cold bias tee connected through an isolator to a broadband cooled HFET amplifier with 30 dB gain and about 10 K noise temperature (including isolator losses). The IF system bandwidth is 1250 to 1750 MHz. In some experiments we used a room temperature IF amplifier with a noise temperature of 150 K. After further amplification, the IF power is measured with a microwave detector connected to a lock-in amplifier with its reference obtained from the chopper. The setup is aligned by using the HEB device itself as a detector and observing the depression of the device current due to the laser power.

Microwave Measurements

The microwave measurements were performed by utilizing a dipstick setup. The dipstick apparatus used in these measurements consists of a device mounting block immersed in LHe or positioned just above the LHe surface and a low loss, thermally insulated, cable. The impedance characteristics were recorded on a network analyzer operated at a very low power level. Calibration was accomplished in part by using the device at zero volt bias as a superconducting short. The parasitic characteristics of the device mount were taken into account by simulating the mount in Sonnet ***em*** and by performing one further meas-

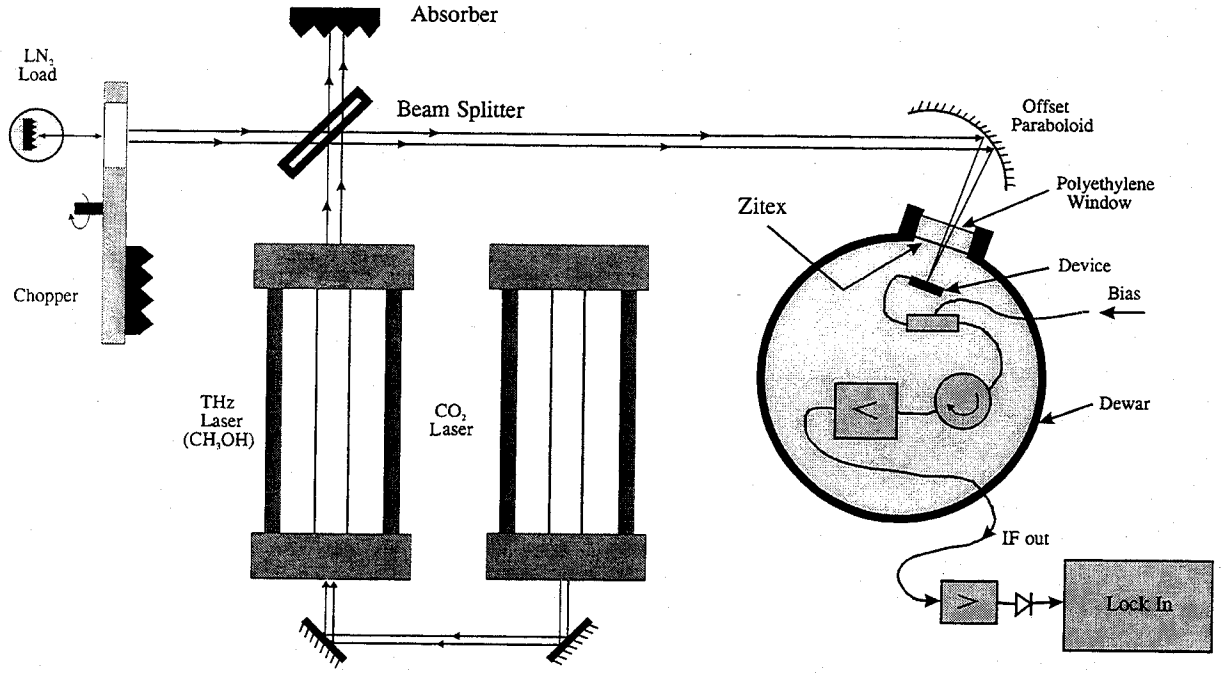

Figure 5: Optical layout for noise measurements.

urement with the device replaced with an indium wire short. The subsequent calibration calculations were done with the Hewlett-Packard MDS package.

We have previously measured the bandwidth of an earlier generation of NbN devices at about 15 GHz. It is sometimes difficult to interpret these measurements due to the very low frequency. However, measurements at 140 GHz have been shown to correlate well with measurements in the 600 GHz range [8]. We have therefore started to perform measurements of mixer bandwidth at 94 GHz in a dipstick waveguide setup.

IV. RESULTS AND DISCUSSION

Laser Pumping of the Device

The best device available for the preliminary measurements was one fabricated at MSPU integrated with a regular spiral antenna. The device substrate was thicker than required for the 1.3 mm diameter lens

and was instead waxed to a 2 mm lens. After alignment of the device to the laser beam, we were able to obtain sufficient suppression of the device current due to the laser power as depicted in Figure 6. The device temperature was 4.73 K and the critical temperature was 7.5 K. In the particular case shown, the LO power produced an IV-curve which is almost identical to one recorded at an elevated temperature of 6.81 K (a heater was then used to heat the device). The significance of this observation is that the device is heated to an electron temperature close to T_c by the laser power as required for optimum mixer operation. The near coincidence of the two curves is expected since the LO radiation is at a frequency much higher than the superconducting gap frequency and LO heating effects should then produce results close to those due to thermal heating.

The IF power in a 50 MHz bandwidth was measured for three conditions: (i) device superconducting at V=0; (ii) with optimum DC bias but without LO power; (iii) with optimum DC bias and the LO power on. The change in IF power from (i) to (iii) amounted to 8 dB. From this we can estimate the device

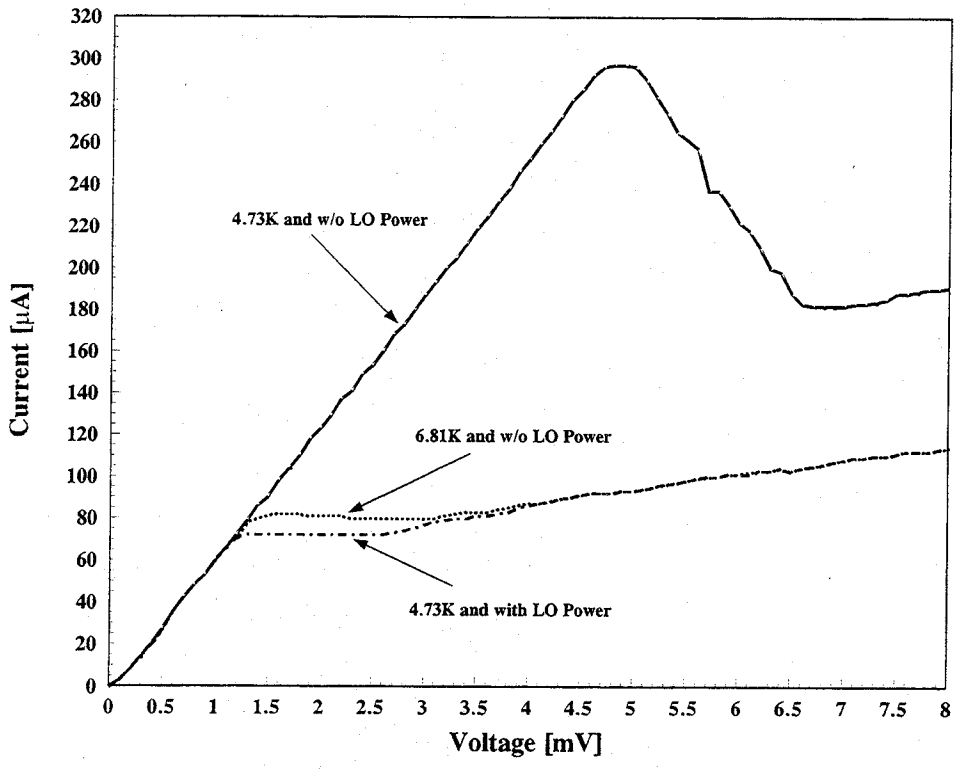

Figure 6: I-V characteristics of quasi optically coupled NbN device.

output noise temperature (T_{out}) to be in the range 40-80 K. The uncertainty is due to our incomplete knowledge of the amplifier noise temperature. This value of T_{out} is in the expected range.

We were also able to measure the amount of laser power absorbed by the device utilizing the IV-curves. The power absorbed at what would be a typical optimum operating point was 800 nW. Note the very small LO power which can be made even smaller in future devices with somewhat smaller device dimensions. The measured laser power after the paraboloid mirror was 2.5 mW. The ratio of these numbers gives an estimate of the optical coupling loss of 35 dB. Such a high value is not uncommon in quasi-optical HEB experiments so far since the gaussian modes are rarely perfect; nor are they well matched between the laser and the antenna/lens combination. These problems will need to be attended to before sources such as the photomixer, with available power at best in the microwatt range, can be utilized. We are continuing our experiments to obtain a measurement of noise temperature. We also expect to improve the optical coupling by using the optimum antenna/lens combination which was not available before the conference[2].

Impedance Measurements

We have pursued accurate measurement techniques for the device impedance in order to obtain useful information to characterize the device without the need to perform THz measurements. Mixing measurements at low GHz frequencies are often more difficult to interpret. Previous published data of the microwave impedance for NbN were obtained by [12] and [13]. We have tested our calibration techniques on an older 10 nm device as shown in Figure 7. The agreement with theory is better than in previous measurements: The real part follows the theoretical model closely whereas the imaginary part fits well above 200 MHz but shows an extra capacitive contribution at very low frequencies. We do not have a satisfactory explanation for the deviation of the imaginary part at low frequencies at this point, but note that other measurements [12][14] show a similar tendency. Data for a fairly large Nb device follow theory very well [15]. Future measurements on the newer generation of films will be performed with even more precise calibration. We will also obtain bandwidth measurements at 94 GHz for the new devices. A long-term goal is to measure

[2] The 1.25 THz version of our log-periodic antenna/device has since been tested at 650 GHz at Chalmers University of Technology and yields a receiver noise temperature of 1750 K. This design is thus validated at the lower frequency [Ekstrom, private communication].

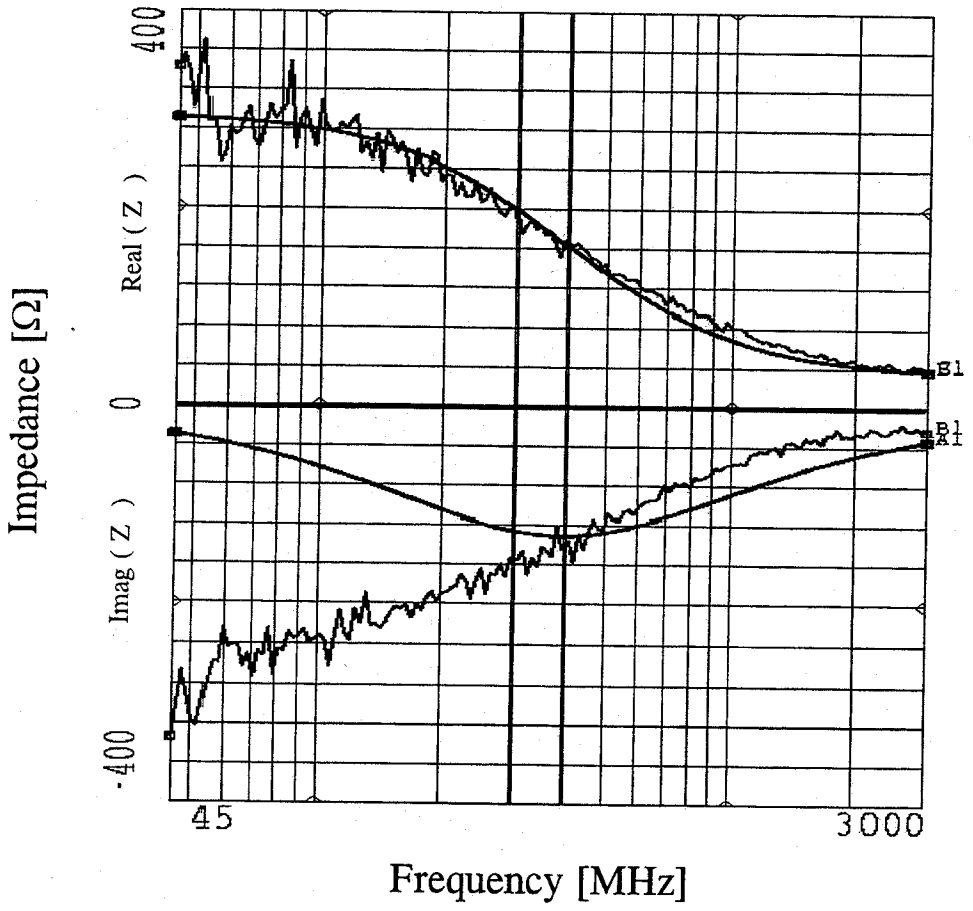

Figure 7: Theoretical and experimental impedances of a 10 nm NbN film.

the conversion gain bandwidth at THz frequencies utilizing a laser LO and a sideband generator as the RF source [7].

V. CONCLUSION

We have shown that lasers can be quasi-optically coupled at THz frequencies to NbN HEB mixer devices integrated with log-periodic or spiral antennas and small silicon lenses. The very small LO power to be expected from such devices when optimally matched (less than 1 microwatt) has been verified. We have also demonstrated improved measurements of the microwave impedance of the device. Noise temperature measurements will be performed in the near future.

VI. ACKNOWLEDGMENT

This work was supported by the Russian Program on Condensed Matter (Superconductivity Division) under Grant No.93169, as well as grants from the National Science Foundation (ECS-9313920), The National Research Council, and NASA (NRA 93-OSSA-06). We acknowledge help from Ms. Teresa Sanchez with device fabrication and Mr. Konstantin Il'in in the laser experiments and for development of the 94 GHz measurements. Dr. A. Verevkin also helped with the latter. Millimetrix provided access to their IR mask-aligner. We gratefully acknowledge their assistance with this crucial step in our fabrication process.

VII. REFERENCES

[1] J. Kawamura et al., "Low Noise NbN Lattice-Cooled Superconducting Hot-Electron Bolometric Mixers at Submillimeter Wavelengths", submitted to the APL, 1996.

[2] J. Kawamura et al., "NbN Hot-Electron Bolometric Mixer at Submillimeter Wavelengths", this symposium.

[3] H. Ekstrom et al., "Gain and Noise Bandwidth of NbN Hot Electron Bolometric Mixers," Accepted for publication in Appl. Phys. Lett., 1996.

[4] S. Verghese, K. A. McIntosh, and E. R. Brown, "Widely Tunable Photomixers Using Fiber-Coupled Diode Lasers", this symposium.

[5] E. Gerecht et al.,"Hot Electron Mixing in NbN at 119 Micrometer Wavelength", Proc. Of the Intern. Semicond. Device. Res. Symp., Charlottesville, VA, pp 619-622, Dec. 1995.

[6] E. Gerecht et al., "Optimization of Hot Electron Bolometer Mixing Efficiency in NbN at 119 Micrometer Wavelength", Seventh Intern. Symp. Space THz Technology, Charlottesville, VA, March 1996.

[7] E. R. Mueller and J. Waldman, "Power and Spatial Mode Measurements of Sideband Generated, Spatially Filtered, Submillimeter Radiation", IEEE Trans. Microw. Theory Techniques, MTT-42, 1891, 1994.

[8] P. Yagoubov, G. Gol'tsman, B. Voronov, and E. Gershenzon, "The Bandwidth of HEB Mixers Employing Ultrathin NbN Films on Sapphire Substrate, Seventh Intern.Symp.Space THz Technology, Charlottesville, VA, p. 290, March 1996.

[9] S. Cheredricheuko et al., "Large Bandwidth of NbN Phonon-Cooled Hot Electron Bolometer Mixers on Sapphire Substrates", this symposium.

[10] D. F. Filipoviz, S. S. Gearhart, and G. M. Rebeiz, "Double-Slot Antennas on Extended Hemispherical and Elliptical Dielectric Lenses", IEEE Trans. Microw. Theory Techniques, MTT-41, 1738, 1993.

[11] S. S. Gearhart et al., "Wide-Band 760 GHz Planar Integrated Schottky Receiver ", IEEE Microw. Guided Lett., 3, 205, 1993.

[12] H. Ekstrom, B. Karasik, E. Kollberg, G. Gol'tsman, and E. Gershenzon, "350 GHz NbN Hot Electron Bolometer Mixer," Sixth Intern.Symp.Space THz Technology, Pasadena, CA, p. 269, March 1995.

[13] H. J. Kawamura, R. Blundell, C.-Y.E. Tong, G. Gol'tsman, E. Gershenzon, and B. Voronov, "NbN Hot-Electron Mixer Measurements at 200 GHz," Sixth Intern.Symp.Space THz Technology, Pasadena, CA, p. 254, March 1995.

[14] B. S. Karasik et al., "A Low-Noise Superconductive Nb Hot Electron Mixer at 2.5 THz", this symposium.

[15] H. Ekstrom, B. Karasik, E. Kollberg, and S. Yngvesson, "Conversion Gain and Noise of Niobium Superconducting Hot-Electron Mixers", IEEE Trans. Microw. Theory Techniques, MTT-43, 938, 1995.

Noise-bandwidth of Diffusion Cooled Hot-Electron Bolometers

Peter J. Burke, R.J. Schoelkopf, D.E. Prober
Depts. of Applied Physics and Physics, Yale University, New Haven, CT 06520-8284

A.Skalare, W.R. McGrath, B.Karasik, M. Gaidis, B.Bumble, H.G. LeDuc
Jet Propulsion Laboratory, California Institute of Technology, Pasadena• CA 91109

In recent years, superconducting hot-electron bolometers have demonstrated promising performance as low-noise mixers in THz receivers. Already, excellent results have been attained at rf frequencies of 0.5 THz[1], 1.2 THz[2], and 2.5 THz[3]. An important technological issue is the intermediate frequency gain and noise bandwidth for these mixers. We have therefore measured the spectrum of the output noise as well as the conversion gain for devices of several different lengths to study how the mixer noise of hot-electron bolometers depends on the intermediate frequency.

The gain-bandwidth, the frequency at which the conversion gain drops by 3 dB relative to its low frequency value, is given by $1/\tau_{thermal}$. The output noise at low intermediate frequencies is dominated by thermal fluctuation noise, while at high intermediate frequencies Johnson noise dominates the output noise. Since the spectrum of the output noise at low frequencies (where thermal fluctuation noise dominates) has the same dependence on frequency as the conversion gain, the mixer noise (T_{mix} (DSB) = $T_{out}/2\eta$, with η =SSB conversion efficiency) will be independent of frequency up to the crossover where the Johnson and thermal fluctuation noise are comparable. Therefore, the noise-bandwidth, the frequency at which the mixer noise is 3 dB higher than its low frequency value, can be larger than the gain-bandwidth.

We have measured the spectrum of the output noise and the conversion gain from 0.05-8 GHz under identical conditions for both diffusion and phonon-cooled Nb bolometers, using a 20 GHz LO. We do indeed find that the noise-bandwidth is 1.5 to 2 times higher than the gain-bandwidth, and that the low-frequency value of the mixer noise is low, $T_{mix} < 300$ *K(DSB).* We have done these measurements on a variety of devices varying in length from 0.08 μm to 3 μm, where the gain-bandwidth[4] varies between 100 MHz and > 6 GHz. We will also present modeling of this data, including modeling of the dependence of the noise and conversion efficiency as a function of dc bias and LO power.

References

[1] A. Skalare, W. McGrath, B. Bumble, H. LeDuc, P. Burke, R. Schoelkopf, and D. Prober, "Large bandwidth and low noise in a diffusion-cooled hot-electron bolometer mixer," *Applied Physics Letters,* vol. 68, no. 11, pp. 1558-1560, 1996.
[2] A. Skalare, W. McGrath, B. Bumble, and H. LeDuc *submitted to IEEE Transactions on Applied Superconductivity,* 1996.
[3] B. Karasik, M. Gaidis, W. McGrath, B. Bumble, and H. LeDuc *submitted to IEEE Transactions on Applied Superconductivity,* 1996.
[4] P. Burke, R. Schoelkopf, D. Prober, A. Skalare, W. McGrath, B. Bumble, and H. LeDuc, "Length scaling of bandwidth and noise in hot-electron superconducting mixers," *Applied Physics Letters,* vol. 68, no. 23, pp. 3344-3346, 1996.

A SUBMILLIMETER SIS RECEIVER COOLED BY A COMPACT STIRLING-JT REFRIGERATOR

J.Inatani, T.Noguchi, S.C.Shi, and K.Miyazawa
Nobeyama Radio Observatory, National Astronomical Observatory
Nobeyama, Nagano 384-13, Japan
H.Masuko, S.Ochiai, and Y.Irimajiri
Communications Research Laboratory, Ministry of Posts and Telecommunications
Koganei, Tokyo 184, Japan
M.Kyoya, K.Narasaki, and S.Tsunematsu
Sumitomo Heavy Industries, Ltd.
Niihama, Ehime 792, Japan
M.Murakami and D.Okamoto
University of Tsukuba
Tsukuba, Ibaraki 305, Japan

Abstract

We have built a prototype SIS receiver for submillimeter observations in space, which is based on a compact Joule-Thomson cooler combined with a two-stage Stirling refrigerator. Cooling capacity, 30 mW at 4.5 K, 200 mW at 20 K, and roughly 3 W at 100 K, has been achieved with the electric power consumption less than 260 W. A 500 GHz SIS mixer and two HEMT amplifiers are well cooled.

Introduction

It is desirable to use the SIS mixer in space, as well as on the ground, for highly sensitive astronomical or global atmospheric observations at millimeter and submillimeter wavelengths. However, the SIS mixer has to be cooled to 4 K, either with liquid helium or by a mechanical refrigerator. Although there are several trade-offs between these two cooling methods, a refrigerator is getting to be preferable for a long life mission. A single-stage Stirling refrigerator has already established its reliability in space, and a two-stage Stirling is also getting such quality. On the other hand, for the purpose of cooling to 4 K in space, the Joule-Thomson cooler seems to be the only practical solution today among several mechanical coolers. But technical reports of its experimental investigations are not so many. We designed and built a thermal prototype of a 500 GHz SIS mixer receiver, intended for the future space applications, which was cooled by a J-T cooler combined with a two-stage Stirling refrigerator.

4 K Joule-Thomson Cooler

We built a small J-T cooler which has a nominal cooling capacity of 30 mW at 4.5 K. Its major components are a helium gas compressor, J-T valve, 4 K stage, and five heat exchangers (HEX-1 to HEX-5). Schematic structure of the whole refrigerator is shown in Fig. 1. HEX-4 and HEX-5 are precooled to 100 K and 20 K by a two-stage Stirling refrigerator. For the J-T

compressor, we used two units of the Stirling-type compressors which are connected in series to achieve the compression ratio of about 16. Additional valves are operated to get a one-way flow of helium gas. For making the J-T effect, we used a small needle valve, whose conductance is controlled manually by means of a gas pressure actuator. For heat exchangers HEX-1, -2, and -3, concentric CuNi tubes are adopted with optimized dimensions.

Nominal cooling capacity of the two-stage Stirling is 200 mW at 20 K, and 1W at 80 K at the same time. But this first stage has the ability to cool 1.5 W at 100 K. Details of the two-stage Stirling refrigerator are described in Kyoya et al.(1994).

The present experiment was designed to operate three channel SIS mixer receiver. In this case, heat load at 100 K is very critical, as shown in the following. So we added a single-stage Stirling, which has a capacity of 1 W at 80 K, to assist the first stage cooling. However, this could be removed in the smaller version of the receiver (one or two channel receiver).

Receiver Cryostat

We built a receiver cryostat based on the above mentioned combined refrigerator. The goal of the present experiment was to demonstrate a submillimeter SIS mixer successfully operating with a small refrigerator which could be used in space. So we concentrate on the thermal performance of the refrigerator and the cryostat. Mechanical supporting structures in the cryostat are not yet well designed to survive the shock and vibration expected in launching phase. Calculated thermal balance of this cryostat is shown in Table 1.

It characterizes this type of cryostat that the heat load to the 4 K stage is small. Heat dissipation of the SIS mixer is negligible. Major heat loads are a radiation leaking through an IR filter and the IF cable connected to the HEMT amplifier. Total load to the 4 K stage is estimated about 14 mW. But the present version of the J-T cooler was designed to have a capacity of 30 mW for safety. So we have a large margin in the 4 K cooling capacity.

On the other hand, heat loads to the 20 K stage and the 100 K stage are very large. Major heat loads to the 20 K stage are the heat dissipation of the IF amplifiers and the precooling of helium gas for the J-T cycle. We used a HEMT amplifier at 2.0 - 2.5 GHz, which is composed of two transistors with a total gain of 27 dB. The HEMT device is usually recommended to be biased with a nominal condition such as a drain voltage of 2 V and a drain current of 10 mA. If this were inevitable, we would have to deal with 20 mW dissipation for each transistor. But actually we found that some HEMT devices keep a good noise temperature, with a little decrease of gain, even when the drain voltage is decreased to 1 V and the drain current to 5 mA. Although this behavior is not common to any model of HEMT devices, it is the case for some devices (e.g. MGF4318D). In Table 1, the the power dissipation of 10 mW is assumed for each HEMT device.

Major heat load to the 100 K stage is thermal radiation from the 300 K wall of the cryostat and from the RF input window (25 mm in diameter). A 40-layer MLI (multi-layer-insulation) is put between the 300 K wall and the 100 K radiation shield. In order to reduce thermal input from the RF window, an optical path with a wire-grid is used such as in Fig.3. This is to reduce the IR coupling to the 100 K shield by means of separating the submillimeter path

(which looks at the IR filter) from the IR path (which looks at metal surface with low emissivity).

Helium gas precooling for the J-T cycle generates the heat load of 100-120 mW at 20 K and 180-255 mW at 100 K. These values correspond to the 4 K cooling capacity of 30 mW. They could be reduced when the 4 K capacity is reduced.

500 GHz SIS Mixer

We put a waveguide-type 500 GHz SIS mixer on the 4 K stage, together with two superconducting magnetic coils and an ellipsoidal mirror. The mixer uses a pair of Nb/AlOx/Nb junctions connected in parallel (PCTJ, Noguchi et al.(1996)), whose resonance frequency is designed at 480 GHz. Schematic drawing of the mixer is given in Fig.4. Details of the SIS mixer are described in Shi et al.(1996). Diagonal feed horn is used for simplicity. A high permeability metal is used for the magnet core to increase the magnetic field at the junction. Actually the current of several 10 mA was sufficient to suppress the Shapiro steps.

Experimental Results

Although three channel receiver was assumed in Table 1, the SIS mixer and the HEMT amplifiers were actually installed only for one channel in the experiment. Only one RF window was open, and only two HEMT amplifiers were dissipating heat including 20 K and 80 K stages. But structures, wires, and IF cables were actually the same as calculated in Table 1. So the actual heat load in the experiment is estimated to be smaller by 410 mW at the first stage, by 50 mW at the second stage, and by 4 mW at the third stage, respectively, from each value in Table 1.

It took about 70 hours to cool the mixer from room temperature to 4.3 K. In the final steady state where the SIS mixer and the HEMT amplifiers are successfully in operation, the balanced temperatures were 106 K at the first stage, 23 K at the second stage, and 4.3 K at the third stage. Helium gas flow-rate in the J-T cycle was 1.3 NL/M (normal-liter per minute). Helium gas pressures were 14.9 kg/cm^{2}A before the J-T valve, and 1.1 kg/cm^{2}A behind it. With this condition the J-T compressor consumes the electric power of 79 W at 35 Hz, and the Stirling compressor does 115 W at 15 Hz for the two-stage cold head and 60 W at 50 Hz for the single-stage cold head. So the total power consumption was 254 W at the AC power source to drive the compressors.

Noise performance of the receiver was measured by means of the usual Y-factor method between 300 K and 77 K loads. LO, at 470-480 GHz, was generated by a Gunn diode oscillator and two cascaded multipliers (x2x3) , and was injected to the mixer through a 75 μm thick Mylar film (its calculated reflectivity is 7.5 %). Measured Y-factor for the whole system was roughly 1 dB, though the same mixer shows the Y-factor of 2.4 dB (Tsys= 220 K) in the other cryostat which has a simpler RF input optics. The present worse performance seems to be attributable to imperfect optical alignment and to the residual effect of the Shapiro steps. The latter remains in the present experiment, not because of insufficient magnetic field but probably due to magnetic flux trapped in the mixer.

Conclusion

We have built a 500 GHz SIS receiver cooled by the Joule-Thomson cooler which is assisted by the two-stage and single-stage Stirling refrigerators. The whole cooling system worked well as designed, and the SIS mixer and the HEMT amplifiers were good in operation. The cooler power consumption was 254 W. It could be largely reduced by removing the single-stage Stirling refrigerator, and by optimizing the J-T compressor to 15 mW capacity at 4.5 K.

Acknowledgements

We acknowledge Nitsuki, Ltd. who built a low power consumption HEMT amplifier for this experiment.

References

M.Kyoya, K.Narasaki, K.Ito, K.Nomi, M.Murakami, H.Okuda, H.Murakami, T.Matsumoto, and Y.Matsubara, "Development of two-stage small Stirling cycle cooler for temperatures below 20 K," *Cryogenics*, **34**, N0.5, 431, 1994

T.Noguchi, S.C.Shi, and J.Inatani, "An SIS mixer using two junctions connected in parallel," *IEEE Trans. Appl. Supercond.*, **5**, 2228, 1995

S.C.Shi, T.Noguchi, and J.Inatani, "Development of a 500 GHz Band SIS Mixer," *IEEE Trans. Appl. Supercond.*, **7**, 1995 (in press)

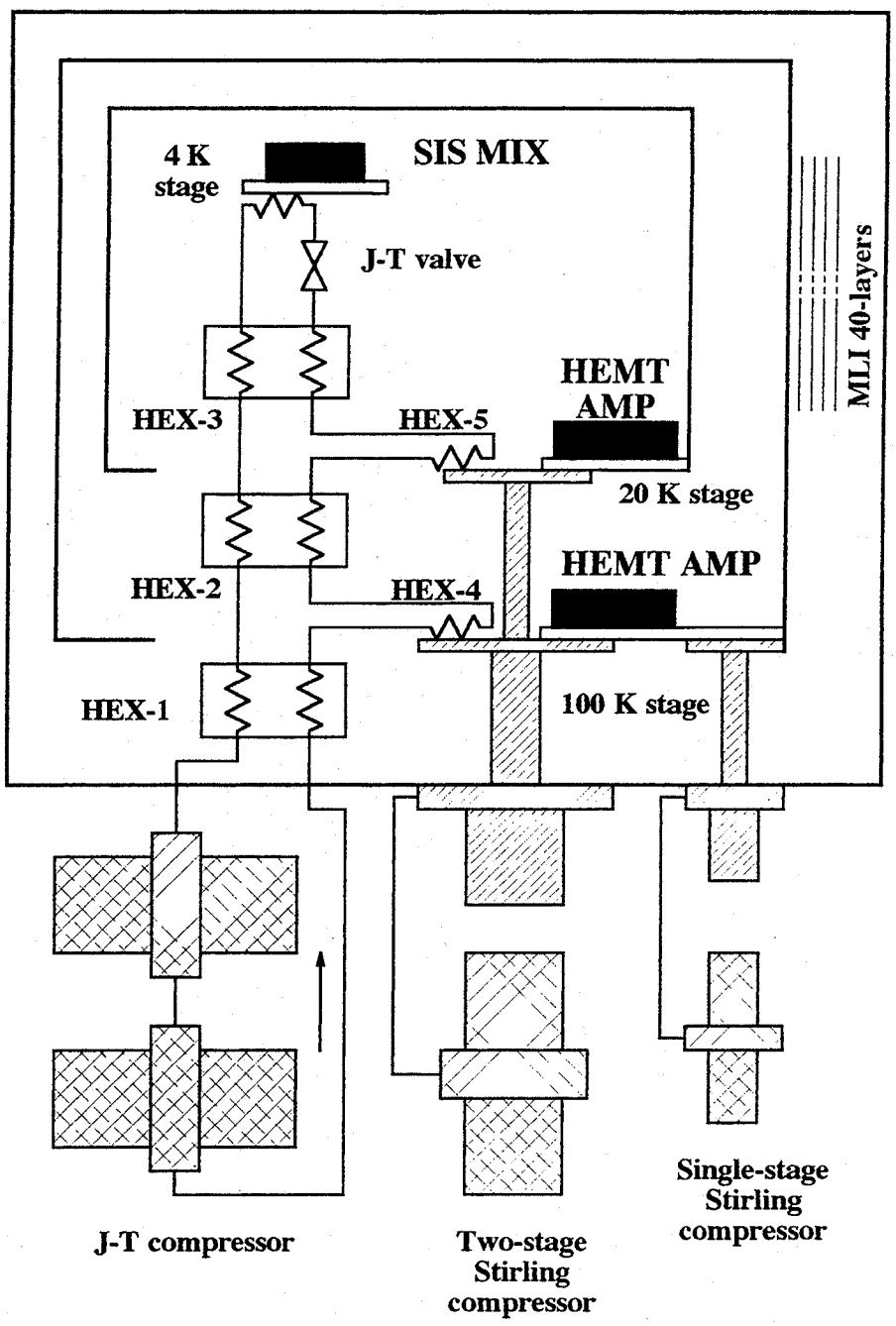

Fig. 1 A small Joule-Thomson cooler which is combined with two Stirling refrigerators: one is two-stage cycle and the other is single-stage cycle. Cooling capacity of 30 mW at 4.5 K is obtained with total power consumption of 254 W.

Items	Types	Heat Load at Each Stage			Assumptions
		1st Stage	2nd Stage	3rd Stage	
		mW	mW	mW	
RF Input Window	rad.	537	9	6	3 windows (25 mm dia. each)
Wall(area with MLI)	rad.	620	26	0	MLI 40-layers
Wall(area without MLI)	rad.	1396			
Supporting Pipes	cond.	218	16	4	3 GFRP pipes at each stage
IF Coaxial Cables	cond.	23	8	2	3 CuNi coax. cables
DC Bias Wires	cond.	9	1	0	18 Manganin wires (0.1 mm)
DC Bias Current	heat source	21	11	0	10 mA each
SCM Coil	cond.	28	7	1	6 Manganin wires (0.5 mm)
SCM Current	heat source	1	0	0	10 mA each
Temp. Monitors/Heaters	cond.	54	14	1	30 wires
HEMT AMP (1st stage)	heat source	60			3 amplifiers (6 HEMTs)
HEMT AMP (2nd stage)	heat source		60		3 amplifiers (6 HEMTs)
SIS MIX (3rd stage)	heat source			0	
J-T Gas Precooling	heat source	255	120		for 30 mW at 4.3 K
Total Load at Each Stage (mW)		3222	272	14	
Equilibrium Temperatures (K)		109 K	24 K	4.5 K	

Table 1 Calculated thermal balance of a 500 GHz SIS mixer receiver, which has three SIS mixers at the 4.5 K stage, three HEMT amplifiers at the 20 K stage, and another three HEMT amplifiers at the 100 K stage.

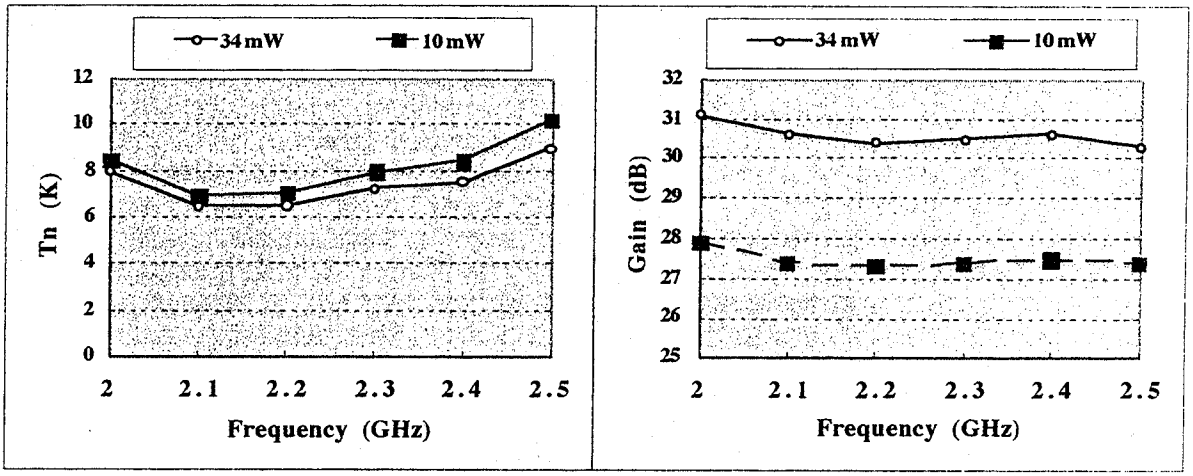

Fig. 2 The noise temperature and gain of a 2.0-2.5 GHz amplifier with two HEMT devices (MGF4318D). Two different bias conditions are applied. In case(i), Vd= 2 V, Id1= 7 mA, and Id2= 10 mA, which means the power dissipation of 34 mW. In case(ii), Vd= 1 V, Id1= 5 mA, and Id2= 5 mA, which means the power dissipation of 10 mW. The noise temperature does not deteriorate so much even when the DC power dissipation is largely reduced.

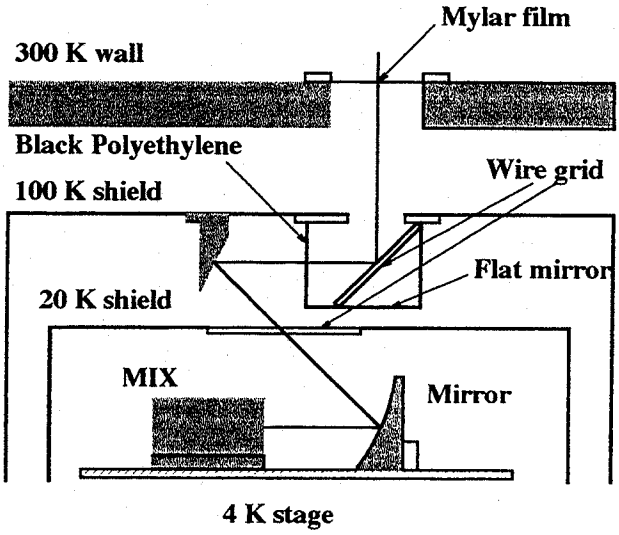

Fig. 3 Thermal radiation from the RF window is one of major heat loads to the 100 K stage. This figure shows one possible method to reduce it. Submillimeter RF will look at a black-polyethylene film (IR filter) which has a high IR emissivity, but IR will look at a metal surface which has a low IR emissivity, so the IR coupling between 300 K and 100 K will be reduced.

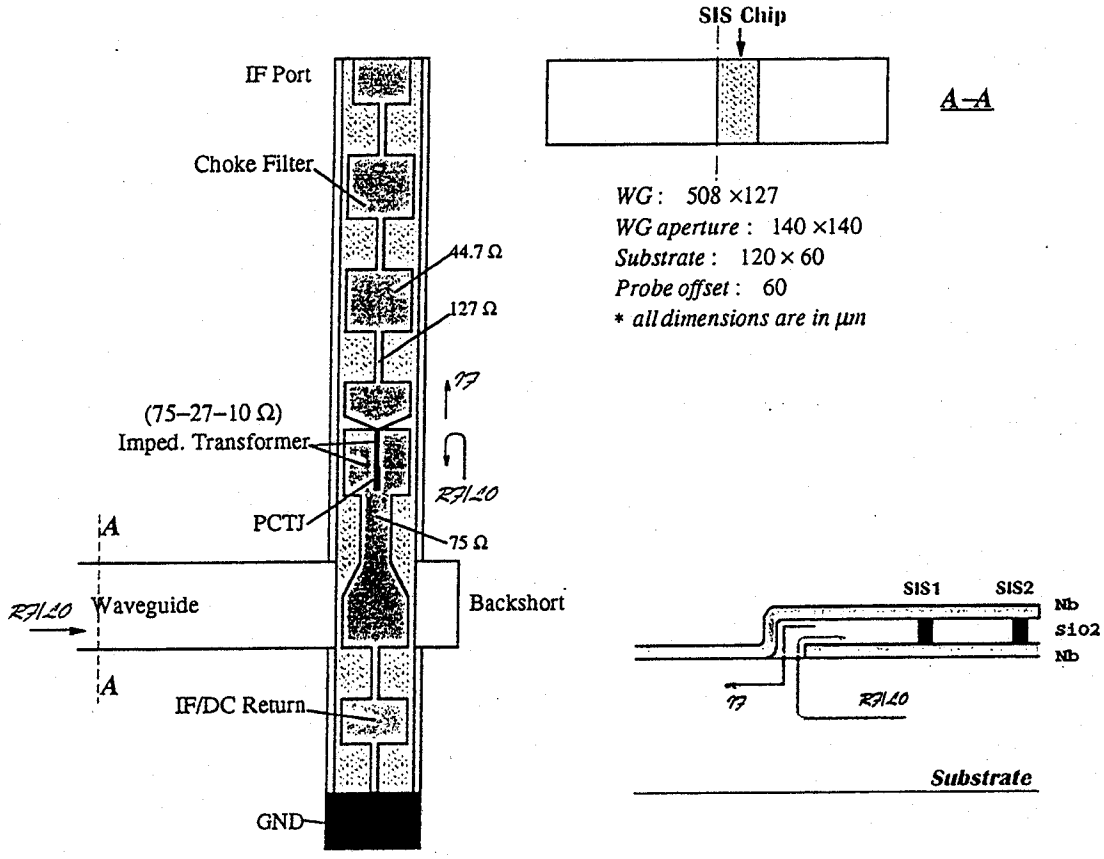

Fig. 4 Schematic drawing of the 500 GHz waveguide-type SIS mixer, which is used in the present experiment. Broad-band characteristics more than 20 % is predicted in a simulation based on the FEM (Finite Element Method) with a fixed backshort.

STUDY OF A QUASIOPTICAL SUPERCONDUCTING INTEGRATED RECEIVER FOR IMAGING APPLICATIONS AT 400-700 GHz

Sergey V. Shitov [1], Valery P. Koshelets [1], Andrey M. Baryshev [1], Lyudmila V. Filippenko [1], Willem Luinge [2], Jian-Rong Gao [2, 3], and Petri Lehikoinen [4].

[1] Institute of Radio Engineering and Electronics, Russian Academy of Sciences, Mokhovaya 11 Moscow 103907, Russia, *Sergey@hitech.cplire.ru, Sergey@sron.rug.nl*

[2] Space Research Organization of the Netherlands, P.O.Box 800, 9700 AV Groningen, the Netherlands.

[3] Department of Applied Physics and Materials Science Center, University of Groningen, Nijenborgh 4, 9747 AG Groningen, the Netherlands.

[4] Helsinki University of Technology, Radio Laboratory, Otakaari 5A, FIN 02150 Espoo, Finland.

Abstract

An imaging array receiver for the submillimeter wavelength is being developed. Each of 9 pixels of the array receiver is a single-chip superconducting receiver with dimensions 4 mm x 4 mm x 0.2 mm and contains a planar antenna, an all-Nb SIS mixer, a superconducting local oscillator (FFO) and the necessary coupling circuitry. A prototype design of the array receiver block, its optics and magnetic shielding are discussed. Experimental data for the integrated receiver for high frequency range of 550-700 GHz are reported. A first sample has shown receiver noise temperature of 560 K (DSB) at 645 GHz with optics optimized for 500 GHz. Smooth and permanent tuning has been demonstrated for the integrated LO over frequency range 610-700 GHz. To obtain ultimate coupling for both signals from the antenna and from the integrated LO, the integrated receiver concept with a quasioptical balanced SIS mixer is suggested.

1. Introduction

The term 'Superconducting Integrated Receiver' has been introduced in 1992 with the first attempt to integrate a low-noise SIS mixer and a superconducting local oscillator to form a sensitive single-chip device [1]. Both the light weight and the low power consumption of the device are attractive features for radio astronomy from space, atmosphere monitoring from aircraft, etc. The small size of the integrated devices makes them particularly suitable for a mapping array receiver.

Since the SIS mixers are proven to be the most sensitive front-end detector for a receiver within frequency range of 100 - 700 GHz, and even up to 1000 GHz (see, for example [2] and [3]), our main efforts were put into the study of compatibility of the mixing device with a superconducting Josephson oscillator, in this case a flux flow oscillator (FFO). Such an integration seems not difficult because both devices can be fabricated using the same $Nb/Al/Al_xO_y/Nb$ trilayer [1, 4]. On the other hand, the need for a strong magnetic field to suppress the Josephson effect in the micron-size SIS junction is inconsistent with demand for a relatively weak and stable magnetic field for proper operation of the Josephson oscillator. The solution has been found by integration of superconducting control lines into both SIS

mixer and FFO in a way that the interference between two devices is reduced to very small values. Experimental tests at 500 GHz have shown the receiver noise temperature $T_{rx} \approx 150$ K (DSB) and the acceptable beam pattern of the integrated lens antenna [4, 5]. However, about half of the receiver noise is still associated with both imperfection of the coupling of LO power and signal loss towards the LO.

The main advantages of a flux flow oscillator (FFO) over other Josephson oscillators developed up to date, are its simplicity, frequency and power tunability up to 850 GHz [6]. Since the frequency of FFO is determined by an external magnetic field, an effective magnetic shielding has to be used similar to a SQUID magnetometer. Unwanted noise of (or interference to) the bias circuit may also change the voltage across the FFO resulting in a broader effective linewidth. With a frequency locking technique that has been developed and used for precise measurement of the FFO spectrum; a 200 kHz linewidth at 450 GHz has been measured [7]. It turns out that the linewidth is different for resonant and non-resonant regimes; linewidth is usually wider for a non-resonant regime [8]. The effect of frequency locking to a specific frequency of the tunable resonator is required similar to other oscillators, including the Gunn oscillator. Preliminary experiments on synchronization of the FFO with the external source are not finished yet, but encouraging so far [9].

Recent development of wide-band SIS mixers [10] covering main part of the submm range (400 -700 GHz), makes the potential integration with widely tunable FFO even more attractive. The performance of the integrated receiver at highest possible frequency has not been tested yet. We report here first experimental results of integrated receiver near the gap frequency of Nb (600-700 GHz) where losses might become important. The prototype design of the imaging array receiver for 450-550 GHz is presented. New concept of a quasioptical balanced SIS mixer is discussed to realize maximum possible coupling of both signals from the antenna and from the integrated local oscillator.

2. Experimental Tests of the 650 GHz Receiver

a) Design of Chip and *dc/rf* Interface

All experimental chips are of the same dimensions 4 mm × 4 mm × 0.2 mm. This area contains a double-dipole antenna SIS mixer placed in the center, superconducting local oscillator and all necessary *dc*- and *IF*-interface. Eleven contact pads are located along the edge of the chip and wire bonded by *Al* wire to the printed circuit board (PCB). The PCB provides mechanical support for *dc*- and *IF*-connectors and also springs down the chip against the flat surface of the hyper-hemispherical lens providing sufficient heat contact to the liquid helium bath. Part of the wafer layout is shown in Fig. 1. The receiver chips for frequency range of 550-700 GHz (nominally tuned at 650 GHz) have a smaller size of antenna. The devices with a larger antenna for a frequency range of 400 - 500 GHz are used as a reference since their design has been tested before [5]. The integrated FFO is placed closer to the left-low corner of the chip. The LO power is supplied to the mixer via a superconducting micro-strip transmission line which contains a number of *dc*-blocking elements. For the fabrication procedure and for the details of the chip receiver design see [1, 4].

b) Mixer/Receiver Noise Temperature Test

The 650 GHz integrated mixers have passed two tests: a pre-test at *dc* and a *rf*-test with Fourier Transform Spectrometer (FTS). Both tests have demonstrated that SIS mixer is tuned at a central frequency of about 640 - 650 GHz and the integrated LO is providing

mixer-coupled power of 60-70 nW. The pumped current-voltage characteristic (IV-curve) of the SIS mixer is presented in Fig. 2. The Josephson effect in the mixer is suppressed at about its first minimum by the integrated control line carrying *dc*-current of about 30 mA.

The complete test of the integrated receiver has been carried out in a vacuum cryostat with optical window. The chip mount and optics were the same as used for 500 GHz receiver experiments. The results reported are not corrected for a mismatch due to the optics and window. The data of *rf*-test with external and internal LOs for two temperatures of the LHe bath are presented in Fig. 3. Outside the region of best tuning, the noise temperature is higher for the internal LO that is caused by lack of the LO power.

The high frequency cut-off is found to be very close to the gap frequency of Nb (680 GHz at 4.2 and 700 GHz at 2.5 K, for our samples). The attenuation in the transmission micro-strip line which is carrying LO power from the FFO, becomes high at about gap frequency of Nb. At lower frequencies the pump was found to be low because the FFS become much "shorter" that means unstable operation of the FFO at higher bias current (at higher power).

The sharp drop of the noise temperature T_{rx} that one may expect from the FTS pre-test, was not found around 645 GHz for both internal and external LOs. It could be due to the presence of excessive noise picked up at the *input* of the mixer (i.e. this noise is not dependent on mixer's gain). A more thorough analysis seems necessary to find out whether losses in LO circuits at 645 GHz are crucial for low noise operation of the integrated receiver near the gap frequency of Nb.

c) Antenna Beam Pattern

The receiver antenna beam was formed by two printed dipole antennas integrated with the SIS mixer and two quartz lenses: hyper-hemispherical one (diameter 10 mm) and front lens f = 40 mm (diameter 24.5 mm). The antenna beam pattern was mapped in front of the dewar's window at the distance of about 45 cm. The mapping is based on detection of a broad-beam source which is being translated in front of the cryostat in the plane perpendicular to the receiver beam axis. The antenna beam pattern presented in Fig. 4 shows main sidelobes at the level of about -12...-15 dB. The beam is not perfectly symmetric. A small of misalignment of the antenna with respect to the center of hyper-hemispherical lens can explain the incomplete symmetry of the beam.

d) Integrated Local Oscillator

Since the frequency of Josephson oscillator has fundamental relation with *dc*-voltage across the tunnel barrier of SIS junction, the tuning range of the integrated LO has been tested via measuring the dependence of its bias *voltage* on control line current while the bias *current* of the FFO was kept constant. Figure 5 shows the experimental data on tuning of the FFO. The LO is showing a *continuous* tuning which is almost linear from 550 GHz up to 700 GHz. The point of limited stability indicated in Fig. 5 means that the bias current of the FFO has to be decreased to obtain continuous tuning over this point. The decrease of the bias current means lower output power of the LO.

It has been found recently that the FFO has at least two distinctive regions of operation within the sub-mm range. Resonant operation takes place at bias voltages less than a *boundary* value of $V_{gap}/3$ that associated with a frequency range below 470 GHz [8]. This regime is characterized by presence of resonance Fiske steps (FS) because of low dumping of the junction cavity. The bias voltage of FFO is strongly locked to the FS that means limited tunability of the oscillator (operation is not stable between FS).

A continuously tunable flux flow regime might be realized at higher voltages (frequencies) where FS are dumped by quasi-particle loss, so flux flow steps (FFS) take place. The most important difference between these two regimes is the FFO linewidth (LW). The resonant regime is characterized by FS with much lower dynamic resistance, R_d, and the typical free running LW is relatively low (less than 1 MHz), but poor tunability is the price. In the non-resonant regime ($f \geq 500$ GHz) the dynamic resistance is much higher that is one of the reasons for broadening of LW. The experimental data of a free running FFO are presented in Fig. 6.

The data graph might be split into three regions. The first region has lowest R_d (0.001 - 0.02 Ω) that usually happens in the resonance regime at relatively low frequencies. Within this region the linewidth is following theoretical model [11] and might be associated with a constant fluctuation current of 0.2 μA. The second region is characterized by more sharp increase of LW that can be explained in terms of higher effective temperature. The estimated value of about 27 K is associated with external interference to the FFO. The much wider LW is measured in the non-resonant regime (presented by diamonds). The experimental value for the non-resonant regime is almost one order higher than LW of resonant regime for the same $R_d \approx 0.02$ Ω. This effect might be explained with the recent theory [12] in terms of elastic noise of the fluxon chain in absence of locking resonant conditions.

To realize the FFO operation with LW about (or smaller) than 1 MHz above the *boundary* voltage, two sets of experiments are in progress. In the first experiment devices have an integrated *rf* feed-back circuit to check whether it is possible to create quasi-resonant conditions for the FFO with high damping. The injection locking of the FFO to a 10 GHz synthesized source will be tested in the second set of experiments using an on-chip FFO-multiplier.

3. Imaging Array Receiver Design

The imaging array of 9 pixels in the frequency range 450-550 GHz is planned to be tested within one year from now. The sketch of the main receiving block is presented in Fig. 7. To achieve both dense packaging of the pixels and equal quality of all beams (f/10), use of diffraction limited silicon elliptic lens (diameter 10 mm) is planned in each individual pixel. Silicon elliptical lenses and their anti-reflection coatings from Stycast™ epoxy [3] are manufactured using precision diamond turning. Each pixel is designed to be the same optically, mechanically and electrically for easy replacement. The chip receivers fabricated on silicon substrates will be tested individually to guarantee *the best selection* for both main receiver and its replacement.

Since the FFO is a magnetic field sensitive device, the magnetic shielding is very important. Present design has two magnetic shields: an external tube from μ-metal and an internal one from superconducting material with option to heat it up in order to release trapped flux (see Fig. 7). To study the shield efficiency, the experimental chip receiver has been tested about 10 times during half-year showing reasonably stable and repeatable operation.

4. Balanced SIS Mixer Concept

Since a wide tuning range (400 - 700 GHz) and a reasonably good sensitivity have been demonstrated for a twin-junction double-dipole SIS mixer [10], there is an interest to

combine this device with a Josephson LO into an integrated receiver of superior quality. However, it was found that injection of LO power via micro-strip coupling circuitry is not obvious for the twin-junction mixer. The extra problem of limited LO power is important because both junctions of the balanced mixer have to be pumped to the same level that means approximately twice more power must be coupled from the FFO. A balanced mixer basically allows complete coupling of both signal and LO power (Fig. 8). Two junctions of the mixer are connected in series to the LO, but they are in parallel to the signal coming from the antennas in such way that no leak of the in-phase signal power is possible to the LO path. The optimal signal coupling might lead to a factor of two *lower noise temperature* along with *extra power* coupled from integrated LO. We hope that an integrated receiver with balanced mixer might operate at the level of the best SIS receivers pumped by a 'traditional' LO. A few experimental samples of the balanced receiver are pre-tested at *dc* and ready for further *rf*-study. The bandwidth of the balanced mixer of present design supposed to be about the same as of a single-junction mixer (60 - 90 GHz). Next is the study of an integrated receiver with *balanced wide-band twin-junction mixer*.

Summary

1. The integrated receiver on a base of niobium trilayer Nb/Al/Al_xO_y/Nb is useful up to 700 GHz. Since 1992 integrated receivers of different design have been tested within frequency range 100-700 GHz showing noise temperatures better than 1 K/GHz close to the performance of 'traditional' SIS receivers with external LO.

2. The linewidth less than 1 MHz is typical for integrated LO within the frequency range below 450-470 GHz when operated in the resonant regime. However, much wider linewidth has been observed in the easy-to-tune regime of the FFO at higher frequencies. To improve the spectral resolution of the integrated receiver, tunable frequency- and phase-locking systems are under study.

3. The imaging array receiver of 9 integrated receiver pixels with elliptical silicon lenses is designed and will be complete within one year.

4. The new quasioptical balanced SIS mixer is designed using an advantage of the integrated *rf*-interface that provide complete coupling of power for both input signal source and the local oscillator. This approach may lead to ultimate quality of the integrated receiving device.

Acknowledgments

The work was supported in parts by Russian Program for Basic Research, the Russian State Scientific Program "Superconductivity," and ESA TRP contract No. 11653/95/NL/PB/SC.

References:

[1] V. P. Koshelets, A. V. Shchukin, S. V. Shitov, and L. V. Filippenko, *IEEE Trans. on Appl. Supercond., vol. 3, No. 1, pp. 2524-2527, 1993.*

[2] R. Blundel and C. E. Tong, *Proc. IEEE, vol. 80, pp. 1702-1720, Nov. 1992.*

[3] H. van de Stadt et al. *Proc. **6th** Int.Symp. on Space THz Techn., March 1995, Pasadena USA.* M. Bin, M. C. Gaidis, D. Miller, J. Zmuidzinas, T. G. Phillips, H. G. LeDuc, *Proc. **7th** Int.Symp. on Space THz Techn., March 1996, Charlottesville, USA, pp. 549-560.*

[4] V. P. Koshelets, S. V. Shitov, L. V. Filippenko, A. M. Baryshev, H. Golstein, Th. de Graauw, W. Luinge, H. Schaeffer, H. van de Stadt, *Appl. Phys. Lett. **68** (9), pp. 1273-1275 (February 1996).*

[5] S. V. Shitov, V. P. Koshelets, A. M. Baryshev, L. V. Filippenko, T. de Graauw, J.-R. Gao, W. Luinge, H. van de Stadt, N. D. Whyborn, P. Lehikoinen, *Proc. 7th Int.Symp. on Space THz Techn., March 1996, Charlottesville, USA, pp. 417-425.*

[6] V. P. Koshelets, S. V. Shitov, A. M. Baryshev, I. L. Lapitskaya, L. V. Filippenko, H. van de Stadt, J. Mess, H. Schaeffer, T. de Graauw, *IEEE Trans. on Appl. Supercond., **5**, 3057 (1995).*

[7] V. P. Koshelets, S. V. Shitov, A. V. Shchukin, L. V. Filippenko, and J. Mygind, *Appl. Phys. Lett. (July 1996).*

[8] V. P. Koshelets, S. V. Shitov, A. V. Shchukin, L. V. Filippenko, J. Mygind, A. V. Ustinov, "Self-pumping effects and radiation linewidth of Josephson flux flow oscillators". *Submitted to Phys.Rev.*

[9] V. P. Koshelets, A. V. Shchukin, I. L. Lapitskaya, and J. Mygind, *Phys. Rev B., (1995).*

[10] S. V. Shitov, A. M. Baryshev, V. P. Koshelets, J.-R. Gao, J. Jegers, W. Luinge, H. van de Stadt, Th. de Graauw, *Proc. 7th Int.Symp. on Space THz Techn., March 1996, Charlottesville, USA, pp. 525-535.*

[11] M. J. Stephen, *Phys. Rev. Lett., **21**, 1629 (1968).*

[12] A. A. Golubov, B. A. Malomed, A. V. Ustinov, *Phys. Rev. B, **54**, 3047 (1996).*

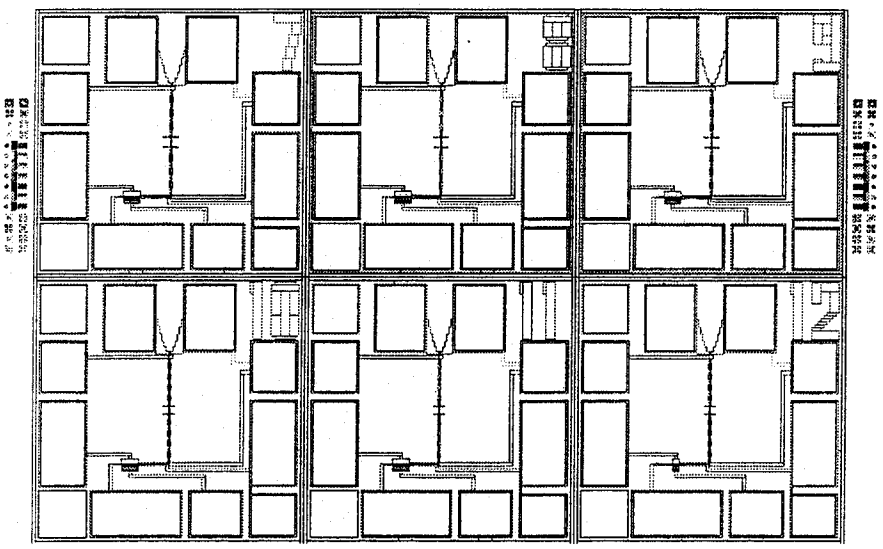

Fig. 1. Layout (partial view) of the quartz wafer containing 15 integrated receiver (only 6 chips are shown). The chip dimensions are 4 mm × 4 mm × 0.2 mm including the area of contact pads (0.7 mm × 0.7 mm). The double-dipole antenna SIS mixer is in the center of each chip; local oscillator (FFO) is at low-left from the mixer. The receivers for operation within 400-550 GHz (larger antennas) and 550-700 GHz (smaller antennas) are fabricated at the same wafer.

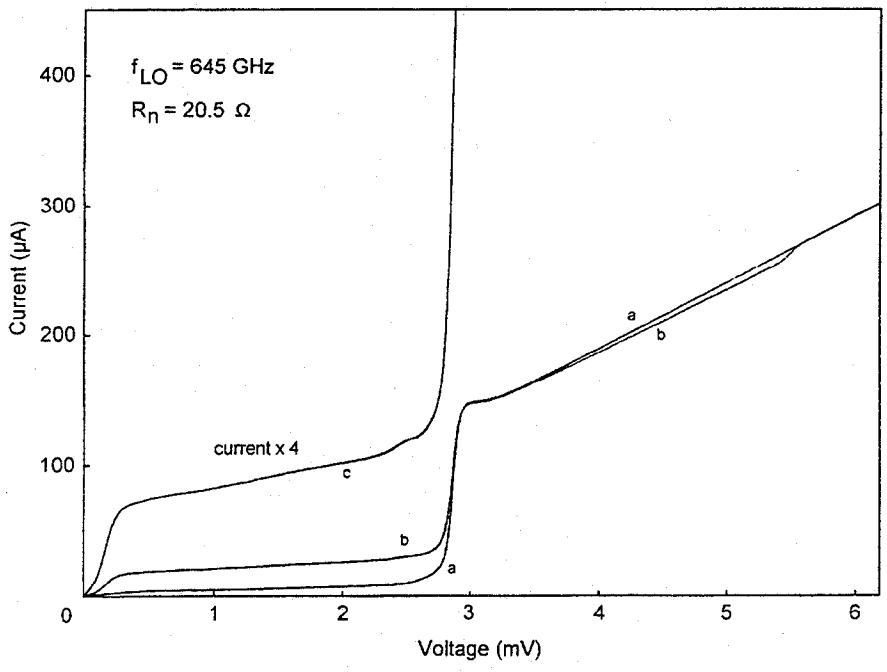

Fig. 2. Unpumped (a) and pumped (b) IV-curves of SIS mixer. The integrated LO at 645 GHz is used. The curve (c) is the same as (b), but it is magnified four times (× 4) in vertical scale.

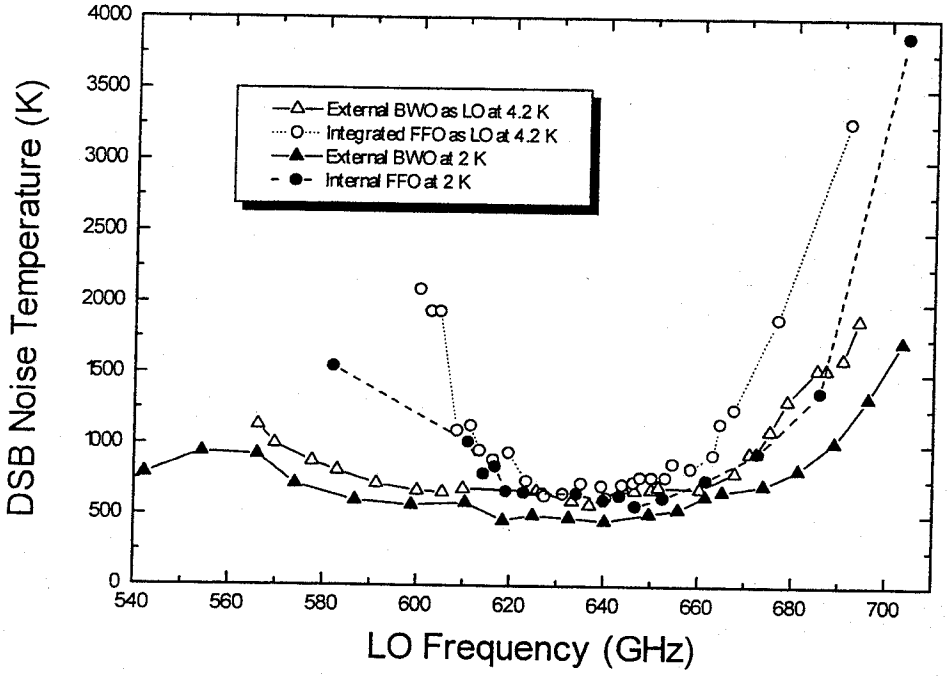

Fig. 3. Noise temperature for the integrated receiver within frequency range 540-705 GHz for both external and internal (integrated) local oscillators at two temperatures of the liquid helium bath.

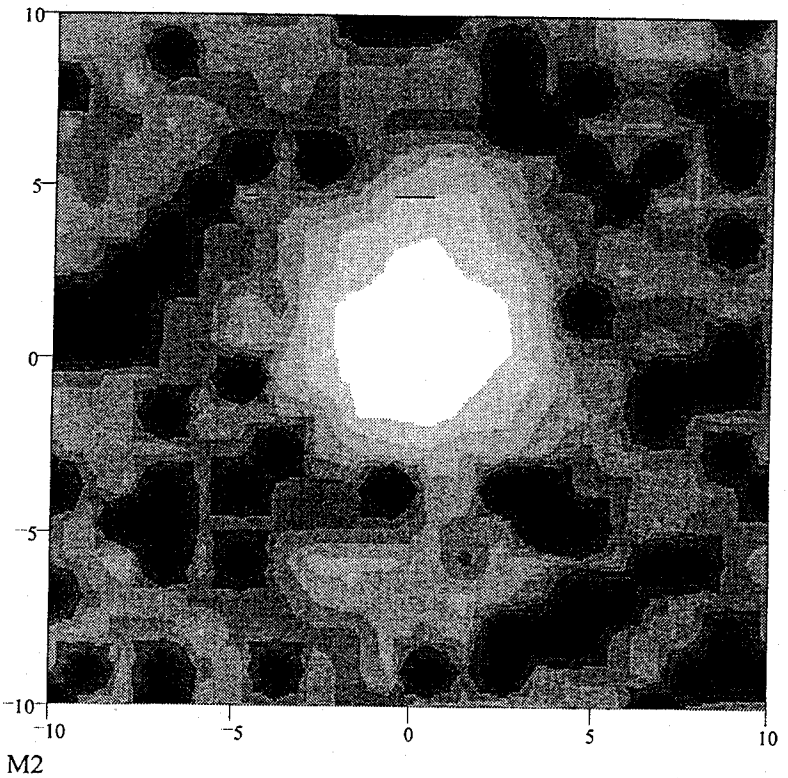

Fig. 4. Contour plot for the antenna beam pattern of the integrated receiver measured in front of the cryostat at 645 GHz. The step of gray scale is 3 dB. Both axes are in angular degrees.

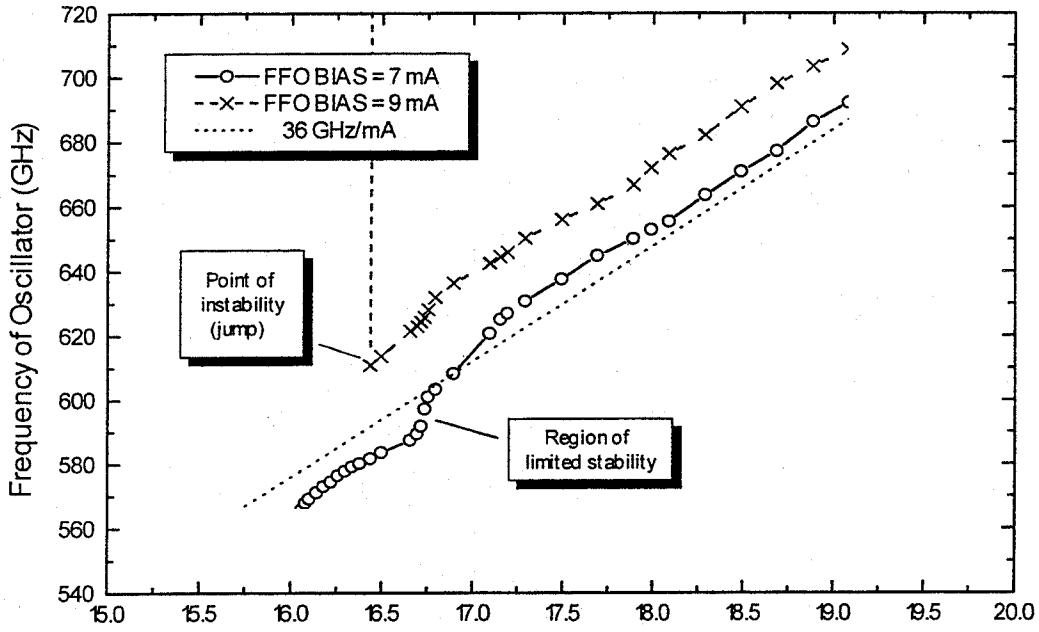

Fig. 5. Tuning characteristic of the superconducting flux flow oscillator (FFO) at about the gap frequency of niobium.

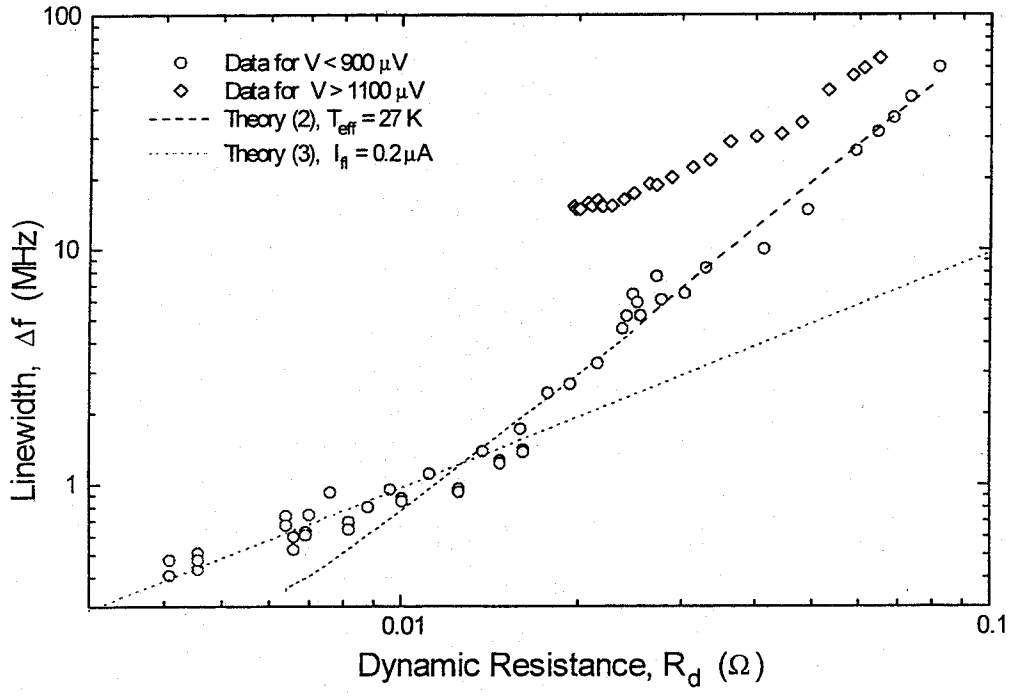

Fig. 6. Experimental data on FFO linewidth for different operating regimes.

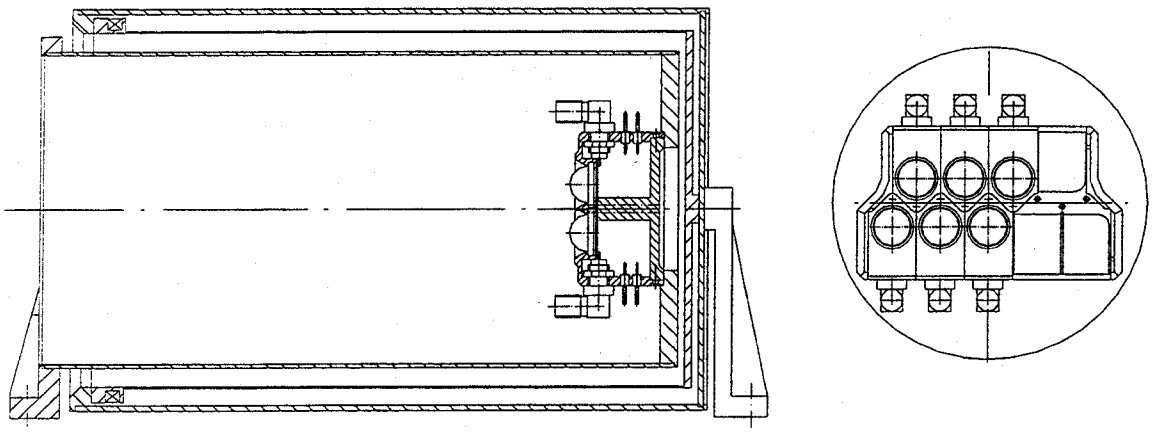

Fig. 7. Design of a prototype imaging receiver with individual silicon single-lens optics at each of 9 pixels. The two-layer shielding is used with the external cylinder from μ-metal and internal one from a superconducting material.

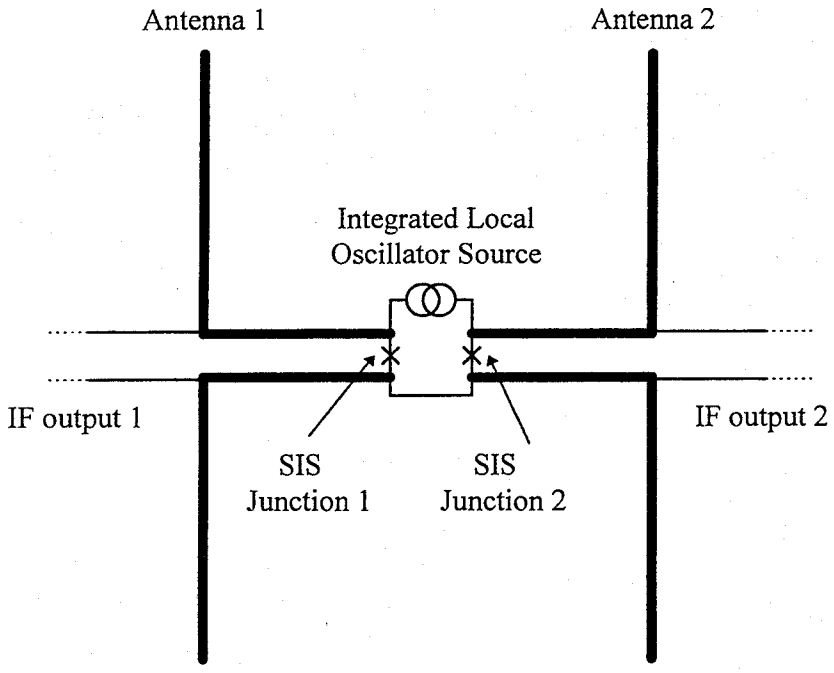

Fig. 8. Schematics of a quasioptical balanced double-dipole antenna SIS mixer. The mixing SIS junctions are connected to the integrated LO in series. Two output signals at IF are phase-shifted (180°) and have to be combined in-phase.

Performance limitations of NbN SIS junctions with Al striplines at 600 - 850 GHz

P. Dieleman, T.M. Klapwijk, H. van de Stadt†,
University of Groningen, Department of Applied Physics and Materials Science Center (MSC) Nijenborgh 4.13, 9747 AG Groningen, The Netherlands.
† Space Research Organisation of the Netherlands, Landleven 12, 9747 AD Groningen, The Netherlands.

M. Schicke, B. Plathner, and K.H. Gundlach
Institut de Radio Astronomie Millimetrique, 300 rue de la Piscine, Saint Martin d'Hères, France.

Abstract

We study the behavior of NbN SIS junctions as radiation detectors with emphasis on the shotnoise generated at voltages below the gap voltage. The intrinsically large subgap current of NbN junctions is carried by pinholes with a conduction attributed to multiple Andreev reflection, leading to transported charges $q >> e$. Using this charge enhancement mechanism we explain the junction shotnoise characteristics in the unpumped case as well as in the pumped case. The measured mixer noise temperature in the pumped case is more than twice that calculated with standard Tucker theory. Measured double side band noise temperatures are 1450 K and 3300 K at 600 and 850 GHz respectively. Main limitations to the receiver sensitivity are the loss in the aluminum circuit and the subgap current induced shotnoise.

1 Introduction

Heterodyne mixers consisting of niobium Superconductor-Insulator-Superconductor (SIS) tunnel junctions are sensitive receivers for radio astronomy in the millimeter and submillimeter wavelength range. There is an increasing demand for these devices at frequencies beyond 700 GHz, which is the frequency limit dictated by the energy gap of Nb. Impedance matching circuits of normal metals are used with a relatively low absorption loss[1, 2]. This allows extension of the upper frequency limit to about 1100 GHz, close to twice the gap frequency of Nb. For detection at higher frequencies a superconductor with a larger energy gap is needed. The most obvious candidate is NbN, with a practical energy gap of 4.8 meV corresponding to a frequency limit of 2 THz. A major drawback of NbN junctions is that the current technology for making high current density junctions leads to an intrinsically large subgap (leakage) current due to pinholes in the barrier. In spite of this, recent results at low frequencies with NbN junctions and (partly) Nb striplines are promising[3, 4] as are the results presented in this paper. To identify room for improvement we investigate the limitations to the sensitivity of NbN SIS mixers with emphasis on the use at THz frequencies. At these frequencies impedance matching circuits made of normal metals provide lower losses than structures made of Nb or NbN[5]. The losses in normal metals are appreciable but well understood and unavoidable[2, 5, 6]. Therefore in this article we will focus on the behavior of the NbN junction itself.
The device characteristics are described in part 2, in part 3 the current-voltage and shotnoise characteristics are presented and modeled. Part 4 compares our measured heterodyne mixing results with the values obtained from the model derived in part 3. Part 5 summarizes the outcome and discusses the expected behavior at supra-THz frequencies.

2 Junction characteristics and measurement setup

The NbN junctions used are fabricated by sputtering on unheated 200 μm thick fused quartz substrates. The NbN films are deposited by reactive RF-magnetron sputtering in an argon and nitrogen atmosphere. The barrier is formed by depositing MgO intermittently on a rotating substrate holder. The junction is patterned by reactive ion etching with CF_4 gas. The MgO layer is etched with a phosphoric acid. We present measurements on two junctions, labeled A and B with resonance frequencies 600 and 850 GHz respectively. The junctions have areas of 0.8 μm^2 and normal resistances R_N of 30 Ω (A) and 50 Ω (B) corresponding to a current density of 15 and 9 kA/cm^2. An I,V curve measured at 4.5 K is shown in Fig. 1a. The subgap-to normal resistance ratio, $R_{(3mV)}/R_N$ is 4.5 and is not improved by lowering the operating temperature. The impedance matching structure is a two junction tuning circuit[7]; two junctions separated by a piece of stripline with length l which serves to transform the capacitive part of the impedance of one junction into an inductive reactance which tunes out the capacitance of the other. A second stripline section of length L matches the resulting real resistance to the antenna impedance, taken to be

50 Ω. The width of both striplines is 4 μm. The striplines and antenna consist of sputtered Al layers with a residual resistance ratio defined as $R_{(300K)}/R_{(5K)}$ of about 3. Details of a similar process are described in [8]. The substrate is polished down to 40 – 50 μm thickness and mounted in a mixer block scaled from a 345 GHz mixer[9]. The mixer is cooled to about 4.5 K. A contacting backshort is used as an adjustable mechanical tuning element. A Mylar beamsplitter of 15 μm thickness is used to inject the local oscillator signal at 600 and 680 GHz, a 56 μm thick beamsplitter is used at 850 GHz. The vacuum window consists of 105 μm thick Mylar and a 110 μm black polyethylene sheet at 77 K functions as IR heat filter. The junctions are connected via an integrated low-pass RF filter and a circulator with 0.5 dB loss to the IF amplifier chain with a noise temperature of 3 K and 80 dB gain at 1.5 GHz with 85 MHz bandwidth.

3 Shot noise measurements and modeling

In Fig. 1a the I,V curve and differential resistance are plotted. Clearly the subgap current is much larger than expected from simple tunneling theory[10]. This can be due to *a)* an energy gap spread over the junction area because of inhomogeneous materials quality , *b)* barrier edge effects, *c)* pinhole defects in the barrier. The first can be excluded since this leads to a gap smearing which is indeed observed, but small, ΔVgap < 0.5 mV. Barrier edge damage can be excluded since large area junctions exhibit the same I,V characteristics as smaller ones where the edge effects should be more dominant, if present. Therefore we conclude that the current transport is through pinholes, small defects in the deposited MgO. The observation of subgap harmonic structures in Fig. 1a supports this conclusion, since these occur only in transparent channels. Together with the independence of the I,V curve on temperature they hint at the transport mechanism in these pinholes causing the excess subgap current, multiple Andreev reflection (MAR)[11, 12].

An electron approaching a superconductor can either reflect normally at the interface or take an electron from the Fermi sea to tunnel jointly into the superconductor to form a Cooper pair (Andreev reflection). The charge effectively transported is 2e. The missing electron (a hole) has opposite phase and momentum and will therefore move away from the interface. If the normal conductor is sandwiched between two superconductors the hole will again have a probability for Andreev reflection at the opposite interface. Since the energy of the Andreev reflected particle is exactly as far above the Fermi level as the original particle was below, the back and forth movement can go on until the electron or hole has gained enough energy to tunnel into one of the superconductors at an energy larger than the energy gap. With each Andreev reflection event a Cooper pair is created or destroyed, and a charge 2e is transferred from the normal regime to the superconductor or vice versa. The average total charge q transported after each tunneling event depends on the Andreev reflection probability and therefore on the transmission of the pinhole. The maximum charge in the limit of high pinhole transmission is calculated following KBT[11]. In this limit an electron coming from the normal region is either Andreev reflected or tunnels into the

superconductor. The total current flowing from the left superconductor (at voltage V) to the right superconductor (at zero voltage) is given by the difference of[11]

$$I_{\rm LR} = \frac{1}{eR_N} \int_{-\infty}^{\infty} dE f_0(E-eV)[1-A(E-eV)][1+A(E)+A(E)A(E+eV)+\cdots] \quad (1)$$

and

$$I_{\rm RL} = \frac{1}{eR_N} \int_{-\infty}^{\infty} dE f_0(E)[1-A(E)][1+A(E-eV)+A(E-eV)A(E-2eV)+\cdots] \quad (2)$$

where $f_0(E)$ is the Fermi distribution, $A(E)$ is the Andreev reflection probability. The first term $[1-A]$ denotes the fraction of available electrons in the superconductor which is transmitted into the normal region. The last term $[1+\cdots]$ gives the proper charge transferred, 1 if no Andreev reflections take place, 2 for one Andreev reflection, and so on. At every voltage the currents I_n $(n = 1, 2, \ldots)$ carried by n-electron processes are calculated by splitting up Eqs. 1 and 2 into the n-electron parts. For example I_2 is given by

$$\begin{aligned} I_2 \;=\; \frac{2}{eR_N} \int_{-\infty}^{\infty} dE(\; & f_0(E-eV)[1-A(E-eV)]A(E)[1-A(E+eV)] - \\ & f_0(E)[1-A(E)]A(E-eV)[1-A(E-2eV)]\;) \end{aligned} \quad (3)$$

The factor 2 comes in because 2e is taken across the normal region. The sum of the properly weighted currents nI_n divided by the total current gives the average charge multiple q/e carried. The resulting charge-voltage curve is shown in the inset of Fig. 1b. The charge is calculated over a small voltage range since the calcuation becomes increasingly time consuming at lower voltages. For this reason a much simpler approach is tried to estimate the average charge. The charge is calculated by taking unity Andreev reflection probability for electrons arriving at energies below the gap energy and zero probability for electrons with higher energies, thereby neglecting higher order terms. The resulting average charge is then simply $m \cdot e$ at voltages Vgap$/(m+1)$, lower than the values obtained using the full energy dependence of the Andreev reflection probability. Since in our case a pinhole is considered to have a short length, the total time of an Andreev reflection sequence is short. With this assumption the charge is considered to tunnel simultaneously. Therefore the calculated charge can be used in the standard low-frequency shotnoise equation[13] :

$$P_{\rm shot} = \frac{1}{4}\,(2qIB \coth \frac{qV}{2k_BT} R_{\rm dyn}) \quad (4)$$

This equation yields good correspondence between the current-voltage and shotnoise characteristics of Nb devices[14]. Fig. 1b shows the shotnoise measured with the IF chain described in section 2 together with the curve calculated using Eq. 4. The best fit was obtained using the solid curve in the inset of Fig. 1b, which is the charge calculated neglecting Andreev reflection above the gap (the dotted curve in the inset), multiplied by a factor 1.1. This input charge is lower than the charge calculated following [11] indicating that the pinhole transmission is lower than 1 since this would result in

a lower Andreev reflection probability as used in the approximation. Clearly the IF output curve calculated using the effective charge concept follows the measured result very well. *Hence the shotnoise of a high current density NbN junction is intrinsically more than doubled!* By high current density we mean 10 kA/cm^2 or more, resulting in a $R_{(3mV)}/R_N$ of 10 or smaller with state of the art technology[15, 16]. Similar shotnoise behavior in NbN junctions was previously observed but not understood[17]. Our results agree with a theoretical prediction which was not yet observed that a single normal metal / superconductor structure can produce a shotnoise up to twice that of a structure consisting of two normal metals due to the 2e charge transfer via Andreev reflection[18].

4 Receiver noise measurements

To investigate the effect of the shot noise behavior of the junction on the mixing properties heterodyne measurements are performed at 600 and 850 GHz using standard hot/cold loads. For each frequency the bias voltage, backshort position and local oscillator power is adjusted to give optimum performance. Fig. 2b shows the IF output power at 600 GHz versus bias voltage for input powers corresponding to 77 K and 293 K. Y-factors and corrected receiver noise temperatures are listed in Table 1. Measured loss values of optical components are listed in Table 2. The stripline loss is derived from the measured receiver gain. The calculated stripline loss is close to the measured value, if the aluminum conductivity derived from the series resistance value is taken into account instead of the independently measured Al conductivity. This lowers the residual resistance ratio to about 3. From wideband FTS measurements it was concluded that the resonance frequency is lower than anticipated. This may indicate a specific capacitance that is larger than the 135 fF/μm^2 which we expect for the current densities found[16]. The effective coupling is also not optimal since the design assumed 18 Ω junctions with sizes of 1 μm^2.

Table 1: Measured receiver noise and gain values

Junction	Frequency (GHz)	Y- factor (dB)	T_{REC} (K)
A	600	0.55	1450
A	680	0.45	1700
B	850	0.15	3300

Table 2: Loss in dB of RF components

Junction	Beamsplitter	Window	Heat Filter	Lens + Horn	Stripline
A (600 GHz)	0.32	0.81	0.81	0.22	7.5
B (850 GHz)	2.9	0.13	0.18	0.22	12

The consequence for the mixer noise temperature is that the same voltage dependent q value has to be applied in the calculation of the current correlation matrix H_{ij}

of the Tucker theory[19]. The resulting mixer noise temperatures are listed in Table 3. Since the effective charge q at the optimum bias voltage is about 2.5, the mixer noise temperatures are increased by approximately the same value. The calculated IF output powers are compared with the measured values in Fig. 2b. In the voltage region of the first photon step, the measured and calculated values agree reasonably well, indicating the validity of the method.

Table 3: Measured and calculated mixer noise T_M and loss L_M. The mixer noise values in column *calc* is calculated using $q = e$, the values labeled *corr* are calculated using the full expression for q.

	T_M (K)			L_M (dB)	
Junction	meas	calc	corr	meas	calc
A (600 GHz)	243	80	198	9.1	9.1
B (850 GHz)	204	77	168	8.1	7.8

5 Conclusions

Sensitive THz radiation detection requires small area, high current density SIS junctions. However, the current NbN/MgO/NbN technology is not matured sufficiently to obtain thin pinhole-free tunnel barriers. Whether it will be possible to further improve the technology to produce MgO barriers with less defects remains to be seen. The presence of pinholes results in a large subgap current with intrinsically large shot noise power due to multiple Andreev reflection. Because of this effect it is unlikely that NbN SIS junctions will outperform Nb junctions below 1100 GHz. To illustrate this: The only difference between NbN junctions and Nb junctions is that the latter operates above its gap frequency. If we now compare the mixer noise temperature of Nb at 820 GHz (51 K)[6] with NbN at 850 GHz (204 K) it is clear that Nb even above the gap frequency functions much better than a state of the art NbN junction. Further measurements of NbN devices above 1100 GHz need to be performed to examine the feasibility of SIS detection at these frequencies.

We would like to thank N. Whyborn for the adaptation of the two junction tuning design for waveguides. Helpful ideas, discussions and general assistance of H. Bukkems, S. den Hartog, J.B.M. Jegers, J.R. Gao, W. Hulshoff, D. Nguyen, and H.H.A. Schaeffer are acknowledged. This work was supported in part by the European Space Agency under contract No. 7898/88/NL/PB(SC) and the Stichting voor Technische Wetenschappen.

References

[1] H. van de Stadt, A. Baryshev, P. Dieleman, M.W.M. De Graauw, T.M. Klapwijk, S. Kovtonyuk, G. de Lange, I. Lapitskaya, J. Mees, R.A. Panhuyzen, G. Prokopenko, and H.H.A. Schaeffer, *Sixth Int. Symp. on Space THz Techn.*, March 1995, CalTech. Pasadena, California, USA.

[2] M. Bin, M.C. Gaidis, J. Zmuidzinas, T.G. Phillips, and H.G. LeDuc, *Appl. Phys. Lett.*, **68**, pp. 1714-1716 (1996).

[3] Y. Uzawa, Z. Wang, A. Kawakami, *Seventh Int. Symp. on Space THz Techn.*, March 1996, University of Virginia, Charlottesville, Virginia, USA.

[4] A. Karpov, B. Plathner, J. Blondel, M. Schicke, and K.H. Gundlach, *Seventh Int. Symp. on Space THz Techn.*, March 1996, University of Virginia, Charlottesville, Virginia, USA.

[5] G. de Lange, J.J. Kuipers, T.M. Klapwijk, R.A. Panhuyzen, H. van de Stadt, and M.W.M. de Graauw, *J. Appl. Phys.*, **77**, pp. 1795-1804 (1995).

[6] P. Dieleman, T.M. Klapwijk, J.R. Gao, and H. van de Stadt, to be published in *IEEE Trans. Appl. Super.* 1997.

[7] J. Zmuidzinas, H.G. LeDuc, J.A. Stern, and S.R. Cypher, *IEEE Trans Microwave Theory Tech.* **42**, 698-706 (1994).

[8] B.Plathner, M. Schicke, T. Lehnert, K.H. Gundlach, H. Rothermel, M. Aoyagi, and S. Takada, Appl. Phys. Lett. **69**, pp. 4102- 4104 (1996), M. Schicke, K. H. Gundlach, H. Rothermel, P. Dieleman, and H. van de Stadt, unpublished.

[9] C.E. Honingh, J.J. Wezelman, M.M.T.M. Dierichs, G. de Lange, H.H.A. Schaeffer, T.M. Klapwijk, and M.W.M. de Graauw, *J. Appl. Phys.*, **74**, pp. 4762-4773 (1993).

[10] E.L. Wolf, *Principles of Electron Tunneling Spectroscopy*, p 104 (Oxford University Press, New York, 1985).

[11] T.M. Klapwijk, G.E. Blonder, and M. Tinkham, Physica B+C 109 & 110, 1657 (1982), M. Octavio, M. Tinkham, G.E. Blonder, and T.M. Klapwijk, Phys. Rev. B **27**, 6739 (1983).

[12] N. van der Post, E.T. Peters, I.K. Yanson, and J.M. van Ruitenbeek, Phys. Rev. Lett. **73** 2611 (1994).

[13] D. Rogovin and D.J. Scalapino, *Ann. Physics,* **68**, pp.1-90, (1974).

[14] N.B. Dubash, G. Pance, and M.J. Wengler, *IEEE Trans. Microwave Theory Tech.*, **42**, pp 715-725, (1994).

[15] Z. Wang, Y. Uzawa, and A. Kawakami, to be published in *IEEE Trans. Appl. Super.* 1997.

[16] J.A. Stern, H.G. LeDuc, and A.J. Judas, *Third Int. Symp. on Space THz Techn.*, Ann Arbor, MI, USA., (1992).

[17] N.B. Dubash, M.J. Wengler, private communication.

[18] M.J.M. de Jong and C.W.J. Beenakker, Phys. Rev. B **49**, 16070 (1994).

[19] J.R. Tucker, M.J. Feldman, *Rev. Mod. Phys.* **57**, pp. 1055-1113 (1985).

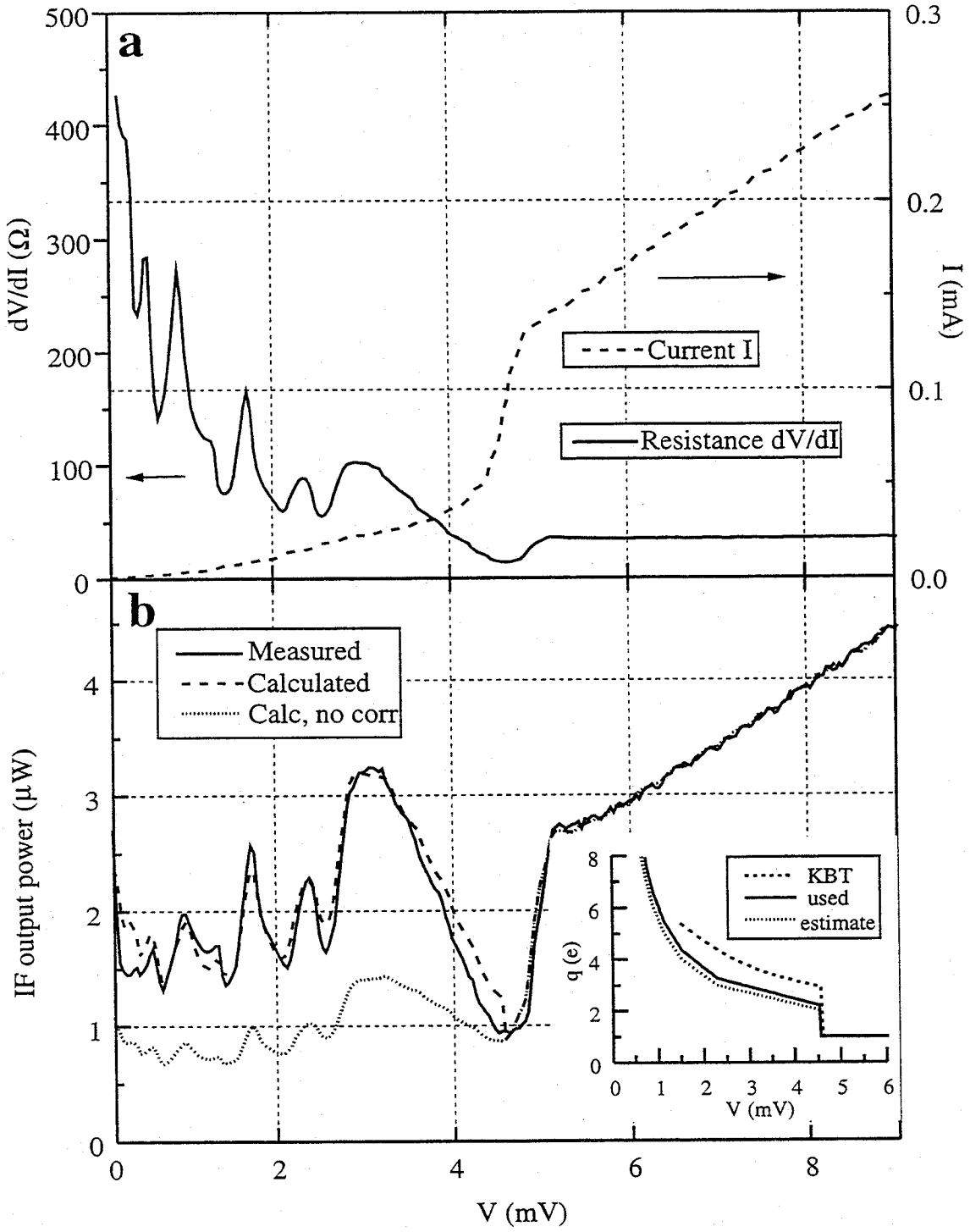

Figure 1: a. I,V and dV/dI characteristics. The dV/dI curve peaks at voltages close to $2\Delta/n$, with $n = 1, 2, 3 \ldots$. b. The output noise power at 1.5 GHz. The dotted curve is calculated using $q = e$, the dashed curve is calculated with the full dependence of q on the voltage as shown by the solid line in the inset. The dashed curve in the inset is calculated as described in the text. Neglecting Andreev reflection above the gap energy results in the dotted curve.

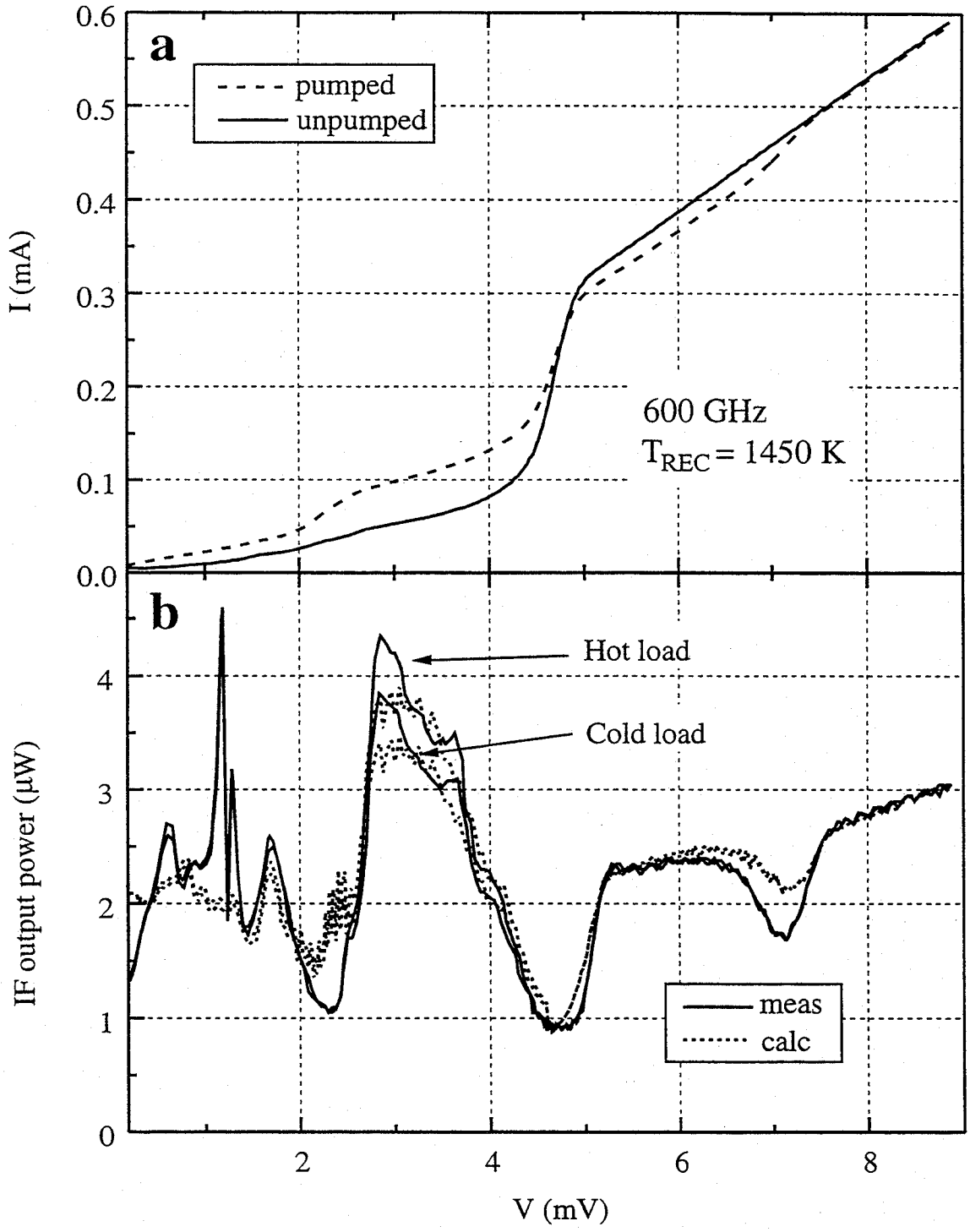

Figure 2: **a.** Pumped and unpumped I,V curves. The pump frequency is 600 GHz. **b.** Measured and calculated IF output power for hot and cold loads. The double peak in the measured IF curve at 1.2 mV is due to incomplete suppression of the ac Josephson effect by a magnetic field, possibly because the junctions had unequal areas. Higher order Shapiro steps at multiples of $hf/2e$ =1.24 mV are reasonably well suppressed.

ALL-NbN QUASI-OPTICAL SIS MIXERS AT TERAHERTZ FREQUENCIES

Yoshinori UZAWA, Zhen WANG, and Akira KAWAKAMI

Kansai Advanced Research Center, Communications Research Laboratory,
Ministry of Posts and Telecommunications, 588-2 Iwaoka, Iwaoka-cho, Nishi-Ku,
Kobe, 651-24 JAPAN

Abstract

We have theoretically and experimentally investigated submillimeter-wave receiver performances employing NbN/AlN/NbN tunnel junctions with high current density and high energy gap. The receiver noise based on parameters for our typical NbN SIS junction were analyzed using Tucker's quantum theory of mixing, which showed that DSB receiver noise temperatures of below $3hv/K_B$ can be achieved by using the NbN SIS junctions for frequencies up to 2 THz. An experimental receiver has been designed and tested for the 1 THz band. The mixer consists of a MgO hyperhemispherical lens with anti-reflection cap, a NbN twin-slot antenna, and NbN tuning circuits. The prepared NbN/AlN/NbN junction size was about 0.5 $\mu m\phi$, and the current density was about 30 kA/cm^2 ($\omega C_J R_N$ = 11 at 1 THz). Although the junctions showed good dc I-V characteristics with a small sub-gap leakage current, the receiver noise temperature measured by the standard Y-factor method was about 2700 K(DSB) at 761 GHz, which is much larger than the theoretical prediction. The relative high noise performance may be caused by the large RF losses in the tuning circuit of polycristalline NbN on the SiO.

1. Introduction

Superconductor-insulator-superconductor (SIS) tunnel junction based on NbN is the best candidate for terahertz mixer elements, because NbN has a large gap frequency of up to 1.4 THz compared to about 700 GHz for conventional Nb. According to theoretical calculations by Feldman [1], SIS mixers should exhibit good performance at frequencies up to twice the superconducting gap frequency, which is 2.8 THz for all-NbN tunnel junctions. SIS mixers using all-NbN junctions can therefore almost cover the whole submillimeter wave band. However, simple scaling arguments pose some problems in fabricating SIS mixers based on NbN at the end of submillimeter wave-lengths. This issue is discussed in Ref. [1], which is that the NbN junctions must have small junction area of 0.1 μm^2 and the critical current density of 40 kA/cm^2 at 1 THz for the condition of $\omega C_J R_N = 4$, assuming the specific capacitance of 60 $fF/\mu m^2$.

We have developed NbN/AlN/NbN tunnel junctions with high quality and high current density up to 54 kA/cm^2 [2,3], and demonstrated excellent noise performances in the 300 GHz band by using these junctions with Nb tuning circuits[4,5]. In order to develop the great potential of the high current density NbN SIS junctions at terahertz frequencies (above the gap frequency of Nb), it is essential to fabricate all-NbN mixers or NbN mixers with normal metal tuning circuits. In this report, we show the theoretical prediction of the receiver noise temperature based on an experimental I-V curve of the typical NbN junctions, and the preliminary results on fabrication and testing of all-NbN quasi-optical SIS mixers at terahertz frequencies.

2. Theoretical Noise Performance

We have made simulation of the DSB receiver noise temperatures employing quasi-five port model based on Tucker's quantum theory of mixing at frequencies up to around twice the gap frequency of NbN [6]. The I-V curve of a NbN/AlN/NbN tunnel junction used in our simulation is shown in Fig. 1. This was obtained from the measurement for the NbN SIS junction with the current density of 20 kA/cm^2 and the size of 1 $\mu m\phi$. The junction has the

small leakage current and the strong non-linearity at the gap voltage of about 5.3 mV which corresponds to the gap frequency of 1.3 THz. We assumed that the junction capacitance with the specific value of about 100fF/μm^2 was tuned out at each simulation frequency by an external circuit. Both the RF embedding admittance and the IF load resistance seen by the intrinsic SIS junction were taken to be $1/R_N\ \Omega^{-1}$ and 50 Ω, respectively. The IF frequency is 1 GHz and IF amplifier noise temperature is 2 K. The results for optimum receiver noise temperature at the physical temperature of 4.2 K are shown in Fig. 2. At each frequency, the pumping strength α and bias voltage were optimized. As seen in Fig. 2, the simulation predicts that sensitive SIS receiver noise temperature of below $3h\nu/K_B$ can be achieved by using the NbN/AlN/NbN junctions for frequencies up to 2 THz. This result is encouraging.

3. Experimental Results

3.1 Mixer Design

In our mixers, a quasi-optical structure employing a substrate lens is used to couple the RF radiation to the junctions. An optical micrograph of our mixer chip is shown in Fig. 3. On a 0.3-mm-thick single-crystal MgO substrate, two NbN/AlN/NbN junctions in parallel were integrated with a single-crystal NbN twin-slot antenna and NbN tuning circuits. The procedures for fabricating the junctions are described in Ref. [5]. The mixer designs utilizing twin-slot antennas and two-junction tuning circuits have successfully demonstrated low noise performances and wide-band operations as described in many papers [7-10]. We chose the antenna dimensions as followings: the slot length is $L = 0.33\lambda$, the width is $W = 0.05L$, and the separation is $S = 0.17\lambda$. Here λ is the free-space wavelength at the center frequency. These dimensions are originally for the silicon substrate ($\varepsilon_r = 11.5$), and the antenna impedance become a value of $Z_{ant} = 33\ \Omega$ at the center frequency [8]. In case of our mixer using the MgO substrates ($\varepsilon_r = 9.6$), the antenna impedance may be a little bit different from 33 Ω at the design frequency, but we assumed the antenna impedance to be 35 Ω. The slot antennas are connected to the NbN SIS junctions with NbN coplanar-waveguide (CPW) transmission lines having the characteristics impedance of 35 Ω.

The NbN/AlN/NbN tunnel junctions are assumed to be the size of 0.7 μmϕ and the

current density of 30 kA/cm^2. The capacitance for the 30 kA/cm^2 junction was calculated from the following expression obtained by measurements for our high current density NbN SIS junctions ;

$$\mathrm{Log}C_S = 1.85 + 0.16\log J_C,$$

where C_S is the specific capacitance in fF/μm^2, and J_C is the current density in kA/cm^2 [11]. Thus, the assumed junction has the normal state resistance of 37 Ω and the junction capacitance of 47 fF/μm^2, which gives the $\omega C_J R_N$ product of 11 at 1 THz.

The two-junction tuning circuit employing a NbN microstripline is used to tune out the SIS junction capacitance, and connected to the center conductor of CPW-lines. The NbN microstripline consists of a 300-nm thick NbN for the strip, a 250-nm thick SiO (ε_r = 5.5) for the microstrip dielectric, and a 180-nm thick NbN for the ground plane on the single-crystal MgO substrate. Since we had not measured the penetration depth of NbN thin films fabricated on the SiO underlayers, we assumed the penetration depth to be 180 nm measured for NbN films on the single-crystal MgO [12, 13].

The mixer chip, whose dimensions are 4 x 4 x 0.3 mm, is clamped on the flat surface of a 3-mm radius hyperhemispherical MgO lens. As MgO has a relatively large dielectric constant of 9.6, the reflection loss at the surface of the lens is about 26 % in case of no matching layer. To reduce the reflection loss, we put a thermoformed matching layer of polyimide film [14]. This material has not only a dielectric constant of 3.46, necessary for the λ/4 matching layer, but also excellent physical, electrical, and mechanical properties at cryogenic temperature. We used the 50-μm thick film which corresponds to the λ/4 thickness at around 800 GHz.

3.2 Noise Performances

The receiver set-up is basically the same as described in Ref. [5]. The incoming radiation entered the dewar through a 0.5-mm-thick Teflon vacuum window. Thin Zitex infrared filters cooled to 77 K and 4.2 K were used to block infrared radiation from the 4.2-K

components in order to reduce thermal load and temperature gradients. Local oscillator (LO) power was provided by a optically pumped HCOOH laser [15], and was introduced into the signal path through a 16-μm-thick mylar beam splitter. LO power was adjusted by rotating a wire-grid in front of the LO source. The heterodyne receiver noise measurements were made using the standard Y-factor method with room-temperature (295 K) and liquid-nitrogen-cooled (77 K) loads. No corrections were made for losses in front of the receiver.

The prepared junctions have current density of around 30 kA/cm^2, and the size of 0.5 μmϕ, lower than the design value of 0.7 μmϕ. Fig. 4 shows I-V characteristics for the receiver at 761 GHz with and without LO power. The receiver IF output in response to hot and cold loads is also shown in Fig. 4 as a function of bias voltage. The small subgap leakage current and large gap voltage as used in our noise simulation are observed in the unpumped I-V curve. The gap voltage is 5.2 mV, corresponding to a gap frequency of 1.26 THz. The normal state resistance for each junction is about 72 Ω, which is twice the design value. Photon-assisted tunneling steps were clearly observed with LO applied.

The IF responses to hot and cold loads show a receiver noise temperature of 2700 K (DSB), which is much larger than the theoretical prediction. Moreover, the measured receiver noise at around 1 THz using a optically pumped CH_3OD laser was much worse. The relative high noise performances may be caused by the large RF losses in the tuning circuit of polycrystalline NbN on the SiO. In addition, the penetration depth used in our design may be different from that of actual value. It is very difficult to fabricate single-crystal NbN thin film on the SiO. Polycrystalline NbN film has larger surface resistance and longer London penetration depth compared to single-crystal NbN film [16]. To overcome this problem, we will attempt to use single-crystal NbN for tuning circuits or self-compensated NbN SIS junction [17].

4. Conclusion

Submillimeter-wave receiver performances employing our high current density NbN/AlN/NbN tunnel junctions have been investigated theoretically and experimentally. The

theoretical prediction showed that DSB receiver noise temperatures of below $3h\nu/K_B$ can be achieved by using the NbN SIS junctions for frequencies up to 2 THz. However, the experimental receiver designed for the 1 THz band showed poor performances with the noise temperature of 2700 K at 761 GHz. The main reason for the high noise performance may be the large RF losses in the tuning circuit of polycristalline NbN on the SiO. Thus, the existing problem for developing low noise terahertz receivers is material properties of tuning circuits rather than NbN SIS junction properties. We are continuing to explore the fabrication of NbN/AlN/NbN tunnel junctions with single-crystal NbN tuning elements or self-tuned NbN SIS junctions, and to test their noise performance at terahertz frequencies.

Acknowledgments

We thank Professor Takashi Noguchi and Dr. Sheng-Cai Shi of Nobeyama Radio Observatory for their valuable discussions on the simulation of receiver noise performances. This work was supported in part by the Joint Research Fund of National Astronomical Observatory.

References

[1] M.J. Feldman, Int. J. Infrared Millimeter Waves, 8, 1239 (1987).

[2] Z. Wang, A. Kawakami, Y. Uzawa, and B. Komiyama, Appl. Phys. Lett., 64, 2034 (1994).

[3] Z. Wang, A. Kawakami, and Y. Uzawa, Appl. Phys. Lett., 70, 114 (1997).

[4] Y. Uzawa, Z. Wang, and A. Kawakami, Appl. Phys. Lett., 69, 2435 (1996).

[5] Y. Uzawa, Z. Wang, and A. Kawakami, To appear in IEEE Trans. Appl. Supercond., 7 (1997).

[6] S.C. Shi, J. Inatani, T. Noguchi, and K. Sunada, Int. J. Infrared Millimeter Waves, 14, 1273 (1993).

[7] J. Zmuidzinas, H.G. LeDuc, J.A. Stern, and S.R. Cypher, IEEE Trans. Microwave Theory Tech., 42, 698 (1994).

[8] J. Zmuidzinas, N.G. Ugras, D. Miller, M.C. Gaidis, H.G. LeDuc, and J.A. Stern, IEEE Trans. Appl. Supercond. 5, 3053 (1994).

[9] M.C. Gaidis, H.G. LeDuc, M. Bin, D. Miller, J.A. Stern, and J. Zmuidzinas, IEEE Trans. Microwave Theory Tech., 44, 1130 (1996).

[10] M. Bin, M.C. Gaidis, J. Zmuidzinas, and T.G. Phillips, Appl. Phys. Lett., 68, 1714 (1996).

[11] Z. Wang, Y. Uzawa, and A. Kawakami, To appear in IEEE Trans. Appl. Supercond., 7 (1997).

[12] B. Komiyama, Z. Wang, and M. Tonouchi, Appl. Phys. Lett. 68, 562 (1996).

[13] Z. Wang, A. Kawakami, Y.Uzawa, and B. Komiyama, J. Appl. Phys., 79, 7837 (1996).

[14] DuPont-Toray Co., 5-6 Nihonbashi-honcho, 1-chome, Chuo-ku, Tokyo 103, Japan.

[15] Y. Uzawa, Z. Wang, A. Kawakami, and B. Komiyama, Appl. Phys. Lett. 66, 1992 (1995).

[16] S. Kohjiro, S. Kiryu, and A. Shoji, IEEE Trans. Appl. Supercond., 3, 1765 (1993).

[17] V.Yu. Belitsky, W.L. Kollberg, Proc. of Seventh Int. Symp. on Space Terahertz Technology, 234, Charlottesville, VA, Mar. 1995.

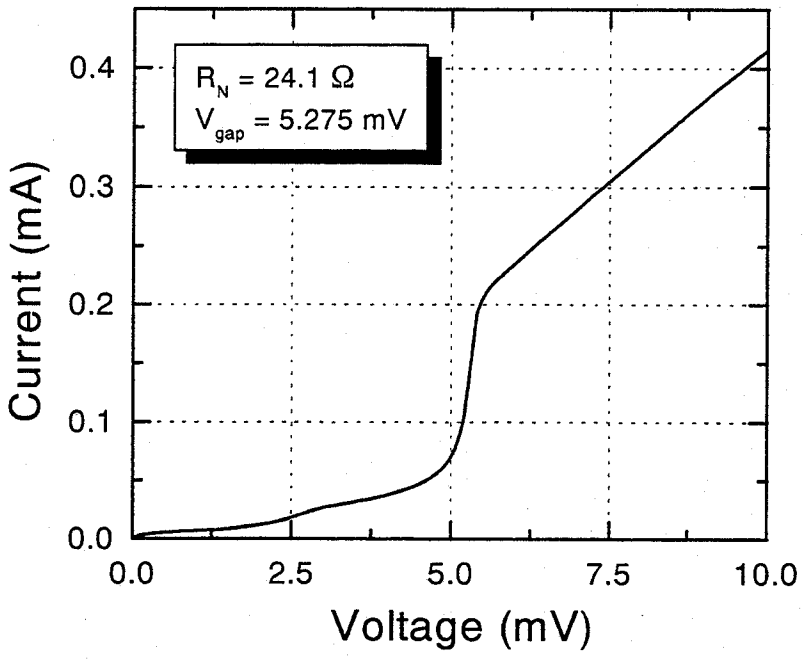

Fig. 1. I-V curve of a practical NbN/AlN/NbN tunnel junction for the performance simulation of the SIS receiver.

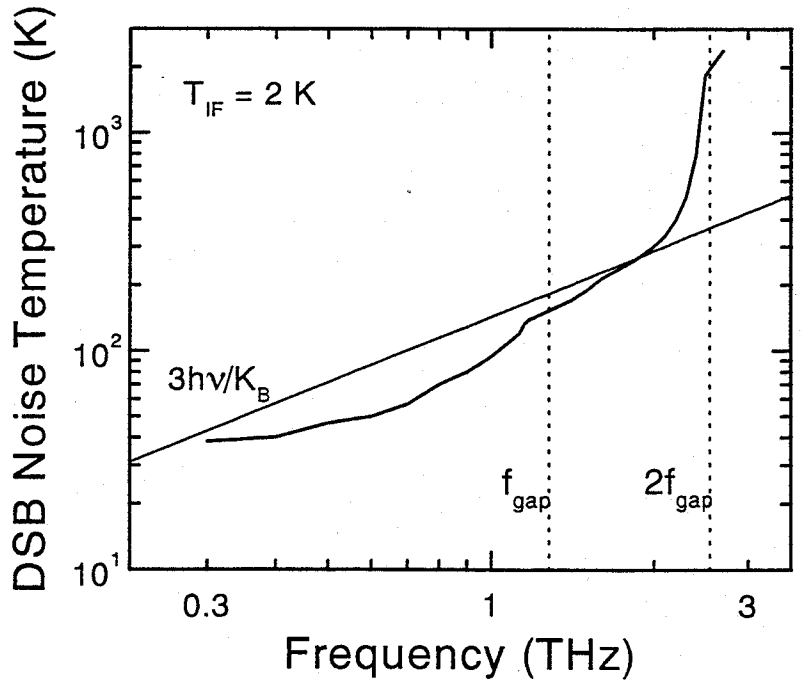

Fig.2. Theoretical sensitivity of the NbN SIS receiver based on the practical I-V curve

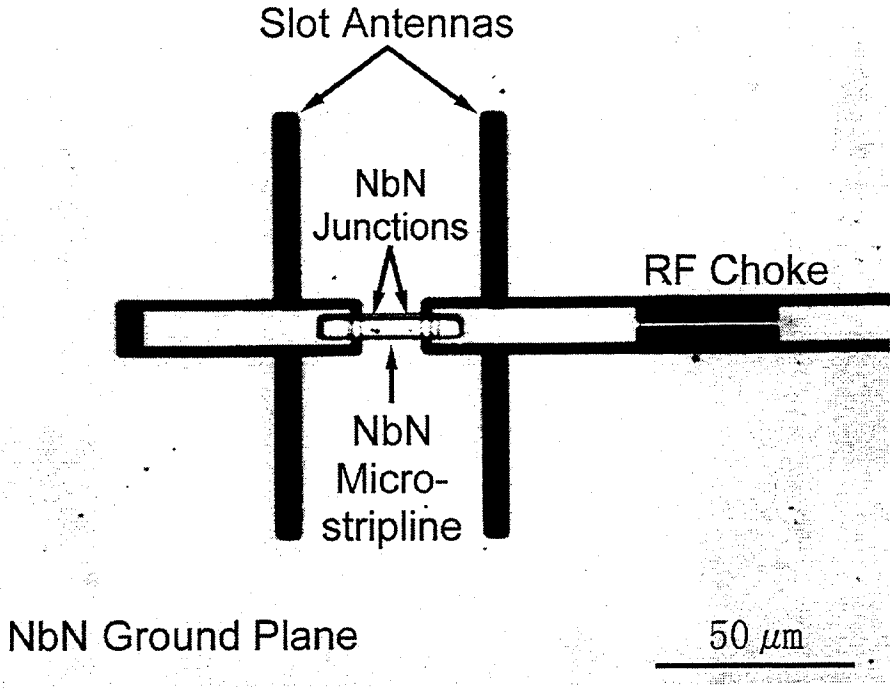

Fig. 3. Optical micrograph of the 1 THz NbN/AlN/NbN mixer. Two NbN junctions in parallel with integrated tuning circuits are fabricated with a twin-slot antenna. Each junction is approximately 0.5 μm in diameter.

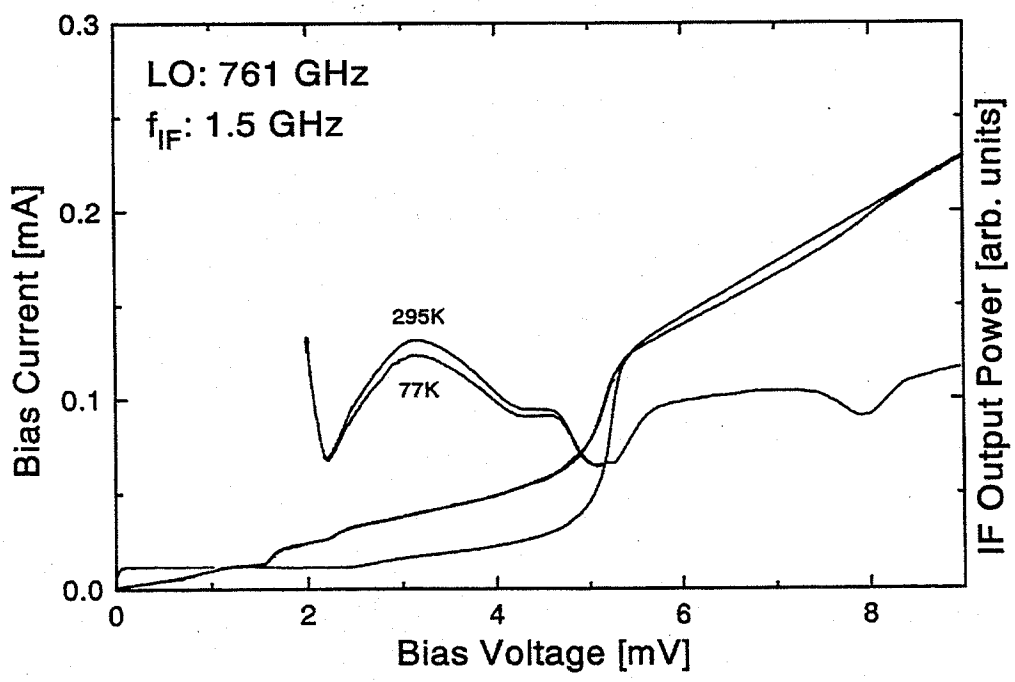

Fig. 4. Heterodyne response of the receiver at 761 GHz. Shown are the I-V curve for the parallel NbN/AlN/NbN junctions with and without LO power. Also shown is the IF power as a function of bias voltage for hot (295 K) and cold (77 K) loads.

Low-Loss NbTiN Films for THz SIS Mixer Tuning Circuits

J. W. Kooi[1], J. A. Stern[2], G. Chattopadhyay[1],
H. G. LeDuc[2], B. Bumble[2], J. Zmuidzinas[1]

[1] California Institute of Technology, MS 320-47, Pasadena Ca 91125
[2] Center for Space Microelectronics Technology/JPL, Pasadena, CA 91108

Abstract

Recent results at 1 THz using normal-metal tuning circuits have shown that SIS mixers can work well up to twice the gap frequency of the junction material (niobium). However, the performance at 1 THz is limited by the substantial loss in the normal metal films. For better performance superconducting films with a higher gap frequency than niobium and with low RF loss are needed. Niobium nitride has long been considered a good candidate material, but typical NbN films suffer from high RF loss. To circumvent this problem we are currently investigating the RF loss in NbTiN films, a 15K Tc compound superconductor, by incorporating them into quasi-optical slot antenna SIS devices.

Introduction

There is a strong astronomical interest to construct sensitive heterodyne receivers above 700 GHz, which is the bandgap energy of niobium. Niobium is the material of choice in nearly all Superconducting-Insulating-Superconducting tunnel junction (SIS) mixers. Niobium has a bandgap energy of (2Δ) of 700 GHz. Above this frequency the photons have enough energy to break Cooper pairs within the superconductor. This results in a very steep increase in the absorption loss of niobium films, as is shown in Figure 1. To circumvent this problem, up to 1.2 THz at least, we are developing quasi-optical SIS devices with NbTiN films[1]. Many of these devices show I-V resonances up to 1 THz, indicating that the loss continues to be low up to the gap frequency (1.2 THz). Comparison of circuit simulations and FTS measurements indicate that the resistivity of the NbTiN just above Tc is about 60 $\mu\Omega$-cm, which computes to a phase velocity of 0.21c for NbTiN microstrip lines with a 200 nm SiO dielectric. The critical temperature of the NbTiN films is around 15K and the gap voltage about 5.2 mV. Several different devices have been tested up to 650 GHz, all of which can be categorized in the following three groups.

I. NbTiN ground plane, Nb wiring and Nb/Al-O_x/Nb junctions

II. NbTiN ground plane and wiring, NbTiN/MgO/NbTiN junctions

III. NbTiN/Nb ground plane and wiring, Nb/Al-N_x/NbTiN junctions

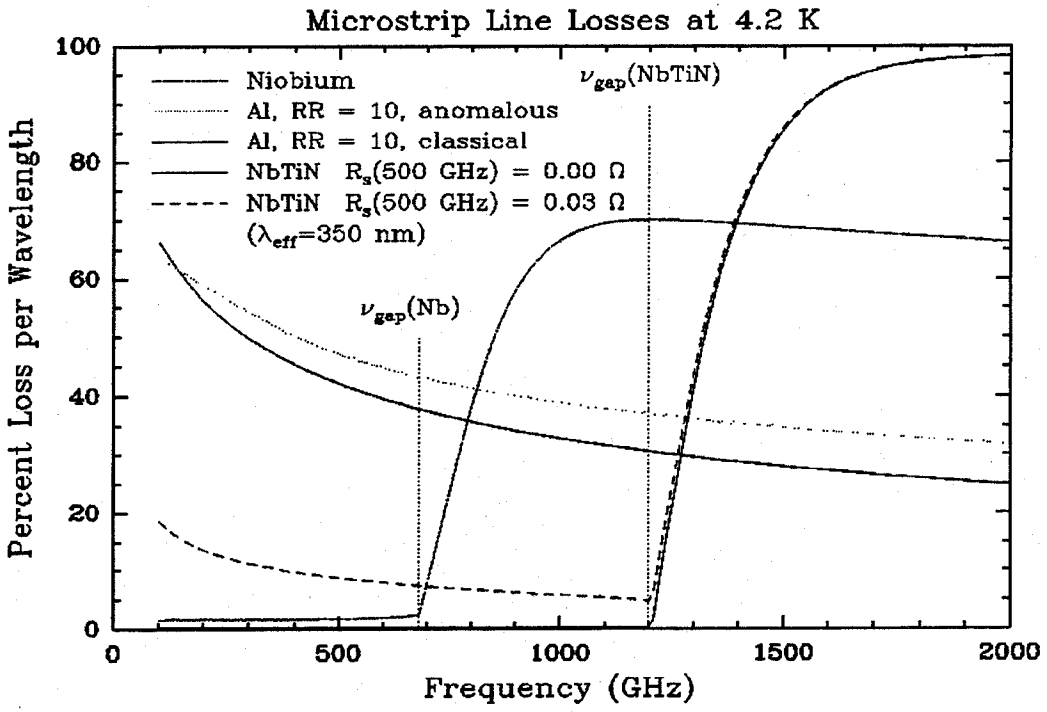

Fig. 1 RF loss of microstrip lines made with several different materials.

I. NbTiN Ground Plane, Nb Wiring and a Nb/Al-O_x/Nb Junctions

Since we did not know the material properties (mechanical and electrical) of the NbTiN superconducting films, we first fabricated double slot antenna devices with an existing mask designed for niobium [1, 2]. The devices had a NbTiN ground plane, Nb/Al-O_x/Nb junction, and niobium wiring. We have made direct detection Fourier Transformer Spectrometer (FTS) measurements and hot/cold heterodyne measurements near the peak of the FTS response, at 639 GHz. The frequency response measured with the FTS fits quite well with our circuit calculation if we assume that the NbTiN films have essentially no loss. Significant discrepancies arise between theory and experiment if the surface resistance of the NbTiN film is assumed to be 0.1 Ω/square. We also deduce from our circuit simulations a phase velocity of about 0.21c and a penetration depth on the order of 230 nm. For comparison, niobium films have a penetration depth of 80 nm. As an interesting side note, the heterodyne result of 110K at 639 GHz proved to be one of the most sensitive un-corrected receiver measurements at this frequency to date. Clearly the loss in the

NbTiN ground layer is very low. A 9μm mylar LO injection beamsplitter was used during the duration of the heterodyne measurement.

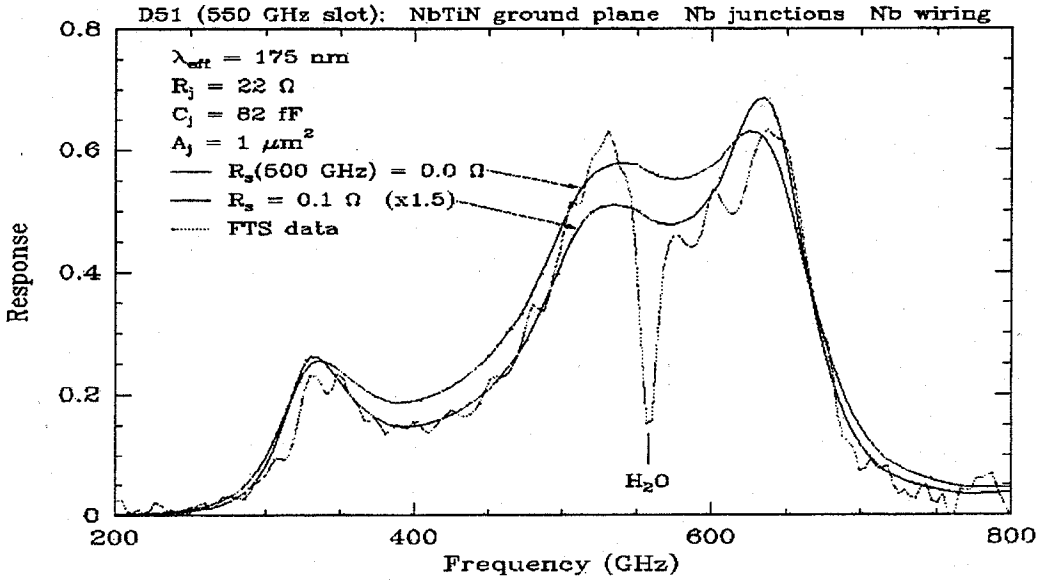

Fig. 2 FTS measurement of a Nb/Al-Ox/Nb junction with NTiN groundplane.

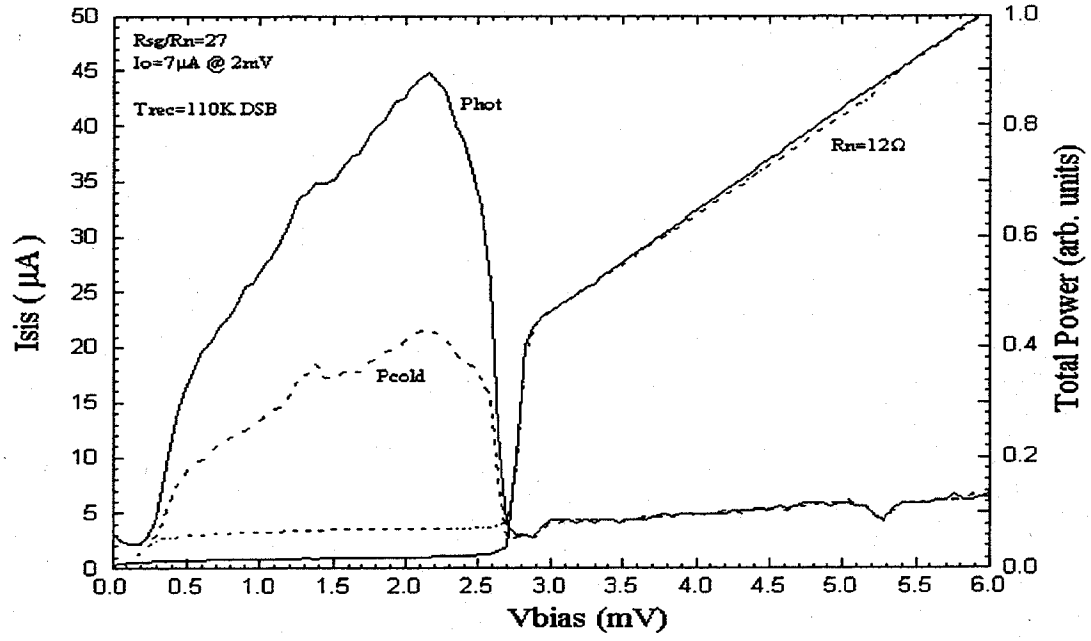

Fig. 3 Heterodyne response of a Nb/Al-Ox/Nb junction with NTiN groundplane at 639 GHz.

Once an understanding of the phase velocity and penetration depth of the NbTiN films was gained, we designed two different double slot antenna circuit layouts for further experimentation.
The first design was for an all NbTiN device with a NbTiN/MgO/NbTiN junction, and the second design was optimized for an Nb/Al-O_x/Nb junction. The difference being that, according to our computer simulations to FTS fits, the specific capacitance of a MgO barrier is on the order of 140-160 fF/μm^2. Nb/Al-O_x/Nb junctions with similar current density have a specific capacitance around 85 fF/μm^2.
The RF capacitive impedance of a 0.5 μm^2 NbTiN/MgO/NbTiN SIS junction at 1 THz is less than 2 Ohm, which makes it very difficult to match. Due to its lower capacitance, Al-O_x would be a preferred barrier except that we were not successful in fabricating high quality NbTiN junctions with Al-O_x barriers. A third barrier was used, Al-N_x, which has a reported specific capacitance similar to that of Al-O_x but is better suited to the fabrication process. There are good indications that Al-N_x has a lower barrier height than Al-O_x, and is thermally more stable.

II. NbTiN Ground Plane and Wiring, NbTiN/MgO/NbTiN Junction

As discussed, a 0.5μm^2 NbTiN/MgO/NbTiN SIS junction at 1 THz presents a mere 2 Ohm of reactance and the I/V characteristics are similar to the well known "washed-out" NbN I/V curves. Nonetheless, these devices are still of interest because of the relatively high energy gap, $(2\Delta) = 1200$ GHz, and low RF loss. To verify that these films do indeed show improved performance over NbN devices, we have measured several of these devices over a wide range of current densities. Figure 4 shows the FTS response with three different circuit simulation fits for a junction with a RnA product of 42 Ω-μm^2. Though the fits are not perfect, it does enable us to put a upper limit on the loss (0.03-0.06Ω/square), get an estimate for the junction capacitance (132fF/μm^2 for a RnA product of 42 Ω-μm^2) and resistivity (60$\mu\Omega$-cm). We have also measured MgO devices with RnA products as low as 8 and as high as 60 Ω-μm^2. The specific capacitance, according to circuit simulations fits to the FTS data, for these particular device were 163 fF/μm^2 and 125 fF/μm^2 respectively.
The NbTiN/MgO/NbTiN SIS junction heterodyne measurement presented in Figure 5 has a receiver noise temperature of 250K DSB. This is several factors better than results reported with NbN devices at similar frequencies.

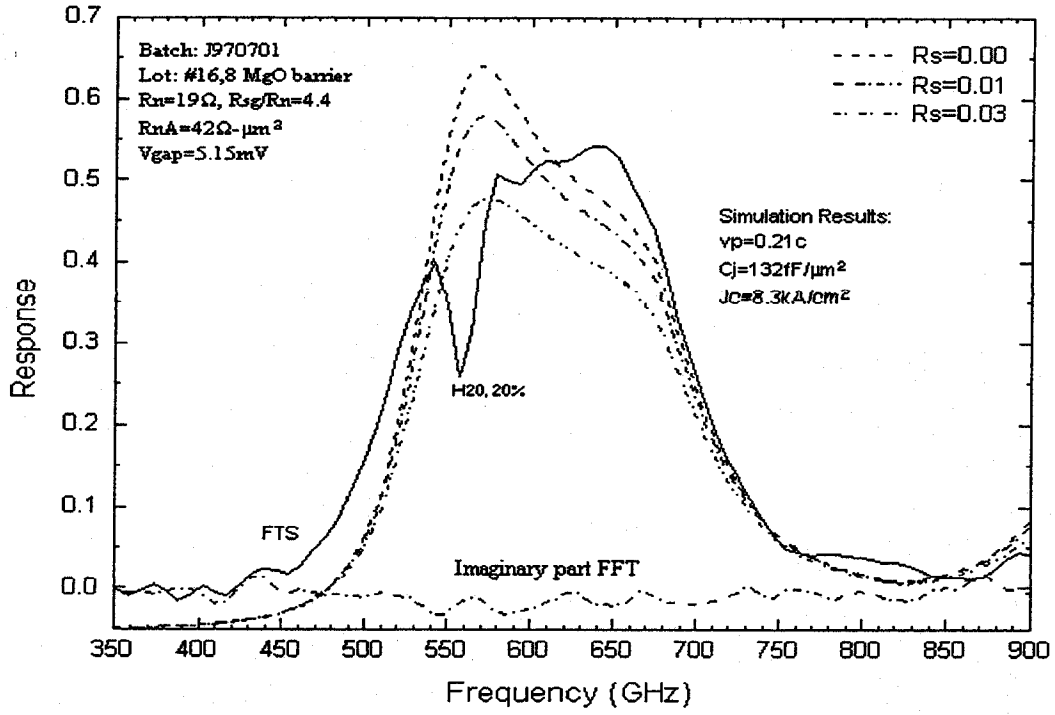

Fig. 4 FTS response of an All NbTiN junction with MgO barrier.

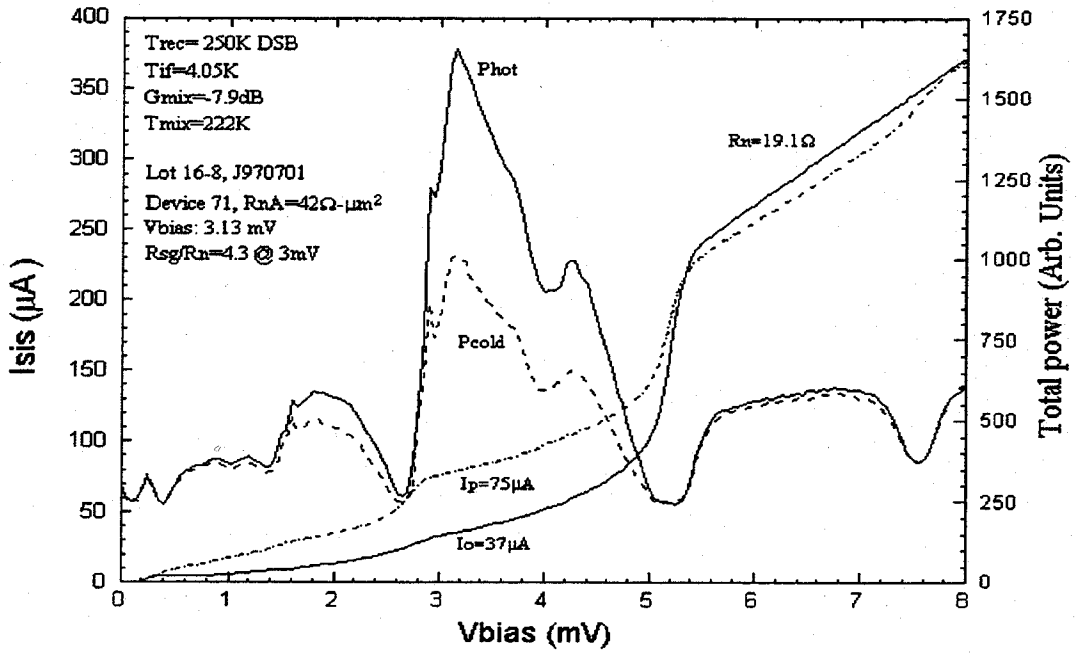

Fig. 5 Heterodyne response of an All NbTiN junction with MgO barrier at 638 GHz.

III. NbTiN/Nb Ground Plane, NbTiN Wiring, Nb/Al-N_x/NbTiN Junction

A promising technology for THz applications is the use of an Al-N_x barrier rather than MgO barrier. This should result in a reduced specific capacitance, making the RF match to these devices at 1 THz more realistic. Josephson resonances in the I/V curve of many of these devices show resonances up to 2.1 mV. In Figure 6 we present a device that shows a rather nice resonance at 800 GHz. Unfortunately the I/V curve showed a weak-link break around 5 mV, and no heterodyne data is available for this particular device. Note that the junction gap voltage is at 3.5 mV. The devices discussed here were fabricated with a 100 Angstrom niobium layer on top of the NbTiN ground plane. This was done because Aluminum can readily be deposited on top of a niobium base electrode, but not easily on NbTiN.

The sum gap of the 100 Angstrom niobium and NbTiN counter electrode is 3.5 mV as shown in Figure 6. Our calculations show that the absorption loss in the very thin niobium film is significant enough to effect the RF performance above 700 GHz, the gap frequency of niobium.

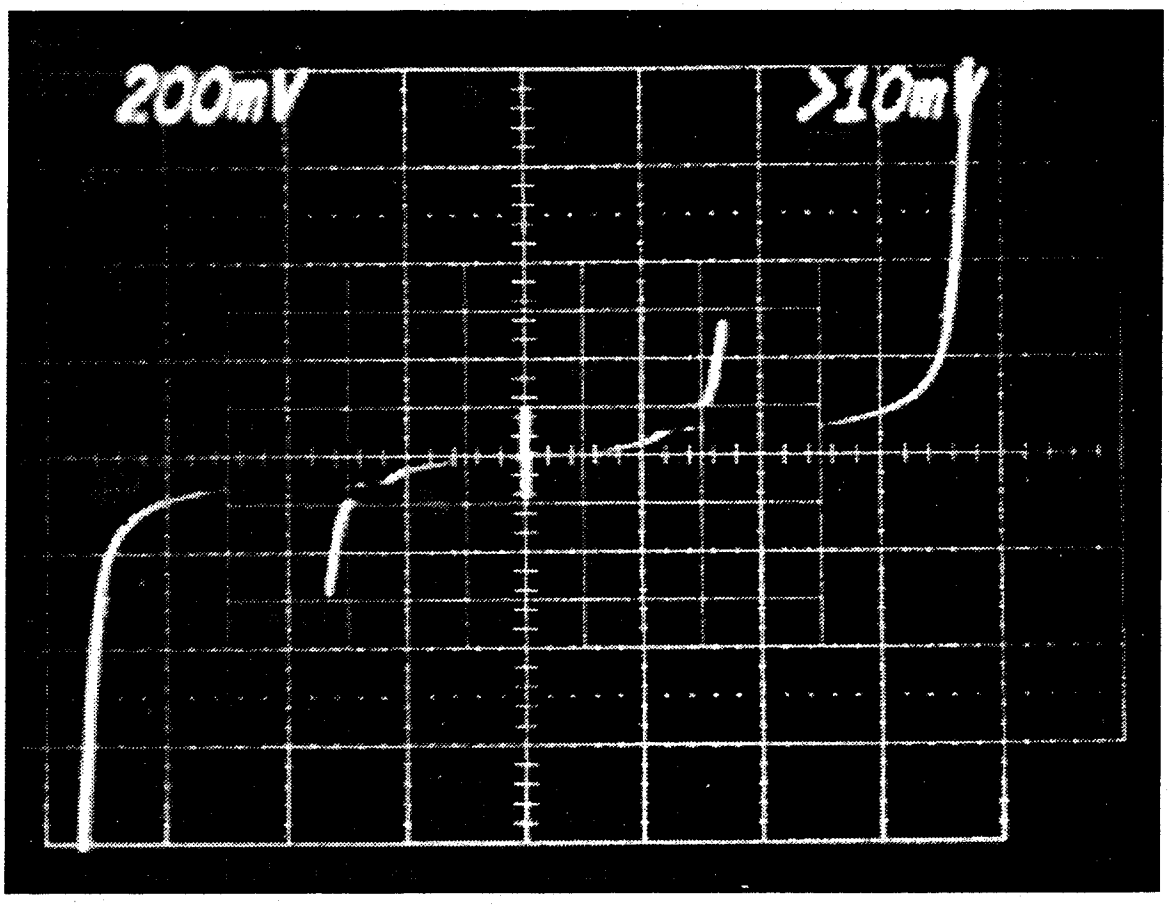

Fig. 6. Josephson resonance at 800 Ghz of a Nb/Al-N_x/NbTiN junction
. Horizontal scale: 1mV/division, Vertical scale: 20μA/division

A new process is currently under development at JPL which will etch completely through the 100 angstrom niobium layer on top of the NbTiN base electrode, except for where the junction is patterned. This should solve the RF loss issue in the niobium film, yet still allow good quality IV curves with gap voltages around 3.5 mV. This technology is therefore particularly interesting for THz applications.

RF circuit simulations show a 3 dB bandwidth of about 120 GHz for these devices, which is in good agreement with the measured FWHM bandwidth of 115 GHz on our FTS. The small RF bandwidth is indicative of a low loss RF tuning circuit. In fact the 3 dB bandwidth of a similar device with aluminum wiring is 450 GHz [3].

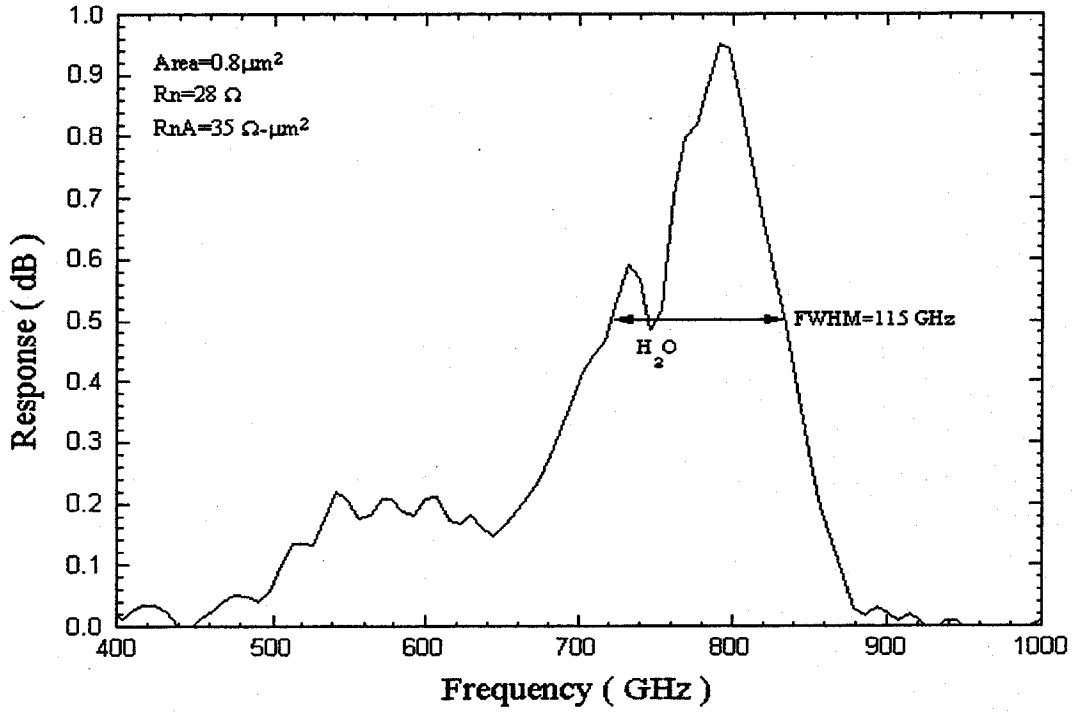

Fig. 7 Direct Detection response of a 950 GHz designed Nb/Al-N_x/NbTiN junction with NbTiN groundplane and wire layers.

Since no more high quality 950 GHz devices were available for this fabrication run, we turned our attention to a 650 GHz device. The direct detection response is shown in Figure 8. The measurement was made at two different resolutions and it shows a resonance that is shifted down from the 650 GHz design frequency to 590 GHz, approximately 10%. Heterodyne measurements at 588 GHz gave a 195K DSB noise temperature.

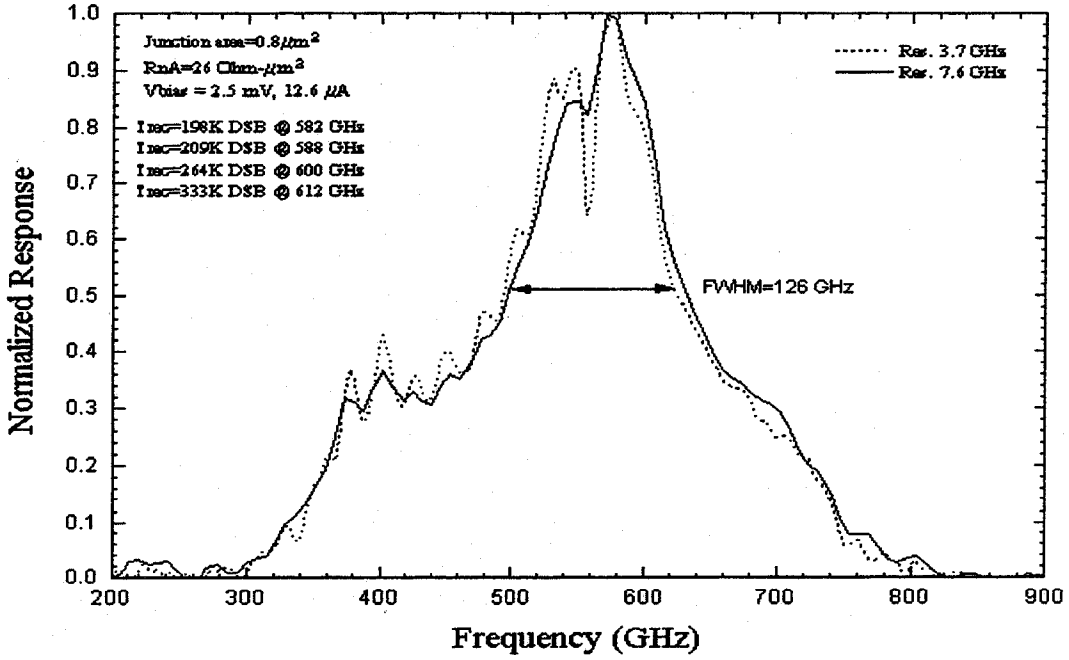

Fig 8 FTS response of an Al-N_x barrier junction designed to resonate at 650 Ghz. RnA=26Ω-μm^2

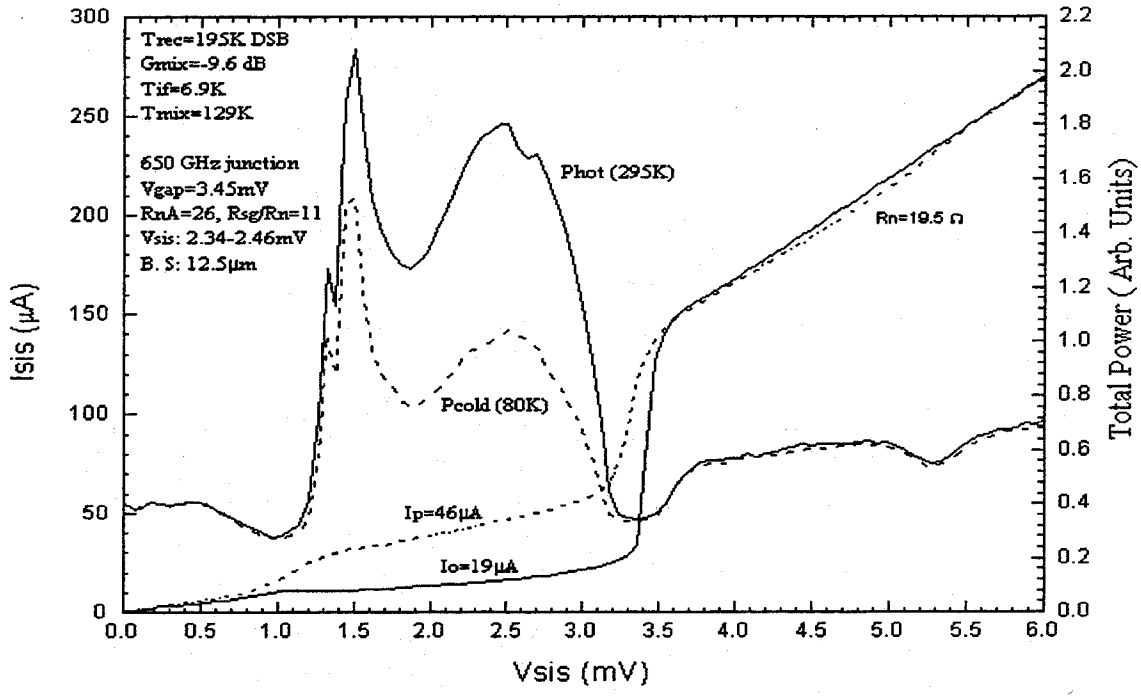

Fig 9 Heterodyne response if an Al-N_x barrier junction at 588 GHz.

The standard IF shot noise calibration technique[4] gave a mixer noise temperature of 129K and a mixer gain of -9.6 dB. The mixer conversion loss is somewhat higher than expected. The reason for this is not very clear since we are below the gap frequency of niobium. However if the loss in the NbTiN tuning circuit were significant would have expected a broadened RF response.

Conclusion

Clearly, our preliminary measurements demonstrate that NbTiN films show great promise for use in low-loss tuning circuits for SIS mixers at 1 THz. However, much work remains to be done to turn this promise into reality. Numerous technical difficulties must be overcome before a stable, reproducible fabrication process is available, which is necessary for the production of optimized devices. Several different junction configurations are currently under investigation as it is not clear which one will perform best up to 1.2 THz.

New devices have recently become available, and we anticipate testing them at 800 GHz in the very near future.

Acknowledgments

This work was supported in part by NASA grants NAG5-4890 and NAGW-107, NAG2-1068, the NASA/JPL Center for Space Microelectronics Technology and the Caltech Submillimeter (NSF grant AST-9615025).

References

1. **J. Zmuidzinas and H.G. LeDuc,** "Quasi-Optical Slot Antenna SIS Mixers", *IEEE transactions on Microwave Theory and Techniques*, Vol. 40. No. 9, pp. 1797-1804, Sept 1992.

2 **M. Gaidis, H. G. LeDuc, M. Bin, D. Miller, J. A. Stern and J. Zmuidzinas,** "Characterization of low noise quasi-optical SIS mixers for the Submillimeter Band", *IEEE transactions on Microwave Theory and Techniques*, Vol. 44, No. 7, pp. 1130-1139, July 1996.

3 **M. Bin, M. C. Gaidis, J. Zmuidzinas, T. G. Phillips and H. G. Leduc,** "Quasi-Optical SIS mixers with Normal-Metal Tuning Structures", IEEE Transactions on Applied Superconductivity, Vol. 7 (2), Part 3, pp 3584-3588, Jun. 1997.

4 **D.P. Woody, R.E. Miller, and M.J. Wengler,** "85-115 GHz Receivers for Radio Astronomy," *transactions on Microwave Theory and Techniques*, Vol. 33, pp.90-95, Feb. 1985.

DESIGN, ANALYSIS AND SCALE MODEL TESTING OF FIXED-TUNED BROADBAND WAVEGUIDE TO MICROSTRIP TRANSITIONS

J.L. Hesler, K. Hui, R.M. Weikle, II, and T.W. Crowe
Department of Electrical Engineering
University of Virginia
Charlottesville, VA 22904

Abstract

We have designed and tested broadband fixed-tuned waveguide to microstrip transitions in which the probe is extended across the waveguide. We have performed scale-model testing of several configurations of waveguide to microstrip transitions, and have measured a fixed-tuned bandwidth of 32%. Simulations of these structures were performed using Hewlett Packard's High Frequency Structure Simulator (HFSS). The sensitivity of the transition bandwidth to changes in geometry and microstrip circuit layout are discussed.

Introduction

Many mixers and multipliers use waveguide at their input because of the availability of waveguide flanges and horns, which allow for efficient coupling of power into the waveguide over a broad bandwidth. Once inside the waveguide, it is often convenient to transition into a shielded microstrip channel in order to simplify the integration of filters and nonlinear devices into the mixer or multiplier. One method to make a broadband transition is to use a probe inserted partially across the waveguide, which can be designed to provide excellent coupling across an entire waveguide band [1]. However, in certain circumstances it is desirable to extend the probe across the input waveguide, thus allowing for the possibility of a current path thru to a channel on the other side of the waveguide. This paper describes the design and scale-model testing of a broadband fixed-tuned waveguide to microstrip transition in which the probe is extended across the waveguide. In addition, several geometries of waveguide to microstrip transitions are examined, and their bandwidths are compared for different tuning configurations.

Summary of Modeling Results for Different Geometries

A schematic of the basic probe design is shown in Fig. 1, where tuning is provided by a waveguide backshort and a termination in one of the microstrip channels. For this modeling it was assumed that the microstrip channel was terminated by either an ideal open or short circuit at some length down the channel. For transitions which are designed solely to provide an IF or DC signal ground, it is possible to provide a microstrip short circuit termination. However, for structures in which it is desirable to continue the line through there will be a filter terminating the channel.

There were two main transition geometries modeled during this study. Fig. 1(a) shows a transition in which the quartz circuit is oriented parallel with the E-plane of the waveguide. In the geometry shown in Fig. 1(b), the quartz is mounted perpendicular to the waveguide E-plane. The waveguide height for both geometries was chosen to be 1/3 height. Reducing the height was found to be necessary to achieve broadband operation with this transition. Simulations of these transitions were performed using Hewlett Packard's High Frequency Structure Simulator

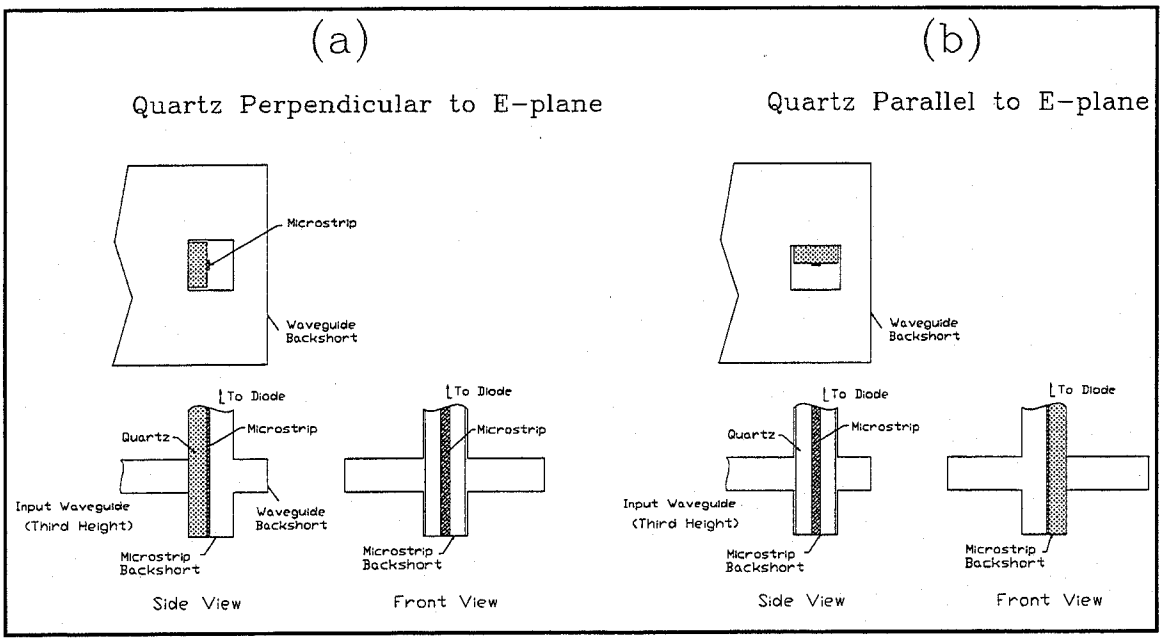

Fig. 1. Schematic of the basic waveguide to microstrip transition design with (a) quartz substrate perpendicular to waveguide E-plane and (b) substrate parallel to E-plane.

(HFSS). The structure was solved with two waveguide and two microstrip ports, and the effect of the waveguide and microstrip tuning lines was taken into account using the linear S-parameter simulator of Hewlett Packard's Microwave Design System (MDS).

Fig. 2 shows the maximum thru coupling from the waveguide to the microstrip line at a single frequency as a function of the microstrip line length before the termination, where at each channel length the waveguide backshort position has been optimized for peak coupling. A microstrip line impedance of 81 Ω was used for the transition of Fig. 2. Both the open and short circuit terminations have two positions within the first 180 degrees of microstrip line electrical length which allow for unity thru coupling, as marked in Fig. 2 by SC1, SC2, OC1, and OC2. Fig. 3 shows the fixed tuned variation of the return loss versus frequency across the band for each of these points of unity coupling. As shown in Fig. 3, a transition with an open circuit termination just inside the microstrip channel was predicted to provide the best bandwidth performance. Neither of the short circuit positions were predicted to provide as broad a bandwidth as the open circuit.

One key design parameter is the microstrip line impedance. Fig. 4 shows the variation of the transition bandwidth versus line impedance, where the bandwidth has been defined as the range over which the return loss is greater than 20 dB. For the remaining simulations, a microstrip impedance of 81 Ω was used so that the transition would be relatively broad band while not incurring excessive conductor loss.

Table 1 summarizes the simulation results for a number of transition geometries. There are several things to note in Table 1:

- For the transition with the quartz perpendicular to the waveguide E-plane, the microstrip circuit can be placed with the metallization facing either the waveguide backshort or the input waveguide. In all cases the bandwidth was found to be larger when the microstrip metallization faced the waveguide backshort.

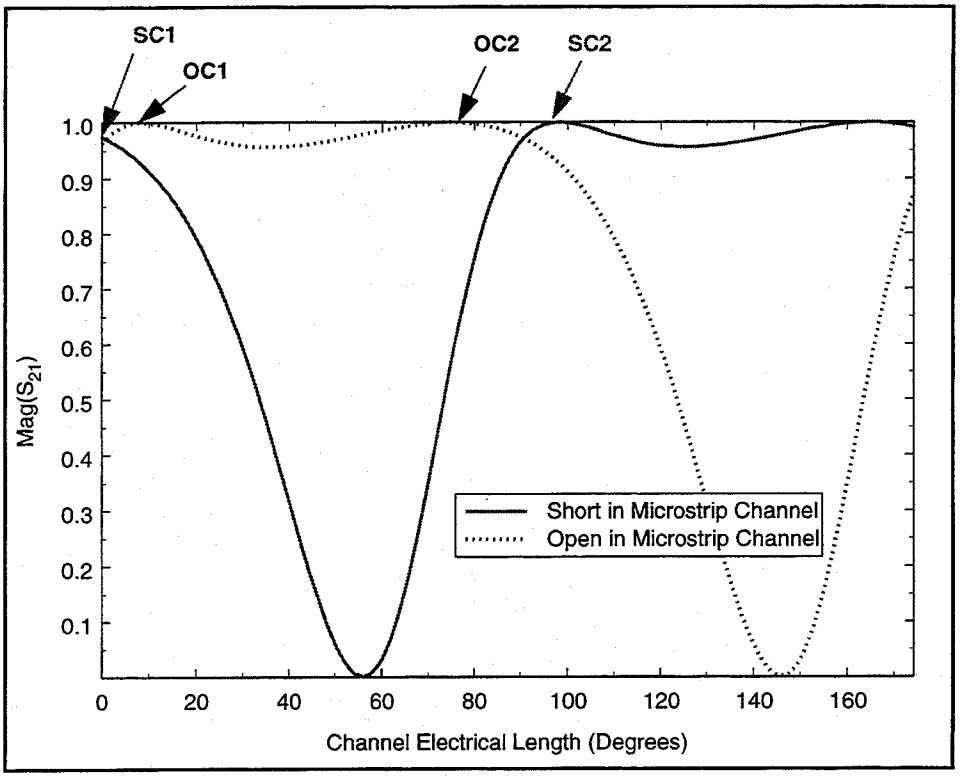

Fig. 2. Maximum thru coupling versus microstrip channel length with open and short circuit terminations in microstrip channel. For each channel length, the waveguide backshort was optimized for peak thru coupling.

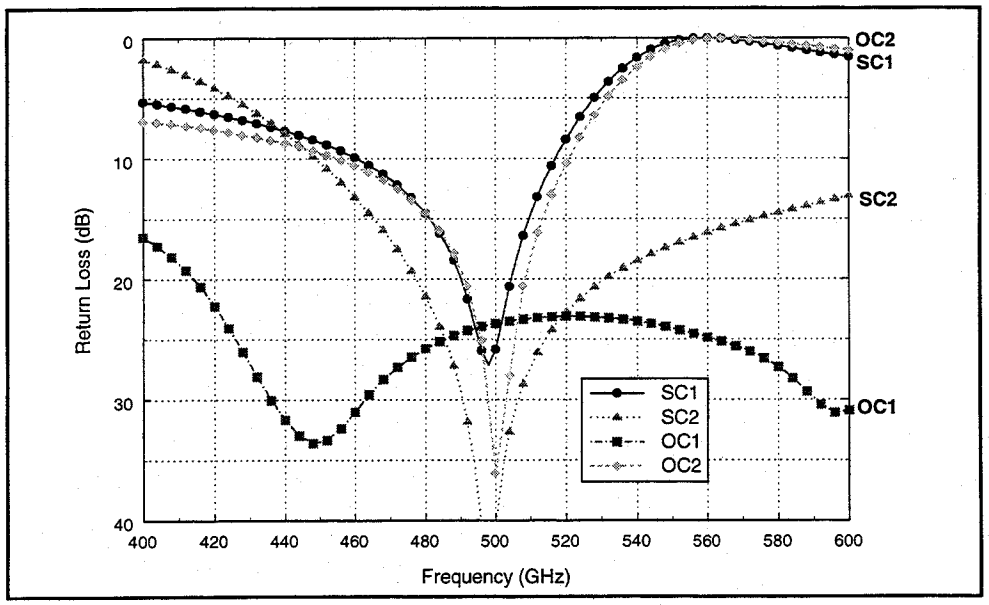

Fig. 3. Fixed tuned variation of the return loss versus frequency across the band for each of the points of unity coupling shown in Fig. 2. These curves are for a transition centered at 500 GHz.

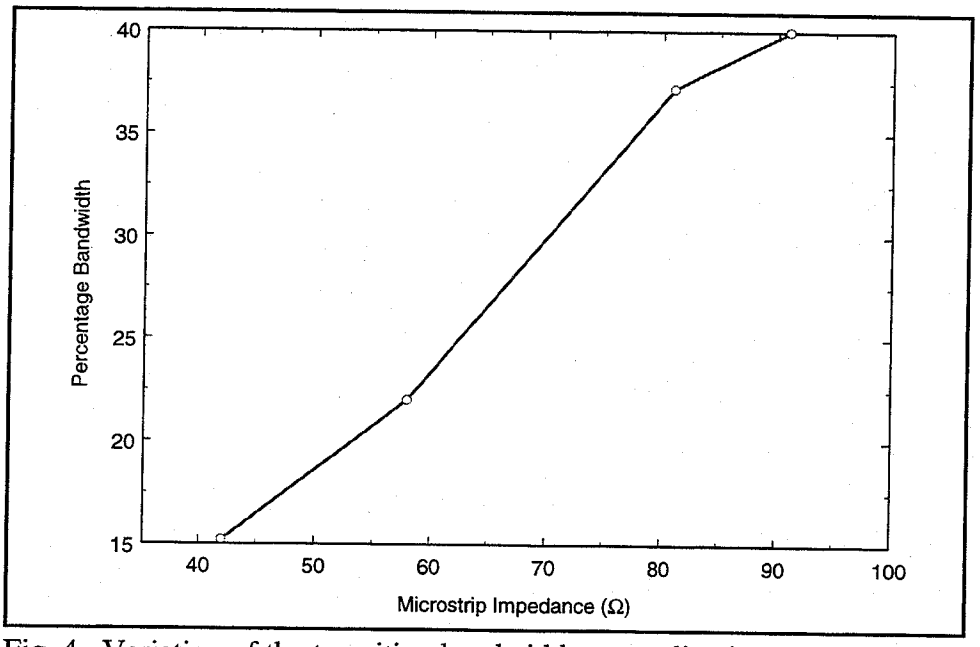

Fig. 4. Variation of the transition bandwidth versus line impedance for the transition of Fig. 1(a). The bandwidth has been defined as the range over which the return loss is greater than 20 dB.

Table 1: Summary of simulation results for waveguide to microstrip transitions.

Quartz ∥ or⊥ to E-plane	Microstrip Metallization Facing	Microstrip Impedance (Ω)	In Waveguide	In Microstrip Channel	BW (%)
⊥	backshort	42	thru line	short open	2.6 15.2
⊥	backshort backshort input input	81	thru line	short open short open	10.8 37.2 2.6 12.6
⊥	backshort backshort input input	81	cross (1.2x12.4 mm)	short open short open	33.2 34.8 9.4 15
⊥	backshort	81	cross (6.2x12.4 mm)	short open	16 22.4
⊥	backshort	81	cross (0.6x12.4 mm)	short open	29.6 31.4
⊥	backshort	91	thru line	short open	15.2 40
∥	-	85	thru line	short open	9.6 21.2
∥	-	85	cross (2.5x11.4 mm)	short open	15.2 23.2
∥	-	85	cross (7.6x11.4 mm)	short open	11.2 16.8

- The transition with the quartz perpendicular to the waveguide E-plane was found to have larger bandwidth than a similar transition with the quartz parallel to the E-plane.
- In an attempt to increase the transition bandwidth, simulations were performed for a transition in which a cross shape is added to the microstrip metallization in the waveguide, as shown in Fig. 5. For a transition with a short circuit termination in the microstrip channel, the cross was found to increase the bandwidth from about 10.8% to 33.2%. The cross has a less significant effect for the transition with an open circuit termination in the microstrip channel. The effect of the cross width on the transition bandwidth is shown in Fig. 6.
- Placing a cross in the microstrip metallization has little effect when the quartz is parallel to the waveguide E-plane.

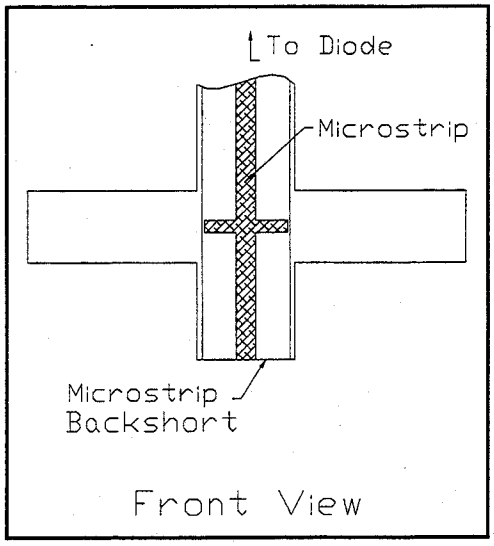

Fig. 5. Schematic showing cross in the microstrip metallization in the waveguide.

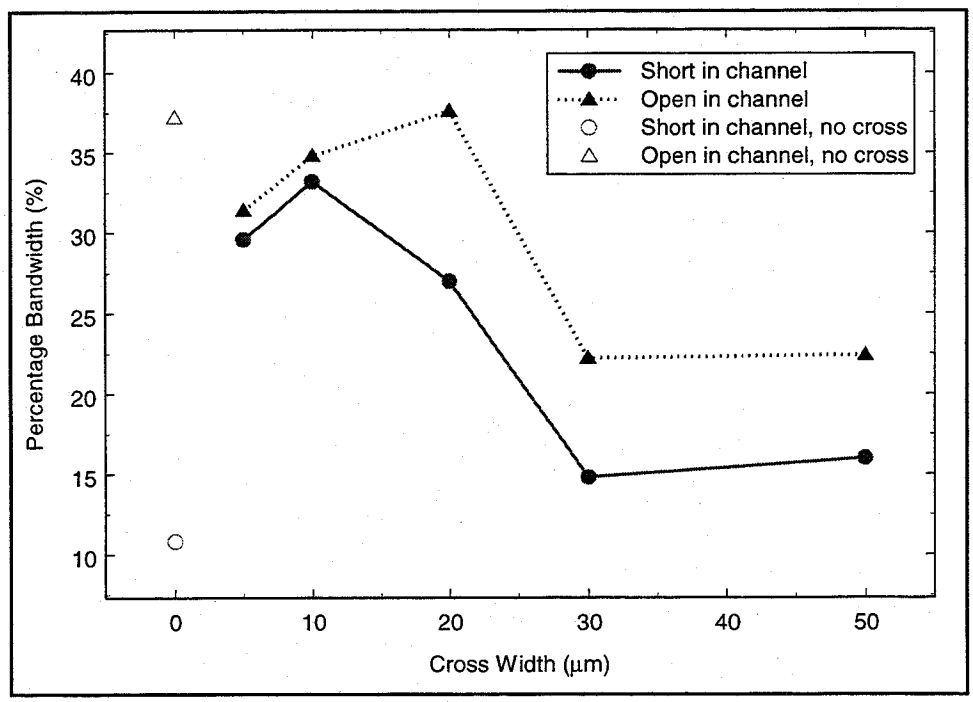

Fig. 6. Effect of the cross width on the transition bandwidth. The bandwidth has been defined as the range over which the return loss is greater than 20 dB.

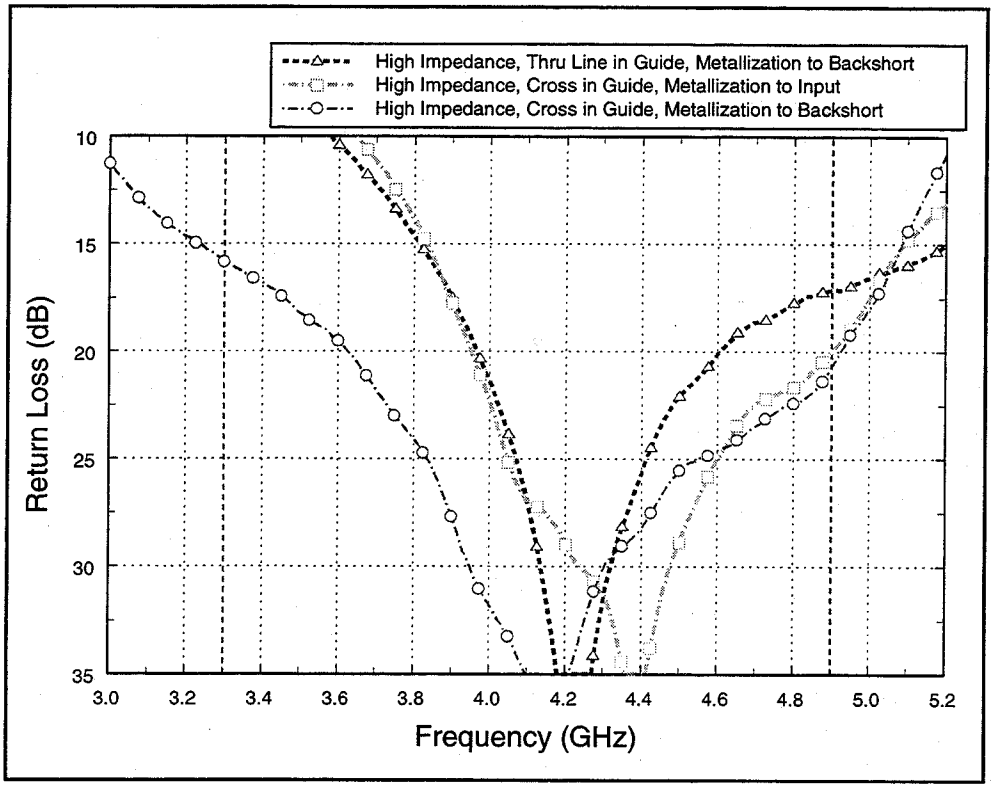

Fig. 7. Measured results using a 3.3-4.9 GHz scale model (the vertical dashed lines mark the edges of the waveguide band). The waveguide and microstrip backshorts were fixed across the waveguide band.

Measured Results

Measurements were made on a scale model waveguide with a frequency band from 3.3 to 4.9 GHz. The reduced height waveguide dimensions for the scale model were 10.0x58.0 mm. The microstrip channel dimensions were 14.7 mm wide by 12.2 mm high, with a quartz substrate thickness of 4.4 mm. For the scale modeling, the quartz was modeled using C-Stock AK-4 plastic stock with adjusted dielectric constant [2] with a relative dielectric constant of 4.0.

Fig. 7 shows measured plots of return loss versus frequency for several waveguide to microstrip transitions. For all of these plots the waveguide and microstrip backshorts were held fixed across the band. The bandwidth for the transition using the high impedance microstrip line with a short circuit termination increased by more than a factor of two when the cross-bar was introduced. The scale model measurements also showed the decrease in bandwidth performance when the microstrip metallization faces toward the input waveguide.

Conclusions

This paper discusses a fixed tuned waveguide to microstrip transition in which the probe is extended across the waveguide. By the introduction of the cross-bar, the fixed-tuned bandwidth of the thru microstrip transition with a built in signal ground was more than doubled. The transition was found to be relatively insensitive to misalignment of the cross-bar from the center of the guide. Also, the design of the cross-bar is insensitive to changes in cross-bar length

and width, although it is believed that additional bandwidth can be gained by fine-tuning of these parameters. Using these results, a broadband transition can be designed which allows for the possibility of continuing the IF or DC lines across the waveguide, which can be advantageous for certain mixer or multiplier configurations.

Bibliography

1. J.L. Hesler, W.R. Hall, T.W. Crowe, R.M. Weikle, II, B.S. Deaver, Jr., R.F. Bradley, and S.-K. Pan, "Fixed-Tuned Submillimeter Wavelength Waveguide Mixers Using Planar Schottky Barrier Diodes," to be published in the *IEEE Trans. Microwave Theory Tech.*, May 1997.

2. C-Stock AK-4, Cuming Corp., 230 Bodwell St., Avon, MA 02322.

An Investigation of the Input Impedance of a Microstrip Probe in Waveguide.

S. Withington and G. Yassin

Department of Physics,
University of Cambridge,
Madingley Rd, Cambridge.

Abstract

We derive an expression for the input impedance of a one-sided microstrip probe in waveguide. By "one-sided" we mean an insulated probe that extends only part way across the waveguide. This arrangement contrasts with the "Eisenhart and Kahn" or "double-sided" configuration, where the probe extends the whole way across the waveguide and is earthed at both ends. Our analysis is based on the spectral-domain method and is able to take into account the dielectric substrate on which the thin-film antenna is deposited. In submillimetre-wave components, the thickness of the substrate is 10-20% of the width of the waveguide, and the substrate has a significant effect on performance. We have examined the validity of our model by carrying out extensive impedance measurements at 5GHz. A key feature of the paper is that we compare the general characteristics of the one-sided probe, in the context of SIS mixers, with those of the two-sided probe. We show that the bandwidth of a probe that stretches only part way cross the waveguide is very much greater than the bandwidth of a probe that stretches all of the way across the waveguide. Moreover, the input resistance is lower and more suited to SIS tunnel junctions. We also show, analytically, that the input impedance is almost independent of axial orientation.

I Introduction

Waveguide-mounted superconducting tunnel junctions have been used as mixers in low-noise submillimetre-wave receivers for many years. It is usual practice to couple the tunnel junction to the waveguide by locating it at the centre of a thin, conducting strip which extends the whole of the way across the waveguide and which is earthed at both ends. As the demands on the technology grow, however, it is important to ask whether this arrangement is optimum or whether some other arrangement would be more effective. In particular, we are interested in getting the greatest possible bandwidth out of the waveguide to tunnel-junction transition, and in extending the frequency of operation to above 1THz where conventional waveguide becomes small and difficult to manufacture.

The double-sided probe, which was analysed rather elegantly by Eisenhart and Khan [1], is known to be effective, but has the disadvantage that it is is not possible to obtain low values of input impedance (50 Ω or less) without significantly reducing the height of the waveguide—even when an adjustable backshort tuner is used. As we shall see later, this property is intrinsic to the Eisenhart and Khan configuration, and is a consequence of the fact that the device is most naturally described by an input admittance. That is to say, the contributions from the scattered evanescent modes add up in parallel and influence the real part of the input impedance in a complicated way. In the one-sided probe, however, the contributions from the scattered evanescent modes add up in series, and only the propagating fundamental mode couples to the resistive part of the input impedance. As a consequence, the input impedance is relatively independent of frequency and is straightforward to control.

In a previous paper we developed an expression for the input impedance of a free-standing, one-sided microstrip probe [2]. In this paper we include in the model the dielectric substrate on which the thin-film antenna is deposited. In submillimetre-wave components the dielectric can occupy a significant fraction of the waveguide and must therefore be taken into account. We verify the integrity of the theory by performing a range of experiments, at 5GHz, on a scale model. At the end of the paper, we compare the general characteristics of one-sided probes and two-sided probes in the context of submillimetre-wave SIS

mixers.

The full-wave analysis of a probe in a waveguide is not an easy problem. The task is particularly complex if one wants to take into account the field radiated by the aperture through which the feeding transmission line passes—clearly, this additional complexity does not arise in the case of the Eisenhart and Khan probe. Despite the complications, Collin [3] has provided a solution, based on the *space-domain* dyadic Green's function, for the input impedance of a cylindrical probe in a rectangular waveguide. First he employed the method of moments, in conjunction with Galerkin's technique, to derive a general expression for the input impedance of a probe; then he performed substantial analytical manipulations to get a fast numerical algorithm. A similar approach, based on the method of moments, has also been used to calculate the input impedance of a microstrip probe [4]. In this case, however, the conventional Galerkin method, which results in a large matrix equation where each matrix element is found by double integration, was employed. This method requires a great deal of computing time even though the supporting dielectric substrate is not taken into account.

In this paper, we develop further the basic technique reported by Ho and Shih [5] to produce an expression for the input impedance of a microstrip probe. The approach is based on the reciprocity theorem and the spectral-domain method. An important feature of the theory is that the Fourier transforms of the current and field distributions are related—through the *spectral* dyadic Green's function—by an algebraic rather than an integral equation. Moreover, the expression for the spectral Green's function is much simpler and easier to obtain than the space-domain version—especially for dielectrically-loaded waveguide. The spectral-domain approach also has the advantage that modal properties of the dielectrically-loaded probe are brought out clearly, and we can determine how thick the substrate can be before higher-order modes introduce resonant features into the input impedance.

To verify the validity of the theory, we carried out extensive measurements on a scale model. A frequency range of 4-6GHz was chosen in order to scale the operation of a 450-500GHz mixer block by a factor of a 100. We measured the complex input impedance of a variety of different probes—various lengths, widths, and backshort locations.

Such data is surprisingly rare in the literature, and in most cases only the return loss is given, which is not sufficient to provide a sensitive test of the theories. To isolate the behaviour of the probe from that of the probe-backshort combination, we measured the input impedance of the probe with both ends of the waveguide terminated with matched loads.

II Basic Theory

In Fig. 1, we show the geometry of a microstrip probe. The probe is assumed to be fed by a current source I_{in} which is connected between the base of the probe and the wall of the waveguide. This source causes a potential difference V_{ab} to be established, through which the input impedance of the probe can defined according to

$$Z_{in} = \frac{V_{ab}}{I_{in}} \; . \tag{1}$$

Using the reciprocity theorem [6],[7], we can derive an expression for V_{ab} in terms of the current density on the surface of the probe J_x and the tangential electric field in the waveguide E_x; in this way, we obtain the expression

$$Z_{in} = -\frac{1}{I_{in}^2} \int\int\int E_x(r) J_x(r) dV \; . \tag{2}$$

When evaluating the above integral we assume that the current is distributed sinusoidally over the length of the probe. This assumption allows a great deal of simplification and eventually leads to an elegant solution for the input impedance. It is nevertheless also possible to obtain the real current distribution as a bi-product of the solution of a full-wave numerical analysis by expanding J_x in terms of a set of basis functions and then calculating the coefficients of the expansion by using standard iterative techniques. Experimental results show that the use of a simple one-term expression is sufficient for most practical purposes. We therefore write

$$J_x(x, y, z) = J_0 \delta(y - d) u(z) \sin k(x_1 - x) \tag{3}$$

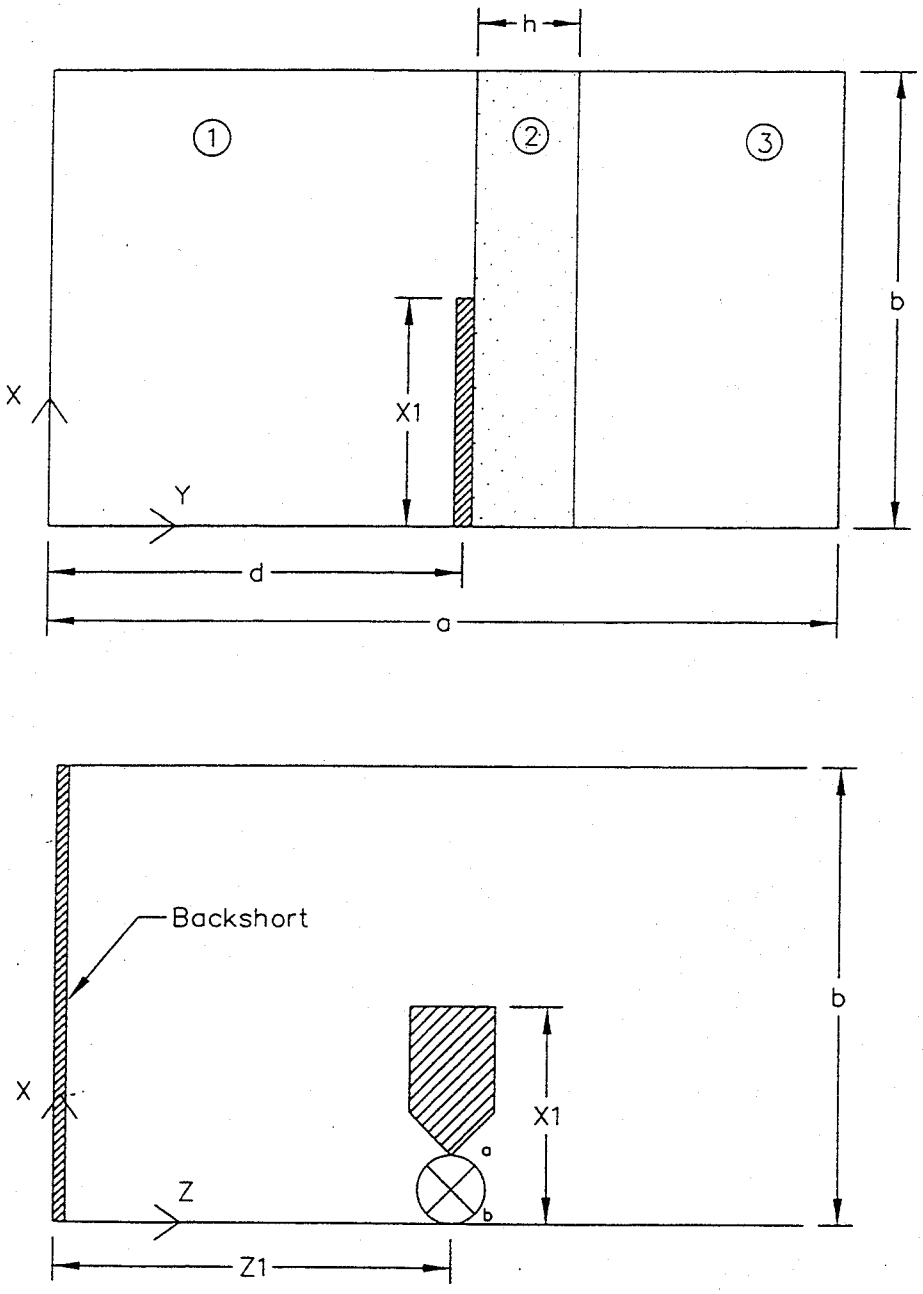

Figure 1: A microstrip probe.

for $x < x_1$ and zero otherwise. $u(z)$ describes the current density distribution across the width of the probe and can be written as

$$u(z) = \frac{1}{\pi} \frac{1}{\sqrt{1 - (\frac{z - z_1}{w})^2}} \qquad |z - z_1| < w \ , \tag{4}$$

where w is the half width of the probe. Notice that in the first instance we are assuming that the plane of the probe is in the E-plane of the waveguide: we shall call this type of probe a 'longitudinal probe' as distinct from a 'transverse probe' where the plane of the probe is transverse to the direction of propagation. In the following treatment, we shall neglect the transverse components of the current J_z and the electric field E_z.

To apply the spectral-domain method to our problem we first replace the current and field in (2) by their Fourier transforms and apply Parseval's theorem in three dimensions to obtain

$$Z_{in} = -\frac{1}{2\pi b} \frac{1}{I_{in}^2} \sum_{n=-\infty}^{+\infty} \sum_{m=-\infty}^{+\infty} \int_{-\infty}^{+\infty} \tilde{E}_x(\alpha, \gamma, \beta) \tilde{J}_x(\alpha, \gamma, \beta) \, d\beta \tag{5}$$

where

$$\tilde{J}_x(\alpha, \gamma, \beta) = (2j) \sin \frac{m\pi d}{a} J_o(|\beta w|) \left[\frac{k}{k^2 - \alpha^2} (\cos \alpha_n x_1 - \cos k x_1) \right] \ . \tag{6}$$

To derive the above expression we Fourier transformed the current distribution of (3) by using the method of images. In addition, boundary conditions on the field distributions require

$$\alpha_n = \frac{n\pi}{b} \ . \tag{7}$$

The input impedance can now be calculated by using the spectral-domain relationship between the current and field distributions. Neglecting the transverse component of the field and current, which we find to be justified experimentally, we obtain

$$\tilde{E}_x(\alpha, \gamma, \beta) = \tilde{G}_{xx}(\alpha, \gamma, \beta) . \tilde{J}_x(\alpha, \gamma, \beta) \tag{8}$$

where

$$\tilde{G_{xx}}(\alpha, \gamma, \beta) = \frac{\alpha^2}{\alpha^2 + \beta^2} Z^e + \frac{\beta^2}{\alpha^2 + \beta^2} Z^h \ . \tag{9}$$

Here $\tilde{G_{xx}}(\alpha,\gamma,\beta)$ is the longitudinal component of the dyadic Green's function. Z^e and Z^h are the Green's functions associated with the LSE and LSM modes. According to the scheme we can can take into account the presence of the supporting dielectric substrate merely by using the appropriate Green's function. Substituting (6) in (5) and using the residue theorem we can now obtain an expression for the input impedance:

$$Z_{in} = \frac{j}{kb}\sum_{n=0}^{+\infty}\delta_n \sum_{m=1}^{+\infty}\lim_{\beta\to\beta_{mn}}\left\{\left(\frac{\beta-\beta_{mn}}{k}\right)\right. \tag{10}$$
$$\left[J_o(\beta w)\left(\sin\frac{m\pi d}{a}\right)\left(\frac{\cos\alpha_n x_1-\cos kx_1}{\sin kx_1}\right)\right]^2$$
$$\left.\left(\frac{k^2}{k^2-\alpha_n^2}\right)^2 .\tau_{mn}(\beta).\tilde{G}_{xx}(\alpha_n,\gamma,\beta)\right\} .$$

In the above equation, β_{mn} are the poles of $\tilde{G}_{xx}$ which satisfy the relation

$$\beta_{mn}^2 = k^2+\gamma_m^2-\alpha_n^2 \tag{11}$$

and $\delta_n = \begin{cases} 1 & \text{for n=0} \\ 2 & \text{otherwise} \end{cases}$. Also $\tau_{mn}(\beta)$ is the reflection coefficient of the termination at z=0. It can be written as

$$\tau = \begin{cases} 2j\sin\beta z_1 \exp -j\beta z_1 & \text{for a lossless backshort} \\ 1 & \text{for a matched termination} \end{cases} . \tag{12}$$

Equation (10) gives the input impedance of a microstrip probe that lies in the E-plane of a rectangular waveguide. This equation applies to all dielectric thicknesses and all probe locations.

An important case, which can be treated by the above theory, is the free-standing planar probe; that is to say we ignore the dielectric substrate. In this case, the Green's function is given by

$$\tilde{G}_{xx}(\alpha,\gamma,\beta) = \frac{jR_0}{\gamma/k}\left[\frac{1-\alpha_n^2}{k^2}\right]\left(\frac{\sinh^2\gamma d}{\sinh\gamma a}\right) . \tag{13}$$

Computing the limit yields $\gamma_m = jm\pi/a$, and the input impedance of the probe becomes

$$Z_{in} = -\frac{2jR_o}{k^2ab}\sum_{n=0}^{+\infty}\sum_{m=1}^{+\infty}(-1)^m\delta_n\left[J_o(\beta w)\left(\sin\frac{m\pi d}{a}\right)^2\right.$$
$$\left.\left(\frac{\cos\alpha_n x_1 - \cos kx_1}{\sin kx_1}\right)\right]^2 \times \frac{\sin\beta_{mn}z_1}{\beta_{mn}/k}\frac{e^{-j\beta_{mn}z_1}}{[1-(\alpha_n/k)^2]} \qquad (14)$$

where the propagation constant is now simply

$$\beta_{mn} = \left[k^2 - (\frac{m\pi}{a})^2 - (\frac{n\pi}{b})^2\right]^{1/2} : \qquad (15)$$

k is the propagation constant of free space, R_o is the impedance of free space, and J_o is the ordinary Bessel function.

At this stage, before the dielectric is included in the model, it is instructive to compare (14) with the equivalent expression derived by Eisenhart and Khan for the input impedance of a probe which extends the whole way across the waveguide and which is earthed at both ends. Assuming a gap of width $2g$ and taking into account the presence of the backshort, we obtain [1]

$$Z'_{in} = \left(\sum_{n=0}^{+\infty}\frac{1}{Z_n}\right)^{-1} \qquad (16)$$

where

$$Z_n = \frac{jR_o b}{a}\sum_{m=1}^{+\infty}\frac{1}{\delta_n}\left[\frac{\mathrm{sinc}(|\gamma_m|w)\sin(\frac{m\pi d}{a})}{\mathrm{sinc}(\alpha_n g)\cos(\frac{n\pi h}{b})}\right]^2 \qquad (17)$$
$$\times\left[1-(\alpha_n/k)^2\right]\frac{\sin\beta_{mn}z_1}{\beta_{mn}/k}e^{-j\beta_{mn}z_1}$$

and $h = b-2g-x_1$: h and $x1$ are the distances from the edges of the gap to the walls of the waveguide. Comparing (14),(16) and (17) we notice that the two expressions have some striking similarities. In particular, in each case the total input impedance consists of a combination of elemental impedances, where the elemental impedances essentially reflect the fact that energy is either stored or dissipated by each of the

TE_{mn} and TM_{mn} waveguide modes. In contrast, however, in the case of the microstrip probe, the terms add up in series, whereas in the case of the Eisenhart and Kahn probe the terms add up in parallel. Consequently, for the microstrip probe the real part of the input impedance is due solely to the lowest-order propagating mode; whereas for the Eisenhart and Khan probe, the real part of the input impedance is influenced by the large number of high-order non-propagating modes. This basic and important difference results in the Eisenhart and Khan probe being characterised by a high value of input impedance whereas the microstrip probe is characterized by a relatively low value of input impedance. Moreover, the input impedance of the two-sided probe has a complicated frequency dependence. In order to reduce the input impedance of the Eisenhart and Kahn probe, and to increase the bandwidth, the height of the waveguide is usually reduced by a factor of about 4, but this modification increases the conduction losses and the manufacturing complexity—both of which are extremely important if one wants to manufacture components for the THz frequency range.

We can now write the final design equations for the input impedance, $Z_{in} = R_{in} + jX_{in}$, of a free-standing microstrip probe in single-moded waveguide as

$$R_{in} = \frac{2R_o}{k\beta_{1o}ab}\tan^2(\frac{kx_1}{2})\sin^2(\beta_{1o}z_1)J_o^2(\beta_{1o}w)\sin^4(\frac{\pi d}{a}) \tag{18}$$

$$X_{in} = X_{10} + \frac{2R_o}{k^2ab}\left[\sum_{m=2}^{\infty} X_{m0} + \sum_{n=1}^{+\infty}\sum_{m=1}^{+\infty} X_{mn}\right] \tag{19}$$

$$X_{10} = \frac{R_o}{k\beta_{1o}ab}\tan^2(\frac{kx_1}{2})\sin 2(\beta_{1o}z_1)J_o^2(\beta_{1o}w)\sin^4(\frac{\pi d}{a}) \tag{20}$$

$$X_{mn} = -(-1)^m\delta_n\left[J_o(|\beta_{mn}|w)\left(\sin^2\frac{m\pi d}{a}\right)\left(\frac{\cos\alpha_n x_1 - \cos kx_1}{\sin kx_1}\right)\right]^2 \times\frac{\sinh|\beta_{mn}|z_1}{|\beta_{mn}|/k}\frac{e^{-|\beta_{mn}|z_1}}{[1-(\alpha_n/k)^2]} \tag{21}$$

where X_{10} is the inductive contribution of the propagating mode and X_{mn} is the expression inside the double summation (14). It is interesting to notice that for $w \to 0$, (18) becomes identical to Collin's formula for the input resistance of a coaxial probe[8].

A question often asked is 'what happens to the input impedance of a planar probe when it is rotated about its axis?' Clearly, some device configurations will favour the longitudinal probe whereas other device configurations will favour the transverse probe. The above theory can easily be modified to cover the situation where the probe is transverse to the direction of propagation. First we imagine that the current distribution in the $x-z$ plane, at $y=d$, is given by

$$J_x = J_o \sin k(x_1 - x)\delta(z_1)u(y) \ . \tag{22}$$

The corresponding electric field can be obtained through the spectral-domain method in exactly the same way as before, and then the terms in the expression for the input impedance are modified as follows:

$$Z_{mn}|_{\text{Transverse}} = \left\{ \frac{J_o(|\gamma_m w|)}{J_o(|\beta_{mn}|)} \right\}^2 Z_{mn}|_{\text{Longtitudinal}} \ . \tag{23}$$

It interesting to notice that the difference between the input impedance of the longitudinal probe and the input impedance of the transverse probe is very small. We therefore conclude that the orientation of the probe can be chosen for mechanical convenience alone.

Having now discussed the general properties of probes by considering the free-standing case, we would like to include the supporting dielectric substrate. Moreover, we would like to make the modification to the longitudinal probe because the longitudinal probe is the most useful configuration for "split-block" technology [9]. We can calculate the input impedance of the new geometry by using (10) and inserting the Green's function for a three-layer dielectric system. This modification is straightforward to make in the spectral-domain because the transverse resonance technique can be used to derive $\tilde{G}_{xx}(\alpha_n, \gamma, \beta)$. Applying the immittance method [10] we find that

$$Z^e = \frac{y_2 Ct_3 + y_3 Ct_2}{Ct_2 Ct_3 + Ct_1 Ct_3 y_2/y_1 + Ct_1 Ct_2 y_3/y_1 + y_3/y_2} \tag{24}$$

and

$$Z^h = \frac{z_2 Ct_2 + z_3 Ct_3}{z_1 z_2 Ct_1 Ct_2 + z_1 z_3 Ct_1 Ct_3 + z_2 z_3 Ct_2 Ct_3 + z_2^2} \tag{25}$$

where

$$Ct_1 = \coth \gamma_1 d, \quad Ct_2 = \coth \gamma_2 h, \quad Ct_3 = \coth \gamma_3 a - (d+h) \ ; \tag{26}$$

also

$$y_i = \frac{\gamma_i}{j\omega\epsilon_i}, \qquad z_i = \frac{\gamma_i}{j\omega\mu} \tag{27}$$

where the subscript denotes the region of the cross section, 1,2 or 3, under consideration, see Fig. 1.

Numerically, a difficult aspect of evaluating the impedance is finding the transverse propagation constant γ. Although one is simply finding the roots of the transcendental equations derived through the transverse resonance method (or equivalently the poles of the Green's function) subject to the auxiliary conditions

$$\beta_{mn}^2 = k_i^2 + \gamma_{mi}^2 - \alpha_n^2 \,, \tag{28}$$

for all i, the problem is complicated because the system is three-layered and poles and closely-spaced roots exist. It is therefore a little awkward to ensure that all of the roots and poles are found and that the poles are removed. It turns out to be much more straightforward to perform this task if one assumes that the dielectric is placed symmetrically in the waveguide and the transverse-resonance equations are simplified accordingly. We have found, for geometries of practical interest, that the results are almost identical to the more complicated case when one places the dielectric slightly off axis. In all cases, however, we use a current distribution which is on-axis regardless of whether or not we approximate the off-axis Green's function with the on-axis Green's function. In general terms, an important feature of the method is that the transverse resonance equations lead to a clear understanding of the modes that can propagate in the dielectrically-loaded section of the waveguide, and this has important implications for the bandwidths of probes, as we shall see later.

III Experimental Results and Discussion

To investigate the above theory, we manufactured a scale model of a 400-500GHz mixer block. The waveguide had dimensions of a=47mm and b=22mm, and the probe was fed by an SMA connector which was inserted into the centre, ($d = a/2$), of the broad wall. The central conductor of the SMA connector penetrated 0.5mm into the waveguide and a copper-foil probe was soldered to the end. The dielectric

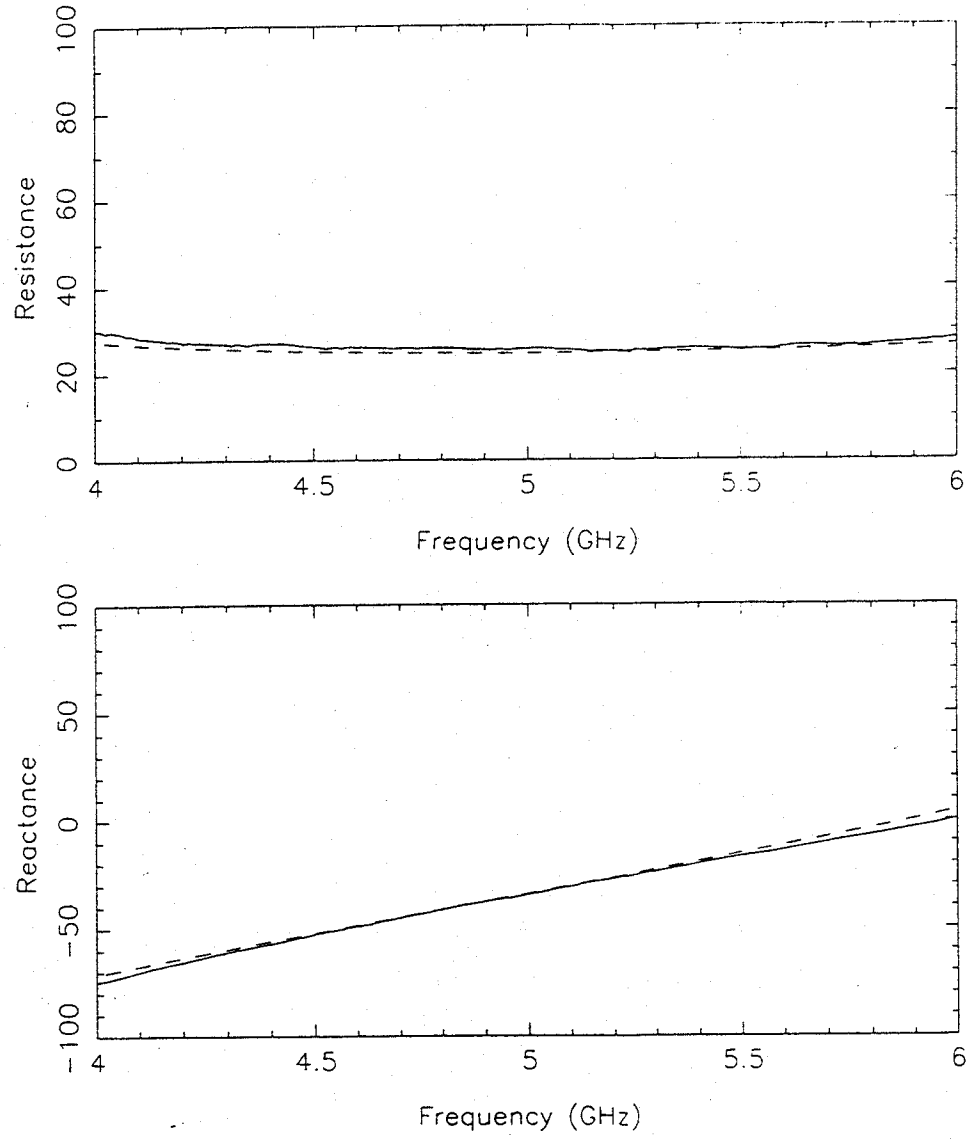

Figure 2: The input impedance of a doubly-matched microstrip probe as a function of frequency. The probe was orientated in the longitudinal direction, no dielectric was used, w =3mm, and $x1$ =12mm. The dotted lines correspond to the experimental data and the solid lines to the theoretical model.

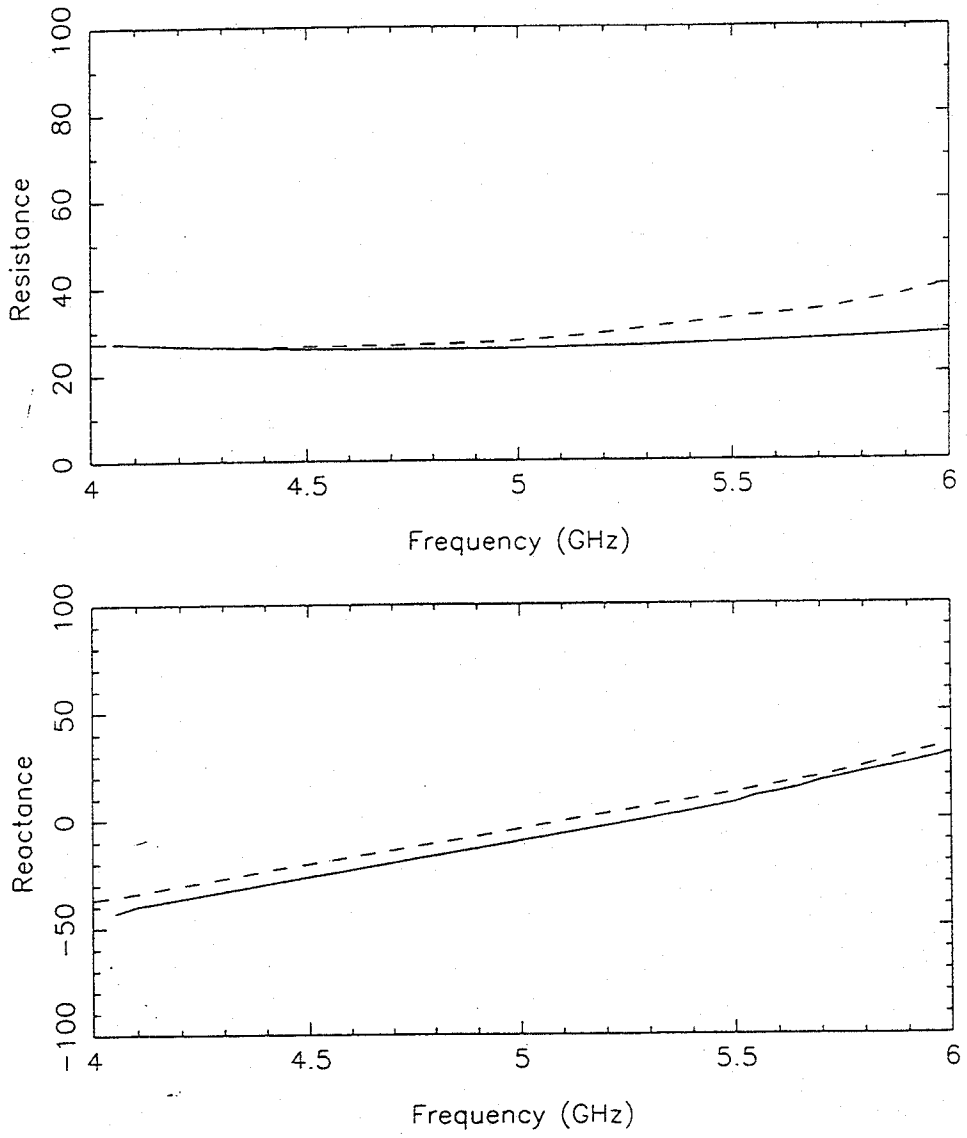

Figure 3: The input impedance of a doubly-matched microstrip probe as a function of frequency. The probe was orientated in the longitudinal direction, the PTFE dielectric was 7mm thick, w =3mm, and $x1$ =12mm. The dotted lines correspond to the experimental data and the solid lines to the theoretical model.

was 7mm thick and was made out of PTFE. Originally, we attempted to use Nylon 66 because its dielectric constant is similar to that of quartz. Unfortunately, however, although the reactive part of the input impedance agreed well with theory, the real part was higher than predicted and this seems to have been due to the known high losses in Nylon 66. To remove the effects of reflections from the ends of the dielectric we tapered the substrate over a distance of approximately 100mm. In addition, we verified the effectiveness of the tapers by measuring the return loss, without a probe but with the dielectric, looking into into one end of the waveguide with the other terminated with a match load. The reflections from the ends of the substrate were at a level of below -15dB. A major advantage of the arrangement described here is that a short circuit can be applied at the wall of the waveguide in order to establish a well-defined reference plane for the impedance measurements. It is substantially more difficult to do well-calibrated impedance measurements on an Eisenhart and Kahn probe.

In order to separate out the intrinsic behaviour of the probe from that of the the probe-backshort combination, we terminated both ends of the waveguide with matched loads. The real and imaginary parts of the input impedance were then measured by using a Vector Network Analyser. In Fig. 2 we show the input impedance of a doubly-matched probe as a function of frequency. In this case the probe was 3mm wide and 12mm long and no dielectric was included. In Fig. 3 we show the input impedance when a 7mm thick PTFE substrate was included. Firstly, it can be seen that theory and experiment agree extremely well in both cases. Secondly, it can be seen that the dielectric does influence the behaviour of the probe even in the case where the dielectric is relatively thin compared to the width of the waveguide and the dielectric constant is low. More specifically, the real part of the impedance is changed very little, but the imaginary part changes significantly. The difference occurs of course because the imaginary part is determined by local, non-propagating modes, whereas the real part is determined by non-local propagating modes. An important observation is that the microstrip probe is essentially a low-impedance structure with a typical input resistance in the range 10-60Ω. This range is ideally suited to the characteristic impedances of microstrip lines. From the point of view of SIS mixers, the probe can be used for

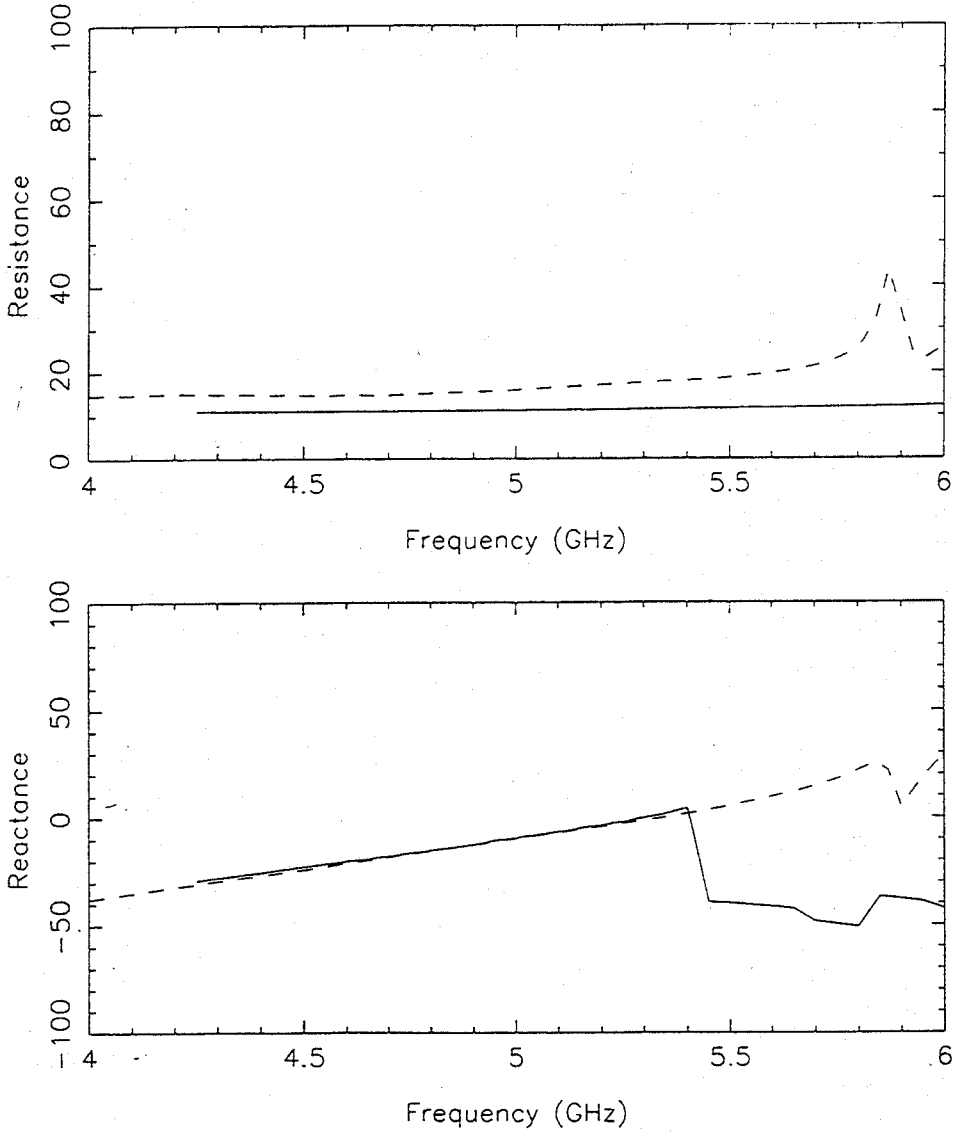

Figure 4: The input impedance of a doubly-matched microstrip probe as a function of frequency. The probe was orientated in the longitudinal direction, the Nylon 66 dielectric was 7mm thick, w =3mm, and $x1$ =9mm. The dotted lines correspond to the experimental data and the solid lines to the theoretical model.

feeding SIS tunnel junctions over broad frequency ranges without the need to reduce the height of the waveguide [11].

An important observation when performing the experiments was that for dielectric constants of 3.8, high-order modes can start to propagate in the dielectric-loaded waveguide, over the frequency range considered, in addition to the lowest-order LSE and LSM modes. This leads to a stronger dependence on frequency than one would like. The effect is shown in Fig. 4 where Nylon 66 has been used in place of PTFE. The theoretical model cuts off at a frequency of 5.4 GHz due to the onset of high-order modes—although we could include them in the model if desired—and the experimental data shows a peak due to a resonance between high-order modes. In the context of mixers this means that as the substrate is made thicker the bandwidth of the probe is reduced. This behaviour and the frequency at which it occurs is fully predicted and can be understood by means of our theory. In fact we find, for practical mixers, that high-order modes in the probe are more influential in determining the bandwidth than high-order modes in the IF channel [12]. Another notable feature of Fig. 4 is that experiment and theory do not agree when one looks at the real part of the impedance, but they do agree when one looks at the reactive part. We believe that this effect is due to the very high microwave losses that are known to be associated with Nylon 66.

IV Conclusions

We have derived an expression for the input impedance of a microstrip probe in waveguide. In the case where the dielectric is extremely thin and can be neglected, the expression can be reduced to a very simple analytical form. In the case where the dielectric is taken into account, the expression is more complicated but straightforward to evaluate numerically. A major advantage of developing a theory of this kind, over simply relying on three-dimensional electromagnetic simulators, is that one gets a clear understanding of the underlying physics involved.

Our work on microstrip waveguide probes leads us to the following conclusions:

1. For the two-sided probe the effects of the propagating and non-propagating modes add up in parallel leading to a high input

impedance with a narrow bandwidth. This is intrinsic to the structure and can only be overcome by reducing the height of the waveguide. For the one-sided probe the impedances associated with the individual modes add up in series leading to a low-impedance broadband structure. In fact only the lowest-order propagating mode makes a contribution to the real part of the input impedance.

2. With the one-sided probe a low-impedance broad-band structure can be made without reducing the height of the waveguide. In fact for THz operation it may well be possible to use oversize waveguide.

3. For the one-sided probe we have shown that the axial orientation of the film has very little influence on the input impedance, meaning that the orientation can be chosen for mechanical convenience alone. To our knowledge this is the first time that this effect has been proven theoretically.

4. When a supporting dielectric substrate is included, the modal behaviour becomes more complicated and it is necessary to keep the substrate thiner than some certain value to avoid resonances and achieve broad-band operation. Normally, one keeps the substrate thin to avoid high-order modes in the IF filter and not to avoid high-order modes in the probe. In practice it seems that the probe dictates how thick the substrate should be.

In summary, we feel that a well-designed one-sided probe is better than a two-sided probe.

References

[1] R.L. Eisenhart and P.J. Khan, "Theoretical and experimental analysis of a waveguide mounting structure," IEEE Trans. Microwave Theory Tech., vol. MTT-19, pp. 706-717, 1971.

[2] G. Yassin and S. Withington, "Analytical expression for the input impedance of a microstrip probe in waveguide," Int. J. Infrared Millimeter Waves, vol. 17, pp. 1685-1705, 1996.

[3] R.E. Collin, *Field Theory of Guided Waves*, IEEE Press: New York, pp. 471-483, 1991.

[4] F. Chen and W. B. Dou ,"Full-wave analysis of a waveguide-to-microstrip transition for millimeter wave applications," Int. J. Infrared and Millimeter Waves, vol. 16, pp. 641-652, 1995.

[5] T.Q. Ho and Yi-Chi Shih, "Spectral-domain analysis of E-plane waveguide to microstrip transition," IEEE Trans. Microwave Theory Tech., vol. MTT-37, pp. 388-392, 1989.

[6] W.L. Weeks, it Electromagnetic Theory for Engineering Applications, John Wiley & Sons, Inc.: New York, 1964.

[7] V.H. Rumsey "Reaction concept in electromagnetic theory," Phys. Rev., vol. 94, pp. 1483-1491, 1954.

[8] R.E. Collin, *Field Theory of Guided Waves*, McGraw-Hill: New York, 1960.

[9] S. Withington, G. Yassin, M. Buffey, and C. Norden, "A horn-reflector antenna for high-performance submillimetre-wave imaging arrays," Int. J. Infrared and Millimeter Waves, vol. 18, pp. 341-358, 1997.

[10] T. Uwano and T. Itoh, "Spectral Domain Approach," in *Numerical Techniques for Microwave and Millimeter-Wave Passive Structures*, Ed. T. Itoh, John Wiley & Sons, New York, 1989.

[11] A.R. Kerr and S.-K. Pan, "Some recent developments in the design of SIS mixers," Int. J. Infrared Millimeter Waves, vol. 11, pp. 1169-1187, 1990.

[12] S. Withington and G. Yassin, "Spectral-Domain Analysis of Submillimetre-Wave Microstrip Filters," Int. J. Infrared and Millimeter Waves, vol. 14, pp. 1975-1984, 1993.

ELECTROMAGNETIC ANALYSIS OF FINLINE MIXERS

G. YASSIN, S. WITHINGTON AND R. PADMAN
Department of Physics, University of Cambridge,
Madingley Road, Cambridge CB3 OHE, UK

ABSTRACT

We describe the electromagnetic design of antipodal finline SIS mixers. An important part of the mixer is the section of antipodal finline which transforms the high impedance of the waveguide ($\approx 300\Omega$) to the low impedance of the microstrip ($\approx 15\ \Omega$) in which the tunnel junction is located. We review the numerical methods that were used to calculate the electrical properties of the finlines, taking into account the finite thickness of the metallisation. We also explain how the transmission line taper was synthesized using an optimum taper method. The design procedure is illustrated by outlining the experimental behaviour of a 230GHz mixer, and scale model results are presented for a mixer which is currently being developed for 345 GHz.

INTRODUCTION

On previous occasions we have reported the design and performance of an antipodal finline mixer at 230 GHz. The arrangement comprises a diagonal waveguide horn, an antipodal finline transition and a miniature superconducting microstrip line which contains the tunnel junction. This mixer combines the directivity and low sidelobe levels of metallic horns with the simplicity, ease of manufacture and repeatability of planar-circuit technology. The noise performance and bandwidth of the mixer are comparable to the best waveguide mixers, and the mixer is easy to operate and does not employ mechanical tuning (Yassin *it al, 1997)*.

A key feature of the design is the use of a low impedance antipodal finline to transform the waveguide into a microstrip line. The two superconducting films which form the finline are deposited on one side of a quartz substrate and are separated by a thin oxide layer. Since the thickness of the oxide layer cannot easily be made thicker than $\approx$ 400nm and the width of the microstrip line cannot be made narrower than $\approx 3\mu$m the embedding impedance of the device is low. More precisely, taking a microstrip width of $w = 3\,\mu$m, a dielectric thickness of $h = 400\,$nm (dielectric constant of SiO_2=5.8), and a metallization thickness of $t = 400\,$nm we obtain a source impedance of $15.5\,\Omega$ (Yassin and Withington, 1995).

One disadvantage of the finline mixer is that the waveguide-to-microstrip transition is rather difficult to design. In this paper we shall describe the electromagnetic methods that were used to design the finline tapers. As is well known,

a difficulty when calculating the properties of miniature superconducting microstrip lines is that the metallization thickness cannot be neglected when it is comparable to the transmission line dimensions. In the case of microstrip lines the effect can be taken into account by using methods such as conformal mapping. In the case of finlines the problem is particularly difficult because of the complicated geometry and the dispersive nature of the multilayer structure. To date, we have calculated the electrical properties of finlines by using a combination of the ridged waveguide model and the spectral domain method, corrected for thickness by Wheeler's approximation. We have verified the conclusions of our theoretical work by performing measurements on scale models and investigating in some detail the performance of a 230 GHz mixer. In this paper we shall also describe a method based on matching the electromagnetic fields at the discontinuities in the cross section of the waveguide. An important advantage of this method is that it is capable of dealing with metallisation thickness rigorously and can be applied easily to a whole variety of finline configurations. Although the calculations can only yield cutoff frequencies, rather than propagation constants and characteristic impedances, knowledge of the former is sufficient to synthesize finline tapers, as we shall see later.

TAPER SYNTHESIS

The conventional way to taper a quasi-TEM transmission line is to taper the geometry according to the impedance profile. This method has two disadvantages. The first is due to the fact that the characteristic impedance of a non-pure TEM mode is not uniquely defined and the second is that the calculation of the characteristic impedance of finlines with thick metallisation and all gap dimensions is not easy. We design our transmission lines according to an "Optimum Taper Method" which only requires knowledge of the propagation constant (and the cutoff frequency) as a function of lateral dimensions. This method is based on minimizing the coupling coefficient χ^{-+} between the incident and reflected waves along a quasi-TEM transmission line. The end product is a minimum-length high-pass section which gives a return loss lower than a specified design value R_{max} at frequencies above a predetermined frequency f_0.

The reflection coefficient of a TEM taper of length L can be approximated by

$$R(f_o, L) = -\int_0^L \chi^{+-} \exp[-2j \int_0^z \beta(f_o, z')dz']dz \ . \tag{1}$$

To solve this equation we need to know the propagation constant, a problem we shall consider in the next section. In addition it has been shown that for any finline structure, the coupling coefficient can be written as (Hinken, 1983)

$$\chi^{+-} = \frac{1-(f_c/f_o)^2/2}{1-(f_c/f_0)^2} \cdot \frac{1}{f_c} \cdot \frac{df_c(z)}{dz} \tag{2}$$

where z is the coordinate along the taper and f_c is the cutoff frequency of the finline. The above equation can be written in the form

$$R(f_o, L) = C \int_0^{2\theta} K(\xi) \exp[-j\xi]d\xi \tag{3}$$

where $\xi(z) = \int_0^z 2\beta(f_0, z')dz'$, $2\theta = \xi(L)$ and C is a normalization constant so that

$$\int_0^{2\theta} K(\xi)d\xi = 1 \tag{4}$$

which yields

$$C = ln\left[\frac{f_{c1}}{f_{c2}}\left(\frac{1 - f_{c2}^2/f_o^2}{1 - f_{c1}^2/f_o^2}\right)^{\frac{1}{4}}\right] . \tag{5}$$

Here, f_{c1} and f_{c2} are the cutoff frequencies at the two ends of the taper. For a given distribution $K(\xi)$ we can then calculate the required taper length (or the value of θ) which yields a return loss which is less than a specified design value R_{max}. Moreover the distribution which gives the minimum value of R for a given length is the Dolph-Chebyshev polynomial (Spolder, 1979). Synthesis of the finline taper then proceeds as follows:

1. Determine the initial and final gaps of the finline section s_1, s_2 and calculate the corresponding cutoff frequencies f_{c1}, f_{c2}.

2. Choose a function $K(\xi)$ which gives the coupling coefficient distribution along the taper in the ξ-space, where the variable ξ is related to the variable z along the taper by $\xi(z) = \int_0^z 2\beta(f_0, z')dz'$. Calculate the normalization constant C and use eqn. (3) to determine the value of θ for the specified value of R_{max}.

3. Use the relation between the coupling coefficient and the cutoff frequency for both the unilateral and the antipodal configurations to obtain the cutoff frequency distribution $f_c(\xi)$. This relation can be written as

$$\begin{aligned} f_c(\xi) &= f_{c1}\left[F/2 + \sqrt{F^2/4 + (1-F).\exp[4CI(\xi)]}\right]^{-\frac{1}{2}} \\ F &= (f_{c1}/f_o)^2 \\ I(\xi) &= \int_0^{\xi} K(\xi')d\xi' \end{aligned} \quad . \tag{6}$$

4. Calculate the corresponding finline gap from the known cutoff frequency using the transverse resonance approach or any other method (eg. spectral domain analysis)and then synthesize the taper using the relation

$$\Delta z = \frac{\Delta\xi}{2\beta(f_0, \xi)}) . \tag{7}$$

The design of the microstrip taper was also based on the above method, but in this case an analytical expression could be derived to compute the characteristic impedance Z_0 as a function of the longitudinal coordinate z which can be written as (McGinnis and Beyer, 1988)

$$Z_0(z) = Z_{01}\exp\left\{\frac{1}{2}\ln(\frac{Z_{02}}{Z_{01}})\left[\sin[\pi(\frac{z}{L} - \frac{1}{2})] + 1\right]\right\} . \tag{8}$$

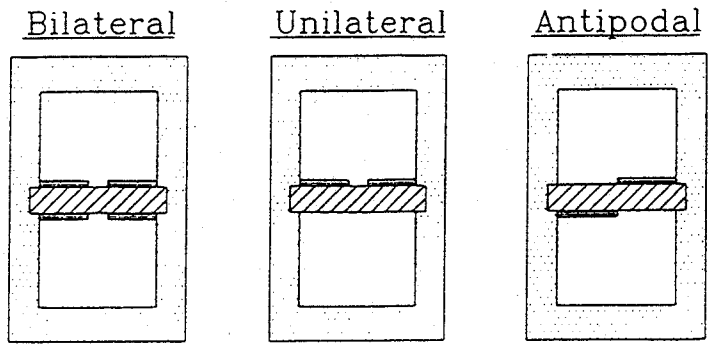

FIGURE I The main finline configurations

This approach is convenient since the characteristic impedance of a microstrip line is unambiguously defined and can be calculated accurately using the conformal mapping method (Yassin and Withington, 1995).

We employed the above approach to design the waveguide to microstrip transition and found that a taper length of two wavelengths is sufficient to match the 300Ω impedance of the loaded waveguide to the 15.5Ω impedance seen by the junction.

CALCULATION OF THE ELECTRICAL PARAMETERS OF FINLINES

A schematic view of the well known finline configurations is shown in Fig. 1.

This structure has been investigated thoroughly in the literature, assuming infinitely-thin metallisation. It is, however, extremely difficult to identify a single full-wave analysis that can be applied to all types of finlines and yet take into account the finite thickness of the fins. One must, therefore, use several analysis techniques and approximations that can, jointly, be used to cover the whole of the waveguide to microstrip transition.

To put the analysis into context we first consider a magnified view of a chip geometry which was designed for a 230 GHz mixer as shown in Fig. 2.

The RF transmission line comprises a transition from waveguide, to modified antipodal finline, to microstrip. The fins (which constitute the base and the wiring layers) are made out of Nb and are separated by a 300 nm of SiO_2 and deposited on a 170 μm thick quartz substrate. In the region before the fins overlap the thickness of the SiO_2 layer is much less than that of the quartz substrate, and the transmission line behaves like a unilateral finline. The impedance in this section is brought down from several hundred ohms to 80 Ω as the finline gap is reduced from the height of the waveguide to about one micron. As the fins overlap the structure needs to be treated as an antipodal finline whose properties are mainly determined by the thin oxide layer rather than the thick quartz sheet, which from this stage onwards merely supports the structure. When significant overlap is achieved, the section behaves like a parallel-plate waveguide with an effective width equal to that of the overlap region. When the width becomes

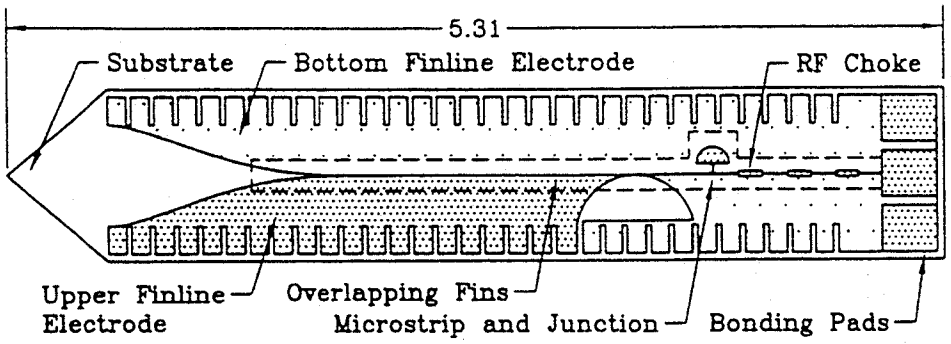

FIGURE II A schematic view of the mixer chip geometry.

large enough such that fringing effects can be ignored, transition to microstrip is performed which in turn is tapered to the required width of about 4 μm. We therefore conclude that the type of sections that we need to analyse, in order to synthesize the transition, are as follows:

1. A unilateral finline on a quartz substrate.
2. An antipodal finline with small overlap.
3. A parallel plate waveguide and microstrip with a large width-to-height ratio.

We shall now describe the various methods that may be employed to analyse the individual sections.

Spectral Domain Analysis (SDA)

Spectral Domain Analysis is a well established full-wave method for analysing multi-layer planar circuits with infinitely thin metallisation. Extensive theoretical work, which was carried on unilateral finline, revealed that there is only a mild dependence of the characteristic impedance on the film thickness and that the dependence of the propagation constant on the thickness is extremely small over much of the waveguide band (Kitazawa and Mittra, 1984). We therefore conclude that the Spectral Domain Method is recommended for calculating the electrical properties of the first section of the transition since it accurately accounts for dispersion which is significant in unilateral finlines with relatively large gaps. The method that we used, which is regarded as being computationally efficient, is well documented in the literature and therefore only a brief description is required here.

Let E_x and E_z represent the tangential electric fields across and along the gap of the finline and let J_x and J_z represent the transverse and longitudinal currents in the fins. In ordinary spatial analysis, the fields and currents are related by an integral equation with the dyadic Green's function as the kernel. In SDA however we relate the Fourier transform of these quantities by a matrix

as follows

$$\begin{pmatrix} \tilde{J}_x(\alpha_n) \\ \tilde{J}_z(\alpha_n) \end{pmatrix} = \begin{bmatrix} G_{xx}(\alpha_n,\beta) & G_{xz}(\alpha_n,\beta) \\ G_{zx}(\alpha_n,\beta) & G_{zz}(\alpha_n,\beta) \end{bmatrix} \begin{pmatrix} \tilde{E}_x(\alpha_n) \\ \tilde{E}_z(\alpha_n) \end{pmatrix} \quad (9)$$

where $\alpha_n = \frac{n\pi}{b}$ is the Fourier parameter of the x-coordinate and $G(\alpha,\beta)$ is the dyadic Green's function in the Fourier domain. Expressions for $G(\alpha,\beta)$ corresponding to a three layer waveguide (unilateral finline) and two layer waveguide (bilateral finline) may be found in the literature. The dyadic Green's function for the antipodal finline is a combination of the two layer and three layer systems. It is worthwhile noting that the simplest expressions for $G(\alpha,\beta)$ are those found using a transverse-resonance-like method called the immittance approach (Zhang and Itoh, 1987). In fact the poles of $G(\alpha,\beta)$ give the roots of the transverse resonance equations of a loaded waveguide.

The above matrix equation is solved using Galerkin's method. The electric fields E_x, E_y are expanded in terms of known basis functions ξ and η

$$\tilde{E}_x(\alpha_n) = \sum_{i=1}^{M} a_i \tilde{\xi}_i(\alpha_n) \quad (10)$$

$$\tilde{E}_z(\alpha_n) = \sum_{i=1}^{M} b_i \tilde{\eta}_i(\alpha_n) \quad (11)$$

$$. \quad (12)$$

After taking the inner products of the above equations with $\tilde{\xi}_i$ and $\tilde{\eta}_i$, using Parseval's theorem and taking advantage of the fact that at any point across the finline either the current or the tangential electric field vanishes, we obtain a 2M $\times$ 2M set of linear equations. The coefficients of the resulting determinant have the form

$$A_{ij}^{uv} = \sum_{n=0}^{\infty} \tilde{\xi}_i(\alpha_n) G_{uv}(\alpha_n,\beta) \tilde{\eta}_j(\alpha_n) \; . \quad (13)$$

A wide range of basis functions have been chosen to solve the resulting set of homogeneous equations. We recommend the Legendre polynomials for the transverse field and sinusoidal functions for the longitudinal field. For a unilateral finline we may choose

$$\xi_m(x) = P_{2(m-1)}(2x/w) \quad (14)$$

$$\eta_m(x) = \sin(\frac{2m\pi x}{w}) \; . \quad (15)$$

The reason for this choice is that Legendre polynomials yield accurate results for both wide and narrow gaps provided that at least the first five terms are used. Moreover since those polynomials form a complete set and satisfy the electric fields edge condition for large values of m, they may be used for more computationally demanding applications such as higher order modes or loss calculations.

In our designs we employed the Spectral Domain Technique to calculate the cutoff frequency and propagation constant at the start and the end of the taper

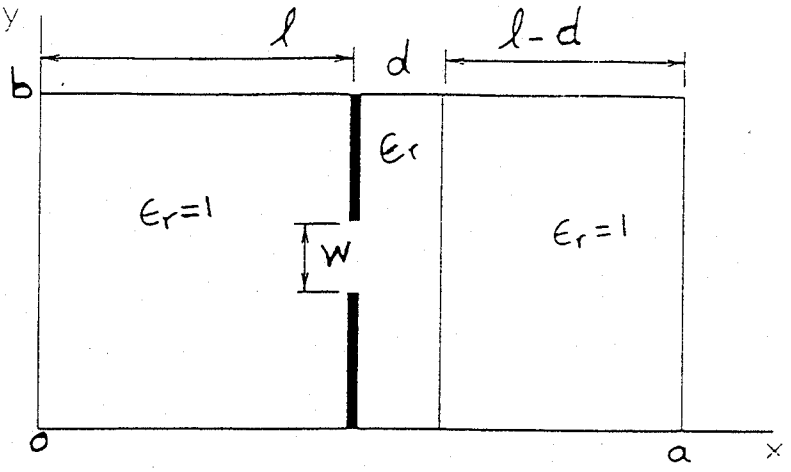

FIGURE III Transverse Resonance Calculation for Unilateral finline

and to validate the results obtained using the transverse resonance method, which we shall describe later. We also employed this method to provide a list of numbers to taper the second section. For this section we corrected for the finite thickness of the fins by applying Wheeler's approximation to the overlap region. The recommended basis functions for the antipodal finline are also a combination of Legendre polynomials and sinusoidal functions (Mirshekar-Syahkal and Davis, 1982)

The Transverse Resonance Approach

The Spectral Domain Method yields accurate results for unilateral finlines. When employed design tapers in conjunction with the optimum taper method described previously, however, a doubly iterative procedure results, which makes it computationally complicated. An alternative method which is simpler and yet gives accurate results is a transverse resonance method which takes into account the presence of the dielectric (Schieblich, Piotrowski and Hinken, 1984). We shall describe how this method can be applied to thin metallisation although it could be extended to handle thick films with the disadvantage of extra complexity. Let a and b be the width and height of the waveguide respectively and k_c the cutoff wavenumber as shown in Fig. 3.

The transverse resonance equation for a loaded waveguide is

$$-\cot(k_c l) - \cot[k_c(l-d)] + \frac{B}{Y} = 0\,. \tag{16}$$

Expressions for the normalized susceptance were then derived using an equivalent circuit which for a centred gap gave the following result

$$\begin{aligned}
&\tfrac{B}{Y} = \tfrac{b}{\pi} k_c[2P_1 + \epsilon_r(P_2 + P_3)] \\
&P_1 = \ln[csc(\tfrac{\pi w}{2b})] \\
&P_2 = r_d.\arctan(\tfrac{1}{r_d} + \ln\sqrt{1+r_d^2}) \\
&P_3 = r_b.\arctan(\tfrac{1}{r_b} + \ln\sqrt{1+r_b^2}) \\
&r_d = w/d \quad r_b = w/b
\end{aligned} \tag{17}$$

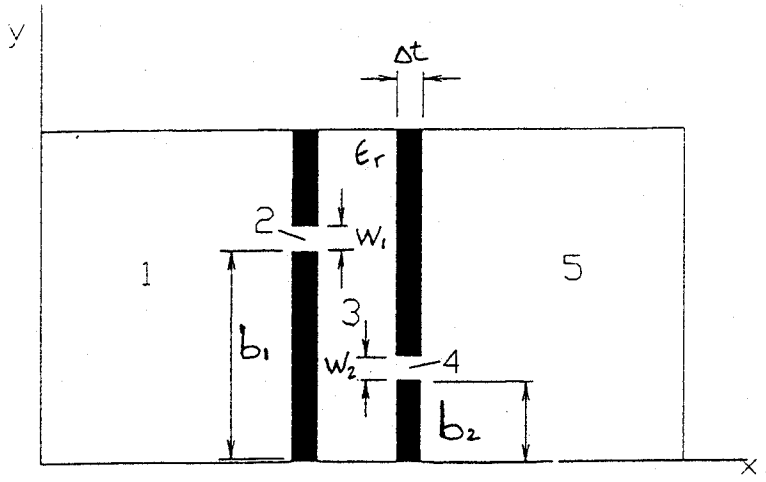

FIGURE IV A cross section for the three finline structures

The propagation constant β is found from the calculated cutoff frequency using the equivalent dielectric constant ϵ_{eq}

$$\begin{aligned} \beta/k_o &= \sqrt{\epsilon_{eq}[1-(\frac{f_c}{f})^2} \\ \epsilon_{eq} &= (f_{co}/f_c)^2 \end{aligned} \tag{18}$$

where f_{co} is the cutoff frequency for $\epsilon_r = 1$. We have designed and tested scale model unilateral finline tapers of length 1λ and measured excellent return losses across the full waveguide band.

The Field Matching Method

The arrangement for calculating the properties of finline using field matching is shown in Fig. 4 (Saad and Schunemann, 1982). This arrangement allows us to find a solution which is applicable to the three main finline configurations. For example, the gap centred unilateral finline is obtained by taking $b_2 = 0, d_2 = b$ and an antipodal finline is obtained for $b_1 = 0, b_2 = b - d_1$. Assuming that the fields are at cutoff, the arrangement may be considered to be a parallel plate waveguide with conductors located at $x = 0$ and $x = a$. The fins and dielectric are then considered as discontinuities and the fields are matched at the four interfaces. Since media 1 and 5 are identical, an eigenvalue problem is obtained which leads to a linear set of algebraic equations.

The solution can elegantly be represented by the equation

$$\mathbf{Ax} = \mathbf{b} \tag{19}$$

where $\mathbf{b}$ is an N-element constant vector, $\mathbf{x}$ is the unknown N-element vector whose components give the expansion coefficients of the fields in the five regions (once those coefficients are known the fields are known) and $\mathbf{A}$ is an N $\times$ N matrix whose components are functions of the unknown cutoff wavenumber k_c. Explicit expressions for the elements A_{mn} and the components of b_n are given in (Saad and Schunemann, 1982). It is interesting to notice that this method is can be used of calculating the parameters of the higher order modes in addition to those of the dominant mode which is required for designing the taper.

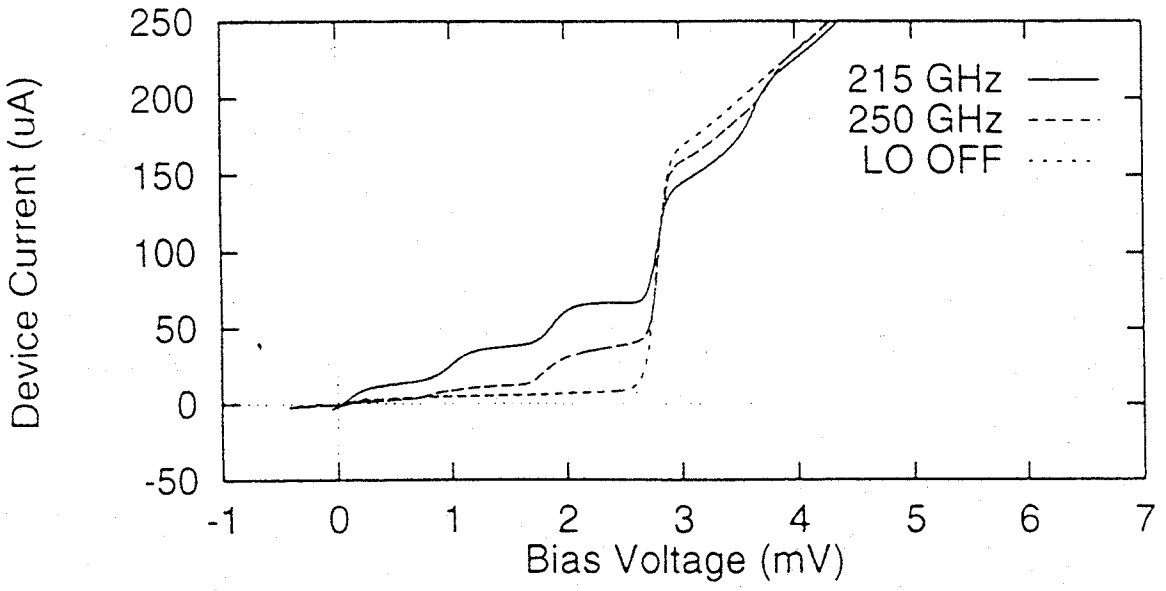

FIGURE V Pumped I-V Curves showing the effect of the tuning stub

Experimental Results

At present we are in the process of designing a broad band finline mixer for 345GHz. The performance of this mixer will be compared with that of a broad-band probe-type mixer, and the one with the best performance will be used in a receiver that is being developed explicitly for observing highly-redshifted extragalactic spectral lines (WEASEL). We have therefore designed and tested several scale model finline taper sections using the method described above. In Fig. 5 we show the return loss of a back-to-back unilateral finline with a taper length of $\approx 1\lambda$. The waveguide dimensions were $a = 47.5$ mm and $b = 22.2$ mm and the thickness of the quartz substrate was 6.0 mm, which scales the real mixer by a factor of about 75.

It can be seen that the return loss is -15 db over most of the waveguide band (4-6 GHz). We matched the empty to the loaded waveguide using one dimensional linear dielectric tapers of length $1/2\lambda$, at both ends of the substrate. We have chosen this arrangement for its simplicity although we were able to verify that the periodic variations which limited the return loss to its present values are in fact resonances which result from the mismatches at the dielectric interfaces and they are not intrinsic to the transition itself.

Finally we present the latest results which were obtained with the 230GHz finline mixer which was developed for the MARS project (Padman and Blundell, 1995). We tested the mixer over a frequency range of 213-265GHz and obtained an average noise temperature of $\approx$ 60K over this range. In fact the frequency band of operation was limited by the availability of local oscillator power rather than a rapid deterioration of the mixer performance. Our measurements clearly show that the bandwidth of the mixer is determined by the tuning stub rather than the finline transition itself. Examples of the performance of the 230GHz mixer are shown in Figs. 5 and 6.

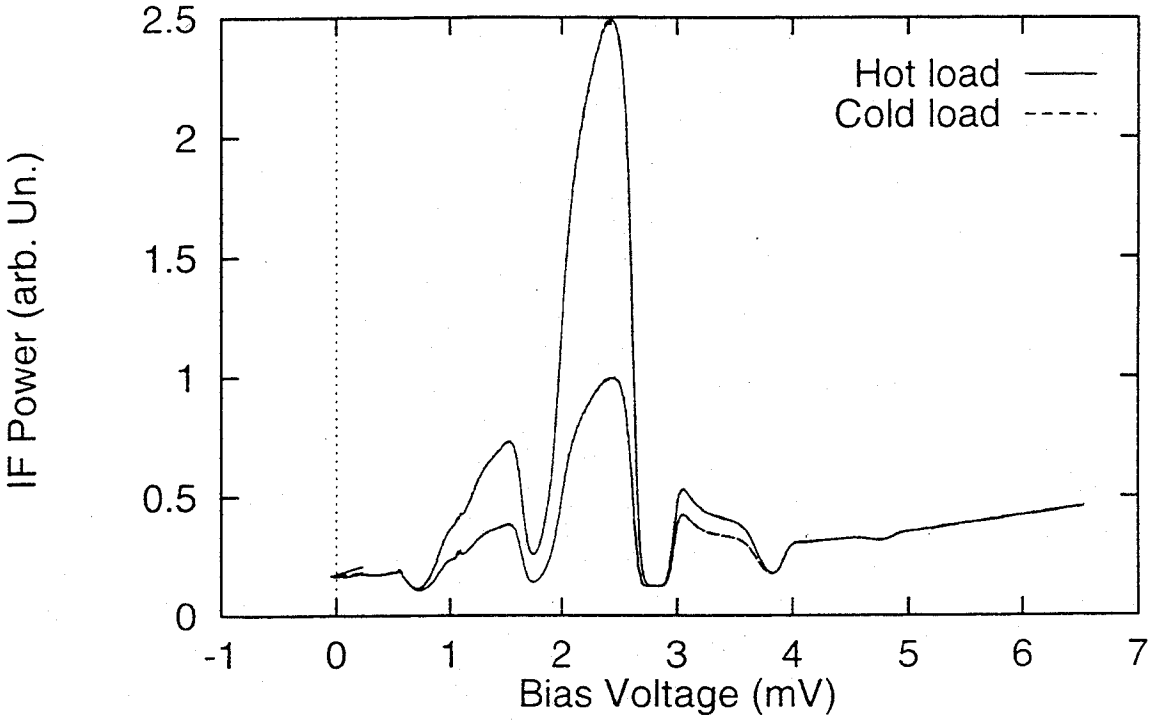

FIGURE VI Hot and cold load measurements at 250 GHz

ACKNOWLEDGEMENTS:

The electromagnetic design work described in this paper is part of a much larger project to develop a range of finline mixers. We would like to acknowledge the work of our collaborators at the University of Cologne, in particular Karl Jacobs, for their excellent work on the development of fabrication techniques for finline mixer chips.

REFERENCES

Yassin, G., Padman, R., Withington, S., Jakobs, K. and Wulff, S. "A broad band 230 GHz finline mixer for astronomical imaging arrays ," Elctron. Lett. Vol. 33, PP. 498–500, 1997.

Yassin, G. and Withington, S. "Electromagnetic models for superconducting millimeter–wave and submillimeter–wave microstrip transmission line," J. Phys. D: Appl. Phys. **28** PP. 1983–1991, 1995.

Hinken, J. H., "Simplified analysis and synthesis of finline tapers," Arch. Elek. Ubertragung., vol. 37, pp. 375–380, 1983.

Sporleder, F. and Unger, H. G. *Waveguide Tapers Transitions and Couplers.* Stevenage: Peregrinus, 1979.

McGinnis, D. P. and Beyer, J. B. "A broad-band microwave superconducting thin–film transformer," IEEE Trans. Microwave Theory Tech., MTT–36, PP. 1521–1525, 1988.

Kitazawa, T. and Mittra, R. "Analysis of finline with finite metallization thickness" IEEE Trans. Microwave Theory Tech., MTT–32, pp. 1484–1487, 1984.

Zhang, Q. and Itoh T. "Spectral domain analysis of scattering from E-plane circuit elements," IEEE Trans. Microwave Theory Tech., MTT–35, PP. 138–149, 1987.

Mirshekar-Syahkal, D. and Davies J. B. "An accurate, unified solution to various finline structures, of phase constant, characteristic impedance and attenuation," IEEE Trans. Microwave Theory Tech., MTT–30, PP. 1854–1861, 1982.

Schieblich, C. Piotrowski, J. K. and Hinken, J. H. "Synthesis of optimum finline tapers using dispersion formulas for arbitrary slot width and locations," IEEE Trans. Microwave Theory Tech. MTT–30, PP. 1638–1644, 1984.

Saad, A. M. K. and Schunemann, K. "Closed form approximations for finline eigenmodes," IEE Proc. H., Microwave Opt. & Antenna, pp. 253–261, 1982.

Padman, R. and Blundell, R. "MARS–The MRAO array receiver system," in *Multi– feed Systems for Radio Telescopes*, ASP Conf. Series, Vol. 75, PP. 155, 1995.

INJECTION LOCKED 100 GHz LO NETWORK, FOR A 32 CHANNEL 220 GHz IMAGING ARRAY

Israel Galin[1], David S Zacharias[2]

[1]GenCorp Aerojet - P.O. Box 296, 1100 W. Hollyvale St., Azusa, CA 91702
[2]ZAX, Millimeter-Wave Corporation - 555 W. Allen Ave., San-Dimas, CA 91773

Abstract

Multi-channel array receivers, for millimeter-wave (MMW) imagers, require local-oscillator distribution network with challenging electrical and packaging performance. This paper presents a local-oscillator (LO) distribution network driving 32 subharmonic (X2) mixers, of a 220 GHz imaging array. The LO distribution network features 32 outputs - each injection-locked and phase controlled relative to a master oscillator - yielding more than 20 mW power at each output. The waveguide network configuration facilitates LO distribution to a compactly packaged, 12" linear array of mixers. The paper provides a complete description and data for this MMW LO distribution network.

LO/Mixer Technological Mismatch, Creates Challenges/Opportunities

Designers of MMW multi-channel receiver front-ends face a challenge/opportunity, originated with the mismatch between the available local-oscillators (LOs) output power, and the required LO drive for mixers. MMW LOs employing InP Gunn devices are designed for maximum possible output power - typically ~50 mW at 100-150 GHz - while individual mixers require LO drive typically of only ~10 mW.
Hence, single MMW LOs are capable of driving 2-4 separate mixers, simultaneously, through LO power divider networks. Larger MMW multi-channel receivers (≥5 mixers) require LO power combining/coherent networks and LO power dividing networks.
The added complexity of multi-channel MMW receivers promise in fact, economical and technical system enhancements. In the final analysis, LO distribution networks may facilitate system cost reduction, reduction in DC power consumption per receiver channel, and/or reliability augmentation through efficient LO redundancy.

This paper presents a local-oscillator distribution network embodied in a compact, efficient, and relatively simple structure, which is driving 32 subharmonic (X2) mixers of a 220 GHz imaging array. This LO distribution network is implemented as a simple network of separate oscillators, frequency injection locked and than phase matched, to yield coherent outputs - avoiding the complications commonly associated with power combining networks.

LO Distribution Network - Structure Description

Figure 1 depicts the 32 output 100 GHz LO waveguide distribution network (produced by ZAX Millimeter Wave Corporation) which consists of sixteen free-running output oscillators, each employing a single InP Gunn device. Each output oscillator feeds separately a 1:2 power divider (matched terminated magic-T), yielding thirty-two outputs. A three port circulator yields a nominal 20 dB isolation - to minimize load pulling - between each free running oscillator and its respective pair of loads, at the 1:2 power divider outputs. Each circulator also facilitates frequency injection locking, of each of the sixteen free-running output oscillators, to a single master oscillator, through a 1:16 power divider (a network of 15 matched terminated magic-Ts). Finally, the LO distribution network's thirty-two outputs are separately provided with adjustable phase shifters yielding, in addition, to a single frequency locked outputs also outputs phase matching.
All oscillators are biased through separate voltage regulators - to minimize pushing effects.
This LO distribution network is compactly packaged to accommodate all 32 output ports in a linear 12" array, for interface with a similar size array of 200 GHz subharmonic (X2) pumped mixers [1].

LO Distribution Network - Electrical Characteristics

Some of the most important electrical parameters of this LO distribution network feature:

- A DC power consumption of all seventeen oscillators combined approximates 30 W, with a total current of 3.4 A (1.5-2.2 W per oscillator) - resulting in LO DC consumption of ~0.9 W, per receiver channel.
- Each of the 32 output ports provides a minimum of 20 mW of power at 100 GHz.
- Each of the 16 output oscillators delivers a minimum of 50 mW power.
- The master oscillator output power is some 75 mW providing an injection power of some 3 mW to each output oscillator.
- The frequency-versus-temperature coefficients of all oscillators (master or outputs) are matched, and each oscillator is set for 1-2 MHz/°C - designed to insure a frequency locking band over some 100-200 MHz (locked frequency over a 25±15 °C operating temperature).

Acknowledgment

The work described in this paper was carried out and funded in part under a NASA contract NCC1-203.

Reference

[1] I Galin, "A 220 GHz Subharmonic (x2) Mixer - For Ultra-Wideband Array Applications", The 20th International Conference on IR and MM-Waves, Orlando 1995.

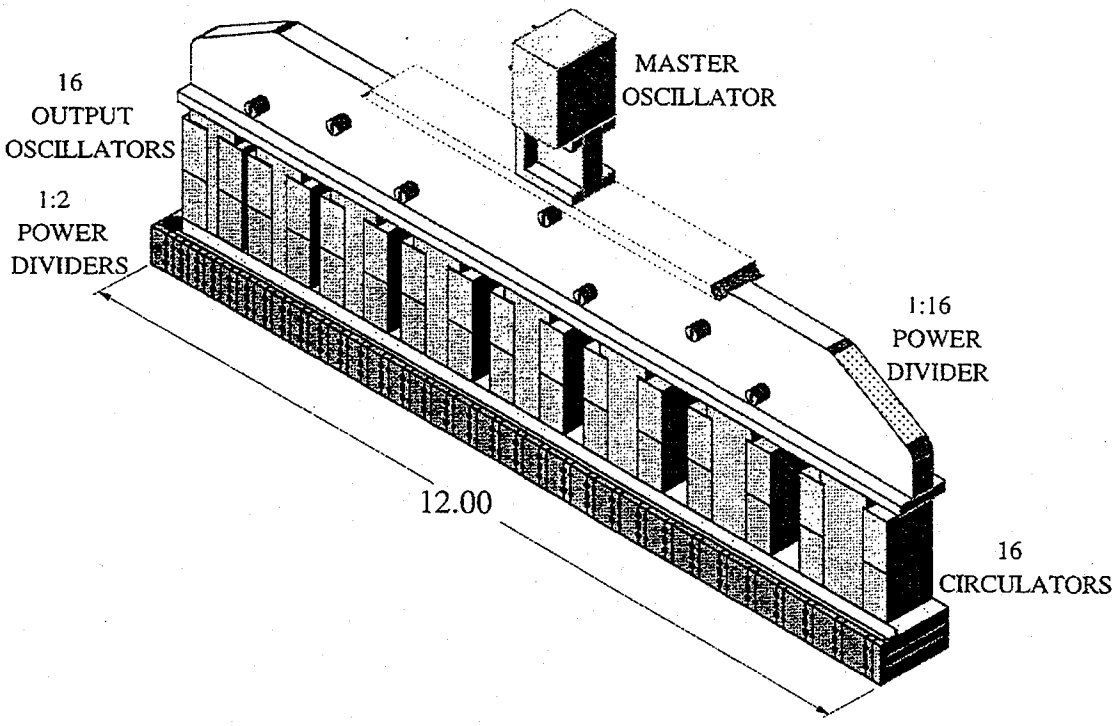

Figure 1

100 GHz LO waveguide distribution network - 32 output ports packaged in a linear 12" array.

LASER MICROMACHINING OF SILICON: A NEW TECHNIQUE FOR FABRICATING HIGH QUALITY TERAHERTZ WAVEGUIDE COMPONENTS[1]

C. K. Walker, G. Narayanan, H. Knoepfle, J. Capara, J. Glenn, A. Hungerford
Steward Observatory, University of Arizona, Tucson, AZ 85721

and

T. M. Bloomstein, S. T. Palmacci, M. B. Stern, and J. E. Curtin
Lincoln Laboratory, Massachusetts Institute of Technology, Lexington, MA 02173

ABSTRACT

One of the main obstacles encountered in designing low noise, high efficiency, heterodyne receivers and local oscillator sources at submillimeter wavelengths is the quality and cost of waveguide structures. At wavelengths shorter than 400 micrometers, rectangular waveguide structures, feedhorns, and backshorts become extremely difficult to fabricate using standard machining techniques. We have used a new laser milling technique to fabricate high quality, THz waveguide components and feedhorns. Once metallized, the structures have the properties of standard waveguide components. Unlike waveguide components made using silicon wet-etching techniques, laser-etched components can have almost any cross section, from rectangular to circular. Under computer control, the entire waveguide structure (including the corrugated feedhorn!) of a submillimeter-wave mixer or multiplier can be fabricated to micrometer tolerances in a few hours. Laser etching permits the direct scaling of successful waveguide multiplier and mixer designs to THz frequencies. Since the entire process is computer controlled, the cost of fabricating submillimeter waveguide components is significantly reduced. With this new laser etching process, the construction of high

[1]The Lincoln Laboratory portion of this work was performed under a cooperative research and development agreement (CRDA) with the University of Arizona. Opinions, interpretations, conclusions, and recommendations are those of the author and are not necessarily endorsed by the United States Government.

performance waveguide array receivers at THz frequencies becomes tractable. In this paper we describe the laser etching technique and discuss test results from a micromachined 2 THz feedhorn.

1 Motivation

The vast majority of radio receivers, transmitters, and components that operate at millimeter and submillimeter wavelengths utilize waveguide structures in some form. This is because waveguide is a well characterized, low-loss, transmission medium which can be readily fashioned into a variety of high-quality circuit and quasi-optical components. The long history of development of waveguide components provides a broad base of knowledge from which to synthesize and evaluate new designs. In addition, new computer aided design tools (*e.g.* Hewlett Packard's High Frequency Structure Simulator) provide a straightforward way of optimizing even complicated waveguide structures. Unfortunately, at frequencies above 1 THz, waveguide dimensions become so small (less than 0.23 by 0.116 mm) that fabrication utilizing conventional machining and electroforming techniques becomes extremely difficult, expensive, and/or impossible. Indeed, for situations where even modest sized heterodyne array receivers are being considered, the practical frequency limit to utilizing conventional machined waveguide structures is much lower ($\sim$ 500 GHz). This situation is unfortunate, since, due to their lower loss and tuning flexibility, waveguide mixers have been found to (in general) outperform quasi-optical mixers both electrically and optically at frequencies where both have been constructed. Clearly, a new way of machining small waveguide structures is needed in order to reap the benefits of waveguide at THz freqencies.

In the past, silicon wet etching techniques have been employed as an alternative to conventional machining [1, 2]. The main disadvantage of the wet etching technique is that one is forced to follow the $< 100 >$ or $< 110 >$ crystal plane in the silicon. This severely limits the types of structures that can be produced. The process is well suited to making wide-angle pyramidal horns or straight sections of single height waveguide. However, it cannot readily be used to make waveguide structures in which the height of the waveguide is stepped down (*e.g.* in an impedance transformer) or tapered (either rectangular or circular). These structures are needed to make efficient feedhorns.

In this paper we introduce a new laser micromachining technique for fabricating high quality, low-cost waveguide structures for frequencies up to $\sim$ 10 THz. With this process, waveguide components of varying height and width can be machined to $\sim$ 1 μm accuracy. As a test of the viability of the laser micromachining technology, we conducted beam pattern measurements on a 2 THz corrugated feedhorn made using this process.

2 Waveguide Fabrication

2.1 Laser Induced Microchemical Etching of Silicon

Laser processing offers several advantages for machining parts in the micro-domain. Compared to conventional machining, smaller feature sizes with greater mechanical tolerances can typically be achieved due to the high focusability of laser light and ability to deliver intense sources of energy with high precision. Since laser machining is a non-contact process, there is no mechanically-induced material damage, tool-wear, or machine vibration from cutting forces. This can lead to finer finishes, improved accuracy, and less process overhead. A number of different materials ranging from metals and polymers to composites and ceramics have been successfully machined using lasers, traditionally using ablative techniques.

For the waveguide application, we employ a laser-induced microreaction initially developed for trimming and trench etching of silicon in semiconductor microfabrication [3,4,5]. As explained below, there are several important advantages to using chemical action for the controlled removal of material. The basic process is shown schematically in Figure 1. An argon-ion laser is used to locally heat a portion of the silicon substrate in a chlorine ambient. At the onset of melting, volatile silicon chlorides are formed. Due to the highly non-linear activation energy of the process, the reaction is confined almost exclusively to the molten zone. Also, silicon is bound into volatile products unlike ablative techniques which due to their explosive nature, can lead to particulate formation. These are often very difficult to remove due to significant attractive forces in the micro-domain. Chemical activation also reduces the energy requirement for removal minimizing the potential for cracking. Using a crystalline material such as silicon also has the benefit that unetched portions of the molten zone regrow epitaxially to crystalline quality. This allows controlled thin shavings to be removed plane

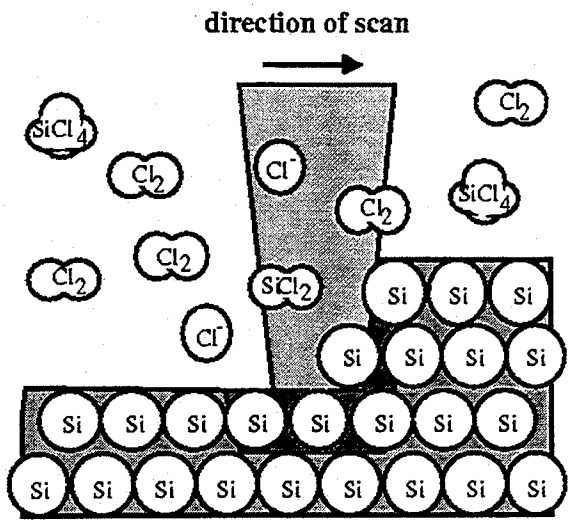

Figure 1: Schematic representation of laser direct write etching of silicon in a chlorine ambient. Using high NA optics, the reaction zone can be confined to the necessary micrometer resolutions demanded for microelectronics processing.

by plane with no change in etch rate. In this manner, structures can be built up by limiting the etch depth at each scan plane [6,7].

In practice, this etch depth can be maintained to approximately one micrometer shavings using low-inertia galvanometers to rapidly deflect the beam. The basic set-up of the optical scanning system and vapor cell used are similar to those of previously developed laser-direct write systems [8]. As shown schematically in Figure 2, the output of a 15-Watt argon ion laser is expanded to a 16 mm beam using an 8× telescope. The beam is deflected using a commercial X-Y scanner [9] through an achromatic lens which serves as the focusing element. The focused beam is introduced through a quartz cover-glass into a stainless-steel vapor cell containing the sample. The vapor cell has ports for gas inlet and outlet, pressure head, and thermocouple. The wafer surface is typically biased to approximately 100° C using an IR-illumination source incident on the substrate from the backside. Filtered, 99.9% pure research grade chlorine is slowly flowed over the wafer surface at 20 SCCM to limit the build-up of products. A cold trap is also placed before the vacuum pump to protect it

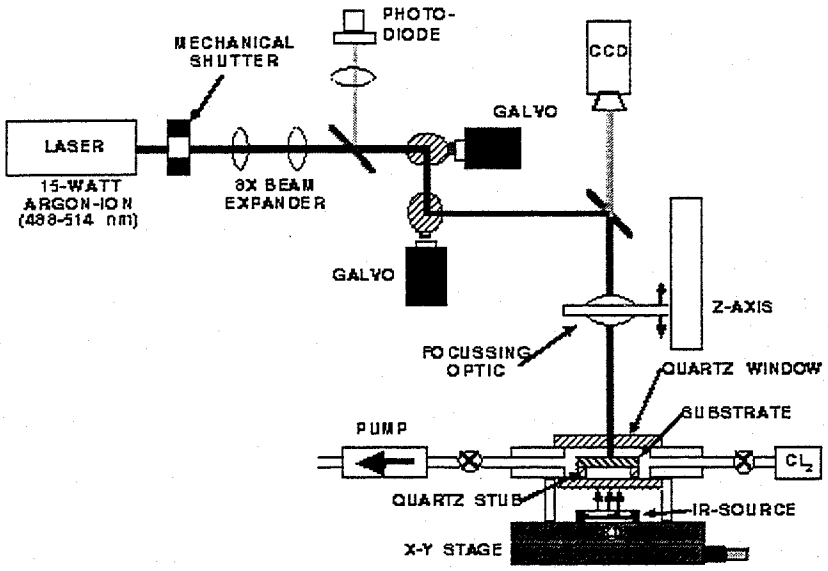

Figure 2: Schematic diagram of galvanometer based scanning apparatus. A higher power objective (not shown) can be slid in place of the focusing optic to allow more detailed analysis of the surface. For etching high aspect ratio structures, a circular polarizer is placed in the beam path to improve edge uniformity due to the selective reflectivity of the S and P polarization components along the side-walls.

from the corrosive gas. The reaction is observed through the focusing optic with a charge coupled device (CCD) camera. A high power 50× objective is also mounted on a linear translation stage containing the focusing element allowing details on the surface to be more closely examined in-situ. The scanning system is driven directly from computer generated patterns which can be constructed using a commercial solid-modeling software package or via software using a toolbox of simple shapes.

A detailed description of the process physics can be found in [10]. Below, we summarize the results. The volumetric removal rate (Vol Rate) is found experimentally to scale according

to:

$$\text{Vol Rate} = 10^4 \mu\text{m}^2/\text{s}(\text{T}_\text{A}/300\text{K})^{0.8}\omega_\text{m}$$

where T_A is the temperature of the ambient gas and ω_m is the diameter of the molten zone. The proportionality constant is determined by the complicated transport and reaction dynamics, particularly from gas phase chemical reactions which alter the dynamics through compositional changes and heats of reaction. The temperature scaling is due to the improved diffusive transport of species to and from the chemically active area in the gas-phase localized above the molten zone. The gas ambient temperature (equal to the bias temperature of the substrate) can be continually increased to approximately 700 K. At higher temperatures, significant background etching of the substrate occurs. Additional laser energy can also initiate a self-sustained reaction leading to highly damaged and coarse looking surfaces. The removal rate is also found to scale directly with the radius of the molten zone. This linear scaling of removal rate with reaction zone is characteristic of systems with three dimensional transport such as in the combustion of fuel droplets. The melt zone diameter is dependent on the laser power, optical coupling, and thermal properties of silicon. In practice, the melt zone can be varied from 1 to 25 μm using a 15 Watt argon-ion laser running multi-mode. This leads to removal rates ranging from approximately 10^4 $\mu\text{m}^3/\text{s}$ (0.036 mm^3/hr) to 5×10^5 $\mu\text{m}^3/\text{s}$ (1.8 mm^3/hr). By virtue of the scaling law, smaller, higher frequency waveguide components can be fabricated in *even less* time since volumetric removal rates scale linearly with melt zone diameter, or resolution, while the total volume of the device scales cubically with length scale. For instance, a similar 1.62 THz waveguide at 4-μm resolution can be etched in one-fourth the time of an 810 GHz version etched at 8-μm resolution.

As an example of a laser micromachined part, a proof-of-concept demonstration was made of a portion of an 810 GHz and 2 THz circular to rectangular mode matching waveguide. In the initial prototyping of the 810 GHz waveguide structure, an approximately 8 μm diameter laser-induced reaction zone (6-μm laser beam spot size) is swept across the surface at 5 cm/s removing 1 μm shavings per plane at a rate of $10^5\mu\text{m}^3/\text{s}$. Higher scanning velocities can be used to increase depth resolution. Improved lateral resolutions, if necessary, are possible over critical dimensions through power modulation of the laser beam. Figure 3 shows a portion of the waveguide structure etched in 1 hour (a duplicate mating piece must be fabricated). A larger portion of the feedhorn is shown in Figure 4. For the 2 THz

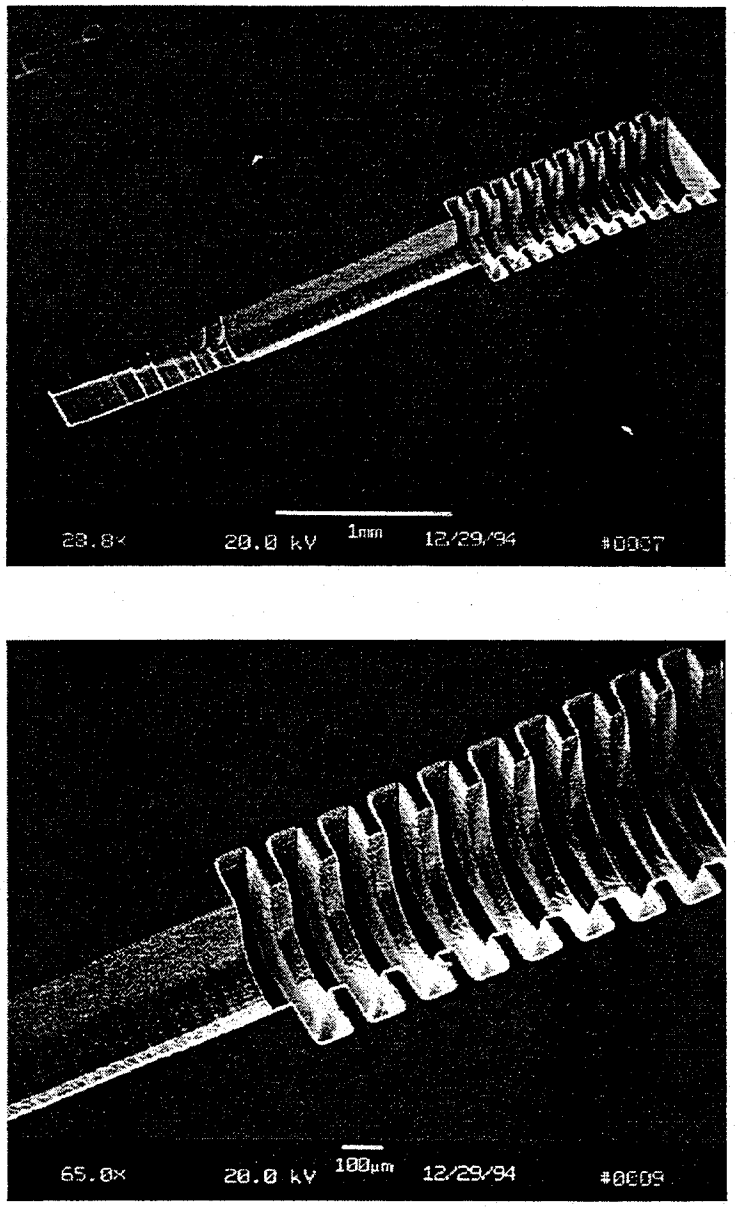

Figure 3: (a) Scanning Electron Micrograph (SEM) of portion of an 810 GHz feedhorn structure. The structure was etched using 4.3 Watts of laser power focused into a 6 μm spot in 200 Torr of chlorine gas. The laser beam was scanned at 5 cm/s and incrementally moved 2 micrometers between line scans. Under these conditions, nominally 1 μm shavings are removed per pass of the laser over the surface. The total etch time is one hour, not including the overhead time for pattern generation and stage motion. (b) SEM close-up of ridges.

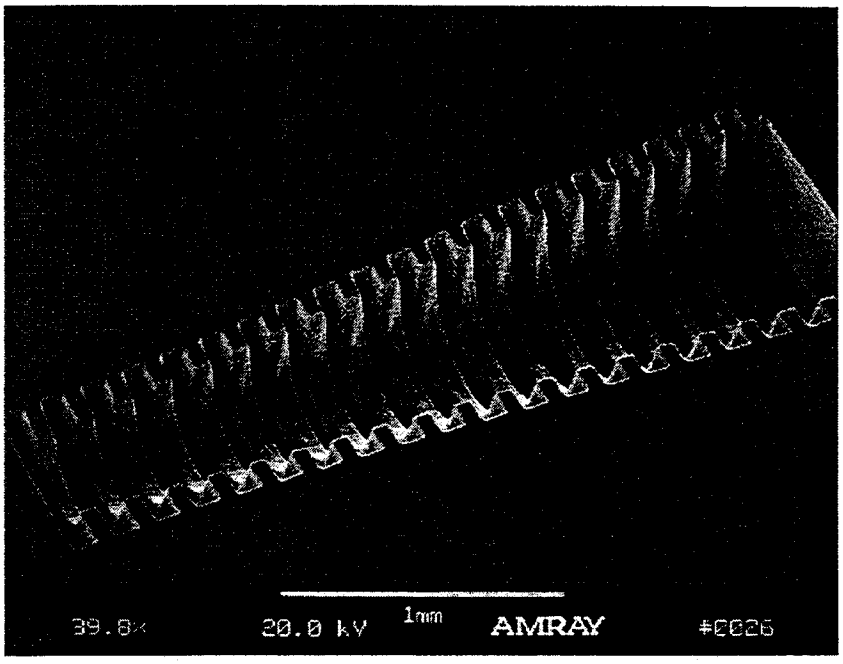

Figure 4: SEM of the first twenty-ridges in the feedhorn portion of the 810 GHz structure. The same processing conditions described in Figure 3 were used. This extended portion of the feedhorn required two hours to fabricate, not including the overhead time for pattern generation and stage motion.

device, an approximately 4 μm (3-μm laser beam spot size) diameter laser-induced reaction zone is swept across the surface at 4 cm/s removing 0.65 μm shavings per plane at a rate of $5 \times 10^4 \mu m^3/s$. Figure 5 show scanning electron micrographs of the structures.

Waveguide surface roughness values measured with atomic force microscopy are typically on the order of 200 nm RMS. This surface quality is already sufficient to provide low-loss waveguide performance to $\geq$ 10 THz. The RMS surface roughness can be reduced even further, to under 25 nm, using standard polishing etches based on HF-HNO_3-$HC_2H_3O_2$ solutions.

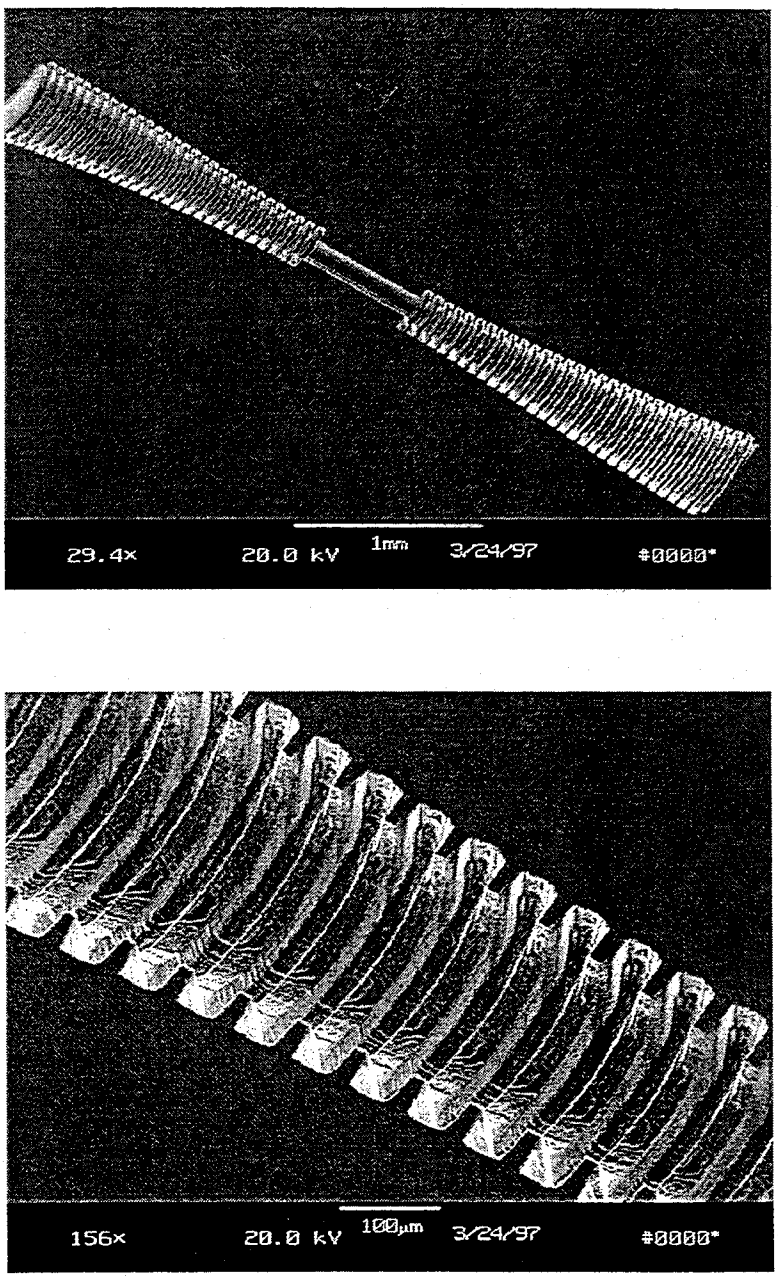

Figure 5: (a) SEM micrograph of replicated version of 2 THz waveguide structure. The original structure was etched using 3 Watts of laser power focused into a 4 μm spot in 200 Torr of chlorine gas. The laser beam was scanned at 4 cm/s and incrementally moved 2 micrometers between line scans removing 0.65 μm shavings per pass of the laser over the surface. (b) SEM close-up of ridges.

2.2 Device Replication

Although the process can be used to produce prototypes relatively quickly, to produce large format arrays, it becomes more practical to replicate the etched devices. We are currently working on a polymer based replication process [11] to produce high performance, low-cost, focal plane arrays at THz frequencies. This molding process has shown extremely high fidelity in reproducing features down to sub-micrometer detail. A negative of the silicon etched master is first made by casting polydimethylsiloxane (PDMS) over the etched surface which has been first fluorinated with tridecafluoroctaltrichlorosilane (TDTS). Due to the high elastomeric constant and low interfacial free energy between PDMS and the surface, it can be readily pulled apart from the silicon master. A low-viscosity polymer precursor, such as uv-curable epoxy, polyurethane, or polymethylmethacrylate is then flowed over the elastomer negative, filling the structure through capillary action. After curing, the elastomer is pulled from the epoxy replica for further reuse. A portion of a replicated version in five minute uv-cured epoxy of a 2.0 THz waveguide structure is shown in Figure 6 showing the excellent fidelity of the process. After the structures are replicated in epoxy, 0.3 μm of gold are sputtered onto the waveguide surface. The structures are then mated using uv-cureable epoxy in a double sided aligner we have implemented. Cross-hairs etched off to the side of the waveguide on the silicon master and masked during the gold sputtering are used as guides in the mating procedure. A summary of the replication and coating process is shown in Table 1.

3 Beam Pattern of a 2 THz Laser Micromachined Feedhorn

Using the process described above, two 2 THz corrugated feedhorns were fabricated in an end-to-end arrangement as shown in Figure 5a. The feedhorn design follows that of [12] and has 30 corrugations. The two horns are connected by a short (0.164 mm) section of circular waveguide. Once the two halves of the horn blocks have been aligned and mated, they are clamped into a test fixture (Figure 7). The beam of one feedhorn looks through a far-infrared, low-pass filter (0.8 mm thick crystalline quartz with garnet powder and a black

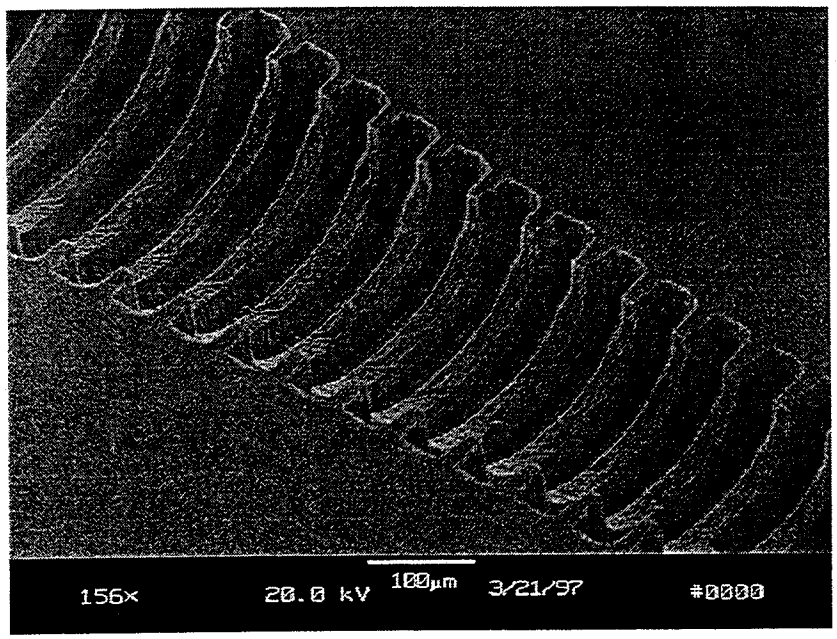

Figure 6: SEM micrograph of replicated version of 2 THz waveguide.

polyethylene layer) and polyethelene vacuum window into an anechoic chamber. It is this feedhorn on which the beam pattern measurement is performed. An additional ($\sim 25\mu$m) layer of black polyethylene was placed across the vacuum window to further reduce the possibility of near/mid infrared light leaks. The second feedhorn looks down into a reflective cavity containing a doped silicon bolometer [13] designed to operate at 4 K. Together the low-pass filter and feedhorns limit the frequency response of the bolometer to between ~ 1.4 and 2.4 THz. The voltage output of the bolometer is proportional to the power intercepted by the input feedhorn over this frequency range. The downward looking cryostat containing the detector assembly is mounted on top of an air tight anechoic chamber as shown in Figure 8. The humidity in the chamber can be lowered by filling it with dry nitrogen gas and/or with a tray of dessicant. The chamber contains a large (42" travel), computer-controlled, X-Y stage. A calibrated, upward looking, black-body source is mounted on the stage and serves as the signal source for beam pattern measurements. For the measurements described here, the temperature of the blackbody source was set to 950 K. The blackbody aperture is

Table 1: Replication and Gold Sputtering Process

1. LASER ETCH WAVEGUIDE	
2. PRIME SUBSTRATE WITH RELEASE AGENT AND CREATE ELASTOMER MASTER FROM PDMS (NEGATIVE TONE)	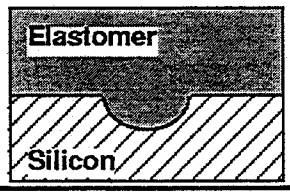
3. REPLICATE ELASTOMER IN UV-CURED EPOXY ON ACETATE SUBSTRATE	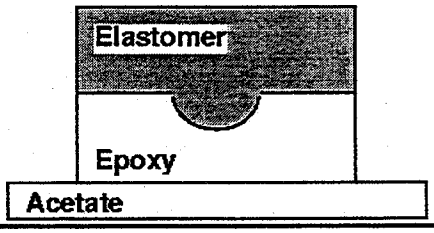
4. PEEL OFF ELASTOMER AND ACETATE AND SPUTTER GOLD ON EPOXY REPLICA	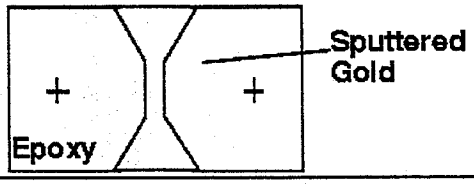

chopped at 20 Hz. Beam pattern measurements are made by scanning the blackbody under the test dewar and synchronously detecting the bolometer output using a lock-in amplifier. The control computer records the position of the black body source along with the corresponding lock-in amplifier output. The distance between the black body source and feedhorn (234 mm) provides an angular resolution of $\sim 1.47°$.

Figure 9 shows cross-scans of the 2 THz feedhorn. The plots indicate the feedhorn's beam is nearly Gaussian with no measurable sidelobes to the noise floor of the map ($\sim$ 11 dB). There is a small asymmetry in the beam patterns, probably the result of a slight misalignment between the two halves of the horn block. The FWHM of the beam profile is $\sim 20°$, close to the value of 19.3° derived from the horn's beamwaist, $\omega_o = 0.33\,d$, where d is the diameter of the feedhorn aperture ~ 0.506 mm.

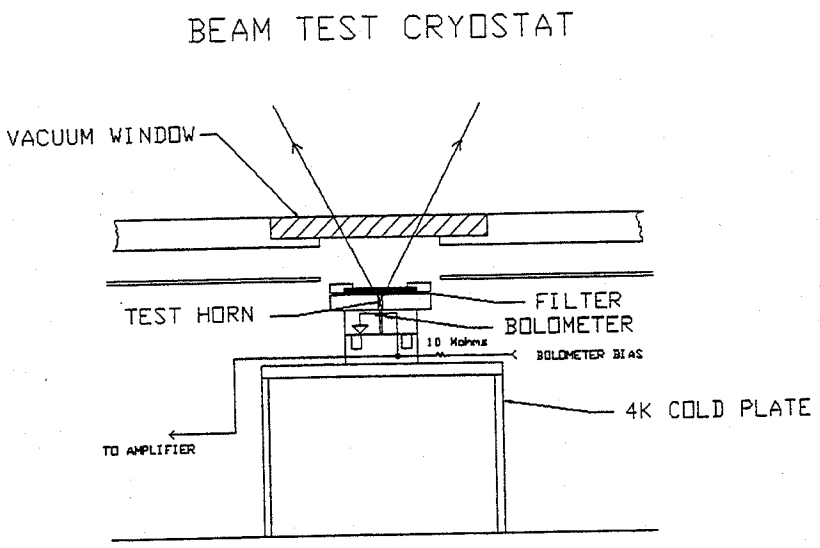

Figure 7: Cross section of feedhorn test fixture mounted in the cryostat. The beam of one feedhorn looks through a far-infrared, low-pass filter (0.8 mm thick crystalline quartz with garnet powder with a black polyethylene layer) and polyethelene vacuum window into an anechoic chamber. The second feedhorn looks down into a reflective cavity containing a doped silicon bolometer [13] designed to operate at 4 K.

4 Applications

4.1 Mixer Arrays

With this new micromachining technology it is now possible to consider the construction of large format arrays of high-performance THz waveguide receivers. Figures 10, 11a, 11b, and 11c illustrate how a 2 THz array of hot-electron bolometer mixers could be constructed using this technology.

Figure 10 is an assembly diagram of the mixer array. The design uses an array of corrugated feedhorns, each with a reduced-height waveguide transition (Fig. 11a). The

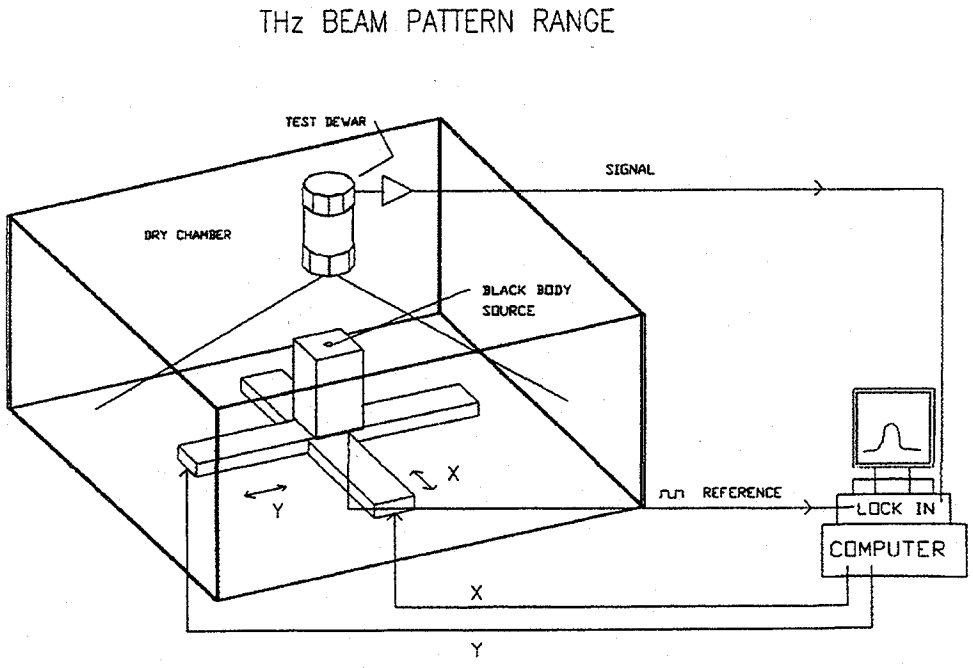

Figure 8: THz Beam Pattern Range. The chamber contains a large ($42'' \times 42''$ travel), computer-controlled, X-Y stage. A calibrated, upward looking, black-body source is mounted on the stage and serves as the signal source for beam pattern measurements.

reduced-height waveguide should provide an excellent match to the real part of the bolometer impedance, permitting the use of only a single, fixed backshort.

At high frequencies ($\geq$ 650 GHz) it becomes nearly impossible to manually mount detectors across small waveguide structures. In order to avoid this problem, mixing devices for the array are fabricated on $\sim$1 μm thick silicon nitride membranes. To date, this approach has been successful with SIS junctions up to frequencies of $\sim$850 GHz. Here, the bolometers are fabricated on membranes which span an aperture with the dimensions of the reduced height waveguide used in the 'horn block'. These apertures are formed by etching a pyramidal hole from the backside of the silicon wafer supporting the membrane (see Fig. 11b). As with the horn block, all exposed surfaces of silicon are gold plated to provide conduction. The bolometers are placed in the center of the waveguide. Low pass filtering is provided by a

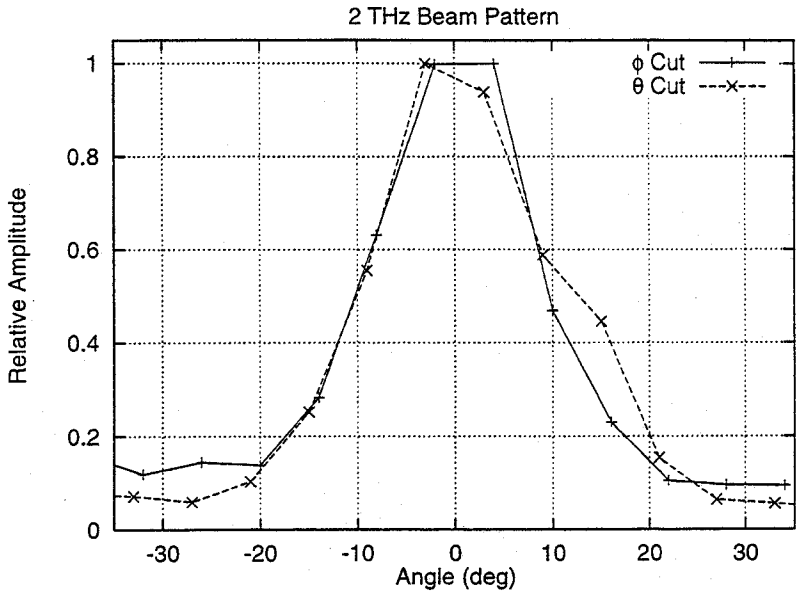

Figure 9: Beam cross scans of the micromachined 2 THz feedhorn. The θ and ϕ cuts are othogonal to each other.

microstrip circuit (see Fig 11c). Each IF output of the array is wire bonded to a microstrip matching network located just outside the periphery of the Bolometer Array Block. Bolometer bias is provided through the matching network.

The fixed backshort is a pyramidal structure designed to fit the cavity behind the membrane. The backshorts can be readily made by wet-etching silicon through an SiO mask evaporated on the wafer [2]. Once etched, the backshort wafer is gold plated.

4.2 Other Applications

With laser micromachining it now becomes possible to incorporate reactive posts and irises in submillimeter waveguide designs. These structures would be particular useful in providing a low-loss alternative to the end-loaded and radial stubs often used to tune out the capacitance of SIS junctions in waveguide mixer mounts. Below the gap frequency of niobium ($\sim$ 690 GHz), where such stubs are less lossy, the addition of a properly chosen post or iris can increase the instantaneous bandwidth of the mixer significantly over what would be achieved with the tuning stub alone.

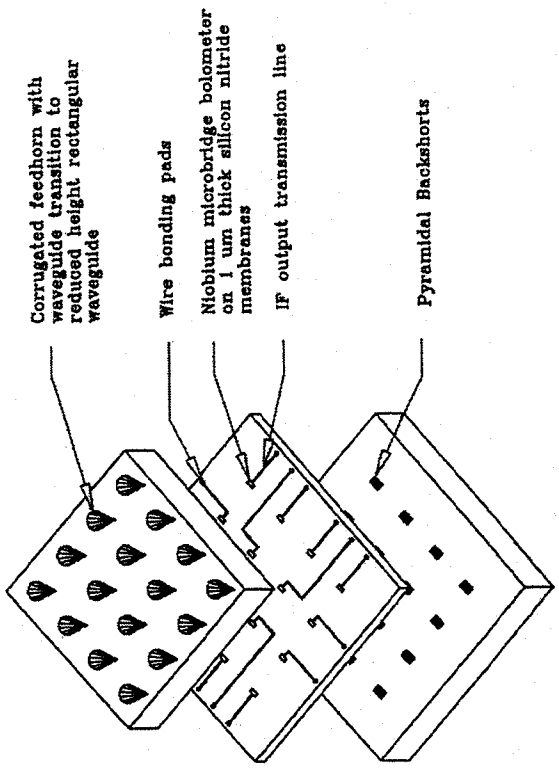

Figure 10: Silicon micromachined array mixer assembly diagram. The array mixer consists of three blocks: a feedhorn block, a bolometer array block on which HEBs are fabricated across silicon nitride windows, and a backshort block. The horn block is laser micromachined. The bolometer array block and the backshort block are micromachined out of silicon using wet etching techniques.

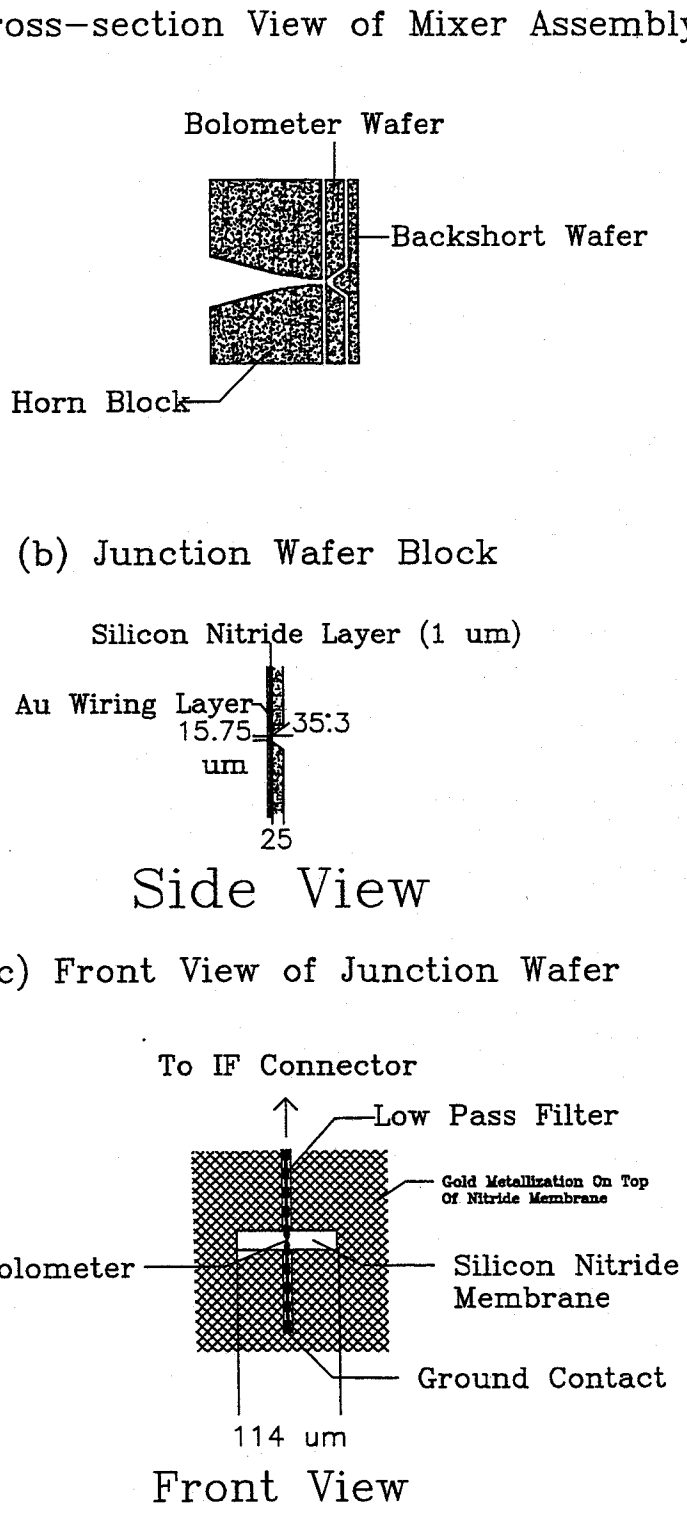

Figure 11: Detailed drawings of a typical mixer in the array.

The design and construction of solid state frequency multipliers is often more difficult to achieve than a single mixer [14]. The ability to micromachine reduced height waveguide with the option of including irises and posts, will allow the designer greater flexibility in the construction of high efficiency THz LO sources than have been available in the past.

Laser micromachining can also be used to make high performance submillimeter-wave phase gratings [15, 16]. These gratings can serve as quasi-optical LO power splitters for submillimeter array receivers.

The laser micromachining and replication process permits the construction of large numbers of high-efficiency feedhorns. Such horns could provide an alternative to Winston cones in large format bolometer arrays where single mode optics are desired.

5 Summary

1. We have introduced a new technology for the fabrication of waveguide devices which are difficult or impossible to manufacture using conventional techniques. We envision structures operating at 1 through 10 THz (feature sizes of 300-30 micrometers) can be fabricated with this technology.

2. With this technology it is now possible to construct large-format, waveguide imaging arrays at THz frequencies.

3. This technology can also be used in the construction of efficient LO sources and quasi-optical components at THz frequencies.

6 References

1 R. McGrath, C. K. Walker, M. Yap, and Y. Tai, IEEE Microwave and Guided Wave Letters, vol 3, 61, 1993.

2 G. Rebeiz, G. W. Regehr, G. Wade, D. B. Rutledge, R. L. Savage, L. Richard, N. C. Luhmann JR, Int. J. of IR ans MM Waves, vol 8, 1249, 1987.

3 D.J. Ehrlich, R.M. Osgood, Jr., and T.F. Deutsch, Appl. Phys. Lett., 38, 1018, 1981.

4 G.V. Treyz, R. Beach, and R.M. Osgood, Jr., J. Vac. Sci. Technol. B. 6, 37, 1988.

5 G.V. Treyz, R. Beach, and R.M. Osgood, Jr., Appl. Phys. Letters 50, 475, 1987.

6 T.M. Bloomstein and D.J. Ehrlich, in Technical Digest of Transducers (IEEE, New York, 1992), pp. 507-511, 1991.

7 T.M. Bloomstein and D.J. Ehrlich, Appl. Phys. Lett. 61, 708, 1992.

8 Y.S. Liu, "Sources, optics, and laser microfabrication systems for direct writing and projection lithography" in Laser Microfabrication, edited by D.J. Ehrlich and J.Y. Tsao (Academic Press, San Diego, ch. 1., 1989.

9 See M3 Scanner/Driver User's Manual, Rev. A (General Scanning, Inc. Watertown, MA, 1992).

10 T.M. Bloomstein, Sc.D. Thesis, Massachusetts Institute of Technology, 1996.

11 E. Kim, Y. Xia, and G.M. Whitesides, Nature 376, 581, 1985.

12 B. M. Thomas, IEEE Trans. Antennas and Propagation, 26, 267, 1978

13 Infrared Laboratories Inc., 1808 E 17th St., Tucson, Az.

14 N. Erickson, 1997, this volume.

15 G. F. Delgado and Bengtsson, 1194, Microwave and Optical Technology Letters, vol. 7, No. 18, pp. 831-834.

16 T. Klein, G. A. Ediss, R. Güsten, C. Kasemann, 1997, this volume.

INEXPENSIVE RECEIVER COMPONENTS FOR MILLIMETER AND SUBMILLIMETER WAVELENGTHS

Thomas W. Crowe*, Philip J. Koh*, William L. Bishop*, Chris M. Mann, Jeffrey L. Hesler*, Robert M. Weikle, II*, Perry A. D. Wood*, and David Matheson****

*Applied Electrophysics Laboratories
Department of Electrical Engineering
University of Virginia
Charlottesville, VA 22901

**Space Science Department
Rutherford Appleton Laboratory
CHILTON, DIDCOT, OXON
OX1 1OQx, United Kingdom

Abstract

In recent years there has been excellent progress in the development of millimeter and submillimeter wavelength components such as mixers and multipliers. Particularly, SIS mixers have yielded sensitivity near the quantum limit at frequencies approaching 1 THz and hot-electron bolometric mixers now promise similar performance above 1 THz. However, for many applications the cost of building and maintaining cryogenic systems is prohibitive. In such cases, GaAs Schottky diode technology remains a very attractive option, provided the sensitivity requirement is not so great, particularly now that planar (whiskerless) diodes are yielding good performance. However, even in the case of Schottky mixers and multipliers, the cost of machining the waveguide blocks can be prohibitive, particularly at THz frequencies and/or when array applications are considered. In this paper we summarize two techniques which allow low cost manufacturing of millimeter and submillimeter wavelength components.

I. BACKGROUND

The most successful millimeter and submillimeter wavelength components, such as oscillators, multipliers and mixers, generally use traditional metal blocks which are fabricated by standard machining techniques. These components yield excellent coupling to the electronic circuit elements, are highly reliable, and are relatively straight-forward to design. However, the cost of fabricating such blocks can be prohibitively high, particularly as the frequency is increased and/or arrays of components are considered.

Typical components are formed by the so-called "split-block" technique, where the circuit structures are formed on a single face of two (or more) metal blocks which are then pieced together to form the complete components. This process has two primary advantages, the machining is, in principle, straight forward and the circuit components, such as filters, coupling structures and diodes, can be easily placed into the block during assembly. Although this process has been extended to the THz frequency region [1], and has lead to the development of many successful systems, the cost of the required machining tools and the expertise required greatly increase the expense and fabrication time of such components. In fact, the high cost of machining such components is perhaps the primary factor which limits

the extension of millimeter-wave technology to large scale applications such as collision avoidance radars, personal communications, aircraft landing systems, and contraband detection.

We are developing two methods which have the potential to greatly reduce the manufacturing costs of millimeter and submillimeter-wave components. The first is a method of Mastering, Molding and Casting by which many inexpensive copies are produced from an initial "Master" by a process of molding and casting. Although the formation of the original Master will often be done by standard machining techniques, the final casting of many components will greatly reduce the per piece cost. The second method allows the formation of high quality horns, waveguides and channels directly in a silicon wafer by novel micromachining techniques.

II. COMPONENT FABRICATION BY MASTERING, MOLDING AND CASTING

Molding and casting has a long and successful history of fabricating inexpensive components for myriad applications. The basic process involves three major steps, as is depicted in Fig. 1.

1) The fabrication of an original master, which has all of the dimensional characteristics of the desired component.
2) The formation of a mold, or molds, from the master, which maintain all of the essential features but in a "negative polarity".
3) The final production of many parts, geometrically identical to the master, from the molds through a casting process.

However, the fabrication of millimeter and submillimeter wavelength components by casting has not, to our knowledge, previously been reported. The demand for extremely small features and precise component alignment requires special techniques and materials. The new Mastering, Molding and Casting (MMC) process which we propose[1], incorporates several novel techniques and each of the fundamental process steps is optimized for high frequency waveguide component fabrication. This MMC process is not one of merely replicating an existing part, but rather it is an integrated manufacturing technology.

The design of the master is quite different from the design of standard machined waveguide blocks since the geometry must be optimized for the subsequent molding and casting process. The fabrication of the master is naturally a critical step, and is in most regards as difficult and costly as the fabrication of a standard component. However, in forming the master we have the advantage that its mechanical, electrical, thermal and other properties need not be optimized for use as a final component. For example, it need not be electrically conductive or suitable for temperature cycling. Rather the material used for the master can be selected for its machinability and suitability as a master component. Furthermore, great resources can be

---

1. Provisional patent applied for March 26, 1997, "Mastering, Molding and Casting (MMC) Technology for High Precision, Fabrication of Millimeter and Submillimeter Wavelength Hollow Waveguides, Channels, Horns and Assemblies."

expended on the master since it will be used to fabricate many final parts. Masters can be made with composite structures and can be formed with a combination of additive and subtractive methods. The cost of the master is spread over the many final parts that are cast, provided, of course, that a market exists for a sufficient number of components.

Only a few commercially available materials are suitable for the formation of the mold in this process. The primary concerns are maintenance of the critical dimensions, ruggedness of the mold, and excellent release properties. We have used a silicone material for the mold and we have also developed a unique mold formation fixture and techniques which secure the master and the mold resin, reinforce the mold for excellent dimensional control and facilitate efficient mold fabrication. Fig. 2 shows one of the silicone molds as well as a master and casting of a test structure consisting of a 585 GHz waveguide section and two diagonal horns. As can be seen from the figure, the mold was formed in a metal ring to give it structural reinforcement and make it easier to handle.

In the casting process we have used a specially selected polyurethane material although other casting resins such as epoxies may be suitable. The mechanical and thermal properties of this casting resin are very critical. Essentially, the polyurethane is poured into the mold, cured and then removed. However, care must be taken to eliminate air bubbles at the surface of the casting which can create pits in the final waveguides or horns. Several techniques have been developed to form the back side of the casting without further machining. Also, such things as the curing process and the removal of the casting from the mold must be carefully planned to avoid damage to the mold and/or the casting.

In order to complete the fabrication process we have coated our cast components with gold in a sputter deposition system and then electroplated additional gold to a thickness of a few microns. At this point we have tested the dimensional accuracy of the castings. Fig. 3 shows scanning electron micrographs of a small portion of a master and a casting. We have also assembled cast components by the split block technique. Although we have noticed a small but appreciable "bowing" of the castings, we have found that with a small amount of pressure the components can be brought into intimate contact along the entire contact surface. This problem is now being addressed through improvements of our process and we do not expect it to cause appreciable difficulty. Finally, we have immersed the completed components into liquid nitrogen. Upon warming we see no noticeable change, either in the dimensional quality, or the final gold surface.

We have successfully used this MMC process to fabricate a complete 585 GHz mixer of the design described by Hesler [2]. This involved the machining of a master for each half of the block, the formation of molds, the casting and metalization of the block halves, and the installation of the quartz microstrip circuit with the planar Schottky diode as well as the SMA connector for dc bias and IF output. The measured beam pattern of the cast horn was as expected from the design and very comparable to that achieved with a traditional block. With a non-optimized diode, a mixer noise temperature of 12,000K (DSB) was measured. Although this is about a factor of five worse than our best result at this frequency, it is better than we had previously achieved with this particular diode design in a conventional machined mixer block. Further measurements with optimized diodes are now in progress.

III. THE FABRICATION OF COMPONENTS BY MICROMACHINING

In general terms, the fabrication of components by micromachining involves the use of techniques and processes developed by the microelectronics industry for the fabrication of complex integrated circuits. Through the use of micromachining we hope to be able to simultaneously fabricate many complete split block components on large silicon wafers. Although this general idea is not new, previous attempts have suffered from significant drawbacks. For example, Rebeiz [3] has fabricated mixer assemblies based on micromachined horns and detector elements integrated onto silicon nitride membranes. However, since his horns were formed directly on the (111) crystal faces of silicon, their flare angle was roughly seventy degrees, as determined by the crystal planes. This large flare angle is not conducive to the formation of the excellent beam patterns required for most applications. Other groups have tried to develop standard components using photoresist formers [4], upon which waveguides could be formed. These efforts suffer from two difficulties, first the photoresists available were not thick enough to form the relatively large features needed at millimeter wavelengths and second the resists were difficult to remove from within the newly formed waveguide channel. Also, the problem of forming excellent horn antennas on the silicon wafer was not solved.

In our micromachining work we have solved these problems by inventing a new way to micromachine horns in silicon crystals and using a new photoresist material which easily achieves the dimensions required.[2] Our process consists of two basic steps, the etching of an initial horn structure directly into the silicon substrate and the subsequent use of the EPON SU-8 [5] photoresist to complete the horn and form the necessary waveguides, channels and other physical features of the block.

Etching of a Horn with Small Flare Angle

Our method of etching the horn into the silicon wafer results in a shape that is very similar to a traditional diagonal horn, except that the angles of the aperture are not ninety degrees, but rather 70 and 110 degrees. The horn is formed by etching into the silicon wafer with a selective etch through a silicon dioxide mask. The flare angle of the horn is determined by an easily controlled angle in the original SiO2 etch mask. An SEM photo of such an etched half-horn is shown in Fig. 4. Note that the wafer has been diced to open the aperture of the horn and that the silicon etch was timed to yield a flat (100) surface on the bottom of the aperture, rather than a full diagonal horn.

Formation of Integrated Waveguides and Channels

To form the desired integrated waveguides and channels a layer of the extra thick resist [5] is spun onto the silicon wafer. This resist fills the horn and forms a planarized surface above the silicon wafer. This resist can be as thick as 500 microns, and multiple layers can be used to

---

2 Provisional patents applied March 26, 1997, "A Preferential Crystal Etching Technique for the Formation of Millimeter and Submillimeter Wavelength Horn Antennas," and "Integration of Hollow Waveguides, Channels and Horns by Lithographic and Etching Techniques."

achieve even greater thickness. The resist is then exposed through a mask that defines the horn and the waveguide channels. Before development, a second layer of resist is added. It is exposed in the shape of the horn, waveguide and also the microstrip channel. Both layers of resist can then be exposed simultaneously to clear the volume of the horn, waveguide and channel. The remaining resist is subsequently cured and the entire wafer is metalized, yielding the final split block mixer as shown in Fig. 4.

We also use a third layer of the resist to form alignment pins to aid the assembly of the mixer block. To date we have successfully assembled a complete mixer, but it has not yet survived a complete mixer test. Although we believe the structure can be made to be quite robust, we have not yet completely worked out the details of the alignment pins. We have also found that the materials used do not survive cooling to 77K in a liquid nitrogen bath. We are presently working to build and test our first micromachined mixer and exploring methods to solve the cryogenic cooling problems.

IV. SUMMARY

We are developing two techniques that will allow the inexpensive fabrication of mixer, multiplier and oscillator blocks. The first uses a novel Mastering, Molding and Casting (MMC) technique to form many inexpensive split blocks from a specially designed master. To date we have demonstrated the process by building a complete 585 GHz Schottky mixer of the design described by Hesler [2]. The resulting product is of high quality and very robust. Although we have made preliminary noise temperature measurements, we have not yet tested the mixer with a high quality Schottky diode.

The second technique involves a novel micromachining process. In this process we have invented a method to micromachine high quality horns with small flare angles which are aligned in the plane of the silicon wafer. Although the horn shape is still dictated by the silicon crystal planes, we can achieve small flare angles simply by controlling the shape of a simple photolithography mask. Also, the beam shape can be further adjusted by controlling the silicon etch time and the thickness of the layers used to form the waveguides and channels of the mixer. Through the use of the new photoresist, we have successfully integrated high quality rectangular waveguides and microstrip channels with the horns. The resulting structure is an accurate reproduction of Hesler's 585 GHz mixer. To date, we have not completed a mixer assembly, due to minor problems with the integrated alignment pins. When this process is perfected we expect to be able to fabricate dozens of mixers simultaneously on a single silicon wafer.

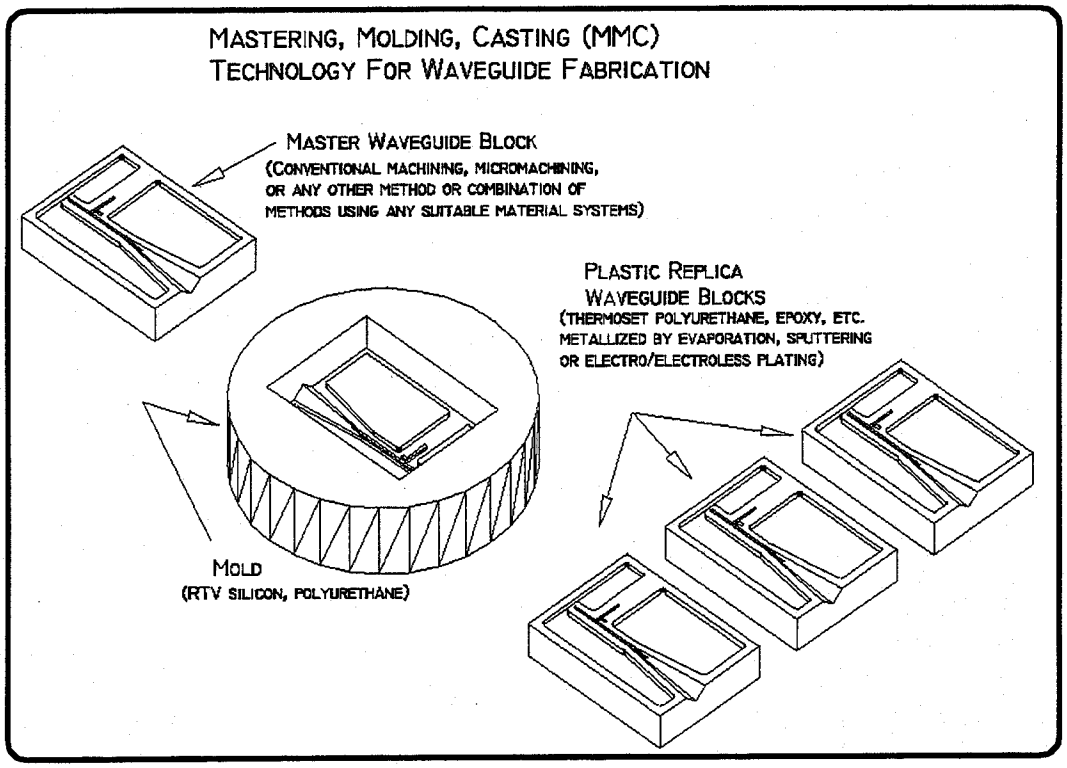

Figure 1. The basic principle of fabricating split-block components by the method of Mastering, Molding and Casting (MMC).

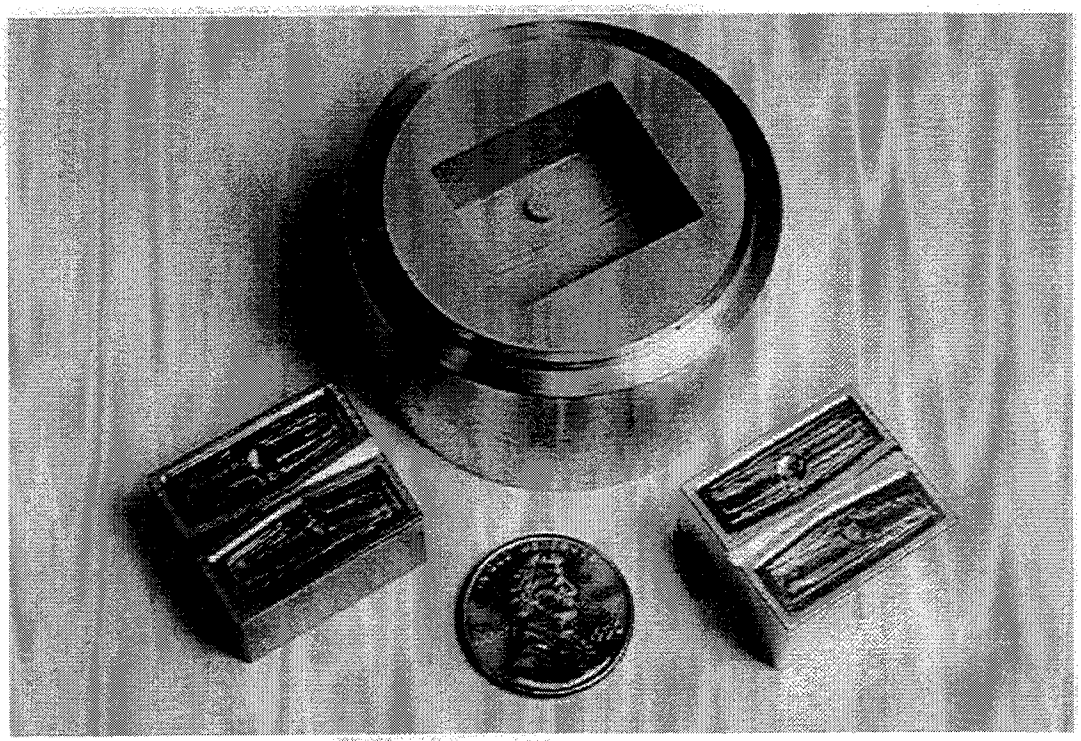

Figure 2. A photograph of a master (left), the silicone mold and a gold coated casting (right). The circuit is a 585 GHz waveguide and two diagonal horns.

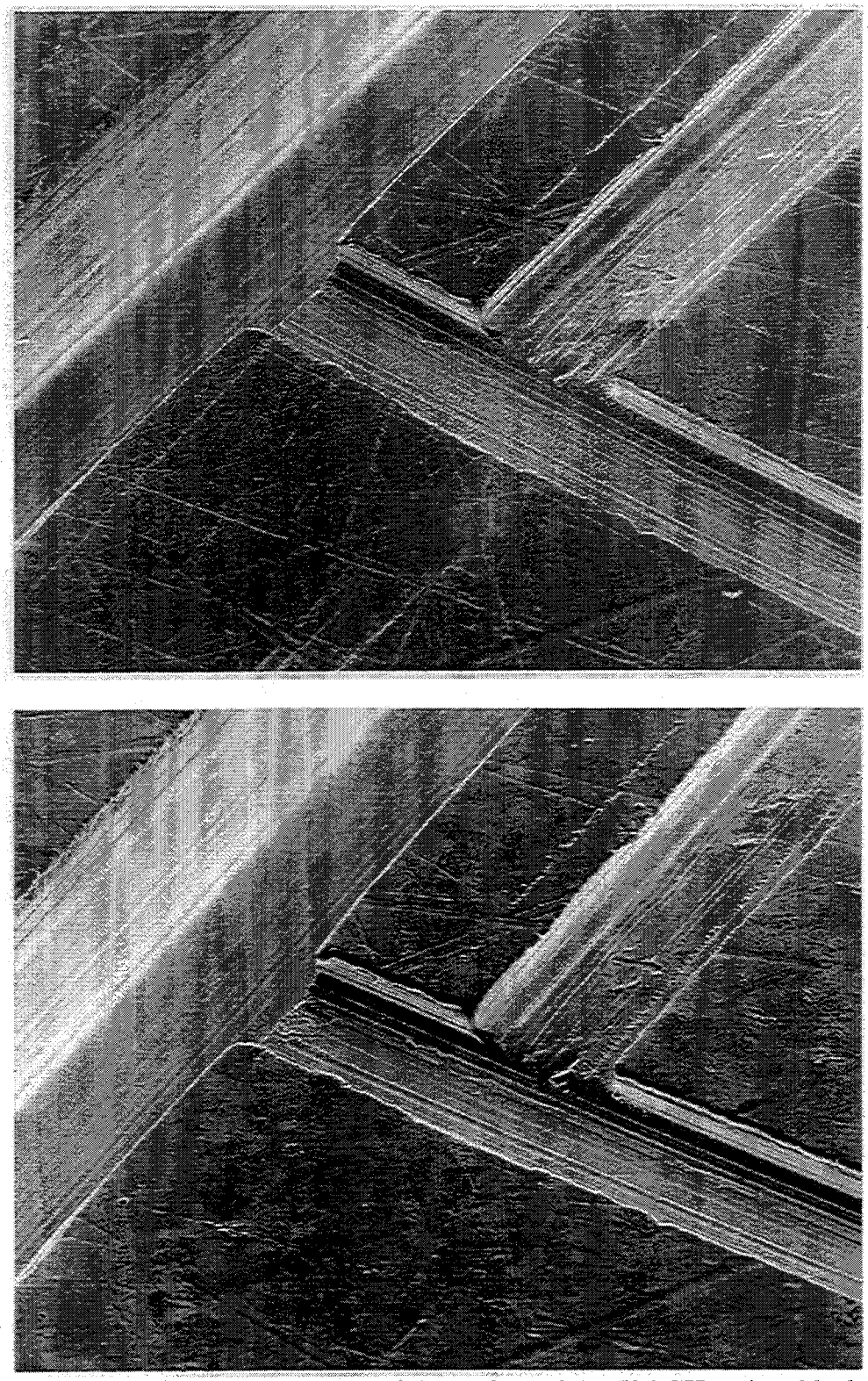

Figure 3. A SEM comparison of the surface of the 585 GHz mixer block master (top) and the metalized casting (bottom). The casting accurately reproduces the waveguide channels. The fine machine marks are reproduced but are partially filled in by thick plated gold.

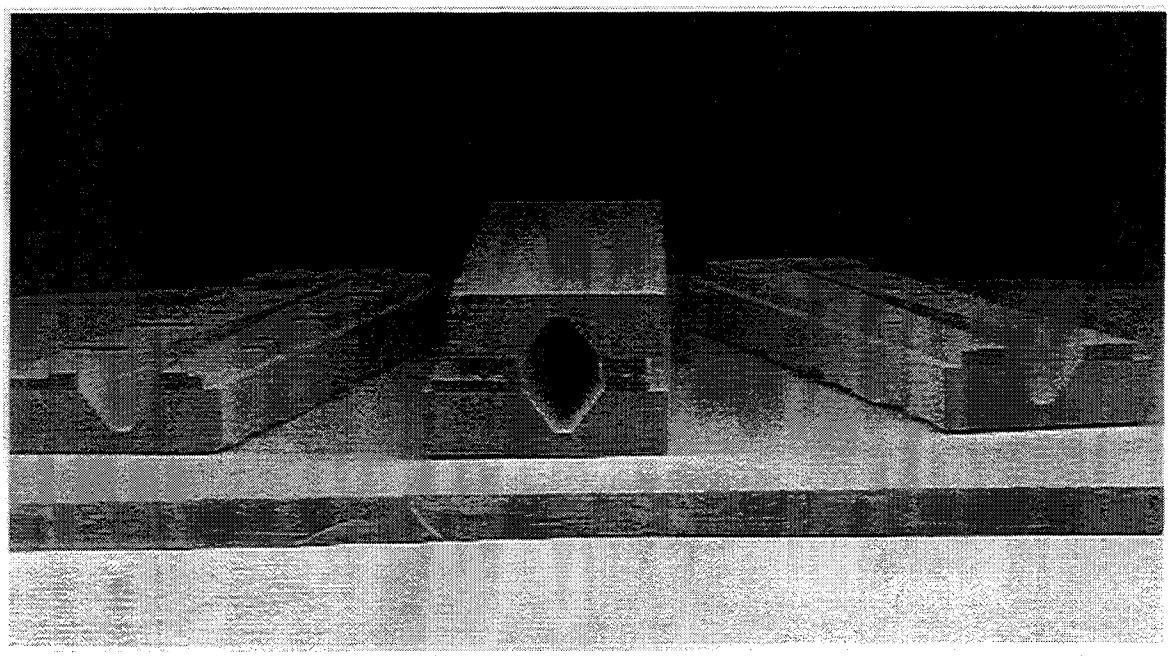

Figure 4. A SEM photo of an assembled 585 GHz micromachined mixer and two half blocks. Note the narrow taper of the integrated horn.

ACKNOWLEDGEMENT

The development of the MMC and micromachined components has been supported by the Army Research Laboratory under the Microelectronics Research Collaborative Program (UMd subcontract Q281601). The testing of the components was supported by a grant from the US Army National Ground Intelligence Center (DAHC90-91-C-0030).

REFERENCES

[1] B.N. Ellison, M.L. Oldfield, D.N. Matheson, B.J. Maddison, C.M. Mann, S.M. Marazita, T.W. Crowe, P. Maaskant, W.M. Kelly, "First Results for a 2.5 THz Schottky Diode Waveguide Mixer," Seventh Intl. Symp. Space THz Tech., Charlottesville, March 12-15, 1996.

[2 J.L. Hesler, W.R. Hall, T.W. Crowe, R.M. Weikle, B.S. Deaver, R.F. Bradley, S.-K. Pan, "Fixed Tuned Submillimeter Wavelength Mixers Using Planar Schottky Barrier Diodes," IEEE Trans. Microwave Theory and Tech., May 1997.

[3] G.M. Rebeiz, "Millimeter-Wave and Terahertz Integrated Circuit Antennas," Proc. IEEE Vol. 80, No. 11, pp. 1748-1770, Nov. 1992.

[4] D.A. Brown, A.S. Treen and N.J. Cronin, "Micromachining of Terahertz Waveguide Components with Integrated Actuve Devices," Proc. 19th Int. Conf. on IR and Millimeter Waves, pp. 359-360, Oct. 1994.

[5] K.Y. Lee, N. LaBianca, S.A. Rishton, S. Zolgharnain, J.D. Gelorme, J. Shaw, T.H.-P. Chang, "Micromachining Applications of a High Resolution Ultrathick Photoresist," J. Vac. Sci. Technol. B 13(6), pp. 3012-3016, Nov/Dec 1995.

THE COMPLETE ANALYSIS OF A 91.33 TO 274 GHz SCHOTTKY BARRIER VARACTOR FREQUENCY TRIPLER

R. E. Lipsey, C. Mann[1], S. H. Jones, and J. Thornton[1]

Department of Electrical Engineering, University of Virginia, Charlottesville, VA 22903
[1]Millimeter Wave Technology Group, Rutherford Appleton Laboratory, Chilton, Didcot, U.K.

Abstract

A complete analysis of a SBV frequency tripler has been performed. This analysis was achieved through the development of a unique tripler block based on the mounting structure proposed by Eisenhart and Khan. Using the boundary conditions imposed by Eisenhart and Khan, an analytical model of the waveguide structure was derived and simulated. With the linear RF circuit decomposed into an analytical model, the Drift-Diffusion Harmonic-Balance numerical simulator was used to accurately model the performance of the active non-linear device in the linear embedding circuit. The results of the RF circuit simulations combined with the numerical device Harmonic-Balance simulator is then compared to experimental results and demonstrates a high degree of accuracy over a wide range of output backshort positions.

I. Introduction

In the drive to create solid-state heterodyne mixers at frequencies above 1 THz, the provision of sufficient local oscillator power becomes a critical issue [1]. Since substantial power has been reported from solid-state LO chains around 300 GHz (6-8 mW) [2 -3], a final tripler stage using a Schottky Barrier Varactor diode (SBV) with an efficiency of 6% would provide enough power to drive a single-diode harmonic mixer at frequencies near 2 THz. There are, however, significant difficulties in the design of triplers at these high frequencies. These difficulties include the design of the Schottky device, idlers and filters, as well as reliable and reproducible RF circuits to effectively couple power to and from the multiplier diode. In order to effectively couple the power into and generate power from the SBV frequency tripler, the embedding impedances of the RF circuit must be carefully designed relative to the diode. The analysis of traditional tripler waveguide structures requires the use of such programs as Hewlett Packard's High Frequency Structure Simulator (HFSS). However, simulations run for such complex structures in HFSS are extremely CPU intensive. In an attempt to create a tripler waveguide structure that lends itself to straight-forward analytical calculations for the embedding circuit impedances, a mounting waveguide based on the structure proposed by Eisenhart and Khan [4] has been developed [1], and reported here. Using the boundary conditions imposed by Eisenhart and Khan, an analytical model of the waveguide structure was derived and simulated in Mathematica. The embedding impedances presented by the linear RF circuit were calculated over a wide range of backshort positions in a matter of minutes. With the linear RF circuit decomposed into an analytical model, Computer Aided Design (CAD) techniques can be used to accurately model the performance of the active nonlinear device in the linear embedding circuit.

In this paper, we report on the use of the novel fully self-consistent physics based large signal time- and temperature-dependent Drift-Diffusion Harmonic-Balance (DDHB)

[5-6] analysis of the active device combined with the electromagnetic modeling of the waveguide based on the Eisenhart and Khan analysis. The DDHB simulator models carrier transport through the bulk region of the SBV by a set of coupled nonlinear differential equations and requires that the linear RF circuit embedding impedances be known. The combination of these tools has, for the first time, provided a means for the complete analysis of a high frequency tripler. The results of the RF circuit simulations combined with the CAD programs are compared to the experimental results for the 91.33 to 274 GHz tripler block. These results demonstrate a high degree of accuracy over a wide range of backshort positions and predict similar output powers to experimental results (i.e. 2.5 mW at 274 GHz).

II. The Tripler Waveguide Structure

The diode mount used in this work was a 230 to 290 GHz tripler based closely on the structure reported in [7]. The block employed the use of crossed LO and output waveguides, backshort and E-plane LO tuners, a backshort for output tuning, a single diode with facility for d.c. bias, and two quarter-wave transformer sections between the idler and the output waveguide. Figure 1 presents a detailed diagram of the internal configuration of the tripler waveguide structure used. The input power from the LO is coupled into the SBV via a waveguide probe, and a stripline filter on the probe prevents power at the higher harmonics from leaking back into the input waveguide. The diode is mounted in the idler waveguide approximately a quarter wavelength (at the fundamental LO frequency) from the idler to output waveguide transition in which only the fundamental LO frequency is in cut-off. The idler serves as a resonant cavity in which a standing wave in the second harmonic exists but cannot propagate into the output waveguide. The two transformers transition the idler into the output waveguide and serve to increase the circuit bandwidth. D.C. bias is provided to the device via a 140 Ω transmission line bias filter.

To create a waveguide circuit for the SBV in which the embedding impedances can be set and optimized with a high degree of confidence, the mounting structure was designed based on the waveguide proposed by Eisenhart and Khan [4] (shown in figure 2). This was accomplished by mounting the SBV to the rectangular output waveguide by connecting the waveguide wall to the diode via a thin quasi-two dimensional post. This is analogous to the rectangular waveguide structure proposed by Eisenhart and Khan and the reduced mathematical structure is shown in figure 3. By using this precise geometry, the mathematical analysis of Eisenhart and Khan can be used to accurately and quickly calculate the diode embedding impedance. Multiplier waveguide circuits have not previously been designed using a quasi-two dimensional post; hence, the method of Eisenhart and Khan could not be accurately implemented.

A very brief derivation of the embedding impedance as calculated for this structure (figure 3) using the method of [4] follows. The restrictions $w' < 0.25$ and $g' < 0.25$ on the dimensions of the waveguide structure apply. The embedding impedance is found from the combination of the impedance of the waveguide structure (the mode pair impedance), the degree of coupling between the post and the gap for a given mode pair, and the waveguide terminations with non-zero reflection.

The mode pair impedance (the series combination of the TE_{mn} and the TM_{mn} contributions) for the waveguide structure is given by

$$Z_{mn} = \frac{j\eta b}{ak} \frac{(k^2 - k_y^2)}{(2-\delta_0)(k_x^2 + k_y^2 - k^2)^{1/2}} \tag{1}$$

where

$k_x = \frac{m\pi}{a}$ $k_y = \frac{n\pi}{b}$ $k = \frac{2\pi}{\lambda}$ λ = free space wavelength

η = characteristic impeance of free space

$\delta_0 = 1$ if n = 0

$\delta_0 = 0$ if n $\neq$ 0.

The parameters *a* and *b* define the waveguide geometry. As can be seen in equation (1), Z_{mn} is only a function of *m, n,* and the waveguide geometry.

The degree of coupling between the post and the gap to a particular mode pair impedance is given by the coupling factors which are defined as

post coupling factor $k_{pm} = \sin k_x s \left(\frac{\sin\theta_m}{\theta_m} \right)$ where $\theta_m = \frac{m\pi w}{2a}$ (2)

gap coupling factor $k_{gm} = \cos k_y h \left(\frac{\sin\phi_n}{\phi_n} \right)$ where $\phi_n = \frac{n\pi g}{2b}$ (3)

Since the waveguide may be terminated under non-matched conditions, the following expression results for a terminated mode pair impedance $Z_{Tmn} = Z_{mn}\tau$ where

$$\tau = \frac{1 + \rho_{1mn}\exp(-2\Gamma_{mn}l_1) + \rho_{2mn}\exp(-2\Gamma_{mn}l_2) + \rho_{1mn}\rho_{2mn}\exp(-2\Gamma_{mn}(l_1 + l_2))}{1 - \rho_{1mn}\rho_{2mn}\exp(-2\Gamma_{mn}(l_1 + l_2))} \tag{4}$$

$\Gamma_{mn} = (k_x^2 + k_y^2 - k^2)^{1/2}$

ρ_{1mn} and ρ_{2mn} are the complex reflection coefficients at terminations 1 and 2

l_1 and l_2 are the distances to terminations 1 and 2 from the post (see l_1 and l_2 in figure 1(a)).

The total gap impedance, Z_{gap}, is the parallel combination of all mode pairs and is given by

$$Z_{gap} = \frac{1}{\sum_{n=0}^{N_1} \frac{1}{\sum_{m=1}^{M_1} Z_{Tmn} \left(\frac{k_{pm}}{k_{gn}}\right)^2}} \tag{5}$$

where M_1 and N_1 are the truncated limits of summation for the n and m modes, respectively. Typical values for millimeter wave devices are $M_1 = 12$ and $N_1 = 8$.

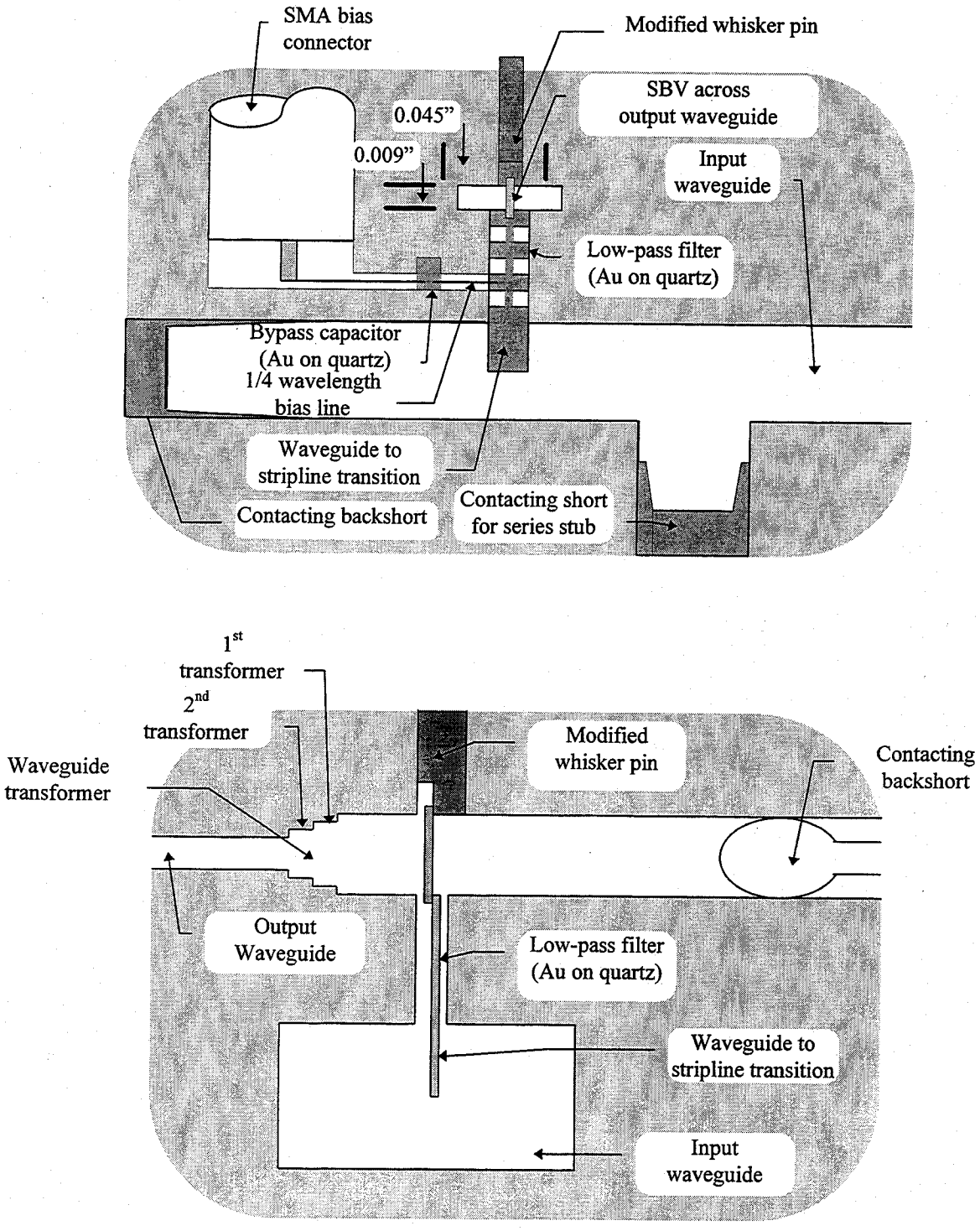

Figure 1 Schematic of the 200-290 GHz tripler waveguide structure showing (a) the block cross-section detailing the input waveguide and (b) the block cross-section detailing the output waveguide

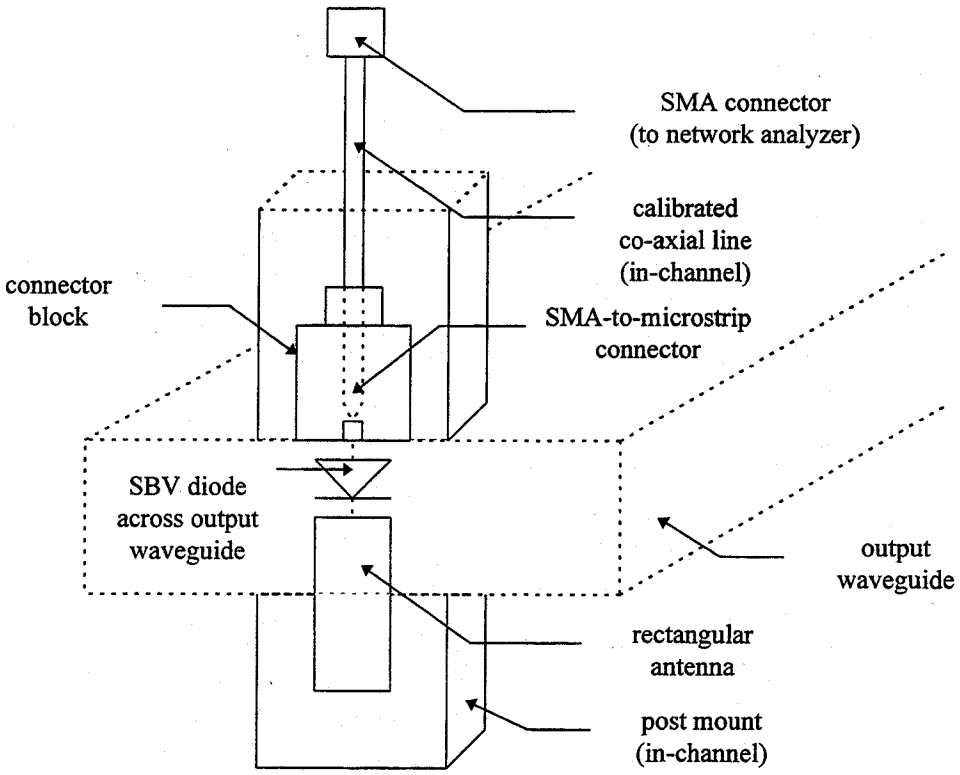

Figure 2 Cross-section of output waveguide structure

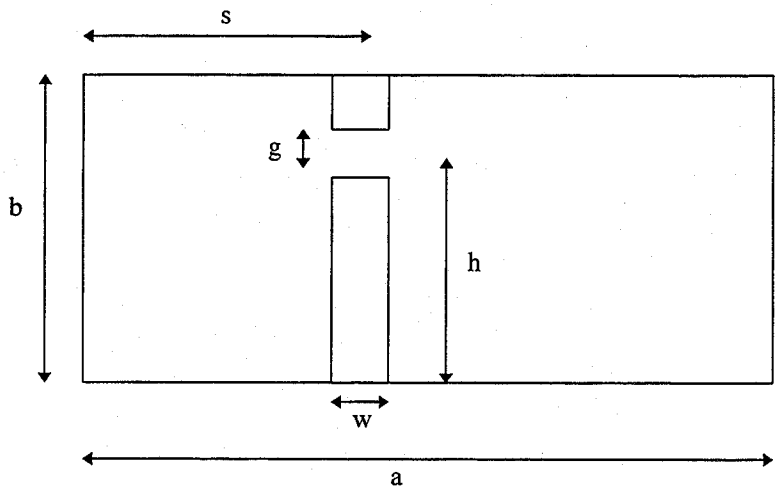

a = waveguide width
b = waveguide height
g= gap size
h = gap position (center of gap from bottom)
s = post position (center of post from side)
w = post width

Also,
s' = s / a = normalized post position
h' = h / b = normalized gap position
w' = w / a = normalized post width
g' = g / b = normalized gap size

Figure 3 Waveguide Mount Proposed by Eisenhart and Khan [1]

Because the tripler waveguide structure's embedding impedances versus backshort position can be decomposed into an analytical expression, this mounting block lends itself to rapid and accurate simulation. Software was written in Mathematica to solve equation (5) and the embedding impedance was calculated at the second, third, and fourth harmonics versus backshort position which were then used as inputs to the device simulators (which require the harmonic components of the linear embedding circuit). The calculated embedding impedances are shown in figure 4.

III. Numerical Device/Harmonic-Balance Simulation

The UVA 5M4 diode was used as the SBV in the tripler block with device parameters summarized in table 1. The UVA 5M4 diode is moderately doped and has a thin active layer which increases the device cut-off frequency and aids in high frequency tripling. However, the thin active layer also leads to low breakdown voltages and constrains the maximum input pump power relative to the embedding impedance for optimal efficiency. A cross-sectional schematic of the diode is presented in figure 5.

Table 1 Nominal Diode Parameters for the UVA 5M4

Diode	Diode Doping Density (cm^{-3})	Active Layer Thickness (μm)	Anode Diameter (μm)	Mobility (cm^2/Vs)
5M4	5.0×10^{16}	0.31	4.7	6200

In order to model the performance of the nonlinear active device in the linear embedding circuit, two independent CAD tools have been used. The first CAD tool is an equivalent circuit/harmonic-balance simulator (ECHB) based on the work of Siegel and Kerr [8]. The second is a large signal time- and temperature-dependent Drift-Diffusion Harmonic-Balance (DDHB) simulator [5]. For the ECHB, the Schottky Barrier Varactor (SBV) is modeled by its d.c. current versus voltage and d.c. capacitance versus voltage characteristics. This equivalent circuit model is then embedded into a harmonic-balance algorithm based on the multiple reflection technique [8] and the embedding impedances calculated as described above are incorporated. Although the ECHB technique is fast and has good convergence properties (converged solutions are on the order of five minutes on an IBM RS6000), analytical modeling techniques such as these do not provide a means for studying electron transport phenomena due to their macroscopic nature, and fail to accurately predict device performance at high frequencies [9]. This failure is attributed to the fact that equivalent circuit models cannot account for the actual physics of electron transport within the device. In particular, effects such as current saturation, velocity saturation, and transit time [6] phenomenon are not modeled using the ECHB code. Therefore, the novel physics-based Drift-Diffusion Harmonic-Balance simulator was employed.

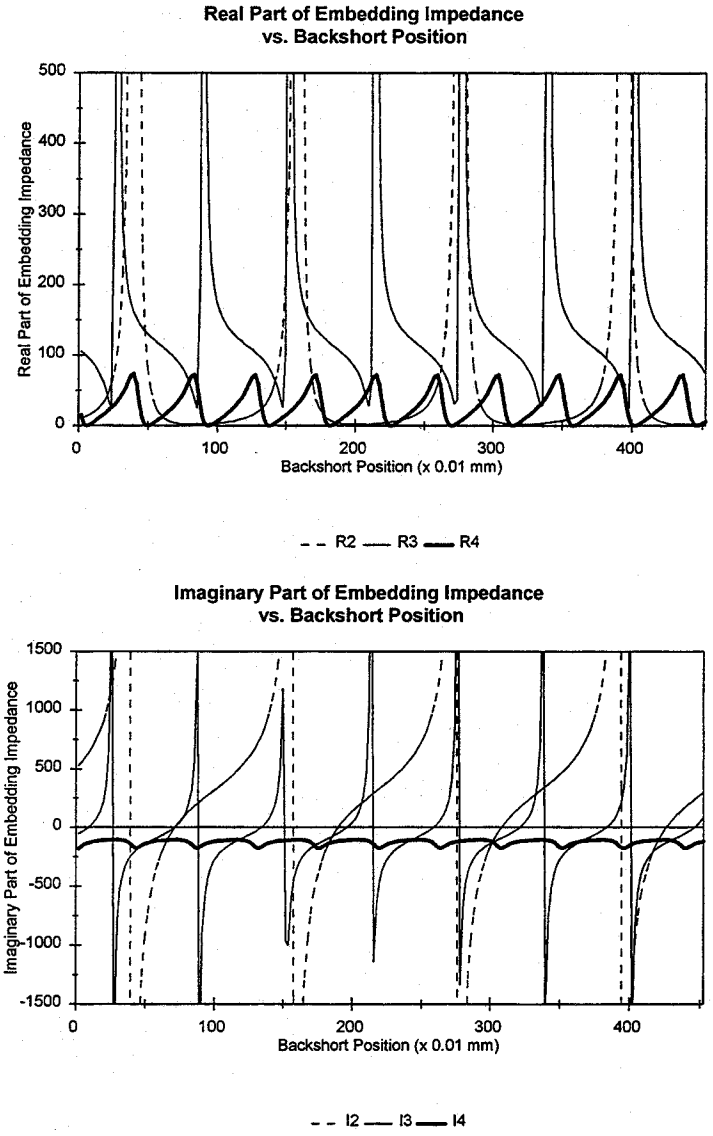

Figure 4 Calculated Embedding Impedances vs. Backshort Position

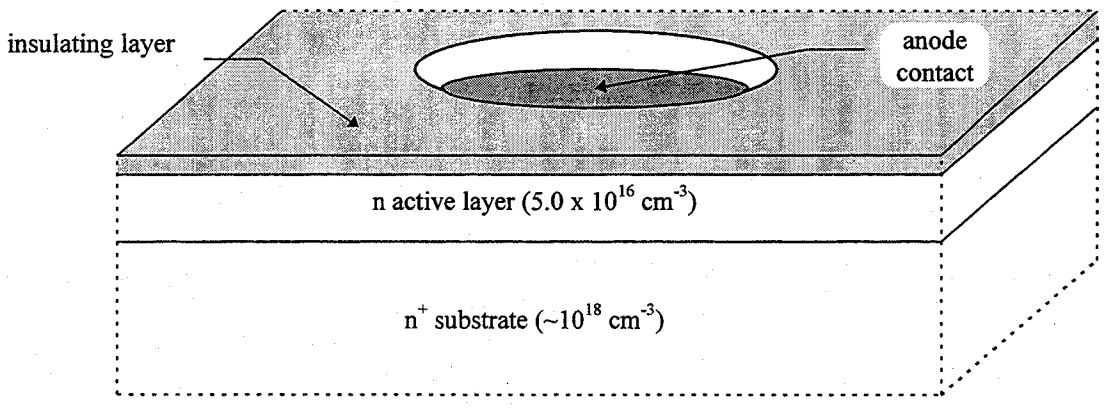

Figure 5 Typical cross-section of the UVA 5M4 GaAs SBV

Since this numerical device simulator self-consistently calculates the displacement and particle current throughout the entire device, the total electron current is accurately calculated. Carrier transport through the bulk region of the SBV is described [10] by a set of coupled nonlinear differential equations. This drift-diffusion analysis is based on the first two moments of the Boltzmann transport equation coupled to Poisson's equation. The resulting equations are

$$\frac{\partial n(x,t)}{\partial t} = \frac{1}{q}\frac{\partial J_n(x,t)}{\partial x}, \tag{6}$$

$$J_n(x,t) = q\mu_n(x,t)n(x,t)\frac{\partial \Phi_n(x,t)}{\partial x}, \tag{7}$$

and

$$\frac{\partial}{\partial x}\left[\varepsilon(x)\frac{\partial \Psi(x,t)}{\partial x}\right] = q\left[n(x,t) - N_D(x,t)\right], \tag{8}$$

where

$$n(x,t) = n_{i,ref}\exp\left[\frac{q}{kT}\left(\Psi(x,t) + V_n(x) - \Phi_n(x,t)\right)\right], \tag{9}$$

and where n is the electron density, q is the electron charge, J_n is the electron particle current density, Φ_n is the electron quasi-Fermi potential, Ψ is the electrostatic potential, $n_{i,ref}$ is the intrinsic electron density in the reference material (GaAs or InP), k is Boltzmann's constant, T is the absolute temperature, and V_n, μ_n, N_D, and ε are the spatially-dependent alloy potential [10], electron mobility, donor impurity concentration, and dielectric permittivity, respectively. Two types of mobility were considered for the simulations. First, a constant low field mobility derived from Monte Carlo simulations [11-12] was used. Second, in order to account for hot electron effects and high-field velocity saturation effects, a d.c. field-dependent mobility was computed as outlined in [13] using the Monte Carlo simulator of [11-12].

For accurate modeling of SBVs, current transport through the bulk device is combined with thermionic and thermionic-field emission current imposed at the metal-semiconductor contact. This approach is analogous to the analytical thermionic-emission/diffusion theory of Crowell and Sze [14]. Following the work of Adams and Tang [15-16], we have adopted a current density boundary condition at the metal-semiconductor interface which assumes a drifted Maxwellian electron distribution. This boundary condition allows us to avoid the unphysical accumulation of electrons at the metal-semiconductor interface near the flat-band voltage. The resulting current density interface constraint at x=0 is

$$J_n(0,t) = qv_{r,n}\left[n(0,t) - n_0\right] \tag{10}$$

where $n(0,t)$ is the electron density at the metal-semiconductor interface and n_0 is the equilibrium electron density at the interface. The effective surface recombination velocity for electrons is

$$v_{r,n} = v_d + \sqrt{\frac{2kT}{\pi m^*}} \left\{ \frac{\exp\left[-v_d^2\left(\frac{m^*}{2kt}\right)\right]}{1+\mathrm{erf}\left(v_d\sqrt{\frac{m^*}{2kT}}\right)} \right\} \tag{11}$$

where m^* is the effective electron mass at the metal-semiconductor interface. The amount of drift in the electron distribution at the metal-semiconductor interface is modeled as

$$v_d = \frac{J_n(0,t)}{qn(0,t)}. \tag{12}$$

The electrostatic potential at the metal-semiconductor interface, assuming a constant potential of zero for the metal is,

$$\Psi(0,t) = \frac{\chi_{ref} - \Phi}{q} \frac{kT}{q} \ln\left(\frac{N_{C,ref}}{n_{i,ref}}\right) \tag{13}$$

where χ_{ref} is the electron affinity in the reference material, Φ is the metal work function, and $N_{C,ref}$ is the total effective conduction band density of states in the reference material. The barrier height at the metal-semiconductor interface, Φ_b, is given by the first term in equation (11) multiplied by the electronic charge. This barrier height is lowered due to the Schottky effect by the amount

$$\Delta\Phi_b(t) = \sqrt{\frac{q|\xi(0t,)|}{4\pi\varepsilon(0)}} \tag{14}$$

where $\xi(0,t)$ is the electric field at the metal-semiconductor interface.

Through careful investigation of solution methods and the use of the one-dimensional state variables J_n, Φ_n, Ψ, *and* D we have developed a robust method with excellent numerical convergence and good speed. The carrier transport equations are solved for a given bias voltage, and subject to the metal-semiconductor (anode) interface constraints and an ohmic contact (cathode) boundary condition, using the coupled equation Newton-Raphson method (a one-dimensional finite difference analysis).

IV. Simulation Methodology

In order to simulate the performance of the SBV in the tripler block, the embedding impedances of the linear RF circuit were calculated using the model developed in Mathematica at 275 different output backshort positions for 0.01mm increments (as described in section II). Before beginning the set of 275 simulations for each CAD tool (ECHB & DDHB), each simulator required its own unique set of input specifications. A summary of the input parameters for the UVA 5M4 diode for each simulator (excluding the diode geometry) are provided in table 2.

Table 2 Inputs to the ECHB simulator

Barrier height (Φ)	-1.0 V
Current vs. Voltage curve fit parameter (η)	1.08
Capacitance vs. Voltage curve fit parameter (Γ)	0.5
Zero bias capacitance (C_0)	15×10^{-15} F
Saturation Current (I_{sat})	2.7×10^{-17} A
Series Resistance (R_s)	8.0 Ω
Input pump frequency (f_{in})	91.33 GHz
Input pump power (P_{in})	50.0 mW
d.c. bias (V_{dc})	-4.5 V

Inputs to the DDHB simulator

Barrier height (Φ)	-1.0 V
Number of time steps per period	501
Mobility	6200 cm^2/Vs for constant mobility simulations $\mu(\xi,t)$ for field-dependent simulations
Input pump frequency (f_{in})	91.33 GHz
Input pump power (P_{in})	50.0 mW
d.c. bias (V_{dc})	-4.5 V

Because the first harmonic embedding impedance is independently tunable from the higher harmonics using the two input tuners, a point of reference needed to be established to compare the experimental results with the CAD simulators. The chosen point of reference was at the point of experimental maximum third harmonic output power. The experimental embedding impedances for the second, third, and fourth harmonics at the chosen point of reference were calculated and the point of maximum simulated third harmonic output power was determined for each simulator. This point was found by iteratively conjugate matching the first harmonic embedding impedance to the determined intrinsic device impedance of the diode (solved for by each simulator) until the circuit embedding impedance was within 1% of the intrinsic device impedance. A conjugate match at the fundamental was chosen since the diode absorbs the maximum amount of available input power under conjugate match conditions, and a minimal amount of power is reflected. Table 3 presents the determined optimal first harmonic impedances for the three simulators

Table 3 Comparison of the determined first harmonic intrinsic device impedance

	ECHB	DDHB w/ constant low field mobility	DDHB w/ d.c. field-dependent mobility
First harmonic impedance	128 - j 292	49 - j 191	48 - j 186

V. Comparison of Experiment and Theory

After the inputs to each simulator were specified and the first harmonic embedding impedance for each simulator had been determined, simulations over a range of output backshort positions were performed (tuning backshort output waveguide section show in figure 1(b)). For both the ECHB and DDHB with d.c. field-dependent mobility simulators, simulations were performed over the 275 different backshort positions. After completing these simulations, sixty simulations were performed using the DDHB with

constant low field mobility simulator around the point of maximum third harmonic output power for comparison purposes. At a typical backshort position, a converged ECHB simulation was reached with one to two minutes and a converged DDHB (with either mobility function) simulation was reached in approximately five to ten hours (simulations were performed on an IBM RS6000).

For each simulation, the device was biased at -4.5 V and driven with 50 mW of available input power consistent with the experimental data (the reflected power at the LO port was minimized using the technique described above). The results of the measured power at the 275 different backshort positions are presented in figure 6 and compared with the predicted powers of the ECHB and DDHB with d.c. field-dependent mobility simulators.

As figure 6 illustrates, there is good agreement between both simulators and the measured data for relative power and spacing of the major power peaks. Although the relative magnitude of the major peaks is better predicted by the ECHB simulator, only the DDHB simulator with d.c. field-dependent mobility correctly predicts the power in the minor peaks.

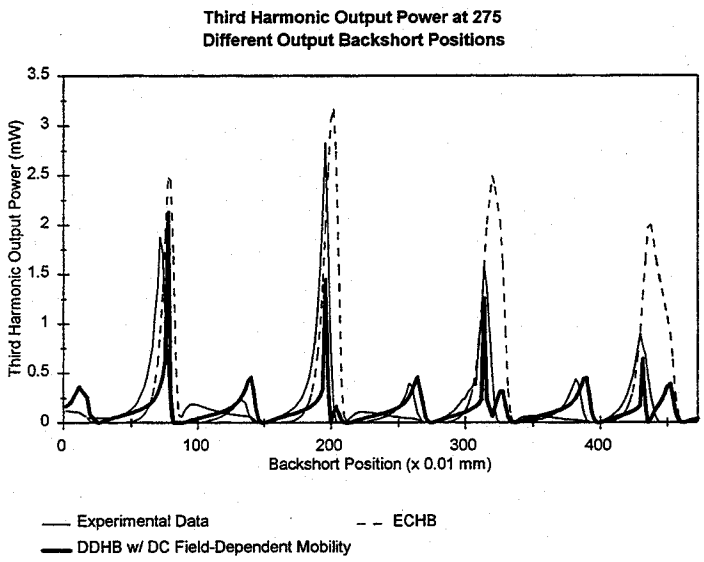

Figure 6 Comparison of predicted and measured third harmonic output power for the tripler block at 275 different output backshort positions

To better understand why the ECHB simulator fails to predict the minor peaks, a set of 60 different backshort positions spanning the second minor and major peaks was simulated using the DDHB simulator with constant low field mobility. Because the DDHB simulator with d.c. field-dependent mobility accurately predicts the relative power in the minor peaks, we wanted to investigate whether the dynamics of a field-dependent mobility gave rise to the power in the minor peaks or the modeling of electron transport was responsible. Figure 7 presents a comparison of the three simulators with the experimental data.

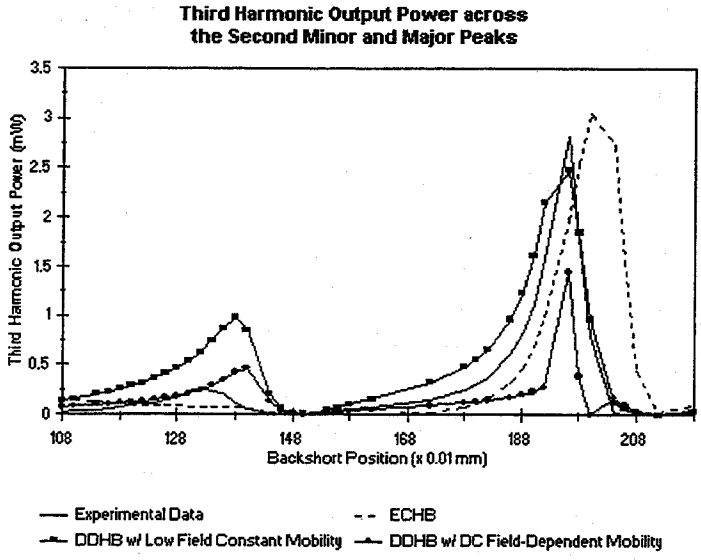

Figure 7 Comparison of predicted and measured output power for the tripler block for the ECHB and DDHB with d.c. field-dependent and constant low field mobilities over the second minor and major peaks

As can be seen from figure 7, the DDHB simulator with constant low field mobility correctly predicts and more accurately models the relative power in the minor peak. Also, the DDHB simulator with constant low field mobility more accurately predicts the relative power over the other simulators over the range of backshort positions. This suggests that the DDHB simulator with constant low field mobility most accurately predicts the performance of this tripler block. The ECHB simulator does not accurately reflect the relative power in the minor peaks due to the inaccurate determination of the diode impedance. Since there is a high degree of electron transport phenomenon occurring in the high doped short diode, the diode impedance is calculated at the wrong steady state phase and magnitudes of the voltage and current.

To determine the effect the calculated fourth harmonic embedding impedance (which has the most approximations made) had on the DDHB simulator with d.c. field dependent mobility, the set of 60 different backshort positions spanning the second major peak was re-simulated with the fourth harmonic embedding impedance shorted ($Z_4 = 0.1 + j0$). The results of these simulations are presented in figure 8. As illustrated by figure 8, the fourth harmonic impedance does not significantly affect the simulation results. This result supports the conclusion that the DDHB simulator with constant low field mobility most accurately predicts the performance of this tripler block.

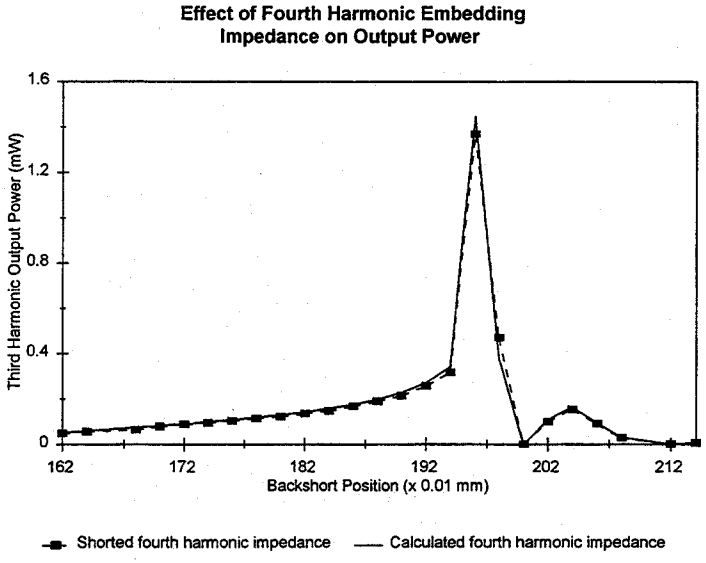

Figure 8 Effect of the fourth harmonic embedding impedance on third harmonic output power for the DDHB with d.c. field-dependent mobility over the second major peak

One set of final simulations was performed to determine the relationship between the first harmonic impedance and the third harmonic output power. These simulations were performed to determine the significance of the conjugate match specification at the first harmonic described earlier. Simulations were performed at the point of maximum third harmonic output power using the DDHB simulator with d.c. field-dependent mobility (for reasons of simulation speed) by changing only the real or imaginary part of the first harmonic impedance while leaving the unchanged part of the impedance set to that of table 4.3. The results of these simulations are shown in figure 9. As can be seen in figure 9, the point of maximum third harmonic output power is little affected by changes in either the real or imaginary parts of the first harmonic embedding impedance over some range of impedance values. This suggests some flexibility on the experimental setup of the tripler block for tuning at the LO.

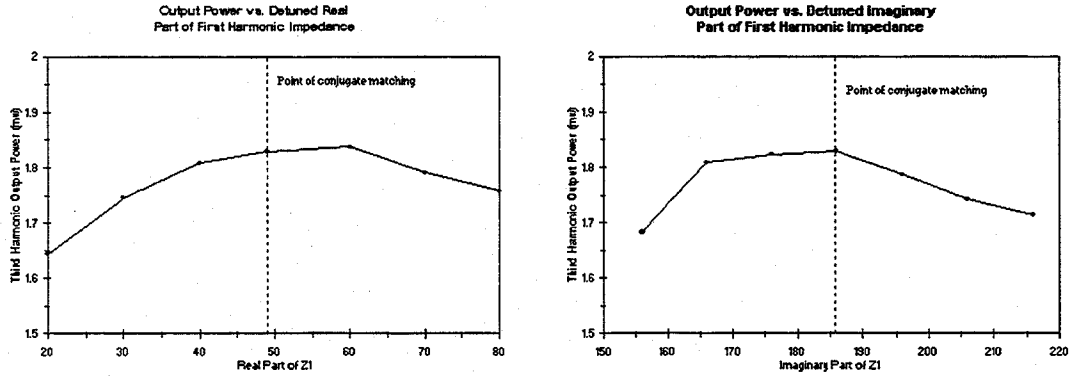

Figure 9 Comparison of maximum third harmonic output power vs. (a) real part of the first harmonic embedding impedance ($\mathrm{Im}\{Z_1\} = j186$) and (b) imaginary part of the first harmonic embedding impedance ($\mathrm{Re}\{Z_1\} = 49$)

VI. Simulation Results and Discussion

Once the comparison between the experimental data and the simulation results had been completed, an investigation of the ECHB and DDHB with d.c. field-dependent and constant low field mobility simulators was performed. All three simulators have the ability to generate steady-state current and voltage vs. time information. A comparison of the current vs. time and voltage vs. time at the second minor and major peaks of figure 6 are presented in figure 10. Although the ECHB simulator offers a significant advantage over its DDHB counterpart in terms of simulation time, there are significant limitations of the ECHB simulator. Both the ECHB and DDHB simulators provide current and voltage vs. time information, but only the DDHB simulator provides a means for studying the internal physics of device operation. Because of the microscopic nature of the DDHB simulator, both electron concentration and electric field across the device over time are solved for and are available as output. The numbers 1-5 on figure 10 represent instances where electron concentration and electric field vs. position were taken at the time corresponding to the number. Because the ECHB does not provide a means for analyzing these values, no numbers are listed on these plots. Figure 11 presents a comparison of the physics of device operation for the DDHB simulator with constant low field mobility and the DDHB simulator with d.c. field-dependent mobility at the second minor and major peaks.

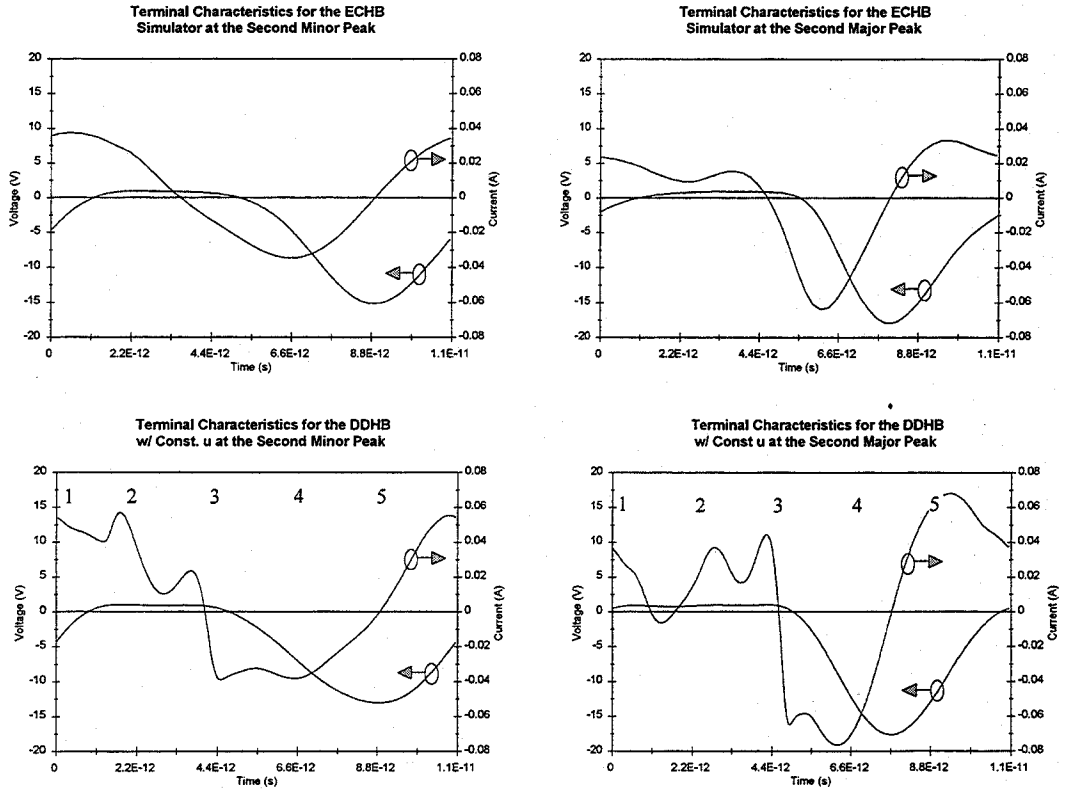

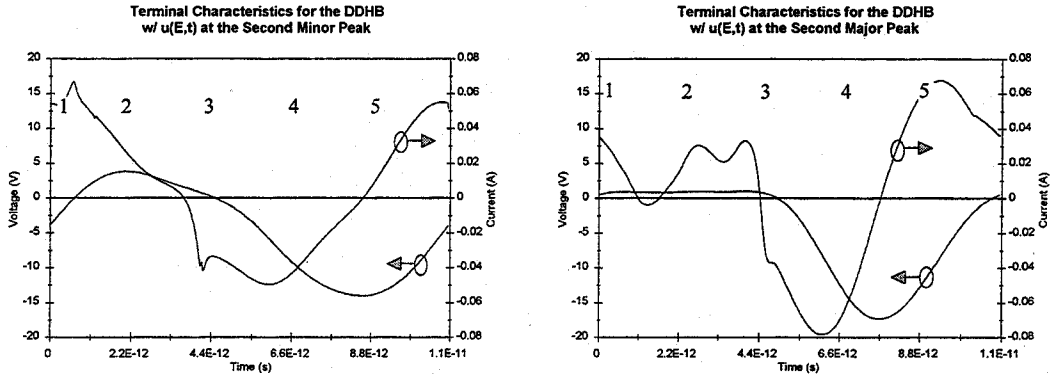

Figure 10 Comparison of the terminal characteristics for (a) the ECHB simulator (b) the DDHB simulator with constant low field mobility and (c) the DDHB simulator with d.c. field-dependent mobility at the second minor and major peaks

As can be seen from figure 10, both the ECHB and DDHB with d.c. field-dependent and constant low field mobility simulators predict similar output waveforms for the periodic voltage. The significant differences between the different simulators truly become apparent in the periodic current waveforms. Although the relative phase

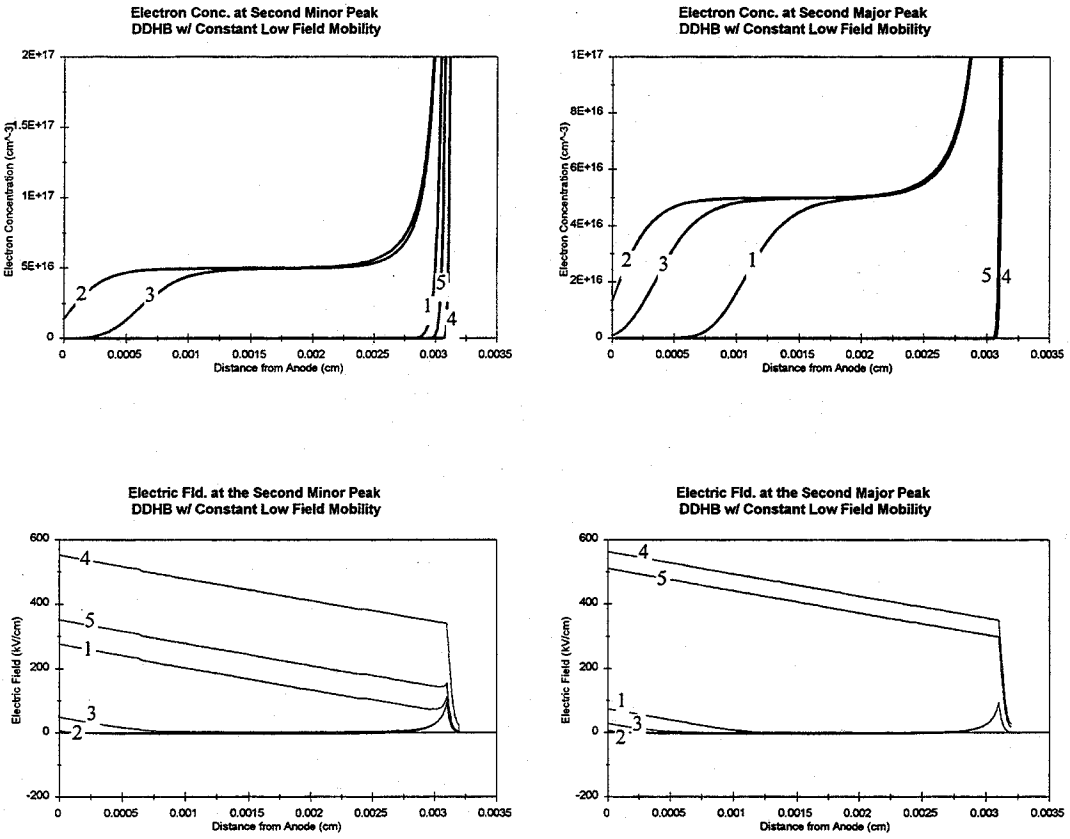

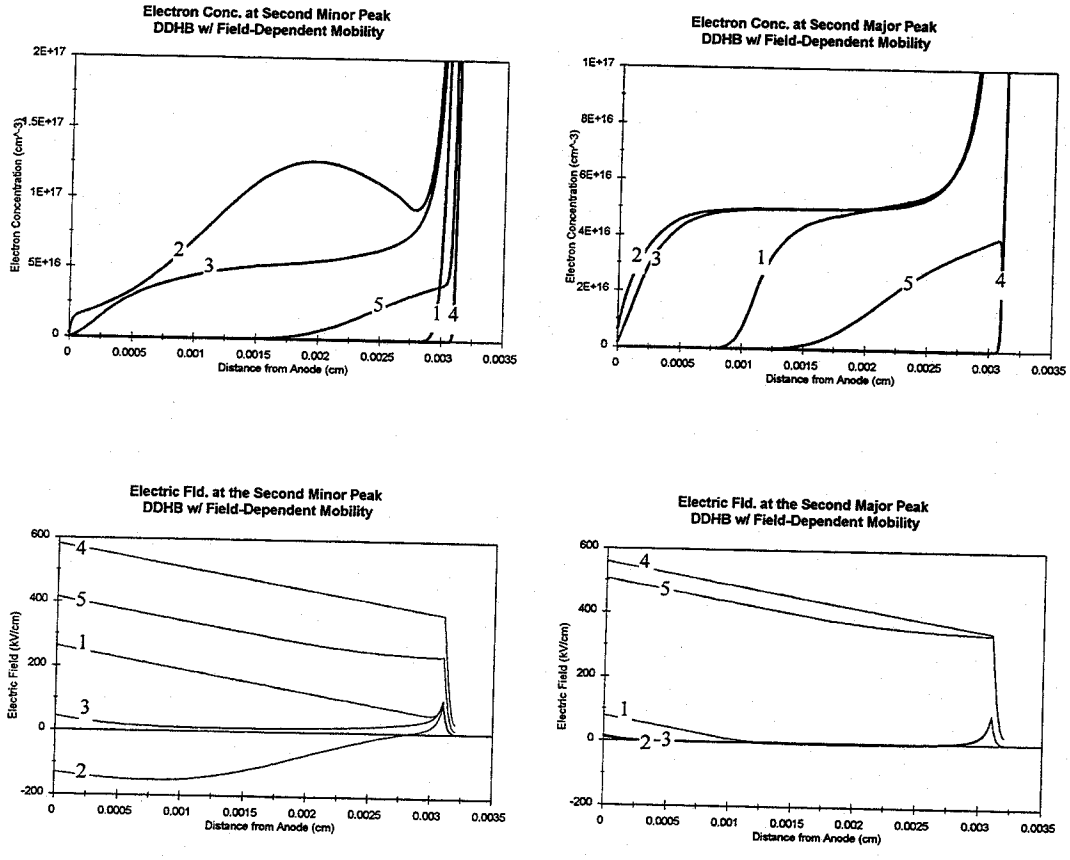

Figure 11 Comparison of electron concentration and electric field over the length of the active layer at five evenly spaced intervals over one period for both the second minor and major peaks for (a) DDHB with constant low field mobility and (b) DDHB with d.c. field-dependent mobility

differences between the voltage and current waveforms are similar for the different simulators, the ECHB simulator predicts a current waveform with fewer high frequency components and a lower peak to peak swing. Both the DDHB simulator with d.c. field-dependent mobility and constant low field mobility predict similar current waveforms with similar magnitudes. The relative maximums and minimums in the current waveform for the DDHB simulator with d.c. field-dependent mobility appear more exaggerated than that of the DDHB simulator with constant mobility. This exaggeration most likely arises from velocity saturation effects accounted for in the simulator which incorporates a non-static mobility with field-dependence.

Figure 11 demonstrates the power of the DDHB simulator for studying the physics of electron transport in the device. Both the DDHB simulator with d.c. field-dependent mobility and constant low field mobility predict that the device will fully deplete. The differences in the electron concentration gradients between the two different mobility models arise from velocity saturation effects [6]. As the magnitude of the voltage is increasing, the electrons towards the anode experience large electric fields (as seen in figure 11) but cannot reach the same velocity as the electrons towards the cathode so that weak electron concentration gradient across the depletion edge is created. The

depletion edge broadens as the faster electrons move toward the cathode. As the magnitude of the voltage is decreasing, the fast electrons in the low field region recompress the depletion edge. Also as the voltage decreases, the electron diffusion gradient is acting in the same direction as the movement of the electrons which helps create a sharp electron concentration gradient across the depletion edge. These gradient changes do not arise in the constant low field mobility model because there is no field dependence on the velocity and thus no saturation velocity.

The plots of the electric field vs. position over time in figure 11 illustrate that punch through occurs in the device (the electric field within the active layer does not go to zero) and that the fields become larger than the critical field (~500 kV/cm) for the device. This suggests that the device is being driven well in breakdown which may be limiting the tripling performance.

VII. Conclusions

In an attempt to handle the complex nature of tripler waveguide circuits, a tripler block incorporating the boundary conditions of Eisenhart and Khan was developed by Rutherford Appleton Laboratory. The boundary conditions of Eisenhart and Khan allow for the accurate analytical calculation of the linear RF embedding circuit impedances. A model was developed in Mathematica to calculate the embedding impedances at the second, third, and fourth harmonics as a function of the output backshort position. In order to simulate the performance of the active non-linear device in the linear embedding circuit, both equivalent circuit harmonic-balance (ECHB) and drift-diffusion harmonic-balance (DDHB) CAD tools were used. The ECHB simulator offers superior solution times (on the order of 100 times faster than the DDHB simulator). The self-consistent DDHB simulator both with d.c. field-dependent mobility and constant low field mobility offers the ability to study the internal physics of electron transport in the active non-linear device. Since these CAD tools require the embedding impedances as inputs to the simulator, the accurate nature of the calculations made in Mathematica were made possible by the Eisenhart and Khan boundary condition specifications. The ECHB and DDHB simulators were used to simulate the performance of the tripler block over a wide range of output backshort positions. The results of these simulations were compared with experimental measurements made over the same set of backshort positions. The results suggest that although the ECHB simulator can accurately predict the experimental data at some backshort positions, only the DDHB simulator can accurately predict the tripler block performance over a wide range of output backshort positions. This is a direct result of the inability of the ECHB simulator to accurately predict the diode impedance; hence the phase and magnitudes of the steady state voltage and current are incorrect as the embedding circuit impedance varies. For the first time, the combination of the analytical model specifying the linear RF circuit and an accurate self-consistent CAD tool simulating the active non-linear device in the linear RF circuit can accurately predict the performance of a millimeter wave tripler block. This combination has for the first time allowed for a complete analysis of a tripler block.

Acknowledgments

This research has been sponsored by NSF grant #ECS-9412931. The authors greatly appreciate many important discussions with Tom Crowe, Rob Jones, and Greg Tait.

References

[1] John Thornton, "An Analytical Model for a Rectangular Antenna in Metallic Enclosure and its use for the Optimization of a 250 GHz Source for Antenna Characterization," July 1996, p. 1-3.

[2] P. Zimmermann, "Frequency Multipliers and LO Sources for the Submillimeter Wave Region," Proc. ESA Workshop on Millimeter Wave Tech. and Appl., Dec. 1995.

[3] P. J. Koh, W. C. B. Peatman, T. W. Crowe, Neal R. Erickson, "Novel Planar Varactor Diodes," 7th Int. Symp. Space THz Technology, March 1996.

[4] R. L. Eisenhart and P. J. Khan, "Theoretical and Experimental Analysis of a Waveguide Mounting Structure," *IEEE Trans. on Microwave Theory and Tech.*, Vol. 19, No. 8, August 1971.

[5] J. R. Jones, "CAD of Millimeter Wave Frequency Multipliers: An Experimental and Theoretical Investigation of the Heterostructure Barrier Varactor," Doctoral Dissertation, University of Virginia, January 1996.

[6] R. E. Lipsey, S. H. Jones, J. R. Jones, T. W. Crowe, L. F. Horvath, U. V. Bhapkar, and R. J. Mattauch, "Monte Carlo Harmonic-Balance and Drift-Diffusion Harmonic-Balance Analyses of 100-600 GHz Schottky Barrier Varactor Frequency Multipliers," Submitted to *IEEE Electron Dev.*, November 1996.

[7] J. W. Archer, "An Efficient 200-290 GHz Frequency Tripler Incorporating a Novel Stripline Structure," *IEEE Trans. on Microwave Theory and Tech.*, Vol. 32, No. 4, April 1984.

[8] P. H. Siegel, A. R. Kerr, and W. Hwang, "Topics in the Optimization of Millimeter-Wave Mixers," NASA Technical Paper 2287, 1984.

[9] J. R. Jones, S. H. Jones, G. B. Tait, "Self-Consistent Physics Based Numerical Device/Harmonic-Balance Circuit Analysis of Heterostructure Barrier and Schottky Barrier Varactors including Thermal Effects," *Proceedings of the Sixth International Symposium of Space Terahertz Technology*, March 1995, p. 423.

[10] E. L. Kollberg, T. J. Tolmunen, M. A. Frerking, and J. R. East, "Current Saturation in Submillimeter Wave Varactors," *IEEE Trans. on Microwave Theory Tech.,* Vol. 40, No. 5, May 1992, pp. 831-838.

[11] U. V. Bhapkar, "Monte-Carlo Simulation of GaAs Schottky Diodes for Terahertz Frequencies," Doctoral Dissertation, University of Virginia, 1995.

[12] U. V. Bhapkar and R. J. Mattauch, "Monte Carlo Simulation of Terahertz Frequency Schottky Diodes," *Proceedings of the 1995 International Semiconductor Device Research Symposium*, Vol. 1, Dec. 1995, pp. 263-265.

[13] M. F. Zybura, S. H. Jones, G. B. Tait and J. R. Jones, "100-300 GHz Gunn Oscillator Simulation through Harmonic Balance Circuit Analysis Linked to a Hydrodynamic Device Simulator," *IEEE Microwave Guided Wave Lett.*, Vol. 4, No. 8, August 1994, p. 282.

[14] C. R. Crowell and S. M. Sze, "Current Transport in Metal-Semiconductor Barriers," *Solid-State Electron*, Vol. 9, No. 11/12, Nov./Dec. 1966, pp. 1035-1048.

[15] J. Adams and T. W. Tang, "A Revised Boundary Condition for the Numerical Analysis of Schottky Barrier Diodes," *IEEE Electron Dev. Lett.*, Vol. 7, No. 9, Sept. 1986, pp. 525-527.

[16] J. Adams and T. W. Tang, "Computer Simulation of Boundary Conditions for Schottky Diodes," *Elec. Lett.*, Vol. 25, No. 16, Aug. 1989, pp. 1098-1100.

POWER AND SPATIAL MODE MEASUREMENTS OF A SIDEBAND GENERATOR SUBMILLIMETER-WAVE SOURCE

Eric R. Mueller

DeMaria ElectroOptics Systems, Inc.

1280 Blue Hills Ave., Bloomfield, CT 06002

(860) 243-9557

Jerry Waldman

University of Massachusetts Lowell

Submillimeter-Wave Technology Laboratory

Lowell, MA 01854

W. E. Nixon

US ARMY National Ground Intelligence Center

Charlottesville, VA 22902-5396

Abstract

Coherent, black-body-referenced measurements of submillimeter-wave sideband generator (SBG) output power are reported here. This SBG utilizes a submillimeter-wave laser, microwave synthesizer, and high frequency Schottky diode to produce tunable radiation. An output power 10.5 μW at a drive frequency of 1.6 THz has been obtained, and SBG radiation was efficiently separated from the laser driver with Si etalons. The power measurements were made using a dual CO_2-Submillimeter-wave laser system and two Schottky diodes, one as the sideband generator and one as the coherent receiver. The SBG efficiency of four different models of University of Virginia (UVa) diodes were studied and the output mode of the sideband (without the unshifted laser present) was also easured. Finally, the design of a single-sideband submillimeter-wave receiver is presented.

I - Introduction

Tunable sources of submillimeter-wave radiation are rare. The most common source uses a high-temperature blackbody coupled with a Fourier Transform Spectrometer to effectively simulate a tunable source.[1] While such a system can have wide bandwidth, the output power is very small in the submillimeter (on the order of 1 nW per wavenumber of bandwidth[2]) and the practical resolution is limited by the instrument size and maximum allowable time for a scan.

The desire for a narrow-band, tunable source, has prompted the development of a number of other techniques. One approach is the free electron laser (FEL). In a FEL, electrons are first sent through an accelerator and then through a series of magnets to cause the electrons to undulate. The resulting emitted radiation is coherently reinforced thus producing a coherent beam whose frequency can be tuned. While FEL's have very impressive tuning bandwidths, they also suffer from great complexity, emission at higher harmonics, and rms frequency instability of at least 0.05%.[3] Another technique involves the mixing of two CO_2 lasers in a MIM diode.[4] This method has been shown to produce roughly 200 nW of power and some tuning flexibility, $\sim \pm 120$ MHz about each selected CO_2 line. Further tuning range has been achieved, at the expense of roughly a factor of three in output power, by adding a microwave source to the mixing scheme.[5] Recently a method involving the mixing of two near IR lasers in a device fabricated from LT GaAs, photomixing, has demonstrated promising results.[6]

In the technique utilized in the present work, the SBG, a submillimeter laser is mixed with a microwave source in a Schottky diode. This was first demonstrated in 1978 by D. D. Bicanic et. al.[7] and H. R. Fetterman et. al.[8, 9] and has subsequently been achieved by a number of other groups.[10, 11] Several review articles have been published on SBG's in recent years.[11 - 14]

The sidebands produced in this manner are radiated from the coupling antenna and typically separated from the unshifted laser using a diplexer. The achieved separation

efficiency usually results in a beam with the sideband power roughly 20 dB below the unshifted laser.[15] In the current work we have employed two silicon reflection etalons to improve separation. In the resulting beam the sideband is 20 dB above the unshifted laser, a 40 dB improvement.[34] This allowed examination of the spatial beam profile through conventional mode scans with an apertured incoherent detector. Spatial aperture techniques combined with careful optical adjustment yielded a reasonably pure spatial mode.

The remainder of this paper will describe results in separate sections: II - Coupling the Laser to the Diode; III - Coherent Measurement of the Sideband Power; IV - Sideband Separation and Spatial Mode Performance; V - Single-Sideband Submillimeter-Wave Receiver; VI - Summary and Conclusions.

II - Coupling the Laser to the Diode

In order to make the most efficient use of available laser power one must optimize the coupling of the laser mode to the antenna pattern of the corner-reflector-mounted diode. Several papers have been published on this topic[16 - 18] and scaled model experiments have been performed.[8, 19] Based on these results we decided, as have other groups,[20] to have the bottom face tilted away thus resulting in a 4 λ antenna mounted in a dihedral, instead of a "cats eye" corner-cube. Tilting of the bottom face of the mount by 19° resulted in a 9 dB decrease in backreflected laser radiation and no observed degradation in receiver noise temperature. The above results were measured with a bolometer and a beamsplitter in the former case, and by performing noise temperature measurements, with identical corner-reflectors with and without tilted bottom faces, in the latter case.

In the present study, coupling experiments were performed in order to confirm the optimal coupling parameters predicted by Grossman,[18] namely that the beam waist w_0 be 1.82 λ at the diode. In our experiments the size of a collimated Gaussian laser beam was

varied and subsequently measured using a computer-controlled translation stage and an apertured LHe-cooled bolometer. The collimated beam then propagated to a 59.7 mm focal length off-axis parabolic reflector as the final optic before the diode. To determine which beam size was optimal, the Schottky's non-linear video responsivity was measured over a range of incident power levels between 1 and 10 mW for each tested configuration. This was necessary since these Schottky diodes are known to be non-linear video detectors above ~ 100 μW.[21] Assuming the paraxial wave equation to be correct for systems employing optics this fast,[22] and using the predicted waist size and location for an off-axis parabolic reflector focusing a Gaussian beam[23] (we cannot scan at the focus of the parabolic reflector due to spatial constraints), we have confirmed the optimal waist size at the diode

$$w_0 = 1.82\,\lambda, \qquad (1)$$

for a 4 λ antenna mounted 1.2 λ from each face of a dihedral.[18] Further we have observed that this coupling is quite sensitive; a waist size of 2λ produces noticeably weaker diode response and waists smaller than that of condition (1) also result in significantly less response. As the predicted[23] waist size approaches λ, the correction terms to the paraxial equation become important, and thus our "assumed" waist at the diode is slightly too small.

III - Coherent Measurement of the Sideband Power

The apparatus for the sideband power measurement is shown in Figure 1. The submillimeter lasers are independent systems each pumped by a nominal 100 W, CW CO_2 laser. The LO and Drive lasers were running the 191.61960 μm laser line[24] in CH_3OH (1564.5187 GHz) and were tuned to operate roughly 3 MHz apart.

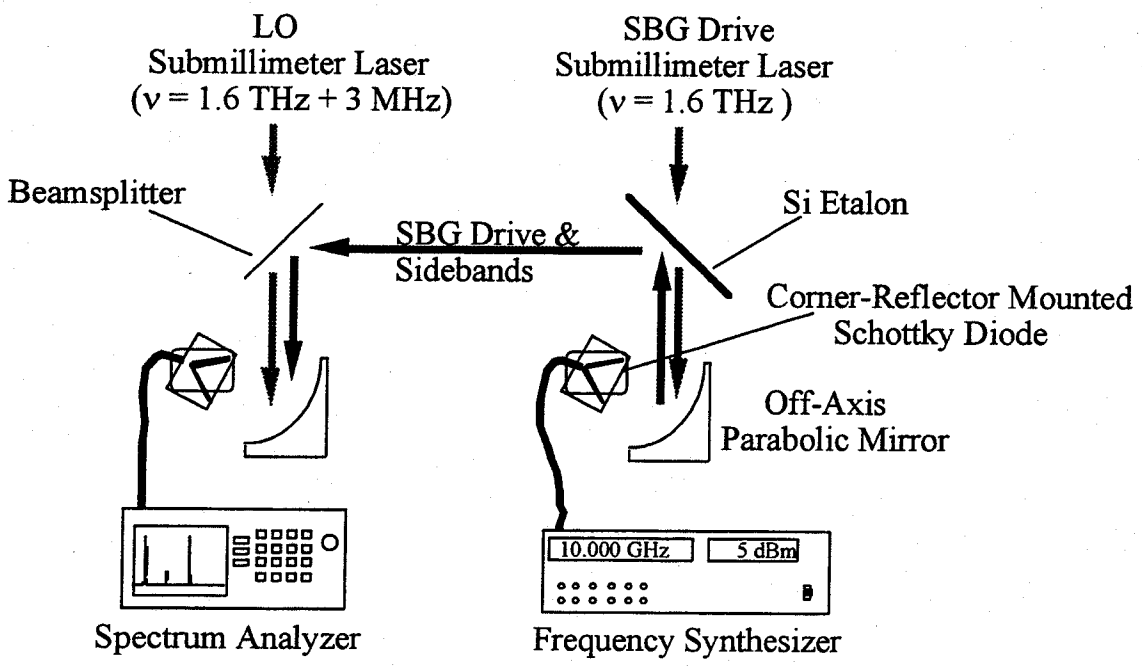

Figure 1: Apparatus used for sideband power measurements. Not included in the figure, is an amplifier placed between the receiver diode and the spectrum analyzer.

This separated the upper and lower sideband by 6 MHz and also served to separate the sidebands from any pick-up signal present at the microwave synthesizer frequency. Without this separation, signal at the synthesizer frequency picked-up by the receiver could be mistaken for sideband radiation. The synthesizer was operated at 10 GHz and provided ~ 5 dBm of microwave power at the diode. The Si etalon will be described in detail in the next section. Essentially, it transmits nearly 100% of the laser radiation while reflecting 80% of the sideband radiation. The 1 mil Mylar® beamsplitter has a reflectivity of 50% for s-polarized radiation at this wavelength.[25] The power of the LO was measured to be 5.5 mW and the Drive laser power was measured for each diode tested. The laser power data was obtained with a Keating Absolute Power Meter.[26] The receiver diode was a University of Virginia (UVa) model 1T17 and the SBG diode was one of the following: 1T7, 1T12, 1T17, 1T15.

In order to accurately measure the sideband power, it was necessary to measure the conversion loss of the receiver diode. This was done *in-situ* by placing a cold load and

chopper in the beam path between the two Schottkys and performing measurements of the system noise temperature for different values of IF temperature. This procedure was performed 5 times in order to assure accuracy. With this data the conversion loss and mixer temperature can be determined from[27]

$$T_{sys} = T_M + L_c T_{IF} \qquad (2)$$

where T_{sys} is the system noise temperature, T_M is the mixer temperature, L_c is the conversion loss, and T_{IF} is the noise temperature of the IF electronics. Since the measurement was performed *in-situ* the conversion loss included the 3 dB contribution of the beamsplitter. The measured conversion loss was 17.3 dB which corresponds to a diode conversion loss of 14.3 dB. This fairly poor value of L_c is mostly due to the ~2.5 dB measured impedance mismatch at 10 GHz,[28] and to a lessor extent, the fact that 2.8 mW of LO power is not quite enough to optimize this receiver at 1.6 THz.

With the above information, the gain of the IF chain, and the fact that the etalon reflects 80% of the sideband, the power in the sideband can be determined by measuring the power at the IF. Namely,

$$P_{sideband} = P_{IF} - G_{IF} + L_c + 1\ dB_{(etalon\ loss)} \qquad (3)$$

where $P_{sideband}$ is the single sideband power in dBm, P_{IF} is the IF power in dBm, G_{IF} is the gain of the IF chain, and L_c is the conversion loss of the receiver. The IF power was measured with the spectrum analyzer set to a resolution bandwidth of 100 kHz and the amplitude accuracy of the spectrum analyzer was checked against two calibrated power meters. The accuracy of the P_{IF} readings is dominated by spectrum analyzer calibration error which is less than 0.5 dB.

A typical IF spectrum is presented in Figure 2. The resolution bandwidth was set to 30 kHz for this data to clearly resolve the mechanical-vibration-induced integrated-laser-linewidth. It is important to note that the noise floor shown in Figure 2 is the noise floor of the spectrum analyzer and not that of the receiver. The fairly weak pick-up signal

from the microwave synthesizer is clearly seen in the figure and smaller peaks from other laser modes are also observed.

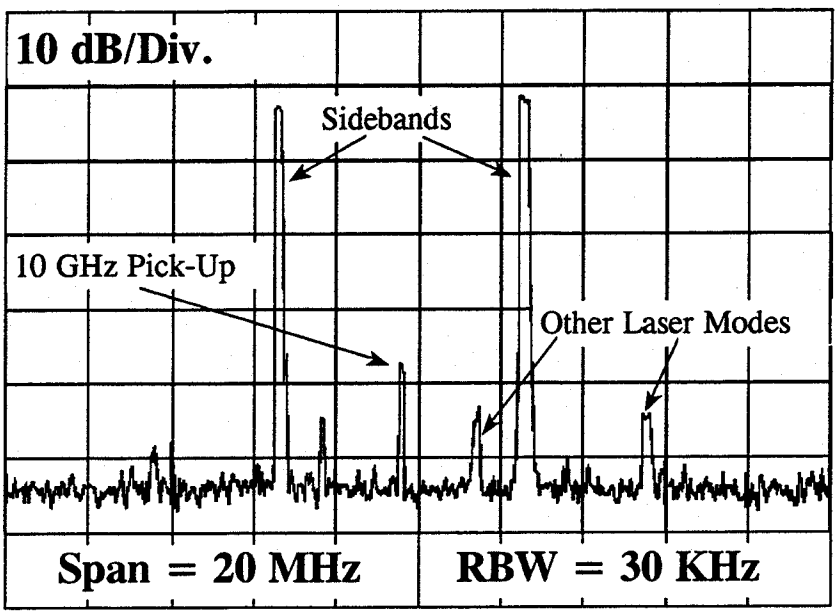

Figure 2: Typical IF spectrum. The pick-up signal is at the synthesizer frequency, and the upper and lower sidebands are separated by two times the difference frequency of the submillimeter lasers.

A summary of SBG diode performance is presented in Table 1. The Drive power was measured for each diode and then the SBG efficiency was calculated by dividing the single-sideband (SSB) power by the Drive laser power. Any error in the above measurement will only serve to underestimate the sideband power either through not coupling all of the sideband power into the receiver, or due to the fact that the IF exhibits ~100-150 kHz of jitter due to laser mirror vibrations. However, we believe that we are coupling the sideband into the receiver well and the IF jitter should be almost completely accounted for by the resolution bandwidth used in the power measurements.

Table 1

Respective sideband generator performance of four different models of Schottky diodes. The SBG efficiency is defined as the single-sideband power divided by the Drive laser power.

UVa Diode Model	SBG Efficiency	SSB Output Power
1T7	6×10^{-5}	0.6 μW
1T12	5×10^{-4}	6.6 μW
1T17	4×10^{-4}	4.2 μW
1T15	8×10^{-4}	10.5 μW

In examining Table 1 it is important to note that several contactings of the same diode can each lead to somewhat different performance. The results presented in Table 1 represent experiments performed with: 1 - 1T7 diode; 3 - 1T12 diodes, 2 - 1T17 diodes, and 1 - 1T15 diode.[29] The best results of these experiments are shown in Table 1 but the diode-to-diode variation was less than 1.5 dB, for a given model. Thus the 1T12 and 1T17 appear to be about on par, the 1T7 is clearly lower in efficiency, and the 1T15 is clearly the best tested. The results compare well with noise temperature and required LO power for these diodes at 184.3 μm.[21] Namely, the 1T15 achieves better noise temperature and requires roughly 3 dB less LO power to be optimized. Our conclusion is that the Drive power couples better into the 1T15 probably owing to its low junction capacitance (0.41 fF) and series resistance (14.4 Ω). The 1T15 has a nominal anode diameter of 0.25 μm making it very sensitive to static and other damage. Nevertheless this diode was operated in the SBG system for a week and no degradation in performance was observed. It should also be noted that the 3 - 1T17 diodes are slightly better receivers than the 1T12 diodes. The 1T17's tend to exhibit lower conversion loss.

IV - Sideband Separation and Spatial Mode Performance

Almost any experiment will benefit from pure, predictable, spatial mode performance of the source and some measurements may even require it. Examination of the mode of the sideband radiation requires either removing the unshifted laser from the beam, or scanning a coherent receiver through the beam. The latter approach is expected to be fraught with technological difficulties and thus the former technique was employed. Reflection etalons were designed using available ultra-high-precision complex index of refraction data on high-purity Si.[30] Using the Fresnel equations for a multilayered system,[31] a program was written to find a practical etalon thickness where, at an angle of incidence of 45°, the unshifted laser would be almost completely transmitted but the sideband radiation would be highly reflected. The calculated performance is presented in Figure 3. As demonstrated there, the 3 dB reflection bandwidth of the etalon is ~20 GHz and the reflection behavior will cyclically repeat with higher offset frequency.

While the calculation indicates that the laser radiation reflection should be 43 dB down, it was observed to be 23 dB down. In an effort to understand this discrepancy a more complete calculation was performed[32] including the effects of Gaussian beam walkoff.[33] This calculation predicts the reflection to be - 25 dB, in reasonable agreement with experiment, considering that the absorption loss is neglected in reference 33.

With roughly 10% of the laser radiation being reradiated from the antenna,[34] ~10 mW of laser Drive power, and 5 - 10 μW of sideband power, approximately 40 dB of unshifted laser radiation had to be removed from the beam so that conventional mode scans of the SBG radiation could be conveniently performed. The use of two etalons provided this rejection. After careful alignment of the etalons, the unshifted laser was 20 dB below the sideband. This was measured by placing a bolometer with a 2 mm diameter aperture in center of the beam and turning off the frequency synthesizer to see only the unshifted laser. While this measurement was performed, the DC bias point of the diode was varied over the entire safe range to confirm that the diode bias point change caused by the presence of the microwave source did not effect the amount of reradiated laser.

Further, the 20 dB ratio of sideband power to laser power was confirmed at several other points in the beam.

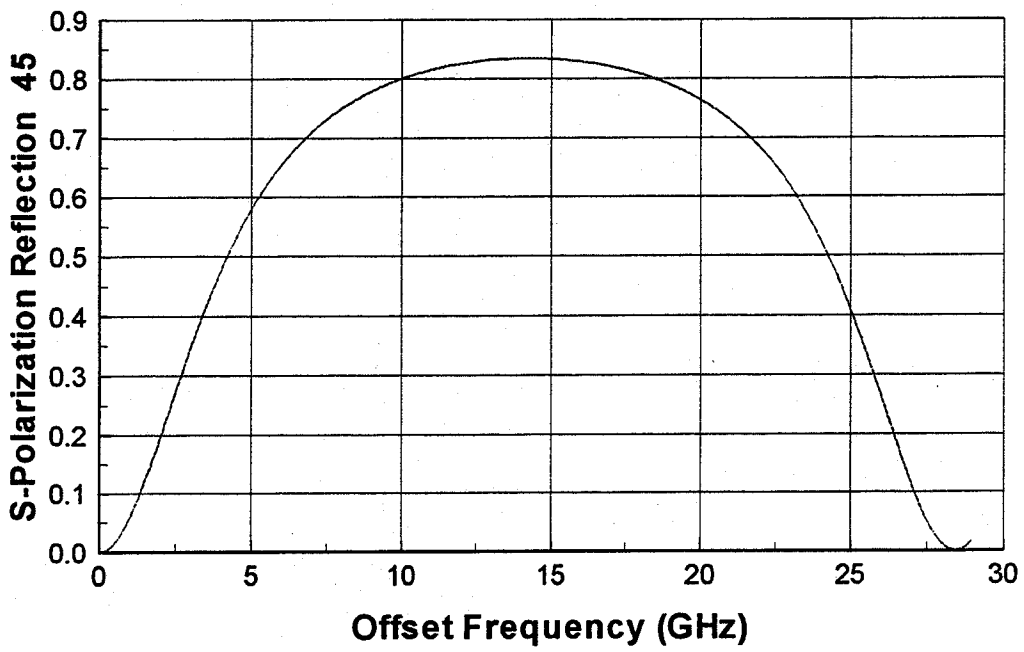

Figure 3: S-Polarization reflection versus offset frequency for the 1576.75 μm thick Si etalon used in the measurements. Zero offset corresponds to the laser center frequency, 1564.5187 GHz.

A typical antenna pattern of one of the mounted diodes is presented in Figure 4. This pattern was measured by UVa.[28] With the diode located at the focal point of the off-axis mirror, the expected output mode would be the collimated antenna pattern. Examination of Figure 4 leads one to believe that the output mode will not be a good Gaussian. Initial SBG mode scans confirmed this and revealed some structure due to cross-polarized radiation. This is to be expected since the antenna cannot be perfectly aligned in the dihedral. The cross-pol structure was eliminated with a polarizer placed in front of the SBG diode.

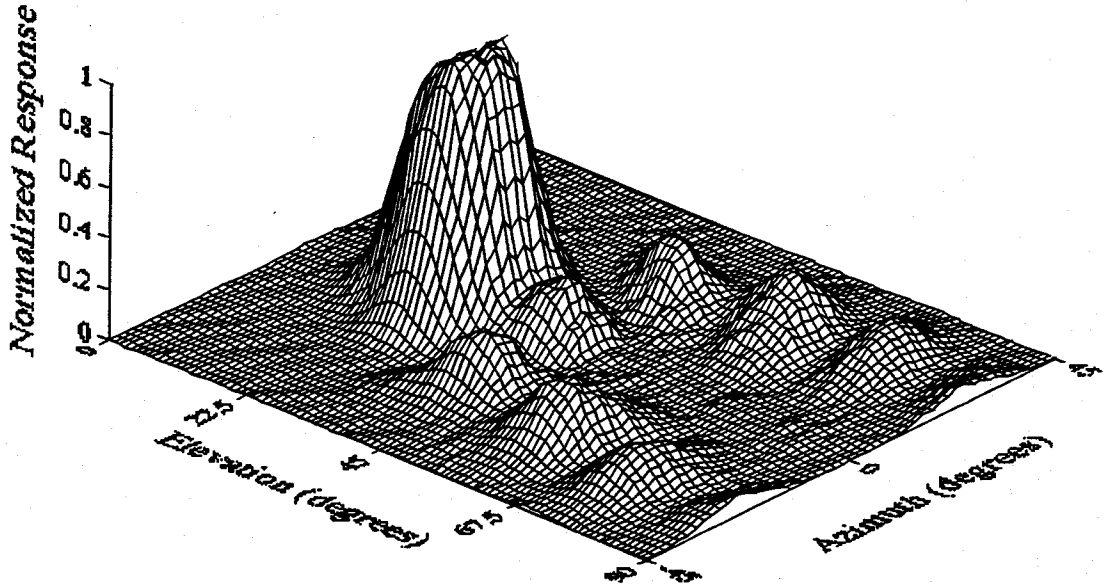

Figure 4: Antenna map of a diode mounted in a dihedral. Zero degrees elevation corresponds to the antenna parallel to the laser propagation direction. At zero degrees azimuth the dihedral is symmetric with the incident beam.

The first attempts to improve the mode involved careful adjustment of the diode orientation. This was accomplished with a five degree of freedom stage. While these efforts were somewhat successful, the resulting mode was so sensitive to corner-reflector alignment and individual diode antenna alignment that exchanging SBG diodes resulted in very different output modes. The final approach used to improve the mode employed two spatial filter apertures (SF's) to redefine the beam and effectively select only the central portion of the main beam. The first SF was somewhat oversized and located ~ 2" from the second etalon while the second SF was undersized and 19" from the first SF. The first SF removed rapidly diffracting structure on the skirts of the beam while the second selected the main lobe of the remaining beam. The resulting mode is presented in Figure 5. The sidelobes are ~18 dB down from the peak. The mode scan in Figure 5 is the result of subtracting a scan made with the synthesizer off from a scan made with the synthesizer on. This was done to insure that the unshifted laser present in the beam did not affect the

low-level data on the skirts of the beam. As expected, this subtraction caused no significant shift in the data.

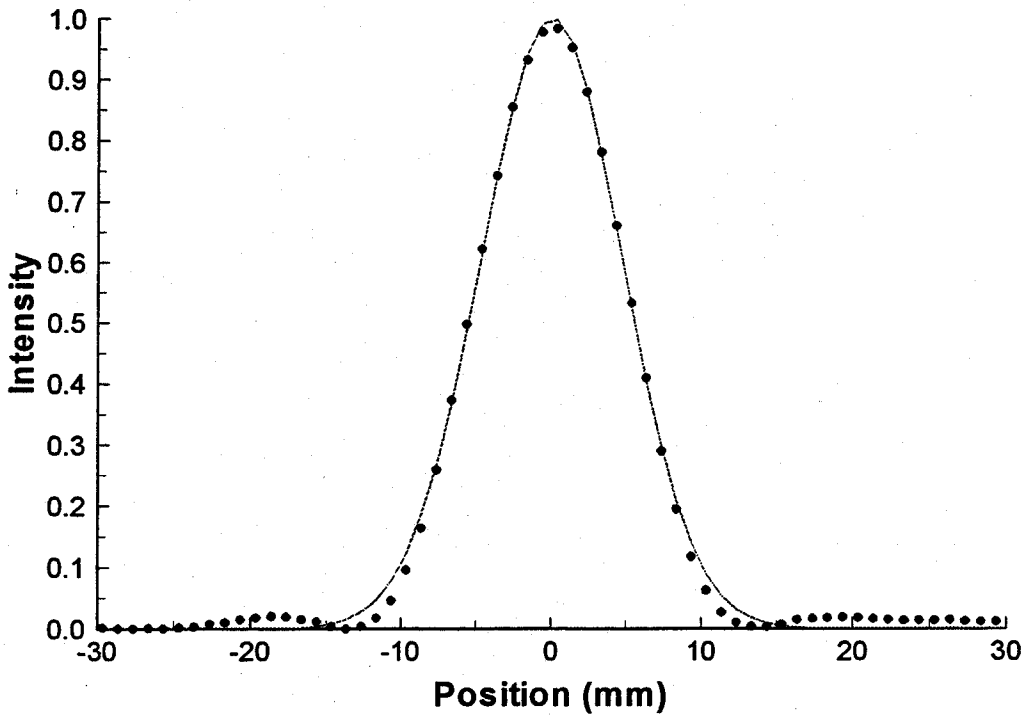

Figure 5: Mode scan of the sidebands. The data was taken using a bolometer with a 2 mm aperture and a computer-controlled translation stage. The solid line is the best fit Gaussian to the data, neglecting data that is more than 7 dB below the peak.

The second SF in the system was small enough that fairly noticeable diffraction was observed near it. However, the propagation of the mode further in space was well predicted by the paraxial equations[35] once the beam was 20 - 25" from the second SF. Four different SBG diodes were tested in the system once adequate mode performance was obtained. All of these produced virtually the same mode pattern beyond the two SF's. The SF's did unfortunately cause a loss of about 3 - 5 dB in sideband power in the beam.

While this method of sideband separation keeps both sidebands in the beam we have developed a receiver which will be respond to only one of the sidebands.[36] This receiver design is presented in section V, below.

V - Single-Sideband Submillimeter-Wave Receiver

A single sideband (SSB) receiver has been developed and implemented for use with a submillimeter SBG. While the sideband generator emits both an upper and lower sideband, and even some unshifted laser radiation, the receiver responds to only one sideband. The operator of the system can choose which sideband to receive. Rejection of the undesired signal is accomplished through selective frequency shifting coupled with the use of a commercially available single-sideband microwave mixer. This receiver is fully coherent, preserving phase and amplitude information.

The advantages of coherent reception include: greatly improved sensitivity (NEP's in the range of 10^{-19} W/Hz are typical)[37], phase and amplitude measurement, predetection bandwidth narrowing through IF bandwidth narrowing, and discrimination between upper and lower sidebands (as will be shown here). This section will describe the operation of the coherent SSB receiver by tracing the mixing products through the system.

A block diagram of the receiver is shown in Figure 6. The lasers are operated with one laser on line center and the other tuned 2 MHz above line center.[14] The first laser is the drive for the sideband generator and the second laser is the LO for the reference and receiver Schottkys. In the example presented in Figure 6 the microwave synthesizer is operated at 12 GHz and the frequency-shifting synthesizer is operated at 16 MHz.
The lower-case letters **a** - **e** denote locations where frequency content will be illustrated. Before describing frequency content it is important to note that since the laser frequency ν is in the THz range mixing products of frequency ν or greater will be rapidly attenuated in the coax or waveguide connecting the remaining portions of the circuit, and can be ignored. With this in mind, the first-order frequency content at position **a** is

2 MHz, (a)

and at position **b** is

14 MHz
18 MHz (b)

16 MHz (LO mixer leakage)

2 MHz (RF mixer leakage).

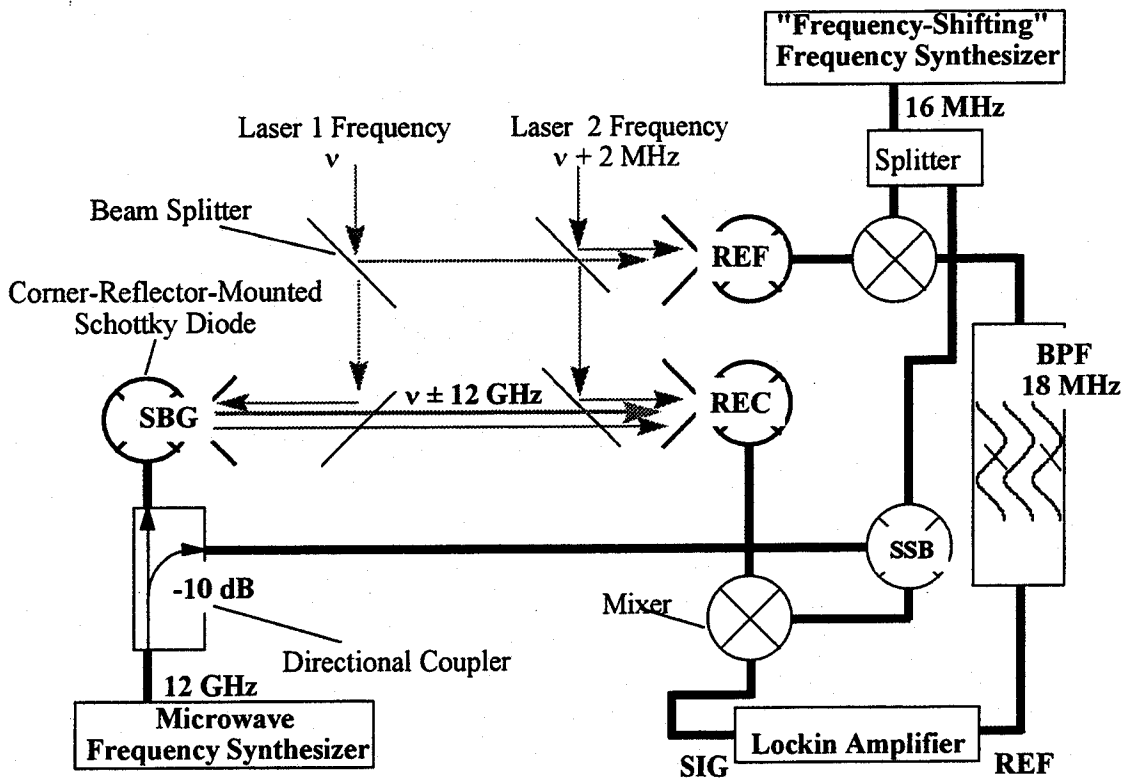

Figure 6: Block Diagram of the SSB receiver. The bandpass filter (BPF) is centered at 18 MHz and has a 3 dB width of 400 kHz.

Before examining position **c** one must remember that a number of frequencies enter the receiver Schottky. Considering only first-order sideband generation, in the interest of brevity, the following spectrum enters the receiver: ν + 2 MHz (Laser 2, LO), ν + 12 GHz (Upper Sideband), ν - 12 GHz (Lower Sideband), and ν (Laser 1, Unshifted Drive).

Therefore the first-order frequency content at **c** is

2 MHz

12 GHz (u, l)

$$\begin{array}{l} 12\ \text{GHz} - 2\ \text{MHz (u)} \\ 12\ \text{GHz} + 2\ \text{MHz (l)} \\ 24\ \text{GHz (u, l)} \end{array} \qquad \text{(c)}$$

where (u) and (l) denote upper and lower submillimeter sidebands, respectively. If at this point one simply mixed (3) with the microwave synthesizer signal, the upper and lower sideband would both be at 2 MHz, and DC. Next, examining location **d**, the frequency content is

$$12\ \text{GHz} + 16\ \text{MHz}, \qquad \text{(d)}$$

neglecting the other component which is at least 28 dB down, as a result of the image rejection of the SSB mixer.[38] Using this as the LO for the mixer prior to **e**, noting that the electronics between position **c** and the mixer prior to **e** will not pass 2 MHz, at position **e** the first order frequency content is,

$$\begin{array}{l} 16\ \text{MHz (u, l)} \\ 18\ \text{MHz (u)} \\ 24\ \text{GHz} + 14\ \text{MHz (u)} \\ 14\ \text{MHz (l)} \\ 24\ \text{GHz} + 18\ \text{MHz (l)} \\ 12\ \text{GHz} \pm 16\ \text{MHz (u, l)} \\ 36\ \text{GHz} + 16\ \text{MHz (u, l)}. \end{array} \qquad \text{(e)}$$

One can now see that the upper submillimeter sideband has been mixed down to 18 MHz, while the lower submillimeter sideband has been mixed down to 14 MHz.

If a bandpass filter centered at 18 MHz is placed after **b**, the two-phase lockin (I - Q demodulator) will be locked to the upper sideband. Further, as the sideband frequency is tuned, the upper sideband will always be at 18 MHz. The lockin will track any laser jitter since it is coincidentally measured with the reference Schottky. The lower

submillimeter sideband can be chosen instead of the upper by simply tuning laser 2 to be 2 MHz below laser 1.

A further advantage of this circuit stems from the fact that the reference Schottky never "sees" the sideband radiation. Therefore the problem of cross-talk through sideband radiation in the LO laser path is eliminated.

V - Summary and Conclusions

An accurate measurement of the power of a submillimeter sideband generator has been performed and output power at ~ 1.6 THz of 10.5 μW has been obtained. Optimal coupling parameters at one frequency have been confirmed, $w_0 = 1.82\lambda$, and good spatial mode performance has been achieved. A technique has been presented for removal of unshifted laser radiation and this technique has been demonstrated to provide a beam with the sideband 20 dB above the unshifted laser. If the above etalon technique were used in a very wideband system the periodic "holes" in the etalon reflection could be compensated for by designing etalons with different null spacing, ie. different thickness, and performing one frequency scan for each etalon set.

A single-sideband receiver for use with a submillimeter sideband generator has been developed. The rejection of the unwanted sideband is achieved through selective frequency shifting in the IF electronics. This receiver permits the user to select which submillimeter sideband to demodulate, eliminates the cross-talk problem, and allows for correction of laser drift through adjustment of the "frequency-shifting" synthesizer.

Acknowledgments

We are grateful for the technical assistance of the UVa Semiconductor Device Laboratory, the UVa Far-Infrared Receiver Laboratory, and in particular to D. W. Porterfield and P. A. Wood. This work was supported by the US ARMY, NGIC under contract number DAHC90-91-C0028.

References

1. R. J. Bell, Introductory Fourier Transform Spectroscopy, New York: Academic Press (1972)

2. This number can be estimated based on the results found in E. K. Plyer, D. J. C. Yates, and H. A. Gebbie, "Radiant Energy from Sources in the Far-Infrared," J. Opt. Soc. Am. **52**(8), 859 (1962).

3. J. Burghoorn, J. P. Kaminski, R. C. Strijbos, T. O. Klaassen, and W. Th. Wenckebach, "Generation of subnanosecond high-power far-infrared pulses by using a passive resonator pumped by a free-electron laser," J. Opt. Soc. Am. B **9**(10), 1888 (1992)

4. K. M. Evenson, D. A. Jennings, F. R. Petersen, "Tunable far-infrared spectroscopy," Appl. Phys. Lett. **44**, 576 (1984)

5. I. G. Nolt, J. V. Radostitz, G. Dilonardo, K. M. Evenson, D. A. Jennings, K. R. Leopold, M. D. Vanek, L. R. Zink, A. Hinz, and K. V. Chance, J. Mol. Spec. **125**, 274 (1987)

6. E. R. Brown, K.A. McIntosh, F. W. Smith, J. Appl. Phys. **73**, 1480 (1993), and K. A. McIntosh, E. R. Brown, K. B. Nichols, O. B. McMahon, W. F. DiNatale, & T. M. Lyszczarz, Appl. Phys. Lett. **67**(26), 3844 (1995)

7. D. D. Bicanic, B. F. J. Zuidberg, and A. Dymanus, "Generation of continuously tunable laser sidebands in the submillimeter region," Appl. Phys. Lett. **32**(6), 367 (1978)

8. H. R. Fetterman, P. E. Tannenwald, B. J. Clifton, W. D. Fitzgerald, and N. R. Erickson, "Far-ir heterodyne radiometric measurements with quasioptical Schottky diode mixers," Appl. Phys. Lett. **33**, 151 (1978)

9. W. A. M. Blumberg, H. R. Fetterman, and D. D. Peck, "Tunable submillimeter sources applied to the excited state rotational spectroscopy and kinetics of CH_3F," Appl. Phys. Lett. **35**(8), 582 (1979)

10. J. Farhoomand, G. A. Blake, M. A. Frerking, and H. A. Pickett, "Generation of tunable laser sidebands in the far-infrared region," J. Appl. Phys. **57**(5), 1763 (1985)

11. P. Verhoeve, E. Zwart, M. Versiuis, M. Dtabbels, J. J. ter Meulen, W. Leo Meerts, and A. Dymanus, "A far infrared sideband spectrometer in the frequency region 550-2700 GHz," Rev. Sci. Instrum. **61**(6), 1612 (1990)

12. D. D. Bicanic, Infrared and Millimeter Waves, Vol. 7, Academic Press, p. 285 (1983)

13. G. A. Blake, K. B. Laughlin, R. C. Cohen, K. L. Busarow, D.-H. Gwo, C. A. Schmuttenmaer, D. W. Steyert, and R. J. Saykally, "The Berkeley tunable far infrared laser spectrometer," Rev. Sci. Instrum. **62**(7), 1701 (1991)

14. E. R. Mueller, & J. Waldman, IEEE Trans. on Microwave Theory & Techniques **42**(10), 1891 (1994)

15. K. B. Laughlin, Ph. D. Thesis, Department of Chemistry, Univ. Cal. Berkeley, p. 72, Ann Arbor, Michigan: University Microfilms International (1988)

16. H. Krautle, E. Sauter, and G. V. Schultz, "Antenna Characteristics of Whisker Diodes used as Submillimeter Receivers," Infrared Phys. **17**, 477 (1977)

17. H. Krautle, E. Sauter, and G. V. Schultz, "Properties of a Submillimeter Mixer in an Open Structure Configuration," Infrared Phys. **18**, 705 (1978)

18. E. H. Grossman, "The Coupling of Submillimeter Corner-Cube Antennas to Gaussian Beams," Infrared Phys. **29**, 875 (1989)

19. E. Sauter, G. V. Schultz, and R. Wohlleben, "Antenna Patterns of an Open Structure Mixer at a Submillimeter Wavelength and of its Scaled Model," Int. J. Infrared MMW **5**, 451 (1984)

20. Ref. 15, p. 85

21. P. A. Wood, "Analysis of High Frequency Effects in GaAs Schottky Barrier Diodes", Ph. D. Thesis, Department of Electrical Engineering, University of Virginia (1994)

22. G. P. Agrawal, and D. N. Pattanayak, "Gaussian beam propagation beyond the paraxial approximation," J. Opt. Soc. Am. **69**(4), 575 (1979)

23. S. Withington, and J. A. Murphy, "Gaussian-mode Analysis of "Thin" Mirrors," Proc. Fourth Int. Symp. on Space THz Techno., p. 211 (1983)

24. W. J. Weber (Ed.), CRC Handbook of Laser Science and Technology, Volume II, Gas Lasers, Boca Raton, Florida: CRC Press, Inc., p. 461 (1982)

25. This can be calculated using the Fresnel equations[31] and the fact that Mylar® has an index of refraction of 1.85 (H. A. Gebbie, and N. W. Stone, Infrared Phys. **4**, 85 (1964)).

26. Thomas Keating Ltd., Billingshurst, West Sussex, England

27. J. W. Archer, Infrared and Millimeter Waves, Vol. 15, Academic Press, p. 4 (1986)

28. D. W. Porterfield, UVa Far-Infrared Receiver Laboratory (1993)

29. W. C. B. Peatman, P. A. D. Wood, D. Porterfield, T. W. Crowe, and M. J. Rooks, "Quarter-Micrometer GaAs Schottky Barrier Diode with High Video Responsivity at 118 μm," Appl. Phys. Lett. **61**(3), 20 (1992)

30. A. J. Gatesman, R. H. Giles, and J. Waldman, "High-precision reflectometer for submillimeter wavelengths", J. Opt. Soc. Am. B, **12**(2), 212 (1995), and A. Gatesman, Ph. D. Thesis, Department of Physics, University of Massachusetts Lowell (1993). At 191.84803 μm, n = 3.4160, and k = 0.000057.

31. R. M. A. Azzam, and N. M. Bashara, Ellipsometry and Polarized Light, New York: North-Holland Publishing Co., p. 285 (1979)

32. A. Gatesman, personal communication (1993)

33. J. C. Cotteverte, F. Bretenaker, and A. Le Floch, "Jones matrices of a tilted plate for Gaussian beams," Appl. Opt. **30**(3), 305 (1991)

34. The tilting of the bottom of the corner-reflector left only reradiated laser in the outgoing beam. The amount of reradiated power was measured with the Keating power meter.

35. H. Kogelnik, and T. Li, "Laser Beams and Resonators," Appl. Opt. **5**(10), p. 1550 (1966)

36. E. R. Mueller, "Frequency-Shifting Submillimeter Single-Sideband Receiver", Int. J. IR & MMW, **15**(4), 665 (1994)

37. P. A. D. Wood, W. C. B. Peatman, D. W. Porterfield, and T. W. Crowe, "GaAs Schottky Diodes for THz Mixing Applications", Proc. Fourth Int. Symp. on Space THz Technol., p. 377 (1993)

38. The SSB mixer was purchased from MITEQ Inc. in Hauppauge, NY.

TERAHERTZ EMISSION FROM *p*-TYPE GERMANIUM LASERS DOPED WITH NOVEL ACCEPTORS

O. D. Dubon,[1,2] D. R. Chamberlin,[1,2] W. L. Hansen[1] and E. E. Haller,[1,2]
Lawrence Berkeley National Laboratory[1]
Department of Materials Science and Mineral Engineering[2]
University of California, Berkeley, CA 94720, USA
and
L. A. Reichertz, G. Sirmain, E. Bründermann, A. M. Linhart and H. P. Röser
DLR, Institute for Space Sensor Technology, Rudower Chaussee 5, D-12489 Berlin, Germany

Abstract

We have studied the stimulated emission from Ge single crystals doped with the multivalent acceptors Be, Zn, and Cu. Unlike those containing shallow acceptors, lasers doped with the double acceptors Be and Zn exhibit stimulated emission over the full frequency range of 1 to 4 THz. First results on Ge doped with the Cu triple acceptor show that emission between 1.5 and 4 THz can be achieved. By using crystals that contain these novel dopants, we have increased the duty cycle up to the 10^{-2} range which is one order of magnitude higher than the maximum duty cycle reported for shallow acceptor doped lasers.

I. Introduction

The interest in a compact, tunable local oscillator for the heterodyne detection of THz radiation has led to considerable interest in the *p*-type Ge hot-hole laser as a potential continuous wave (cw) source in the 1 to 4 THz range. This laser operates in crossed electric (E) and magnetic (B) fields at liquid helium temperatures. Stimulated emission arises from a) intervalence band (IVB) transitions from the light- to the heavy-hole subbands and b) cyclotron resonance (CR) transitions between Landau levels of the light-hole subband. Thus far these lasers have been shown to operate only in a pulsed mode achieving an output power as high as a few Watt and duty cycles in the 10^{-3} range.[1] The operating principles of these lasers are explained in detail elsewhere.[2]

The emission spectrum of lasers operating in the IVB mode has previously been shown to consist of two regions, the "low frequency" (1.0-1.8 THz) and the "high frequency" (2.4-4 THz) region. It has been recently demonstrated that internal absorption of the radiation by neutral acceptors suppresses the emission between the low and high frequency region.[3] Until recently, all previous spectral investigations have been performed with crystals doped with shallow hydrogenic acceptors (mostly Ga), all of which exhibit internal hole transitions that partially overlap in energy with IVB transitions. There has therefore been a strong interest in producing lasers from Ge crystals that are doped with deeper acceptors.

Here we present spectral measurements of the stimulated emission from Be-, Zn- and Cu-doped Ge crystals. Neutral Be, Zn, and Cu have ionization energies of 25, 33, and 43 meV, respectively, and therefore should not lead to self-absorption. Laser action from multivalent-acceptor-doped Ge crystals was recently demonstrated.[4,5] We show that stimulated emission from these materials can be achieved over the full range of 1 to 4 THz.

II. Sample preparation and measurement

For this study we used samples from two Czochralski-grown crystals, one doped with Be and the other with Zn. Wafers were lapped sequentially in 600 and 1200 mesh SiC powder/water slurries and polish-etched in a 4:1 HNO_3:HF mixture. Ohmic contacts were formed on the wafer surfaces by boron ion implantation with doses of 1×10^{14} and 2×10^{14} cm^{-2} at 33 and 50 keV, respectively. 200 Å of Pd and 4000 Å of Au were then rf sputtered onto the implanted surfaces. Annealing for 1 hour at 300 °C in a N_2 ambient was performed to remove implantation damage and activate the boron acceptors in the implanted layer. The wafers were crystallographically oriented and cut into parallelepipeds. The freshly exposed surfaces were re-lapped, and the bar-shaped samples were re-etched in the 4:1 HNO_3:HF mixture.

The crystals were characterized by variable temperature Hall-effect measurements and photothermal ionization spectroscopy (PTIS) in order to determine the type and the concentration of the different impurities present in the crystals. For both crystals we determined a majority dopant concentration of 1.5×10^{14} cm^{-3} and a residual net shallow acceptor (mostly B and Al) concentration of 1.0 to 2.0×10^{12} cm^{-3}.

Copper doping can be readily obtained in Ge crystals by thermal diffusion. This makes Cu-doped Ge an attractive material for producing these hot-hole lasers.[6] In this study a wafer 6 mm thick was cut from a Czochralski-grown, *p*-type Ge ingot with a residual shallow acceptor concentration of $2x10^{11}$ cm^{-3}. It was lapped and etched in the manner described above. A 1000 Å layer of Cu was rf sputtered onto the wafer as a diffusion source. The wafer was crystallographically cut to produce sample geometries with dimensions slightly larger than the final device. Each laser crystal was cleaned and annealed separately in an ampoule sealed under vacuum. In-diffusion of Cu was performed for 40 hours at a fixed temperature of 700 °C. The ampoules were quenched rapidly in ethylene-glycol to reach the desired substitutional Cu concentration of $1x10^{15}$ cm^{-3}.

Reference samples 1 mm thick were cut at each end of the laser crystals to check the Cu concentration, the homogeneity of Cu along the length of each laser crystal and the concentration of residual shallow impurities (acceptor and donor contaminants). Hall effect measurements performed on these samples show the homogeneity of the Cu acceptors to be better than 20%. These measurements reveal a residual shallow acceptor net concentration in the low 10^{12} cm^{-3} range which is approximately five times higher than the concentration measured for unannealed samples. We relate this shallow acceptor concentration increase, at least in part, to the dissociation of hydrogen-acceptor complexes.[7] The residual acceptors are Al and Ga impurities in a 1:1 concentration ratio according to PTIS measurements. The concentration of compensating shallow donors lies in the low 10^{11} cm^{-3} range and is attributed to phosphorus impurities.

Upon completion of Cu in-diffusion and characterization of the annealed crystals, the laser crystal surfaces were lapped and polish-etched to their final dimensions. Ohmic contacts were formed on two opposite surfaces in the same manner described previously.

The laser samples were mounted between two copper electrodes and placed inside a superconducting magnet in a liquid helium cryostat. Electric field pulses with lengths of 1 to 2 μs were applied. The high refractive index of germanium enables laser operation without external resonators, the laser surfaces forming an internal cavity. The radiation was detected in the Faraday configuration with the outcoupling direction parallel to the magnetic

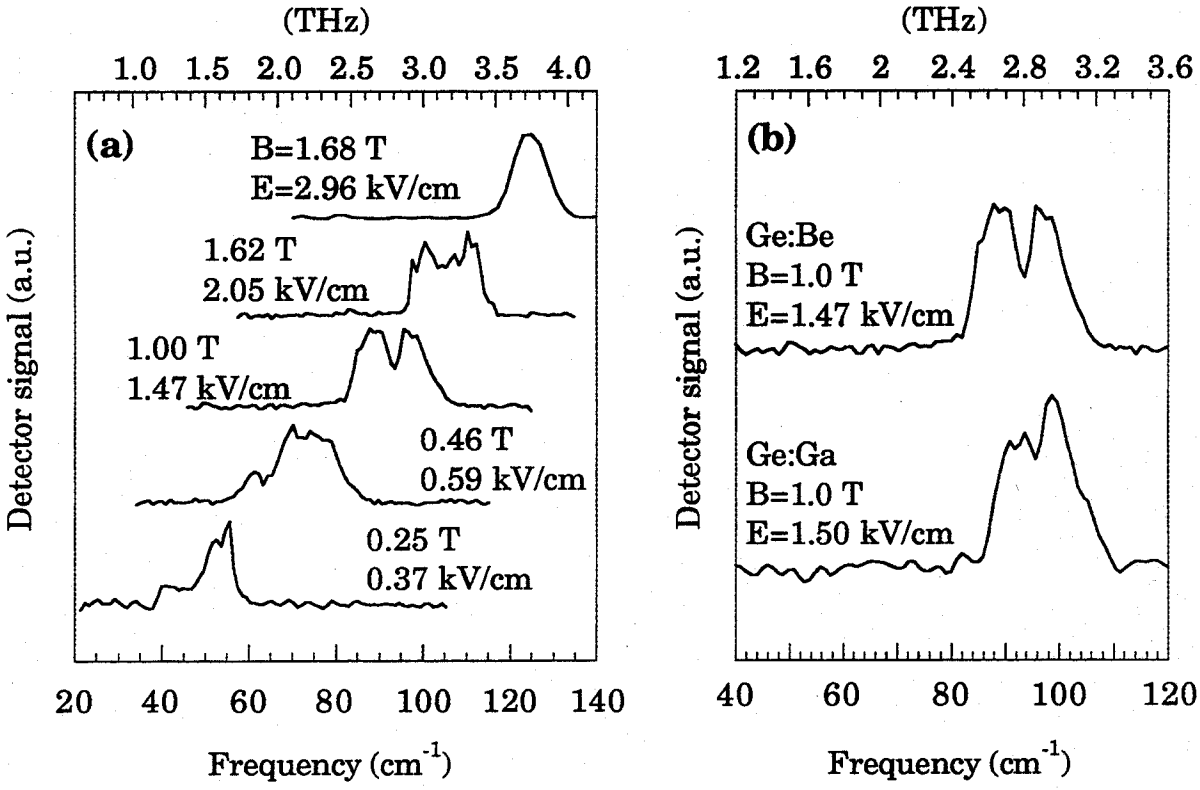

Figure 1. (a) Stimulated emission spectra from Ge:Be for various combinations of E and B fields. The spectral resolution is 1 cm^{-1} (0.03 THz) except for the spectrum measured at 1.68 T which has a resolution of 2 cm^{-1} (0.06 THz). (b) Stimulated emission from Ge:Ga (4x4x25 mm^3, Ga concentration of $8x10^{13}$ cm^{-3}) compared to Ge:Be tested under the same conditions, including crystallographic orientation with respect to the E and B fields.

field. We measured the emission spectra by Fourier transform spectroscopy using a Michelson interferometer and a broadband 4.2 K bolometer.

III. Results and discussion

Figure 1(a) shows the emission spectra of a 4x4x20 mm^3 Ge:Be laser for different combinations of E and B fields. The magnetic field was oriented parallel to the long axis of the crystal which pointed along a [110] crystallographic direction. The E field was applied along a [001] direction.

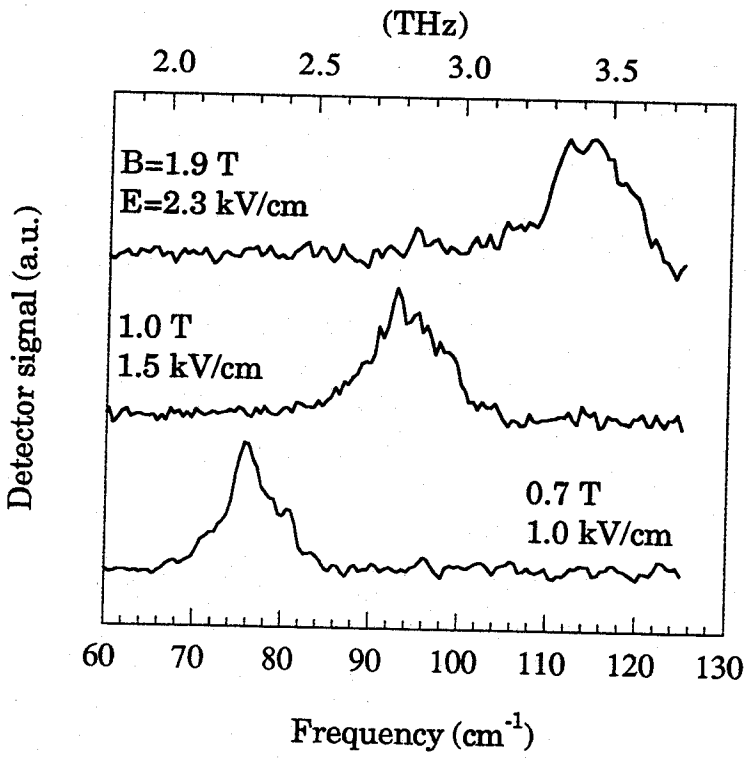

Figure 2. Stimulated emission spectra from Ge:Cu for various combinations of E and B fields. The spectral resolution is 0.5 cm^{-1} (0.015 THz).

By varying both fields we were able to achieve IVB stimulated emission throughout the range of 1 to 4 THz unlike the case for Ga-doped Ge lasers which exhibit an emission gap between 1.8 and 2.4 THz. The emission of Zn-doped germanium lasers possesses the same spectral characteristics displayed in Fig. 1(a). In addition, we find that outside the spectral region where dopant self-absorption occurs, double acceptor doping does not change the character of the emission spectrum [Figure 1(b)]. These results clearly demonstrate that the observed emission is related to the intrinsic properties of the Ge valence band and is not due to the nature of the dopant species.

Figure 2 shows the emission spectra of a 4.5x39.2x6.0 mm^3 Ge:Cu laser. As in the case of the Be- and Zn-doped samples, the magnetic field was oriented parallel to the long axis of the crystal along a [110] direction. However, the Ohmic contacts were made on the 6.0x39.2 mm^2, [110]-oriented surfaces. With this configuration we have observed stimulated emission in

the range of 2.1 to 3.6 THz. In addition, we have measured the spectrum for the same laser crystal but with the contacts (and hence the electric field) oriented in a [001] direction similarly to the Be-doped Ge lasers. We find that the spectral range of the emission broadens and have observed lasing between 1.5 and 4 THz. Changing the direction of E redistributes the hole population within the valence subbands, and lasing conditions are achieved between different levels as reflected by the differing ranges in the emission spectra.

The onset of stimulated emission at a higher photon energy for the case of Ge:Cu compared to Ge:Be is related to the deeper ground state of the copper acceptors. The stronger localization of the Cu-acceptor ground state requires that higher electric fields be applied in order to impact ionize the neutral Cu centers.[8] In the range of small E fields (and small B fields) where lasers normally operate, stimulated emission is not achieved due to the low density of holes in the valence band. Because of the partial ionization of Cu acceptors throughout the operating E-B conditions, Cu-doped Ge lasers can operate with acceptor densities that are significantly higher than for lasers containing either single or double acceptors.

By removing the effect of dopant self-absorption and improving the power dissipation of the laser during operation, we have reached record duty cycles as high as 2.5%. Also, we have observed additional features in the emission spectra of these materials.[9] Studies on the nature of this new emission are under way.

IV. Conclusion

We have shown stimulated emission from Be-, Zn- and Cu-doped Ge single crystals. By doping with these acceptors and significantly reducing the shallow impurity background during crystal growth, we have been able to produce lasers that are continuously tunable from 1 to 4 THz. Understanding the dynamics of terahertz emission in these new materials systems will be crucial to the development of a cw p-Ge laser.

Acknowledgments

The authors are grateful to J.W. Beeman (LBNL), K. Roderick (LBNL), and W. Esch (MPIfR Bonn) for their technical support. This work was performed

with facilities at the Lawrence Berkeley National Laboratory operated under U.S. DOE Contract No. DE-AC03-765F00098.

1 E. Bründermann, A.M. Linhart, H.P. Röser, O.D. Dubon, W.L. Hansen and E.E. Haller, Proc. of 7th Int'l. Symp. on Space Terahertz Technol., Charlottesville, VA, USA, p. 187 (1996).

2 For a comprehensive review see: E. Gornik and A.A. Andronov (Eds.), *Optical and Quantum Elec.*, Special issue **23** (2), S111-S310 (1991). Also see: E. Bründermann, H.P. Röser, W. Heiss, E. Gornik and E.E. Haller, *Appl. Phys. Lett.* **67**, 3543 (1995); and E. Bründermann, A.M. Linhart, H.P. Röser, O.D. Dubon, W.L. Hansen and E.E. Haller, *Appl. Phys. Lett.* **68**, 1359 (1996).

3 W. Heiss, K. Unterrainer, E. Gornik, W.L. Hansen and E.E. Haller, *Semicond. Sci. Technol.* **9**, 638 (1994).

4 E. Bründermann, A.M. Linhart, L. Reichertz, H.P. Röser, O.D. Dubon, G. Sirmain, W.L. Hansen and E.E. Haller, *Appl. Phys. Lett.* **68**, 3075 (1996).

5 G. Sirmain, L.A. Reichertz, O.D. Dubon, E.E. Haller, W.L. Hansen, E. Bründermann, A.M. Linhart and H.P. Röser, *Appl. Phys. Lett.* **70**, 1659 (1997).

6 H.H. Woodbury and W.W. Tyler, *Phys. Rev.* **105**, 84 (1957); and R. N. Hall and J. H. Racette, J. Appl. Phys. **35**, 379 (1964).

7 N.M. Haegel and E.E. Haller, *SPIE* **659**, 188 (1986).

8 P.R. Bratt, "Impurity germanium and silicon infrared detectors" in *Semiconductors and Semimetals*, edited by R.K. Willardson and A.C. Beer (Academic Press, New York, 1977), Vol. 12, p. 39.

9 L. A. Reichertz, O.D. Dubon, G. Sirmain, E. Bründermann, W.L. Hansen, D.R. Chamberlin, A.M. Linhart, H.P. Röser and E.E. Haller, submitted for publication (1997).

Tunable THz-laser for applications in FIR astronomy

E. Bründermann, A.M. Linhart, L.A. Reichertz, G. Sirmain and H.P. Röser
DLR, Institute of Space Sensor Technology, D-12484 Berlin, Germany
O.D. Dubon, D.R. Chamberlin, W.L. Hansen and E.E. Haller
Lawrence Berkeley National Laboratory and University of California, Berkeley, CA 94720, USA

Abstract

We summarize recent results of Ge:Be lasers reaching duty cycles up to 2.5%. We have studied the laser emission of a small Ge:Be laser cube with a volume of 27 mm^3 and a Be concentration of $1.5x10^{14}$ cm^{-3} by using permanent magnets. The laser was operated in a standard closed-cycle He refrigerator, and the laser intensity was measured as a function of temperature. The laser emission detected in the Voigt configuration revealed linear polarization.

I. Introduction

We plan to develop a compact, tunable, and continuous wave THz laser within the next 2-3 years. The laser will operate as a local oscillator in heterodyne receivers preferably on the platform SOFIA (Stratospheric Observatory for Infrared Astronomy) or on the space station.

In our previous reports [1, 2] we have demonstrated the capabilities of the p-type germanium laser as a possible tunable THz laser. The pulsed p-type Ge laser operates in crossed electric and magnetic fields at temperatures from 4 to 20 K. Typically, the crystal is immersed in liquid helium (LHe) and emits a reasonable output power of a few watts. A more detailed description of the lasing mechanism, crystal preparation and experimental set-up have been published [1, 2]. The laser fulfills several local oscillator requirements: tunability from 1 to 4 THz [3], single line operation and mode line widths below one MHz [4].

The limited observation time on airplanes and satellites requires a high duty cycle or continuous wave operation. Therefore, the main drawback of the p-Ge laser is its pulsed operation. With the development of a new type of Ge laser [3,5,6] and the miniaturization of Ge lasers [7], it seems to be possible to overcome this problem. Figure 1 displays our progress to the present duty cycle of 2.5%, i.e., emission of 32 µs long laser pulses at repetition rates close to 1 kHz.

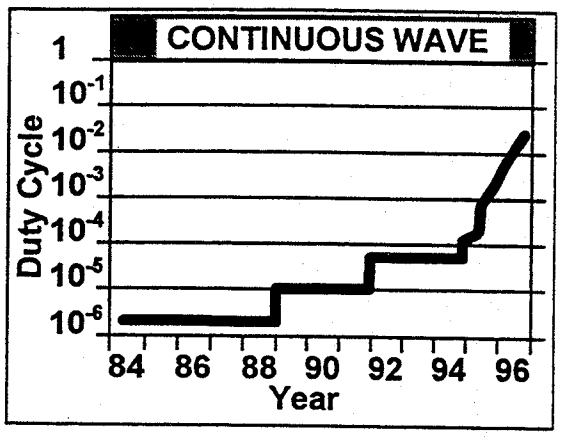

Figure 1: Improvements in the duty cycle since the invention of Ge lasers. New lasers with double acceptors (Ge:Be) have a drastically increased duty cycle.

II. Ge:Be laser operation with permanent magnets

The reduced size of our laser crystals leads to lower demands on power supplies and on the size of the magnets and makes small table-top cryostats viable for laser operation. We have built a table-top standard LHe-cryostat with a horizontal superconducting coil. We mounted the p-Ge laser in vacuum simplifying the construction of external resonators.

Recently, p-Ge laser operation using permanent magnets in LHe has been reported [8]. A tunable permanent magnet was proposed by using so called 'magic spheres' enabling a tunable magnetic field from 0 to 4 T [9].

Figure 2 displays the laser emission of a Ge:Be laser cube with a volume of 27 mm^3 mounted between one, two and three pairs of NdFeB permanent magnets reaching magnetic fields across the crystal of 0.43 T, 0.61 T and 0.69 T, respectively. Each individual magnet had a size of 10x10x6 mm^3.

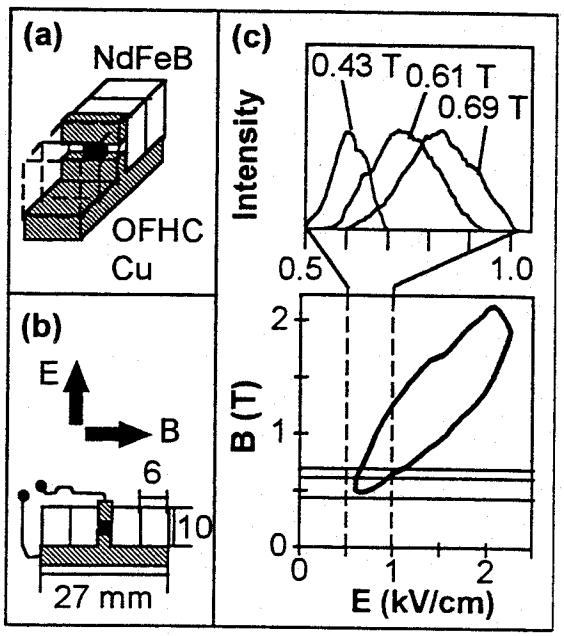

Figure 2: (a) set-up of a 27 mm^3 Ge:Be laser cube with 2 pairs of NdFeB permanent magnets and OFHC copper heat sinks, (b) cross-section of laser set-up in crossed electric and magnetic fields in the Voigt configuration, (c) Ge:Be laser radiation as a function of the electric and magnetic field was found in the area enclosed by the thick line using a tunable superconducting magnet. Horizontal lines indicate magnetic fields of 0.43 T, 0.61 T and 0.69 T reached with 1, 2 and 3 pairs of permanent magnets, respectively. The measured intensities were normalized.

The electric contacts and heat sinks were made from oxygen-free high-conductivity copper (OFHC) to improve cooling. The necessary condition of crossed electric and magnetic fields for Ge laser operation is naturally achieved by using the self-attractive force of the magnets aligning themselves perpendicularly to the electric contacts (Fig. 2(a),(b)). The radiation was detected in the Voigt configuration perpendicular to the magnetic field. Figure 2(c) shows the Ge:Be laser radiation as a function of the electric field for each permanent magnet configuration. For comparison, the active laser area as a function of electric and magnetic fields using a tunable superconducting magnet was measured. With the superconducting magnet we detected the laser radiation in the direction of the magnetic field in the Faraday configuration.

III. Ge:Be laser operated in a closed-cycle He refrigerator

Permanent magnets allow LHe-free operation of Ge lasers at temperatures up to 20 K. Therefore, we were able to demonstrate laser operation in a closed-cycle He refrigerator [10]. Figure 3 gives an overview of the experimental set-up used to investigate the Ge:Be laser cube in the closed-cycle machine. The cooling power of the CTI-Cryogenics cryocooler limited the minimum temperature to 14.3 K without electric excitation of the laser crystal.

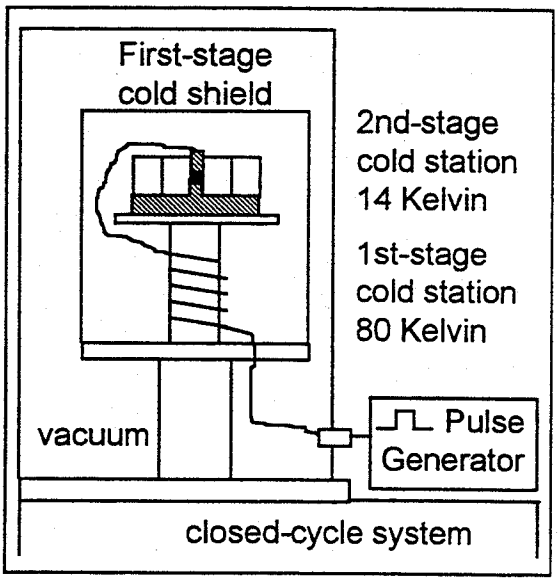

Figure 3: Permanent magnet laser set-up mounted in a closed-cycle machine. The machine specifications allowed a minimum temperature of 14.3 K on the 2nd-stage cold station. The electric pulse for excitation of the laser crystal was delivered by a pulse generator with variable pulse duration and repetition rate.

The laser crystal was excited by an electric field pulse. The laser radiation was directed through four windows made of black polyethylene, Teflon (PTFE) and TPX (poly 4-methyl pentene-1) onto a Ge:Ga photodetector [11] in a LHe-cryostat (Fig. 4(a)). The detected laser signal was observed directly on a digital oscilloscope.

The experiments with 1, 2 and 3 pairs of permanent magnets show an increase of laser intensity with magnetic field accompanied by an increase of the limiting laser temperature up to 20 K (Fig. 4(b)). The duty cycle for the Ge:Be laser cube in the closed-cycle machine reached values of up to 0.03% in comparison to 0.6% in LHe because of the limited cooling power of 0.5 W which raised the second-stage cold station temperature to 20 K. Modern closed-cycle machines can reach 4.2 K at a heat input of 1 W and 10 K at a load of 10 W which corresponds to the maximum dissipated electrical power of our best laser crystals in LHe.

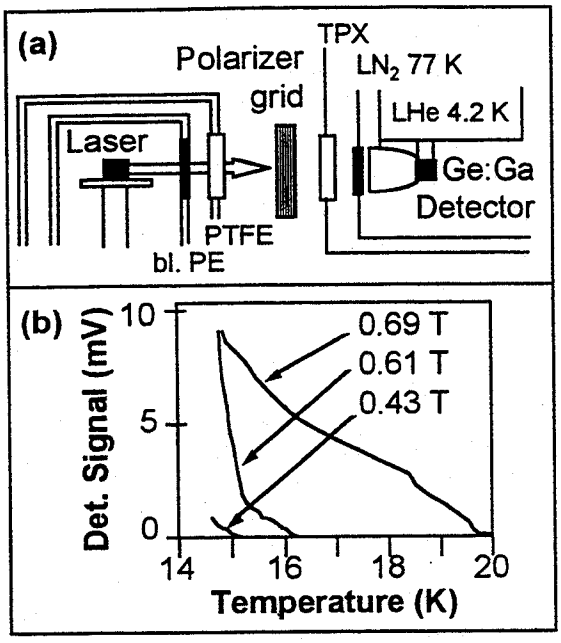

Figure 4: (a) Experimental set-up for measuring the polarization of the Ge:Be laser and temperature dependencies. (b) Laser intensity as a function of temperature and magnetic field.

IV. Polarization of the Ge:Be laser in Voigt configuration

The polarization was measured by introducing a rotating grid polarizer in the air-gap between the closed-cycle machine and the detector cryostat (Fig. 4(a)). The measured signal intensity passing the polarizer grid deviated from the theoretical curve of linear polarization due to the non-ideal polarizer (Fig. 5). With a 2.5 THz emission line of a gas laser with a Brewster window resulting in 100% linear polarization, we reproduced the same curve as measured with the Ge laser. The result is in accordance with theory for emission in the Voigt configuration which imposes quantum mechanical selection rules for linear polarization. In addition, the polarization is directed parallel to the magnetic field indicating the involvement of cyclotron resonance transitions [3]. We measured the emission in the Faraday configuration with the table-top LHe-cryostat. The polarization was found to be elliptical.

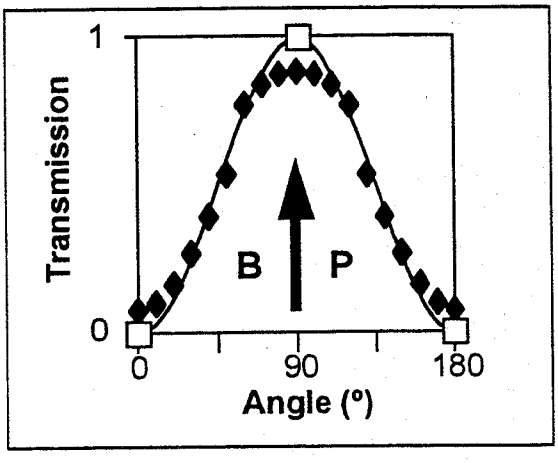

Figure 5: Polarization of the Ge:Be laser radiation. An ideal polarizer is defined by the open squares and the calculated function. Diamonds show the measured signal intensities indicating linear polarization P parallel to the magnetic field B.

V. Summary and conclusions

We have demonstrated that Ge lasers can meet the requirements of local oscillators for future THz heterodyne receivers. They feature linearly polarized radiation, a single mode tunability from 1 to 4 THz with narrow line widths, LHe-free operation in a closed-cycle machine with permanent magnets, and a high duty cycle of 2.5%. In the desired continuous wave mode the homogeneous Ge laser transition will result in single mode operation only defined by the quality and stability of the external resonator.

Further improvement of the laser geometry, the doping level, the cooling environment, the use of external resonators with mesh outcouplers and the application of uniaxial stress will reduce the total applied power and improve the heat dissipation. Careful crystal and surface preparation including crystal growth, contact formation and materials characterization might enable us to design a crystal with which we may reach the ultimate goal of continuous wave operation with mW output power.

Hot electron bolometers require only μW pumping power and operate in the same temperature range as Ge lasers [12]. Therefore, a future heterodyne receiver might consist of an array of hot electron bolometers integrated with a p-Ge laser in a standard table-top cryostat or closed-cycle machine.

We acknowledge the use of facilities at the LBNL operated under US DOE contract DE-AC03-76SF00098.

References

[1] E. Bründermann and H.P. Röser, 'Tunable p-Ge Laser in the Frequency Range from 1 to 4.5 THz', *Proc. 6th Int. Symp. on Space Terahertz Technology*, 159-166 (1995).

[2] E. Bründermann, A.M. Linhart, H.P. Röser, O.D. Dubon, W.L. Hansen and E.E. Haller, 'Miniaturization of p-Ge lasers: progress toward a tunable, CW THz laser', *Proc. 7th Int. Symp. on Space Terahertz Technology*, 187-194 (1996).

[3] O.D. Dubon, D. Chamberlin, W.L. Hansen, E.E. Haller, L.A. Reichertz, G. Sirmain, E. Bründermann, A. M. Linhart and H.P. Röser, 'Terahertz emission from p-type germanium lasers doped with novel acceptors', this conference issue.

[4] E. Bründermann, H.P. Röser, A.V. Muravjov, S.G. Pavlov, V.N. Shastin, 'Mode fine structure of the FIR p-Ge Intervalenceband Laser measured by Heterodyne Mixing Spectroscopy with an optically pumped ring gas laser', *Infrared Phys. Technol.* **1**, 59-69 (1995).

[5] E. Bründermann, A.M. Linhart, L. Reichertz, H.P. Röser, O.D. Dubon, W.L. Hansen, G. Sirmain and E.E. Haller, 'Double acceptor doped Ge: A new medium for inter-valence-band lasers', *Appl. Phys. Lett.* **68**, 3075-3077 (1996).

[6] G. Sirmain, L.A. Reichertz, O.D. Dubon, E.E. Haller, W.L. Hansen, E. Bründermann, A.M. Linhart and H.P. Röser, 'Stimulated far-infrared emission from copper-doped germanium crystals', *Appl. Phys. Lett.* **70**, 1659-1661 (1997).

[7] E. Bründermann, A.M. Linhart, H.P. Röser, O.D. Dubon, W.L. Hansen and E.E. Haller, 'Miniaturization of p-Ge lasers: progress toward continuous wave operation', *Appl. Phys. Lett.* **68**, 1359-1361 (1996).

[8] K. Park, R.E. Peale, H. Weidner and J.J. Kim, 'Submillimeter p-Ge laser using a Voigt-configured permanent magnet', *IEEE J. Quantum Electron.* **32**, 1203-1210 (1996).

[9] H.A. Leupold, A.S. Tilak and E. Potenziani, 'Adjustable Multi-Tesla Permanent Magnet Field Sources, *IEEE Trans. Magn.* **29**, 2902-2904 (1993).

[10] E. Bründermann and H.P. Röser, 'First operation of a far-infrared p-Germanium laser in a standard closed-cycle machine at 15 Kelvin', *Infrared Phys. Technol.* **38**, 201-203 (1997).

[11] E.E. Haller, 'Advanced Far Infrared Photoconductors and Bolometers', *Infrared Phys. Technol.* **25**, 257-266 (1985) and *Infrared Phys. Technol.* **35**, 127 (1994).

[12] A.V. Bespalov, G.N. Goltsman, A.D. Semenov and K.F. Renk, 'Determination of the far-infrared emission characteristic of a cyclotron p-germanium laser by use of a superconducting Nb detector', *Solid State Comm.* **80**, 503-506 (1991).

Investigations of High-Resistivity, Undoped GaP Crystal for Quasi-Phasematched Difference Frequency Generation to Produce Terahertz Frequency Local Oscillators

Gregory S. Herman
Science Applications International Corporation
1 Enterprise Parkway, Suite 300
Hampton, Virginia, 23508

Stephen P. Sandford
NASA Langley Research Center, M/S 468
Hampton, Virginia, 23681

We are investigating high-resistivity, undoped GaP crystal as a useful nonlinear optical material for producing terahertz frequency local oscillators using nonlinear optical frequency conversion, a.k.a. laser mixing. Diffusion-bonded stacked (DBS) crystal structures are being developed for quasi-phasematched nonlinear optical frequency conversion from Near-Infrared (NIR) to Far-Infrared (FIR) wavelengths. Sellmeier equations predict coherence lengths for this interaction in GaP to be approximately 960 micrometers. To increase conversion efficiency, a resonantly-enhanced difference-frequency generation scheme is being employed.

At NASA Langley Research Center, a system is being developed whereby a small percentage of the pump and signal laser energy (1064 nm and 1074 nm, respectively) is diverted and used to actively frequency-lock the pump and signal lasers to adjacent longitudinal modes of an ultrahigh finesse Fabry-Perot reference cavity, thereby greatly enhancing their relative stability. Frequency stability measurements made at NASA Langley with low power lasers using Pound-Drever-Hall locking combined with a new cavity locking technique have demonstrated submillihertz linewidths. The majority of the pump and signal laser energy is than coupled into an external cavity that surrounds the DBS GaP structure to build up the field intensity at the pump and signal wavelengths while the idler wave (118 micrometers) is coupled out.

Tuning must be made in increments of the free spectral range of the reference cavity (~3 GHz). Tuning between resonances can be achieved by altering the length of the reference cavity. Depending on the desired system efficiency, frequency-stability, and complexity, the signal laser can either be another Nd:YAG laser operating at 1074 nm (for the 2.5 terahertz OH line), a diode-pumped solid-state laser with a different host material, such as GSGG, or a 532-pumped optical parametric oscillator, operating near degeneracy, which could achieve continuous tuning from 100 GHz to 3.0 THz.

Investigation of Surface Profiles of a Reflector from Near-field Beam Measurements

M. T. Chen[1] and C. E. Tong[2]

[1]Institute of Astronomy and Astrophysics
Academia Sinica, Taipei, Taiwan 115.
e-mail : mchen@biaa.sinica.edu.tw

[2]Harvard-Smithsonian Center for Astrophysics,
60 Garden St., Cambridge, MA 02138.

ABSTRACT

We have investigated a technique to map out surface defects of a reflector from near-field vector measurements. In our experiment a near-field range is set up to measure the beam reflected from a test surface at 240 GHz. A full-wave numerical method based on a vectorial Green's function is implemented to project the measured beam profile onto the mirror's surface. We then examine the differential phase pattern constructed from two separate scans, one with a known artifact and another without, to reveal features due to the artifact. Our experiments demonstrate that resolution down to a few degrees in phase can be obtained with this method.

I. Introduction

This report describes a technique to examine surface defects of reflectors using near-field measurements at a frequency of 240 GHz. The motivation is to investigate the application of such a technique on large parabola reflectors which usually span a few meters in diameter and which require a high accuracy in the surface profile.

In this technique a reflector, which is the test surface, is placed in the near-field of a transmitter, and the reflected beam pattern, including power and phase, is measured with a planar scanner also located at the near field. A computation code based on a vector Kirchhoff integral is implemented to construct, from the scanned data, the complex beam pattern at the reflector surface. Surface defects on the reflector can be associated with anomalous phase pattern in the calculated phase profile.

II. Near-field measurement and numerical calculation technique

The near-field measurement technique presently used is similar to those applied extensively at microwave frequencies. Figure 1 shows a schematic of the measurement setup. The signal is generated from a phase-locked Gunn oscillator operating at 80 GHz. After multiplication, the corrugated feed emits a signal at a frequency of 240 GHz. The reflector is a 90-degree, off-axis paraboloidal mirror with an aperture of 50 mm in diameter. The horn aperture is placed at the focal plane of the mirror with its beam axis perpendicular to the mirror axis. In the scan plane a WR-3 open wave-guide equipped with a harmonic mixer serves as the scanner probe. The scan plane is aligned to be perpendicular to the mirror axis at a distance of 108.2 mm away from the mirror center. The measured signal is down-converted and detected by a vector voltmeter. In the current setup we achieve a dynamic range of 40 dB.

The corrugated feed is made for the Sub-Millimeter Array (SMA) project. In a previous measurement the aperture field of the feed has been shown to conform to the HE11 mode to a purity of better than 99%, and the cross-polar power is less than 0.5% of the co-polar component [1].

The numerical method is a computation program based on a vector Kirchhoff integral [2]. Assuming an arbitrary source located in the half space $z<0$, the electric field at $z > 0$ can be expressed in an integral form, in terms of the field distribution on the plane $z = 0$, as

$$\vec{E}(\vec{r}) = \frac{1}{2\pi}\int_S \frac{e^{ikR}}{R^2}\left[ik - \frac{1}{R}\right]\cdot \vec{R}\times\left[\hat{z}\times\vec{E}(\vec{r}_0)\right]\cdot dS \qquad (1)$$

where k is the propagation constant, $\hat{z}$ the normal vector of the plane $z = 0$, and $\vec{R} = \vec{r} - \vec{r}_0$. Based on the above formulation, a numerical program is implemented to calculate the electric field on a target plane of interest from an initial plane with known field distribution. In our application, the scan data becomes the initial field and the code is used to generate the field pattern on the reflector.

III. Measurements and Results

To simulate surface defects, a small piece of aluminized tape with a thickness of 50 μm, equivalent to 1/25th of the signal wavelength, is attached to the reflector. Two separate scans are carried out; one with a taped reflector, and another without. Both

scanned data are processed to construct their relevant beam patterns on the reflector. Finally, the difference in phases between both runs is used to generate a differential phase map on the reflector surface. By examining the differential phase profile we have avoided the complexity introduced by the setup alignment and the possible intrinsic defect of reflector surface.

Prior to the measurements, simulations of the near-field scanning were carried out to evaluate the effects caused by the discrete sampling points and finite scan area. The simulations assume an ideal field (HE11 mode) in the feed aperture, and the numerical code based on Eq. (1) is used to calculate the scan patterns reflected from both a perfect and a defect paraboloidal mirror. In this case, a reflector with surface defects is simulated by introducing phase delay on part of the reflector surface when calculating the beam pattern projected from the horn aperture. Both the simulated scan data are used to construct the differential phase profiles on the reflector.

Figure 2 shows the contours and a horizontal cut through the center of a phase map from a simulation in which a phase delay of 9 degrees has been added to a region around the center of the reflector. In this case the scanner is assumed to sample the field at a resolution of 81 x 81 points at a regular spacing of 0.625 mm. Also shown in the center cut for reference is this 9 degrees phase delay on the reflector surface. In a subsequent simulation we increase the scan area to 131 x 131 points, and the resulting plots are shown in Fig. 3. Compared with the previous run the phase map shows less phase ripples and a profile more closely related to the added phase artifact (refer to Fig. 3B).

The phase stability of the measurements is a critical factor toward achieving better surface resolution. Short-term phase fluctuation of less than 5 degrees is recorded during a typical measurement run. However, a slow drifting in phase may occur during the measurement due to the environmental change in the setup, which would ruin the result. Thus, too long a scanning duration is avoided. Two different scan sizes have been used in this report. In our setup, it takes about an hour to scan 85 by 85 points, and 100 minutes for a scan of 115 by 115. The distance between each point is 0.6 mm. Figure 4 presents the plots of the phase map obtained from a scan of 85 x 85 points. Accompanying the contours is a plot showing horizontal cut through the maximum peak of the phase map. The main feature in these plots showing the anomalous phase contours, near the center of the reflector, which resembles the shape of the tape. Although it is clear that the tape's cross-sectional profile is not resolved due to insufficient scanning area, a peak value of 13 degrees in the anomalous contours indicated a maximum path-length difference of 45 μm, which is close to the actual thickness of the tape. As shown in Fig. 4B, the phase profile shows that there are a few degrees of peak-to-peak phase fluctuation near the center of the

reflector, and this increases to more than 5 degrees near the edge of the reflector. A surface plot of the phase map is shown in Fig. 4C.

Figure 5 shows the plots from the results constructed from a scan of 115 x 115 points. From the contour map the morphology of the defect area is clearly seen, which in this case is a triangular in shape. In contrast to the simulation of larger scan area, as shown in Fig.3, the tape's profile is still not shown, and the noise floor has somewhat larger fluctuation compared to the previous result. This may be caused by lower signal-to-noise data when the probe is scanning outside the reflector's aperture.

IV. Summary

Using a near-field measurement setup operating at 240 GHz, we have demonstrated that the surface profile of a reflector in the signal path can be examined via a numerical method based on the vector Kirchhoff integral. To achieve better phase resolution of this technique, the phase stability and signal-to-noise in the measurement, and the scan resolution must be improved. In this preliminary report, we have shown that surface defects that introduce a few degrees of phase error on the reflector's surface can be resolved.

References:

1. M. T. Chen, C. -Y. E. Tong, S. Paine, and R. Blundell, "Characterization of Corrugated Feed Horns at 216 and 300 GHz", International Journal of Infrared and Millimeter Waves, Vol. 18, No. 9, pp. 1697-1710, September, 1997.

2. A. J. Yaghijian, "An Overview of Near-field Antenna Measurements", IEEE Trans. Antenna Propagat., vol. 34, pp. 30-45, Jan. 1986.

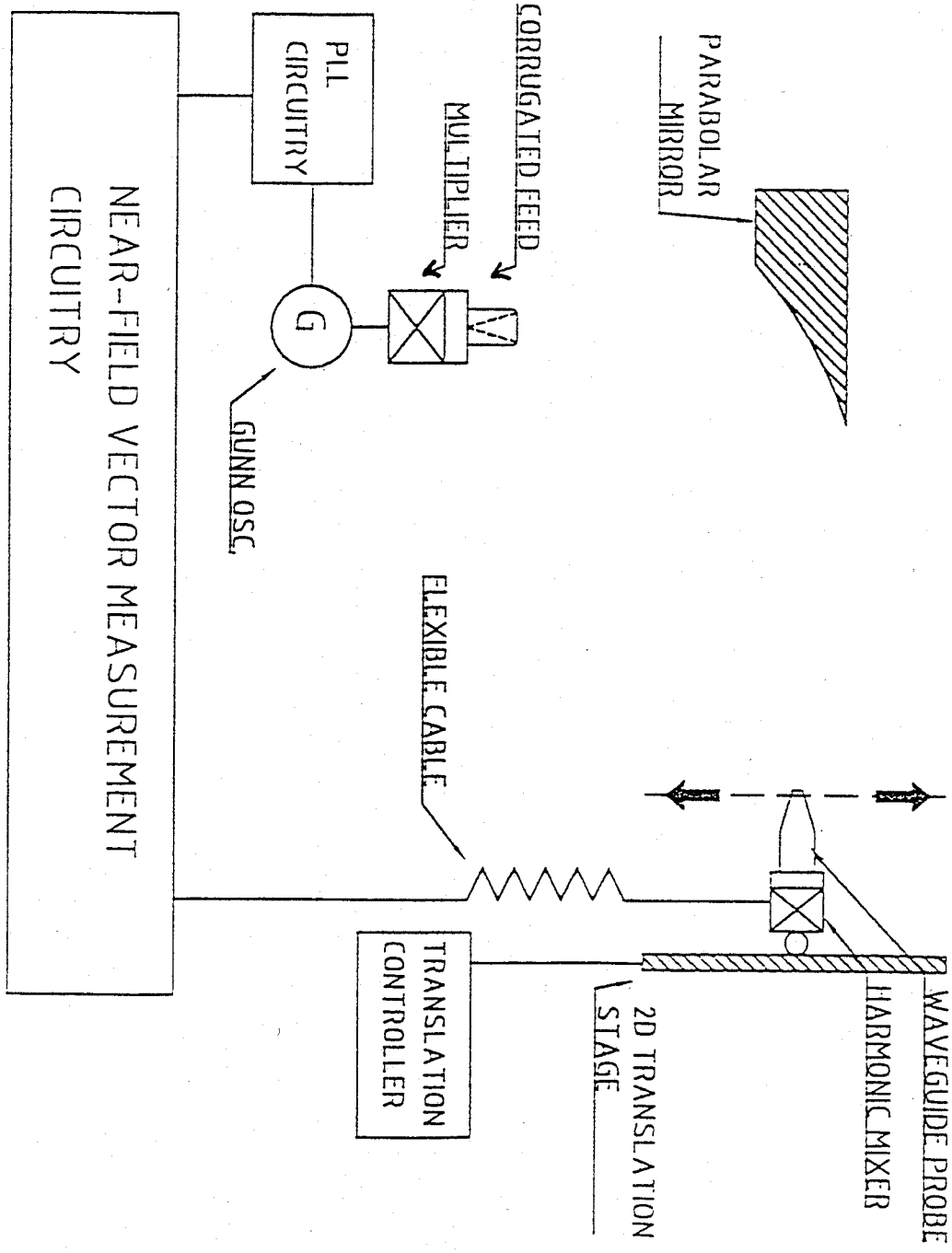

Figure 1. Schematic of near-field measurement setup.

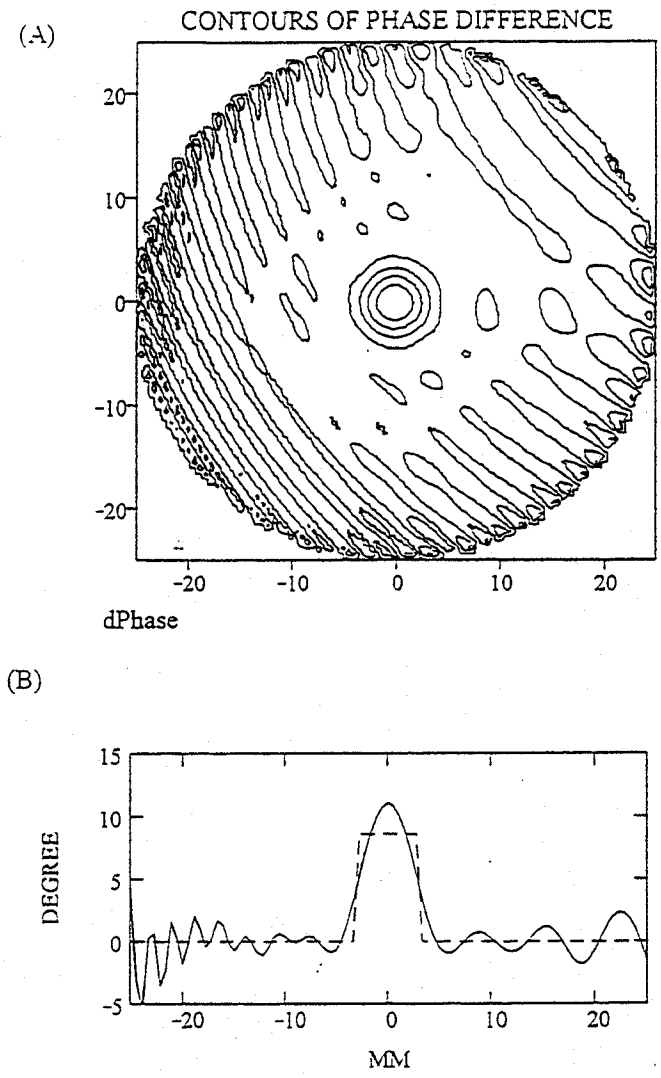

Figure 2. (A) Contour plot of the differential phase map, and (B) a horizontal cut through the contour center on the reflector's surface. The result is obtained from a simulation of 81 x 81 scan points spaced regularly at 0.625 mm in between. The dashed line in (B) is the phase delay used in the simulation as the surface defect.

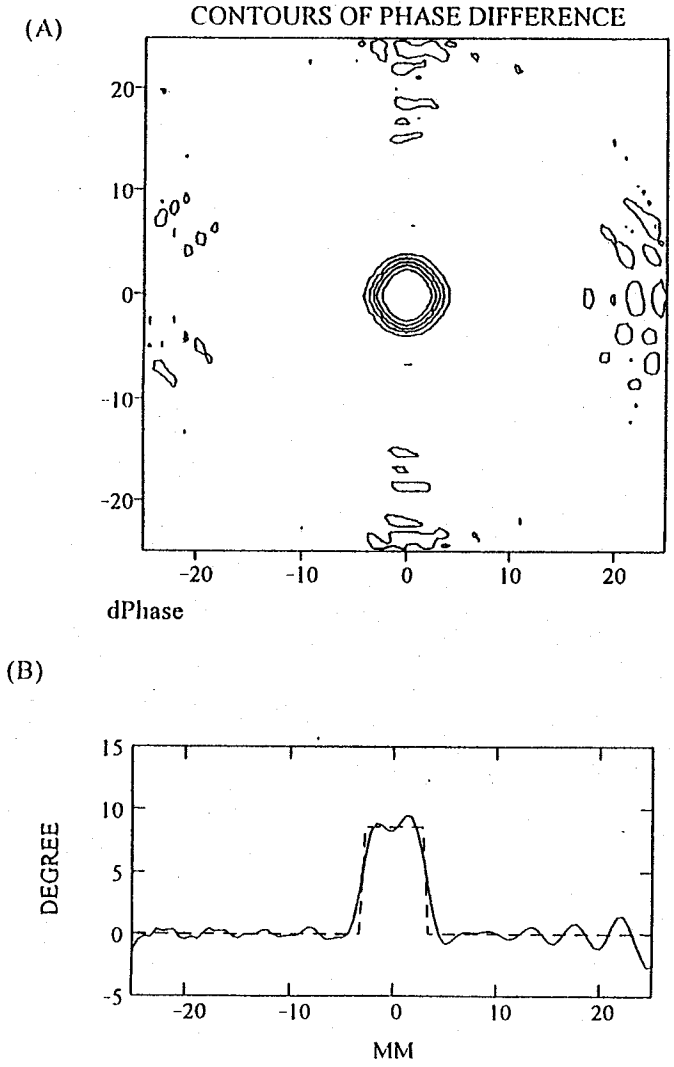

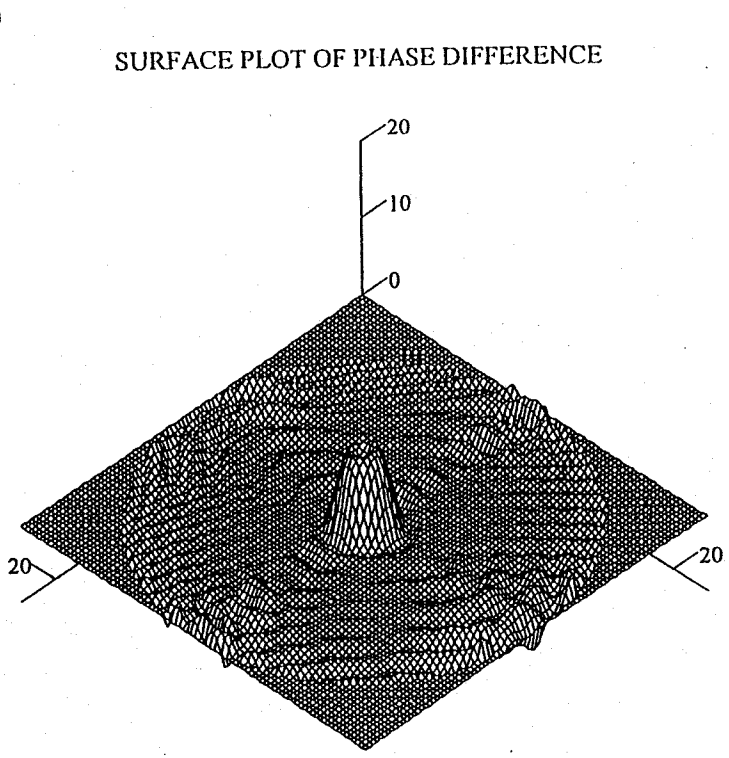

Figure 3. (A) Contour plot, (B) a horizontal cut through the contour center, and (C) a surface plot of the differential phase map on the reflector's surface obtained from a simulation of 115 x 115 scan points spaced regularly at 0.625 mm in between. The dashed line in (B) is the phase delay used in the simulation as the surface defect.

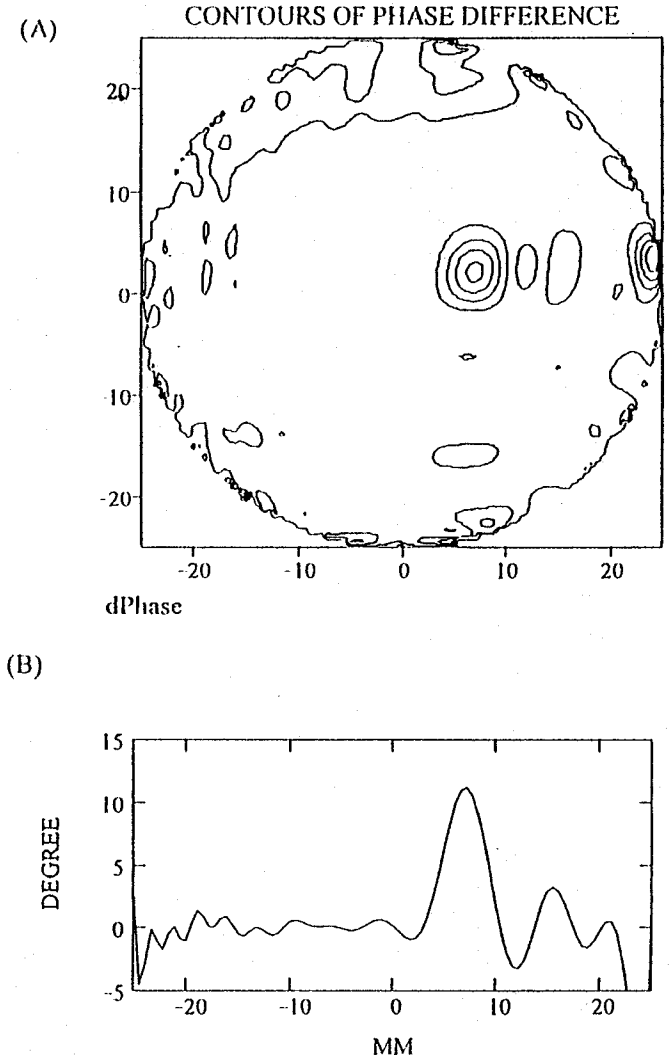

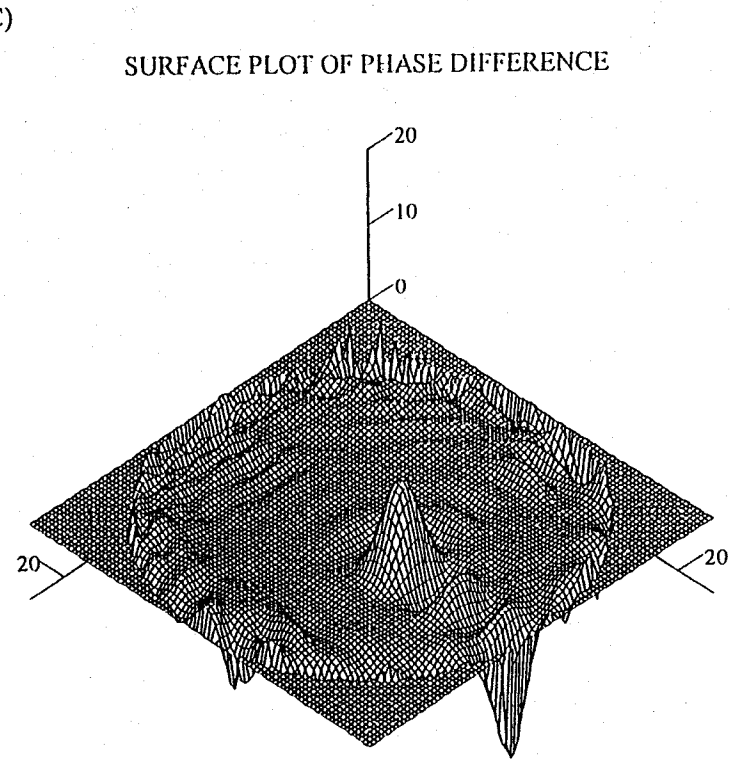

Figure 4. (A) Contour plot, (B) a horizontal cut through the anomalous contour peak, and (C) a surface plot of the differential phase map on the reflector's surface constructed from a measurement result of 85 x 85 scan points spaced regularly at 0.6mm in between.

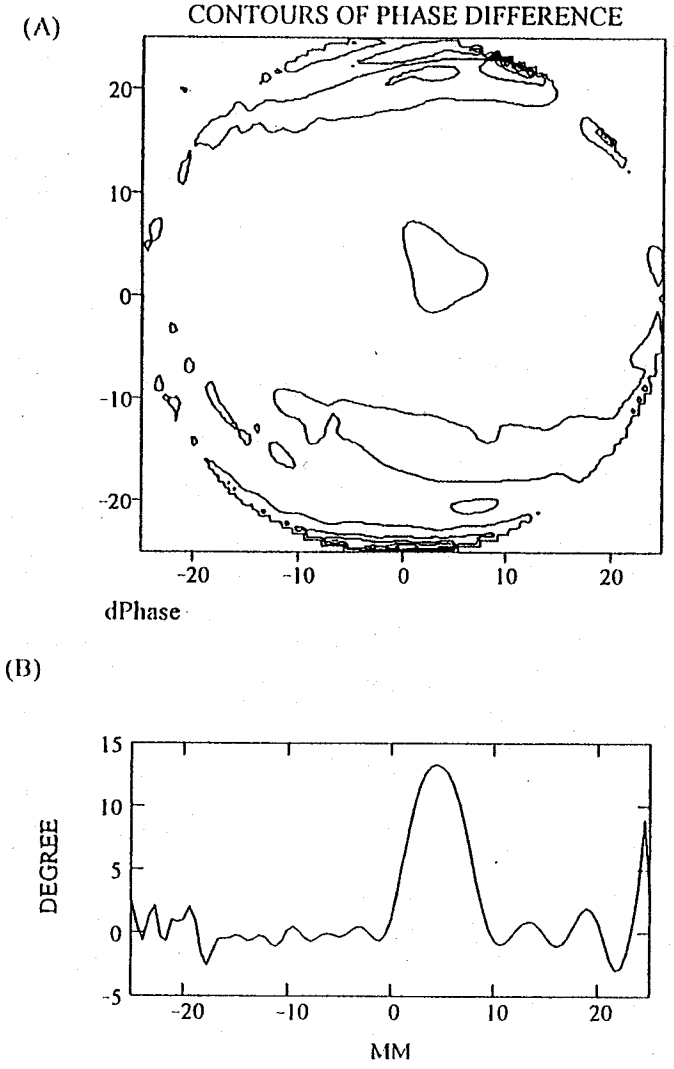

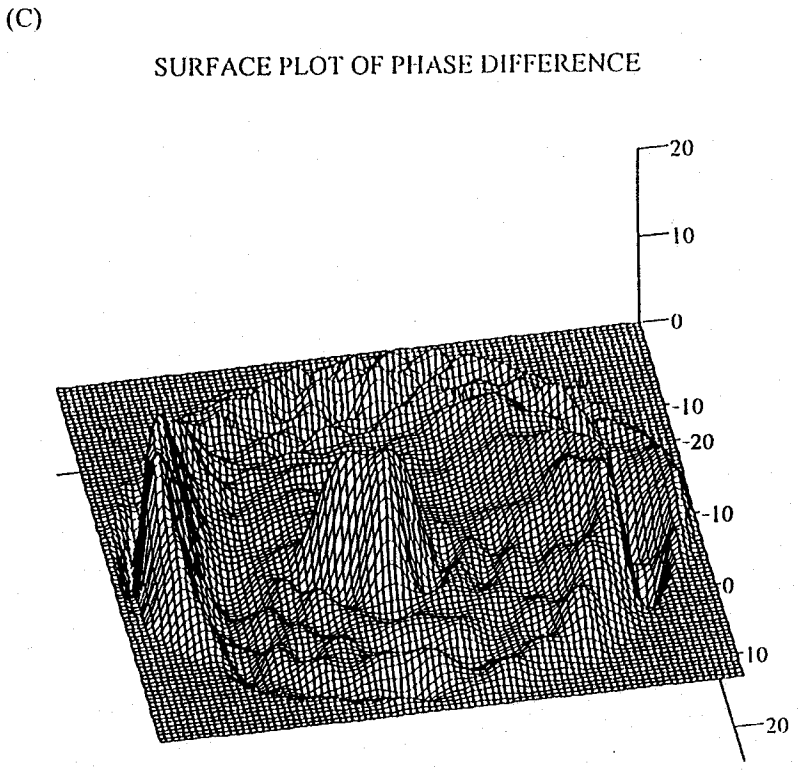

Figure 5. (A) Contour plot, (B) a horizontal cut through the anomalous contour peak, and (C) a surface plot of the differential phase map on the reflector's surface constructed from a measurement result of 115 x 115 scan points spaced regularly at 0.6mm in between.

Modal Analysis of Partially-Coherent Submillimetre-Wave Quasioptical Systems

S. Withington [1] and J.A. Murphy[2],
[1]Cavendish Laboratory, University of Cambridge, UK
[2]St. Patrick's College, Maynooth, Ireland

March 19, 1997

Abstract: We consider the modal analysis of partially-coherent submillimetre-wave quasioptical systems. According to our scheme the cross-spectral density is expanded as a sum of partially-coherent propagating free-space modes. The coherence matrix, the elements of which are determined by evaluating bimodal overlap integrals, completely describes the state of the field at a plane and can be traced through the optical system to another plane by means of a scattering matrix. Whereas diagonalising the scattering matrix gives the natural modes of the optical system, diagonalising the coherence matrix gives the natural modes of the field. As a special case, we consider the case where the field at the source plane is completely incoherent. After developing a number of analytical tools, we demonstrate the technique by analysing the behaviour of a Gaussian-beam telescope. Throughout the paper we emphasise the physical significance of the equations derived.

1 Introduction

We consider the Gaussian-mode analysis of partially-coherent submillimetre-wave quasioptical systems. Our primary aim is to show that the modal techniques that have been developed for the analysis of coherent optics [1, 2, 3] can be extended to cover the case when the field propagating through the system is partially coherent. Partial coherence arises in some form in all problems of practical importance. For example, consider the case where a submillimetre-wave telescope is used to observe an extended radio astronomical source. Usually, for heterodyne receivers, one would calculate the coupling between the detector and the source by propagating the fully-coherent field of the horn 'backwards' through the optical system onto the sky [4, 5]. There is no reason why, however, the analysis should not proceed in the opposite direction; that is to say it should be possible, at least in principle, to propagate the fully-incoherent field of the source 'forward' through the optical system onto the focal plane. In the first case, the field passing through the system is single moded even though the optical system itself is multimoded; whereas, in the second case, the field is multimoded. Clearly, one has to distinguish between the modal properties of the field and the modal properties of the optical system through which the field is passing.

In this paper, we describe a procedure that allows the second-order statistical properties of a field to be traced through a complex system of long-wavelength optical components. The partially-coherent field is constructed from coherent, diffracting free-space modes. A key feature of the scheme is that the description of the *field* is complete—in addition to the description of the *optical system* being complete—and therefore problems of almost any complexity can be solved. For example, we are currently investigating the behaviour multi-mode bolometer imaging arrays, where the state of the overall field is described by a single coherence matrix. Even in the case of a single-

mode detector, the unused, orthogonal modes will be excited by noise, and this noise appears in the analysis in a natural and elegant manner. Not only does the technique allow the throughput of complex systems to be determined, but it also provides a considerable amount of physical insight into the way partially-coherent submillimetre-wave optical systems behave. Looking to the future, it should be possible to study the injection of noise by lossey scattering components and the effects of a fluctuating medium such as the atmosphere. At a deeper level, modal analysis provides an understanding of the thermodynamic entropy of a beam in a such a way that maximum entropy techniques could be used to examine, in some detail, the state of a collimated field from intensity measurements alone.

In the first part of the paper, we review the integral-equation description of the propagation of a partially-coherent field. This form provides the starting point for an analysis in terms of free-space modes. We then describe the way in which the second-order statistical properties of a free-space beam can be decomposed into a sum of partially-coherent modes which propagate easily and which can be scattered at optical components. The form of the partially-coherent field at a plane is fully characterised by a coherence matrix. We show that the coherence matrix can be diagonalised to render the natural modes of the field. These modes are individually fully coherent but have no well-defined phase relationship between each other. In this sense they propagate in an independent manner.

We explain how the elements of the coherence matrix can be determined through bimodal overlap integrals, and we show how the mode set should be chosen so that the field can be represented with near-optimum numerical efficiency. We describe how the coherence matrix can be propagated in both the forward and backward directions. We then consider the special case when the illuminating field is fully incoherent. This situation occurs, for example, when the beam from a radio telescope and all of its sidelobes are coupled into an extended isothermal source. In this case coherence builds up as the field propagates and the natural modes of the field at the output plane are the same as the natural modes of the optical system.

To illustrate the technique we consider in some detail the one-dimensional Gaussian beam telescope. This particular example allows us to demonstrate clearly the basic physical concepts. We assume scalar fields, but this is not an intrinsic limitation of the scheme. The Gaussian beam telescope is analysed in terms of Gaussian-Hermite modes and recursion relationships are used to calculate the scattering matrices of the individual apertures. The behaviour of the whole system is then characterised by a single low-order scattering matrix which is simply the product of the scattering matrices of the individual components. When considering a more complicated system all that needs to be done is to replace the scattering matrix of the Gaussian-beam telescope with that of the actual system under consideration. To complete the paper, we present various useful analytical tools, and demonstrate the overall method by analysing the behaviour of a Gaussian-beam telescope when a partially-coherent field is applied.

2 Classical analysis

We assume that the submillimetre-wave system to be analysed comprises a sequence of components that interact with and scatter a propagating free-space beam [6, 7]. From a classical point of view, assuming for a moment full coherence, the optical system maps the field at the input plane onto the field at the output plane in a linear manner: $E_1(\mathbf{r}_1) \mapsto E_2(\mathbf{r}_2)$. Here, $\mathbf{r}_1$ and $\mathbf{r}_2$ represent position vectors on the input and output surfaces respectively, and a subscript on a quantity denotes the plane over which the quantity is being considered. Because the mapping is linear, we can express

the output field in the form

$$E_2(\mathbf{r}_2) = \int_{S_1} E_1(\mathbf{r}_1)\, K(\mathbf{r}_2|\mathbf{r}_1)\, dS_1 \ , \tag{1}$$

where the integral is evaluated over the input surface S_1. Although, it is tempting to assume that the input surface is flat and perpendicular to the beam, this does not have to be the case, and any surface which contains the beam can be used if the appropriate kernel $K(\mathbf{r}_2|\mathbf{r}_1)$ is known. It is important to appreciate that the kernel is a function of both the input and output coordinates, and therefore the system does not have to be isoplanatic. As a consequence the formalism is applicable in cases where significant aberrations are present. This feature contrasts with Fourier Optics where the kernel has to be space invariant [8].

When cast in its modal form, the above equation can be used to analyse in detail the behaviour of fully-coherent submillimetre-wave optical systems [2]. In many cases, however, the source is not coherent and another level of sophistication is required. If we define the cross-spectral density of an ensemble of random fields to be

$$W_2(\mathbf{r}_2', \mathbf{r}_2) = \langle E_2(\mathbf{r}_2)\, E_2^*(\mathbf{r}_2') \rangle \ , \tag{2}$$

where $\langle\rangle$ denotes the ensemble average, and quasimonochromatic fields are assumed, then through (1) it is trivial to show that the cross-spectral density propagates according to

$$W_2(\mathbf{r}_2', \mathbf{r}_2) = \int_{S_1} W_1(\mathbf{r}_1', \mathbf{r}_1)\, K(\mathbf{r}_2|\mathbf{r}_1)\, K^*(\mathbf{r}_2'|\mathbf{r}_1')\, dS_1 dS_1' \ , \tag{3}$$

where $\mathbf{r}_1$ and $\mathbf{r}_1'$ represent two different points on the input surface. Hence, we can calculate the cross-spectral density on the output surface if we know the cross-spectral density on the input surface. Again it is emphasised that the optical system does not have to be isoplanatic.

A special case arises when the field on the input surface is everywhere fully incoherent. This situation will only occur at the position of a source as any propagation or scattering will induce some degree of coherence, as will be shown later. In the case when the input is fully incoherent we can write

$$W_1(\mathbf{r}_1', \mathbf{r}_1) = I(\mathbf{r}_1)\, \delta(\mathbf{r}_1 - \mathbf{r}_1') \ , \tag{4}$$

where $I(\mathbf{r}_1)$ is the intensity of the source. Substituting in the expression for the propagation of the cross-spectral density, (3), we get

$$W_2(\mathbf{r}_2', \mathbf{r}_2) = \int_{S_1} I_1(\mathbf{r}_1')\, K(\mathbf{r}_2|\mathbf{r}_1')\, K^*(\mathbf{r}_2'|\mathbf{r}_1')\, dS_1' \ . \tag{5}$$

In general, an incoherent source will lead to coherence in the output plane.

Finally, if we are only interested in the intensity of the field at the output plane,

$$I(\mathbf{r}_2) = W_2(\mathbf{r}_2, \mathbf{r}_2) = \int_{S_1} I_1(\mathbf{r}_1')\, |K(\mathbf{r}_2|\mathbf{r}_1')|^2\, dS_1' \ . \tag{6}$$

We can see that for an incoherent source, and for the case where one is only interested in intensity, the output is linear in intensity and the kernel is the square modulus of the kernel associated with the fully-coherent case [9]. This equation describes, of course, the way in which a telescope images the brightness distribution of an astronomical source onto its focal plane.

The imaging properties of optical systems are usually understood in terms of Fourier expansions of the above equations. Unfortunately, Fourier Optics can only be used in the case of ideal, isoplanatic systems, and moreover the equations derived only relate fields at conjugate Fourier planes. What we would like is a simple scheme based on multimode Gaussian optics that allows the statistical properties of a field to be calculated at any intermediate plane.

3 Gaussian-mode expansion of the cross-spectral density

For partially-coherent systems, the quantity we wish to decompose into modes is the cross-spectral density: where, formally, we understand the cross-spectral density to be the time Fourier transform of the mutual coherence function. We can achieve this end by assuming that the optical system under consideration is one member of an ensemble. If the bandwidth is sufficiently narrow so that the coherence length is very much greater than the physical size of the system, the phase at one point in one member of the ensemble is well defined with respect to the phase at another point in the same member of the ensemble. As in the coherent case, the field can then be written as a modal sum [10]:

$$E^i(\mathbf{r},\omega) = \sum_m A_m^i(\omega)\,\psi_m(\mathbf{r},\omega)\ , \tag{7}$$

where we tacitly understand that if the system is two dimensional, the index labelling the mode represents two indices. In this equation, i denotes a particular member of the ensemble, and the frequency dependence of the mode coefficients has been indicated explicitly by ω. Obviously, we can now represent the cross-spectral density at some plane in terms of this expansion:

$$\begin{aligned} W_1(\mathbf{r}_1',\mathbf{r}_1) &= \langle E_1(\mathbf{r}_1)\,E_1^*(\mathbf{r}_1')\rangle \\ &= \sum_m\sum_{m'} C_{m,m'}\psi_{m'}^*(\mathbf{r}_1')\,\psi_m(\mathbf{r}_1)\ , \end{aligned} \tag{8}$$

where

$$C_{m,m'} = \left\langle A_{m'}^{i*} A_m^i \right\rangle\ . \tag{9}$$

The above equation is simply the bimodal expansion of the cross-spectral density. From a physical point of view, the non-negative-definite Hermitian form ensures that a positive intensity is formed when two parts of the field are combined in an interferometer. In the above equation we have dropped the explicit reference to frequency, but it must be remembered that to get the full behaviour over a range of frequencies, the appropriate integration must be carried out.

For convenience we can write the coefficients of the bimodal expansion in matrix form:

$$\mathbf{C} = \left\langle \mathbf{A}^i \mathbf{A}^{i*T} \right\rangle \tag{10}$$

where $\mathbf{A}^i$ is the column vector of mode coefficients corresponding to the i'th member of the ensemble, and $*T$ denotes the conjugate transpose. Clearly, once we know the expansion coefficients $\mathbf{C}$ we have characterised the form of the partially-coherent beam at a plane. The propagation of the coherence matrix in the partially-coherent case is equivalent to the propagation of the mode coefficients in the fully-coherent case.

Although physically appealing the above argument is not mathematically rigorous. The problem lies in the fact that, in order to generate the modal expansions, we tacitly assumed that we could Fourier transform the time-dependent field of each member of the ensemble, and yet it is well known that it is not possible, because of lack of convergence, to Fourier transform the members of a stationary random process. Wolf has considered the modal expansion of three-dimensional stationary random fields in some detail [11, 12]. He showed that in order to avoid the introduction of generalised Fourier transforms, it is possible to set up an ensemble which generates the cross-spectral density as an ensemble average of mode coefficients of ordinary functions. The arguments are somewhat involved, but the outcome is that modal expansions of the above kind are rigorously correct, as physical intuition would suggest. The essential point to bear in mind is that one is propagating a statistical property of the field rather than the field itself, and this quantity, the cross-spectral density, propagates according to Helmholtz equations.

We now need to know how to calculate the mode coefficients when the functional form of the cross-spectral density is known. By a simple extension of the usual overlap integral we find that the elements of the coherence matrix are given by

$$C_{m,m'} = \int_{S_1} W(\mathbf{r}_1', \mathbf{r}_1)\, \psi_{m'}(\mathbf{r}_1')\, \psi_m^*(\mathbf{r}_1)\, dS_1 dS_{1'} \,. \tag{11}$$

In general, we do not know the cross-spectral density at every plane, but there is usually some plane over which the cross-spectral density is known.

4 Natural modes of a partially-coherent field

At this stage we have expanded the cross-spectral density in terms of some basis mode set. We can of course transform to some other basis set and describe the field equally well. It is a basic feature of the Hermitian form given above, that if the cross-spectral density is to remain unchanged under this transformation, the transformation must be unitary. That is to say there is some transformation $\mathbf{U}$, for which $\mathbf{U}\mathbf{U}^{*T} = \mathbf{I}$ and $\mathbf{U}\mathbf{C}\mathbf{U}^{*T}$ is diagonal. Of particular interest is the transformation that diagonalises the coherence matrix. In a sense, the modes found in this way are the natural modes of the field, because then the partially-coherent field is represented by a sum of modes which are individually fully spatially coherent but completely incoherent with respect to each other.

The problem of how to expand the cross-spectral density of a three-dimensional random field in terms of its natural modes has been considered by Wolf [11, 12], who approached the problem not by thinking about the system in which the field is contained but by thinking about the intrinsic properties of the field itself. The solution is to remember Mercer's theorem, which essentially states that if the kernel of a homogeneous Fredholm equation of the second kind is Hermitian and nonnegative definite then the eigenvalue spectrum is discrete, real and the eigenvectors form a complete orthonormal set in terms of which the kernel can be expanded. When looking for a bimodal expansion, it is therefore natural to set up an integral equation of the form

$$\lambda_i \phi_i(\mathbf{r}_1) = \int W(\mathbf{r}_1', \mathbf{r}_1)\, \phi_i(\mathbf{r}_1')\, d\mathbf{r}_1' \tag{12}$$

so that the kernel can be expressed as a weighted sum of eigenfunctions:

$$W(\mathbf{r}_1', \mathbf{r}_1) = \sum_i \lambda_i \phi_i^*(\mathbf{r}_1')\, \phi_i(\mathbf{r}_1) \,. \tag{13}$$

These eigenfunctions, ϕ_i, are the natural modes of the field, and λ_i are the associated eigenvalues.

We can now ask what is the relationship between Wolf's natural mode set and the modes that we have used. If we expand the natural modes as a sum of our—as yet undefined—propagating modes, we have

$$\phi_i(\mathbf{r}_1) = \sum_n A_n^i \psi_n(\mathbf{r}_1) \,, \tag{14}$$

and if we substitute this equation together with the bimodal expansion (8) into the eigenvalue expression (12), we find that

$$[\mathbf{C} - \lambda_i \mathbf{I}]\, \mathbf{A}^i = 0 \,, \tag{15}$$

where now $\mathbf{A}^i$ are the mode coefficients of the natural mode i and λ_i is the associated eigenvalue. Hence, if we know the cross-spectral density at some plane, we can construct the coherence matrix by evaluating the overlap integrals and then we can find the natural modes by finding the eigenvectors through (15).

To understand the physical meaning of these expansions, suppose that we have an ensemble of optical systems, where the field associated with each member of the ensemble is constructed from

spatially-coherent modes, the phases of which are fully incoherent and uniformly distributed with respect to each other. In this case we have

$$C_{mm'} = \left\langle \left|A^i_{m'}\right| \left|A^i_m\right| \right\rangle \left\langle \exp\left[j\left(\theta^i_m - \theta^i_{m'}\right)\right] \right\rangle = \lambda_m \delta m, m' \ . \tag{16}$$

The coherence matrix is diagonal as one would expect. If, however, we now transform to another arbitrary mode set, it is easy to show and physically reasonable, that the mode coefficients become partially coherent and the coherence matrix is no longer diagonal.

In summary, we can expand the cross-spectral density in terms of any convenient mode set by using the bimodal form of the overlap integral. Because the modes are not chosen in any particular way, correlations will exist between the mode coefficients and the coherence matrix will be full. Here we are expanding the cross-spectral density in terms of a set of fully spatially-coherent modes which are partially coherent with respect to each other. If we diagonalise the coherence matrix, we can express the cross-spectral density as a sum of modes which are completely uncorrelated with respect to each other, and therefore have no definite phase relationship between them. These are the natural modes of the optical field defined by Wolf.

Expanding a random process as a sum of orthogonal uncorrelated functions is known as a Karhunen-Loéve expansion, and in general an expansion can be found even when the process is not stationary. For example, in adaptive optics, the randomly distorted phase in the aperture of a mirror is usually expanded in terms of Zernike polynomials. The most efficient functions to use, however, when compensating for phase errors is the Karhunen-Loéve expansion [13] . There is a close relationship between the technique that we are promoting and the techniques of adaptive optics, but it must be appreciated the physical application is very different. In this paper, we are expanding a propagating field, whereas in adaptive optics it is the phase of the field at a plane that is being expanded. Nevertheless it would be particularly interesting to use partially-coherent Gaussian modes to model the behaviour of a submillimetre-wave telescope when a turbulent atmosphere is included.

5 Completely-incoherent sources

Of particular significance is the case where the field at the input plane is fully incoherent and has uniform intensity. This situation occurs for example when the beam of a submillimetre-wave telescope is coupled to a source of uniform brightness. For an incoherent field, we can write

$$W\left(\mathbf{r}'_1, \mathbf{r}_1\right) = I\left(\mathbf{r}_1\right) \delta\left(\mathbf{r}_1 - \mathbf{r}'_1\right) \ . \tag{17}$$

Substituting this form into the bimodal overlap integral we find

$$C_{m,m'} = \int_{S_1} I\left(\mathbf{r}_1\right) \psi_{m'}\left(\mathbf{r}_1\right) \psi^*_m\left(\mathbf{r}_1\right) dS_1 \ . \tag{18}$$

Now if the source has uniform brightness

$$C_{m,m'} = I_o \delta_{m,m'} \ ; \tag{19}$$

that is to say all of the modes are excited equally and independently. It can be shown that because of completeness this statement must be true regardless of what mode set is used. Physically, this must be true because the resultant field cannot contain any spatial information. In matrix form, we have for a uniform incoherent source

$$\mathbf{C} = I_o \mathbf{I} \tag{20}$$

where $\mathbf{I}$ is the identity matrix. Obviously, if the brightness over the plane of the source is not uniform, correlations must be induced between modes even though the source itself is incoherent. This behaviour is to be expected classically because the van Cittert-Zernike theorem tells us that correlations exist in the far field of a source of finite size even when the source itself is incoherent.

6 Propagating the correlation matrix

It is well known that a coherent field can be traced through a submillimetre-wave optical system by multiplying the mode coefficients of the incoming beam by a scattering matrix. Moreover, if the optical system comprises a number of optical components then the scattering matrix associated with the overall system is simply the product of the scattering matrices associated with the individual components [2]. This procedure is fundamentally based on the modal expansion of equation (1). That is to say the input and output fields, and the kernel, are expanded in terms of a convenient set of modes prior to evaluating the integral. In the case of a partially-coherent beam, we need to find the modal equivalent of equation (3); or in other words, we need to ask how the coherence matrix can be traced through an optical system once the scattering matrix is known.

We know that for each member of the ensemble we can propagate the field according to the usual Gaussian mode scattering matrix $\mathbf{S}$. Hence if the field at the input plane has mode coefficients $\mathbf{A}^i$ then the field at the output plane has mode coefficients $\mathbf{B}^i$ where

$$\mathbf{B}^i = \mathbf{S}\mathbf{A}^i \,. \tag{21}$$

The coherence matrix at the output plane therefore becomes

$$\left\langle \mathbf{B}^i \mathbf{B}^{i*T} \right\rangle = \mathbf{S} \left\langle \mathbf{A}^i \mathbf{A}^{i*T} \right\rangle \mathbf{S}^{*T} \,; \tag{22}$$

or

$$\mathbf{D} = \mathbf{S}\mathbf{C}\mathbf{S}^{*T} \,, \tag{23}$$

where $\mathbf{D}$ is the coherence matrix at the output plane, $\mathbf{S}$ is the usual coherent-mode scattering matrix, and $\mathbf{C}$ is the coherence matrix at the input plane. Hence we can calculate the scattering matrix associated with the optical system in the usual way, and then calculate the coherence matrix at the output plane if we know the coherence matrix at the input plane. Numerically, the procedure is very straightforward, and the scattering matrix only has to be calculated once for a given optical system. The scattering matrix contains all of the information necessary to propagate a coherent or incoherent field. Notice also that if the optical system under consideration is varying with time, as would be the case for a turbulent atmosphere above a telescope, then the ensemble average should include the time-varying scattering matrix.

It is also interesting to ask how we calculate the cross-spectral density at the *input* plane if we know the cross-spectral density at the *output* plane. This is clearly the imaging process in the case where we have complete knowledge about the amplitude and phase of the cross-spectral density in the focal plane. It is straightforward to show that as along as $\mathbf{S}^{-1}$ exists, the cross-spectral density at the input plane is given by

$$\mathbf{C} = \mathbf{S}^{-1}\mathbf{D}\left(\mathbf{S}^{-1}\right)^{*T} \,. \tag{24}$$

In a later paper, we will show how this leads to a general method for reconstructing images even in the case when the imaging array is far from ideal.

7 Analysis of partially-coherent submillimetre-wave optical systems

Before demonstrating the above techniques through the analysis of a particular system, it is useful to review the overall procedure with an emphasis on physical interpretation.

We now know that the properties of a partially-coherent field can be fully characterised by means of a coherence matrix. The coherence matrix is simply a convenient way of organising the

coefficients of a bimodal expansion of the cross-spectral density. The modes used in the expansion can be any orthonormal set, but it is convenient to use a set of modes that propagate easily. Later we will show that Gaussian-Hermite or Gaussian-Laguerre modes are almost ideal. Once the coherence matrix is known, it can be traced forwards or backwards through the optical system by using the ordinary coherent-mode scattering matrix. Finally, once the scattered coherence matrix is known, the cross-spectral density can be reconstructed at the output plane.

It is also straightforward to show that if we combine two fields at a plane that are generated incoherently then the overall coherence matrix is the sum of the two individual coherence matrices regardless of the states of coherence of the individual fields. This particular theory has application for example when a submillimetre-wave beam is truncated by a lossy aperture which injects noise of its own. We will show in a later paper how to calculate the coherence matrix of a lossey, passive component simply from knowledge of its temperature and scattering matrix. In general, therefore, not only can we propagate a partially-coherent field but we can also add in noise generated by lossey components. If required these noise sources can be referenced to one end of the optical system giving a set of noise parameters which completely characterises the noise performance of the system in much the same way as the noise properties of a microwave transistor are characterised by a set of noise parameters which are referenced to the input. In the case of an optical system the noise parameters take the form of a matrix of complex temperatures.

It is vitally important to appreciate that the coherence matrix characterises the modal properties of the field at a plane whereas the scattering matrix completely characterises the modal properties of the optical system. The two are, of course, distinct. In general, because an arbitrary mode set has been chosen to expand the cross-spectral density, the coherence matrix will be full showing that correlations exist between the modes. We can, however, diagonalise the coherence matrix to give the mode coefficients of the natural modes of the field, that is to say the modes that propagate independently with full spatial coherence but no definite phase relationship between them. The eigenvalues give the amount of power in each mode. In general, even though we do not diagonalise the coherence matrix we should choose a convenient mode set that makes the coherence matrix as near diagonal as possible. In this way the modes chosen will be as close as possible to the true natural modes of the field.

In a previous paper [2], we discussed the diagonalisation of the scattering matrix. In this case the eigenvectors give the mode coefficients of field distributions which pass through the optical system unchanged, and the eigenvalues give the loss associated with the propagation of these fields. These modes are the normal modes of the optical system, and in general any incoming field distribution can be expanded in terms of these modes and propagated through the system simply by multiplying by the eigenvalues. For convenience we choose a mode set that propagates easily and yet which diagonalises as near as possible the scattering matrix. In general the natural modes of the optical system are not the same as the natural modes of the field, and we can ask whether it is more reasonable to choose a mode set that near diagonalises the coherence matrix or a mode set that near diagonalises the scattering matrix.

It is now particularly revealing to ask what happens in the case where an optical system described by a scattering matrix $\mathbf{S}$ is illuminated by a uniform fully-incoherent source. We know that for any mode set the coherence matrix of a fully-incoherent source is diagonal, and therefore the field at the output plane of the optical system is described by

$$\mathbf{D} = I_o \mathbf{S} \mathbf{I} \mathbf{S}^{*T} . \tag{25}$$

It is clear that although the field at the input plane is fully incoherent, the field at the output plane has coherence induced on it due to mode filtering. The induction of coherence is evidenced by the appearance of off-diagonal terms in the output coherence matrix. We know, however, that there is some mode set that diagonalises the scattering matrix—the natural modes of the optical

system—and clearly in this case the coherence matrix at the output plane must also be diagonal. Hence, if the optical system is illuminated by an incoherent field, the natural modes of the field at some plane in the optical system are the same as the natural modes of the optical system itself. This statement seems physically reasonable because all of the coherence induced in the originally incoherent field is due to the optical system.

It is also interesting to note at this stage that spatial coherence will generally build up as modes are filtered. We know that when a low-throughput optical system is illuminated by a coherent source, the output of the system will tend to the lowest-order eigenmode regardless of the precise nature of the incoming field, and this is why submillimetre-wave optical systems always, somewhat conveniently, tend to produce Gaussian beams. In the case of incoherent illumination the situation is somewhat similar, but now as more and more low-throughput components are added, the output field will tend to become more and more coherent. We will demonstrate this effect in the next section.

In summary, it is important to distinguish between the natural modes of the optical system and the natural modes of the field. The natural modes of the optical system are found by diagonalising the scattering matrix whereas as the natural modes of the field are found by diagonalising the coherence matrix. In the case where the incoming field is incoherent the two are, as shown above, identical. If the incoming field is partially coherent, however, the natural modes of the field after passing through the optical system will not be the same as those of the optical system, and the similarities will depend on the degree to which the optical system imposes coherence on the field.

A further important and useful consideration is that the number of significant non-zero eigenvalues found when diagonalising the scattering matrix gives the number of degrees of freedom of the optical system. The number of non-zero eigenvalues found when diagonalising the coherence matrix gives the number of degrees of freedom of the field. Clearly, the number of degrees of freedom of the field can only be as many as the optical system and the two will be the same when the incident field is fully incoherent. In the case where the incoming field is fully coherent, the coherence matrix at any plane will have only one non-zero eigenvalue, a feature which can be traced to the fact that the elements of the coherence matrix factorise. In general, this will mean that because the coherence matrix has N^2 elements it will not be possible to diagonalise. The solution to this apparent paradox is that the modes of the optical system will all, at some level, be excited by noise. In fact it can easily be seen that we can add a noise coherence matrix to a fully-coherent coherence matrix we get a matrix that can be diagonalised, and if the signal to noise ratio is high, one eigenvalue will be much greater than all of the others. The ability to study the signal and noise properties of a field through diagonalisation is a particularly powerful technique. For example, the field 'produced' by a *complete array* of detectors [14] can be described by a *single* coherence matrix, the eigenvalues of which give the relative sensitivities of the pixels. Another example is the thermal radiation emitted by an overmoded horn when a perfect absorber is placed in the overmoded waveguide. Moreover, the diagonalisation of the coherence matrix could be used to diagnose problems in experimentally-derived data. In particular it should be possible to extract the coherent field of interest from background noise. Before leaving the subject of modes, it is also worth pointing out that the coherence matrix just described is the optical analogue of the quantum mechanical density matrix, where a coherent field corresponds to a pure quantum state and a partially-coherent field corresponds to a mixed quantum state.

In addition to diagonalising the coherence matrix for the purpose of investigating the nature of a field, we can also use various other analytical tools. First it should be noticed that the total amount of power in the beam is given by the trace of the coherence matrix:

$$P = \sum_i C_{i,i} = Tr(\mathbf{C}) \,. \tag{26}$$

Now the trace of a matrix is invariant to unitary transformations such as diagonalisation, and

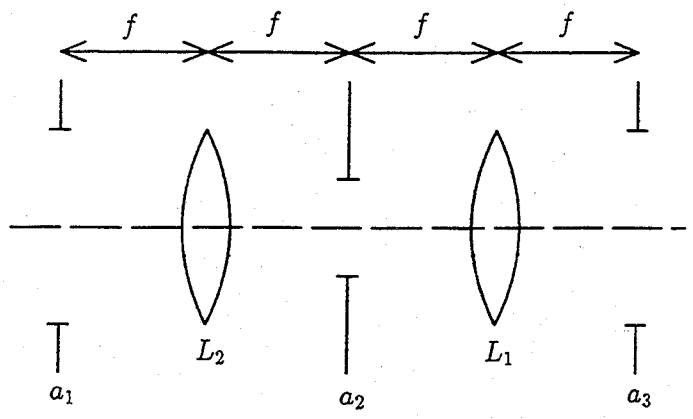

Figure 1: A Gaussian-beam telescope.

therefore, the total amount of power is also given by the sum of the eigenvalues (the eigenvalues are real because the coherence matrix is Hermitian). Physically, this is to be expected because the diagonalised coherence matrix is representing the cross-spectral density as a sum of completely incoherent modes. Moreover, although we will not discuss it in this paper it is likely that the eigenvalues can be used as a measure of the degree of disorder of the whole field, and therefore it should be possible to use maximum entropy techniques to recover mode coefficients from noisy partially-coherent experimental data [15, 16].

Once the coherence matrix is known, we can reconstruct the intensity and degree of coherence of the field. As stated earlier the cross-spectral density is given by

$$W(\mathbf{r}', \mathbf{r}) = \sum_m \sum_{m'} C_{m,m'} \psi^*_{m'}(\mathbf{r}_1) \psi_m(\mathbf{r}_1) \ , \tag{27}$$

and therefore the intensity and degree of coherence can be written

$$I(\mathbf{r}) = W(\mathbf{r}, \mathbf{r}) \tag{28}$$

and

$$\Gamma(\mathbf{r}', \mathbf{r}) = \frac{W(\mathbf{r}', \mathbf{r})}{\sqrt{I(\mathbf{r}') I(\mathbf{r})}} \tag{29}$$

respectively. The one-dimensional forms of these expressions will be used in the next section.

8 Partial coherence and the Gaussian-beam telescope

In the preceding sections we outlined a method by which the behaviour of multimode partially-coherent submillimetre-wave quasioptical systems can be analysed. Although the technique can be used to analyse the behaviour of almost any system—through the use of the appropriate scattering matrix—in this section we shall apply the theory to the Gaussian-beam telescope [1]. Not only does the Gaussian-beam telescope exhibit features which are integral to all systems, but it also produces results which are easily interpreted in terms of classical analysis [17, 18]. In order not to cloud the central features of the model, we shall work in one dimension, but the extension to two dimensions is straightforward.

A diagram of a Gaussian-beam telescope is shown in Fig. 1. This arrangement is important because the field at the input plane is imaged onto the field at the output plane in a frequency-independent way. An important feature of the arrangement is that there are two apertures, one at the input plane and one at the conjugate Fourier plane. In the context of a telescope, one can be regarded as the aperture stop and one as the field stop. Although for convenience we have located

the apertures at particular planes, the technique can easily handle other arrangements. The reason for including apertures in the model is that they limit the throughput of this ideal imaging system as would be the case for any real system with finite-size components.

To begin, we must calculate the scattering matrix of the system. Let us for the moment assume that the fields in the regions between the components are described as sums of propagating Gaussian-Hermite modes. Each mode has the form

$$\psi_m(x) = \left(\frac{\sqrt{2}}{w}\right)^{1/2} h_m\left(\frac{\sqrt{2}x}{w}\right) \exp\left[\pm j\theta\right] \exp\left[\mp \frac{j\pi x^2}{\lambda R}\right] \exp\left[\mp jkz\right] \tag{30}$$

where

$$h_m(u) = \frac{H_m(u) \exp\left[-\frac{u^2}{2}\right]}{\left(\sqrt{\pi} 2^m m!\right)^{1/2}}, \tag{31}$$

and

$$\theta = (m + 1/2)\frac{z}{z_c}, \tag{32}$$

also $H_m(u)$ is the Hermite polynomial of order m in u. It is important to realise that the functions $h_m(u)$ are orthonormal in the sense that

$$\int_{-\infty}^{+\infty} h_m(u)\, h_n(u)\, du = \delta_{mn}. \tag{33}$$

In these equations the symbols have their usual meanings. In particular, w characterises the scale size of the beam at a plane, R characterises the large-scale radius of curvature of the phase front, and θ, the phase slippage between modes, characterises the form of the field as the beam propagates and diffracts. As has already been described in some detail [2], a mode set is not completely defined until the size w_o and position of the waist are stated. Let us defer for a moment a discussion about how the waist size w_o should be chosen. We do know, however, that at for a Gaussian-beam telescope the large-scale phase front of the field at the focal planes is flat, and therefore we can place the waists at these positions.

Having decided on the mode sets, we know that the scattering matrix of the whole system is just the product of the scattering matrices of the individual components. The components in this case are the two apertures and the free space paths between them; as usual the focusing effects of the ideal lenses are taken up by choosing the mode sets appropriately; that is to say the waists at all but the input plane are chosen according to the usual single-mode Gaussian-beam analysis. If we adopt this scheme there is no modal scattering associated with the ideal lenses.

The size of the waist at the input plane is still undetermined, and although any waist would produce a complete mode set in terms of which the field throughout the system could be represented, some particular input waist will be numerically more efficient than others. In a previous paper [2], we discussed at some length that the waist should be chosen to diagonalise as near as possible the scattering matrix, because in this case the Gauss-Hermite mode set chosen is a close as possible to the true eigenmodes of the system. In fact in that paper, we diagonalised the matrix to recover the true eigenmodes and eigenvalues which are known from classical analysis to be prolate spheroidal wavefunctions. Rather than choosing the mode set that best describes the natural modes of the optical system, we could choose the mode set that best represents the natural modes of the field. We know, however, that in the case of a perfectly incoherent source the two converge. In fact the way of choosing the waist described previously is based on the concept of incoherent modes, in the sense that we assumed that the intensity of the beam at a cross section is simply given by the incoherent sum of the individual mode intensities. It seems completely reasonable that the mode set for analysing the behaviour of a partially coherent field is precisely the same as that required for analysing a completely coherent field. We, therefore, assume that the mode set is also appropriate

for any partially-coherent field. We are of, course, merely talking about efficiency of convergence and so the precise choice is not critical anyway.

Hence, as before, we take the input waist of the optimum mode set to be

$$w_1 = \left[\frac{\lambda f a_1}{\pi a_2}\right]^{1/2} \tag{34}$$

where a_1 and a_2 are the radii of the apertures, and f is the focal length of the lenses. Moreover, the number of modes that should be used in the expansion is approximately the Fresnel number c where

$$c = \frac{2\pi a_1 a_2}{f\lambda} \ . \tag{35}$$

We are now in a position to derive the scattering matrix of the Gaussian-beam telescope. First we must calculate the scattering matrices of the apertures. By evaluating the field overlap integral over the output plane of each aperture [19, 20], and taking advantage of the fact that the large-scale phase front is flat at that point, we find that the scattering matrices are given by

$$S_{m,n} = \int_{-\sqrt{2}k_t}^{+\sqrt{2}k_t} h_n(u)\, h_m(u)\, du \ , \tag{36}$$

where $k_t = a/w$ is the normalised truncation. Because the mode set is, by definition, chosen so that the truncation at each stop is the same, we can easily write

$$S_{m,n} = \int_{-\sqrt{c}}^{+\sqrt{c}} h_n(u)\, h_m(u)\, du \ . \tag{37}$$

Hence once we have chosen the Fresnel number, the scattering matrices of the two apertures are the same and given by the expression above. We could, of course, evaluate this matrix numerically, but we have found the following recurrence relationships useful. First we calculate the lowest-order coefficient through

$$S_{00} = \mathrm{erf}\left(\sqrt{c}\right) \tag{38}$$

where $\mathrm{erf}(u)$ is the error function. Then, for all $n+1$ odd we have

$$S_{0,(n+1)} = S_{(n+1),0} = 0 \ , \tag{39}$$

and for all $n+1$ even we have

$$S_{0,(n+1)} = S_{(n+1),0} = -\left(\frac{2}{n+1}\right)^{1/2} h_0\left(\sqrt{c}\right) h_n\left(\sqrt{c}\right) \ . \tag{40}$$

Also, for $(m+1)+(n+1)$ odd

$$S_{(m+1),(n+1)} = S_{(n+1),(m+1)} = 0 \ , \tag{41}$$

and for $(m+1)+(n+1)$ even

$$\left(\frac{m+1}{n+1}\right)^{1/2} S_{m,n} - \left(\frac{2}{n+1}\right)^{1/2} h_{m+1}\left(\sqrt{c}\right) h_n\left(\sqrt{c}\right) \ . \tag{42}$$

These equations show that power does not scatter between odd and even ordered modes, as would be expected.

We also need the scattering matrices of the free-space paths. These are easily found because we know that the relationship between the focal planes of a Gaussian-beam telescope is a Fourier

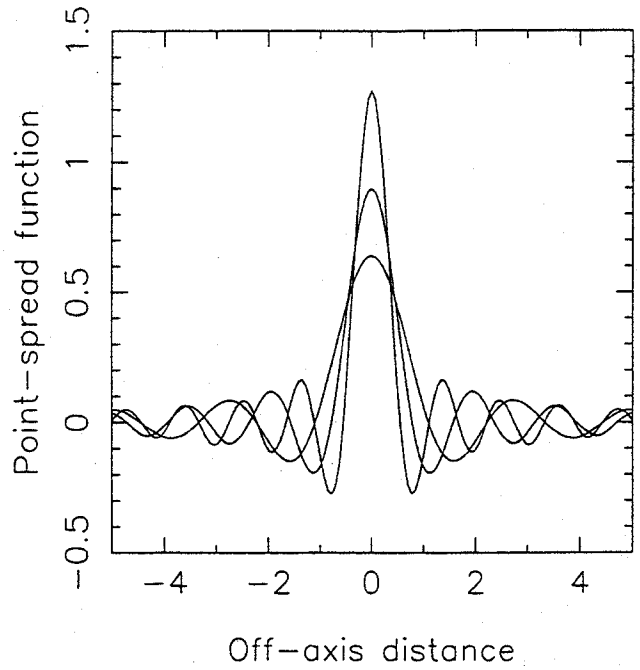

Figure 2: The point-spread functions of Gaussian-beam telescopes having Fresnel numbers of 4,8, and 16. The off-axis distance is normalised to the waist: x/w. Forty eight modes were used to construct these plots.

transform or equivalently that the phase slippage is $\pi/2$ [2]. The scattering parameters of the free-space paths therefore become

$$S_{m,n} = \left[\cos\left(\frac{\pi m}{2}\right) + j\sin\left(\frac{\pi m}{2}\right)\right]\delta_{m,n} \ . \tag{43}$$

If we denote the scattering matrices of the free space paths by $\mathbf{S}_f$ and the scattering matrices of the apertures by $\mathbf{S}_a$ then the scattering matrix of the whole Gaussian beam telescope is simply given by the product

$$\mathbf{S} = \mathbf{S}_f\mathbf{S}_a\mathbf{S}_f\mathbf{S}_a \ . \tag{44}$$

This matrix is extremely simple to generate using the above equations, and it is remarkable that it completely characterises the coherent and partially-coherent behaviour of the system. Also by raising the overall scattering matrix to some power we can calculate the effect of having a sequence of Gaussian-beam telescopes. This technique will be demonstrated shortly.

Now that we have generated the scattering matrix of a one-dimensional Gaussian-beam telescope, we can investigate its response to various different kinds of excitation. Before studying the propagation of partially-coherent radiation, it is worth while verifying the integrity of the scattering matrix by investigating the coherent behaviour. First of all we would like to plot the point-spread function.

The point-spread function is, of course, the output of the system when there is a delta function in the input plane. Moreover, for the Gaussian beam telescope, the input plane is at the position of a waist, where the phase front is flat. Calculating the mode coefficients in the one-dimensional case by evaluating the overlap integral, and then substituting the mode coefficients into the modal

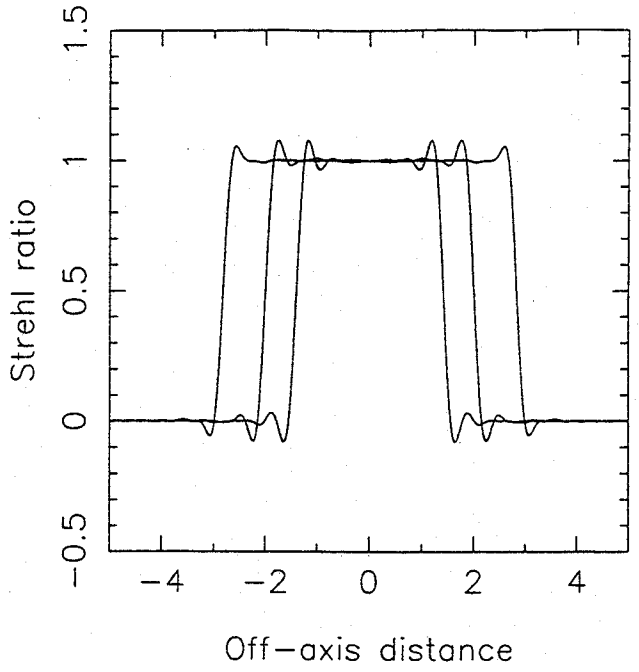

Figure 3: The Strehl ratio as a function of normalised, x/w, off-axis distance of Gaussian-beam telescopes having Fresnel numbers of 4,8 and 16. Forty eight modes were used to construct these plots.

expansion of the field, we find that the point-spread function, at the output plane, is given by

$$E_{psf}(x,x') = \left(\frac{\sqrt{2}}{w}\right) \sum_m \sum_n S_{m,n} h_n \left(\frac{\sqrt{2}x'}{w}\right) h_m \left(\frac{\sqrt{2}x}{w}\right) \tag{45}$$

where $S_{m,n}$ are the elements of the scattering matrix and x' is the position of the delta function in the input plane. In Fig. 2, we show the point-spread functions of a number of Gaussian-beam telescopes. This example demonstrates rather clearly how easy it is to calculate the point-spread function once the scattering matrix is known.

Rather than plotting the point-spread function for different input positions, it would be convenient to have some simple measure of its form. Classically, the crudest method use to use the Strehl ratio, where the Strehl ratio is defined as the height of the central peak normalised to the height of the peak at the central position. The argument being that because of the conservation of energy, any aberrations which spread the point-spread function will also reduce its height. In the case of Gaussian modes it is particularly easy to calculate the Strehl ratio. In fact it is given by

$$S = \frac{\sum_m \sum_n S_{m,n} h_n \left(\frac{\sqrt{2}x}{w}\right) h_m \left(\frac{-\sqrt{2}x}{w}\right)}{\sum_m \sum_n S_{m,n} h_n(0) h_m(0)} . \tag{46}$$

Notice that the sign on one of the Hermite functions has changed to take into account the fact that, in our system, the peak in the point-spread function moves in the opposite direction to the position of the delta function. In Fig. 3 we show the Strehl ratio as a function of position for a number of different Fresnel numbers.

The Strehl ratio is independent of position over the whole of the field of view and this observation simply reflects the fact that we did not include any aberrations in our system. Some ringing can be seen at the edge of the input aperture, and this is a Gibbs phenomena due to the fact that we

are trying to describe the sharp edge of the input aperture with a finite number of modes. This ringing is not an optical effect, but exists merely because we are trying to represent the abrupt disappearance of the input field behind the input aperture. Moreover, it is only a second-order effect in the sense that it only represents a low-level ringing in the point-spread function. In fact Fourier theory gives us a limit to the percentage error in the height of the point-spread function as we move close to the edge of the field of view. The most impressive aspect of these plots is that they demonstrate that a small number of modes can represent the behaviour of the system over a large field of view, and this has significant implications for modelling the behaviour of imaging arrays.

Notice that in all of these plots, we used the expression

$$\frac{x}{w} = \frac{x}{a}\left(\frac{c}{2}\right)^{1/2} \tag{47}$$

in order to generate normalised scales.

We would now like to investigate the behaviour when a fully-incoherent source with a Gaussian intensity distribution is applied to the input. To perform this calculation, we require the coherence matrix. Using the one-dimensional form of the bimodal overlap integral and a cross-spectral density of the form

$$W(x', x) = I(x)\,\delta(x - x') = K^2 \exp\left[-\frac{2(x - x_o)^2}{\sigma^2}\right]\delta(x - x') \tag{48}$$

we find

$$C_{m,n} = K^2\left(\frac{\sqrt{2}}{w}\right)\int_{-\infty}^{+\infty} \exp\left[-\frac{2(x - x_o)^2}{\sigma^2}\right] h_n\left(\frac{\sqrt{2}x}{w}\right) h_m\left(\frac{\sqrt{2}x}{w}\right) dx\,. \tag{49}$$

In Fig. 4, we show the intensity of the field at the output plane of a Gaussian-beam telescope when the Fresnel number is 4, 8, and 16. The normalised width of the effective input field distribution, σ/w, was taken to be 0.707. Superimposed on each plot is the cross-spectral density when the normalised reference position is 0.35: we could, trivially, have chosen any other reference position and the result would have been essentially the same.

For the purpose of generating a highly-incoherent input field distribution, we used 60 modes, but this large number of modes is not actually needed for the analysis. The main feature is, as would be expected, a slight spreading of the output intensity with decreasing Fresnel number and an increasing degree of coherence. What is not seen, because of normalisation, is the large amount of power lost, which would not be the case for a coherent field.

In addition to these plots it is also convenient to look at the behaviour when the input is a flat incoherent field of finite extent. In this case the elements of the coherence matrix are given by

$$C_{m,n} = \left(\frac{\sqrt{2}}{w}\right)\int_{-b}^{+b} h_n\left(\frac{\sqrt{2}x}{w}\right) h_m\left(\frac{\sqrt{2}x}{w}\right) dx\,, \tag{50}$$

where b is the extent of the field. Clearly, in the case where $b \to \infty$, the coherence matrix becomes diagonal, as expected. In Fig. 5 we show the intensity and cross-spectral density at the output plane when the Fresnel number is 4, 8 and 16.

Again the main feature of the plots is the smoothing of the highly-truncated input field and the increase in spatial coherence with decreasing Fresnel number. The cross-spectral densities should be compared with the point-spread functions shown in Fig. 2.

Finally, in Fig. 6 we show a sequence of plots where in each case the top-hat field distribution described above has been applied to a combination of Gaussian-beam telescopes all having a Fresnel number of 4. By simply raising the scattering matrix to the appropriate power, we show the effect of

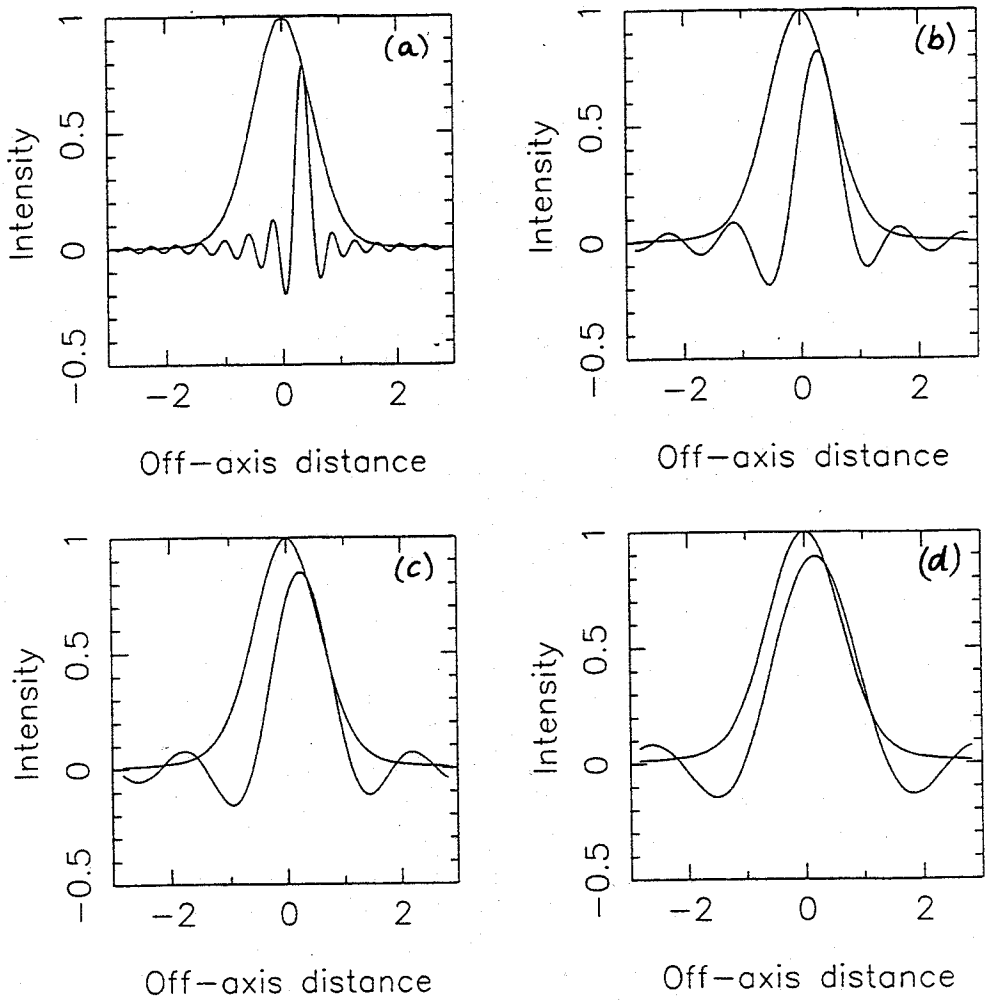

Figure 4: In (a) we show the Gaussian intensity and cross-spectral density of the field at the input plane of a Gaussian-beam telescope. Sixty modes were used, for the purposes of the plot, to synthesize a nearly fully-incoherent field. The Gaussian input field has an effective normalised width of 0.707. In (b),(c) and (d) we show the intensity and cross-spectral density at the output plane when the Fresnel number is 4,8, and 16.

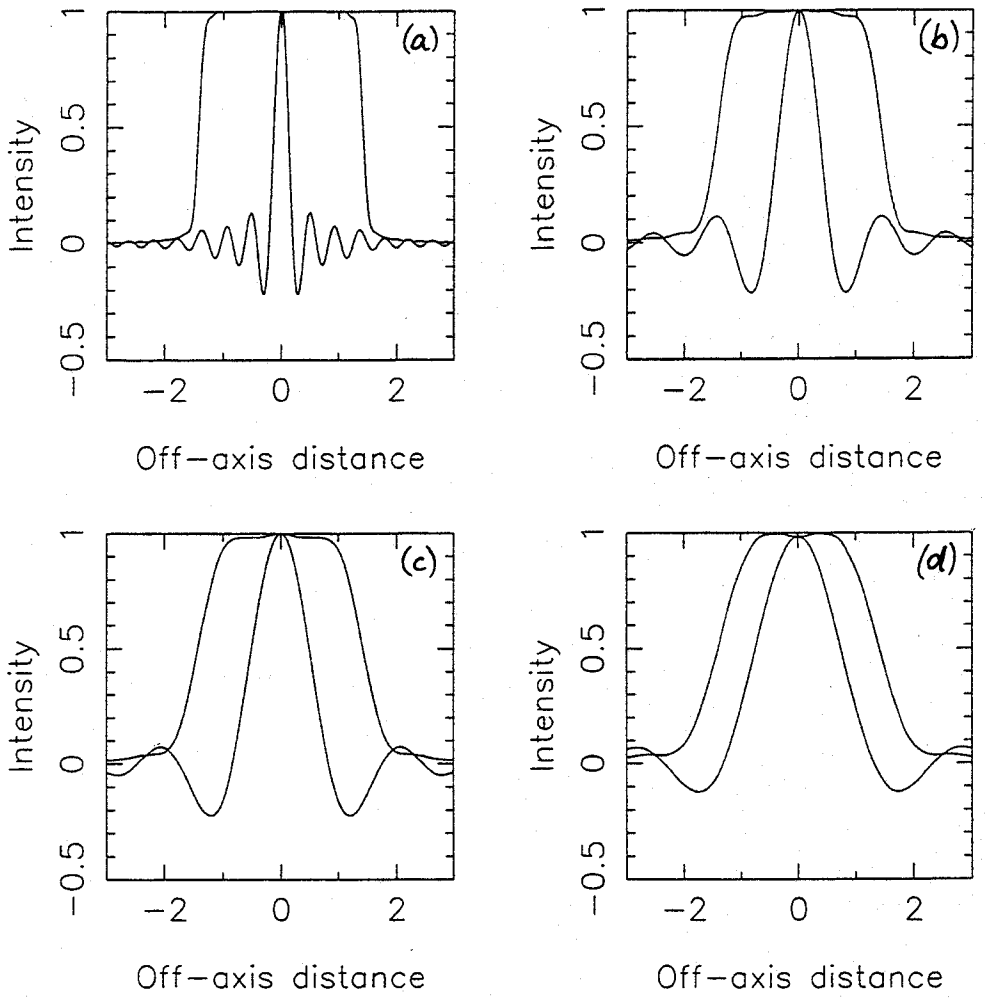

Figure 5: In (a) we show the top-hat intensity and cross-spectral density at the input plane of a Gaussian-beam telescope. Sixty modes were used, for the purposes of the plot, to synthesize a nearly fully-incoherent field. The top-hat input field has an normalised half width of 1.414. In (b),(c) and (d) we show the intensity and cross-spectral density of the field at the output plane when the Fresnel number is 4,8, and 16.

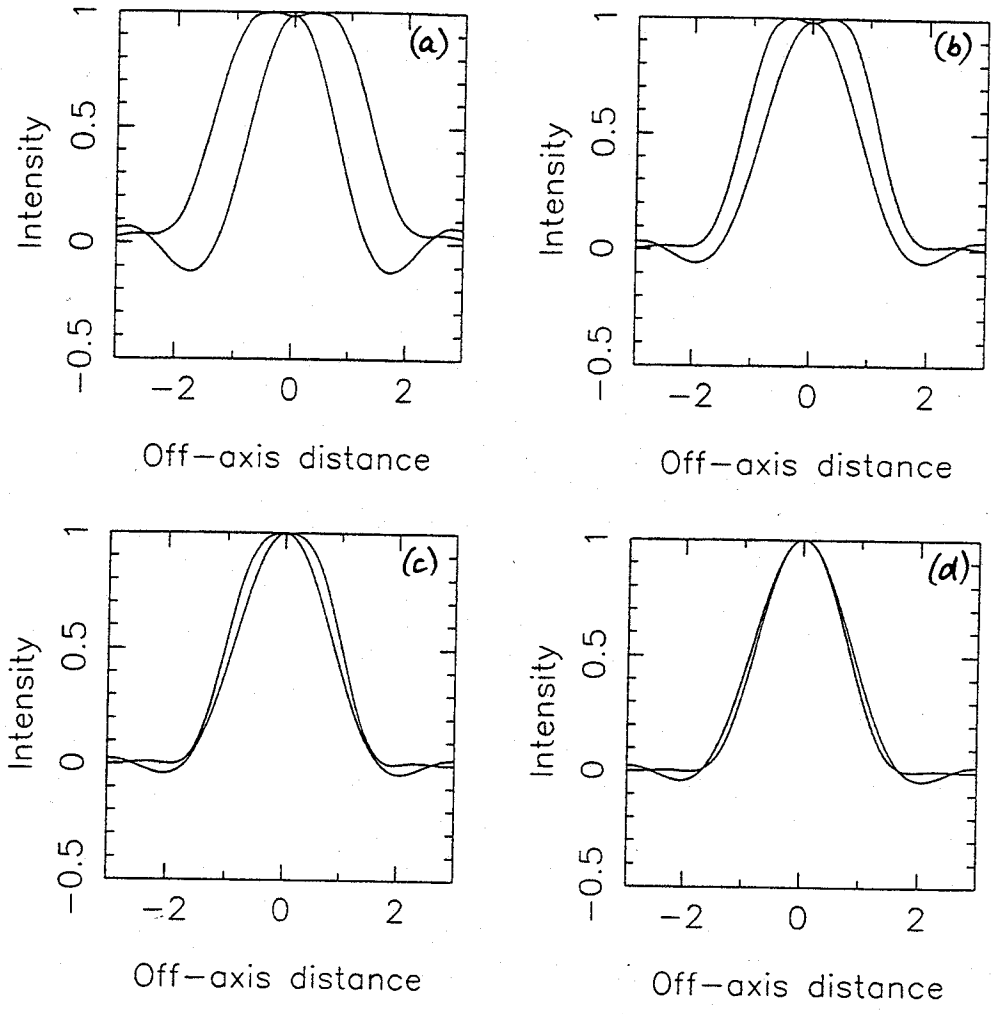

Figure 6: The intensity and cross-spectral density of the field at the output plane of a Gaussian-beam telescope when the Fresnel number is 4 and a fully-incoherent field with a top-hat intensity distribution is applied. (a),(b),(c) and (d) show the outputs when 1,2,4 and 8 identical telescopes are combined in series.

having 2 telescopes, 4 telescope, and 8 telescopes in series. Clearly, this corresponds to adding more and more identical lens systems. It can be seen how coherence builds up due to mode filtering, and after 8 passes a fully-coherent Gaussian field is produced despite having started with fully-incoherent top-hat field. Indeed this is precisely the way in which coherence builds up in a laser cavity [21, 22, 23].

In order to demonstrate the behaviour of the system, we have used fully-coherent and fully-incoherent input fields. It is usual practice in classical optics to work in terms of Gauss-Schell sources [24, 25, 26], where both the intensity and the degree of coherence are Gaussian functions. It is then possible to change the degree of global coherence by varying the relative scale sizes. It would be straightforward to apply such a field to our system in order to investigate general behaviour, but it would not be particularly useful for practical applications. The examples we have studied here, are of course the two limiting extremes of this more general model. Despite these comments, it is interesting to note, that the natural modes of the Gauss-Schell source are Gauss-Hermite functions and the eigenvalues also have a particular form. It would be interesting to investigate the

implications of the scale sizes when such a beam is propagated through a Gaussian-beam telescope. In particular it should be possible to determine what size Gaussian intensity distribution would pass through a system with the minimum amount of loss. Moreover, such an analysis is closely related to the ability to use different approximations when calculating the scattering matrices of apertures. This issue has been discussed in some detail in the context of coherent fields [2], and it would be useful to extend the analysis to incoherent fields.

9 Conclusions

In this paper we have described in some detail a technique for calculating the behaviour of partially-coherent submillimetre-wave quasioptical systems. The technique, like its coherent equivalent, is based on the ability to scatter propagating modes at optical components. The field, instead of being described by a vector is described by a matrix, and this allows much more detail about a field to be traced through a system. In this way it is possible to distinguish between the natural modes of the field and the natural modes of the optical system through which the field is passing.

In the paper, we explained how to calculate the components of the coherence matrix from the known functional form of the cross-spectral density, and also how to propagate the coherence matrix in the forward and backward directions. We also gathered together a collection of tools for analysing performance when the scattering matrix is known. We illustrated the overall method by investigating the behaviour of one-dimensional Gaussian-beam telescopes. In a later paper we will use the same techniques to analyse in some detail the behaviour of arrays of multimode bolometers.

Not only is the method very powerful in a computational sense, but it also leads to considerable insight into the way multimoded partially-coherent quasioptical systems behave. We believe that the method can be extended to allow the noise performance of multibeam bolometer arrays to be calculated, to allow the experimental analysis of beams through maximum entropy techniques, and to allow the statistical properties of systems to be taken into account—for example to model the behaviour of a submillimetre-wave radio telescope with the atmosphere included.

References

[1] P.F. Goldsmith, "Quasioptical techniques at millimetre and submillimetre wavelengths," in Infrared and Millimeter Waves, vol. 6, K.J. Button, Ed. New York: Academic, Ch. 5, 1982.

[2] S. Withington and J.A. Murphy, "Multimode Gaussian optics," 3rd Int. Workshop on Terahertz Electronics, Zermatt, Aug. 1995.

Submitted to Infrared Physics and Technology.

[3] D.H. Martin and J.W. Bowen, "LOng-wave optics," IEEE Trans. Microwave Theory Tech., vol. 41, pp. 1678-1690, 1993.

[4] R. Padman, J.A. Murphy, and R.E Hills, "Gaussian mode analysis of Cassegrain antenna efficiency," IEEE Trans. Antennas Propagat., vol. 35, pp. 1093-1103, 1987.

[5] J.A. Murphy, "Aperture efficiencies of large axisymmetric reflector antennas fed by comical horns,"IEEE Trans. Antennas Propagat., vol. 36, pp.570-575, 1988.

[6] R. Blundell and C.-Y.E. Tong, "Submillimetre Receivers for Radio Astronomy," Proc. IEEE, vol. 80, pp. 1702-1720, 1992.

[7] P.F. Goldsmith, "Quasi-optical techniques," Proc. IEEE, vol. 80, pp.1729-1747, 1992.

[8] J.W. Goodman, "Introduction to Fourier Optics," New York: McGraw-Hill, 1968.

[9] M. Born and E. Wolf, "Principles of Optics," Pergamon Press:1993, section 9.5, pp.480-490.

[10] J.A. Murphy and A. Egan, "Examples of Fresnel diffraction using Gaussian modes," European J. Physics, vol. 14, pp. 121-127, 1993.

[11] E. Wolf, "New theory of partial coherence in the space-frequency domain. Part I: spectra and cross spectra of steady-state sources," J. Opt. Soc. Am., vol. 72, pp. 343-351, 1982.

[12] E. Wolf, "New theory of partial coherence in the space-frequency domain. Part II: Steady-state fields and high-order correlations," J. Opt. Soc. Am. A., vol. 3, pp. 76-85, 1986

[13] F. Roddier, "The problematic of adaptive optics design," in Adaptive Optics for Astronomy, eds. D.M. Alloin and J.-M. Mariotti, Kluwer Academic: The Netherlands, 1994, pp. 89-112.

[14] D.T. Emerson and J.M. Payne, "Multifeed systems for radio telescopes," Astronomical Society of the Pacific Conference Series, vol. 75, 1995.

[15] S. Withington and K.G. Isaak, "Phase retrieval at submillimetre wavelengths using Gaussian Hermite modes," Proc. Fourth International Symposium on Space Terahertz Technology, Los Angeles, April, 1993.

[16] A. Cutolo, A. Esposito, T. Isernia, R. Pierri, and L. Zeni, "Characterisation of the transverse modes in a laser beam: analysis and application to a Q-switched Nd:YAG laser," Applied Optics, vol. 31, pp. 2723-2733, 1992.

[17] G. Toraldo Di Francia, "Degrees of freedom of an image," J. Opt. Soc. Am., vol. 59, pp.799-804, 1969.

[18] M. Bendinelli, A. Consortini, L. Ronchi, and B.R. Frieden, "Degrees of freedom, and eigenfunctions for the noisy image," J. Opt. Soc. Am., vol. 64, pp. 1498-1502, 1974.

[19] J.A. Murphy, S. Withington, and A. Egan, "Mode conversion at diffracting apertures in millimetre and submillimetre-wave optical systems," IEEE Trans. Antennas Propagat., vol. 41, pp. 1700-1702, 1993.

[20] J.A. Murphy, A. Egan, and S. Withington, "Truncation in beam waveguides," IEEE Trans. Antennas Propagat., vol. 41, pp.1408-1413, 1993.

[21] E. Wolf, "Spatial coherence in resonant modes in a maser interferometer," Phys. Lett., vol. 3, pp. 166-168, 1963.

[22] D.C.W. Morley, D.G. Schofield, L. Allen, and D.G.C. Jones, "Spatial coherence and mode structure in the He-Ne laser," Brit. J. Appl. Phys., vol. 18, pp. 1419-1422, 1967.

[23] W. Streifer, "Spatial coherence in periodic systems," J. Opt. Soc. Am., vol. 56, pp. 1481-1489, 1966.

[24] A. Starikov and E. Wolf, "Coherent-mode representation of Gaussian Schell-model sources and their radiation fields," J. Opt. Soc. Am., vol. 72, pp. 923-928, 1982.

[25] F. Gori, "Collett-Wolf sources and multimode lasers," Opt. Commun., vol. 34, pp. 310-305, 1980.

[26] A.T. Friberg and R.J. Sudol, "Propagation parameters of Gaussian Schell model beams," Opt. Commun., vol. 41, pp. 383-387, 1982.

Gaussian Beam Mode Analysis of Imaging Arrays

J.A. Murphy,
St. Patrick's College, Maynooth, Co.Kildare, Ireland
& **Stafford Withington,**
Cavendish Laboratory, Cambridge CB3 0HE, UK

Abstract

In this paper we consider the Gaussian beam mode analysis of imaging arrays on submillimetre-wave radio telescopes. We show how it is possible to describe any of the off-axis beams generated by the array in terms of the same on-axis beam mode set. The mapping process can be easily analysed using a modal approach.

1. Introduction

Focal plane arrays for submillimetre-wave radio telescopes are now being developed at a number of observatories. The imaging process in such systems is nearly always described in terms of Fourier optics [1]. It is more physically meaningful, however, in a telescope coupled to an array of mixers by a quasi-optical beam guide to develop the corresponding Gaussian beam mode model. In general, multi-mode Gaussian Beam Mode Analysis (GBMA) of beam guides is particularly powerful in terms of its conceptual accessibility, offering an intuitive understanding of the way in which submillimetre-wave optical systems operate [2].

This is a new application of Gaussian Beam Mode Analysis (GBMA), as the approach is normally used in modelling a single on-axis beam produced by some horn antenna in a single pixel detection process [3][4][5][6]. Nevertheless, since GBMA should be applicable to any field which is well defined on some input plane, it should be possible, at least in theory, to model an *off-axis* feed horn of an array system in terms of *on-axis* beam modes. However, if the on-axis beam mode set appropriate for a single horn is used, it is obvious that very high order modal contributions are necessary to describe the off-axis

beams. The feasibility of the GBMA depends on finding a more appropriate mode set which can describe any off-axis beam of an array with a modest number of modes, and thus be efficient computationally. In section 2 we describe how the best choice mode set (from a computational point of view) can be selected in a practical way for an array of beams propagating through an optical system of finite throughput. The mode set is parameterized in terms of the most appropriate choice for the beam waist radius, W_o. The mode set, for which the optics can transmit the maximum number of modes intact, is the "best" choice mode set, in the sense that it is the one which minimises the number of modes required in a modal expansion description of the any of the off-axis beams on the output plane (the sky). The number of modes in the best choice set turns out to have a natural relationship to the throughput of the optics and, consequently, the number of independent channels by which information can be transmitted by the optics. An example case of a telescope fed by a 4×4 array of horns is presented to show the power of the approach.

The natural modes of an imaging system of *finite* throughput are the eigenfunctions of the diffraction integral which maps the input aperture (taken to be the field of view of the telescope) onto the sky [2]. Although these modes are not the same as Gaussian beam modes, since finite throughput implies truncation, nevertheless the best choice mode set is a good approximation to the true modes of the system. This is discussed in section 3. In section 4 mapping and image reconstruction is discussed in terms of GBMA. Describing image reconstruction turns out to be very natural from this viewpoint, with the Nyquist rate being related to the total number of modes required in a modal expansion of the image, again emphasising the fundamental physical significance of the best choice mode set. In section 5 we briefly discuss how aberrations can be included in the description.

2. GBMA applied to an array of beams.

2.1. Choosing optimum mode set

Gaussian beam modes are solutions to the wave equation parameterized in terms of an arbitrary beam waist radius W_0 and beam waist position. In practice, for computational efficiency these are chosen so the beam can be described to high accuracy with as few modes as possible [7]. If we are interested in describing the output beam from an optical system fed by an *off-axis* horn, it is not necessary to describe the very high spatial frequency content of the fields of the horn, because truncation and aberrations will cause spatial filtering. Thus, the image produced at the output plane by the optical system will be band limited. Since the spatial frequency content of a mode depends both on the mode number n and the beam width parameter, W_o, we expect that both the best choice for W_o and the number of modes required to describe the beam at the output

plane will be affected by the spatial filtering characteristics of the optical system as well as on the input field distribution. The optimum mode set is the one with the largest number of modes not significantly affected by truncation and vignetting in the process of propagation through the optics from the input plane to the output plane; this is the mode set which requires the minimum number of modes to describe the fields adequately at the output plane.

Two stops are, in fact, required to define the optimum mode set uniquely (the same is true for the definition of throughput). Consider the simple, but instructive, example of an arbitrary field of finite extent at some plane with a finite sized lens in the far field (see figure 1). We assume the field has zero curvature on the input plane, so that the beam waist is best chosen to be there. We define the input and output stop widths in terms of the extent of the input field (field stop) and the radius of the lens (aperture stop). At both the input and lens stop the truncation level depends on the local value of r/W, where r is the radius of the stop. The greater r/W at an aperture is, the greater the number of unscattered modes that will squeeze through. However, the fact that the lens is in the far field of the input plane implies an inverse relationship between the respective beam widths since $W_1 W_2 = \lambda z/\pi$. Therefore, if we decrease W_1, so as to reduce truncation effects on the modes at the entrance stop, and thus allow more modes through without scattering, we unfortunately increase W_2 at the lens causing a greater level of truncation at the exit stop. In this situation we get the greatest number of unscattered modes to squeeze through both apertures, if we arrange that the level of truncation, defined by $t = r/W$, to be the same at both, so that

$$t_1 = \frac{r_1}{W_1} = t_2 = \frac{r_2}{W_2}$$

which since $W_1 W_2 = \lambda z/\pi$, implies

$$W_1^2 = \frac{\lambda z r_1}{\pi r_2}$$

In order to determine the number of modes that can squeeze through a stop, we choose to define a mode as significantly truncated if the coupling of overall power to the transmitted *propagating* mode, $\psi_{n,trans}$, from the incident *propagating mode* is less than 50% (see figure 2). That is, $|\int_A (\psi^*_{n,inc}\psi_{n,trans})dA|^2 = (\int_A |\psi^2_n|dA)^2 < 0.5$, where the subscript A denotes surface integration over the area of the stop. For one-dimensional Hermite modes, it is found that the mode number of the highest order mode which just squeezes through with 50% coupling loss at the stop of width r is given by $n \approx (1.2\, r/W)^2$. The number of modes which "squeeze through" is therefore given approximately by

$$N \approx \frac{4 r_1 r_2}{\lambda z}.$$

The throughput of a stop is defined, in terms of classical optics, to be the product of the area of the stop and the viewing solid angle, $A\Omega$. In this case we can take A to be the

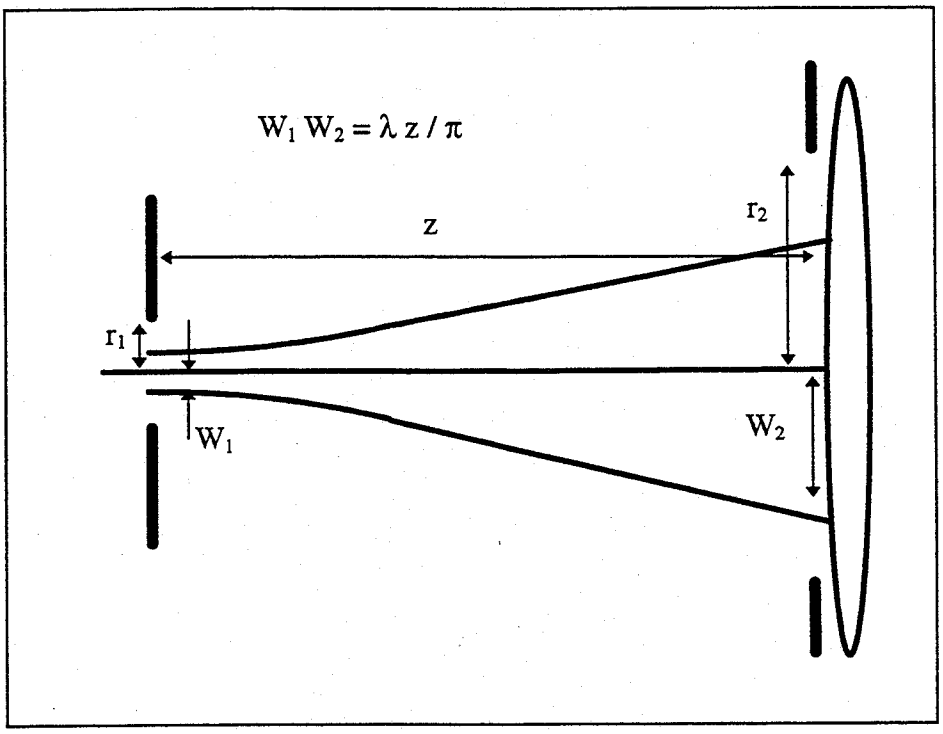

Figure 1. Simple single lens optical system

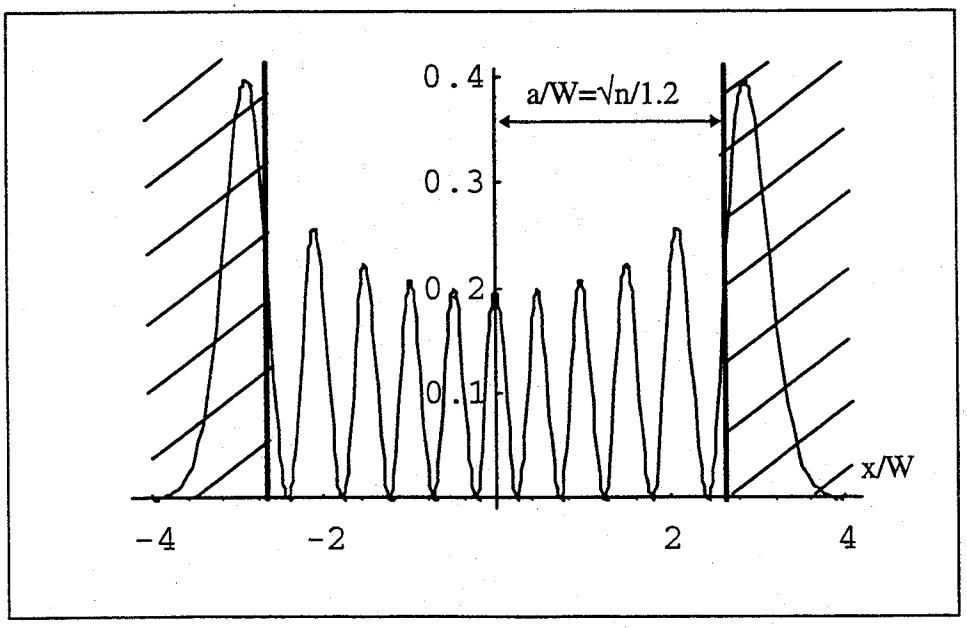

Figure 2. 50% power coupling loss due to beam truncation for h_{10} mode.

area of the entrance stop at the input plane,which defines the physical extent of the field, and Ω to be the solid angle subtended by the lens at the input plane. Thus, since for square apertures, $\Omega = (2r_2/z)^2$ and $A = (2r_1)^2$, we can write $A\Omega = (4r_1r_2/z)^2 = N^2\lambda^2$. Thus, the number of modes transmitted turns out to have a natural relationship to the throughput of the optics.

For a more complicated quasi-optical system the best value of W_o, is effectively defined by the two most truncating stops in the optical train (see figure 3). These can be found by estimating the effect of changing W_o on the resulting truncation levels $t_i = r_i/W_i$ at *each* truncating stop. The various t_i for all of the truncating stops can be plotted as a function of W_o, as illustrated in figure 3. What we seek is the value of $W_o = W_{o,opt}$ for which the value of t_i for the two most truncating stops is as large as possible. As will be seen from observation of figure 3, this occurs when the two relevant curves $t_i(W_o)$ cross. $W_{o,opt}$ then parameterizes the mode set for which the greatest number of modes is transmitted through the system.

2.2. Reconstructing the beam pattern of an array

In practice if we wish to reconstruct the output field to high accuracy we can use a larger number of modes than that defined by the highest order mode that suffers 50% power loss; $2N$ modes is usually more than sufficient. Although we intimated above that any mode that suffered less than 50% power truncation at any stop effectively squeezes through the optics, in practice, of course, the higher order modes do suffer some power attenuation and scattering to other modes [8]. A full scattering analysis needs to be made of the system and the scattering matrix $\mathbf{S}$ evaluated, but just including $(2N)^2$ modes [9]. Since the optimum mode set is used in determining $\mathbf{S}$, it will tend, in fact, to be almost diagonal. The significance of this is discussed further in the next section.

As an example we take an 4×4 square array of *long* square scalar horns of sidelength a, feeding a telescope with, for simplicity, a square aperture of sidelength b. The telescope reflector we will assume to be in the far field of the array, at distance of $z = f$, the focal length of the telescope. We can take the aperture field of the horn to be given by $E_h = E_o \cos(\pi x/a)\cos(\pi y/a)$. The best fit Gaussian beam to E_h has a beam width parameter at the horn apertures of $W_h = 0.350a$; thus, to a good approximation the field at a horn mouth can be taken to be $E_h = E_o \exp(-(x^2+y^2)/W_h^2)$. If we assume a 10dB edge taper at the telescope aperture (of width D_t), then for the Gaussian beam approximation to E_h at the telescope, $W_{ht} = 0.466D_t$. This implies that $W_h = \lambda f/\pi W_{ht} = 0.684\lambda F$, fixing $a = 1.95\lambda F$, where F is the F-ratio of the telescope beam given by $F = f/D_t$. For a single on-axis horn beam it would be adequate to use a mode set parameterized by a beam width parameter of W_h, to describe the beam propagation. The best choice of W_f for the array on the focal plane, however, depends also on the extent of the array, which

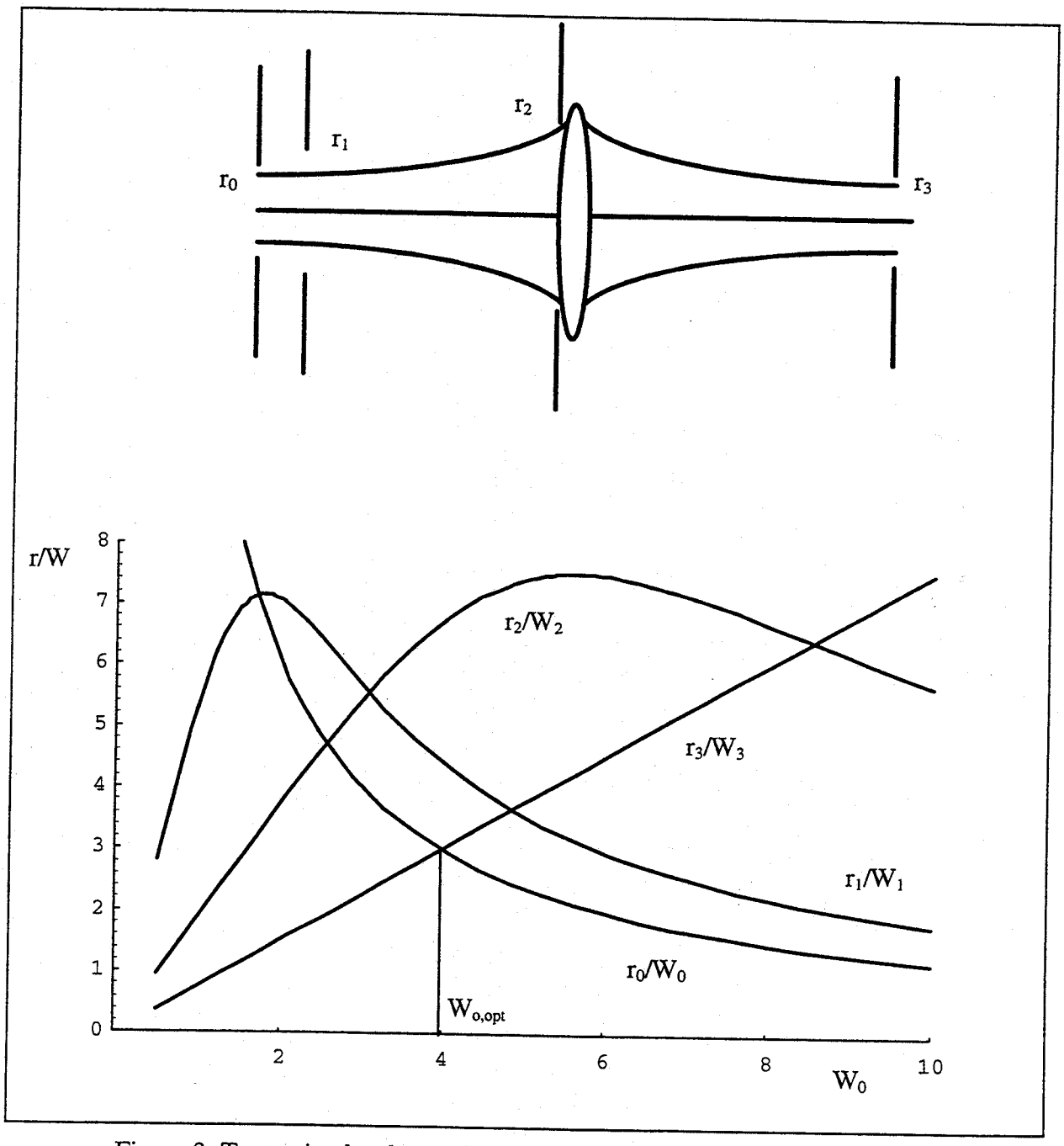

Figure 3: Truncation levels as a function of W_0 for stops in optical system.

defines the input pupil as well as the exit pupil. W_f is given by

$$W_f = \sqrt{\frac{\lambda f.4a}{\pi D_t}} \approx 1.58\lambda F = 0.808a.$$

We expect to be able to adequately describe the 4×4 array of beams on the sky with $(2N \times 2N)$ modes, where

$$N \approx (1.2 \times 2a/W_f)^2 \approx 9.$$

Figure 4 shows a 1-dimensional cut through the array of beam patterns reconstructed on the sky.

3. Integral Analysis - interpreting the best choice mode set.

The natural modes of an imaging system of finite throughput are the eigenfunctions of the diffraction integral equation which maps the input plane onto the output plane[2]. Assume that we have some optical system, and that we wish to find the field at the output plane, E_2, corresponding to a given field at the input plane, E_1. By linear superposition, the field at the output plane is expressible in the form [2]

$$E_2(\mathbf{r}_2) = \int_{P_1} E_1(\mathbf{r}_1) K(\mathbf{r}_2|\mathbf{r}_1) dS$$

where $\mathbf{r}_1$ and $\mathbf{r}_2$ are coordinates in the input and output plane respectively, and $K(\mathbf{r}_2|\mathbf{r}_1)$ is the appropriate kernel, also known as the point spread function or transfer function. In the case of any array the kernel is the field pattern on the sky of a point radiator (or detector) at the plane defined by the imaging array. This function includes the influences of all the optical components.

From the modal (or eigenfunction) point of view we can look for field distributions, $\phi(\mathbf{r})$ that remain unchanged after passing through the system:

$$\lambda\phi(\mathbf{r}_2) = \int_{P_1} \phi(\mathbf{r}_1) K(\mathbf{r}_2|\mathbf{r}_1) dS$$

The fact that in general $|\lambda| \leq 1$, implies that mode attenuation in the system is possible. This happens through a process of truncation and diffraction which nevertheless reproduces the input field distribution at the output plane. These eigenfunctions can be thought of as modes of the system rather than free space modes. In fact, if the optical system is perfect, in the sense of producing no truncation or aberrational effects, the $\phi(\mathbf{r})$ clearly have the same functional form as the Gaussian beam modes, at least in the limit of the Fresnel approximation [10], [11]. We can expand any field in terms of these normal modes. Thus, $E_1(\mathbf{r}_1) = \sum A_n \phi_n(\mathbf{r}_1)$, while $E_2(\mathbf{r}_2) = \sum A_n \lambda_n \phi_n(\mathbf{r}_2)$.

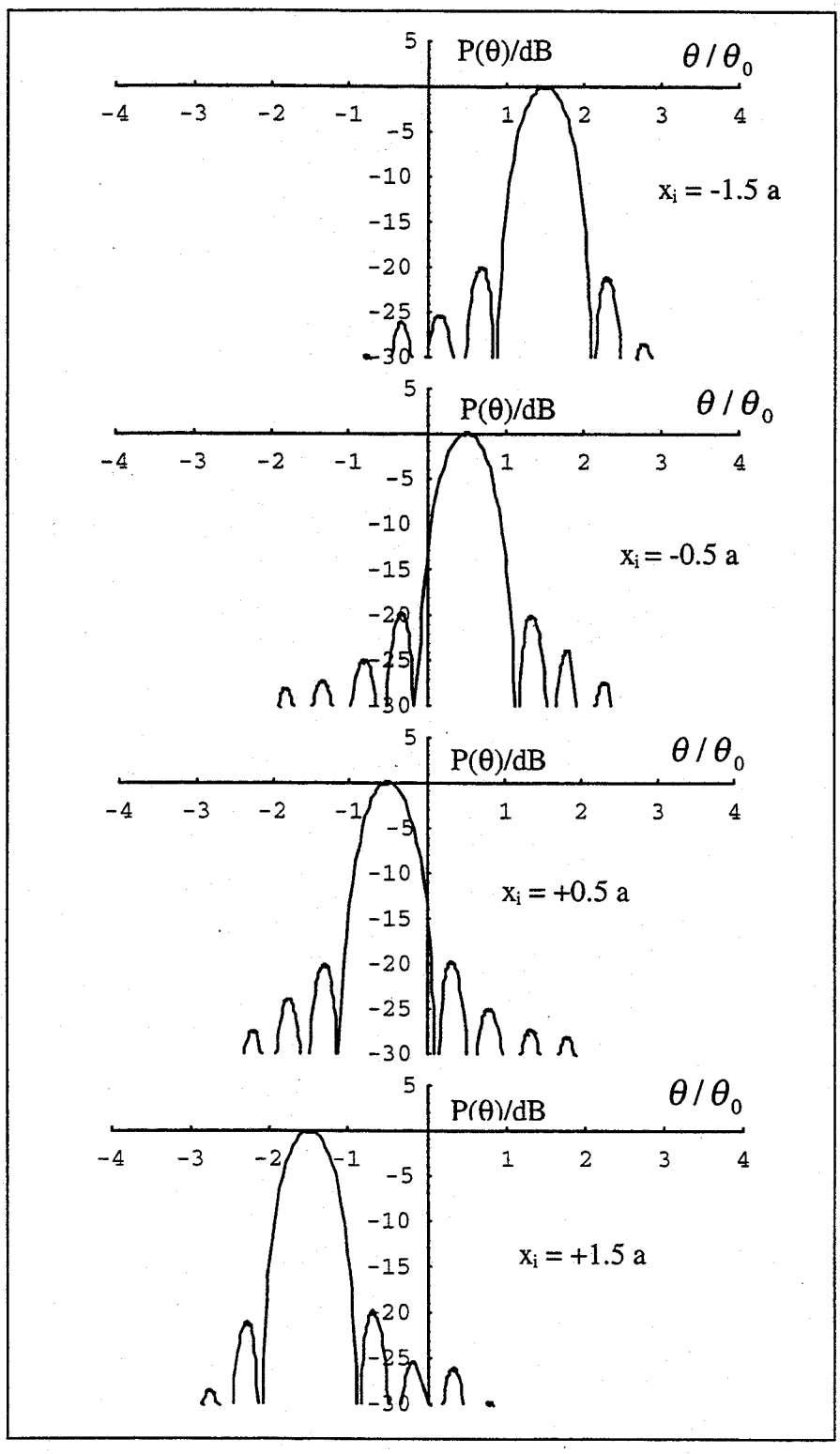

Figure 4: Beam patterns on sky due to an array of horn antennas (produced with an 18×18 mode set). Note: $\theta_0 = a / f$

In any real quasi-optical system clearly the optical components (lenses, mirrors, stops, pupils etc.) making up the beam guide will be finite in size, and may introduce aberrations into the beam. If we analyse propagation through such a system using propagating Gaussian beam modes, rather than applying the diffraction integral, we have to take into account the fact that the beam is no longer in free space as it propagates in the vicinity of an optical component. Boundary conditions are introduced by such components, and only certain linear combinations of the free space modal solutions are possible at the aperture (analogous to the modes in a waveguide). This situation can be handled using scattering matrix analysis [9], where an incident free space mode is regarded as having its power attenuated both because of truncation, and because the truncated mode that results is not a pure propagating mode, so that there is scattering of some of the transmitted power to other modes as well. This scattering process may happen many times in a real quasi-optical system and an overall scattering matrix for the system $\mathbf{S}$ can be computed.

For the best choice of W the scattering effect is minimised on the maximum number of modes, resulting in the scattering matrix $\mathbf{S}$ for the optical system being approximately diagonal. These beam modes, ψ_n, are therefore good approximations to the true eigenmodes of the optical system for those modes for which the magnitude of the eigenvalue is effectively unity, $|\lambda| = 1$. We can in fact derive the eigenvalues and Gaussian beam mode expansions for the eigenfunctions of the integral equation by computing the eigenvalues and eigenfunctions of $\mathbf{S}$, defined by $\mathbf{S}\boldsymbol{\chi}^n = \lambda_n \boldsymbol{\chi}^n$. Here $\boldsymbol{\chi}_i$ is a vector of mode coefficient $\{\chi_i^n\}$, in terms of which ϕ_n can be expanded $\phi_n = \sum_i \chi_i^n \psi_i$. (Note that even though it may not be always possible to derive ϕ_n analytically by solving the eigenvalue integral equation, it often still possible to obtain a mode expansion of the solution.)

4. GBMA of Mapping

Consider a source field with a brightness distribution $B(\theta, \phi)$, which is to be mapped by a radio telescope fed by an array of horns. When the source is observed with an antenna of power pattern $P(\theta, \phi)$, a flux density S_o is observed given by [12]

$$S_o = \int_{source} B(\theta, \phi) P(\theta, \phi) d\theta d\phi$$

In the imaging system $P(\theta, \phi)$ represents one of the array of beam patterns produced by the telescope. Consider off-axis horn i, with a field across its aperture expressed as an expansion in terms of the optimum mode set, and given by

$$E_i(x, y) = \sum_{m,n} A_{mn}^i h_m(x; W) h_n(y; W).$$

Here $h_m(x;W)$, etc., represents a Hermite Gaussian mode of order m, parameterized by the optimum beam width parameter, W, and defined by

$$h_m(x;W) = \frac{H_m(\sqrt{2}x/W)}{\sqrt{2^m m!\sqrt{\pi/2}\,W}} \exp\left(-\frac{x^2}{W^2} - j\frac{\pi x^2}{\lambda R}\right).$$

The corresponding telescope beam pattern is given by $P_i(\theta,\phi) = |E_{i,s}(\theta,\phi)|^2$, where $E_{i,s}(\theta,\phi)$, the field pattern on the sky, is given by $E_{i,s}(\theta,\phi) = \sum_{m,n} C^i_{mn} h_m(\theta;\omega) h_n(\phi;\omega)$, with the C^i_{mn} related to the A^i_{mn} via the usual scattering relationship

$$C^i_{mn} = \sum_{m,\mu,n,\nu} S_{m\mu,n\nu}\, A^i_{\mu\nu},$$

(in matrix notation $\mathbf{C} = \mathbf{SA}$.) Note, that here ω is the corresponding best choice beam width (in angle) on the sky, assuming small angles. Since we have chosen to analyse the problem in terms of the optimum mode set, we can define the scattering matrix to be finite in size so that $m_{\max} = \mu_{\max} = n_{\max} = \nu_{\max} = N$, where N is mode number of the highest order mode that just suffers less than 50% power coupling loss at each of the two most truncating stops. Thus, C^i_{NN} is the highest order mode coefficient, and the highest order mode in the expansion at the output plane for $E_{i,s}(\theta,\phi)$ is $h_N(\theta;\omega)h_N(\phi;\omega)$.

$P_i(\theta,\phi)$ can be written as the bandlimited *bi-modal* sum

$$P_i(\theta,\phi) = \sum_{m,m',n,n'}^{N} (C^i_{mn})^* (C^i_{m'n'})\, [h_m(\theta;\omega)^* h_{m'}(\theta;\omega)][\, h_n(\phi;\omega)^* h_{n'}(\phi;\omega)].$$

It is possible, however, to write this in a more convenient form. The product $[h_m(\theta;\omega)^* h_{m'}(\theta;\omega)]$ is a polynomial p of order $m+m'$ in θ/ω, multiplied by a Gaussian term $\exp(-(\theta/\omega)^2)$, to be squared

$$\begin{aligned}[h_m(\theta;\omega)^* h_{m'}(\theta;\omega)] &\propto H_m(\sqrt{2}\theta/\omega)\exp(-(\theta/\omega)^2)\; H_{m'}(\sqrt{2}\theta/\omega)\exp(-(\theta/\omega)^2).\\ &= p_{m+m'}(\theta/\omega)\exp(-2(\theta/\omega)^2)\end{aligned}$$

But *any* polynomial of order $m+m'$ can be written as a *finite* orthogonal series of Hermite polynomials,

$$p_{m+m'}(\theta/\omega) = \sum_{0}^{m+m'} \eta_k H_k(c(\theta/\omega)),$$

where c is any constant. Therefore, if we define $\omega_P = \omega/\sqrt{2}$, the bi-modal product $[h_m(\theta;\omega)^* h_{m'}(\theta;\omega)]$ can clearly be re-expressed precisely in terms of a finite sum of Hermite Gaussian modes (with the Gaussian beam width, ω_P),

$$[h_m(\theta;\omega)^* h_{m'}(\theta;\omega)] = \sum_{k}^{m+m'} \chi_k h_k(\theta;\omega_P)$$

Thus, $P_i(\theta,\phi)$ becomes a standard beam mode expansion of the form

$$P_i(\theta,\phi) = \sum_{k,l}^{2N} P_{kl}^i \; h_k(\theta;\omega_P) \; h_l(\phi;\omega_P),$$

where the mode coefficients P_{kl}^i are

$$P_{kl}^i = \sum_{m,m',n,n'=0}^{N} \left(C_{mn}^* C_{m'n'} \xi_{mm'k} \xi_{nn'l}\right),$$

and

$$\xi_{mm'k} = \int h_k(\theta;\omega_P) \; [h_m(\theta;\omega)^* h_{m'}(\theta;\omega)] \; d\theta$$

Note that $h_k(\theta)$ is real (i.e. $R = \infty$), so $h_k(\theta) = h_k(\theta)^*$. Clearly, if the mode expansion for the horns A_{mn}^i and the scattering matrix for the system $S_{m\mu,n\nu}$ are known, then the P_{kl}^i are readily calculable. ω_P is best choice beam width parameter for the mode set for describing the beam pattern on the sky, $P_i(\theta,\phi)$, as any other value for ω would require a larger number of modes than $2N \times 2N$ in the modal expansion.

V_i represents a measurement of the flux coupled from the celestial source to the ith horn, [12], [13].

$$V_i = \int P_i(\theta,\phi) B(\theta,\phi) \; d\theta d\phi = \int |E_{i,s}(\theta,\phi)|^2 \, B(\theta,\phi) \; d\theta d\phi.$$

Using the natural mode expansion for $P_i(\theta,\phi)$, the relationship for V_i becomes

$$V_i = \int \sum_{k,l}^{2N} P_{kl}^i \; h_k(\theta;\omega_P) \; h_l(\phi;\omega_P) B(\theta,\phi) \; d\theta d\phi,$$

which can clearly be re-expressed as

$$V_i = \sum_{k,l}^{2N} P_{kl}^i B_{kl},$$

where

$$B_{kl} = \int h_k(\theta;\omega_P) h_l(\phi;\omega_P) B(\theta,\phi) \; d\theta d\phi.$$

We therefore have generated a set of simultaneous equations for the B_{kl}. Assuming the equations are linearly independent, we can therefore, by measuring V_i at $2N \times 2N$ positions of the horn, solve for the B_{kl}. The equation for B_{kl} indicates that it is possible to express $B(\theta,\phi)$ as a mode expansion

$$B(\theta,\phi) = \sum_{k,l}^{2N} B_{kl} \; h_m(\theta;\omega_P) \; h_n(\phi;\omega_P).$$

However, the sum is finite, since B_{kl} can only be determined for k and $l \leq 2N$, indicating in terms of mapping that only a bandlimited image of $B(\theta, \phi)$ (in terms of spatial frequencies) can be reconstructed from a set of measurements V_i.

The relationship with Nysquist sampling can be derived in a straightforward manner. Consider the case where the beam width parameter at the telescope focal plane is W_f, and the corresponding beam width at the telescope is W_t. If the telescope is in the far field of the focal plane then, $W_f W_t = \lambda f/\pi$. For an array with a field of view of d_v, the number of propagating modes is given by both $N = (1.2d_v/2W_f)^2$, and $N = (1.2D_t/2W_t)^2$, so that we obtain

$$N = 1.44\frac{\pi d_v D_t}{4\lambda f} \approx \frac{d_v}{F\lambda}.$$

In order to obtain the reconstruction of the source brightness to the highest resolution of the telescope we need to take approximately $2N$ measurements with the horn array. But, this implies a sampling interval of approximately $2d_v/F\lambda$, exactly the same as the Nyquist sampling rate! The measurements are best made at equal intervals, though this is clearly not necessary for the recovery process. In fact beam distortion (due to aberrations in the optical system feeding the telescope) in the case of arrays often results in slight differences in the inter-beam intervals on the sky.

Since the Gaussian beam modes are not the true eigenmodes for the system, but rather approximations to the true eigenmodes, choosing the value for N to be given by the order of the mode that suffers just less than 50% power coupling loss is to some extent arbitrary. However, if N is set much larger, the highest order C^i_{mn} will have very small values, and the inversion process will become unstable. A similar concern arises in a Fourier optics approach, as the highest spatial frequency contributions to the image can only be measured with vanishingly small accuracy, which in the presence of noise may not be the reliably extracted.

We illustrate the mapping process with a one-dimensional example. Again we consider an array of 4 horns. Figure 5 illustrates the inversion process. The input source intensity pattern is a uniform extended source with sharp edges. The image on the focal plane of the telescope has elongated wings. The reconstructed (deconvolved) field using the beam mode approach shows sharp edges, with some ringing effects because of the finite number of modes used (inevitable with a top-hat distribution).

5. Aberrations

We can deal with aberrations in a natural way within the beam mode description of mapping, since the effect is to change the mode coefficients C^i_{mn} for the output field expansion [14],[15]. Aberrations cause mode distortion at an optical component, introducing extra

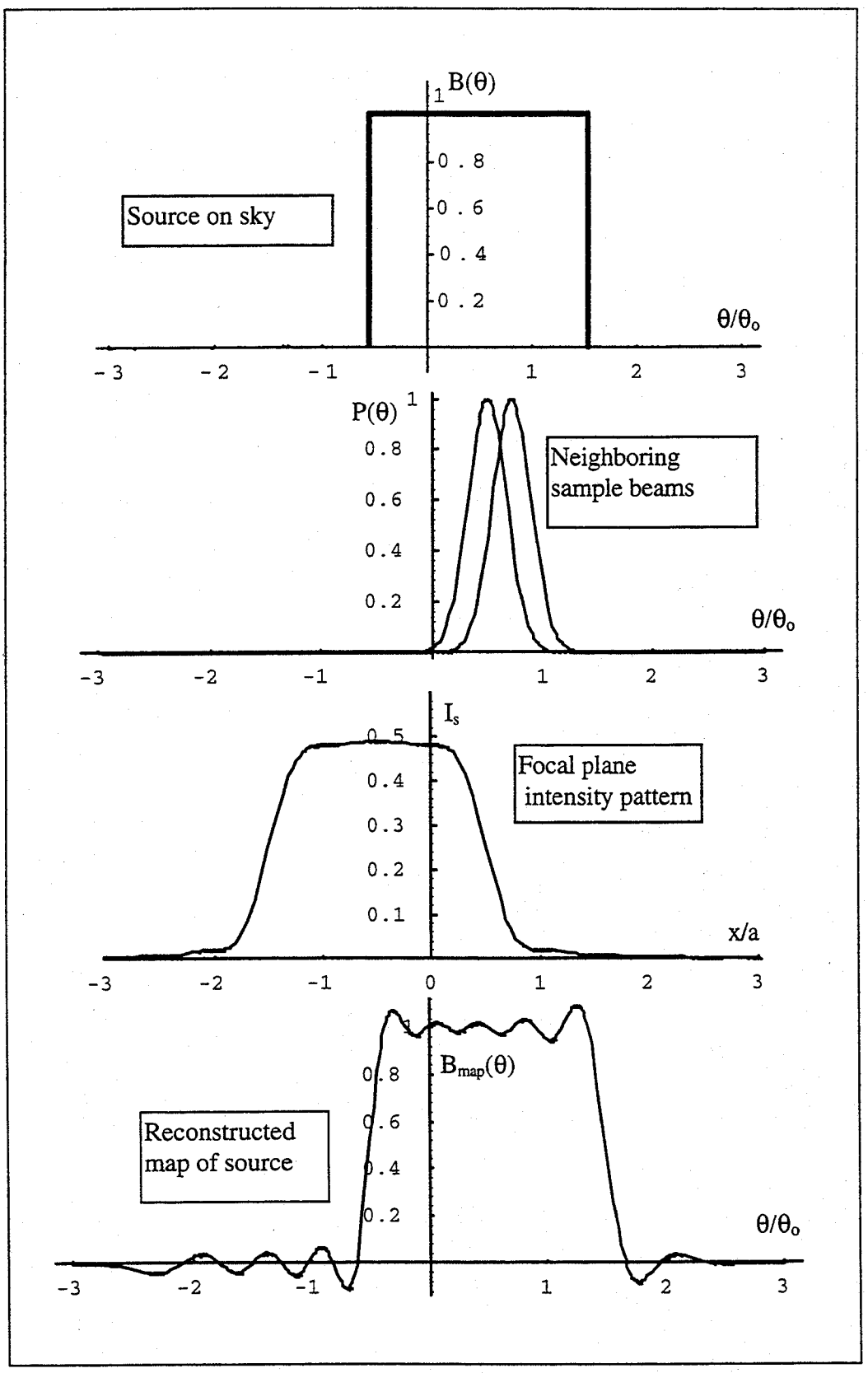

Figure 5. Mapping of extended sources

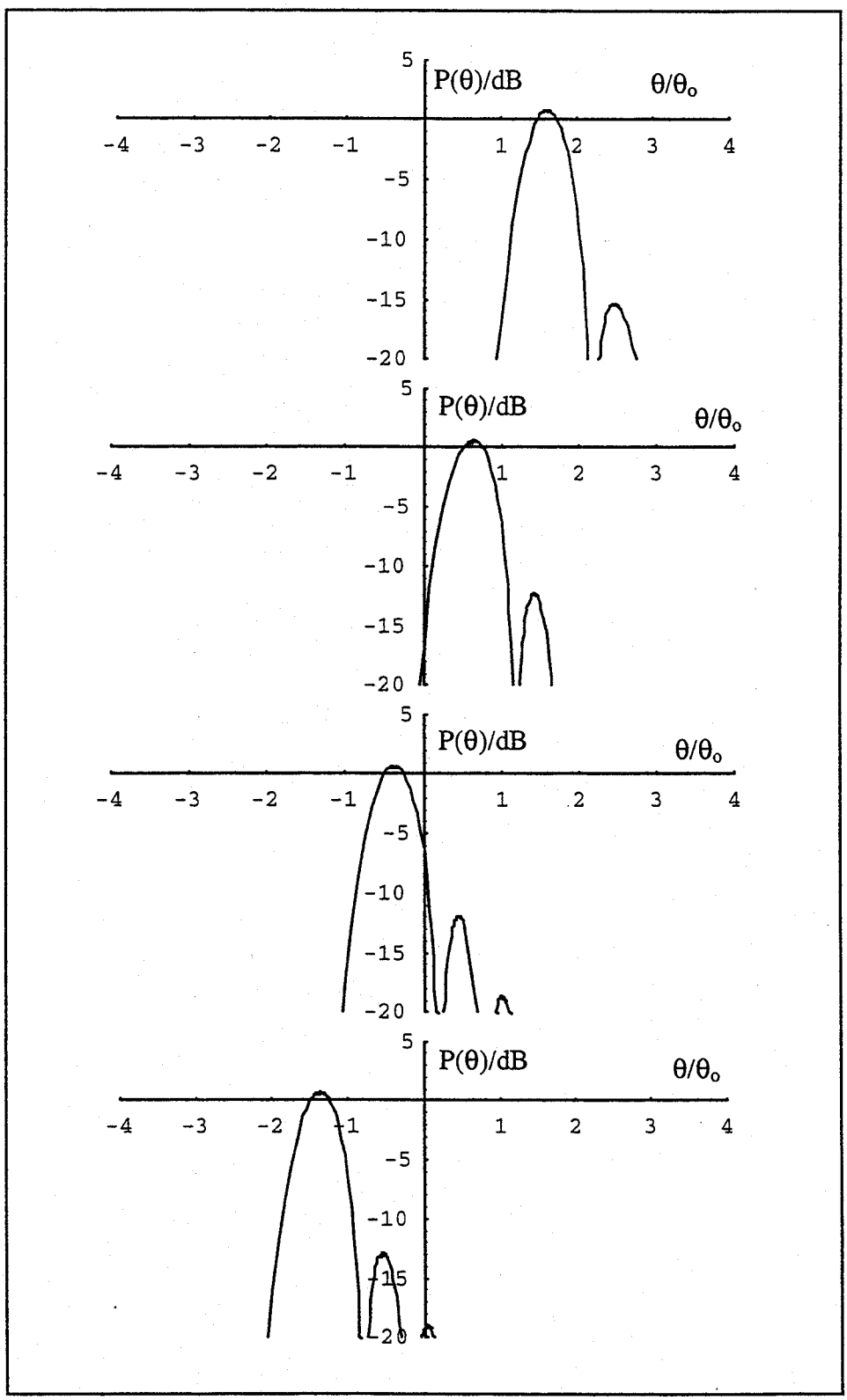

Figure 6. Effect on output beam patterns of a one dimesional aberration function of form $\Phi(x) = \exp(-j\alpha x^2)$ at aperture stop of telescope. Note: $\theta_0 = a / f$

inter-modal scatterings of the propagating modes (see figure 6). In severe cases such an effect may result in more severe attenuation at subsequent stops in the system than would otherwise be the case, with a consequent reduction in the overall total number of modes that can propagate from the input to the output plane. Also, for beams at the edge of the array we might expect more severe aberrational effects, so that the output beams on the sky are not ideal replicas to the on-axis beam. In the theory of Fourier optics this variation in the beam pattern across the output plane causes problems for the analysis, whereas in Gaussian beam mode theory only the mode coefficients for the beam are affected, and thus no difficulty arises. In fact, different types of horns could be used for the array, generating a non-identical set of output beams on the sky, without causing any problems for the reconstruction process (provided the mode coefficients for the horns are known, as well as the scattering matrix of the system.) Figure 6 illustrates the distorted set of beam patterns calculated using GBMA, that result in a one-dimensional array with a non-negligible phase error across the aperture stop of the imaging array.

6. Conclusions

We have considered in detail how to choose the best mode set, in terms of computational efficiency, with which to describe beam propagation in quasi-optical multi-beam systems. For the best choice only a finite and well defined number of modes are propagated by the system. This number is related to the throughput of the optical system giving physical significance to that mode set choice.

We have also considered how the mapping of incoherent sources can be expressed in terms of modal analysis. The reconstruction process becomes one of solving a set of straightforward linear equations. Aberrational effects can also be included.

References

[1] J.W. Goodman, "Introduction to Fourier Optics," New York: McGraw-Hill, 1968.

[2] S. Withington and J.A. Murphy, "Multimode Gaussian Optics," Proc 3rd Int Workshop on THz Electronics, Zermatt, Aug/Sept 1995.

[3] P.F. Goldsmith,"Quasi-optical techniques at millimeter and submillimeter wavelengths," in Infrared and Millimeter Waves, Vol6, K.J. Button, Ed. New York: Academic, Ch. 5, 1982.

[4] R. Padman, J. A. Murphy and R.E. Hills, "Gaussian mode analysis of Cassegrain antenna efficiency," IEEE Trans Antennas Propagat, vol 35, pp 1093-1103, 1987

[5] J. A. Murphy, "Aperture efficiencies of large axi-symmetric reflector antennas fed by conical horns," IEEE Trans Antennas Propagat., vol. 36, pp.570-575, 1988.

[6] S. Withington and J.A. Murphy, "Analysis of diagonal horns through Gaussian-Hermite modes," IEEE Trans Antennas Propagat, vol. 40, pp 198-206, 1992

[7] C. Aubry and D. Bitter, "Radiation pattern of a corrugated horn in terms of Laguerre-Gaussian functions," Electronic Letters, vol 11, pp. 154-156, 1975.

[8] J.A. Murphy, A. Egan and S. Withington, "Truncation in beam waveguides," IEEE Trans Antennas Propagat, vol 41, pp1408-1413, 1993.

[9] J.A. Murphy, S. Withington and A. Egan, "Mode conversion at diffracting apertures in millimetre and submillimetre-wave optical systems," IEEE Trans Microwave Theory Tech, vol 41, pp 1700-1702, 1993.

[10] J.A. Murphy and A. Egan, "Examples of Fresnel diffraction using Gaussian beam modes," European J Phys, vol 14, 121-127, 1993.

[11] M. Born and Wolf, "Principles of Optics," Pergamon Press:1993.

[12] J.D. Kraus, "Radio Astronomy," 2nd. Ed., Cygnus-Quasar, 1986

[13] K. Rohlfs, "Tools of Radio Astronomy," Springer Verlag, 1986.

[14] S. Withington, J.A. Murphy and K.G. Isaak, "Representation of mirrors in beam waveguides as inclined phase-transforming surfaces," Infrared Phys Technol, vol. 36, pp 723-734, 1995

[15] J.A. Murphy and S. Withington, "Perturbation analysis of Gaussian-beam-mode scattering at off-axis ellipsoidal mirrors," Infrared Phys Technol, vol. 37, pp 205-219, 1996.

LO BEAM ARRAY GENERATION AT 480 GHZ BY USE OF PHASE GRATINGS

T.KLEIN, G.A.EDISS, R.GÜSTEN, H.HAUSCHILDT, C.KASEMANN
Max-Planck-Institut für Radioastronomie, Auf dem Hügel 69, 53121 Bonn, Germany

ABSTRACT

For the MPIfR's 480 GHz-heterodyne-array, 16 SIS mixer elements have to be driven by the local oscillator power of two LO-chains. In order to split the power of each LO into one subarray of 8 mixer elements in a conventional way a complicated beam splitting foil complex is necessary. A more elegant way to couple the LO-power is to generate the required beam array with a phase grating. Such devices have been developed at optical wavelengths and are potentially suitable for quasi optical applications.
We will report upon the design of such gratings for quasi optical systems. Theoretical considerations and first measurements of binary phase gratings at 480GHz for a 3x3 beam array will be presented, as well as calculations of more efficient multilevel gratings. The design of the grating for the array receiver will be discussed.

INTRODUCTION

To couple LO-power equally into each receiver element of a submm heterodyne array an optical power dividing system is required. There are several possible solutions for such a system. The straight-forward one is to extend the power divider for a one channel system into a dividing system for an array by splitting the LO beam with a combination of power dividing foils as described in [1,2]. As simple as this idea may be for linear arrays, for two dimensional arrays it becomes more complicated.
A more elegant way for imaging one LO beam to a mixer array is the use of a phase grating as practiced at optical wavelengths for decades and as proposed for the submillimeter range in [3,4]. It is the purpose of this paper to show our considerations of phase gratings and calculations for a grating design which generates the image of one subarray of the MPIfR's heterodyne array.

THEORY

We use a theory of phase gratings based on the scalar theory of diffraction which can be described mathematically by fourier optics [5].
The typical setup for signal array generation by a phase grating is shown in fig.[1]. The first lens of a gaussian telescope is illuminated by the gaussian beam generated by the LO feed and produces a beam waist in its focal plane, where the grating is positioned. At optical wavelengths this setup yields an uniform illumination of the grating with a plane wave. However at submillimeter wavelengths the illumination is gaussian and only at the waist position a planar phasefront can be assumed. The grating structure causes an additive phase distribution to the zero phase gaussian beam. The second lens of the gaussian telescope images the diffraction orders produced to an object plane at distance f (focal length of the lens). The intensity distribution in the output plane is given by

$$I(x,y) = \left| \int e^{-\frac{x'^2+y'^2}{\omega_0^2}} \cdot t(x',y') \cdot e^{\frac{-2\pi i(xx'+yy')}{\lambda f}} \, dx' \, dy' \right|^2 \qquad (1)$$

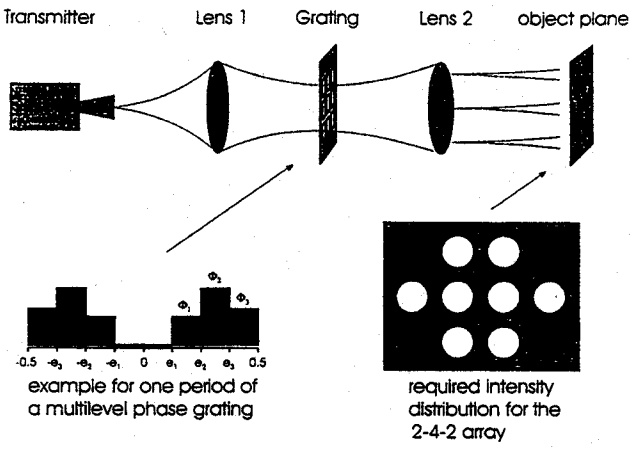

FIGURE I Typical setup for signal array generation by a phase grating. The grating is positioned in the focal plane of the two lenses, where a plane phasefront can be assumed. After diffraction by the grating the output spots can be observed in the output plane, the focal plane behind the second lens.

which is the complex fourier transform of the amplitude distribution of the incident beam with waist ω_0 and the transparency function $t(x,y)$ of the grating. The problem to solve is the determination of $t(x,y)$ under the condition to generate the required array pattern with high efficiency.
The calculations can be reduced to an one dimensional problem [6,7] if $t(x,y)$ is separable. Then $t(x,y)$ can be written as

$$t(x,y) = t_1(x)t_2(y) \tag{2}$$

If further $t_{1,2}$ is determined to be a stepped function with M transition points e_n at phase levels ϕ_n

$$t_{1,2}(z) = \sum_{n=0}^{M} e^{2\pi i\phi_n} \cdot rect\left[\frac{z - \frac{1}{2}(e_{n+1} - e_n)}{e_{n+1} - e_n}\right] \tag{3}$$

the amplitude maxima of the diffraction orders are calculated to be

$$a_0 = \sum_{n=0}^{M} 2(e_{n+1} - e_n)e^{2\pi i\phi_n} \tag{4}$$

$$a_m = \frac{1}{m\pi}\sum_{n=0}^{M} \left[sin(2\pi m e_{n+1}) - sin(2\pi m e_n)\right] e^{2\pi i\phi_n} \tag{5}$$

where a_0 is the 0^{th} and a_m the m^{th} order. One period of a grating corresponding to equation 3 is shown in figure 1. The symmetry of the structure is a further limitation on the number of solutions because only symmetric configurations of orders (a_m=a_{-m}) can be obtained. This limitation is useful if a symmetric configuration is required because the number of iterations is reduced.

RESULTS

The solutions for $t_{1,2}$ can be found by varying e_n and ϕ_n in eqn. (4) and (5). The optimized transparency function is obtained if a maximum fraction of the incident power is coupled uniformly into the required output pattern. To achieve this goal the efficiency function for a one dimensional grating η_{1D}

$$\eta_{1D} = \sum_{m=-M}^{+M} a_m^* a_m \tag{6}$$

and the error function ρ

$$\rho = \sum_{m=-M}^{+M} \left| 1 - \frac{a_m^* a_m \cdot (2M+1)}{\eta_{1D}} \right| \tag{7}$$

indicate the quality of the solutions during the iteration procedure.
For the "2-4-2" beam pattern of the MPIfR's heterodyne array (see fig.1) we first calculated the transparency function t_1 as a solution for a 3×3 array and t_2 for a 4×4 array and combine $t_1(x) \cdot t_2(y)$ to obtain a 3 × 4 beam array with high efficiency. Then by a second optimization process the undesirable beams in the four corners were suppressed by increasing the efficiency for the eight beams belonging to the required pattern.

Solutions for 3×3 beam arrays

For $2M + 1$ required spots M transition points have to be varied if the number of different phase levels is limited to 2 (binary grating). In this case M=1 and the phase is shifted between 0 and π. The results for maximum efficiency are shown in table I. Note that the overall efficiency η_{1D}^2 is only 44% in this case. An improvement can be achieved by use of more phase levels. For four different phase levels three transition points are necessary (M=3) and 2M+1=7 spots are generated. To suppress the 2^{nd} and 3^{rd} order only the 0^{th} and 1^{st} orders are considered in eqn. (6) and (7). Table II summarizes the parameters for two representative results. The intensity

TABLE I Solutions for a binary grating with M=1

e_1	$\|a_0\|^2$	$\|a_1\|^2$	η_{1D} [%]
0.132	0.223	0.220	66.4
0.368	0.223	0.221	66.4

TABLE II Solutions for a four level grating with M=3

e_1	e_2	e_3	ϕ_1	ϕ_2	ϕ_3	$\|a_0\|^2$	$\|a_1\|^2$	$\|a_2\|^2$	$\|a_3\|^2$	η_{1D} [%]
0.15	0.25	0.40	0.125	0.625	0.750	0.304	0.296	0.011	0.013	89.6
0.10	0.22	0.30	0.125	0.500	0.750	0.305	0.298	0.015	0.014	90.2

response of 2-dimensional gratings ($t_1 \cdot t_2$) were then simulated using these results. In agreement with the calculated efficiencies the far-field amplitude distribution (see fig.2) generated by the four level grating the 2^{nd} order beams are largely suppressed compared with the response of the binary grating. The far-field phase distributions are also shown to be flat over the main beams. The grating structures become more complicated with increasing number of different phase levels. The binary grating (see fig.3 right) made of PTFE has been fabricated in our workshop with a numerical controlled machine. The accuracy achieved by this method is limited by the physical behavior of PTFE during the machining. The measured amplitude response (fig.3 left) indicates this fact. The nine required beams were detected but differ in intensity by up to 5dB for the corner beams on the left side. Also the beamshapes show poor features. The grating structure produces the required Bragg angle indicated by the measured distance of 22mm between two adjacent beams.

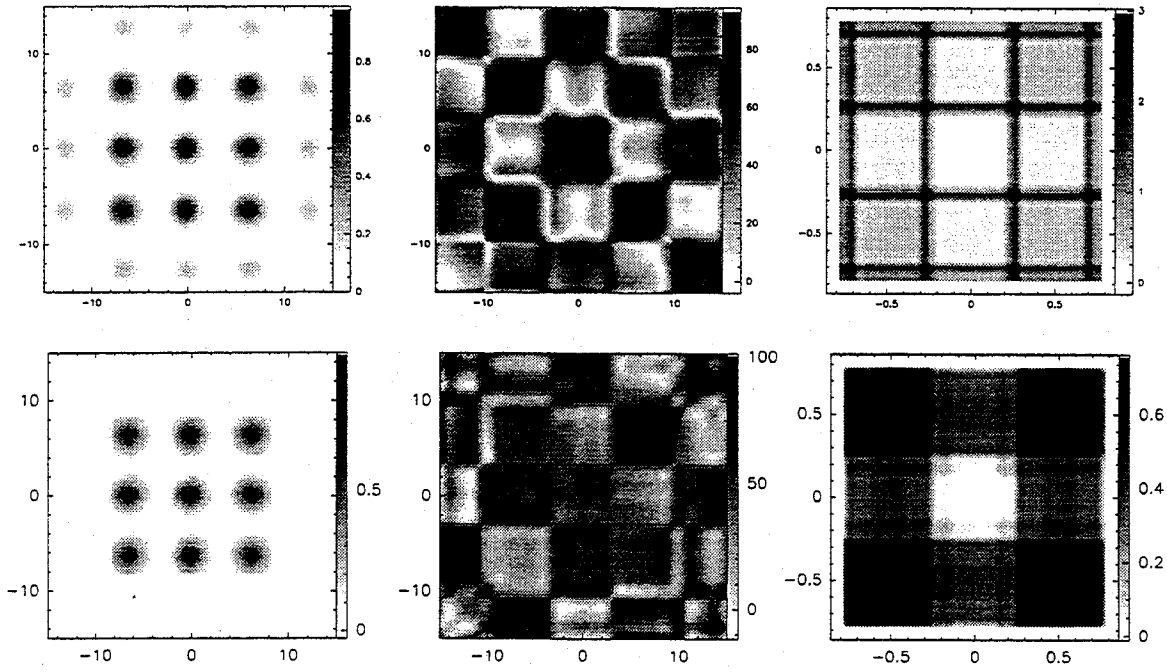

FIGURE II Far-field amplitude pattern (left), phase (middle) and grating structure for a 3 × 3 (right) binary (top) and a four level grating (bottom). The response of the binary grating shows considerable intensities in the higher orders yielding a lower efficiency. Amplitude greyscales are linear and normalized to one. The diffraction angle is in degrees, phase greyscales are in degrees and grey scales of the phase levels are $0,\pi$ and 3π for the binary and fractions of π for the four level grating. The grating period is normalized to one.

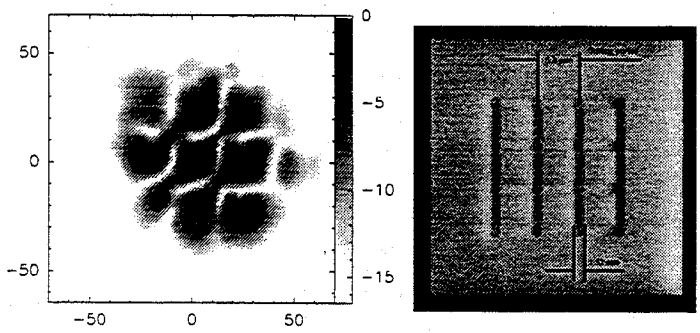

FIGURE III Very first measurement of a binary phase level grating at 460GHz for a 3×3 array. The measured intensity (left plot) is greyscaled and the coordinates in the object plane are mm. The PTFE-grating fabricated with a numeric controlled machine is shown on the photograph (right).

Solutions for 4×4 beam arrays

To generate a beam array with an even number of spots (such as 4×4) the 0^{th} diffraction order has to be suppressed and if equal distances between the beams are required only the odd numbered orders are to be maximized. We calculated binary and four level gratings once more for the case M=3 by suppressing the 0^{th} and 2^{nd} orders and put the results shown in table III into the simulation yielding the far field patterns in figure 4. The two dimensional intensity response of the four level grating is shown to be more uniform than that of the binary grating in addition to 12% efficiency improvement.

TABLE III Solution for a binary and a four level grating with M=3 and suppressed even numbered orders

	e_1	e_2	e_3	ϕ_1	ϕ_2	ϕ_3	$\|a_0\|^2$	$\|a_1\|^2$	$\|a_2\|^2$	$\|a_3\|^2$	η_{1D} [%]
binary	0.025	0.250	0.470	1	0	1	0.0004	0.174	0.0004	0.178	70.7
4 level	0.100	0.250	0.425	1.50	0.625	1.125	0.006	0.205	0.004	0.206	83.0

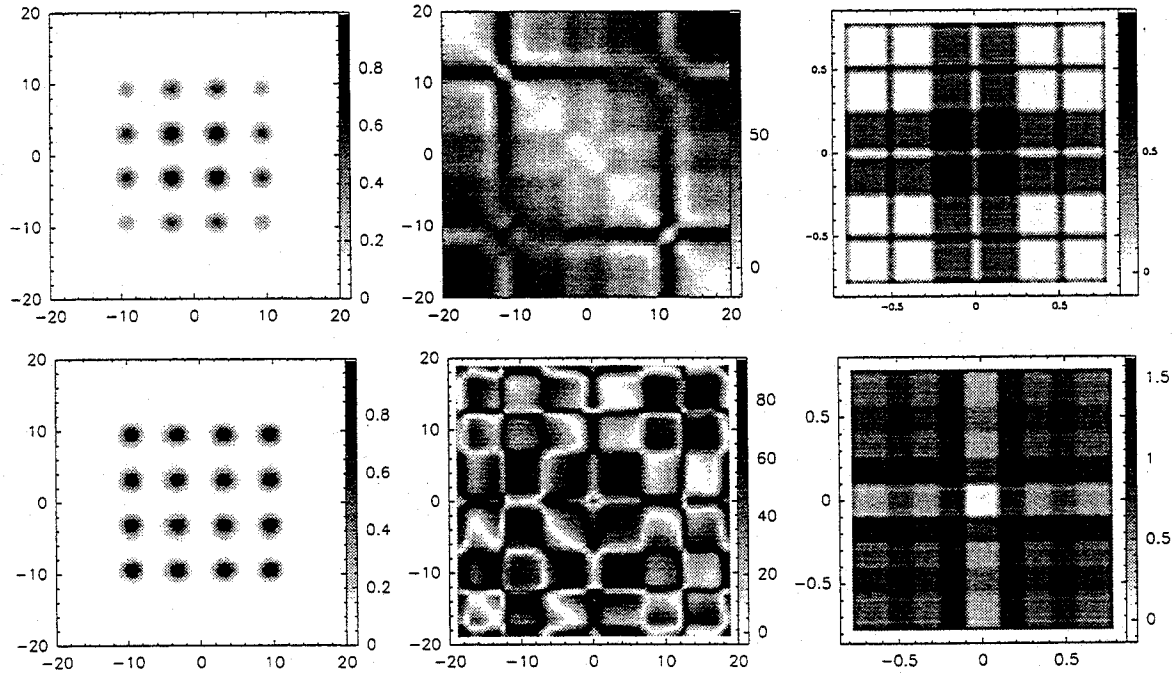

FIGURE IV Far-field amplitude (left), phase pattern (center), and grating structure (right) for a 4×4 array with a binary (top) and a four level grating (bottom)

Bandwidth

We used the four level grating calculated for a linear four beam array and center frequency ν_o=475GHz to check the bandwidth of the device. Varying the frequency means a change in phase delay (given by the phase levels) and a deviation of the transition points in the grating period caused by the wavelength dependence of the period P given by

$$P = \frac{\lambda f}{a} \tag{8}$$

with wavelength λ, distance a between two adjacent beams of the object array and the focal length f of the transforming lens. The shape of the intensity distribution in the object plane is shown in figure 5 for the range 400-540GHz. The usable bandwidth of about 60GHz (~13% of the center frequency) is mainly due to the change of the beam separation as a consequence of the wavelength dependence of the Bragg angle.

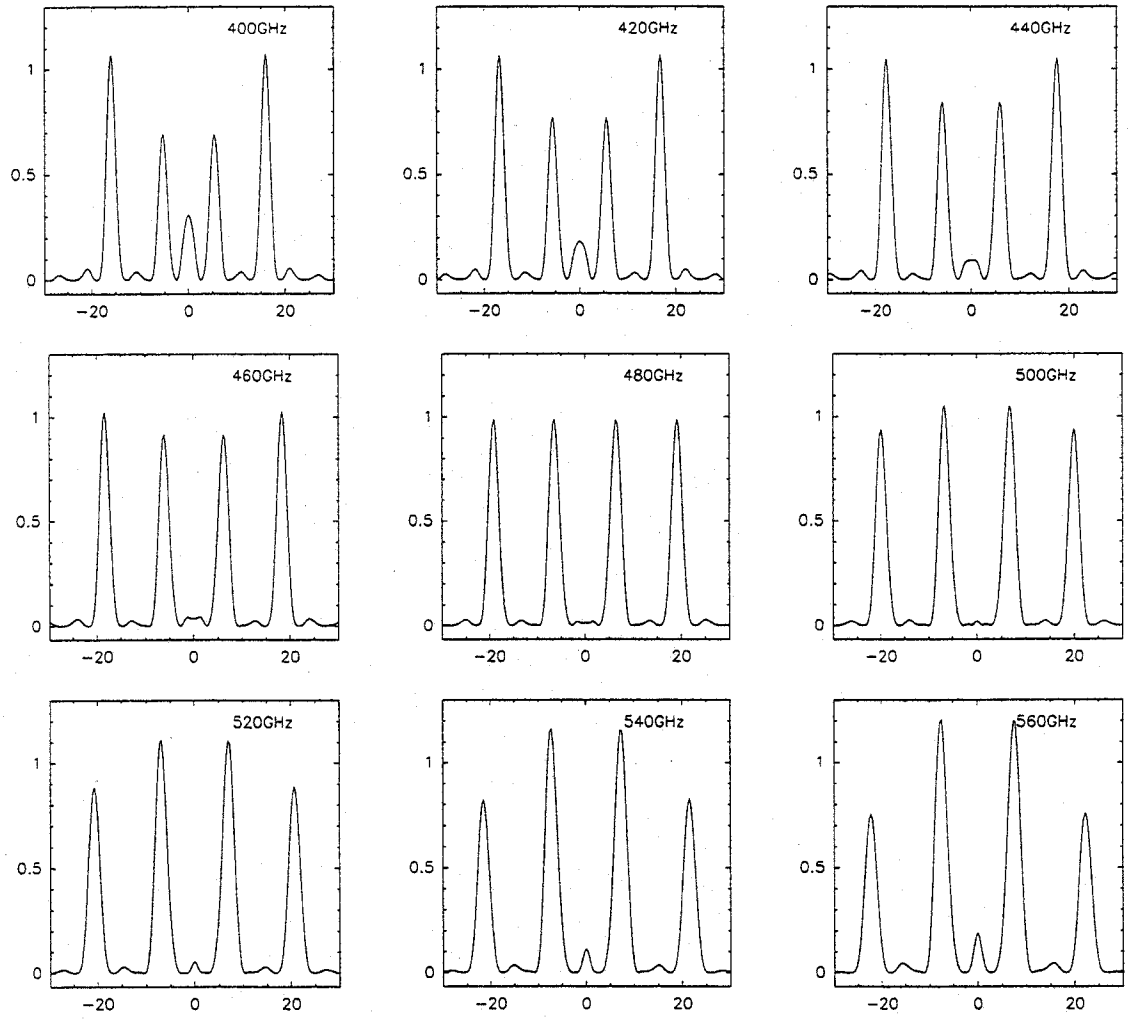

FIGURE V The calculated farfield amplitude patterns of the four spot grating at various frequencies shows the usable bandwidth of the grating is from 440GHz to 520GHz when the grating is optimized for a center frequency of 475GHz.

Solution for a 4×3 beam array

The results of the calculations for a three and a four beam linear array were combined to provide a solution for a 4×3 2-dimensional array. Because of the requirement of highest efficiency the two four level solutions were chosen.
Due to the suppression of the odd numbered orders for the four beam array the grating period has to be multiplied by a factor 2 in one dimension to obtain equally spaced beams. The resulting patterns are shown in figure 6. The combination of $t_{3beam} \cdot t_{4beam}$ yields an efficiency of 74% and is a

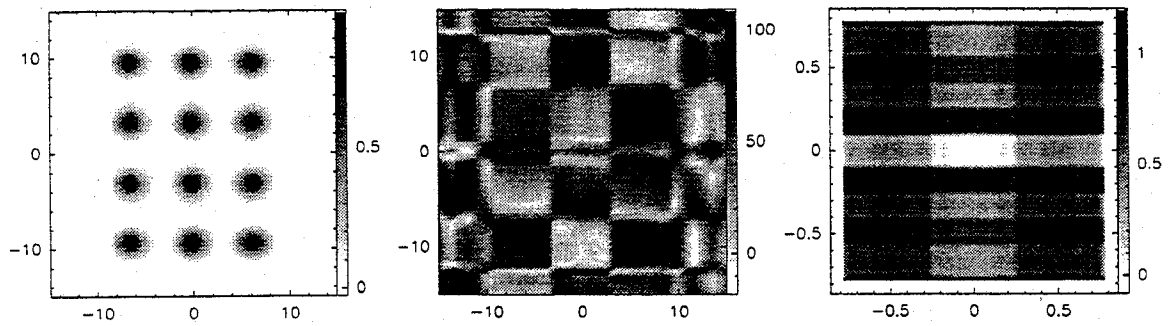

FIGURE VI Amplitude (left) and phase (center) patterns for the combined four phase level solutions (table 1 and 4). The grating structure (right side) is the result of the combined solutions. Intensity is linear greyscaled and the diffraction angle is in degrees.

potential solution for the required 2-4-2 array (figure 1). Because of the high output power available by the LO chains of the heterodyne array less than 1% of the LO power is required to drive each SIS-junction individually. If the losses in the further optics of the LO path can be assumed to be less than 6dB, sufficient power is coupled into each mixer.
In the next step we tried to optimize the grating structure for the 2-4-2 configuration (see fig.1). The resulting gratings had higher efficiencies, however they became more complicated and the size of the structures were very small (sometimes below the limit of the wavelength). This indicates that the starting function (the solution above) is too close to or is itself a local maximum in the set of solutions. Better results (fig.7), with a 15% efficiency improvement, were obtained starting the optimizing routine with the solution for the four beam linear array (tab.3) because here the routine starts at zero for the 2^{nd} dimension.

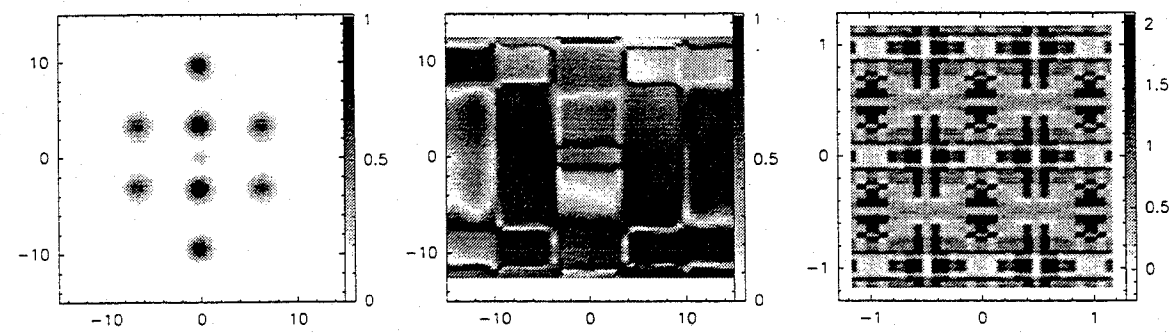

FIGURE VII Amplitude (left) and phase (center) patterns for the optimized grating structure (right). Intensity is linear greyscaled (normalized to one) vs. the diffraction angle in degrees.

CONCLUSIONS

We have presented the designs for various binary and multilevel gratings which can be used as wideband LO couplers for the MPIfR heterodyne array receiver. Measurements of a test 3×3 beam

phase grating have been given, and show reasonable agreement with the theory. The final design of a grating optimized for 8 beams (2-4-2 configuration) with a high enough efficiency to supply the LO required for each mixer will be manufactured and tested in the near future.

REFERENCES

[1] R. Güsten, G.A. Ediss, H. Hauschildt, C. Kaseman, M.Scherschel: "A 16-Element 480 GHz Heterodyne Array for the Heinrich-Hertz-Telescope (HHT)", ASP Conference Series, Vol.75,1995, D.T. Emerson and J.M. Payne (eds.)

[2] T. Klein, G.A. Ediss, R. Güsten, H. Hauschildt, C. Kaseman: "Quasi-Optical Measurements for the MPIfR 16-Element 480 GHz Heterodyne Array", Proceedings of the Fourth International Workshop on Terahertz Electronics, University of Erlangen-Nürnberg, Germany,1996

[3] G.F. Delgado, J.F. Johansson: "Quasi-optical LO injection in an imaging receiver: an electro optical approach", ASP Conference Series, Vol.75, 1995

[4] J.A. Murphy, S.Withington, M.Heanue: "Dammann gratings for local oscillator beam multiplexing" ASP Conference Series, Vol.75, 1995

[5] J.W. Goodman: "Introduction to Fourier Optics", McGraw-Hill, New York,1968

[6] S.J. Walker, J. Jahns: "Array generation with multilevel phase gratings", J. Opt. Soc. Am., Vol 7, No.8,1990

[7] H.Dammann, E.Klotz: "Coherent optical generation and inspection of two dimensional periodic structures", Optical Acta, Vol 24, No.4, pp505-515, 1977

HOLOGRAM CATR FOR MM- AND SUBMM-WAVELENGTHS: A PROGRESS REPORT

T. Hirvonen, P. Piironen, J. Ala-Laurinaho, A. Lehto, A. V. Räisänen,
Radio Laboratory, Helsinki University of Technology,
P.O.Box 3000, FIN-02015 HUT, Finland
E-mail: thi@radio.hut.fi

Abstract-A development work of a 2.4 m × 2.0 m hologram for testing the 1.1 m offset reflector of Odin satellite at 119 GHz is reported. The design is based on the combination of physical optics (PO) and finite difference time domain (FDTD) method. Feasibility of a submillimeter wave hologram CATR is studied theoretically.

1. Introduction

In a hologram type of compact antenna test range (CATR), the feed horn transmits a spherical wave onto one side of a computer-generated amplitude hologram structure which modulates the field such that a planar wave is emanated on the other side of the structure. The antenna under test (AUT) is illuminated with this plane wave. The extent of the volume enclosing the plane wave is called the quiet-zone. The required field-quality of the quiet-zone is driven by the required measurement accuracy of the AUT. Typical requirements are a peak-to-peak amplitude ripple of less than 1 dB and a peak-to-peak phase ripple of less than 10° in the quiet-zone. The advantage of a hologram is its less stringent surface accuracy requirement than that of a reflector which is the traditional collimating element used in CATRs [1,2]. Figure 1 illustrates a facility layout employing a hologram CATR.

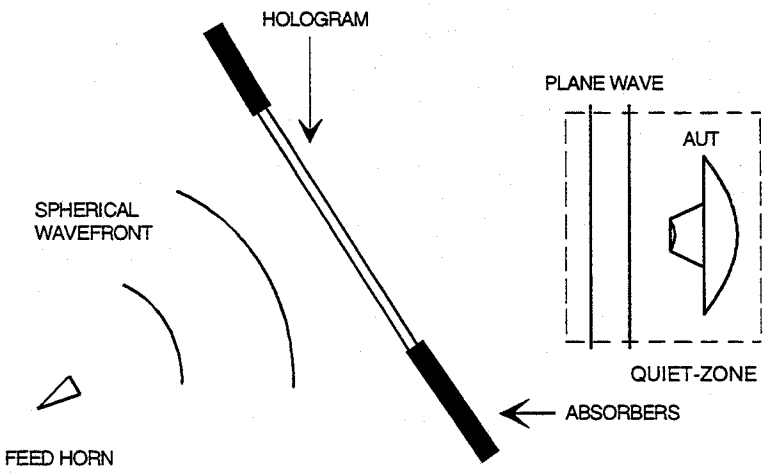

Figure 1. Hologram CATR.

Helsinki University of Technology (HUT) participates in an international, mainly Swedish, Odin satellite project. Odin satellite program is being developed for monitoring aeronomical and astronomical spectral lines. The satellite has a heterodyne receiver at 119 GHz and four heterodyne

receivers at submillimeter wave frequencies between 486 and 580 GHz. The satellite has an offset reflector antenna. The diameter of the main reflector is 1.1 m. The telescope will be tested with a hologram type of a CATR at 119 GHz.

In this paper, the idea of a hologram CATR and the basis of the theoretical analysis are briefly reviewed. The theoretical analysis is based on physical optics (PO) and finite difference time domain (FDTD) method [2,3]. Main emphasis is on the development work of a large 2.4 m × 2.0 m millimeter wave hologram for the Odin telescope tests, and on the current status of the submillimeter wave hologram CATR at HUT.

2. Hologram theory

The binary structure of the amplitude hologram is given (see also [4])

$$T_B(x',y') = \begin{cases} 0, & 0 \le 0.5\left[1+\cos\Psi(x',y')\right] \le b, \\ 1, & b < 0.5\left[1+\cos\Psi(x',y')\right] \le 1, \end{cases} \tag{1}$$

where $b = 1-(1/\pi)\arcsin a(x',y')$. The phase is modulated by the locations of the slots and the amplitude is modulated by the variations of the slot widths. x', y' are the coordinates in the hologram plane, and $0 \le a(x',y') \le 1$ is a real function proportional to the relation between the output and input amplitudes so that the hologram compensates the amplitude variation of the input field and adds an amplitude taper to the amplitude of the output field. The phase term is $\Psi(x',y') = \psi(x',y') + 2\pi\nu x'$, where ν denotes the spatial carrier frequency which separates the diffraction orders produced by the hologram, $\psi(x',y')$ is the normalized phase of the input field in the plane of the hologram. The desired plane wave leaves the hologram at an angle of $\theta = \arcsin(\nu\lambda)$, so that the unwanted diffraction orders do not disturb the quiet-zone of the CATR. The structure of the hologram is derived from the known incident field and the required aperture field, which radiates a plane wave to the quiet-zone. As a result, the hologram consists of narrow curved slots in a conducting plane [2].

The field in the quiet-zone is calculated by using physical optics (PO). The formula for the quiet-zone field is

$$\mathbf{E}(x,y,z) = \int_S E_a(x',y')\frac{1+jkR}{2\pi R^3}e^{-jkR}\left[\mathbf{u}_y(z-z') - \mathbf{u}_z(y-y')\right]dS', \tag{2}$$

where $R = \sqrt{(x-x')^2+(y-y')^2+(z-z')^2}$ is the distance from a point in the aperture to a point in the quiet-zone. In Equation (2), the polarization of the feed antenna is in the $\mathbf{u}_y$-direction. $E_a(x',y')$ is the complex field in the aperture of the hologram. It is calculated with a two-dimensional finite difference time domain (FDTD) analysis. The FDTD prediction is performed across the hologram at a fixed value of y' using the complex field of the feed antenna, in the plane of the hologram, as an excitation. Applying the FDTD analysis incrementally across the entire hologram produces the near-field result which can be integrated (PO) over the hologram surface to

produce the quiet-zone field. Analyzing a single hologram in this way would be prohibitively time consuming taking several months of CPU time on a super computer. However, because the hologram pattern varies slowly with respect to the y'-coordinate, it is sufficient to perform the FDTD analysis at a given $y' = y_n$ and calculate the PO integration over one line in the x-direction, and evaluate the quiet-zone field in the plane at the corresponding $y = y_n$. This analysis was validated by designing, fabricating, and measuring a 55 cm diameter hologram for 119 GHz. The structure of the hologram optimized the quiet-zone field at vertical polarization. Figure 2 shows the theoretical and measured quiet-zone field of the hologram CATR based on the 55 cm diameter hologram. In this case, the optimization was carried out at $y' = 0$ only, and it is more thoroughly reported in [2,3].

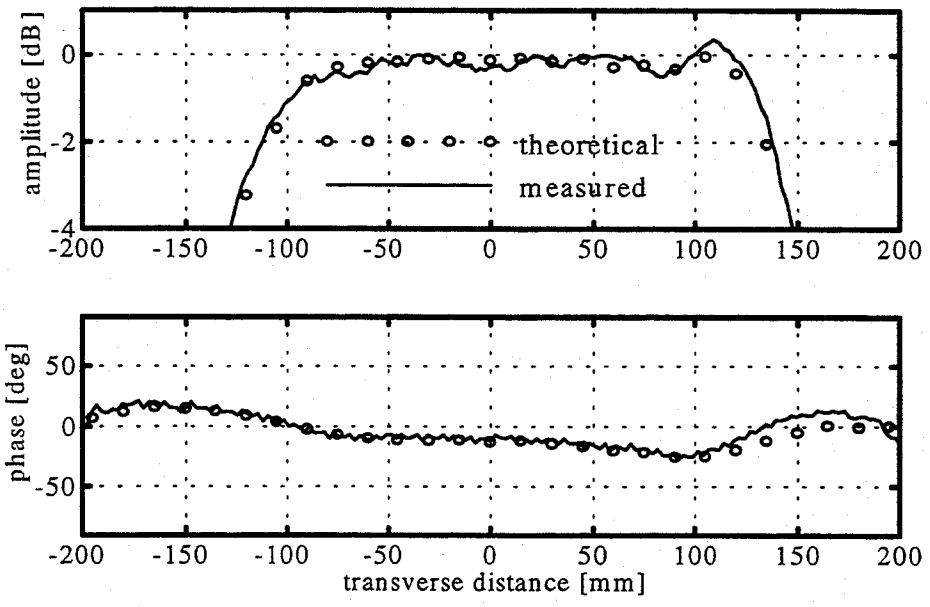

Figure 2. Theoretical and measured quiet-zone field of the 55 cm diameter hologram.

3. Millimeter wave hologram for Odin tests

The purpose of the Odin antenna testing is to verify the radiation pattern of the antenna. In the first phase, during summer of 1997, the radiation pattern of the antenna integrated with the quasioptical feed system will be measured. In the second phase, in the beginning of 1998, the antenna with the quasioptics will be measured after it is mounted on the satellite.

3.1. Hologram design

The size of the facility depends mainly on the required size of the quiet-zone and the way the hologram is illuminated. There is also a slight dependence on the frequency. In this case a 2.4 m × 2.0 m elliptic hologram is designed. The corrugated horn as a feed is placed 6.0 m away from the hologram. The structure of the hologram optimizes the quiet-zone field at vertical polarization 6 m behind the hologram. The plane wave is designed to leave the hologram in an angle of 33.0°. The

thickness of the dielectric film is 75 μm, and the thickness of the copper layer is 35 μm. The relative permittivity of the film is 3.3.

The task of the iterative design procedure is to generate a hologram structure which produces such an aperture field $E_a(x', y')$ which radiates a plane wave to the quiet-zone. The aperture field is calculated with the FDTD analysis after the hologram is generated (Equation (1)). The quiet-zone field is calculated by integrating the aperture field (Equation (2)). Until the quiet-zone field meets the requirements, the hologram needs to be regenerated with changed slot widths and locations in different parts of the hologram. In practice, the problem is to find a proper weighting function $W(x', y')$ for the term $a(x', y') = W(x', y') / \left| E_{\text{feed}}(x', y') \right| \le 1$ which determines the widths of the slots. In the case of the large hologram, the optimization was carried out at $y' = 0$, 250 mm, 500 mm, and 750 mm. The weighting function is as follows

$$W(x', y') = 0.5 \cos^{10}\left[\left(\frac{\rho'}{\rho_e'}\right)^6\right]\left[1.7 - 0.9\cos\left(\frac{x'}{1.2}\right)\right] w_1(x') w_2(x'), \tag{3}$$

where

$$w_1(x') = \begin{cases} 0.92 - 0.08\cos[\pi(x'-0.3)/0.5], & -0.2 \le x' \le 0.8, \\ 1.0, & \text{elsewhere}, \end{cases}$$
$$w_2(x') = \begin{cases} 1.018 + 0.018\cos[\pi(x'+0.45)/0.3], & -0.75 \le x' \le -0.15, \\ 1.0, & \text{elsewhere}, \end{cases} \tag{4}$$

and ρ_e' is the radius of the ellipse, and $\rho' = \sqrt{(x'-\xi)^2 + y'^2}$ which means that the hologram is generated asymmetrically in order to have an asymmetric illumination in the x-direction [5]. The phase in the quiet-zone may be tuned by adding an extra phase term to $\Psi(x', y')$ as explained in [2]. In practice, this means that certain parts of the hologram are generated by using a slightly different angle than 33.0° into which the plane wave is launched. In this case

$$\theta = 33.0 \cdot \theta_1(x') \theta_2(x'), \tag{5}$$

where

$$\theta_1(x') = \begin{cases} 1.00004 - 0.00004\cos[\pi(x'+0.25)/0.25], & -0.5 \le x' \le 0.0, \\ 0.99984 - 0.00016\cos[\pi(x'-0.5)/0.3], & 0.2 \le x' \le 0.8, \\ 1.0, & \text{elsewhere}, \end{cases}$$
$$\theta_2(x') = \begin{cases} 0.99995 - 0.00005\cos[\pi(x'-0.7)/0.1], & 0.6 \le x' \le 0.8, \\ 1.0, & \text{elsewhere}. \end{cases} \tag{6}$$

As a result, the hologram consists of 557 curved slots. The widths of the slots are 0.1–1.3 mm. Figure 3 shows the weighting function (Equation (3)) in the x- and y-direction.

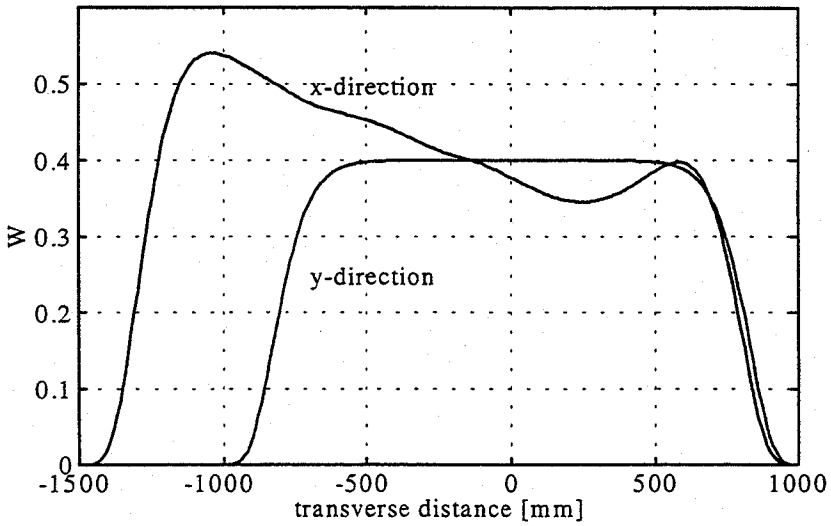

Figure 3. Weighting function in the x- and y-direction.

3.2. Hologram fabrication

The optimized pattern of the hologram is printed on a film with a high-precision plotter. In this case, the resolution is about 760 dots per inch. This film is used as a mask when the pattern is transferred to a copper plated Mylar sheet covered with a photoresist. The fabrication procedure is similar to that used for making printed circuits (silk-screen printing).

The largest size of a high-precision print is 1.2 m × 1.0 m (available in Finland), and 1.0 m wide copper plated Mylar is available. In the pattern transfer and etching procedure, patterns up to about 2.5 m long and over 1 m wide can be fabricated. Furthermore, it is highly desirable to avoid any kind of joints, especially those in the direction of the slots (i.e. vertical), in the center of the hologram. Thus, the hologram is made of three pieces and by using seven masks as shown in Figure 4. The joints of the masks are shown as dashed lines, and the solid lines are the joints between the three pieces. The center part is fabricated by joining three masks together in the pattern transfer process producing a 2.4 m × 1.0 m center part in the etching. The upper and lower parts are fabricated by joining two masks together, respectively. Finally, the three pieces are spliced together by using 50 mm wide and 30 μm thick polyester tape on both sides of the film. The curved lines in Figure 4 illustrate the slots of the hologram.

First version of the 2.4 m × 2.0 m hologram made of three pieces has been fabricated. However, due to unexpected errors in the fabrication, the slots of the hologram are 100–200 μm too narrow producing an erroneous quiet-zone field. Thus, at the moment, only the theoretical quiet-zone field of the large hologram is given, Figure 5. A new, corrected version is under construction.

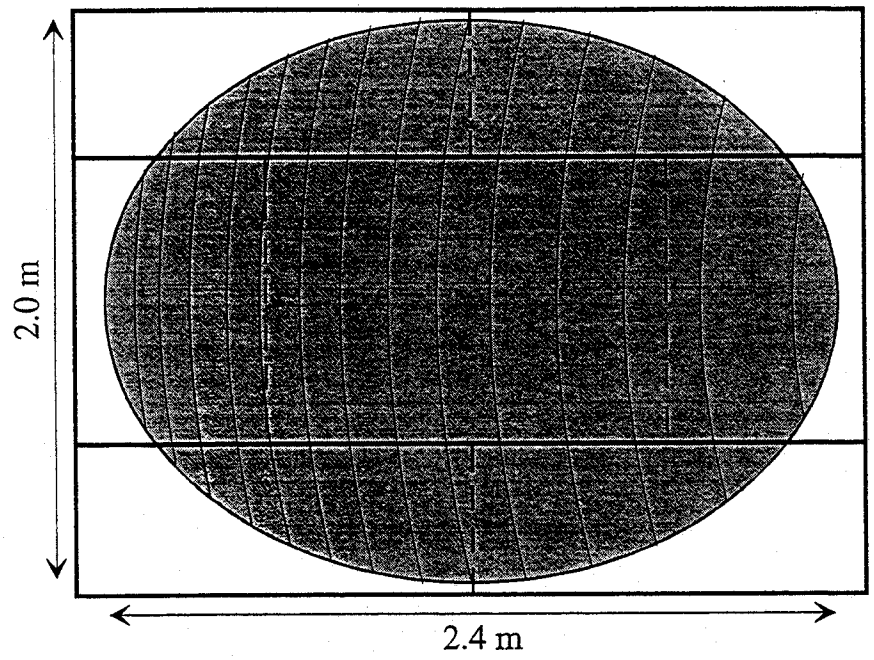

Figure 4. Layout of the hologram fabrication.

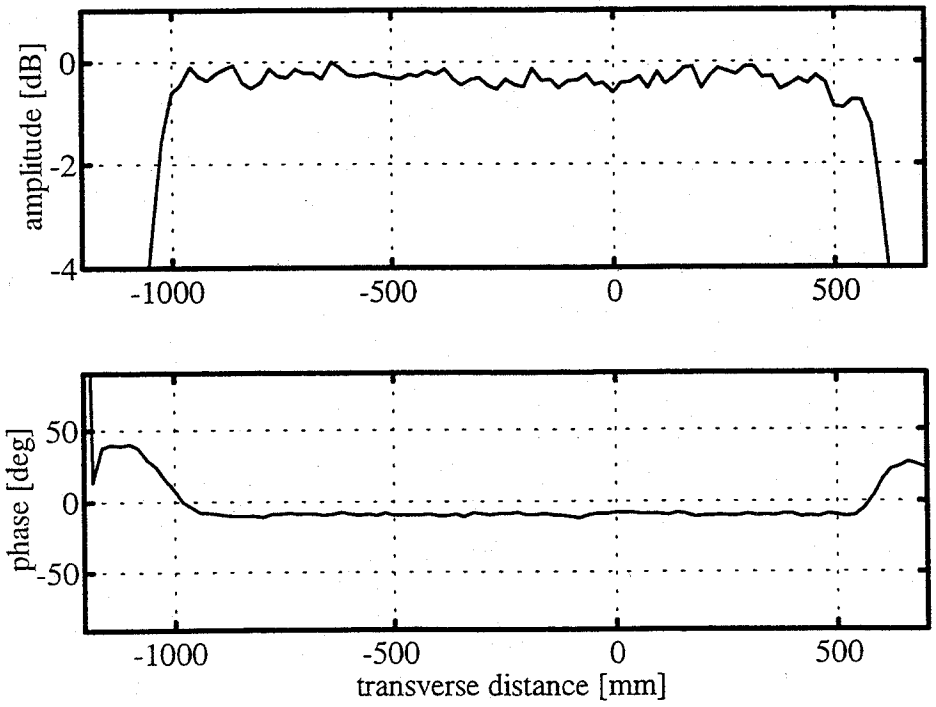

Figure 5. Theoretical quiet-zone field of a CATR employing a 2.4 m × 2.0 m hologram at 119 GHz.

4. Submillimeter wave hologram

The European Space Agency (ESA) is currently examining the use of space-based radiometric instruments to probe the atmosphere in the 200–1000 GHz region. Recently, the Radio Laboratory participated in a study where possible antenna measurement facilities up to 1500 GHz were examined in detail [6]. In this study, the feasibility of a submillimeter wave hologram CATR was theoretically studied by using the combined PO and FDTD method described above. The analyses include the effects of fabrication errors of the hologram pattern and various feed displacements on the quiet-zone field. Also the effect of joints, resulting from the fabrication of the hologram of several pieces, is discussed in [6]. Based on these results, the quality of the attainable quiet-zone at submillimeter wavelengths may be estimated. As an example, part of the results of the performance analysis of a submillimeter wave hologram CATR is given here.

Fabrication errors are due to the inaccuracies of the three main steps in the fabrication procedure: 1) mask (inaccuracy of the printer and the limited size of the graphics file), 2) pattern transfer, and 3) etching. Furthermore, the fabrication errors may be divided into systematic errors and random errors. Due to systematic fabrication errors, all the slots of the hologram are wider or narrower than in an ideal case. Because of the random errors the slots are randomly either wider or narrower than in an ideal case. The order of magnitude of the systematic errors due to each of the three steps of the fabrication procedure may be estimated at 10 μm in the width of the slot. This means that ±30 μm is the worst case, and ±17 μm is the RSS case. The random errors are considered to be due to the limited size of the graphics file or the resolution of the precision printer, and it means that the edges of the curved slots are serrated instead of being smooth. This error is not exactly random but may well be estimated with a normally distributed random error in the widths of the slots. In the case of the millimeter wave hologram [2], this error was measured to be 9 μm. However, a better resolution is achievable.

The effect of these inaccuracies has been estimated at frequencies of 200 and 500 GHz with 20 cm diameter holograms optimized for vertical polarization. In the analysis, the widths of the slots were changed by ±10 μm, ±30 μm , and ±50 μm. The standard deviation in a case of random errors was 5 μm, 10 μm, and 20 μm. The effect of the joints (and gaps) was studied by introducing a 100 μm wide gap in the center of the hologram (at 119 GHz the effects of larger gaps have been studied as well). Figure 6 shows the effect of various fabrication errors on the quiet-zone field compared to the ideal case at 500 GHz. The amplitude curves have been vertically shifted in order to separate them from each other.

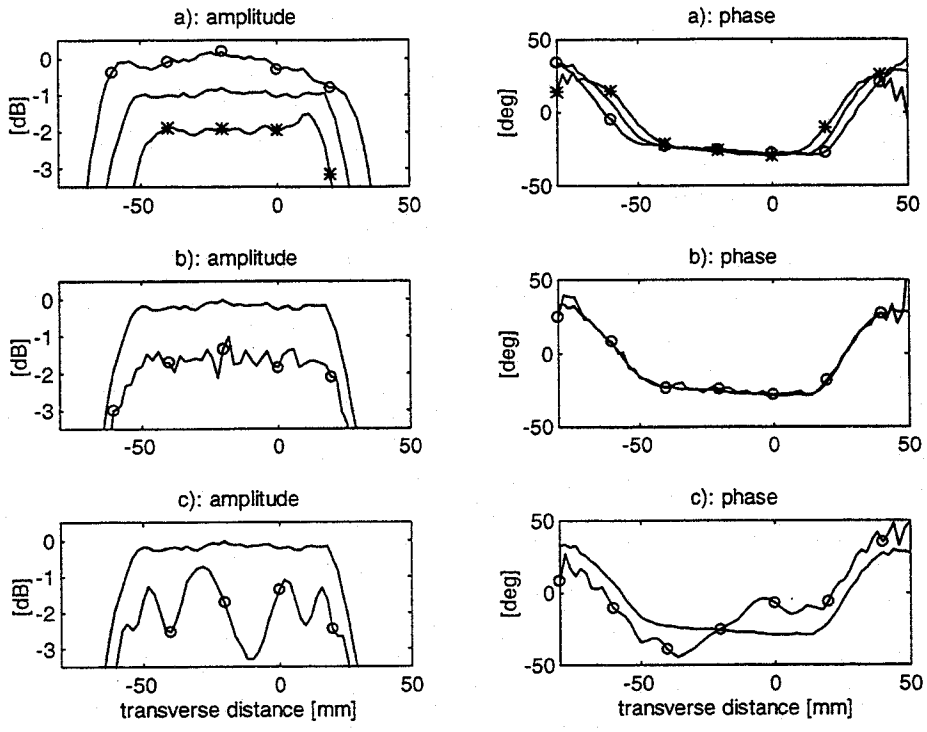

Figure 6. a) Effect of the ± 30 μm systematic fabrication errors: ideal case (-), + 30 μm (o) and – 30 μm (*), b) effect of the random error, σ = 10 μm (o), c) effect of a 100 μm vertical gap in the center of the hologram (o).

The effect of a specific error depends on the frequency, the geometry of the facility (i.e. focal length and diameter of the hologram), and the weighting function. However, these results should give a realistic estimation of the feasibility of a submillimeter wave hologram CATR. Systematic fabrication errors increase slightly the quiet-zone ripple, but the main effect is the change of the size of the quiet-zone. Random errors clearly increase the amplitude and phase ripple in the quiet-zone, and the highest possible resolution of the printer should be utilized. Vertical gaps in the hologram structure have been found to be very undesirable in the development of the 2.4 m × 2.0 m hologram for the Odin tests at 119 GHz. This analysis and those made at 119 GHz confirm that vertical joints should be avoided.

5. Conclusion

A hologram type of compact antenna test range (CATR) utilizes a computer-generated amplitude hologram to form the desired plane wave from the feed horn spherical wave. The analysis method based on physical optics (PO) and finite difference time domain (FDTD) method is validated by comparing the theoretical and experimental results of a CATR employing a 55 cm diameter hologram at 119 GHz. The design, fabrication method, and the theoretical quiet-zone field of a CATR based on a 2.4 m × 2.0 m hologram is presented. Furthermore, feasibility of a submillimeter wave hologram CATR is studied theoretically.

Acknowledgments

The authors are grateful to Mr. Lauri Laakso and Mr. Lorenz Schmuckli for helping in the mechanical aspects related to the testing of the holograms in this work.

6. References

[1] Tuovinen, J., Vasara, A., Räisänen, A.: A new type of compact antenna test range at mm-waves. *Proceedings of the 22nd European Microwave Conference*, Espoo, 1992, pp. 503–508.

[2] Hirvonen, T., Ala-Laurinaho, J., Tuovinen, J., Räisänen, A.: A compact antenna test range based on a hologram. Accepted for publication in *IEEE Transactions on Antennas and Propagation*, 1997.

[3] Ala-Laurinaho, J., Hirvonen, T., Tuovinen, J., Räisänen, A. V.: Numerical modeling of a non-uniform grating with FDTD. Accepted for publication in *Microwave and Optical Technology Letters*, 1997.

[4] Vasara, A., Turunen, J., Friberg, A. T.: Realization of general nondiffracting beams with computer-generated holograms. *Journal of Optical Society of America A,* Vol. 6, 1989, pp. 1748–1754.

[5] Ala-Laurinaho, J., Hirvonen, T., Räisänen, A.: Optimization of a submillimeter wave hologram CATR. To be appeared in *Proceedings of the IEEE AP-S International Symposium*, 1997.

[6] Foster, P. R., Martin, D., Parini, C., Räisänen, A., Ala-Laurinaho, J., Hirvonen, T., Lehto, A., Sehm, T., Tuovinen, J., Jensen, F., Pontoppidan, K.: Mmwave antenna testing techniques–Phase 2. *MAAS Report 304*. ESTEC Contract No 11641/95/NL/PB(SC), 1996.

THE IRAM 230 GHz MULTIBEAM SIS RECEIVER

K.-F. Schuster, J. Blondel, M.Carter, A. Karpov, J. Lamb
B.Lazareff, F. Mattiocco, S. Navarro, J.-L. Pollet
IRAM
Institute of Millimetre Radio Astronomy
300 rue de la piscine, 38406 St Martin d'Heres

Abstract:
We present the optical, electrical and cryogenic design of the SIS 230GHz heterodyne array receiver for the IRAM 30m telescope. This telescope receiver combination will offer unique possibilities for high resolution mapping at mm wavelengths. The design of the multibeam receiver includes compact low loss optics including a possibility for field derotation. The size of the dewar window and therefore the heat load on the closed cycle refrigerator can be kept small and independent of the number of mixer elements The receiver will use SIS mixers in waveguide technology including a waveguide LO coupling scheme. The SIS mixers will have single variable backshorts which allow for SSB tuning. We discuss theoretical and experimental results of the receiver optics, which characterise the image quality and coupling efficiency.

Introduction:
The interest in array receivers for mm-radio telescopes originates from the idea that such receivers should allow for an increase in mapping speed over single-beam receivers. As the noise temperatures of existing receivers have constantly decreased over the last years, more and more attention is drawn to the possibility of mapping with high efficiency even during suboptimal weather conditions where the system temperature may be more influenced by the sky emission. Array receivers are the obvious solution to this demand. The considerable effort in the development of such receivers should pay off with a clear improvement in mapping speed (factor 5-10).
Increased mapping speed is however not the only advantage of array receivers. Array receivers also allow for various self-calibration schemes, which can reduce sky noise and improve relative calibration. Furthermore, with chopping between different elements of the array a maximum point source sensitivity can be achieved.
In practice there are currently two possible ways to achieve a real improvement in mapping speed. On one side it is possible develop an array with a very large number of elements with simple electrical and mechanical construction but probably mediocre performance in terms of noise temperature and optical coupling. On the other hand one can think of a moderate sized array with an optimised element performance very close to that of a single or dual channel receiver.
For the IRAM 30m telescope a moderate sized high performance array is more attractive than a very large array with mediocre single element performance because the number of beams is

limited anyway by the Nasmyth apertures. Such a solution is also better adapted to the still very limited availability of suitable wideband backends. IRAM decided to develop a medium sized array receiver (with 9 then 18, with possible future extension to maximal 32 elements) with high efficiency single elements reaching the performance of state of the art single channel receivers and the following specifications:

- Close Spacing of Beams (2 FWHM)
- Possible Field Derotation
- $T_{DSB} < 50$ K
- RF Bandwidth 206-275 GHz
- IF Bandwidth 1 GHz
- SSB Operation Option.

Optics:

The optics of a suitable array receiver should have very low loss and allow for field derotation. The constraints to be considered in any design are given by the telescope apertures, the maximum heat load on the dewar, the tolerable aberrations and last but not least the very limited space in the receiver cabin.

We chose a combination of a modified Gaussian telescope and a truncated lens array (Fig. 1). The external warm part of the optics is purely reflective. A combination of two off axis elliptical mirrors forming the Gaussian telescope with a moderate demagnification factor of 1.4 turned out to be useful for several reasons.
The external ambient temperature mirror focuses the beams onto a relatively small dewar window (∅ 9 cm). The primary aperture field is reimaged as a topheat function onto the dewar window. Therefore all energy coming from the telescope passes through a well-defined diameter at the dewar entrance.
By placing the warm elliptical mirror as the top mirror in a K-mirror derotator combination the incidence angles (and therefore the aberrations) as well as the spatial dimensions of the K-mirror can be kept small.
The cold part of the optics consists of the second elliptical mirror and flat which folds the beams onto a crossed wire grid. This grid separates out the different polarisation of the beams, which are finally coupled over truncated lens arrays into the individual corrugated feed horns.
The performance of the optics was investigated with the software packages ASAP and ZEMAX. We used ZEMAX to minimise aberrations occurring from the combination of two off axis ellipsoids with varying relative orientation due to the derotator movement. The optimisation resulted in a configuration where the mirrors had unchanged effective focal lengths but considerably lower conical constants. In other words we could improve the imaging performance of the system for different K-mirror positions by making the mirrors more spherical.

The radiation field of a point source was calculated at the position of the horn aperture with ASAP. From there a coupling to the horn can be derived by means of overlap integrals. In this calculations we assumed a linear relation between the point source position and the position of the horn e.g. we assumed an undistorted field of view. Figure 2 shows the calculated coupling for different positions across a diagonal of the image plane. A good coupling can be achieved for a field of 4x4 beams. The decrease in coupling with increasing diagonal offsets is a combination of beam distortion and deviations from the assumption of undistorted field

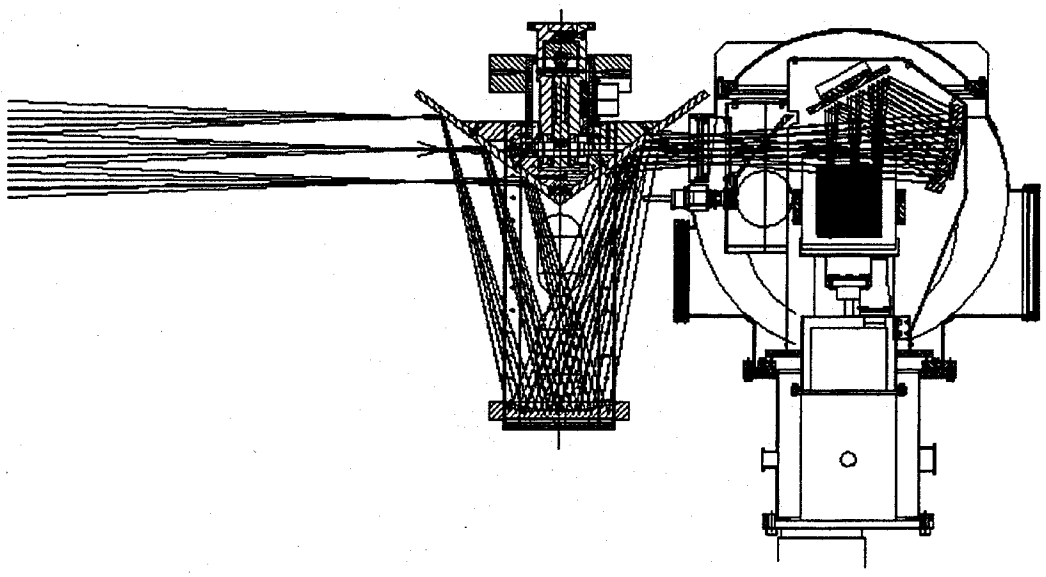

Fig. 1 : Layout of the 230 Hz SIS multibeam receiver. Although only nine beams are indicated the occupied field of view corresponds to a 4x4 field covered with beams separated by 2 FWHM . The horns of the mixers are orientated perpendicular to the plane of view.

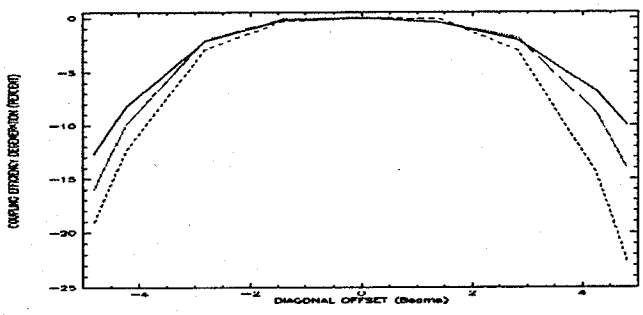

Fig 2.: Coupling efficiency across the field of view. The maximum coupling at the centre corresponds to the theoretical limit of 85 %.

To experimentally verify the optical layout all optical components including the cutted lens array and the aperture of the dewar window was mounted on a breadboard. The characteristics of the optics was measured by using the foreseen corrugated mixer horn as an emitter (200-260 GHz) while the resulting pattern was measured in a plane in front of the optics close to the location of the telescopes secondary focal plane.

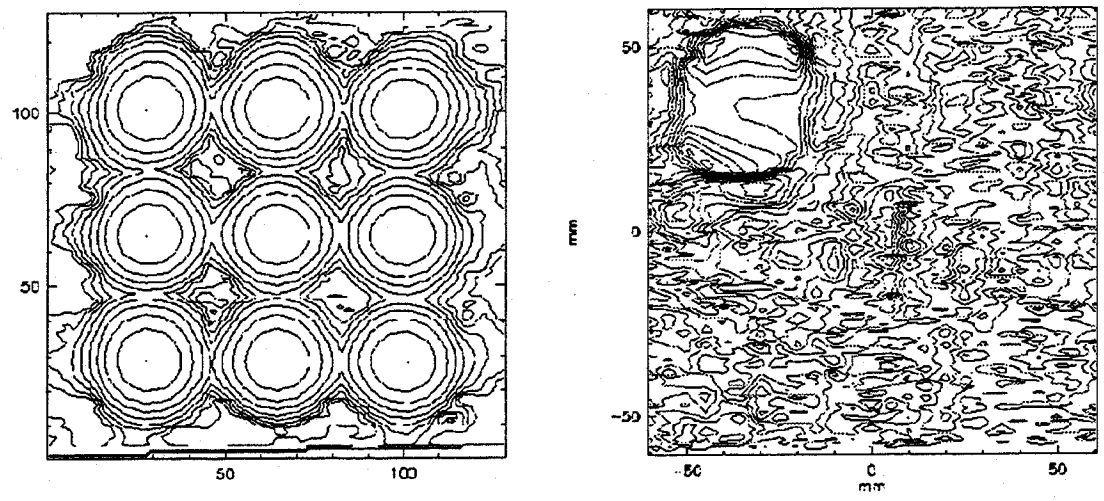

Fig 3. : Left: Measured amplitude pattern of the assembled receiver optics in 5 dB steps.
Right. : Measured phase pattern of a single beam, contours in 10 degrees steps.

The planar measurement was done with a waveguide probe mounted on a remote controlled XY table. Phase and amplitude were recorded with the set-up described in [1]. Fig 3 shows the amplitude pattern of the array. The beams are very clean and sidelobe levels are lower than 25 dB. The individual beams are arranged in a perfect 3x3 pattern with displacements smaller than 0.2mm corresponding to a deviation from the ideal pattern of less than 0.15 arcsec on the sky.

The correct position of the beams is however not the only necessary condition, a proper and common illumination of the subreflector by all pixels is equally important. To verify such an operation we performed a two-dimensional fit of a fundamental gaussian mode to the measured amplitude and phase distribution of each pixel (see Table 1). The maximum angular deviation of the beams is about 0.004 radians corresponding to a misalignment of about 8 cm at the 2 meter wide secondary. The results therefore show that all beams are illuminating the secondary mirror of the telescope equally well for a common focus.

As the derotator is very critical to align we developed a high precision mechanics which allows a compact motor drive under the rooftop mirrors of the K-mirror. By laser alignment we found that the beams move less than 0.5 mm in the focal plane which corresponds to a movement of 0.36" on the sky. Such a beam displacement is tolerable without changing the pointing model of the telescope.

Pixel	w0 [mm]	z0 [mm]	αx [rad]	αy [rad]	η
1	11.2	-16	0.001	0.002	0.99
2	10.9	-16	0.002	0.001	0.98
3	11.2	-12	-0.003	0.001	0.99
4	10.2	-37	0.001	-0.001	0.98
5	11.5	-36	0.001	-0.001	0.99
6	11.3	-80	0.002	-0.002	0.98
7	11.1	-60	0.0	0.0	0.98
8	11.2	-70	-0.001	0.001	0.99
9	11.1	-11	-0.002	0.0	0.98

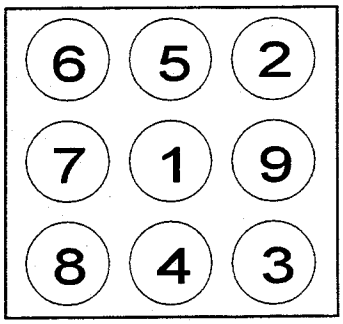

Table 1: Result of two-dimensional fits to nine pixels in the focal plane in front of the receiver optics. w0 designs the waist radius and z0 the position of the waist in direction of the beam propagation. αx and αy are the angle of the best fit gaussian beams in respect to the normal vector as defined by the measurement plane. Because η is not the final beam efficiency it should best be considered as a quality parameter of the fit.

LO Distribution :

The LO distribution is entirely made in WG technology which allows a very compact optical design. The LO power is generated separately for each polarisation of the array by a gunn-tripler combination. This power is then split up by an optimised 3 way power splitter

a)

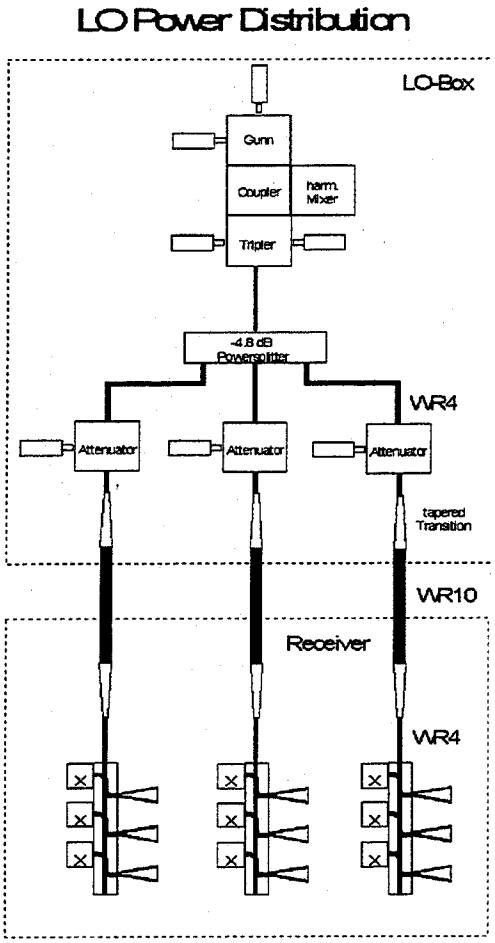

b)

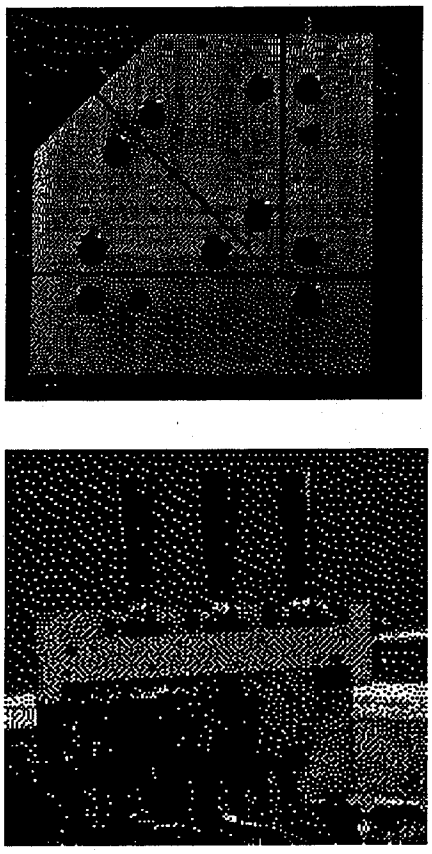

Fig. 3: a) LO power distribution scheme for one polarisation. Waveguide power splitter (upper photo) and triple mixer waveguide coupler unit (lower photo).

(see Fig. 3) followed by an attenuator in each branch. Three mixers are provided with LO power by a serial triple coupler built as a sidewall hole coupler (coupling 15 dB). This arrangement emerges from a compromise between available LO power and the necessary flexibility to adjust the LO power for different mixers of the array (see below). The connection between the external LO box and the couplers on the 4 K stage of the receiver is done by overmoded waveguides in order to reduce losses. First results of the triple mixer unit indicate a possible operation of the mixers within the defined specifications.

[1] M. Carter, S. Halleguen, B. Fouilleux , Proceedings of the 5th International Workshop on Terahertz Elektronics, Sep. 1997, Grenoble, France.

A Superconducting Sub-millimeter Wave Limb Emission Sounder (SMILES) on the Japanese Experimental Module (JEM) of the Space Station for Observing Trace Gases in the Middle Atmosphere

Harunobu Masuko, Satoshi Ochiai, and Yoshihisa Irimajiri
Communications Research Laboratory (CRL), Ministry of Posts and Telecommunications
4-2-1, Nukui-kita-machi, Koganei, Tokyo 184, Japan
Phone: +81-423-27-7544, Facsimile: +81-423-27-6110, E-Mail: masuko@crl.go.jp

Junji Inatani and Takashi Noguchi
Nobeyama Radio Observatory, National Astronomical Observatory (NAO/NRO)
Nobeyama, Minami-maki-mura, Minami-saku, Nagano 384-13, Japan
Phone: +81-267-98-4382, Facsimile: +81-267-98-2684, E-Mail: inatani@nro.nao.ac.jp

Yukiei Iida, Naomi Ikeda, and Noritaka Tanioka
Tsukuba Space Center, National space Development Agency of Japan (NASDA)
2-1-1, Sengen, Tsukuba, Ibaraki 305, Japan
Phone: +81-298-52-2277, Facsimile: +81-298-52-2299, E-Mail: yiida@rd.tksc.nasda.go.jp

ABSTRACT

Trace gases such as ClO, BrO, HO_2, etc. from the upper troposphere to the stratosphere play important roles in the depletion of the ozone layer and are closely related to the climate change. Emission spectroscopy using a low-noise heterodyne technique in the sub-millimeter wave range is the most promising method to remotely measure the ozone and these trace gases. The space-borne limb emission sounder can globally observe the 3-dimensional distributions of these trace gases. We submitted a proposal for an experiment of a Superconducting Sub-millimeter Wave Limb Emission Sounder (SMILES) on the Exposed Facilities of the Japanese Experimental Module (JEM) of the Space Station, and the proposal was accepted by the Space Development Board and the Science and Technology Agency of Japan in March 1997. The JEM/SMILES will be operated at 640GHz-band with 10-14GHz IF frequencies. The parallel-connected-twin-junctions (PCTJ) type SIS mixers developed in NAO/NRO will be used for the ultra-high sensitive receiver. The operation conditions for the SIS receiver will be achieved by a compact Joule-Thomson refrigerator combined with a two-stage Stirling refrigerator. In this experiment, we are aiming to demonstrate the effectiveness of the sub-millimeter wave limb emission spectrometry in observing the atmospheric environment from space, to attempt an application of superconduction in space, and to operate a mechanical 4K-refrigerator in space. The JEM/SMILES is a pre-phase of SMILES on an atmospheric environment observing satellite, ATMOS-C1, which is planned to be launched around 2006.

1. BACKGROUND

The depletion of the stratospheric ozone is caused by trace gases, such as ClO, BrO, HO2, etc., in the stratosphere. Climate change is closely coupled with chemistry interactions in the Lower-Stratosphere and the Upper-Troposphere. Scientific issues for the understanding of Ozone Depletion and Climate Change concern the understanding of the chemical processes related to trace gases, the understanding of the coupling between the dynamic and the chemical processes, and the understanding of the interactions between the Troposphere and the Stratosphere, the Equatorial region and the Mid-latitudes, and the Mid-latitudes and the Polar regions. The first issue, concerning chemical processes related to trace gases, requires the simultaneous observations of ozone, water vapor, and the trace gases in the Stratosphere and the upper Troposphere, together with the atmospheric temperature and pressure. The second issue, concerning dynamic and chemical process coupling, requires high time and spatial resolution. The third issue, concerning regional interactions, requires 3-dimensional global observations, with diurnal and seasonal variations.

Sub-millimeter wave limb emission sounding from space has many advantages in meeting these requirements. Many kinds of the trace species have intense spectral bands in the sub-millimeter wave range (Pickett et al., 1992). Heterodyne spectroscopy can achieve high spectral resolution, such as 1MHz or less, i.e. $\Delta\lambda/\lambda$~1E-06, which is very effective for precise observations. Emission measurements day and night independent of sun-light in any regions are the best way for global observations and are essential for understanding the diurnal cycles of the chemical processes. The limb sounding technique gives high sensitivity and sufficient height resolution of nearly 2km. Figure 1 shows an overview of limb sounding from space. Measurements in the sub-millimeter wave range are less dependent on atmospheric temperature, and are not affected by aerosols and

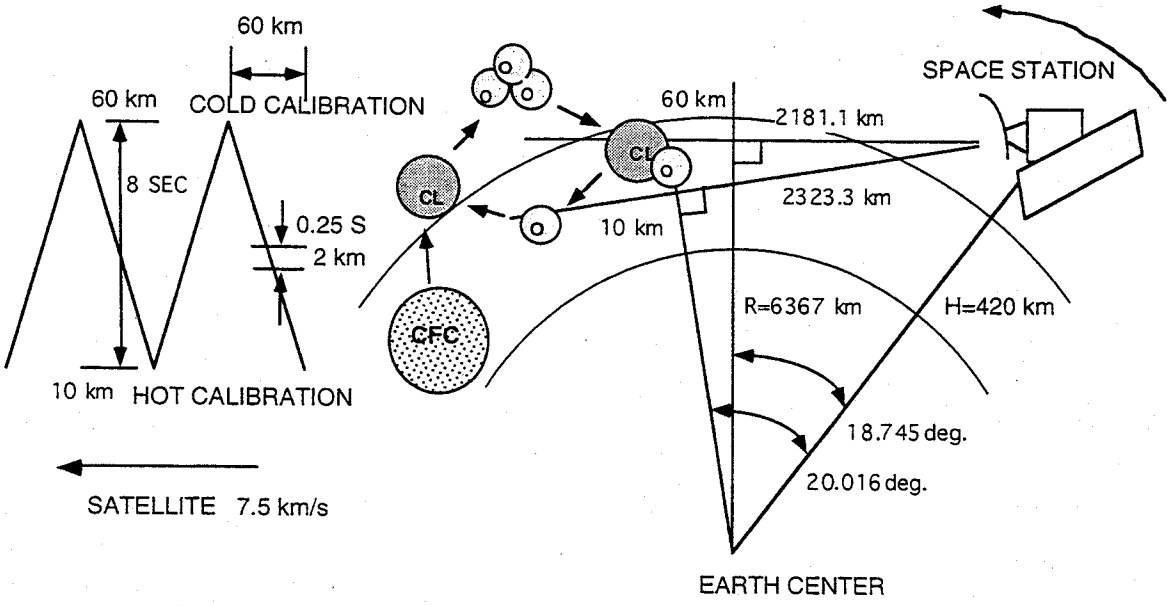

Figure 1. Over view of limb emission sounding.

chemical processes. The conditions make precise observations possible. There are well-provided spectroscopic data bases in the sub-millimeter wave lengths, which are essential for reliable observations. In addition, the heterodyne system can be compacted both in size and weight.

On the other hand, there should be engineering breakthroughs to satisfy the scientific requirements. Measurements of very weak signals with short integration time demand ultra-high sensitivity (ultra-low noise temperature). Figure 2 shows examples of the faint spectra of BrO and HOCl. The best solution to measure such very weak signals is to use a superconductor receiver. Short sub-millimeter waves, such as 0.5mm or less, are profitable for observing the various trace gases up to high altitude range with high signal-to-noise ratio. Figure 3 shows comparison of the ClO spectra in the different frequency bands. Measurements with multiple frequency bands, wide bandwidths in intermediate frequencies (IF), i.e. higher IF, and wide-band spectroscopy are required for simultaneous observations of the trace gases, atmospheric temperature, and pressures. Single-side-band (SSB) operation and high-resolution spectroscopy are needed for reliable quantitative observations.

In order to investigate the sub-millimeter wave limb emission sounding of the trace gases and demonstrate advanced technologies in space, we submitted a proposal for an experiment of a Superconducting Sub-millimeter Wave Limb Emission Sounder (SMILES) for the announcement of opportunity (AO) on the use of the Exposed Facility (EF) of the Japanese Experimental Module (JEM) of the Space Station. The AO had been issued by the National Space Development Agency of Japan (NASDA) in October 1996, according to the decision by the Space Development Board and the Science and Technology Agency (STA) of Japan. The proposal was accepted in March 1997. We describe an overview of the experiment of JEM/SMILES in this report.

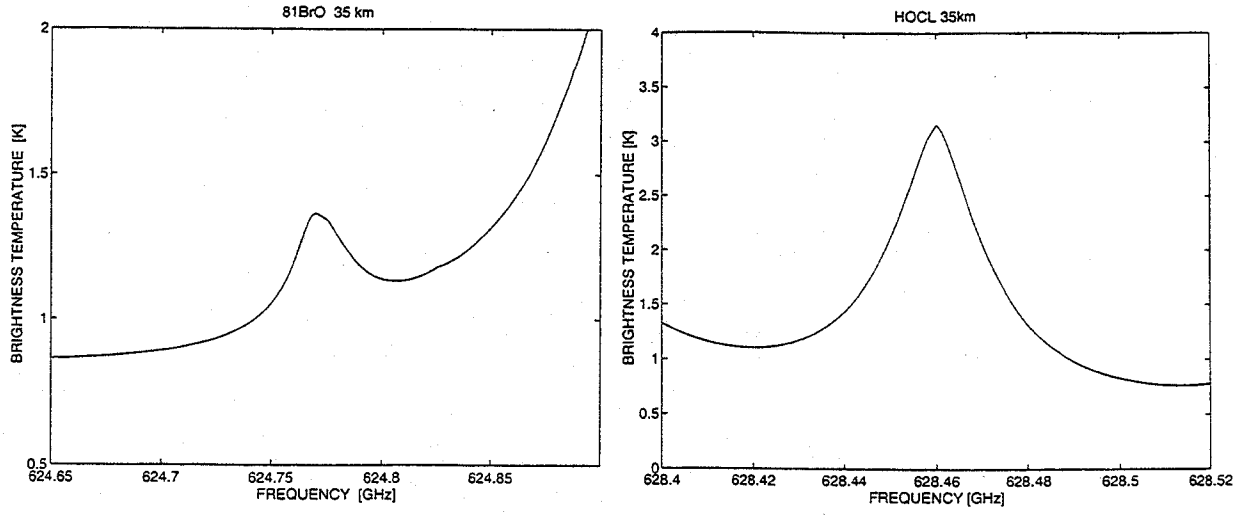

Figure 2. Examples of faint spectra of BrO (left) and HOCl (right) in the sub-millimeter wave range.

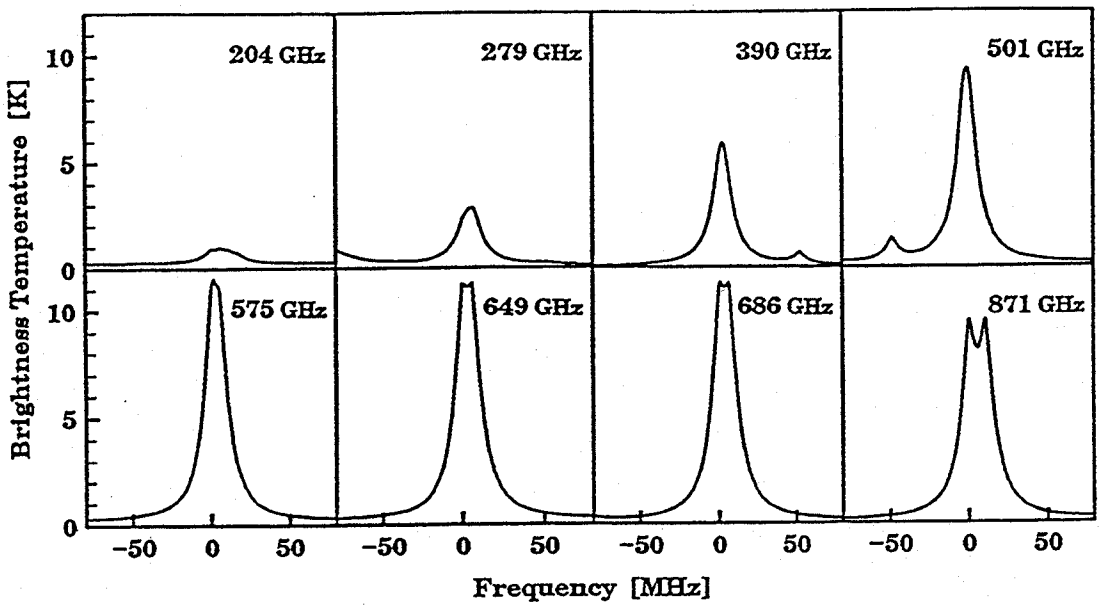

Figure 3. Calculated ClO limb emission spectra in the different frequency bands at the tangent height of 40 km.

2. OBJECTIVES OF THE EXPERIMENT

The experiment of JEM/SMILES has both engineering and scientific objectives. In this experiment, we have proposed to use superconductor-insulator-superconductor (SIS) mixers for the ultra-high sensitive receiver operated around 640GHz. Mechanical cooling is essential for long-term continuous operation of the system. Therefore, the first engineering issue is to establish the key technologies for applications of the sub-millimeter waves, the superconductors (SIS mixers), and the 4K-refrigerator in space. The second engineering issue is to demonstrate the performance of the total system in space. The third engineering issue is to establish the calibration and validation techniques of the system in space.

The first objective for the scientific issues mentioned above is to demonstrate the simultaneous 3-dimensional and global observations of the trace gases in the Stratosphere from space. The second objective is to estimate the accuracy, the possible height range, and other conditions of the observations in each area, i.e. the Equatorial, the Mid-Latitude, and the Polar regions. The third objective is to specifically demonstrate the scientific effectiveness of the observations by investigating the coupling between the chemical processes and the dynamics and regional interactions in the Northern Hemisphere. Recently, the Ozone Depletion processes have been rapidly progressing around the North Pole region.

3. SPACE STATION AND JEM

Figure 4 and 5 show overviews of the configuration of the space station and JEM, respectively. JEM is composed of a pressurized module and a exposed facility. The exposed

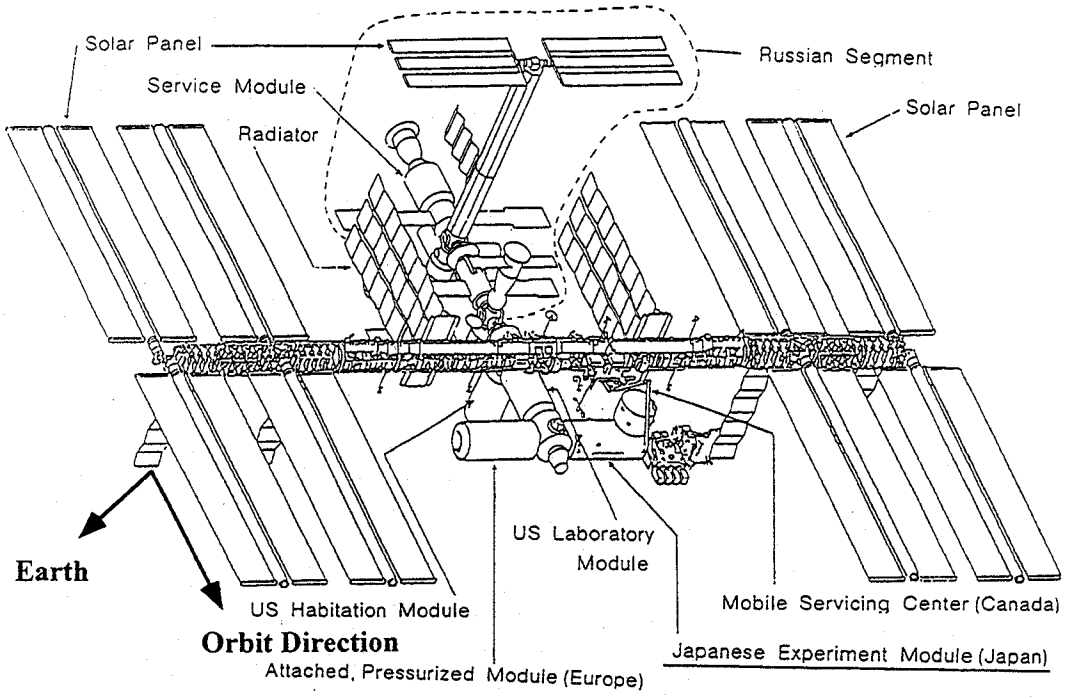

Figure 4. Configuration of Space Station.

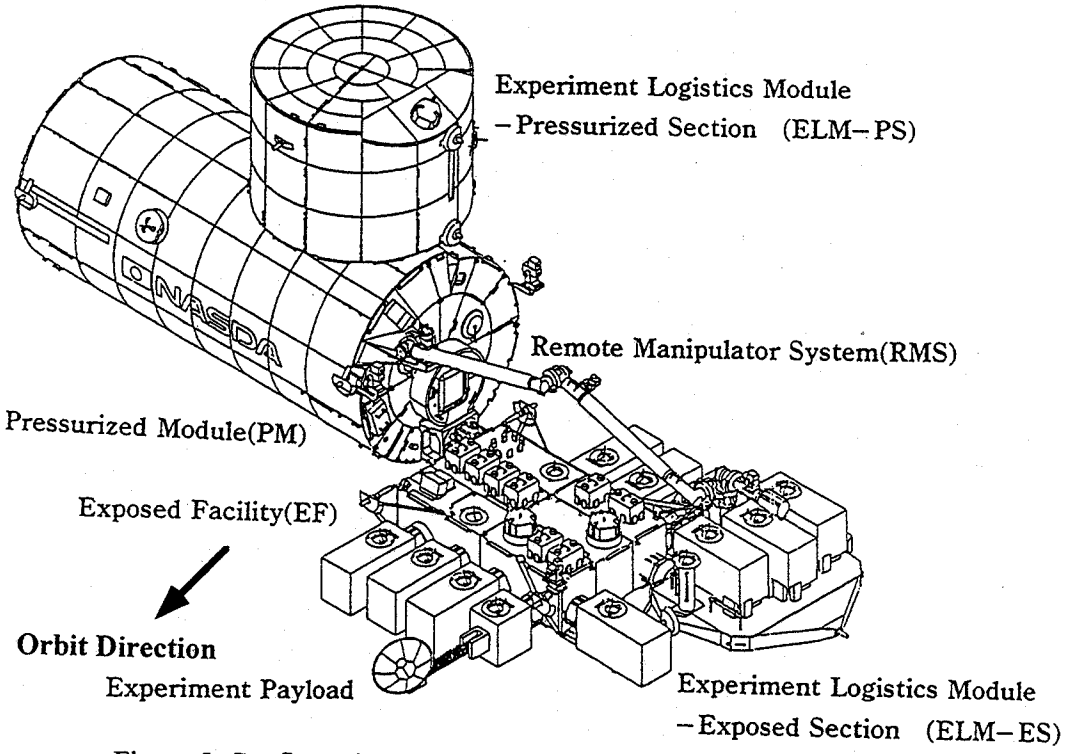

Figure 5. Configuration of the Japanese Experiment Module (JEM).

facility has 10 interface ports to connect the experimental payload units. The use of the interface ports are shared between Japan and US. The AO at this time is for the first use of 4 interface

ports on the Japanese side. Electricity with maximum of 3kW, cooling liquid, and services of signal networks including Ethernet are supplied through the interface ports. The normal interface ports are fit for an experimental payload unit with a maximum weight of 500kg.

The space station has a circular orbit with an inclination angle of 51.6 degrees and a nominal altitude of 407km. No attitude control are made during the inertial flights provided for the microgravity experiments, which results in the attitude drifts up to plus or minus 15 degrees in each of the pitch, roll and yaw directions. In these cases, compensation of the drifts and precise measurements of the attitude become essential for the limb scanning observations.

4. PROPOSED SYSTEM

Almost all of the important trace species, such as ozone, ClO, HCl, HOCl, BrO, HO_2, H_2O-isotope, and O_2-isotope, have absorption bands around 640GHz, and atmospheric opacity is comparatively low around this frequency. Therefore, we have adopted a frequency band around 640GHz for SMILES. Table 1 shows the trace gases observed around this frequency band and the estimated bandwidths to be necessary for the observations. The observation frequencies can be divided into 2 frequency regions. One is used as the lower side-band and the other is used as the upper side-band Both bands are detected separately under SSB conditions. A candidate for the local frequency is 638GHz. In order to satisfy the wide bandwidth observation, an IF of almost 10-14GHz is required. Figure 6 shows a calculated limb emission spectral profile for the upper

Table 1. Objective trace gases, their observation frequencies, and the required band-width (in parentheses, MHz) considered for JEM/SMILES. Local frequency of 638GHz.

SPECIES	624.2-628.6 GHz	646.9-651.9 GHz	COMMENTS
O_3	-	647.840 (600)	Depletion & Green-house Gas
$O^{18}O$	627.773 (600)	-	Temperature/Pressure
ClO	-	649.45 (200)	Ozone Depletion
HCl	625.90-93 (200)	-	Chlorine Reservoir
HOCl	628.46 (100)	-	Chlorine Reservoir
ClO_2	624.271-272 (100)	-	Ozone Depletion
$CH_3{}^{37}Cl$	627.177 (100)	-	Parent Molecule
^{81}BrO	624.77 (100)	-	Ozone Depletion
$H_2{}^{18}O$	-	647.198 (600)	Parent & Green-house Gas
HO_2	625.661/664 (100)	-	Ozone Depletion
H_2O_2	-	647.026 (100)	Hydrogen Reservoir
N_2O	627.748 (600)	[652.834 (600)]	Nitrogen Reservoir
NO	-	651.771-773 (100)	Ozone Depletion
HNO_3	-	650.279 (100)	Nitrogen Reservoir
SO_2	624.344 (100)	-	Volcanic, Aerosol

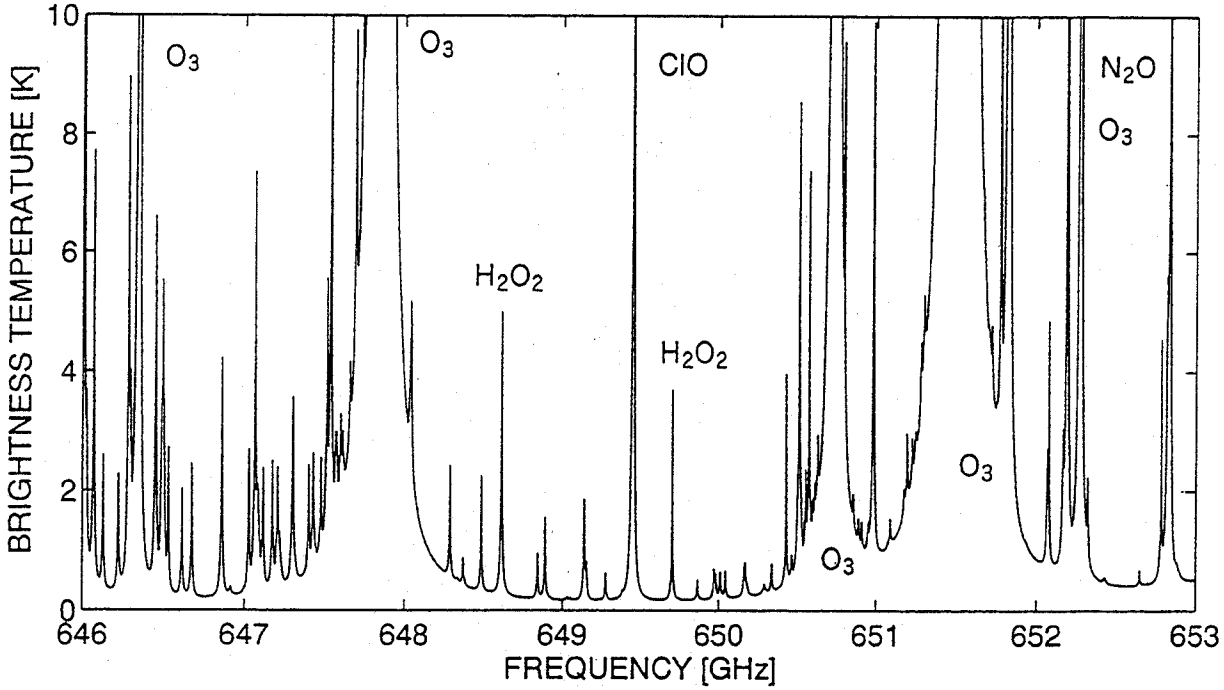

Figure 6. Calculated limb emission spectral profile for the upper side-band region of JEM/SMILES at the tangent height of 35km.

side-band region.

Figure 7 shows the block diagram of the JEM/SMILES system. The system is composed of an antenna sub-system, receiver optics, a phase-locked oscillator, a cryogenic sub-system, a 4K refrigerator, an IF sub-system, spectrometers, and a sub-system of signal processing and system control, in addition to JEM interface equipment and related sub-systems. Table 2 shows the performance required for JEM/SMILES.

The antenna has a elliptical feature with a long axis of nearly 60cm and a short axis of nearly 30cm. The beam width in the vertical direction is designed to be less than 0.06 degrees, by which a height resolution of nearly 2 km can be obtained. A offset Cassegrain type is proposed. The surface accuracy of the antenna is designed to be 9 μm, in order to obtain a high beam efficiency larger than 90%. A thin membrane will be attached in front of the antenna to prevent thermal distortion caused by direct illumination of sunlight. The antenna beam is tilted 45 degrees to the right-hand side, in order that JEM/SMILES can observe the areas with a longitude up to nearly 65 degrees north. The antenna can be moved nearly from -10 to -25 degrees in the elevation direction to mainly compensate for the attitude change in pitch direction. The attitude drift is expected to be very slow. In order to observe the tangent height from 10 to 60km, the antenna is scanned at every 0.05 degrees step in the elevation range of 1.27 degrees. A star sensor will be used for obtaining the precise pointing information. Real-time pointing control is not used in the system.

The quasi-optical transmission system includes reference, calibration, and local signal

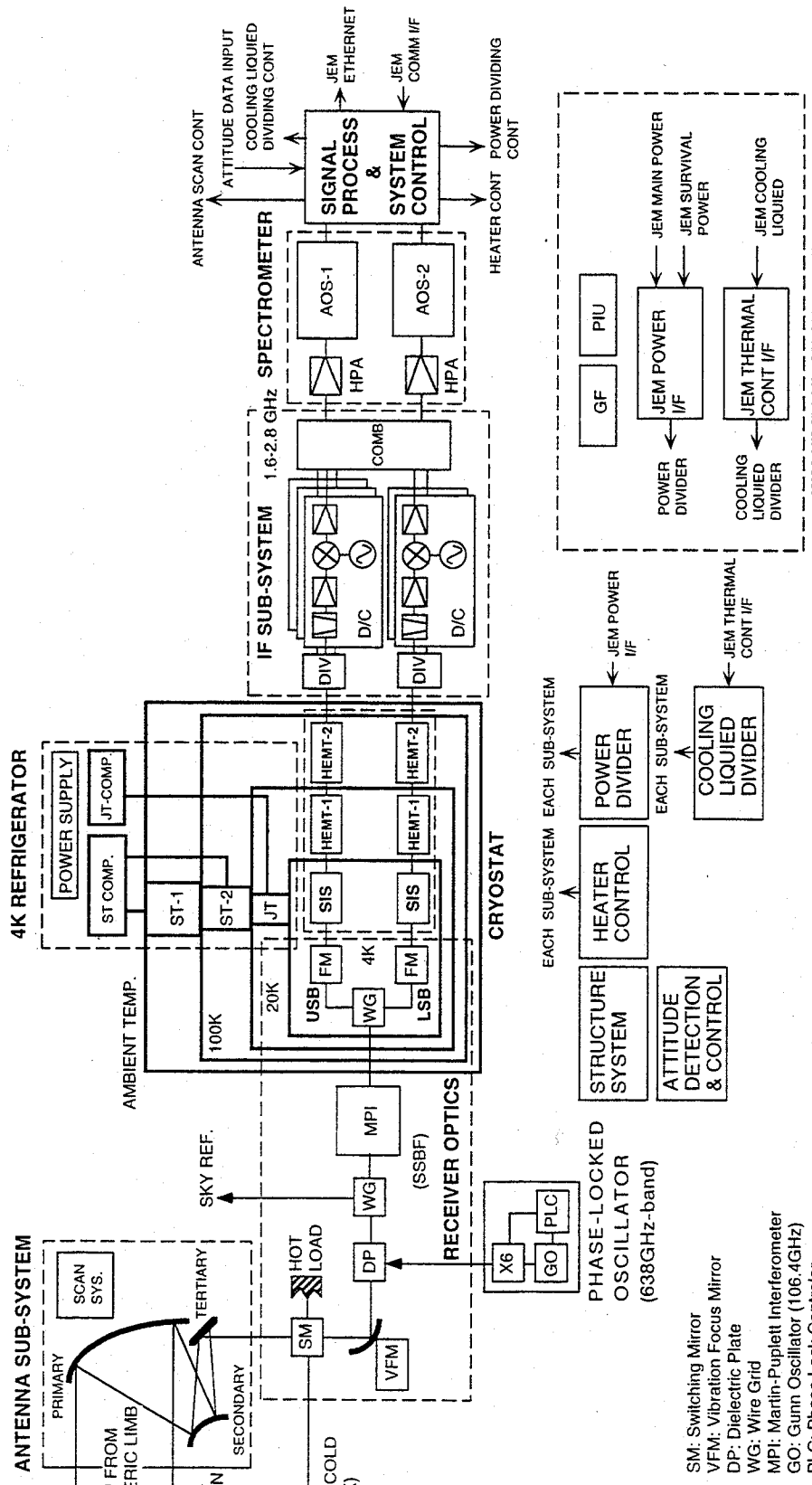

Figure 7. JEM/SMILES SYSTEM BLOCK DIAGRAM

Table 2. Performance of JEM/SMILES

Frequency	640 GHz-Band (624-653 GHz)
IF	10-14 GHz
IF Band-width	Around 4 GHz
System Noise Temperature	Less than 400 K
Integration Time	0.25 seconds
Dynamic Range	10 - 300 K
Spectral Resolution	1 MHz
System Sensitivity	0.8 K
Total Spectral Band-width	2,400 MHz or wider
Observing Species	O_3, $O^{18}O$, ClO, HCl, BrO, $H_2{}^{18}O$, etc.
Expected Observation Accuracy	3 % for O_3, Temperature/Pressure, H_2O 10 % for ClO, HCl, BrO
Data Compression	Band-width Compression by Frequency Synthesis
Quantization	12 bits
Data Rate	150 kbps
Antenna Aperture	0.6 m (vertical) by 0.3 m (horizontal)
Antenna Beam-width	0.055 deg., (elevation) by 0.11 deg. (azimuth)
Height Resolution	2 km
Antenna Scan Range	-10 to -25 deg. in elevation direction only
Observation Height Range	10 - 60 km
Antenna Scan Range for Observation	1.27 deg.
Antenna Scan Step	0.05 deg.
Observation Direction	45 deg. tilted to the right-hand side
Observation Latitudes	65 deg. North - 38 deg. South
Antenna Surface Accuracy	9 μm
Antenna Efficiency	90 % or more
Attitude Precision	Less than 0.05 deg. (Pitch/Roll), 0.1 deg. (Yaw)
Mission Life	1 year
Power	450 W
Mission Weight	224 kg or less
Size	0.8 m (W) by 1 m (H) by 1.85 m (L)

injection. A combination of a Martin-Puplett interferometer (MPI) and a wire-grid polarizer will be used for separate detection of both the lower side-band and the upper side-band signals. The local signal is produced by multiplying 6 times the signal of a phase-locked Gunn oscillator operated at 106.3GHz. The local signal is simply coupled by a thin dielectric film with an efficiency of 5%. A vibrating mirror will be adopted for smoothing standing ripples.

The advantages of the use of SIS mixers is that they are to be able to obtain ultra-low noise temperature and low conversion loss under low local power conditions. A noise temperature of lower than 200K and a conversion loss of less than 5 dB are required for JEM/SMILES. The parallel-connected-twin-junctions (PCTJ) type Nb-AlOx-Nb SIS mixers developed in National Astronomy Observatory, Nobeyama Radio Observatory (NAO/NRO) (Noguchi, et al., 1995) will be used for obtaining ultra-high sensitivity in a wide frequency range under nontuning conditions for space use. The required operation bandwidth is nearly 30GHz, i.e. nearly 5% of the operating frequency. The SIS mixers are used in the waveguide-mount conditions. In addition, to achieve ultra-low noise receivers, we must develop high IF amplifiers (HEMT) operated under cooled conditions with low noise, wide bandwidth, and low power for space use.

The operation conditions of the SIS mixers and the HEMT amplifiers are achieved by a compact-sized low-weight 4K-refrigerator and cryostat system. The 4K-refrigerator is composed of a Joule-Thomson refrigerator combined with a two-stage Stirling refrigerator. The design goal of the cooling capacities is nearly 1.5W for the first stage of 100K, 200mW for the second stage of 20K, and 30mW for the third stage of 4.5K. The total power and weight of the refrigerator will be nearly 250W and 60kg, respectively. The main body of the cryostat is designed to be about 500mm long and to have a diameter of 350mm. The cryostat needs a structure to cut thermal radiation from the outside through the windows, which is one of the largest heat loads for the first stage. Another important issue for the space-qualified cryostat is the mechanical structures to prevent the refrigerators and cooling stages from vibration and launch shock. We have already succeeded in demonstrating the operation of a sub-millimeter wave mixer mounted in the thermal structure model of the cryostat by using a prototype model of the 4K-refrigerator in laboratory level, in collaboration with Sumitomo Heavy Industries, Ltd. (SHI) (Inatani, et al., this issue).

For the effective use of the bandwidths of the spectrometers mentioned below, band compression will be made in the IF sub-system. The frequency bands of each species are divided from the output signals of the HEMT amplifiers, and are synthesized after down-conversion to produce the second IF signals supplied to the spectrometers.

Wide bandwidth, high spectral resolution, and low power are required for the spectrometers to be used for SMILES. A candidate for the spectrometer is an acousto-optical spectrometers (AOS) with a bandwidth of larger than 1.2 GHz and a spectral resolution of about 1 MHz. We are planning to use the 2 AOSs for the JEM/SMILES system.

The acquired data will be transmitted via satellite link prepared on the JEM. The data rate is estimated to be less than 150kbps.

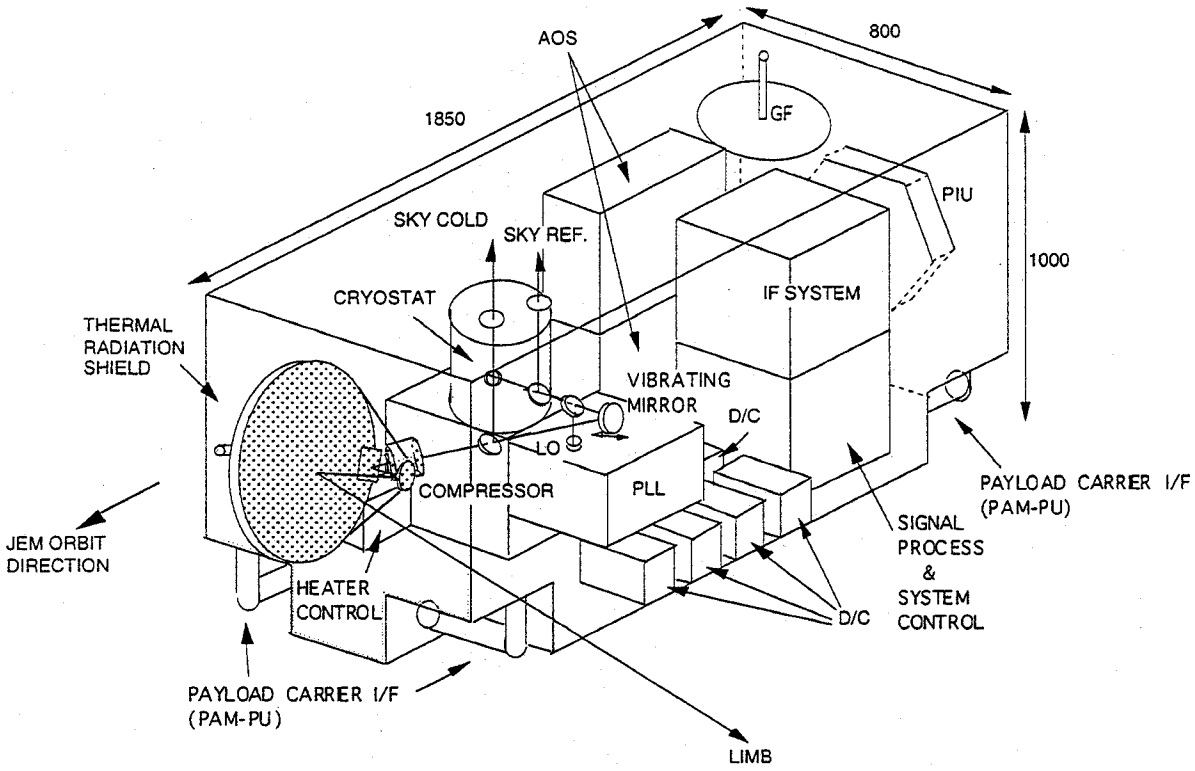

Figure 8. Overview of JEM/SMILES.

The estimated total power and mission weight are 450 W and 224 kg, respectively. The regular size of the JEM/EF experimental unit is 0.8 m (W) by 1.0 m (H) by 1.85 m (L). Figure 8 shows an overview of JEM/SMILES.

4. SCHEDULE AND PLANS

Figure 9 shows the schedule of the JEM/SMILES experiment. According to the present conditions, JEM/SMILES will be launched in 2003 by an H-IIA transportational vehicle (HTV) from the launch site in the Tanegashima-island, Japan. One year of the experiment in space is scheduled. The development period is short, i.e., about 5 years including many kinds of tests for space use. In order to shorten the development period and to decrease the cost, the engineering flight model modified from the engineering model will be launched.

The development of JEM/SMILES will be made under the collaboration of Communications Research Laboratory (CRL), National Astronomical Observatory (NAO), and National Space Development Agency (NASDA) of Japan. CRL and Nobeyama Radio Observatory (NRO) of NAO are responsible for the development of the sub-millimeter wave SIS mixers, the cryostat, and related sections. NASDA is in charge of the development of the antenna sub-system, the 4K-refrigerator, the IF sub-system, etc., together with the construction and the tests of the whole system.

The data processing and distribution are made by NASDA. CRL supports the processing

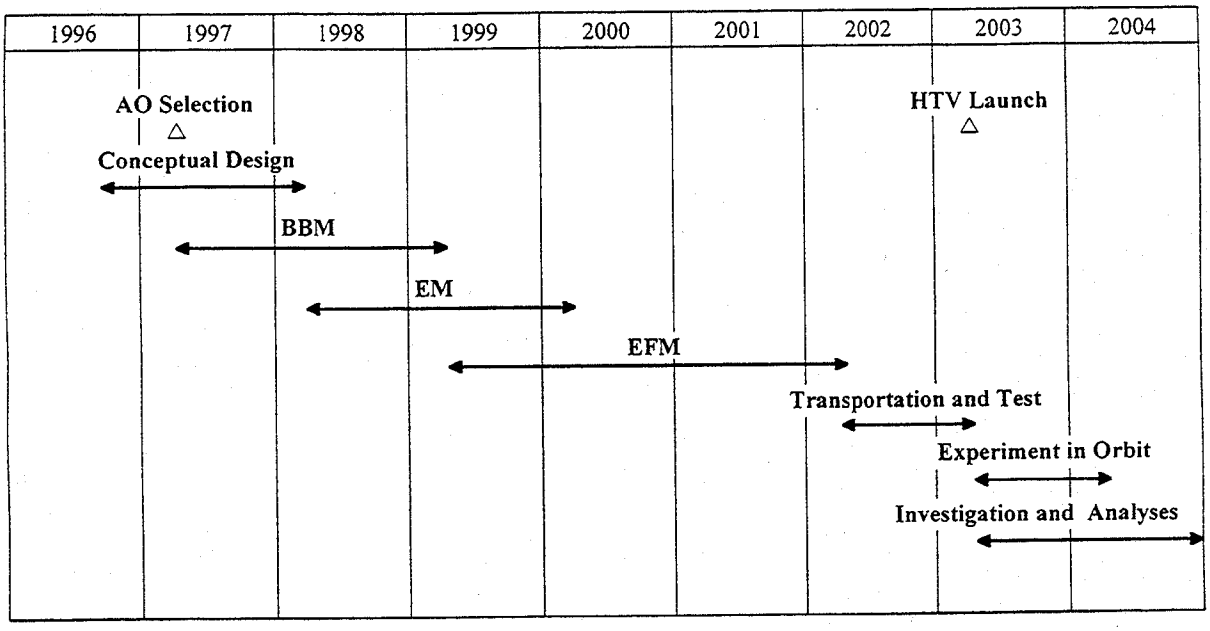

Figure 9. Schedule of the JEM/SMILES experiment.

of the higher level products. A scientist group supported by NASDA and CRL are responsible for the algorithm development and the scientific investigations of the JEM/SMILES experiment including the calibration and validation studies. A research announcement (RA) for the data applications will be issued in near future. The data will be distributed via Internet or an FTP site.

5. SUMMARY

A space-borne limb emission sounder system can globally observe the 3-dimensional distributions of trace gases for the understanding of Ozone Depletion and Climate Change. Communications Research Laboratory (CRL), National Astronomical Observatory (NAO), and National Space Development Agency (NASDA) of Japan are planning to make an experiment for a Superconducting Sub-millimeter Wave Limb Emission Sounder (SMILES) on the Japanese Experimental Module (JEM) of the Space Station to be launched in 2003.

JEM/SMILES will be operated at 640 GHz-band with 10-14 GHz IF frequencies. The PCTJ-type SIS mixers developed in NAO/NRO will be used for the ultra-high sensitive receiver. The operation conditions for the SIS mixers will be achieved by a compact Joule-Thomson refrigerator combined with a two-stage Stirling refrigerators. We are aiming to demonstrate the effectiveness of sub-millimeter wave limb emission spectrometry for observing atmospheric environment from space, to apply superconducting in space, and to operate a mechanical 4K-refrigerator in space. The JEM/SMILES is a pre-phase of SMILES on an atmospheric environment observing satellite, ATMOS-C1, which is planned to be launched around 2006 (ATMOS-C1 Team, 1996).

In addition, extended use of the engineering results of JEM/SMILES can be expected in

wide areas of other fields, such as biological and medical applications, material science and technology, astronomy, and many kinds of precise measurements in space.

In achieving the JEM/SMILES experiment, we are expecting various collaborations with and support from both the scientific and engineering areas in the world.

REFERENCES

ATMOS-C1 Team, Earth Observation Committee/Earth Science & Technology Forum, 1996: "ATMOS-C1 Mission Proposal."

Inatani, J., T. et al., 1997: "A Submillimeter SIS Receiver Cooled by a Compact Stirling-JT Refrigerator, Proc. 8th Int. Symp. Space Teraherz Technology, Cambridge, MA.

Noguchi, T., S.C. Shi, J. Inatani, 1995: "Parallel Connected Twin SIS Junctions for Millimeter and Submillimeter Wave Mixers: Analysis and Experimental Verification, IEICE Trans. Electron., E-78-C (5), 481-489.

Pickett, H.M., R.L. Poynter, and E.A. Cohen, 1992: "Submillimeter, Millimeter, and Microwave Spectral Line Catalogue", JPL Publication 80-23, Rev.3.

Development of a 170-210 GHz 3 ×3 Micromachined SIS Imaging Array

Gert de Lange and Qing Hu
Department of Electrical Engineering and Computer Science
Research Laboratory of Electronics,
Massachusetts Institute of Technology, Cambridge, Massachusetts 02139.

Howard Huang and Arthur W. Lichtenberger
Department of Electrical Engineering
University of Virginia, Charlottesville, VA 22903

Preliminary results from a 3×3 micromachined millimeter-wave focal-plane imaging array with superconducting tunnel junctions as mixing elements are presented. The array operates in the 170-210 GHz frequency range. The micromachined array is mechanically robust and the SIS devices are sufficiently cooled. Uniform DC I-V characteristics of the different elements have been measured. We have implemented integrated tuning structures which show a 3-dB bandwidth of 70 GHz when the junction is used in a video detection mode. Preliminary noise measurements on two of the array elements resulted in lowest DSB noise temperatures of 83 K (@182 GHz) and 125 K (@184 GHz), with a bandwidth of 32 GHz and 20 GHz respectively.

1 Introduction

Imaging arrays of SIS-receivers are of great benefit for the observation of spatially extended sources in astronomy, but the high cost and mechanical difficulties of building an array of waveguide mixers and the poorer beam-quality of open-structure antennas have thus far limited the efforts of actually developing such arrays [1, 2, 3, 4, 5]. SIS-mixers made with micromachined horn antennas offer both a relatively easy, low cost fabrication and excellent Gaussian beam properties and are therefore well suited for the development of imaging arrays. Because of the specific structure of the micromachined horn antenna, interference of IF and DC-bias lines with RF antenna is avoided and also there is no limitation on the element spacing, which are problems of concern in waveguide and open structure antennas. Further advantages for the use of micromachined horn antennas in high frequency imaging arrays are the absence of substrate losses, and the possibilities of integrating a mixing element with super- or semi-conducting electronics (e.g. SQUID IF-amplifiers or Flux-Flow oscillators) [6, 7, 8]. To demonstrate the feasibility of micromachined horn antennas in imaging arrays we are currently testing a 3×3 focal plane SIS imaging array for the 170-210 GHz frequency range (the choice of the frequency range is mainly determined by the availability of the Local Oscillator and the dimensions of the cryostat). In parallel we have developed two

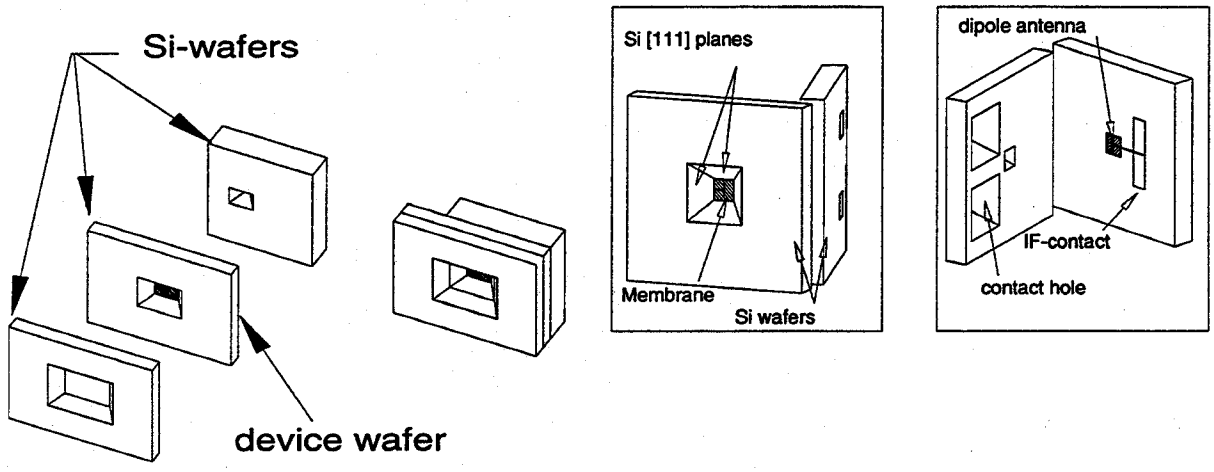

Figure 1: *(a) Overview of assembly of the micromachined horn. (b) Details of a single element of the micromachined array, showing the pyramidal cavity, the membrane, the through holes for the IF/DC connections, and the dipole antenna.*

room-temperature imaging arrays with thin-film Nb as bolometers for the 70-110 GHz and 170-210 GHz frequency range [9].

Micromachined horn antennas consist of a dipole antenna fabricated on a thin ($\sim$ 1 μm) Si_3N_4 dielectric membrane inside a pyramidal cavity etched in silicon (see Fig. 1)[10, 11]. We previously developed a single-element micromachined SIS receiver for the W-band frequency range, which showed a sensitivity comparable to the best waveguide and quasi-optical open-structure receivers [12].

This paper describes the design and fabrication of the 3×3 170-210 GHz imaging array receiver and preliminary noise measurements on the array performance.

2 Receiver Design

The array receiver can be divided into four main parts: the machined horn array, the micromachined array, the magnet, and the IF-output/DC-bias board. An expanded view of the receiver and some details of the individual elements are shown in Figs. 2, 3, and 5.

2.1 Micromachined array

The micromachined array is made of a stack of 4 Si wafers with a total thickness of 1.7 mm. The dipole antenna on the membrane is 0.58 mm long (0.37 λ). In order to have access to the contact pads on the device wafer, through holes are etched in the two wafers forming the apex of the horn (see Fig. 1). A detailed description of the individual micromachined antenna elements and the quasi-integrated horn antenna is given in [13, 14]. The stack of Si wafers forming the micromachined section is aligned with a small x-y-θ stage and the jug for holding the machined horn array. The jug and the alignment stage are positioned with respect to each other with dowel pins. To align two wafers to each other, the wafers are mounted with bee-wax to the alignment stage and to a microscope slide glued to

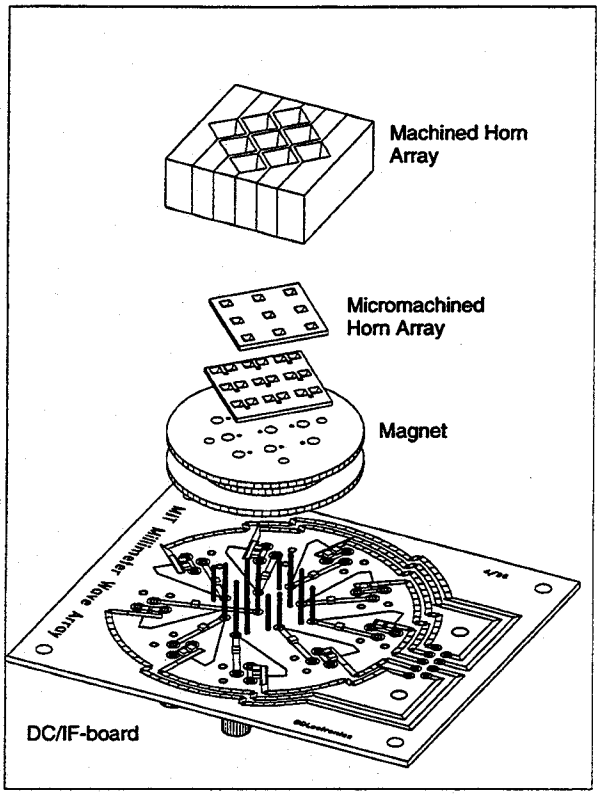

Figure 2: *Expanded view of the array receiver showing the machined horn array, the micromachined array, the magnet, and the DC/IF-board*

the jug. After alignment a small amount of superglue is used to bond the wafers together. The stage is then heated to remove the stack of wafers from the microscope slide. A similar procedure is used to align the micromachined array to the machined array. A typical accuracy of alignment is 20-40 μm.

Two serially connected Nb/Al_2O_3/Nb SIS junctions are used as mixer element whose resistance is matched to the 35-Ω real impedance at the dipole antenna terminals. Typical devices fabricated at the University of Virginia facility have an area of 2.5 μm^2 and a maximum current density of 10 kA/cm^2. For our design, junctions with a current density of 5 kA/cm^2 are required. To optimize the radiation coupling to the capacitive SIS devices, two different types of on-chip tuning structures are implemented, as shown in Fig. 3a. The first type uses an inductive length of microstrip line shorted with a low impedance $\lambda/4$ stub. The low impedance stub has a 90 nm thick (ϵ_r = 40) Nb_2O_5 dielectric and has dimensions of 10×35 μm^2. The microstripline is 6 μm wide and its characteristic impedance is 10 Ω for a 300 nm, ϵ_r=5.6 SiO dielectric layer . Microstrip lengths of 43 μm and 53 μm are used to accommodate variations in the fabrication process. In the second type of tuning structure a capacitive short of the coplanar feedlines of the antenna is used to form an inductive shunt similar to the tuning structure described in Ref [15]. The dimensions of the capacitive short are 20 × 10 μm^2 (with a 90-nm thick Nb_2O_5 dielectric) and distances of 15 and 17 μm between the junction and the edge of the capacitor are implemented.

The size of a single array element on the device wafer is much smaller than the element spacing and the vacant

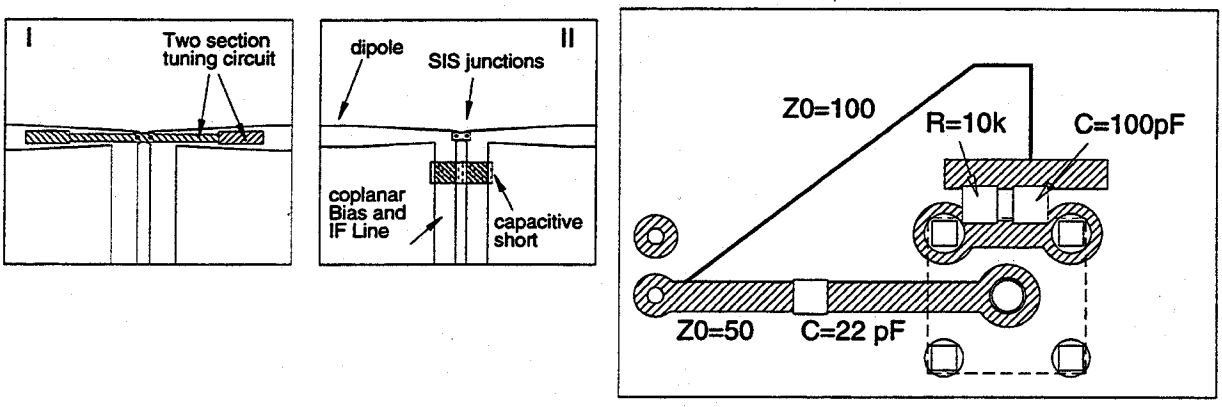

Figure 3: *(a) Details of the two different types of tuning structures incorporated in the mask design. I:two-section stub. II:capacitively shorted coplanar stub. (b) T-bias circuit.*

space on the device wafer is filled up with additional array elements to a total of 36. The positioning of the aperture and backing wafers selects the nine elements forming the array. In the current mask set, four different designs are implemented in order to find an optimum design of integrated tuning structure. In a future design identical devices will be implemented. A single fabrication run will then yield four identical 3×3 arrays.

2.2 Machined Horn Array

The geometry of the machined horn section is similar to the diagonal horn described in Ref [16]. Arrays of diagonal horns can be made with a high packing density and are relatively easy to fabricate on a milling machine with a split block technique. The array is formed by a stack of six gold plated tellurium copper blocks and fabricated at MIT Lincoln Laboratory. To assure the alignment of the separate blocks during the fabrication, a fixture is used in which the blocks are positioned by two dowel pins and mounted under a compound angle. Fabrication of machined arrays for frequencies up to a THz seems to be feasible.

2.3 Optics

As shown in Fig. 2, the minimum spacing of the individual elements of the array is determined by the aperture dimensions of the machined diagonal horn section. For the 200 GHz array the element spacing is 6.5 mm, which is $\sim$ 3.5 beam waist (the $1/e^2$ beam angle of the horn is 16°). The angular separation θ_r of the parallel beams from the array, separated by a distance d, in combination with a lens or reflector of focal length f is $\approx d/f$, whereas the 3dB beam angle θ_{3dB} of a beam with input beam waist w_{in} is 0.59 w_{in}/f. A maximum sampling of the sky requires a 3 dB beam overlap and thus $\theta_r = 2\,\theta_{3dB}$ which gives an element separation of $d = 1.18\,w_{in}$. Our array therefore undersamples the sky, as any horn array will do since the beam waist of the horn is always considerably smaller than the aperture dimensions of the horn [2].

Quasi-integrated horn antennas can be used as a feed for reflector antennas without additonal lenses. Because of the limited diameter (5 cm) of the 77 K heat filter (a 5 mm thick PTFE disk) and the dewar window (a 25 μm thick sheet of polypropylene) in the measurement set-up, a PTFE lens with a focal lenght of 37 mm is used in our set-up, to avoid truncation of the array beams. This lens is at 4.2 K. A second lens (at room temperature) with

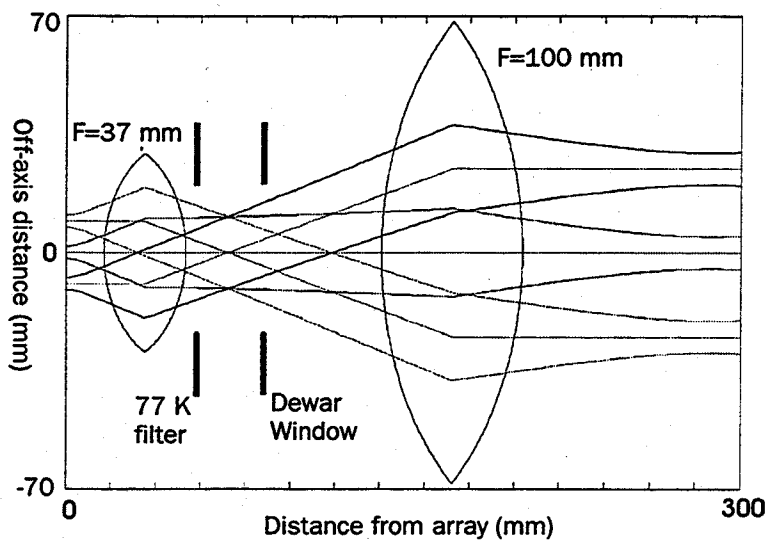

Figure 4: *Optics for the 200 GHz SIS imaging array. The figure shows the beams for the array elements on the diagonal of the array. The F=37 mm lens is located in the dewar.*

a focal length of 100 mm is used to form a gaussian telescope (See Fig. 4). The combination of the two lenses forms a slightly magnified image of the array elements at a 20-cm distance in front of the dewar. This lens set-up is convenient for our test receiver, since we can use a small hot/cold load for the heterodyne measurement and the array is reasonably uniformly illuminated if we use a beam splitter between the two lenses to couple the LO.

2.4 Magnet and DC-IF Board

A single magnet coil (made of copper) with approximately 2500 turns of superconducting 100 μm thick Nb wire (Supercon T48B) is used to suppress unwanted Josephson effects. The geometry of the micromachined array allows the magnet to be in very close proximity of the junction ($\sim$ 1.5 mm). Although the positioning of the magnet (with the magnetic field lines perpendicular to the junction surface) is not preferable, a magnet current of 200-300 mA is sufficient to suppress Josephson effects. The magnet produces a non-uniform magnetic field over the area of the array. Small permanent magnets or magnet coils located in the core of the magnet could be used to correct for this non-uniformity, but are not implemented yet.

In order to have local access to the array elements, through holes are etched in the backing wafers. This avoids the use of long coplanar lines on the device wafer (to bring the signals to the border of the wafer) and thereby increases the available space for mixer elements, reduces possible cross-talk between the different elements, and increases the flexibility of the receiver design. Contact between the array elements and the DC/IF board is made by a modified spring loaded contact pin and a short section of semi-rigid cable in which the center conductor is replaced by a spring loaded contact pin. The spring loaded contact pins are modified by cutting off the sealed end of the pin and extracting a part of the spring located inside the pin. This spring is then used as a flexible contact, instead of the original head. To ensure a reliable contact between the contact pads and the spring contact, the small cavities formed by the through holes in the backing wafers are filled with silver epoxy. The contact pin and the section of semi-rigid cable are mounted in feed through holes in the core of the magnet coil (see Fig. 5). For each array element, one contact pad is connected to the common ground (the core of the magnet) while the other contact

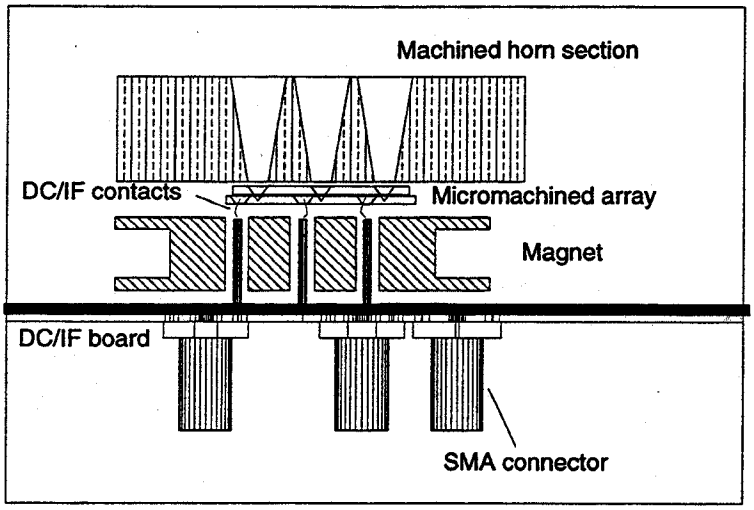

Figure 5: *Details of the receiver assembly*

pad is connected to the DC-IF board via the section of semi-rigid cable. The use of the feed through holes in the copper core of the magnet provide an effective way of shielding IF contact pins for the different elements from each other. In a previous design (without a magnet) severe cross-talk and spurious noise effects were observed in the IF-output signals

The IF/DC-board is made of Duroid 6010 material and contains a T-bias circuit for each array element. Contact between the contact pins and the microstrip line and groundplane on the IF board is made by using tight fitting sockets, soldered on the IF-board. Details of the T-bias design are shown in Fig. 3b. A 50-Ω microstrip line (width=1170 μm) (DC blocked with a 22 pF chip capacitor) connects on one end to the center conductor of a SMA connector and on the other end with the socket for the contact pin. The DC-bias is applied via a 100-Ω $\lambda/4$ line (w=152 μm, l=21 mm), capacitively shorted with a 100 pF capacitor (and a 10-kΩ resistor, to avoid charge build-up).

The array operates with a single IF-amplification stage. Noise measurements on different elements of the array are done by connecting the IF-amplifier to the different IF-ports on the DC/IF Board. The cold stage of the IF-chain consists of a Pamtech LTE 1268K isolator, and a Berkshire Technologies L-1.5-30HI IF-amplifier (40 dB). A further amplification of 60 dB is provided by room-temperature amplifiers outside the dewar. The IF-power is measured in a 35 MHz bandwidth with an HP-436A power sensor at a center frequency of 1.25 GHz (set by a tunable bandpass filter).

3 Device fabrication

The micromachined SIS arrays are made partially at MIT Lincoln Lab and partially at the University of Virginia. The SIS devices are fabricated on 0.38 mm thick (100)-oriented silicon wafers, covered on both sides with a 1-μm thick, low-stress Si_3N_4 layer. The first fabrication step is a reactive ion etch to define the apertures on the aperture side of the wafer, which will later serve as the etch mask in the anisotropic KOH-etch. The next step defines marks (with an Au lift-off) on the other (device) side of the wafer, that are references to the apertures. The patterning of

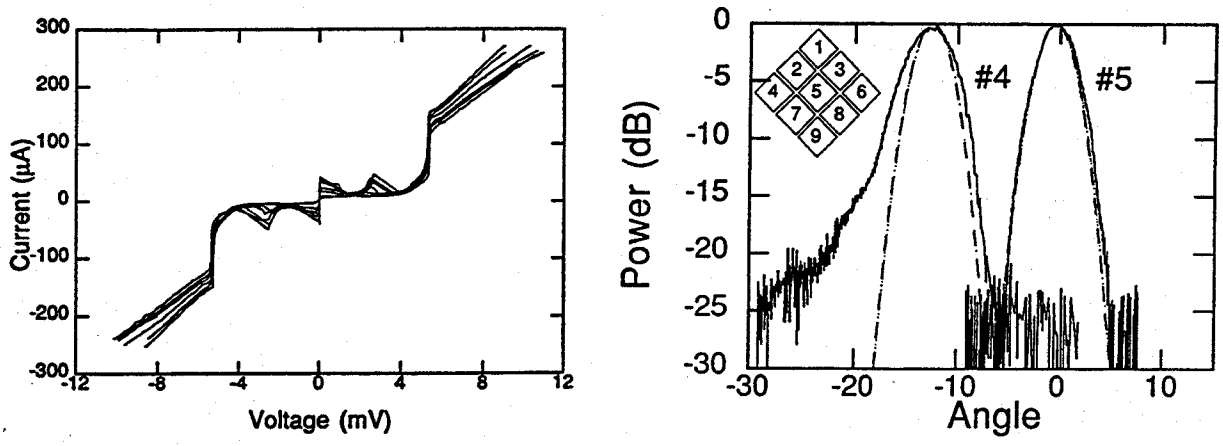

Figure 6: *(a) DC I-V curve of 7 SIS devices of the 9 element array. (b) Measured antenna beam patterns for two elements on the diagonal of the imaging array. The inset shows the device numbering.*

these marks is done using an infrared mask aligner. The marks serve as alignment marks for the antenna definition. The wafers are then shipped to UVA, where the antennas and SIS junctions are fabricated with a modified Selective Niobium Etch Process, described in [17]. Back at MIT the chip is mounted in a Teflon KOH etching mount which isolates the front and back sides of the wafer by sandwiching the wafer between two o-rings. The freestanding membrane is formed by etching the silicon in a solution which contains 20% KOH by weight at 80 ^{0}C for 4-5 hours and another hour at 60 ^{0}C. The last step is used to create smooth sidewalls of the aperture. The final fabrication step is the deposition by E-beam evaporation of a 400-nm Ti/Au layer on the sidewalls of the aperture through a ceramic shadow mask.

4 Results

4.1 DC measurements

A uniform noise performance of the different elements in an array receiver for astronomical observations is of major importance, since an increase in noise temperature of one or more of the elements rapidly reduces the advantage of using an array receiver. This is of special concern for micromachined and quasi-optical array receivers, where one defective element requires replacement of the whole device wafer.

We have thus far tested one device wafer, and results of the DC I-V measurements of 7 SIS devices in the array are shown in Fig. 6a (in this measurement the cryogenic DC contact was not optimized yet, and two devices lost contact during cool-down). The measurements are performed with the mixerblock mounted in the vacuum dewar (at a bath temperaure of 4.2 K). As shown in Fig. 6a the I-V characteristics are fairly uniform, with a $35 - 40\ \Omega$ junction resistance range. The individual elements of the array are sufficiently cooled and show no gap reduction in comparison with an I-V measurement in a LHe bath. Since the overall noise performance of an SIS receiver is not very critical to small changes in subgap current or device resistance, the device uniformity shown in Fig. 6a should be sufficient to obtain a uniform noise performance.

4.2 Antenna Pattern Measurement

As a preliminary test of the antenna patterns of the separate elements in the array, the 45-degree antenna patterns of two elements are measured at a frequency of 182 GHz. The 45-degree plane antenna are obtained by measuring the video response of the elements while rotating the dewar with a rotation stage. Due to the 45 degree angle of the array with respect to the optical table, a combined co- and cross- polarisation is measured. The two elements are at the center and outermost postion on the diagonal of the array, with the antenna beams parallel to the optical table. In this measurement, only the cold lens inside the dewar is used. The measured antenna patterns are shown in Fig. 6b, together with a Gaussian beam profile. The measured radial separation of the beams is 12.5°, and the 10 dB beamwidth of the central beam is 6.8°. Calculated values (using a thin lens approximation) for the beam separation and beam width are 14.4° and 5.2°, respectively. The off-axis element is somewhat wider and shows a non-symmetric shoulder at -17 dB, which we attribute to abberations caused by the lens. Previous measurements of single element quasi-integrated horn antennas [11] and single element [18] and arrays of diagonal horns with waveguide feeds [16] have shown excellent Gaussian antenna beam profiles at frequencies close to 1 THz. Recent measurements on our 95 GHz room-temperature bolometer also show excellent beam properties [19]. Although more thorough tests of the beam patterns of the array have to be performed, our measurements indicate the applicability of quasi-integrated horn antennas in array receivers.

4.3 FTS measurements

The frequency response of the different integrated tuning structures is measured with a Fourier Transform Spectrometer (FTS). The FTS uses a Hg-arc lamp as the broadband millimeter wave source, and is operated in the step-and-integrate mode. In these measurements the devices are biased at a voltage just below the gap voltage and used as a video detector. Fig. 8a shows the result of the measured frequency dependent coupling of three different integrated tuning structures, together with the coupling of a device without integrated tuning structure ([14]). The two section stub with a stub length of 53 μm shows a large increase in bandwidth in comparison with the device without an integrated tuning structure. The peak in the response of this device around 180 GHz is a result of the optimum coupling of the dipole antenna at this frequency. The origin of the observed peak at 300 GHz, which is also observed for the tuning structure with a 43 μm stub length, has not been identified. The tuning stucture with a capacitive short located on the coplanar feed line at 17 μm from the junctions has an optimum coupling at 130 GHz.

4.4 Noise measurements

Results of heterodyne measurements with two elements of the array with the 53-μm long two-section tuning stub are shown in Figs. 8 and 7b. The signal and LO-power are combined by a 97% transmission beam splitter and the IF-power is measured in a 35 MHz bandwidth at a center frequency of 1.25 GHz.

Fig. 8a shows the pumped DC I-V curve and IF-output power of device #4 (see the inset of Fig. 6b for the numbering of the device location) measured at a 182 GHz LO frequency. The maximum Y-factor (measured at the first photonstep below the gap voltage) is 3.7 dB, which results in a 83 $\pm$ 3 K DSB receiver noise temperature (without any correction). Analysis of the receiver noise temperature shows that the mixer gain is -1.4 $\pm$0.8 dB and the mixer noise temperature is 23 $\pm$ 8 K. The IF amplifier noise is 13.6 K (calibrated with the shot noise of the unpumped junction), which gives a total noise contribution of the IF stage of 30 K. The manufacturers specification of the amplifier noise is 4-5 K, which indicates that the current IF-coupling scheme can be substantially improved.

Fig. 8b shows the pumped DC I-V curve and IF-output power of device #7 measured at a 184 GHz LO frequency. This element has a minimum receiver noise temperature of 125 K DSB. As can be seen in Fig. 8a and b, there is a significant difference in the behaviour of the elements under irradiation with LO-power. Device #4 shows photon steps with a width of $2 \times \hbar\omega/e$, as expected in a series array of two junctions; whereas device #7 shows no

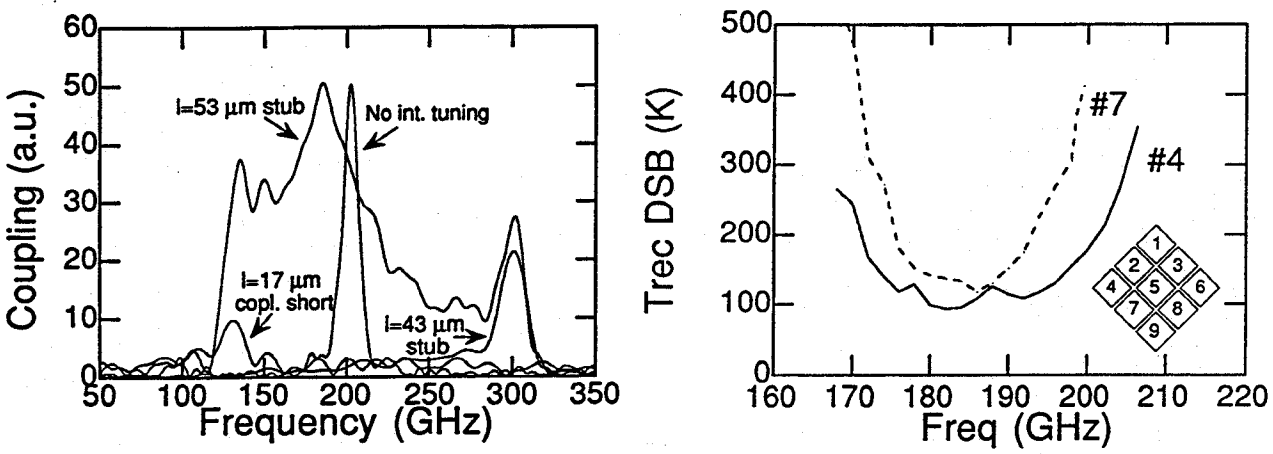

Figure 7: *(a) FTS Measurement of the three devices with different integrated tuning stucture, and one device without integrated tuning structure (b) Receiver Noise temperature for two elements of the imaging array*

clear photon steps below the gap voltage and a structure in the IF-output power of width $\hbar\omega/e$. We contribute this undesirable effect to a non-uniform division of the applied DC-bias voltage and LO-power accross the series array of junctions. At frequencies where the geometric capacitance of the junction is tuned out by the integrated tuning circuit, the junction RF-admittance is determined by the quantum susceptance. Since the quantum susceptance is a sensitive function of bias voltage (especially near the gap voltage), small differences in bias voltage between the two junctions could have a significant effect on the coupling of LO-power. Use of single junction mixers will avoid this type of non-uniformity.

The measured noise temperature as a function of frequency for these devices is shown in Fig. 7b. The 3-dB noise bandwidth for elements #4 and #7 is 32 GHz and 20 GHz respectively. We contribute the difference in the measured bandwidth to the different behaviour of the mixer elements, as explained in the previous paragraph. In a previous measurement on a single element mixer with a backing plane tuned antenna, a bandwidth of 6 GHz was measured [14], showing the effectiveness of the integrated tuning structure in the current design.

Current state-of-the-art waveguide receivers for the 230 GHz astronomy band have DSB noise temperatures of 35-50 K [19, 20, 21]. With a further optimization of the IF coupling and the use of single junction mixer elements, the fabrication of micromachined arrays with a competitive noise temperature for each array element seems feasible. Furthermore, the scalability of the machined and micromachined sections show the promising prospect for the use of micromachined focal plane imaging arrays for frequecies up to 1 THz.

5 Summary

We have described the design and fabrication of a SIS micromachined 3 × 3 focal plane imaging array for the 170-210 GHz range. Measurements show that the micromachined array can withstand thermal cycling and that the devices are sufficiently cooled. Uniform DC I-V characteristics of the different elements have been measured. The use of integrated tuning structures significantly improved the bandwidth of the mixer. Preliminary heterodyne

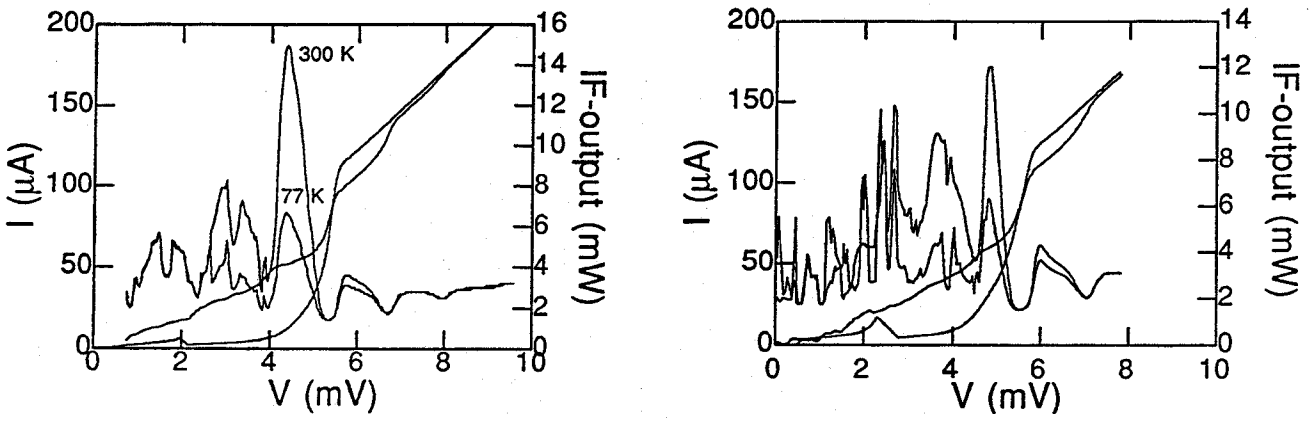

Figure 8: *(a) Pumped I-V characteristics of element #4 at a LO frequency of 182 GHz and the measured IF-output power with a 295 and 77 K input load. (b) Same measurement as in a, but for element #7 and a LO frequency of 186 GHz*

noise measurements on the array elements showed a lowest DSB noise temperature of 83 K with a 3-dB bandwidth of 32 GHz.

6 Acknowledgement

We would like to thank Earle Macedo, Dan Baker,Rich Ralston, Gerry Sollner, Rick Magliocco, Lewis Tedstone, Glenn Willman and William Cummings at MIT Lincoln Laboratory for their help during the fabrication of the devices and the fabrication of the machined horn section. Richard Bradley and Anthony Kerr are acknowledged for their useful suggestions on the dewar and IF-board design. We thank Erik Duerr, Arifuhr Rahman, and Kostas Konistis for their usefull suggestions and help during the measurements. This work was supported by the National Science Foundation under grant No. 9423608-AST, and by NASA under grant No. NAGW-4691.

References

[1] J.M. Payne, *Multibeam Receiver for millimeter-wave radio astronomy*, Rev. Sci. Instrum. **59**, 1911 (1988).

[2] Neal R. Erickson, Paul F. Goldsmith, G. Novak, Ronald M. Grosslein, P.J. Viscuso, Ronna B. Erickson, and C. Read Predmore, *A 15 element Focal Plane Array for 100 GHz.*, IEEE Trans. on MTT **40**, 1 (1992).

[3] Philip A. Stimson, Robert J. Dengler, Peter H. Siegel, and Henry G. LeDuc, in *Proc. of the Third Int. Symp. on Space Terahertz Techn.*, Univ. of Michigan (Univ. of Michigan, Ann Arbor, 1992), pp. 235–242.

[4] P.F. Goldsmith, C.-T Hsieh, G.R. Huguenin, J.Kapitzky, and E.L. Moore, *Focal Plane Imaging Systems for Millimeter Wavelengths*, IEEE Trans. MTT **41**, 1664 (1993).

[5] M.A. Scherschel, G.A. Ediss, R. Güsten, K.H. Gundlach, H. Hauschildt, C. Kasemann, A. Korn, D. Maier, and G. Schneider, in *Proceedings of the Sixth International Symposium on Space Terahertz Technology*, Caltech (Caltech, Pasadena, 1995), pp. 338–343.

[6] John A. Wright, Svetlana Tatic-Lucic, Yu-CHong Tai, William R. McGrath, B. Bumble, and H. LeDuc, in *Proceedings of the Sixth International Symposium on Space Terahertz Technology*, Caltech (Caltech, Pasadena, 1995), pp. 387–396.

[7] J.W. Kooi, M.S. Chan, M. Bin, Bruce Bumble, H.G. LeDuc, C.K. Walker, and T.G. Phillips, *The Development of an 850 GHz Waveguide Receiver Using Tuned SIS Junctions on 1 μm Si_3N_4 Membranes*, Int. J. of IR and MM waves **16**, 1 (1995).

[8] S.V. Shitov, V.P. Koshelets, A.M. Baryshev, I.L. Lapitskaya, L.V. Filippenko, Th. de Graauw, H. Scaeffer, H. van de Stadt, and W. Luinge, in *Proceedings of the Sixth International Symposium on Space Terahertz Technology*, Caltech, (Caltech, Pasadena, 1995), pp. 324–337.

[9] Arifur Rahman, Gert de Lange, and Qing Hu, *Micromachined room-temperature microbolometers for millimeter-wave detection*, Appl. Phys. Lett. **68**, 1 (1996).

[10] G.M. Rebeiz, D.P. Kasilingam, Y. Guo, P.A. Stimpson, and D.B. Rutledge, *Monolithic millimeter-wave two-dimensional horn imaging arrays.*, IEEE Trans. Antennas and Propagation **AP-38**, 1473 (1990).

[11] G.V. Eleftheriades, W.A. Ali-Ahmad, L.P. Katehi, and G.M. Rebeiz, *Millimeter-wave integrated horn antennas: Part I: Theory*, IEEE Trans. Antennas and Propagation **AP-39**, 1575 (1991).

[12] Gert de Lange, Brian R. Jacobson, and Qing Hu, *A low-noise micromachined millimeter wave heterodyne mixer with Nb superconducting tunnel junctions*, Appl. Phys. Lett. **68**, 1862 (1996).

[13] G. de Lange, B.R. Jacobson, and Qing Hu, *Micromachined millimeter-wave SIS-mixers*, IEEE Trans. Appl. Supercond. **5**, 1087 (1995).

[14] G. de Lange, B.R. Jacobson, A. Rahman, and Qing Hu, in *Proc. of the Sixth Int. Symp. on Space Terahertz Techn.*, Caltech (Caltech, Pasadena, California, 1995), pp. 372–386.

[15] S.K. Pan, A.R. Kerr, M.J. Feldman, A.W. Kleinsasser, J.W. Stasiak, R.L. Sandstrom, and W.J. Gallagher, *An 85-116 GHz SIS Receiver Using Inductively Shunted Edge Junctions*, IEEE Trans. MTT **37**, 580 (1989).

[16] Joakim F. Johansson and Nicholas D. Whyborn, *The diagonal horn as a sub-millimeter wave antenna*, IEEE Trans. MTT **40**, 795 (1992).

[17] Arthur W. Lichtenberger, Dallas M. Lea, Robert J. Mattauch, and Frances L. Lloyd, *Nb/Al-Al_2O_3/Nb Junctions with inductive tuning elements for a very low noise 205-250 GHz Heterodyne receiver*, IEEE Trans. MTT **40**, 816 (1992).

[18] H. van de Stadt, A. Baryshev, P. Dieleman, Th. de Graauw, T.M. Klapwijk, S. Kovtonyuk, G. de Lange, I. Lapitskaya, J. Mees, R.A. Panhuyzen, G. Prokopenko, and H. Schaeffer, in *Proceedings of the Sixth International Symposium on Space Terahertz Technology*, Caltech, (Caltech, Pasadena, 1995), pp. 66–77.

[19] Arifur Rahman, Erik Duerr, Gert de Lange, and Qing Hu, *Micromachined room-temperature microbolometers for millimeter-wave detection and focal plane imaging arrays*, submittted for the Proceedings of the SPIE's 11th International Symposium on Aerospace/Defense Sensing, Simulation, and Controls, Orlando, April 1997.

[20] J.W. Kooi, M. Chan, T.G. Phillips, B. Bumble, and H.G. LeDuc, *A low noise 230 GHz Heterodyne Receiver Employing .25 μm^2 Area Nb/AlO$_x$/Nb Tunnel Junctions*, IEEE Trans. MTT **40**, 812 (1992).

[21] J.W. Kooi, M. Chan, B. Bumble, H.G. LeDuc, P.L. Schaeffer, and T.G. Phillips, *180-425 GHz low-noise SIS waveguide receivers employing tuned Nb/AlOx/Nb tunnel junctions*, Int. J. IR and MM Waves **15**, 783 (1994).

[22] A.R. Kerr, S.-K. Pan, A.W. Lichtenberger, and D.M. Lea, *Progress on Tunerless SIS Mixers for the 200-300 GHz Band*, IEEE Microwave and Guided Wave Lett. **2**, 454 (1992).

PRELIMINARY DESIGN OF A 650 GHz SUBHARMONICALLY PUMPED MIXER WITH QUASI-VERTICAL SCHOTTKY DIODES

Ville S. Möttönen[1], Jian Zhang[1], Petri V. Piironen[1], Jyrki T. Louhi[1], Arto O. Lehto[1], Ansgar Simon[2], Chih-I. Lin[2] and Antti V. Räisänen[1]

[1] Helsinki University of Technology, P.O.Box 3000, FIN-02015 HUT, Finland

[2] Institut für Hochfrequenztechnik, Technische Hochschule Darmstadt, D-64283 Darmstadt, Germany

Abstract

Preliminary design of a 650 GHz subharmonically pumped planar Schottky-diode mixer has been carried out. The mixer design is based on the use of scaled models. Before the implementation of the final mixer 2.5/5 GHz and 5/10 GHz scaled models as well as a 216 GHz mixer are designed and tested.

The mixer employs a modified split-waveguide mount design. The mount consists of RF and LO waveguides, an integrated diagonal horn, two sliding backshorts and shielded microstrip channels. The design is compact and fabrication of the mount is easy. Novel quasi-vertical planar Schottky-diodes will be used in the mixer.

The waveguide to shielded microstrip transitions and the filters have been designed and tested by using the 2.5/5 GHz scaled model. After that, a 10 GHz wideband subharmonic mixer has been constructed. Preliminary simulations and measurements predict a conversion loss of 6.7 dB and an IF bandwidth of more than 40 GHz at the scaled frequency of 650 GHz.

1. Introduction

Technology for the next century remote sensing applications is currently being developed by European Space Agency (ESA). In many space based receiver applications technology which does not require cryogenic cooling is preferred. Schottky-diode mixers have the property to work well at either cryogenic or room temperature. Thus, they are well suited in space based receivers. Whisker contacted diodes have shown the best conversion efficiency. Unfortunately, the receiver assembly and the space qualification process are complicated. The use of planar diodes allows easier space qualification with more convenient receiver design and assembly. The development for the replacement of whisker contacted Schottky honeycomb diodes by planar devices has been going on for a number of years.

We are in the process of designing 216 GHz and 650 GHz subharmonic waveguide mixers based on a quasi-vertical antiparallel diode pair configuration [1]. The subharmonic mixing is used because of the requirement for an LO frequency at only about one-half the RF frequency, simple RF diplexing, inherent LO noise suppression and broad achievable IF bandwidth. Consequently, a narrow band filtering for the LO noise suppression is not needed and several

spectral lines can be measured with a single fixed-frequency LO (broadband IF matching possible). The quasi-vertical diode has properties similar to whisker contacted diode. This enables low conversion loss operation.

This paper contains the waveguide mount description, diode description, preliminary design and measurements with the 2.5/5 GHz and the 10 GHz scaled model. Also the modelling of the quasi-vertical planar Schottky-diodes through EM-simulations will be dealt with.

2. Waveguide Mount Description

The mixer employs a modified split-waveguide mount design [2], which has been successfully applied to a subharmonically pumped planar Schottky-diode mixer [3], and is also applicable for a doubler [4]. The primary modification compared to the original design is reduction of the number of sliding backshorts and the use of a bent LO waveguide. Figure 1 shows a schematic of the mixer mount. The RF signal is coupled into a 215 μm x 430 μm (dimensions are for the 650 GHz mixer, dimensions of the 216 GHz mixer are obtained by scaling) waveguide by a diagonal feedhorn and into the shielded microstrip channel by a waveguide to microstrip transition. The RF transition utilizes a microstrip line, which extends across and beyond the input RF waveguide allowing grounding. The LO signal is fed through the bent 425 μm x 850 μm waveguide, the waveguide to microstrip transition and a quartz microstrip LO filter to the antiparallel quasi-vertical Schottky-diode pair. The width and height of the shielded microstrip channel are 120 μm and 100 μm. The quartz substrate is 110 μm wide and 50 μm thick. The IF signal leaves the mixer through an IF filter followed by an SMA connector. The IF channel microstrip line is bonded to the main strip between the waveguides. Noncontacting backshorts will be used in the 216 GHz mixer, while the 650 GHz mixer employes contacting backshorts.

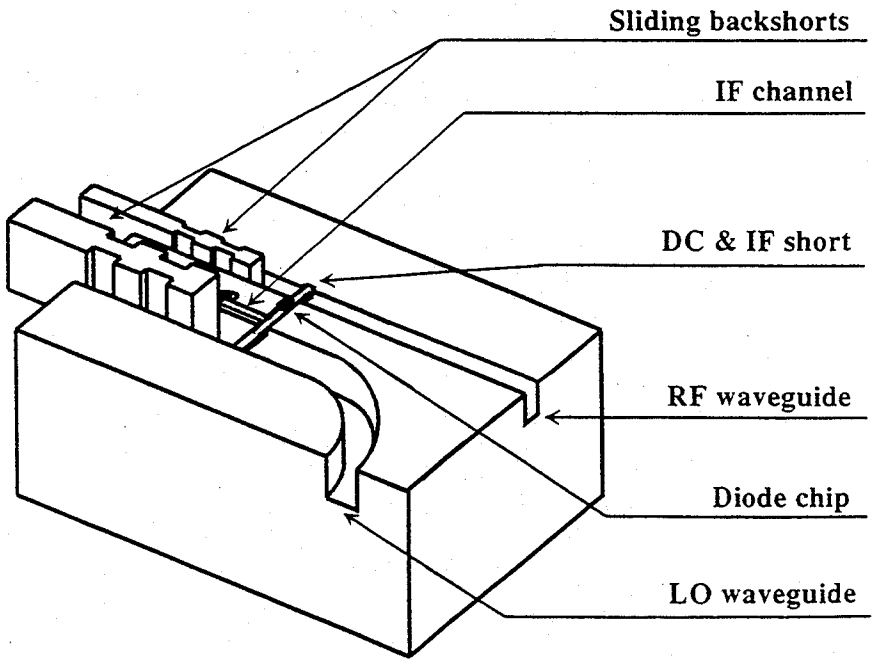

Figure 1. Schematic drawing showing one half of the subharmonic mixer mount (diagonal feedhorn not shown).

3. Mixer Diodes

The subharmonic mixers at 216 GHz and at 650 GHz will utilize a quasi-vertical planar Schottky-diode pair in an antiparallel configuration (APD). The diodes will be manufactured by Technische Hochschule Darmstadt (THD). The diode chip is shown in Figure 2. The chip will be attached onto the quartz substrate by using flip-chip technique as is presented in Figure 3. To reduce the effect of the parasitic impedances, GaAs substrate has to be removed in the 650 GHz mixer. The anode diameter is 0.8 μm on a 70 nm thick epilayer with doping concentration of $3 \cdot 10^{17}$ cm^{-3}. The diode series resistance is 16 Ω, ideality factor 1.1, saturation current lower than $1 \cdot 10^{-16}$ A and a zero bias junction capacitance 1.2 fF. The dimensions of the diode chip are 195 μm long and 110 μm wide. The thickness of the remaining semi-insulating GaAs substrate is reduced to 10-15 μm in order to lower the contribution to the parasitic capacitance. This diode chip will be used in both mixers (216 GHz and 650 GHz). If there is a need for further reduction of the parasitics, the GaAs substrate will be entirely removed after soldering the diode onto the microstrip (Figure 4).

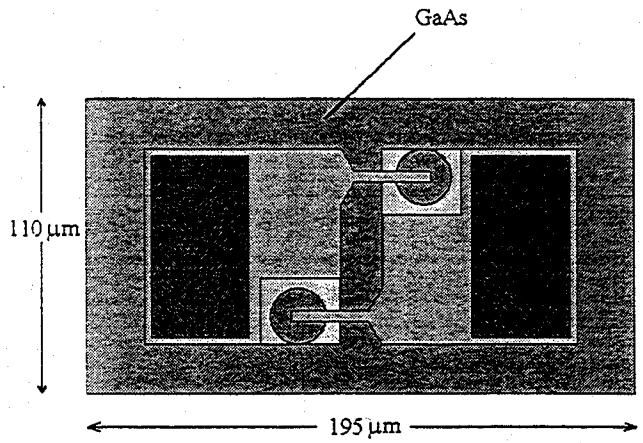

Figure 2. Antiparallel diode chip (APD).

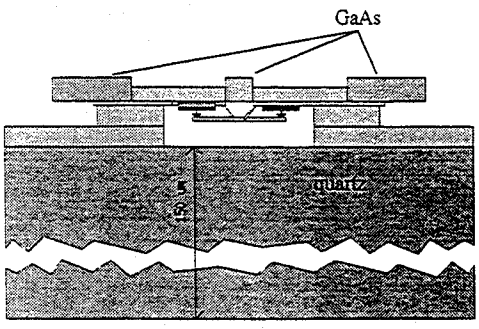

Figure 3. APD with GaAs on a 150 μm thick quartz substrate in the 216 mixer.

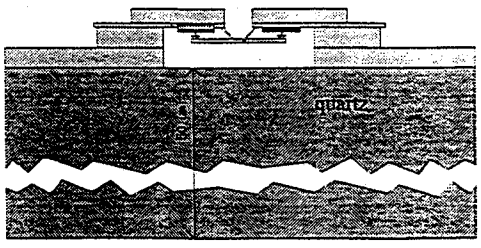

Figure 4. APD without GaAs on a 50 μm thick quartz substrate in the 650 GHz mixer.

4. Preliminary Design

The waveguide to microstrip transitions and the IF and LO filters were designed using the 2.5/5 GHz scaled model. EM-simulations were also carried out in order to verify de-embedding impedances at discrete frequencies and to find out accurate transmission line impedances in the shielded microstrip channel. Hewlett Packard's High Frequency Structure Simulator (HFSS) and an FDTD analysis in APLAC (a tool for circuit simulation developed by Helsinki University of Technology and Nokia Corporation) were used for EM-simulations.

The LO and RF transitions with measurement results are shown in Figures 5 and 6. For the LO transition, a 50 Ω transmission line was used. The width w_l of the 50 Ω line was determined by HFSS. The transition was optimized by changing the length l_w of the transmission line over the LO waveguide and the backshort position. The first step in optimizing the RF transition was to change the width l_1 of the transmission line across the RF waveguide. Further optimimzation was done by changing the width l_2 of the transmission line beyond the RF waveguide. In this way, wideband transitions were obtained.

The sructure of the bandstop filter used for RF and LO rejection is shown in Figure 7. The lenghts and the number of the $\lambda_g/4$ stubs were optimized to obtain desired rejection at stopband. In Figure 8, the measured and simulated (FDTD) insertion loss of the LO filter are shown. With this filter structure, high rejection is easily obtained at a wide band.

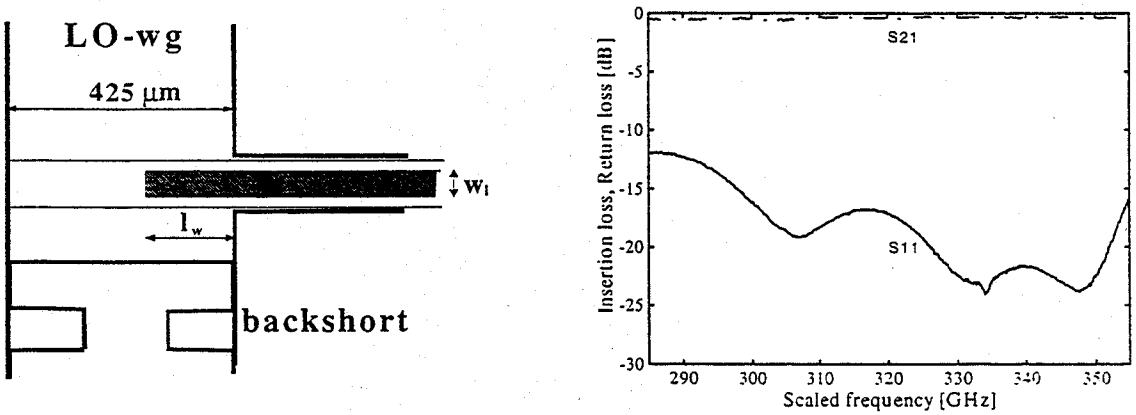

Figure 5. Structure and measured response of LO transition.

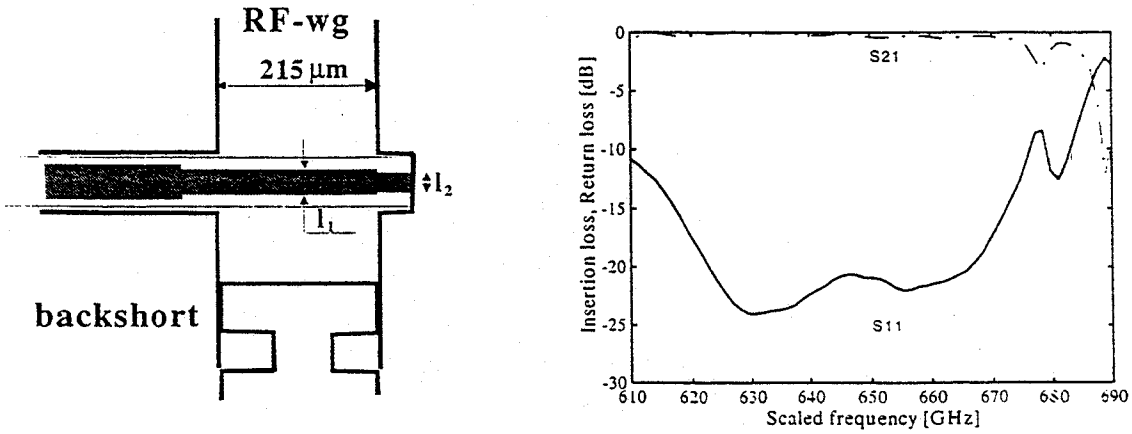

Figure 6. Structure and measured response of RF transition.

Figure 7. Structure of bandstop filter.

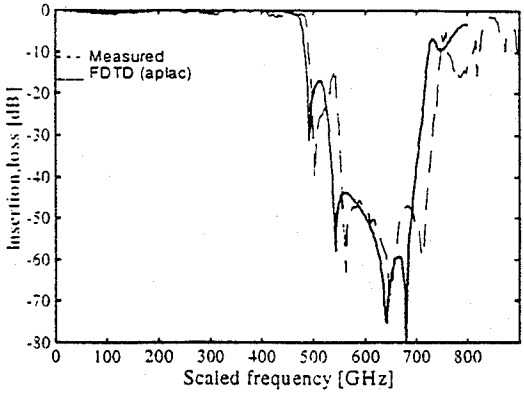

Figure 8. Measured and simulated insertion loss (dB) of LO filter.

A 10 GHz mixer has been designed and preliminary measurements have been done. GaAs beam-lead Schottky diodes have been implemented in the mixer. Diode parameters are given in Table 1 with corresponding impedance values. The diodes were chosen so that the impedance values of the parameters would match as well as possible to those of the 650 GHz mixer diode. The diodes were placed on the microstrip in antiparallel configuration. Harmonic balance analysis in Hewlett Packard's Microwave Design System (MDS) was used in order to find out the diode de-embedding impedances for minimum conversion loss. Simulation results are shown in Table 2. After determination of the de-embedding impedances, a mixer circuit was designed. The mixer circuit is presented in Figure 9. Two bonding wires were used in order to connect the IF channel to the coaxial connector and to the main strip. The diodes were placed near the RF transition in order to minimize signal losses. The measurement results are shown in Figures 10 and 11. In Figure 10, the conversion loss is presented versus the scaled IF frequency. According to the preliminary measurements a scaled IF bandwidth of more than 40 GHz is achievable. The conversion loss versus the LO power requirement is presented in Figure 11. In the simulation of the 10 GHz mixer the LO power was 10 dBm. Measured LO and RF return losses were over 11 dB and over 13 dB at 10 dBm LO power.

Table 1. Parameters of the beam-lead diode.

Series resistance	R_s	10 Ω
Zero junction capacitance	C_{jo}	0.13 pF (122 Ω)
Parasitic capacitance (package)	C_b	0.14 pF (114 Ω)
Parasitic inductance (package)	L_b	0.6 nH (38Ω)
Ideality factor	η	1.18
Saturation current	I_s	$4.46 \cdot 10^{-13}$ A

Table 2. Simulation results of the 10 GHz APD mixer.

RF impedance	Z_{RF}	(10+j5) Ω
LO impedance	Z_{LO}	(14-j20) Ω
IF impedance	Z_{IF}	50 Ω
Conversion loss		6.7 dB
Noise temperature		500 K
P_{LO} requirement		10 dBm

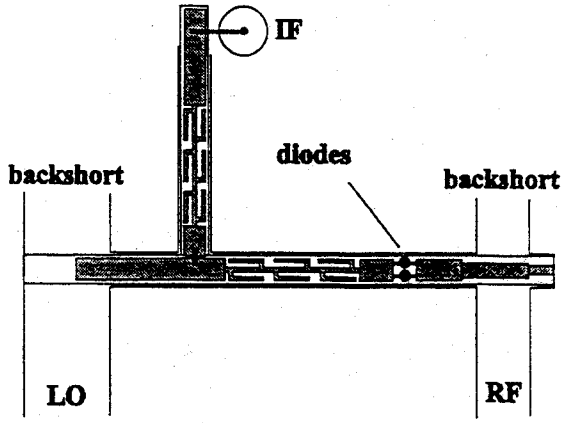

Figure 9. 10 GHz mixer circuit.

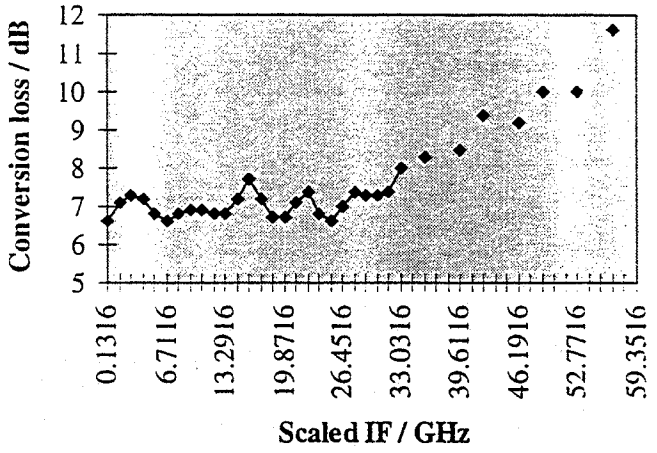

Figure 10. Conversion loss vs scaled IF frequency.

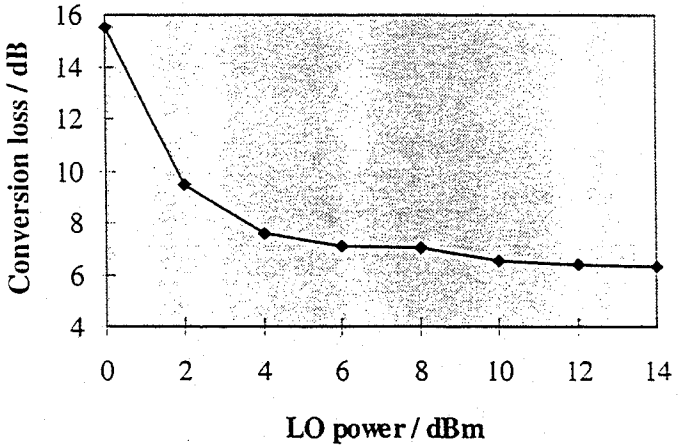

Figure 11. Conversion loss vs LO power.

5. Diode Modelling

In order to obtain a good mixing performance an accurate diode model is required. The equivalent circuit of the Schottky junction has been extensively investigated in [5]. At high frequencies, the parasitic impedances created by the diode chip structure have a significant effect on the mixer performance. We are studying the diode modelling by EM-simulations (HFSS) and broadband measurements. Both diodes, the 216 GHz diode with excess GaAs on the backside of the diode chip and the 650 GHz diode without GaAs, will be modelled. The effects of the associated substrate and the microstrip channel are taken into account by placing the diode chip into the shielded microstrip channel.

The HFSS simulations are made in three main phases. First, only the diode pads and the cathode metallization are simulated. After that, the anode finger is included with the junction short-circuited. Finally, the total capacitance of the junction and the fringing fields are obtained by simulating the diode with the epitaxial layer depleted. In each phase, two-port S-parameters produced by HFSS are compared with the equivalent circuit model so that the entire equivalent circuit is obtained step by step. The optimization routines in MDS are used in order to match the S-parameters with the equivalent circuit and to obtain the circuit element values.

The diode model is shown Figure 12. The subcircuits contain the equivalent circuits for the diode pads. The physical transmission line is used to model the cathode metallization. In the first phase of the simulation, the gap between the anode pad and the cathode metallization is modelled with the parasitic capacitances (C_{g1}, C_{ac} and C_{g2}). The anode finger inductance (L_f) is obtained in the second phase. The fringing field capacitance (C_{fr}) is extracted from the total capacitance obtained in the last phase of the HFSS simulations. After the simulation of the parasitic impedances, the junction model (R_j, C_j, R_s and L_s) is added into the diode equivalent circuit. At the moment simulations are in progress. Measurements will be started during spring -97.

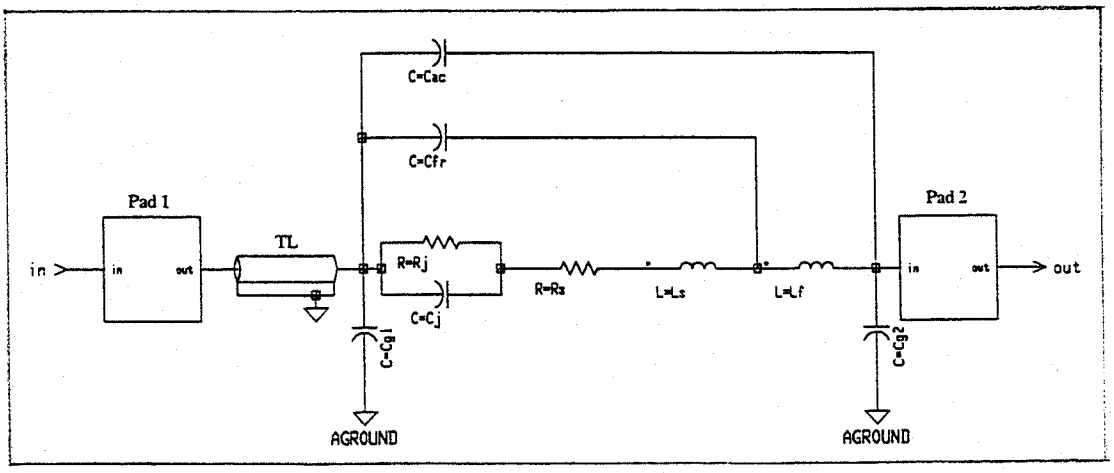

Figure 12. Diode equivalent circuit (the equivalent circuits of the diode pads not shown).

6. Conclusion

Preliminary design of a subharmonic mixer at millimeter and submillimeter frequencies has been carried out by simulations and scaled model measurements. According to the scaled model measurements, a broadband low-conversion-loss subharmonic mixer at 650 GHz can be achieved. This compact mixer structure can be scaled even for higher frequencies. The use of quasi-vertical diodes with properties almost similar to whisker contacted diodes makes low-conversion-loss mixing possible.

References

[1] A. Simon, A. Grüb, V. Krozer, K. Beilenhoff, H. L. Hartnagel, "Planar THz Schottky diode based on a quasi vertical structure", *Proc. Fourth Int. Symp. on Terahertz Technology*, Los Angeles, USA, pp. 392–403, 1993.

[2] A. V. Räisänen, D. Choudhury, R. J. Dengler, J. E. Oswald, P. H. Siegel, "A novel split-waveguide mount design for millimeter- and submillimeter-wave frequency multipliers and harmonic mixers", *IEEE Microwave and Guided Wave Letters*, vol. 3, no. 10, pp. 369–371, Oct. 1993.

[3] A. V. Räisänen, R. J. Dengler, I. Mehdi, J. E. Oswald, D. Choudhury, P. H. Siegel, "Subharmonic mixer with planar Schottky diodes in a novel split-block at 200 - 240 GHz", *IEEE MTT-S Digest*, pp. 775–777, 1994.

[4] J. T. Louhi, "Millimeter wave frequency multipliers based on a planar Schottky varactor", Report S 223, Helsinki University of Technology, Radio Laboratory, March 1997.

[5] J. T. Louhi, A. V. Räisänen, "On the modelling and optimization of Schottky varactor frequency multipliers at submillimeter wavelengths", *IEEE Transactions on Microwave Theory and Techniques*, vol. 43, no. 4, pp. 922–926, April 1995.

BIB Photoconductive Mixers

A. L. Betz and R. T. Boreiko

Center for Astrophysics and Space Astronomy
University of Colorado, Boulder

Abstract

Far-infrared mixers using photoconductive elements offer the promise of quantum noise limited performance at frequencies > 2 THz. The device sizes are $>2\lambda$, so no external antenna is required. Bulk photoconductive mixers, however, must have long absorption lengths because of low doping, and consequently IF bandwidths are limited to 50 MHz. A better device structure using a blocked-impurity-band (BIB) layer allows very high doping in a small device, with a consequent quantum efficiency > 25% and IF bandwidth > 1 GHz, at least in Si-devices. Progress and problems with Ge:Ga mixers for the 2-5 THz range will be discussed along with Si:Sb and Si:As devices for 8-16 THz and 11-22 THz, respectively.

1. Introduction

The sensitivities of heterodyne mixers have advanced to the point that quantum noise limited performance is now the goal between 0.3 and 30.0 THz. Near 0.3 - 0.5 THz, SIS mixers have already achieved double-sideband NEPs close to $4\,h\nu$ per unit bandwidth [1]. At 30 THz (λ =10 μm), receivers using HgCdTe mixers have demonstrated quantum efficiencies of 25%, equivalent to $4\,h\nu$ performance (SSB) or $2\,h\nu$ (DSB) [2,3]. The infrared mixers are reversed biased photodiodes which are sensitive in a frequency range resonant with the bandgap of the intrinsic semiconductor. Between these frequency limits, mixer technology is less developed but rapidly improving. SIS mixers will push up to 1.2 THz, the approximate limit of NbN devices. Above this frequency HEB mixers show promise in achieving 10 $h\nu$ (DSB) performance at 3 THz and maybe even better at 6 THz, because the noise process is independent of frequency [4]. Between 6 THz and 30 THz there are no demonstrated technologies, yet there are many interesting applications in astronomy. Bulk crystals of the extrinsic semiconductors Ge and Si, doped with various elements, have good photoconductive efficiencies between 3 and 30 THz, but inadequate IF bandwidths because

of slow response times. We intend to adapt a new type of photoconductive device called a blocked-impurity-band (BIB) photoconductor to solve this speed problem, and thereby realize a mixer with quantum-noise-limited sensitivity.

Photoconductors and photodiodes can be used as heterodyne mixers because their output current is proportional to the absorbed infrared power: hence a square law response to the incident electric field. For an ideal photodiode, with quantum efficiency η and IF bandwidth B, the heterodyne NEP is given by [5]:

$$\mathrm{NEP} = h\nu B/\eta. \tag{1}$$

Bulk mixers using Ge doped with Ga have been investigated by a number of groups as far-infrared mixers [6-9]. But quantum efficiencies and IF bandwidths of these devices are somewhat poor because of the necessarily low doping levels and the relatively large device sizes.

Devices can be made smaller without sacrifice in quantum efficiency by increasing the doping concentration, but invariably this leads to impurity level banding and a large "dark current". A way of overcoming the impurity band conduction is to use a blocking layer of nearly intrinsic semiconductor at one contact so that impurity band conduction is blocked [10]. With a blocking layer in place, doping in the active region can be increased by a factor 100 with concomitant reduction in the device thickness. For example, Ge:Ga photoconductors, which previously needed to be 1 mm thick to get adequate absorption, can now be only 10 μm thick. Planar fabrication techniques now become applicable, so that device dimensions can be defined by photolithography and doping depths, and large arrays become practical.

2. Device Description

BIB devices are extrinsic photoconductors. This means a donor or acceptor impurity is introduced into the semiconductor lattice so that low lying energy levels are available for photoexcitation. For example, gallium doped into germanium produces hydrogenic energy levels at acceptor sites. Electrons can then be photoexcited into the acceptor sites from the valence band. The valence band hole and impurity band electron are collected at the electrical contacts. The spectral response for the Ge:Ga BIB lies at far-infrared wavelengths between 60-120 cm^{-1} [11]. One can also fabricate a BIB detector using a donor impurities such as Sb or As in a Si lattice [12]. Here the photoexcitation is an electron from a donor site into the conduction band, and the spectral response peaks near 8-15 THz (20-40 μm) for Si:Sb and 11-22 THz (13-26 μm) for Si:As. Of course to prevent thermal excitation of carriers, the devices must be cooled: below 4 K for Ge:Ga devices and below 10 K for the Si:Sb BIB. Si-based BIBs are the most highly developed, and are used in incoherent detector arrays up to

256×256 elements for far-infrared space astronomy [13]. The small detector volume is a major advantage for space applications such as the planned SIRTF Observatory. The low cosmic ray sensitivity for BIBs compared to conventional photoconductors is simply because of their much smaller volumes.

The structure of a Ge:Ga BIB is illustrated in Figure 1. Ga acceptors are doped at a level of about 3×10^{16} cm^{-3} into Ge, which has a donor (impurity) concentration of 4×10^{12} cm^{-3}. The doped and blocking layers are epitaxially grown, with the active region 8 μm thick and a blocking layer with thickness $d = 3.5$ μm. Impurities in the blocking layer are also kept as low as possible (and compensated) at about 10^{12} cm^{-3} to maximize resistivity. The bias contact on the blocking layer is a transparent electrode that passes the infrared radiation. When a negative voltage is applied to the bias lead, electrons in the acceptor impurity band are swept away from the blocking layer over a length called the "depletion" region. The internal electric field in this region is like that in a reversed biased photodiode, and the BIB behaves in a similar manner.

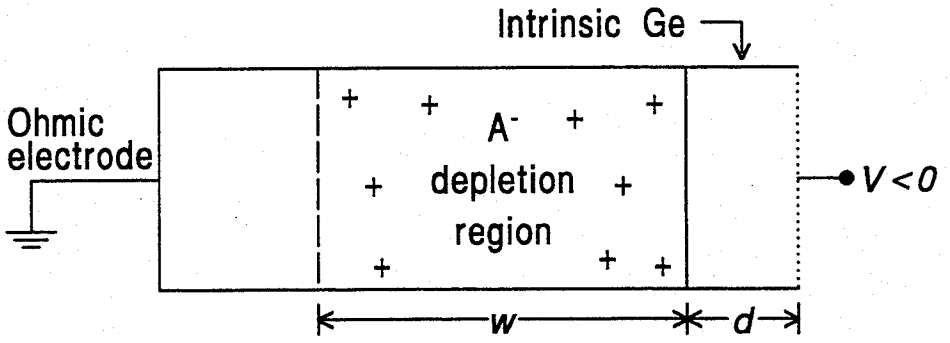

Figure 1: Schematic of a Ge:Ga BIB.

The depletion depth is a function of the applied bias, and is given by the formula [11]:

$$w = \left[(2\epsilon\epsilon_0 V/N_d e) + d^2\right]^{1/2} - d, \tag{2}$$

where V is the applied bias voltage, ϵ the relative dielectric constant (15.4 for Ge), d the blocking layer thickness, and N_d the density of residual donor impurities. Unfortunately, one cannot always increase the bias voltage to deplete the entire detector. The breakdown field for impact ionization of dopants and impurities limits the applied voltage to less than 60 mV for 11.5 μm thick Ge:Ga devices. Under these conditions

the depletion depth is only 2.6 μm, which means most of the "active region" is undepleted. The undepleted portion has a minimal electric field given by Ohm's law, and consequently, a very very slow response (on the order of milliseconds). One could of course use a thinner device better matched to the achievable depletion depth, but this would lower the quantum efficiency. A lower number of undesired donor impurities would also help widen the depletion width for a given bias, but the impurity concentration of 4×10^{12} cm^{-3} for unwanted donor sites (e.g., Sb or As) in a Ge:Ga device is already very low.

Ideally, photons are only absorbed in the depletion region, because only there are the photogenerated carriers rapidly swept away to the electrical contacts. In our reverse-biased photodiode model, g=1, and the carrier lifetime is identical to the transit time, defined (approximately) as:

$$T_r = \frac{L}{\mu E}, \tag{3}$$

where L is the distance between electrical contacts, μ is the carrier mobility, and E is the electric field in the low field limit. The -3 dB bandwidth $B_{-3\,dB}$ for the IF response can be approximated as:

$$B_{-3\,dB} = \frac{1}{2\pi T_r} = \frac{\mu V_{max}}{2\pi L^2}. \tag{4}$$

Consequently, a wide IF requires a thin device with the highest possible bias voltage V_{max}. The RC limited bandwidth is generally much wider than Eq. (4) for a 50 ohm IF system. The limit on bias voltage previously mentioned restricts the maximum electric field for Ge:Ga to ~100 V/cm. For Si devices with more tightly bound sites, the field can exceed 1000 V/cm. In this latter case the carrier drift velocity reaches a terminal value near 10^6 cm sec^{-1}, limited by scattering from neutral impurity sites. BIB devices such as Si:Sb and Si:As, or more exactly those with high energy dopants, have an inherent advantage over Ge:Ga BIBs for this reason. This is evident in Table 1, where the IF bandwidth is estimated for various BIBs which are 10 μm thick.

It should be noted that "compensation" is not used to improve the response time of a BIB mixer. Any increase in donor sites to effect compensation in a Ge:Ga BIB would reduce the width of the depletion region. It would also lower the current gain $g = \tau/T_r$, where τ is the carrier lifetime and T_r is the transit time. Ideally, g =1 for a photodiode where carriers recombine only at the contacts. Lowering the current gain increases the relative noise contribution of the IF amplifier, thereby requiring a higher LO power to achieve quantum noise limited performance. Note that a photoconductive mixer can have a power conversion gain under certain conditions [5,14].

BIB	V_{max}	T_{min}	IF (-3dB)*
Ge:Ga	60 mV	3.3 nsec	50 MHz
Si:Sb	2.0 V	.1 nsec	1500 MHz
Si:As	2.0 V	.1 nsec	1500 MHz

* fully depleted material

Table 1

3. LO Power Requirement

Under the usual condition that $R_s \gg R_{IF}$ (where R_s is the photodiode source impedance and R_{IF} is the IF amplifier input impedance), the LO power required to obtain quantum limited performance (shot noise > IF amplifier noise) can be expressed as:

$$P_{LO} \geq \frac{kT_{IF}\, h\nu}{R_{IF}\, 2\eta g e^2}. \tag{5}$$

For the particular case of an IF amplifier with a 50 Ω input impedance and a noise temperature of 10 K, the required LO power is 1 μW at 3 THz. This LO power requirement can be met with a far-infrared laser even for mixer arrays. A single mixer can be driven by a laser sideband source, which can produce up to 10 μW of tunable FIR power.

Even though the BIB device has a relatively high doping density, its small volume limits the number of absorption sites. Carrier lifetimes must be short or photon fluxes small if power saturation is to be avoided. However, a minimum photocurrent is needed so that the shot noise (quantum noise) dominates over IF amplifier noise. Consequently, the response time must be fast so as to "recycle" the available impurity sites. Figure 2 shows the approximate saturation level for a Ge:Ga device as a function of carrier lifetime. The dotted line shows the LO power level at which shot noise is equal to the input noise of an IF amplifier with T_A =10 K. We see that

the carrier lifetime (transit time) must be significantly less than 10^{-3} sec to prevent hard saturation. Fully depleted devices with response times of 10^{-9} sec consequently do not have a power saturation problem. Undepleted devices, however, are slow and easily saturated.

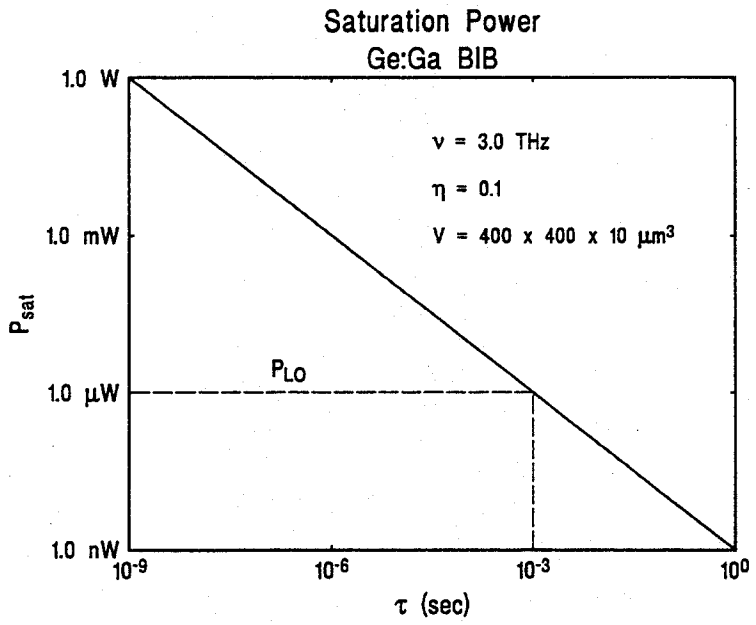

Figure 2: Saturation power for a Ge:Ga BIB as a function of carrier lifetime.

4. Work in Progress

Our results from tests of Ge:Ga BIBs were not promising, but that was not unexpected given the stated limitations of this material. We proceeded because Ge:Ga devices were provided to us first and because our astronomical interests lie at far-infrared wavelengths where this material is sensitive. One big problem with the devices was that they had been fabricated with a very undesirable spike on donor impurities in the active region underneath the blocking layer [15]. The depletion depth under bias conditions was minimal, and consequently the response time was slow and LO saturation was a problem. The Ge:Ga BIBs we tested were from an early attempt at epitaxial growth, and this particular impurity problem can be avoided in subsequent fabrication batches. Nevertheless, it remains to be seen whether Ge:Ga BIBs can ever prove to be competitive with HEB mixers at far-infrared wavelengths.

Si:Sb and Si:As BIBs should be competitive as mixers, not only because they work at higher THz frequencies than the established range of HEB devices, but also because

they have inherent speed advantages over Ge BIBs. Of course a faster response is also needed at higher frequencies if the same Doppler velocity interval is to be observed. We hope that some good results will be available on Si:Sb and Si:As devices by the time of next year's conference. The silicon BIBs can be fully depleted and should have response times fast enough to provide usable IF bandwidths. These BIBs appear to be the only viable technology for high sensitivity heterodyne spectroscopy in the 20-40 μm region.

We thank Dan Watson for providing Ge:Ga BIBs for testing, and also acknowledge useful conversations with him and James Huffman on the properties of these devices. This work is supported by NASA under grant NAGW-2954.

References

[1] Kooi, J.W., Chan, M., Bumble, B., LeDuc, H.G., Bin, M., and Phillips, T.G., "180-500 GHz Low Noise SIS Waveguide Receivers Employing Tuned Nb/AlOx/Nb Tunnel Junctions", Proceedings Sixth International Symposium on Space Terahertz Technology, p. 355.

[2] Spears, D.L., "Planar Heterodyne Arrays with GHz Response at 10 μm", *Infrared Physics*, **17**, 5-8 (1977).

[3] Betz, A.L., "Infrared Heterodyne Spectroscopy in Astronomy", in *Laser Spectroscopy III*, ed. J.L. Hall and J.L. Carlsten, Springer Series in Optical Sciences, vol. 7, pp. 31-38 (1977).

[4] Karasik, B.S., Gaidis, M.C., McGrath, W.R., Bumble, B., and LeDuc, H.G., "A Low-Noise Superconductive Nb Hot-Electron Mixer at 2.5 THz", (these proceedings 1997).

[5] Arams, F.R., Sard, E.W., Peyton, B.J. and Pace, F.P., "Infrared 10.6-Micron Heterodyne Detection with Gigahertz IF Capability", *IEEE J. Quant. Electr.*, **QE-3**, No. 11, 484-492 (1967).

[6] Seib, D.H., "Heterodyne Detection Experiments at 118.6 μm in Ge:Ga", *IEEE J. Quant. Electr.*, **QE-10**, 130-131 (1974).

[7] Dodel, G., Heppner, J., Holzhauer, E., and Gornik, E., "Wideband Heterodyne Detection in the Far-Infrared with Extrinsic Ge Photoconductors", *J. Appl. Phys.*, **54**, 4254 (1983).

[8] Koizumi, T., and Nagasaka, K., "A Gallium Doped Germanium Heterodyne Detector for FIR Plasma Diagnostics", *Infrared Phys.*, **223**, 247-255 (1983).

[9] Park, I.S., Haller, E.E., Grossman, E.N., and Watson, D.M., "Germanium:Gallium Photoconductors for Far-Infrared Heterodyne Detection", *Appl. Optics*, **27**, 4143-4150 (1988).

[10] Petroff, M.D., and Stapelbroek, M.G., U.S. Patent No. 4568960 (1986).

[11] Watson, D.W., and Huffman, J.E., "Germanium Blocked-Impurity-Band Far-Infrared Detectors", *Appl. Phys. Lett.*, **52**, 1602-1604 (1988).

[12] Huffman, J.E., Crouse, A.G., Halleck, B.L., Downes,T.V., and Herter, T.L., "Si:Sb Blocked Impurity Band Detectors for Infrared Astronomy", *J. Appl. Phys.*, **72**, 273-275 (1992).

[13] Herter, T., "IBC Arrays: Present and Future Prospects", in *Infrared Astronomy with Arrays, I*, ed. McLean (Kluwer: Boston 1994), p. 409.

[14] Kingston, R.H., *Detection of Optical and Infrared Radiation*, Springer Series in Optical Sciences, Vol. 10 (Springer-Verlag: Berlin Heidelberg New York 1978)

[15] Watson, D.M., Guptill, M.T., Huffman, J.E., Krabach, T.N., Raines, S.N., and Satyapal, S., "Germanium Blocked-Impurity-Band Detector Arrays I: Unpassivated Devices with Bulk Substrates", *J. Appl. Phys.*, **74**, 4199-4206 (1993).

THE SINGLE-MODE MONOLITHIC SILICON BOLOMETER AS AN ULTRASENSITIVE DETECTOR FOR MILLIMETER WAVELENGTHS

Khurram Farooqui[1], Joshua O. Gundersen[2], Peter T. Timbie[2], Grant W. Wilson[1], Jun-Wei Zhou[3], Christine A. Allen[4], Tina C. Chen[5], S. Harvey Moseley[6], and D. Brent Mott[4]

[1]Department of Physics, Brown University
Providence, RI 02912

[2]Department of Physics, University of Wisconsin
Madison, WI 53706

[3]Princeton Electronics Systems
Princeton, NJ 08512

[4]Solid State Device Development Branch, NASA/GSFC
Greenbelt, MD 20771

[5]Global Science & Technology
under contract to Infrared Astrophysics Branch, NASA/GSFC
Greenbelt, MD 20771

[6]Infrared Astrophysics Branch, NASA/GSFC
Greenbelt, MD 20771

Abstract

We report on the development of a single-mode waveguide-coupled monolithic silicon bolometer for applications in low-background astrophysical observations at millimeter wavelengths. In this device the absorber of the bolometer is a 250 μm wide bismuth-coated silicon substrate oriented along the E-plane of a waveguide. Reflection measurements performed between 75 and 170 GHz show that this coupling scheme is better than 90% efficient. The time constant of these devices is between 2 and 5 milliseconds at the nominal operating temperature of 100 mK. The devices have an electrical responsivity $\approx 2 \times 10^9$ V/W and an electrical noise equivalent power (NEP) $\approx 10^{-17}$ W/$\sqrt{\text{Hz}}$ at ~100 mK.

Introduction

Bolometers are thermal detectors that measure electromagnetic radiation power by converting it to heat. Incoming power is coupled to an absorber which is connected to a heat reservoir through a weak thermal link. The conversion of radiant power to heat in the absorber causes the temperature of the absorber to increase. This rise in temperature is measured by a thermistor (Figure 1).

Bolometers are used in a wide range of applications in astrophysics, particularly in low-background environments where sensitive detectors can be utilized effectively. When cooled below 1 K, bolometers are the most sensitive broadband detectors at millimeter and sub-millimeter wavelengths [1].

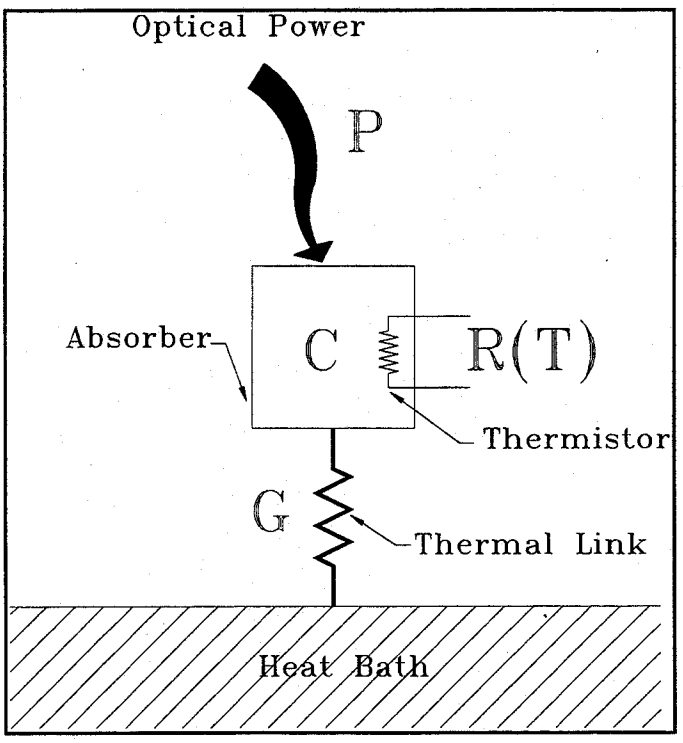

Figure 1: A schematic of a typical bolometer. The absorber has a heat capacity C and is linked to the heat bath by a thermal conductance G. Optical Power P coupled to the absorber causes a rise in temperature above the bath temperature; this change is measured by the thermistor.

We have developed monolithic silicon bolometers for use in an experiment to measure the spatial structure (anisotropy) in the Cosmic Microwave Background (CMB). Since the CMB is an unperturbed relic of the hot Big Bang, studies of its structure can yield a wealth of information about the early Universe. Measurements of anisotropy in the CMB are difficult because the level of anisotropy is five orders of magnitude below the 2.7 Kelvin CMB. As a result, large integration times (~ 100 seconds) are required to obtain enough sensitivity on a single patch of the sky. Our approach is to measure the anisotropy in the CMB using a balloon-borne telescope called the Medium Scale Anisotropy Measurement (MSAM II) [2]. The low atmospheric background at an altitude higher than 30 km allows the use of ultra-sensitive detectors.

The MSAM II radiometer [9] has five channels spanning E, W and D bands: 65-80 GHz, 80-95 GHz, 95-110 GHz, 130-150 GHz and 150-170 GHz. The bands were chosen to take advantage of the window in the atmospheric opacity at microwave frequencies. The broad bandwidth allows higher power coupling to the detectors and increases the sensitivity to the CMB blackbody spectrum. The multiple bands are essential for spectral discrimination between astrophysical foregrounds and the CMB.

At wavelengths shorter than a few millimeters, bolometers are typically coupled to radiation using multimode optical systems such as multimode feed-horns, light pipes and Winston concentrators. However, we have coupled our detectors directly to single-mode waveguide, thereby utilizing the advantages of single-mode technology such as low-sidelobe antennas and high quality filters. In addition, by coupling the detector directly to waveguide, the absorber can be made much smaller than a wavelength. This greatly reduces the time-constant of a thermal detector. Moreover, the cross-section for cosmic ray hits is small.

Coupling Scheme

Monolithic silicon bolometers, introduced by Downey *et al.* [3], have been fabricated at NASA Goddard Space Flight Center [4]. The device consists of a micromachined thin silicon substrate suspended from a silicon frame by silicon legs

which also function as the thermal link to the heat bath. The thermistor is ion-implanted in the substrate. Fabrication by optical lithography allows precise control of detector

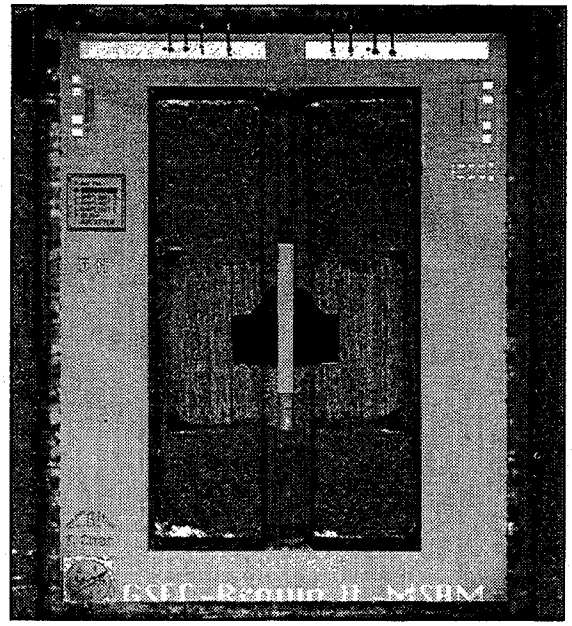

Figure 2: A view of a monolithic silicon bolometer mounted on a WR-6 waveguide block. The block is at 100 mK. The rectangular absorber, oriented along the E-plane of the waveguide, is suspended on 4 silicon legs, which also provide the thermal connection to the silicon frame surrounding the waveguide opening. For scale the inside dimensions of the waveguide are 1.651×0.825 mm.

parameters. The thermistor, the absorber and the thermal link can be optimized separately. Our waveguide-to-bolometer coupling scheme is similar to that introduced by Peterson and Goldman [5] for composite bolometers. However, in our design (Figures 2 and 3) the absorber of the bolometer consists of a thin resistive bismuth film deposited on the narrow silicon substrate oriented along the E-plane. An adjustable backshort in the waveguide behind the absorber is used to match the impedance of the absorber to the waveguide. The thermistor is located outside the waveguide, and the silicon substrate and legs pass through a small slot in the broad wall of the waveguide. Since the thermal contraction of the silicon frame is much smaller than that of the aluminum waveguide mount, the frame cannot be glued directly to aluminum, as it would shatter upon cooling. Instead, a small piece of Invar is press-fit into the mount, and the frame is glued to the Invar piece. The thermal contraction of Invar is close to that of silicon.

To determine the absorber impedance that maximizes power absorption, we measured the reflectance of this design using an X-band scale model. The reflectance was determined to be less than –10 dB across the full waveguide band (8 to 12 GHz) for film

resistances from 75 Ω/square to 180 Ω/square, and was found to depend only weakly on the fraction of the waveguide cross-section covered by the absorber; this fraction was varied from 10% to 25%. Thus, a single bolometer design can be used interchangeably in our E-band, W-band and D-band waveguide mounts.

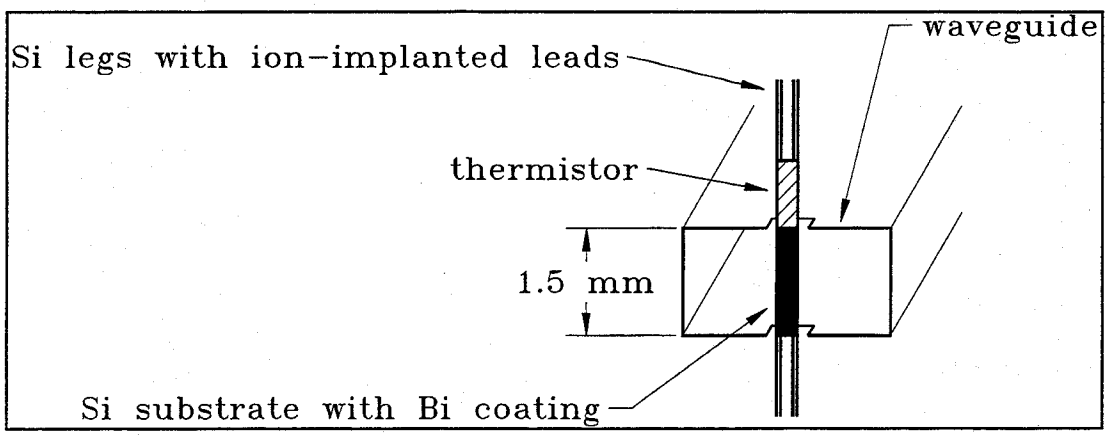

Figure 3: Expanded, perspective view of the bolometer and the waveguide. Silicon legs ($2500 \times 18 \times 10$ μm) provide support and thermal connection to the silicon substrate. The electrical contact to the thermistor is achieved through ion-implanted traces along two of the legs. The substrate thickness is 10 μm. The thermistor is ion-implanted in the substrate.

In the actual bolometers, a 180 nm bismuth layer is deposited on the waveguide portion of the Si. This layer gives an expected impedance of about 80 Ω/square at 4.2 Kelvin, and 20 Ω/square at room temperature. We minimized the reflectance of this structure by adjusting the back short position, with the bolometer cooled to 4.2 Kelvin The reflectance has been measured to be better than –10 dB across the entire band. The bismuth layer is coated with a 100-nm layer of silicon monoxide to prevent exposure to air which has been observed to increase the surface-resistance of bismuth over time [6].

Design and Fabrication

The electrical and thermal properties of the bolometer are determined by the operating temperature, the temperature sensitivity of the thermistor, the thermal conductance of the legs, the heat capacity of the detector, the optical loading and

modulation frequency. Bolometer optimization, including the non-equilibrium noise analysis of Mather [7], is described by Griffin and Holland [8].

In our bolometers, the thermistors are produced by implanting silicon wafers with phosphorus and 50% boron compensation to a concentration near the metal-insulator transition. At this concentration, the phonon-assisted hopping conduction mechanism has a strong dependence on temperature. The behavior of resistance with temperature of the thermistor is described by:

$$R = R_0 \mathrm{Exp}\sqrt{\frac{T_0}{T}} \tag{1}$$

where R_0 and T_0 are experimentally derived constants which are extremely sensitive to doping density. Thus, to accommodate run-to-run implant variations, a minimum of ten wafers are implanted with doses ranging around the optimum in steps of 2.5-5% variation of net dose.

The supporting structure is fabricated from <100> silicon using anisotropic chemical etching. Silicon wafers 300 μm thick are initially back-etched to produce membranes 20-30 μm thick using a thermal-oxide mask and 45% KOH etch bath. Standard photolithographic techniques are used to pattern the oxide mask on the back of the wafers. After thinning, a thick (1.8 μm) Al mask is deposited on the front of the wafer. This layer is subsequently patterned into three successive implant masks to produce first the degenerately doped contact and thermistor leads, followed by two separate implant-masks for the phosphorus and boron thermistor implants. The boron implant is patterned slightly larger than the phosphorus implant to prevent possible shorting of the thermistor around the perimeter by the much more mobile phosphorus during implant and subsequent annealing.

After annealing, an oxide film is deposited using chemical vapor deposition on the front of the wafer to act as an etch mask during the final KOH etching of the bolometer element. The silicon is etched into an "H" pattern as shown in Figure 3. The back of the detector is textured using a dilute ethylenediamine pyrocatechol (EDP) solution in a double boiler temperature bath to provide scattering sites down the legs to

reduce thermal conductance due to phonons. Thus, for the silicon legs, the thermal conductance can be described by:

$$G = G_0 T^3 \tag{2}$$

where G_0 is mainly modified by the design of the leg geometry. Finally, bismuth is deposited on the un-implanted region of the detector to act as the absorber.

Bolometer Performance

The bolometer parameters are optimized for the optical loading and background photon noise expected in flight in each of the five spectral bands. For example, for the 95-110 GHz band, with radiative loading from sky, atmosphere, and 250 Kelvin optics: two mirrors with 0.5% emissivity (estimated), and a 0.020" polypropylene window with 0.5% emissivity (estimated). The optical power and background photon noise are estimated to be 0.3 pW and 6.5×10^{-18} W/$\sqrt{\text{Hz}}$ using a measured system optical efficiency of 30 %. The bolometer is operated at a bath temperature of 100 mK and has T_0 = 14.75 K, $R_0 = 87\Omega$, and G = 2.2×10^{-11} W/K at 100 mK The electrical responsivity at optimum bias was measured to be 1.0×10^{9} V/W. According to Griffin and Holland [8], the only contributions to the bolometer noise are Johnson noise, thermodynamic fluctuations (phonon noise), amplifier noise, and background photon noise. Based on electrical noise measurements made in the dark, we can estimate the detector noise under flight conditions. By combining the estimated detector noise of 8.1×10^{-18} W/$\sqrt{\text{Hz}}$ with the estimated photon noise, we find that the total receiver NEP should be 1.0×10^{-17} W/$\sqrt{\text{Hz}}$. This translates to a receiver sensitivity of 114 $\mu\text{K}\sqrt{\text{sec}}$ for a total-power measurement of a Rayleigh-Jeans source at 15 GHz bandwidth with 30% optical efficiency. The time-constant of the detector has been measured to be 3.5 milliseconds at the optimum bias.

Conclusion

The single-mode monolithic silicon bolometers appear to be extremely promising for balloon- and space-borne observations. The 114 $\mu\text{K}\sqrt{\text{sec}}$ receiver sensitivity can be

compared with the performance of a high electron mobility transistor (HEMT) system under similar conditions. For example, the state-of-the-art W-band HEMT amplifiers which have been developed for the Microwave Anisotropy Probe experiment have a noise temperature of 60 K [10]. For a 15 GHz bandwidth, these amplifiers would have a sensitivity of 490 $\mu K\sqrt{sec}$. The noise of our bolometric system is lower by a factor of 4.

In order to determine how much further our system noise may be reduced, we compare the detector NEP with the expected photon noise at 30 km. As shown in Figure 4, the detector NEP is already comparable to the photon noise from the low-background sources. Further reduction of the detector NEP will not significantly improve the receiver

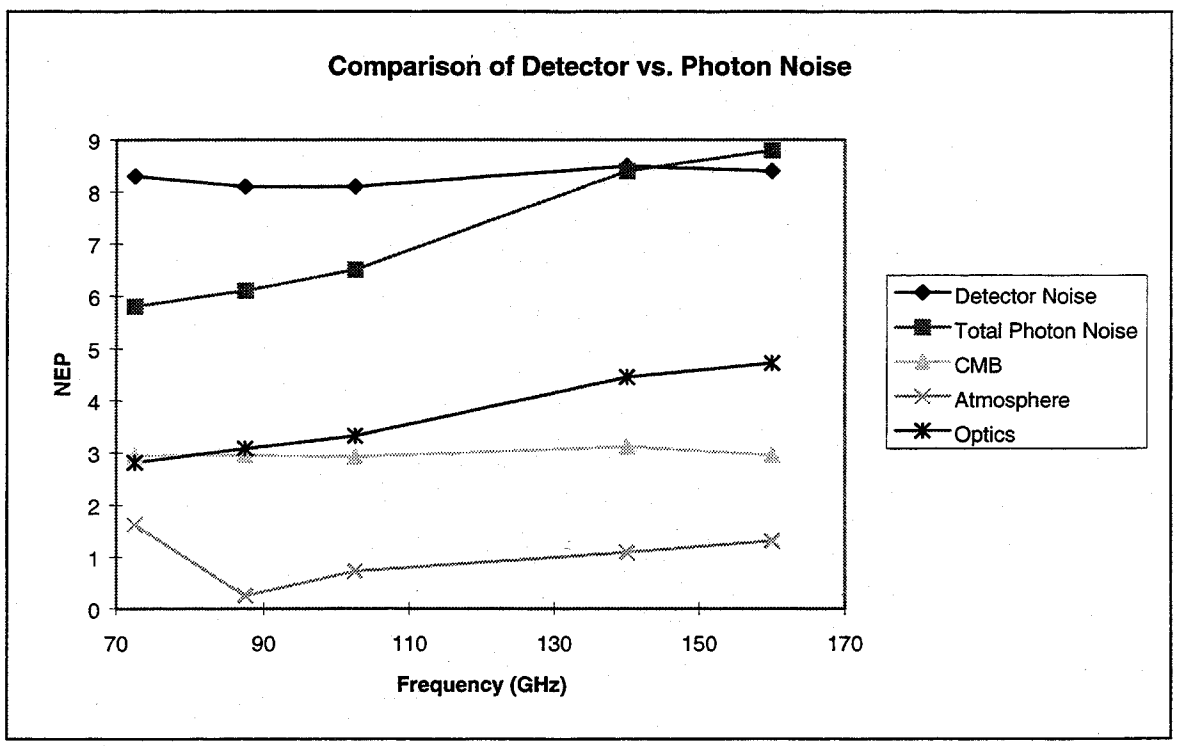

Figure 4: The expected performance of a typical MSAM II bolometer at 30 km is compared with the photon noise in each of the five bands. The total Photon noise is the quadrature-sum of the noise contributions from the CMB, the atmosphere [11] and the 250 Kelvin optics. The most significant contributor to the total photon noise, especially in the higher bands, is the noise from the 250 Kelvin Optics. At 140 GHz and above, the bolometer noise is less than the total photon noise; the instrument is limited by the photon noise.

sensitivity unless the noise contribution from the warm telescope optics is smaller than expected. We will verify our estimate of the noise contribution from the optics and the atmosphere in an upcoming flight of MSAM II.

Acknowledgments

We thank Bob Silverberg and Ed Cheng for helping to provide the detectors, and Stephan Meyer for discussions on bolometer theory. This work was supported by an NSF-PYI award to P.T. (PHY-90588474), the NASA Innovative Research Program (NAGW-2797), and a NASA GSRP award to G.W. (NGT5-50001).

References

1. P.L. Richards, "Bolometers for Infrared and Millimeter Waves", J. Appl. Phys.,**76** (1) (July 1 1994).
2. M. Kowitt *et al.,* "The MSAM/TopHat Program of Anisotropy Measurements", Astro. Lett. And Communications, **32**, 273 (1995).
3. P.M. Downey *et al.,* "Monolithic Silicon Bolometers", Appl. Opt., **23**, 910 (1984).
4. S.H. Moseley *et al.,* Proc. ESA Symp on Photon Detectors for Space Instrumentation, ESA-SP-356, 13 (1992).
5. J.B. Peterson and M.A. Goldman, "Reflectance of Broad Band Waveguide Bolometers", Int. J. Infrared and Millimeter Waves, **9**, 55 (1988).
6. G.S. Tucker, "An Instrument to Search for Small Scale Anisotropy in the Cosmic Microwave Background at 90 GHz", Ph.D. Thesis, Princeton University (1993).
7. J.C. Mather, "Bolometer Noise: Nonequilibrium Theory", Appl. Opt., **21**(6) p1125 (1982).
8. M.J. Griffin and W.S. Holland, "The Influence of Background Power on the Performance of an Ideal Bolometer", Int. J. Infrared and Millimeter Waves, **9**, 861 (1988).

9. G.W. Wilson *et al.*, "Low-Noise Optics for a Measurement of the Anisotropy in the Cosmic Microwave Background Radiation", Proc. of the European Workshop on Low-Noise Quasi-Optics, Bonn, 12-13 Sept. 1994.
10. John Webber, NRAO-CDL, Personal Communication (1997).
11. AT Atmospheric Transmission Software, Dr. Erich Grossman, Airhead Software Company.

Waveguide Coupled Bolometers

Jeffrey B. Peterson
Dept. of Physics
Carnegie Mellon University
Pittsburgh PA 15143

David Osterman
Hypres Inc.
175 Clearbrook Road
Elmsford, NY 10523

Bolometers offer much greater detection bandwidths than are available with heterodyne receiver technology, so bolometers will continue to be used for photometry of continuum radiation from astrophysical sources such as galactic and extragalactic dust emission and the cosmic background radiation. A new bolometer design is presented which couples to waveguide, but which dissipates the Terahertz frequency power in a load resistor that is just a few tens of in microns in size. This load resisitor is located on a microlithographed silicon nitride beam which serves to isolate the load resistor, along with a superconducting transition thermometer, from the 0.3 K cold stage.

Tests of antenna structures, lithographed fliters, transition edge thermometers, and silicon nitride beams will be presented.

Because of the very low heat capacity of the load resistor and thermometer these bolometers will provide sensitivity in the lO^-17 NEP range and time constants of 7 ms without requiring 0.1 K cold stage temperatures, making this technology useful for NASA and ESA missions such as SOFIA and COBRAS/SAMBA.

MIXING EXPERIMENTS AT W-BAND USING HIGH-TC JOSEPHSON JUNCTIONS

O. Harnack, M. Darula, S. Beuven, H. Kohlstedt
Institute of Thin Film and Ion Technology, Research Center Juelich, 52425 Juelich, Germany

Abstract—We report on the mixing properties of high-T_c superconductor (HTS) Josephson junctions. Direct radiation and heterodyne mixing experiments in the frequency range 78 GHz-119 GHz have been performed using $YBa_2Cu_3O_{7-x}$ (YBCO) step-edge junctions (SEJ) and bicrystal junctions (BCJ) on $LaAlO_3$ and MgO substrates. Under external radiation our junctions showed harmonic phase synchronization (Shapiro steps) up to 1.88 THz. Junctions with current voltage characteristics (IVC) close to predictions of the resistively shunted junction model (RSJ) were mounted into a heterodyne mixing setup. Under the radiation of two monochromatic signals we obtained conversion efficiencies around -14 dB in the 11 GHz intermediate frequency (IF) band. In the fundamental mixing regime we observed response at IF at working temperatures up to 72K . We demonstrated the operation of HTS Josephson junctions in the self-mixing mode. The experimental results are in good agreement with simulations using the RSJ model.

I. INTRODUCTION

Mixers based on the Josephson mixing scheme require overdamped junctions. Most of HTS Josephson junctions are naturally overdamped and therefore suitable for this application. Moreover, because of the relatively high energy gap, the operation of mixers based on HTS junctions up to THz frequencies is expected. In contrast, the performance of conventional low-T_c (SIS) mixers degrades above 0.7 THz.

Several groups reported successful mixing experiments using HTS junctions [1,2,3]. In this paper we present an experimental study of the mixing properties of two different types of HTS structures on two different substrates: SEJs prepared on $LaAlO_3$ and MgO substrates and junctions prepared on MgO bicrystal substrates. The aim of our investigations was to compare the heterodyne mixing properties of different HTS Josephson junction types with results of simulations made by using the RSJ model.

II. EXPERIMENTS

A. Samples and fabrication procedure

SEJs and BCJs were fabricated on (100) $LaAlO_3$ (ε_r = 20-24) and (100) MgO (ε_r = 9.6) substrates using laser ablation for film deposition, standard photolithographic processing and ion beam etching for patterning of structures [4]. The junctions were integrated into two different bow-tie antenna designs for a broadband high-frequency coupling (see Fig. 2). This antenna type exhibits a frequency independent impedance characteristic. The antenna structures contained usual microstrip low pass filters with cut-off frequencies between 11 GHz and 100 GHz. The patterned microbridge in the center of the antenna consists of one 2 μm wide Josephson junction.

B. DC and AC junction characterization

Typically, our SEJs on $LaAlO_3$ substrates had a characteristic voltage $V_c=I_cR_n$, where I_c is the critical current and R_n is the normal resistance of junction, in the range between 1 mV and 1.8 mV at 4.2 K. The normal resistance R_n, which is the important parameter for optimization of the impedance matching, was in the range between 10 Ω and 50 Ω. A reduced oxygen concentration in the barrier region of the junction generally results in reduced critical temperature T_c, higher R_n and lower I_c [5]. To achieve optimal junction parameters, e.g., to adjust V_c, a microwave oxygen plasma treatment can be applied (for details see [4]). The BCJs on MgO had R_n from 1 Ω to 4 Ω, I_c between 1.6 mA and 2 mA at 4.2 K. All bicrystal junctions were superconducting up to temperatures close to T_c of the YBCO film (88 K), with I_c=60 μA-90μA at 80 K. Using the simple voltage-frequency relation $f_c=2eV_c/h$, characteristic frequencies f_c in the range between 400 GHz and 1 THz were estimated.

We also investigated the high frequency response to applied microwave radiation with frequencies between 78 GHz and 117 GHz of several junctions on $LaAlO_3$ and MgO. Fig. 1 shows a typical IVC of a MgO-bicrystal junction under 104.5 GHz radiation using a W-band waveguide setup. In the presence of microwave power, the curve exhibits well developed

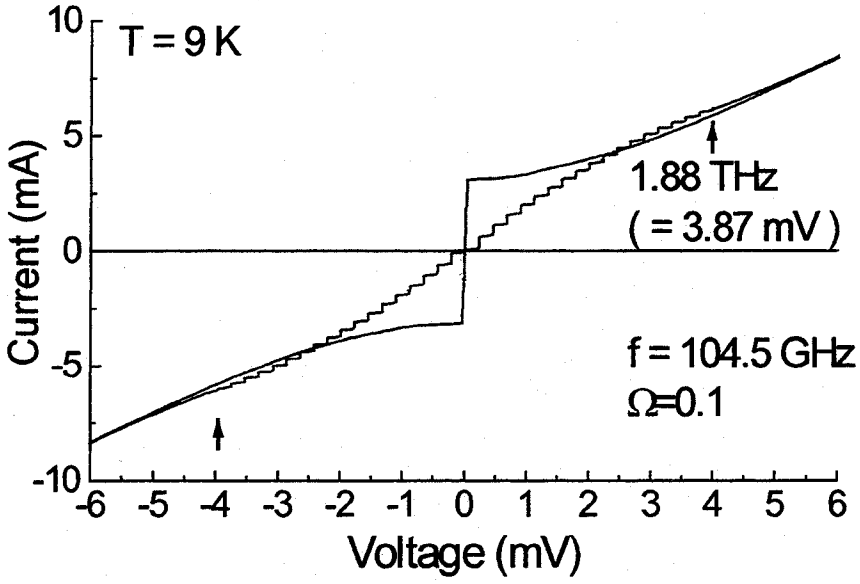

Fig.1. AC characterization of a BCJ on MgO

Shapiro steps at voltages V_n=nhf/2e up to n=18 (≅ 1.88 THz). Here n is the number of the harmonics of the Josephson radiation. This result promises operation of these junctions at THz frequencies. The normalized frequency $\Omega = f/f_c$ was 0.1 in this experiment.

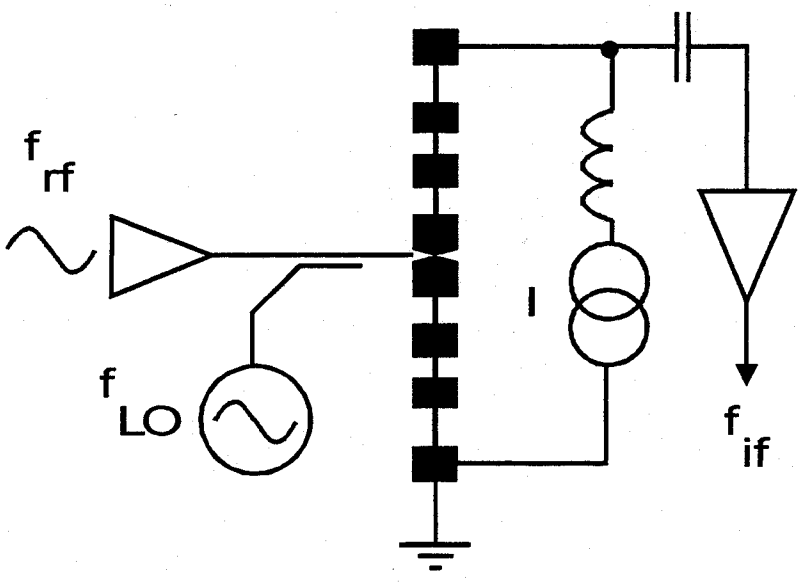

Fig. 2. Scheme of the heterodyne mixer setup

C. Heterodyne Josephson mixing: simulation and experiments

In order to simulate the Josephson mixing we solved numerically the differential equations of the RSJ model including two AC current terms oscillating with f_{rf} and f_{LO}. The obtained time dependencies were transformed into the frequency domain using FFT and the power at $f_{IF}=|f_{rf}-f_{LO}|$ was extracted from the frequency spectrum. In Fig. 3, a result of a complete simulation for different current bias points is plotted. The IVC with Shapiro steps induced by the LO are shown together with clear IF signal maxima between two Shapiro steps. In the heterodyne mixing experiments we used junctions with R_n of 1-50 Ω and V_c of 1 - 2.4 mV. A scheme of our setup is displayed in Fig. 2. In Fig. 4, results obtained for SEJ on $LaAlO_3$ are shown. Under irradiation by a Gunn-oscillator at f_{LO}=90 GHz and a weak signal from a klystron generator at f_{rf}=100.8 GHz, the intermediate frequency power P_{if} detected at 11 GHz shows clear signal peaks up to the 11 th harmonics (990 GHz) of the local oscillator line. SEJs on MgO showed heterodyne mixing response up to the 12th harmonics (1.08 THz) of the local oscillator. With MgO-bicrystal junctions we obtained similar data. Because of the relatively low impedance of these junctions, higher power levels are required to overcome the impedance mismatch. The optimum biasing point for Josephson mixing was located in the middle between two steps in accordance with theoretical prediction.

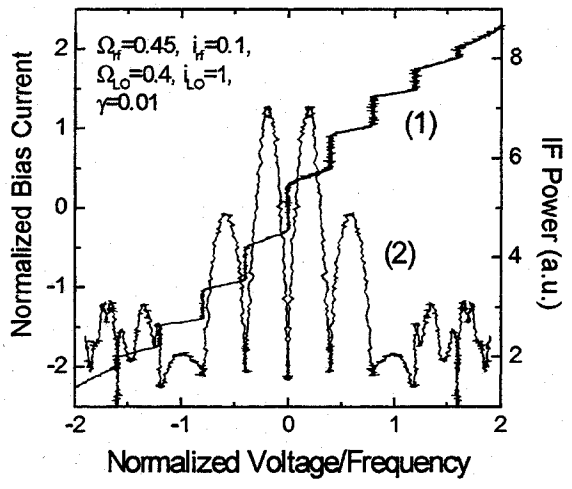

Fig. 3 RSJ model simulation of heterodyne mixing: (1) IVC, and (2) power at IF.

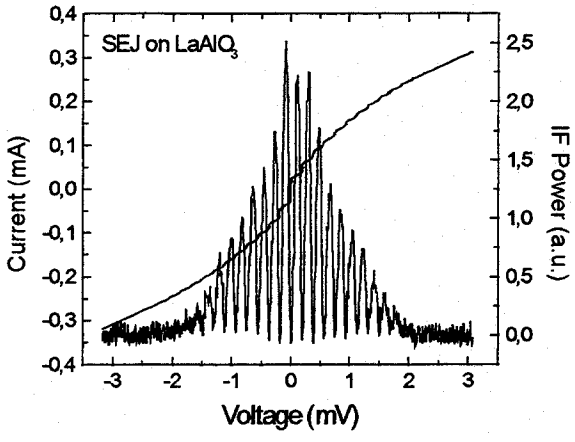

Fig. 4 Mixing experiment using a SEJ at 4.2 K, F_{LO} = 90 GHz, F_{rf} = 100.8 GHz.

D. Temperature effects

Since the characteristic frequency f_c of a Josephson junction is a function of temperature, the normalized frequency Ω, which is the ratio between the incident frequency f and fc, can be influenced by adjusting different working temperatures. Fig. 5 shows the simulated I-V

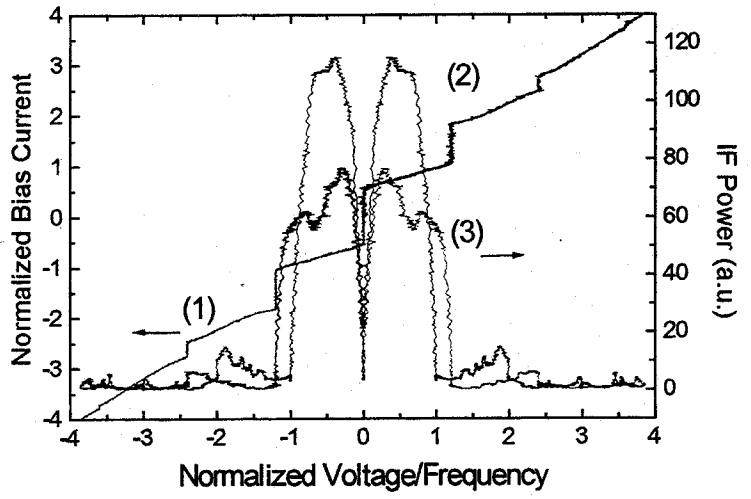

Fig. 5. Simulation of the power at IF for $\Omega = 1$ (2), and $\Omega = 1.2$ (3), IVC for $\Omega = 1.2$ (1)

curve and the power at the IF for $\Omega = 1$ and $\Omega = 1.2$. Fig. 6 displays typical results of mixing experiments using a MgO BCJ at various temperatures between 60 K and 72.4 K. In the experimental and simulated results the IF power follows the differential resistance as indicated by the basic mixer theory based on the RSJ model (e.g., see [6]).

The clearly observable reduction of the available power at the IF with increasing of temperature is due to the increase of the normalized frequency Ω (reduction of f_c). Equivalent to this experiment similar results will be obtained if the working frequency will be increased, keeping the temperature constant.

At temperatures below 60 K, this junction exhibited very high dynamic resistance between the steps, complicating an adjustment of a stable biasing point. This is typically observed if the radiation frequency is much smaller than the characteristic frequency $f_c=2eV_c/h$ of the junction. This shows that the junction parameters (I_c, R_n, V_c) must be optimized for a given

operation frequency. At the same time the value of R_n in the range 30 Ω-100 Ω is important for impedance matching.

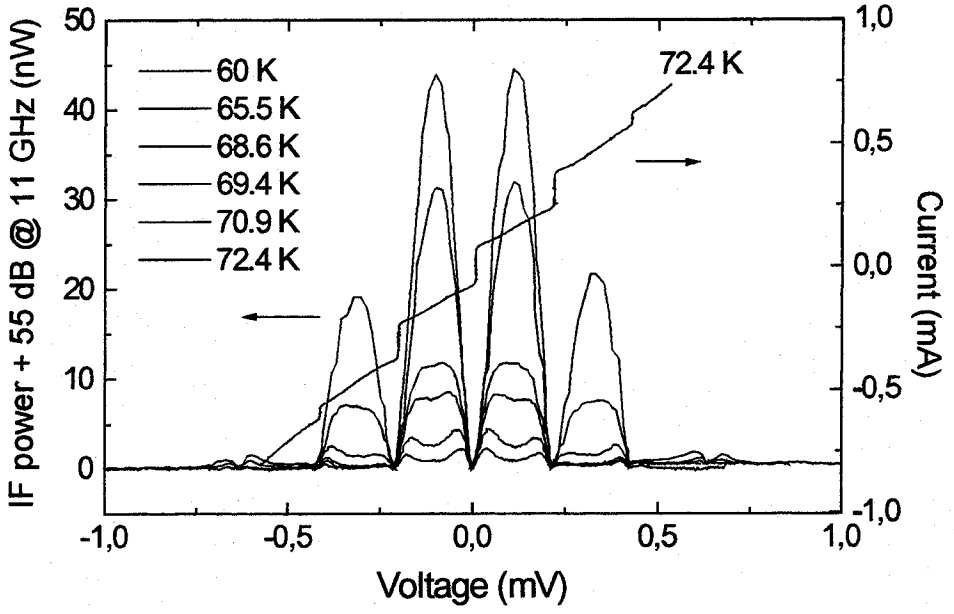

Fig. 6. Measured temperature dependence of Josephson mixing using a BCJ on MgO

E. Conversion efficiency and LO requirements

From mixing experiments using a well matched high ohmic SEJ on $LaAlO_3$ we calculated conversion efficiencies $\eta=P_{if}/P_{rf}$ to be around -14 dB (including losses in the IF matching part). An IF signal response was observed up to a minimum rf-input signal power of approximately 1 pW.

The optimal LO power level for the Josephson mixing process was investigated by measuring the power at the IF for different suppressions of the critical current I_c. The value of the suppressed current I_o depends on the LO power level.

Fig. 7 displays the result of a measurement done by using a MgO-BCJ. The temperature was 70 K, the LO frequency was 101.4 GHz and the signal frequency was 90 GHz. The measured dependency between the available IF power and the ratio of I_o/I_c shows that the

optimum ratio I_o/I_c is approximately 0.5. The LO power consumption in this point was around 40 nW.

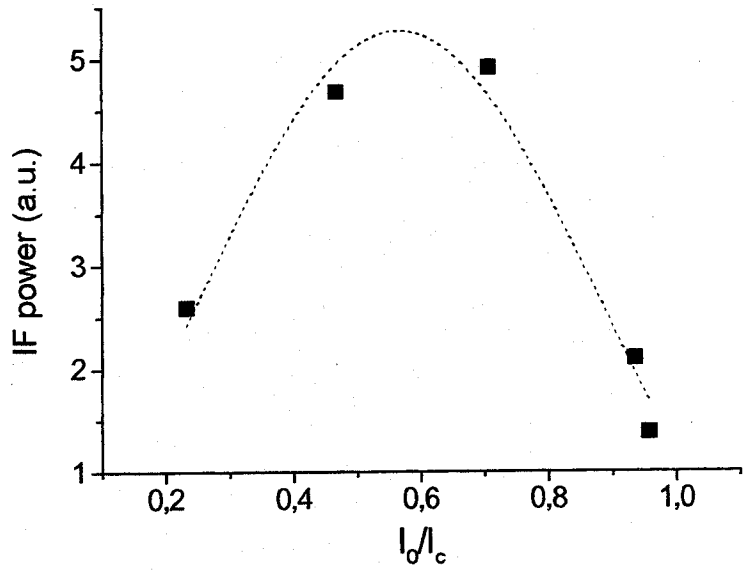

Fig. 7. Power at IF vs normalized suppression of I_c

F. Self-oscillator mixing

An interesting feature of Josephson junctions is the mixing response even without an external local oscillator - the so called self mixing. A typical characteristic of frequency down-conversion with the internal Josephson oscillator radiation is presented in Fig. 8. The MgO-bicrystal junction ($R \approx 4\ \Omega$, $V_c \approx 2.4$ mV at 4.2 K) gives, if irradiated by an external signal (only the first Shapiro step is visible) at 101 GHz, an 11 GHz IF-signal with two clear peaks around each step (101 ± 11 GHz).

The power related to these peaks was around 2 fW. The external microwave power which induced the first step was around 200 nW. The positions of the IF peaks on the voltage scale are well related to the condition for mixing at the first harmonic of the internal Josephson oscillation. The two broader peaks around the 0th Shapiro step represent the radiation of the internal Josephson oscillation detected at 11 GHz ($\cong 22\ \mu$V on the voltage scale).

The linewidth of the down converted signal in this mixing mode is determined by the linewidth Δf of the internal Josephson oscillations. In the case of our Josephson junction Δf was about 2 GHz which is still too high for receiver applications. Arrays of Josephson junctions integrated into suitable resonator structures could overcome this drawback.

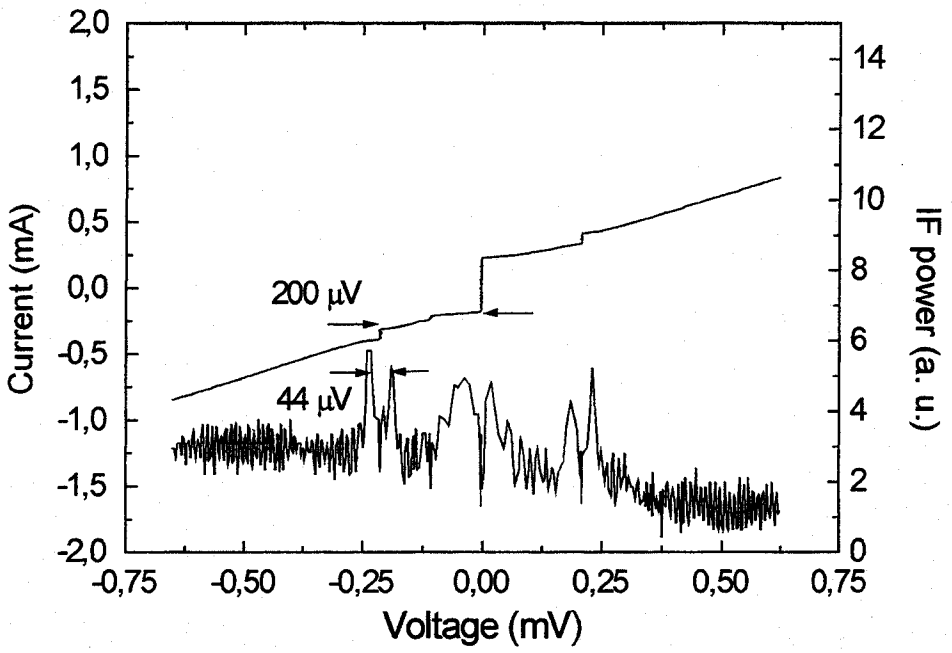

Fig. 8. Self oscillator mixing

III. Conclusion

We investigated the high frequency and mixing properties of step-edge junctions prepared on $LaAlO_3$ and MgO substrates and bicrystal junctions prepared on MgO substrates in the temperature range between 4.2 K and 72 K. These types of junctions showed a behavior in accordance with RSJ model predictions. Using bicrystal junctions on MgO, harmonic phase

synchronization up to 1.88 THz was observed under irradiation by microwaves at 104.5 GHz. We performed heterodyne mixing experiments in the W-band and obtained harmonic mixing response up to frequencies higher than 1 THz with SEJ on MgO. Using high resistance SEJ on $LaAlO_3$ the conversion efficiency of our mixer was -14 dB including the IF losses. IF signal response was observable up to working temperatures around 72 K using a low resistance BCJ on MgO. For the same junction, the required LO power of 40 nW was relatively low. The lowest detectable signal using our receiver system was 1 pW. This fact indicates that further optimization of the impedance matching between the mixer and the HF environment will be necessary.

ACKNOWLEDGMENT

We would like to thank L.E. Amatuni, P. Zimmermann and J. Konopka for useful help and fruitful discussions.

REFERENCES

[1] J. P. Hong, H. R. Fetterman et al., *Appl. Phys. Lett.*, **62,** 22, 1993, p. 2865

[2] Y. Fukumoto, R. Ogawa and Y. Kawate, *Jpn. J. Appl. Phys.*, **32**, 1993, p. 4966

[3] H. Shimakage et al., ASC'96, Pitsburg 1996

[4] O. Harnack, M. Darula, L.E. Amatuni, S. Beuven, H. Kohlstedt, *J. Low Temp. Phys.*, **106**, 3-4, p. 463

[5] K. Herrmann, G. Kunkel, M. Siegel, J. Schubert, W. Zander, A.I. Braginski, C.L. Jia, B. Kabius, K. Urban, *J. Appl. Phys.*, **78**, 1995, p. 1131

[6] T. Van Duzer, C.W. Turner, *Principles of superconducting devices and circuits*, Elsevier North Holland, Inc. (1981)

Eighth International Symposium on Space Terahertz Technology, Harvard University, March 1997

A quasioptical SIS receiver with normal metal tuning for the 800-900 GHz band

F. Schäfer*, P. van der Wal*, E. Kreysa*, K.H. Gundlach**

* Max-Planck-Institut für Radioastronomie, D-53121 Bonn, Germany

** Institut de Radioastronomie Millimetrique, F-38406 St. Martin d'Heres, France

We describe a quasi-optical SIS receiver designed for operation in the 800 - 900 GHz atmospheric window. First results obtained during an observation period in January 1997 at the Heinrich-Hertz-Telescope (HHT) on Mt. Graham, Arizona are presented.

The receiver employs the well established design of using a diffraction limited substrate-lens made of crystalline quartz fed by a double-slot antenna to couple to the incoming radiation [1]-[3]. In contrast to the design variant using silicon as lens material [4], our antenna configuration includes a moveable reflecting backplane to avoid losses due to the backward radiation into the vacuum side. Without backplane these losses would be higher as compared to silicon due to the lower refractive index of the quartz dielectric; on the other hand for the silicon lens an antireflection coating usually has to be applied to reduce the higher reflection loss of the silicon lens. Currently we use no antireflection coating on the quartz lens. A schematic drawing of our optical setup is shown in Fig. 1. It was designed using a theoretical method developed by Prof. V. Hansen and his group [5], which gives the antenna's impedance and its radiation characteristic into a dielectric half space. Results from the calculation of the double-slot input impedance versus reflector distance are shown in Fig. 2. The extended hyperhemispherical lens was shown to provide good quality amplitude and phase patterns by scaled measurements at microwave frequencies [6].

A photography illustrating the mechanical design of the mixer block is shown in Fig. 3. Only few mechanical components are necessary due to the use of a commercially available microwave substrate with thick copper groundplane [7]. It carries the lens assembly on the front side whereas the microwave and bias lines are etched on the substrate side which also supports the superconducting magnet with pole pieces and the reflecting backplane assembly.

The SIS junctions used for this experiment were produced in 1994 at IRAM-Grenoble (France) during a guest period in the junction laboratory. Because the desired operating band of the receiver is well above the gap frequency for niobium films, we decided to use a normal conducting embedding network for the Nb- (Al-oxide)-Nb junction [8]. DC measurements of sputtered aluminum films at 295 K and 4.2 K gave a resistivity near the bulk limit at room temperature and a resistivity ratio (RR) of roughly 11 for a variety of films. At high frequency and low temperature anomalous skin effect losses are the limiting factor for the achievable minimum RF loss in the Al films. According to the theory of metallic conduction, size effects impose an upper

limit on the DC conductivity of thin films. At low temperatures scattering of the conduction electrons from the film surface becomes important if the electron's bulk mean free path is comparable to the film thickness. The result is a maximum RR≈10 for our film thickness of about 200nm, meaning that no further improvement of the RF surface resistance can be expected if this RR is reached. This is because in the pure bulk limit (clean films with thickness large compared to anomalous penetration depth) the RF surface resistance does not depend on the RR [9]. The mixer chip used for the measurements reported here is shown in Fig. 4. It employs the double-junction tuning circuit with antisymmetric feed configuration introduced by Zmuidzinas et al.[10]. We used the cross-line technique [11] to define junctions of roughly 0.8x0.8 μm^2 by optical lithography on two tiny islands of trilayer deposited on the aluminum groundplane. The junction current density is about 15 kA/cm^2. A microphotograph of the junction area of the mixer chips is shown in Fig. 5. These photographs also show the two different thicknesses of the sputtered SiO_2 dielectric layer that were used in the design. In order to realize line impedances of 15-25 Ω with acceptable linewidth (losses) for the antenna feed circuit, 800 nm SiO_2 was used. In contrast, for the radial stub dc-blocks at the slots and for the tuning inductor between the junctions 400 nm SiO_2 was used to realise a low impedance level. This thickness of the dielectric layer results naturally from the crossline-process because about 200nm of SiO_2 are needed for each of the two RIE and liftoff steps.

The receiver cryostat is a standard liquid helium bath type (IR-labs HD3-8). The measurements reported here were done at a mixer block temperature of 4.2 K. The cryostat's atmospheric window is made of 100 μm mylar foil. IR filtering is done by means of a crystalline quartz plate with polyethylene antireflection coating on both sides at 77 K and a resonant fluorogold foil at 4.2 K. The cooled IF section consists of a 3 stage 2 - 4 GHz HEMT amplifier developed at MPIfR; no IF transformer between mixer output and amplifier was used.

During first laboratory tests of the receiver in 1995, a DSB receiver noise temperature of 850 K without any correction for losses had been obtained at a single frequency of 803 GHz using a stabilized FIR laser with $^{15}NH_3$ isotope gas as local oscillator [12]. From subsequent measurements of the receiver bandpass shown in Fig. 6 using a Martin-Puplett interferometer [13], good heterodyne performance could be expected for the entire atmospheric window. When a solid state local oscillator system for the frequency range 795 - 875 GHz got available, we set up a tunable telescope system. The LO system consists of an InP Gunn-oscillator followed by a doubler and tripler stage [14]. A 15 μm mylar beamsplitter couples the local oscillator power to the mixer, two ellipsoidal mirrors at ambient temperature are used to match the mixer beam to the telescope and to the dual-mode horn at the tripler output. Fig. 7 shows the DSB receiver noise temperatures achieved in the laboratory at 4.2 K bath temperature, no corrections for losses were made. The radiation temperatures of the loads at room and liquid nitrogen temperature were corrected according to the Callen and Welton formula [15].

The noise temperature of the IF chain including a cooled isolator was measured by means of a heated 50 Ω load to be12.5 K in a measurement bandwidth of 60 MHz centered at 3 GHz. From these results a conversion loss of ≈11 dB was estimated at 803 GHz. The single measurement included in the figure indicates a DSB noise temperature of 680 K achieved at 810 GHz at the HHT. A plot of the corresponding conversion curves and the junction's IV-curve is given in Fig. 8. The improved sensitivity is attributed to the replacement of the cooled IF amplifier prior to the observation run and to the lower bath temperature of about 3.85 K on the mountain.

During our ten day technical observing run at the HHT in January, an astronomical verification of the receiver's performance could be obtained. As an example Fig. 9 shows the average of 4 continuum subscans across Mars (scanning in azimuth). Deconvolved from the intrinsic size of the planet, a FWHP main beam width of $\Theta_{mb} \approx 9"$ was deduced from the measurements which corresponds to the telescope's diffraction limit. No evidence for side lobe or broad pedestal structure was found to a level of 10-13 dB from this and other measurements carried out. Heterodyne response is demonstrated in Fig. 10, showing the CO (7-6) transition detected towards the carbon rich circumstellar envelope IRC 10216. The integration time was 3 min only for this spectrum taken in rather poor atmospheric conditions ($\tau_{\text{line-of-sight}} \geq 3$).

Acknowledgements

We thank the staff of the workshop at MPIfR Bonn for careful machining of the mixerblock, and the staff of the junction laboratory at IRAM Grenoble for their support during our fabrication run at the junction laboratory. Part of this work was supported by Deutsche Agentur für Raumfahrt-Angelegenheiten (DARA) under contract FKZ 50 00 9102

References

[1] D.B. Rutledge, M. S. Muha, "Imaging Antenna Arrays", IEEE Trans. Antennas Prop., vol. 30, pp. 535-540, July 1982

[2] M. Wengler, D. P. Woody, R.E. Miller, T.G. Phillips, "A Low Noise Receiver for Millimeter and Submillimeter Wavelengths", Int. J. IR and MM Waves, vol. 6, pp. 697-706, 1985

[3] J. Zmuidzinas, H.G. LeDuc, "Quasi-Optical Slot Antenna SIS Mixers", IEEE Trans. MTT, vol. 40, pp1797-1804, Sept. 1992

[4] J. Zmuidzinas, N.G. Ugras, D. Miller, M. Gaidis, H.G. LeDuc, J.A. Stern, "Low-Noise Slot Antenna SIS Mixers", IEEE Trans. Appl. Supercond., vol. 5, pp.3053ff., 1995

[5] H. Aroudaki, T. Vaupel, V. Hansen, F. Schäfer, "Full-Wave Analysis of CPW Fed Slot Antennas for the Submillimeter Wave Region by the Spectral Domain Method", Prog. in Electromagnetic Research Symp. (PIERS), 1994, Nordwijk, Netherlands, Proc., pp. 1-4

[6] F. Schäfer, E. Kreysa, T. Lehnert, K. H. Gundlach, "A Planar SIS Receiver with Logperiodic Antenna for Submillimeter Wavelengths", Proc. 4th Intl. Symp. on Space Terahertz Technologie, 1993, Los Angeles, CA

[7] Duroid 6002, Rogers Corporation, Chandler, Arizona 85226, USA

[8] R.L. Kautz, "Miniaturization of Normal-State and Superconducting Striplines", J. Res. Natl. Bur. Stand., vol. 84, pp 247-259, 1979

[9] R.W. Keyes, E.P. Harris, K.L. Konnerth, "The Role of Low Temperatures in the Operation of Logic Circuitry", Proc. IEEE, vol. 58, pp. 1914-1932, 1970

[10] J. Zmuidzinas, H. G. LeDuc, J. A. Stern, S. R. Cypher, "Two-Junction Tuning Circuits for Submillimeter SIS Mixers", IEEE Trans. MTT, vol. 42, pp. 698-706, April 1994

[11] M. Voss, A. Karpov, K.H. Gundlach, "Submicron Nb-Aloxide-Nb Junctions for Frequency Mixers", Superconductor Science and Technol., vol. 6, pp.373ff, 1993

[12] F. Schäfer, J. Kuhnert, E. Kreysa, K.H. Gundlach, "A quasioptical SIS receiver for the 800-900 GHz band", Proc. of the 3rd Intl. Workshop on Terahertz Electronics, Sept. 1995, Zermatt, Switzerland

[13] J. Gromke, "Spektrale Kalibration von Radiometern im Submm Bereich mit Hilfe eines Martin-Puplett-Interferometers", diploma thesis, Universität Bonn, 1996

[14] Radiometer Physics GmbH, Bergerwiesenstrasse 15, D-53340 Meckenheim, Germany

[15] S.-K. Pan, A.R. Kerr, M.J. Feldman, A. Kleinsasser, J. Stasiak, R.L. Sandstrom, and W.J. Gallagher, "An 85-116 GHz SIS Receiver using Inductively Shunted Edge Junctions", IEEE Trans. MTT, vol. 37, pp. 580ff, 1989

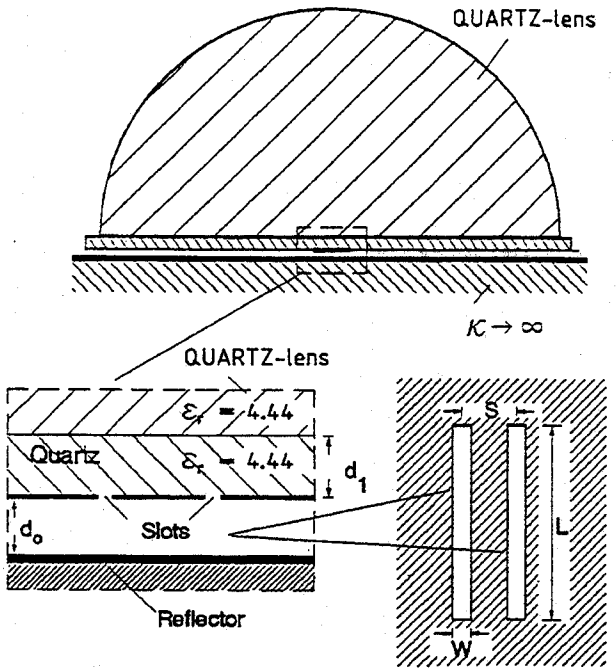

Figure 1: Schematic diagram of the antenna configuration

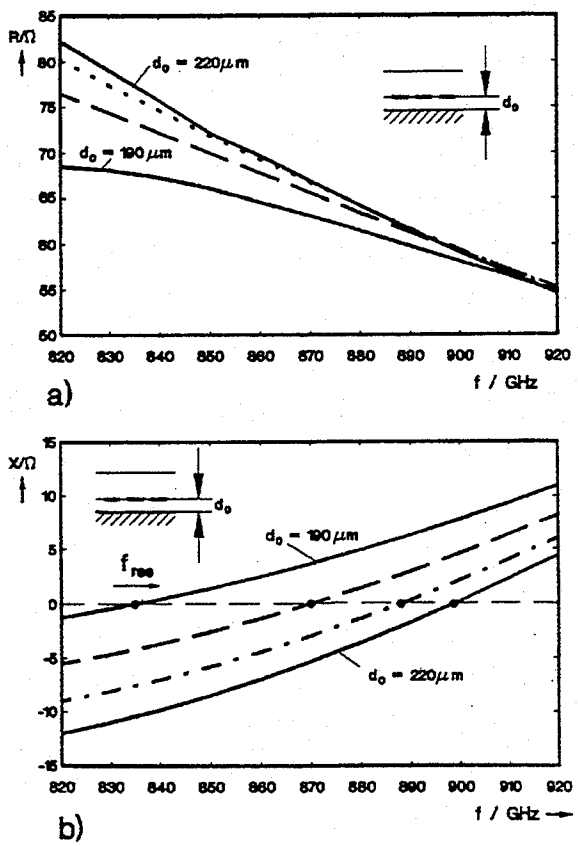

Figure 2: Single slot input impedance for a double slot antenna

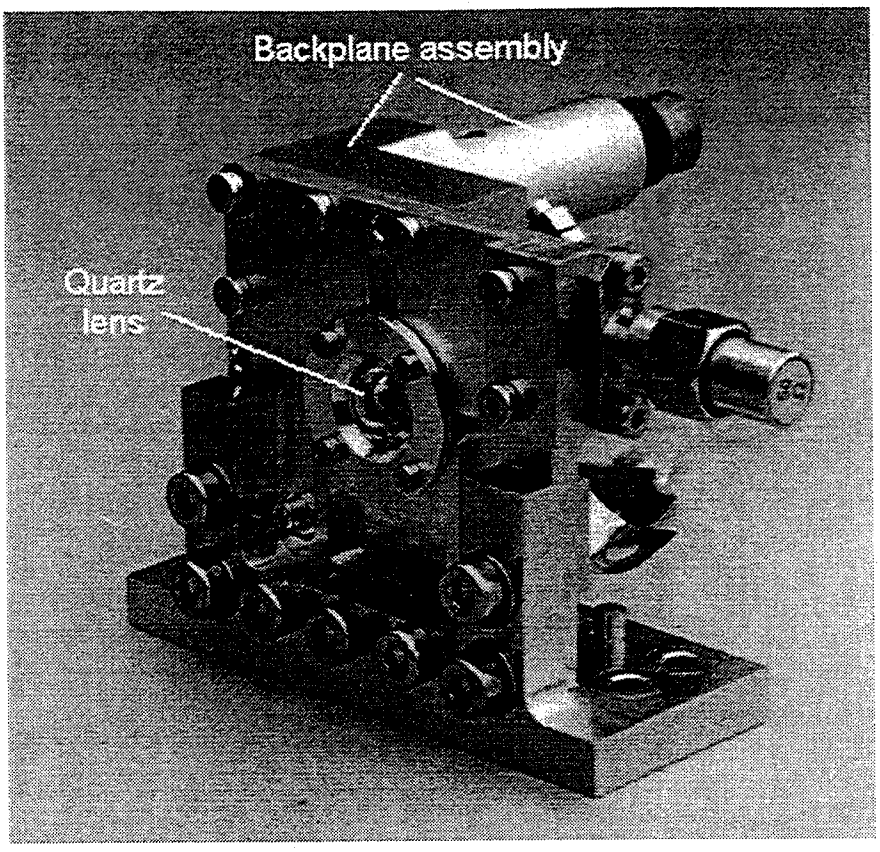

Figure 3: Photograph of the mixer block

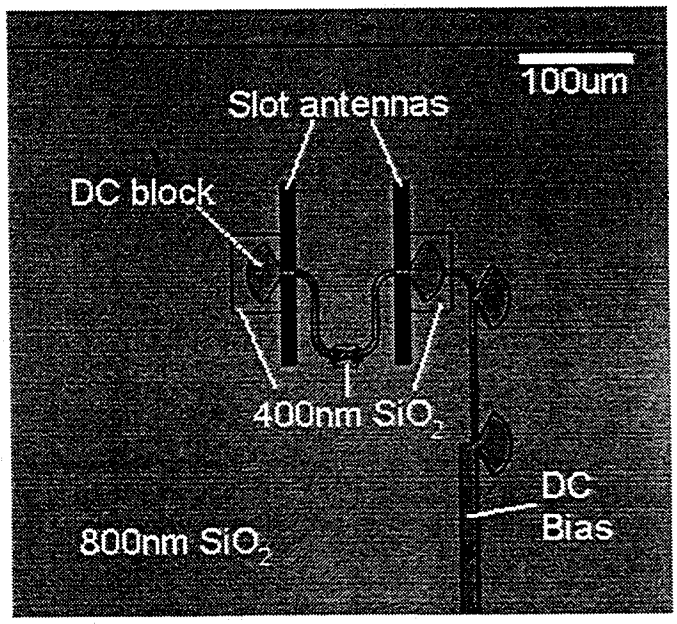

Figure 4: Mixer chip for 800-900 GHz

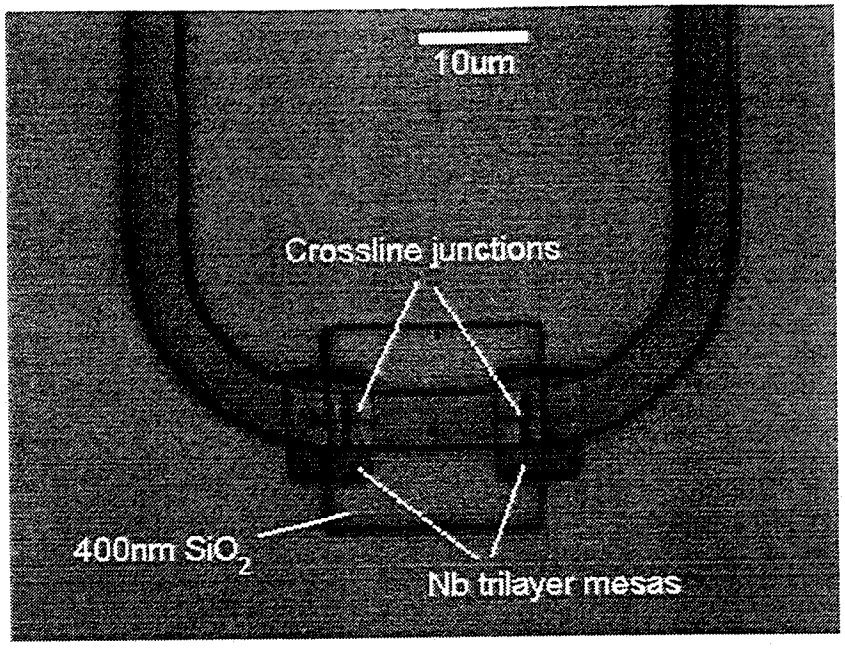

Figure 5: Junction area of the mixer chip

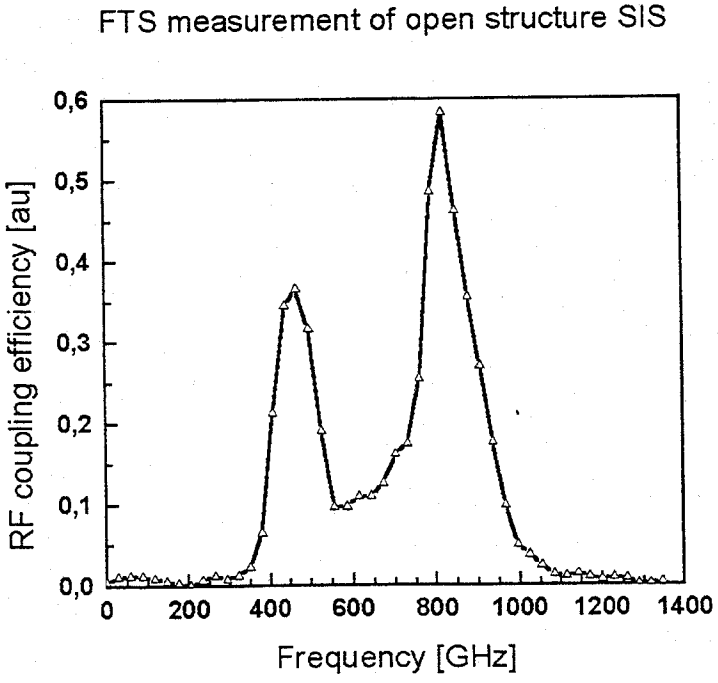

Figure 6: FTS measurement of receiver bandpass

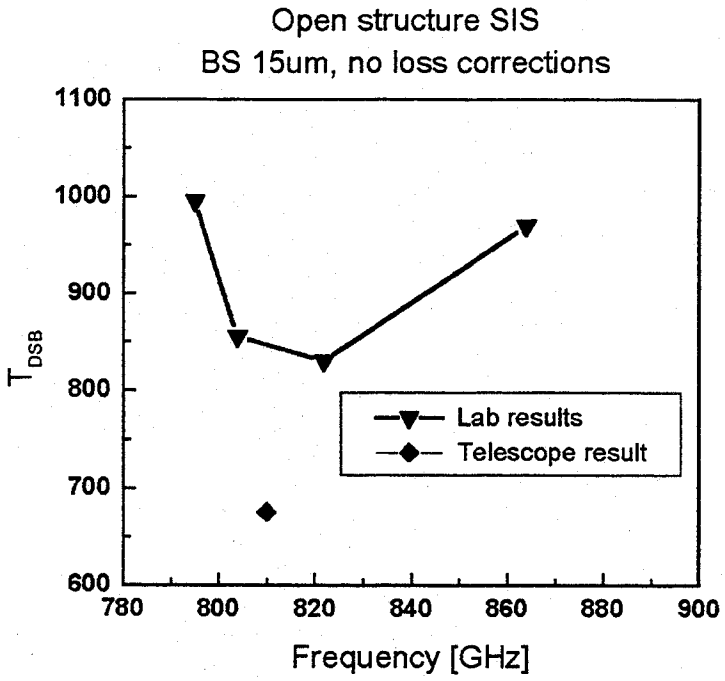

Figure 7: Receiver noise temperatures

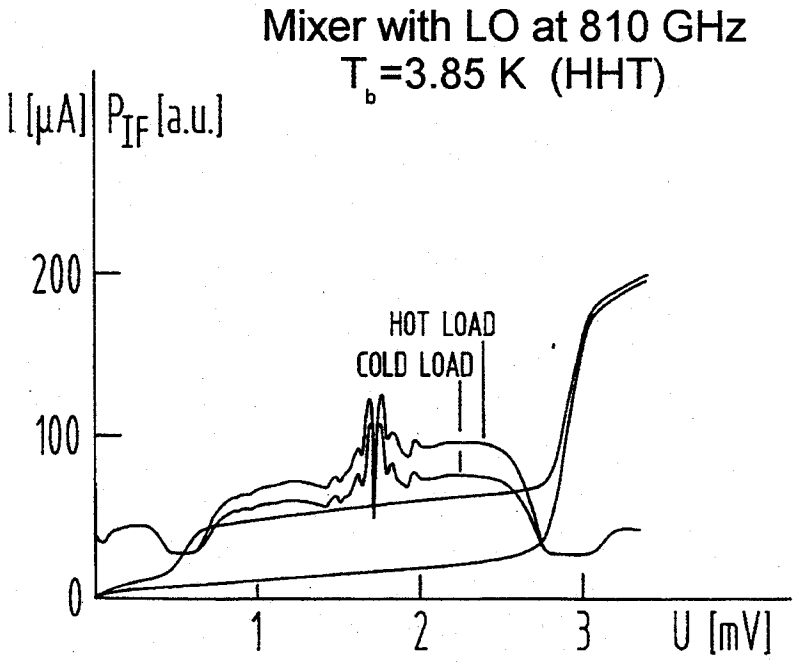

Figure 8: IV and conversion curves for telescope result

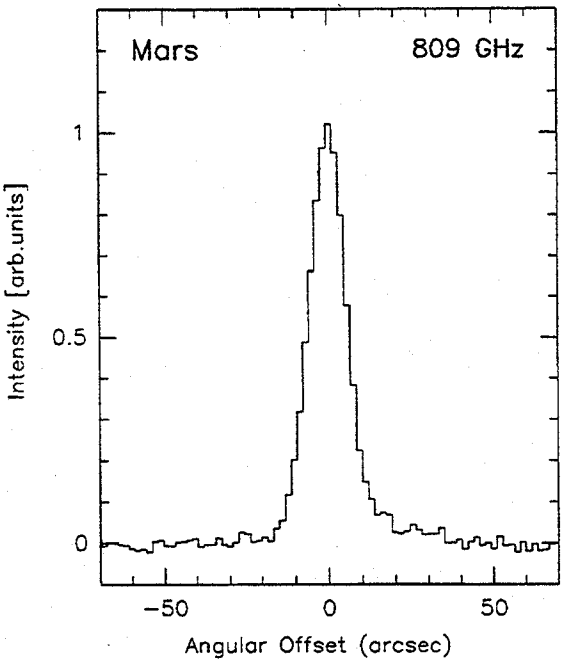

Figure 9: Continuum subscans in azimuth across Mars

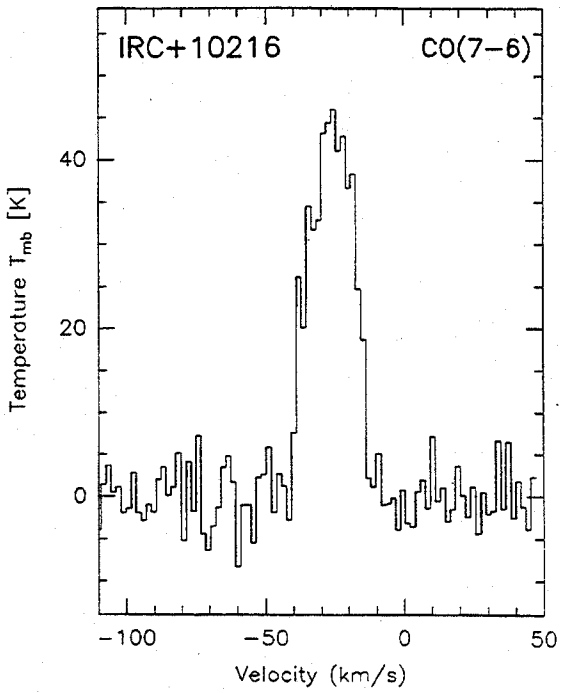

Figure 10: Spectrum of CO (7-6) towards IRC 10216

SIS JUNCTION AS A DIRECT DETECTOR AT 850 μm WAVELENGTH

A. Karpov, J. Blondel, M. Voss, K. H. Gundlach.

Institut de Radioastronomie Millimétrique,

300, rue de la Piscine, F-38406 St. Martin d'Héres, France

ABSTRACT

We have demonstrated the feasibility of a broad band SIS direct detector with a bandwidth up to 70 GHz around 330 GHz. The SIS detector responsivity approaches the quantum limit. The optical noise of 13 mK$\sqrt{s}$ measured with the new direct detector receiver is close to the noise of bolometer receiver developed for radioastronomy at the same wavelength. The SIS direct detector works at 4.5 K instead 0.1-0.3 K required for bolometer receiver.

INTRODUCTION

The cryogenics of a spacecraft submillimeter detector is important for lifetime of the instrument and the duration of a space telescope mission. The basic solution for the 850 μm wavelength channel of the FIRST mission is the 0.1 K He3 cooled semiconductor bolometers.

The direct detection of radiation at millimeter and submillimeter wavelengths via quantum assisted tunneling in a quasiparticle tunnel junction gives an attractive alternative to detection using low-temperature bolometers. A possibility to use a Superconductor - Insulator - Superconductor (SIS) junction as a low noise detector in radioastronomy was discussed since mid-eighties [1].

Only a few experiments have been dedicated to the direct detection in SIS junctions of the mm [2] and submm [3] radiation. Apparently the noise achieved with SIS detectors does not allow one to built an instrument competitive with broad band bolometer receivers used in radioastronomy. Recently we presented a SIS direct detector receiver [4] at $\lambda \approx 850$ μm with the optical noise only 4 - 5 time larger than with a bolometer detector [5]. Below we describe the experiment with SIS detector achieving the same noise as bolometer receiver. The

detector with a Nb/AlOx/Nb junction works at 4.5 K instead 100-300 mK required for bolometer.

SIS DETECTOR

The SIS detector comprises a Nb circuit printed on a 0.1 mm thick quartz substrate with two SIS junctions and a detector block. The sketch of the waveguide detector block is presented in the figure 1. It is a single backshort block with a reduced height 0.78×0.1 mm waveguide. The transition to the 0.78×0.39 mm waveguide is prepared according to [6]. The printed circuit of the mixer is optimized for the individual junction normal resistance of about 25 Ohm and $R_N\omega C \approx 6$.

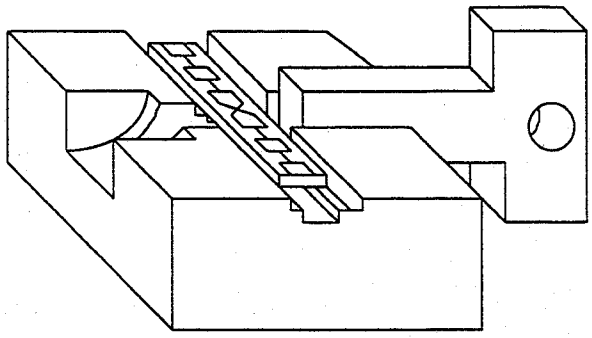

Figure 1. A half of the SIS detector block, the backshort and a quartz substrate with the SIS junctions.

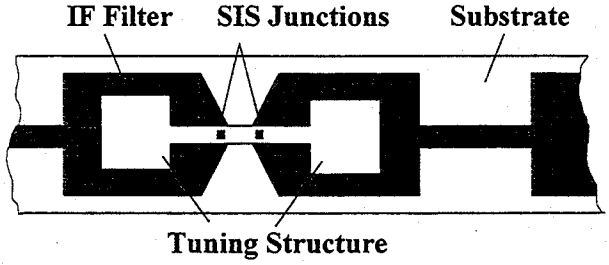

Figure 2. The SIS junctions with individual tuning structure. An L-C microstrip circuit is used to compensate for the junction capacity.

We developed a matching circuit and optimized the SIS detector circuit with the aim to get about 100 GHz effective band of detector operation around 340 GHz [7]. Out of this band the intrinsic capacitance of the junction provides a good rejection of the signal without additional filters normally used with bolometer detectors.

Two Nb-Aloxide-Nb SIS junctions 0.9 μm^2 each with a normal resistance of 30 Ohm are connected in series in the detector circuit. The leacage current at 4 mV is 2.8 μA. The inductive microstrip LC tuning circuit is connected to each of the junctions as a part of interconnection layer in the junction fabrication process (Figure 2). The microstrip is 27 μm long and 4 μm wide. The dielectric layer is in SiO_2 200 nm thick. The DC block capacitance is about 0.4 pF.

EXPERIMENT

The SIS detector responsivity is measured in experiment with a shopper switching the beam of the detector between two black bodies at the different temperatures - an ambient temperature load and a nitrogen cooled load. The variation of the source temperature in this experiment is about 215 K. The switching frequency is 10 Hz. A Ithaco lock-in amplifier is used for the measurement of detected current and of the rms of current fluctuations (optical noise). The optical noise comprises the contributions of the detector, amplifier, receiver optics and parasitics. The optical noise is measured only with the ambient temperature load in front of receiver to avoid the instabilities of nitrogen cooled load.

The same installation is used for detection of a weak monochromatic signal at 330 GHz. In this experiment the detector beam is switched between the ambient temperature black body and a 330 GHz signal source with the power of about $2\ 10^{-10}$ W. The position of the backshort in detector block is adjusted with the aim to get the best responsivity around 330 GHz.

The measured variation of SIS junction current versus bias voltage is presented in Figure 3. The quantum step produced by the 330 GHz signal is presented by a dashed line with + points and the step produced by the broad band black body radiation is presented by a solid line with the ◊ points. The amplitude of the 330 GHz signal is adjusted to get the same maximum detected current of 61 nA as in experiment with the black body.

The measured detected current corresponds to effective bandwidth of the detector of about 70 GHz taking into account the 17 % loss in the detector optics. This band is close to the model prediction and is largely sufficient for the application in radioastronomy. The optical noise of 13 $mK\sqrt{s}$ measured with the new direct detector receiver is close to 15 $mK\sqrt{s}$ noise of the bolometer receiver developed for radioastronomy at the same wavelength [4]. The SIS direct detector works at 4.5 K instead 0.1-0.3 K required for bolometer receiver.

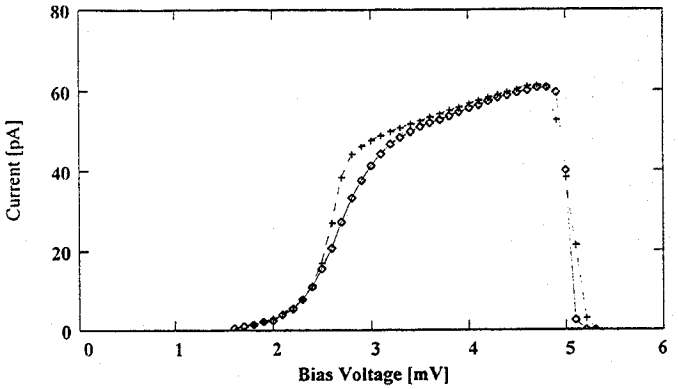

Figure 3. The measured current variation versus bias voltage for a two Nb-Al oxide-Nb junction array. The quantum step with 330 GHz signal (dashed line with +) and with black body radiation (solid line with ◊).

REFERENCES

[1] S. Weinreb, NRAO internal note, September 26 (1986).

[2] H. J. Haffus and K. H. Gundlach, *Int. J. Infrared and Millimeter Waves*, **2**, 809 (1981).

[3] J. D. Prince, B. S. Deaver Jr and S. Withington, *IEEE Trans. on Appl. Superconductivity*, **3**, 1, 2257 (1993).

[4] A. Karpov *et al*, *Applied Superconductivity,* ed. D. Dew-Hughes, UK, (1995), **2**, 1741 (1995).

[5] E. Kreysa *et al*, Memo Nr 72 MPI fur Radioastronomie Div. Millimeter-Technology, (1991).

[6] P. H. Siegel, D. W. Peterson, and A. R. Kerr, *IEEE Tr. Microwave Theory and Techniques*, **MTT-31**, 6, 473 (1983).

[7] A. Karpov *et al*, *IEEE Trans. Appl. Superconductivity*, **5**, 2, 3304 (1995).

Eighth International Symposium on Space Terahertz Technology

Authors and Registered Participants

Juha Ala-Laurinaho
HUT Radio Laboratory
PO BOX 3000
Otakaari 5A, 02015 HUT
FINLAND

Dr. Michael Balister
National Radio Astronomy Observatory
Charlottesville, VA 22903

Dominic J. Benford
Caltech Submillimeter Observatory
Div. of Physics, Mathematics & Astronomy
MS 320-47
Pasadena, CA 91125
DBENFORD@TACOS.CALTECH.EDU

Albert Betz
University of Colorado
CASA/ARL, CB593
Boulder, CO 80309-0593
betz@spot.colorado.edu

William L. Bishop
University of Virginia
Department of Electrical Engineering
Semiconductor Device Laboratory
Charlottesville, VA 22903
wlb@virginia.edu

Raymond Blundell
Harvard-Smithsonian Ctr. for Astrophysics
60 Garden St.
MS 42
Cambridge, MA 02138
rblundell@cfa.harvard.edu

Olga Boric-Lubecke
Jet Propulsion Laboratory
4800 Oak Grove Dr.
MS 306-451
Pasadena, CA 91106

Dr. Richard F. Bradley
National Radio Astronomy Observatory
2015 Ivy Rd.
Suite 219
Charlottesville, VA 22903-1733
rbradley@nrao.edu

Mz. Brugidou
DEMIRM - Observatoire de Paris
61, avenue de l'Observatoire
75014 Paris
FRANCE

E. Bründermann
DLR, Institute for Space Sensor Technology
Rudower Chaussee 5
D-12489 Berlin
GERMANY
ws2t@arzvsl.rz.ba.dlr.de

Jean Bruston
Jet Propulsion Laboratory
4800 Oak Grove Dr.
MS 168-314
Pasadena, CA 91109-8099
bruston@arthur.jpl.nasa.gov

Peter J. Burke
California Institute of Technology
Pasadena, CA 91125
pjburke@cco.caltech.edu

Dr. Michael J. Burns
Jet Propulsion Laboratory
4800 Oak Grove Dr.
MS 302-306
Pasadena, CA 91109-8099
mburns@vaxeb.jpl.nasa.gov

Goutam Chattopadhyay
California Institute of Technology
G.W. Downs Lab of Physics
MS 320-47
Pasadena, CA 91125

Ming-Tang Chen
Institute of Astronomy & Astrophysics
Academia Sinica, IAA
Nankang, P.O. Box 1-87
Taipei 115
TAIWAN
mchen@biaa.sinica.edu.tw

Chi-Chung Chin
Institute of Astronomy & Astrophysics
Academia Sinica, IAA
Nankang, P.O. Box 1-87
Taipei 115
TAIWAN
chin@biaa.sinica.edu.tw

Larry Chu
Sanders, Lockheed Martin
PO Box 868, NHQI-423
Nashua, NH 03061

Tah-Hsiung Chu
Institute of Astronomy & Astrophysics
Academia Sinica, IAA
Nankang, P.O. Box 1-87
Taipei 115
TAIWAN
thc@ew.ee.ntu.edu.tw

Dr. Stephane Claude
Herzberg Institute of Astrophysics
5071 W. Saanich Rd.
Victoria, BC V8X 4M6
CANADA
stephane.claude@nrc.ca

Dr. Thomas W. Crowe
University of Virginia
Department of Electrical Engineering
Semiconductor Device Laboratory
Charlottesville, VA 22902
twc8u@virginia.edu

Gerhard de Lange
Massachusetts Institute of Technology
Research Laboratory of Electronics
77 Massachusetts Ave., Room 36-491
Cambridge, MA 02139
gert@mit.edu

James DeLap
Millitech Corporation
South Deerfield Research Park
South Deerfield, MA 01373
jdelap@millitech.com

Yan Delorme
DEMIRM - Observatoire de Paris
61, avenue de l'Observatoire
75014 Paris
FRANCE
delorme@etoile.obspm.fr

Guy DeMartinis
63 Oak Ridge Road
Reading, MA 01867

Rolf Densing
DLR/DARA
Washington Office
1627 I Street
Washington, DC
rd@dlrdara.org

Pieter Dieleman
University of Groningen
Dept. of Applied Physics
Nijenborgh 4
9747 AG Groningen
NETHERLANDS
dieleman@phys.rug.nl

James Duan
University of Virginia
Department of Electrical Engineering
Semiconductor Device Laboratory
Charlottesville, VA 22903
zd3g@virginia.edu

O. D. Dubon
University of California at Berkeley
Lawrence Berkeley National Laboratory
Berkeley, CA 94720

Jack East
2301 EECS Building
The University of Michigan
Ann Arbor, MI 48109
jeast@eecs.umich.edu

H. Ekström
Saab Ericsson Space AB
S-405 15 Göteborg
SWEDEN
hans.ekstrom@space.se

Neal R. Erickson
Millitech Corporation
P.O. Box 109
S. Deerfield, MA 01373
neal@fcrao1.phast.umass.edu

Khurram Farooqui
Brown University
Department of Physics
Box 1843
Providence, RI 02912
farooqui@het.brown.edu

Roland Feinäugle
German Aerospace Research Establishment
Institute of Space Sensor Technology
Rudower Chaussee 5
D-12489 Berlin
GERMANY
Roland.Feinaeugle@dlr.de

Marc J. Feldman
University of Rochester
Electrical Engineering Dept.
Hopeman Hall
Rochester, NY 14627-0011
feldman@ee.rochester.edu

Israel Galin
GENCORP-Aerojet
Electronic Systems Div., Dept. 8833
100 W. Hollyvale St.
Azusa, CA 91702
galin@ms1.aes.com

J. R. Gao
Space Research Organization
of The Netherlands
P.O. Box 800
9700 AV Groningen
NETHERLANDS
gao@phys.rug.nl

Eyal Gerecht
University of Massachusetts at Amherst
Dept. of Electrical & Computer Engineering
Amherst, MA 01003
gerecht@kira.ecs.umass.edu

Mikhail Gershteyn
Insight Product Co.
P.O. Box 297
Brighton, MA 02135

Bob Giles
UMass - Lowell
Submillimeter Wave Tech. Lab
175 Cabot St.
Lowell, MA 01854

Professor Gregory N. Gol'tsman
Moscow State Pedagogical University
Department of Physics
29 M. Pirogovskaya Str.
119435 Moscow
RUSSIA
goltsman@rpl.mpgu.msk.su

Thomas Goyette
Submillimeter Technology Lab
175 Cabot Street
Lowell, MA 01854
TMG@mps.ohio-state.edu

Urs Graf
Universität zu Köln
I. Physikalisches Institut
Zülpicher Str. 77
D-50937 Köln
GERMANY

Rolf Güsten
Max-Planck Institut für Radioastronomie
Auf dem Hügel 69
53121 Bonn
GERMANY
p212gue@MPIFR-Bonn.MPG.de

Robert Haas
TRW
1 Space Park
MS 1017/E
Redondo Beach, CA 90278
r_haas@qmail4.sp.trw.com

Sybille Haas
Universität zu Köln
I. Physikalisches Institut
Zülpicher Str. 77
D-50937 Köln
GERMANY
haas@ph1.uni-koeln.de

Eugene E. Haller
University of California at Berkeley
Lawrence Berkeley National Laboratory
553 Evans Hall
Berkeley, CA 94720
eehaller@mh1.lbl.gov

Oliver Harnack
Institut für Schicht- und Ionentechnik
Forschungszentrum Jülich GmbH
D-52425 Jülich
GERMANY
harnack@dresden.isi.kfa-juelich.de

Harald Hauschildt
California Institute of Technology
G.W. Downs Lab of Physics
MS 320-47
Pasadena, CA 91125

Gregory S. Herman
NASA LaRC
MS-468
Hampton, VA 23681-0001
g.s.herman@express.larc.nasa.gov

Jeffrey L. Hesler
University of Virginia
Department of Electrical Engineering
Semiconductor Device Laboratory
Charlottesville, VA 22903
jlh6r@virginia.edu

Tavi Hirvonen
Helsinki University of Technology
Radio Laboratory
Otakaari 5A
FIN-02150 Espoo
FINLAND
thi@radio.hut.fi

C. E. Honingh
Universität zu Köln
I. Physikalisches Institut
Zülpicher Str. 77
D-50937 Köln
GERMANY
honingh@ph1.uni-koeln.de

Qing Hu
MIT/MS 36-465
Research Laboratory of Electronics
Cambridge, MA 02139

Shu-I. Hu
Institute of Astronomy & Astrophysics
Academia Sinica, IAA
Nankang, P.O. Box 1-87
Taipei 115
TAIWAN

Kai Hui
University of Virginia
Department of Electrical Engineering
Semiconductor Device Laboratory
Charlottesville, VA 22903
kh2r@virginia.edu

Aimee Hungerford
Steward Observatory
933 North Cherry Avenue
University of Arizona
Tucson, AZ 85721

T. R. Hunter
Harvard-Smithsonian Ctr. for Astrophysics
60 Garden St.
MS 78
Cambridge, MA 02138
thunter@cfa.harvard.edu

Yuh-Jing Hwang
Institute of Astronomy & Astrophysics
Academia Sinica, IAA
Nankang, P.O. Box 1-87
Taipei 115
TAIWAN
yjhwang@biaa3.biaa.sinica.edu.tw

Professor Junji Inatani
Nobeyama Radio Observatory
Nobeyama
Minamisaku
Nagano 384-13
JAPAN
inatani.junji@nasda.go.jp

Kate Isaak
University of Maryland
Department of Astronomy
College Park, MD 20742-2421

Eric Jacobs
UMass Lowell Research Foundation
Submillimeter Technology Lab
175 Cabot Street
Lowell, MA 01854

K. Jacobs
University of Cologne
I. Physikalisches Institut
Zülpicher Strasse 77
50937 Köln
GERMANY

Dr. Stephen H. Jones
University of Virginia
Department of Electrical Engineering
Semiconductor Device Laboratory
Charlottesville, VA 22903
shj2n@virginia.edu

Boris S. Karasik
Jet Propulsion Laboratory
4800 Oak Grove Dr.
MS 168-314
Pasadena, CA 91109-8099
karasik@kbs-mac.jpl.nasa.gov

Alexandre Karpov
Institut de Radioastronomie Millimetrique
300, rue de la Piscine
F-38406 St. Martin d'Heres
FRANCE
karpov@iram.fr

Christoph Kasemann
Max-Planck Institut für Radioastronomie
Auf dem Hügel 69
D-53121 Bonn
GERMANY
ckasemann@mpifr-bonn.de

Akira Kawakami
Kansai Advanced Research Center
Com Rsrch Lab, Ministry of Posts & Telecom.
588-2 Iwaoka, Iwaoka-cho, Nishi-ku
Kobe 651-24
JAPAN
kawakami@crl.go.jp

Jonathan Kawamura
Caltech 320-4T
Pasadena, CA 91125
kawamura@socrates.patnet.caltech.edu

Dr. A. R. Kerr
National Radio Astonomy Observatory
2015 Ivy Rd
Suite 219
Charlottesville, VA 22903
akerr@nrao.edu

Robert Kimberk
Harvard-Smithsonian Ctr. for Astrophysics
60 Garden St.
MS-75
Cambridge, MA 02138
rkimberk@cfa.harvard.edu

Thomas Klein
Max-Planck Institut für Radioastronomie
Auf dem Hügel 69
D-53121 Bonn
GERMANY
tklein@mpifr-bonn.de

Henry Knoepfle
Steward Observatory
933 North Cherry Avenue
University of Arizona
Tucson, AZ 85721
henry@as.arizona.edu

Phil J. Koh
University of Virginia
Semiconductor Device Laboratory
Department of Electrical Engineering
Charlottesville, VA 22903
pjk7u@virginia.edu

Erik Kollberg
Chalmers University of Technology
Ranvage 6
S-412 96 Göteborg
SWEDEN
kollberg@ep.chalmers.se

Konstantinos Konistis
550 Memorial Drive, Apt #1184
Cambridge, MA 02139

Jacob W. Kooi
CalTech - Downs Labs
1200 E. California Blvd.
MS-320-47
Pasadena, CA 91125
kooi@tacos.caltech.edu

Alexay Kozhevnikov
Yale University
217 Prospect St.
New Haven, CT 06511

Carl Kukkonen
Jet Propulsion Laboratory
4800 Oak Grove Dr.
MS 180-604
Pasadena, CA 91109-8099

David Kurtz
University of Virginia
Semiconductor Device Laboratory
Department of Electrical Engineering
Charlottesville, VA 22903
dsk7u@virginia.edu

H. G. LeDuc
Jet Propulsion Laboratory
California Institute of Technology
Ctr for Space Microelectronics Technology
Pasadena, CA 91109
Henry.G.LeDuc@cc2mhb.jpl.nasa.gov

Tracy Lee
Jet Propulsion Laboratory
4800 Oak Grove Dr.
MS 168-314
Pasadena, CA 91109-8099
thlee@serpent.jpl.nasa.gov

C.I. Lin
Lehrstuhl fur Hochfrequenztechnik
Universitat Erlangen-Nurnberg
Cauerstr. 9
D-91958 Erlangen
GERMANY

Victor Lubecke
Riken Photodynamics Research Center
19-1399 Koeji Nagamachi
Aoba-ku, Sendai 980
JAPAN

Willem Luinge
Space Research Center
of The Netherlands
P.O. Box 800
9700 AG Groningen
NETHERLANDS

P. J. I. de Maagt
European Space Agency ESTEC
P.O. Box 299
2200 AG Noordwijk
NETHERLANDS

C. M. Mann
Rutherford Appleton Laboratory
Chilton, Didcot OX1 10QX
U.K.
C.M.Mann@RL.AC.UK

Steve M. Marazita
University of Virginia
Department of Electrical Engineering
Semiconductor Device Laboratory
Charlottesville, VA 22903
smm7k@virginia.edu

Harunobu Masuko
Millimeter Wave Remote Sensing Section
Global Environment Div., Com. Rsrch Lab
4-2-1 Nukui-kita-machi, Koganei
Tokyo 184
JAPAN

W. R. McGrath
Jet Propulstion Laboratory
California Institute of Technology
Ctr for Space Microelectronics Technology
Pasadena, CA 91109
rob@rob-mac.jpl.nasa.gov

Alex McIntosh
MIT Lincoln Laboratory
244 Wood Street
Lexington, MA 02173

I. Mehdi
Jet Propulsion Laboratory
4800 Oak Grove Dr.
MS 168-314
Pasadena, CA 91109-8099
imran@merlin.jpl.nasa.gov

Karl M. Menten
Max-Planck Instute für Radioastronomie
Auf dem Hügel 69
53121 Bonn
GERMANY
kmenten@mpifr_bonn.mpg.de

Dr. James Moran
Harvard-Smithsonian Ctr. for Astrophysics
60 Garden St.
MS-42
Cambridge, MA 02138
jmoran@cfa.harvard.edu

Ville Möttönen
Helsinki University of Technology
Radio Laboratory
Otakaari 5A
FIN-02150 Espoo
FINLAND
vmo@radio.hut.fi

Eric R. Mueller
DeMaria ElectroOptics Systems, Inc.
1280 Blue Hills Ave.
Bloomfield, CT 06002
deos@snet.net

Dr. J. Anthony Murphy
St. Patricks College
Experimental Physics Dept.
Maynooth
Co. Kildare
IRELAND
amurphy@ailm.may.ie

Gopal Narayanan
Steward Observatory
University of Arizona
Tucson, AZ 85721

Petri Piironen
HUT Radio Laboratory
PO BOX 3000
Otakaari 5A, 02015 HUT
FINLAND

Scott Paine
Harvard-Smithsonian Ctr. for Astrophysics
60 Garden St.
MS 78
Cambridge, MA 02138
spaine@cfa.harvard.edu

David Porterfield
University of Virginia
Department of Electrical Engineering
Semiconductor Device Laboratory
Charlottesville, VA 22903
dwp8j@virginia.edu

Dr. Shing-Kuo Pan
National Radio Astronomy Observatory
2015 Ivy Rd.
Suite 219
Charlottesville, VA 22903
span2@polaris.cv.nrao.edu

Daniel E. Prober
Yale University
Department of Applied Physics
Box 208284
New Haven, CT 06520-8482
daniel.prober@yale.edu

D. C. Papa
Harvard-Smithsonian Ctr. for Astrophysics
60 Garden St.
MS 75
Cambridge, MA 02138
cpapa@cfa.harvard.edu

Prof. Antti Räisänen
Helsinki University of Technology
Radio Laboratory
Otakaar 5A
FIN-02150 Espoo
FINLAND
ara@radio.hut.fi

Nagini Paravastu
University of Virginia
Department of Electrical Engineering
Semiconductor Device Laboratory
Charlottesville, VA 22903
np4e@virginia.edu

Jacques Renaud
Harvard-Smithsonian Ctr. for Astrophysics
60 Garden St.
MS-75
Cambridge, MA 02138
jrenaud@cfa.harvard.edu

Jeffrey B. Peterson
Carnegie Mellon University
Department of Physics
Pittsburgh, PA 15213
jbp@cmu.edu

Lance Riley
Jet Propulsion Laboratory
4800 Oak Grove Dr.
MS 168-314
Pasadena, CA 91109

Eric Phipps
University of Virginia
Department of Electrical Engineering
Semiconductor Device Laboratory
Charlottesville, VA 22903
esp5c@virginia.edu

Stephen P. Sandford
NASA/LARC
Bldg. 1202, Room 243
Hampton, VA 23681

Ben Sarpong
University of Virginia
Department of Electrical Engineering
Semiconductor Device Laboratory
Charlottesville, VA 22903
bks8v@virginia.edu

Pat Schaffer
CalTech - Downs Labs
1200 E. California Blvd.
MS 320-47
Pasadena, CA 91125

Dr. Rudolf Schieder
Universität zu Köln
I. Physikalisches Institut
Zülpicher Str. 77
D-50937 Köln
GERMANY
schieder@ph1.uni-koeln.de

R. J. Schoelkopf
Yale University
Department of Applied Physics
429 Becton Center, 15 Prospect St.
New Haven, CT 06520-8482
ROB_SCHOELKOPF@quickmail.yale.edu

Dr. Karl-Friedrich Schuster
Institut de Radioastronomie Millimetrique
300, rue de la Piscine
F-38406 St. Martin d'Heres
FRANCE
schuster@iram.fr

Alex D. Semenov
Universität Regensburg
Institut für Physik III, Angewandte Physik
Universitätstrasse 31
93040 Regensburg
GERMANY
alex.semenov@physik.uni-regensburg.de

Dr. Sheng-Cai Shi
Nobeyama Radio Observatory
Nobeyama
Minamisaku
Nagano 384-13
JAPAN
shencai@nro.nao.ac.jp

Hisashi Shimakage
Kansai Advanced Research Center
Com Rsrch Lab, Ministry of Posts & Telecom.
588-2 Iwaoka, Iwaoka-cho, Nishi-ku
Kobe 651-24
JAPAN
shimakage@crl.go.jp

Sergey V. Shitov
Institute of Radio Engineering & Electronics
Russian Academy of Sciences
Mokhovaya 11
Moscow 103907
RUSSIA
s.v.shitov@sron.rug.nl

Dr. Ansgar Simon
Institut für Hochfrequenztechnik
Technische Hochschüle Darmstadt
Merckstr. 25
D-64283 Darmstadt
GERMANY
hfmwe015@HRZ2.HRZ.TU-Darmstadt.de

Anders Skalare
Jet Propulsion Laboratory
4800 Oak Grove Dr.
MS 168-314
Pasadena, CA 91109-8099
anders@lolita.jpl.nasa.gov

Michael Smith
Harvard-Smithsonian Ctr. for Astrophysics
60 Garden St.
MS-75
Cambridge, MA 02138
msmith@cfa.harvard.edu

R. Peter Smith
Jet Propulsion Laboratory
4800 Oak Grove Dr.
MS 302-306
Pasadena, CA 91109-8099
r.peter.smith@jpl.nasa.gov

Jan Stake
University of Virginia
Department of Electrical Engineering
Semiconductor Device Laboratory
Charlottesville, VA 22903
js7sj@virginia.edu

Anthony Stark
Harvard-Smithsonian Ctr. for Astrophysics
60 Garden St.
MS 78
Cambridge, MA 02138
astark@cfa.harvard.edu

Jeffrey A. Stern
Jet Propulsion Laboratory
4800 Oak Grove Dr.
MS 302-306
Pasadena, CA 91109
jstern@vaxeb.jpl.nasa.gov

Brian Thomas
University of Virginia
Department of Electrical Engineering
Semiconductor Device Laboratory
Charlottesville, VA 22903
bwt2q@virginia.edu

Volker Tolls
Harvard-Smithsonian Ctr. for Astrophysics
60 Garden St.
MS-66
Cambridge, MA 02138
vtolls@cfa.harvard.edu

C.-Y. E. Tong
Harvard-Smithsonian Ctr. for Astrophysics
60 Garden St.
MS 42
Cambridge, MA 02138
etong@cfa.harvard.edu

Eugene Tsiang
Smithsonian Astrophysical Observatory
60 Garden Street, MS 78
Cambridge, MA 02138
etsiang@cfa.harvard.edu

Yoshinori Uzawa
Kansai Advanced Research Center
Com Rsrch Lab, Ministry of Posts & Telecom.
588-2 Iwaoka, Iwaoka-cho, Nishi-ku
Kobe 651-24
JAPAN
uzawa@crl.go.jp

Simon Verghese
Massachusetts Institute of Technology
Lincoln Laboratory
Lexington, MA 02173-9108
simonv@ll.mit.edu

Christopher K. Walker
University of Arizona
Steward Observatory
Tuscon, AZ 85721
cwalker@as.arizona.edu

Zhen Wang
Kansai Advanced Research Center
Com Rsrch Lab, Ministry of Posts & Telecom.
588-2 Iwaoka, Iwaoka-cho, Nishi-ku
Kobe 651-24
JAPAN
wang@crl.go.jp

Sander Weinreb
Department of Astronomy
Graduate Research Center
University of Massachusetts
Amherst, MA 01003

Robert Wilson
Harvard-Smithsonian Ctr. for Astrophysics
60 Garden St.
MS 42
Cambridge, MA 02138
rwilson@cfa.harvard.edu

Stafford Withington
Cavendish Laboratory
Radio Astronomy Group
Madingley Road
Cambridge CB3 OHE
U.K.
stafford@mrao.cam.ac.uk

Perry Wood
University of Virginia
Department of Electrical Engineering
Semiconductor Device Laboratory
Charlottesville, VA 22903
paw7w@virginia.edu

Dave Woody
California Institute of Technology
Div of Physics, Mathematics & Astronomy
Caltech Submillimeter Observatory
Pasadena, CA 91125
dpw@mm.ovro.caltech.edu

Dr. Ghassan Yassin
Cavendish Laboratory
Radio Astronomy Group
Madingley Road
Cambridge CB3 OHE
U.K.
ghassan@mrao.cam.ac.uk

Tao Ye
University of Virginia
Department of Electrical Engineering
Semiconductor Device Laboratory
Charlottesville, VA 22903
ty2k@virginia.edu

Sigfrid Yngvesson
University of Massachusetts at Amherst
Dept. of Electrical & Computer Engineering
Box 35110
Amherst, MA 01003
yngvesson@ecs.umass.edu

Jonas Zmuidzinas
California Institute of Technology
G.W. Downs Lab of Physics
MS 320-47
Pasadena, CA 91125
jonas@ocat.patnet.caltech.edu